NOTICE

The quality of this microform is heavily dependent upon the quality of the original thesis submitted for microfilming. Every effort has been made to ensure the highest quality of reproduction possible.

If pages are missing, contact the university which granted the degree.

Some pages may have indistinct print especially if the original pages were typed with a poor typewriter ribbon or if the university sent us an inferior photocopy.

Reproduction in full or in part of this microform is governed by the Canadian Copyright Act, R.S.C. 1970, c. C-30, and subsequent amendments.

AVIS

La qualité de cette microforme dépend grandement de la qualité de la thèse soumise au microfilmage. Nous avons tout fait pour assurer une qualité supérieure de reproduction.

S'il manque des pages, veuillez communiquer avec l'université qui a conféré le grade

La qualité d'impression de certaines pages peut laisser a désirer, surtout si les pages originales ont été dactylographiées à l'aide d'un ruban usé ou si l'université nous a fait parvenir une photocopie de qualité inférieure

La reproduction, même partielle, de cette microforme est soumise à la Loi canadienne sur le droit d'auteur, SRC 1970, c. C-30, et ses amendements subséquents.

Guidance Control for Automatic Guided Vehicles Employing Binary Camera Vision

Ramesh Rajagopalan

A Thesis

in

The Department

of

Mechanical Engineering

Presented in Partial Fulfillment of the Requirements
for the Degree of Doctor of Philosophy at
Concordia University
Montreal, Quebec, Canada

September 1991

ISBN 0-315-68738-X

Canada

Guidance Control for Automatic Guided Vehicles

Employing Binary Camera Vision

Ramesh Rajagopalan

Abstract

This thesis presents guidance control schemes for a class of Automatic Guided Vehicles (AGVs) employing binary camera vision. These control schemes enable the AGV to follow a given track profile accurately. The accuracy in following tracks has been set based on the current industrial needs for assembly automation. For guidance, the binary camera is continuously focussed on an illuminated track provided on the floor prepared by taping or otherwise. An efficient image processing technique that is capable of identifying the track and recognizing a set of road signs is developed. The image processing scheme provides the instantaneous position and orientation of the longitudinal axis of the vehicle relative to the track and this information is used for guidance control.

This thesis presents three new approaches for guidance control of the vehicle to achieve track following. The first approach employs a camera at the front end of the vehicle. This assures accurate track following of a small section of the vehicle. The steering command is computed using the instantaneous position and orientation offsets of the longitudinal axis of the vehicle relative to the track. The second approach employs an additional camera at the rear end to provide accurate track following of the front and rear ends of the vehicle. In this scheme, the steering command is calculated using control laws that make use of the instantaneous position and

orientation offsets as measured by the front and rear sensors of the vehicle. This scheme employs control equations that are dependent on the presence of track curvature. Further, the choice of control equations is also dependent on the relative position of the front and rear ends of the vehicle with respect to the track. In addition to this, the gains of the control equations are changed in real-time depending on the relative position of the front and rear ends of the vehicle with respect to each other as well as the track. The third approach is a feed forward control scheme for accurate track following of any section of the vehicle as defined by a driving criterion. This is an intelligent method as the vehicle guidance is based on the identified geometry of the track in real-time. The geometry of the track is identified using the motion parameters available upto that instant. The driving criterion defines the positioning of the AGV body on the track, i.e. which section(s) of the AGV has to be on the track. The steering command is computed based on the predicted track profile ahead of the vehicle and the driving criterion.

A methodology to select a suitable wheelbase configuration and combinations of driving and steered wheels without redundancy for optimal kinematic control of AGVs is presented. A criterion is derived for this purpose by considering a generic kinematic model. A prototype AGV with a differential drive and a diamond shaped wheelbase configuration has been built for experimental study. Results of simulations and experiments indicate satisfactory performance.

ACKNOWLEDGEMENT

The author wishes to extend his sincere gratitude and thanks to Dr. R.M.H. Cheng for having rendered supervision, constructive criticism, moral and financial support during the course of this thesis work.

My thanks are to Mr. Gilles Huard for having designed the electronics of the prototype AGV and Mr. Wesley Fitch for his contributions in developing the mechanical structure of the vehicle. Mr. Simon Poon helped me with the development of the software shells for camera imaging and radio link. Ms. Min Huang provided dynamic modelling simulation package to perform simulation studies. Thanks to the staff of the Center for Industrial Control and the technical staff of the Department of Mechanical Engineering for their contributions in a variety of forms.

The author acknowledges the Natural Sciences and Engineering Research Council of Canada (NSERC) awarded to Dr. R.M.H. Cheng for developing an Ambidextrous Automatic Guided Vehicle (AGV) in the form of a strategic grant (grant no. STR0032709) for the period 1987-90. Thanks to the Graduate Awards Office of the Concordia University for the International Student Tuition Fee Remission awarded to me for the periods 1987-88 and 1989-90.

Finally, thanks are due to my wife Mrs. Jayashree for helping me out with this manuscript, and my parents, my brother Dr. Murali, and my uncle Mr. Sadagopan who are responsible for my studies in Canada.

TABLE OF CONTENTS

LIST OF FIGURES

LIST OF TABLES

LIST OF NOTATIONS

F	Floor or inertial frame
R	Reference frame attached to the AGV located at the geometric center 'O'
$\bar{R}$	Instantaneous reference frame attached to the AGV located at the geometric center 'O'
H	Hip coordinate frame for steering column
S	Steering coordinate frame for the steering column
C	Contact point coordinate frame for the wheels
$\bar{C}$	Instantaneous contact point coordinate frame for the wheels
P	Coordinate frame at point **P** on the track
I	Image window coordinate frame
T	Transformation with constant terms are represented like this
ϕ	Represents that the transformation contains variables in addition to constants
${}^{\bar{R}}\phi_{P}$	Position transformation from frame $\bar{R}$ to frame R
${}^{R}T_{H}$	Position transformation from the reference frame 'R' to the hip frame 'H'
${}^{H}\phi_{S}$	Transformation from hip frame 'H' to the steering frame 'S'
${}^{S}T_{C}$	Transformation from steering frame 'S' to the contact frame 'C'
${}^{R}\phi_{C}$	Transformation from reference frame 'R' to the contact point frame 'C'
${}^{\bar{C}}\phi_{C}$	Position transformation for frame 'C' relative to frame '$\bar{C}$'
${}^{\bar{R}}\dot{\phi}_{R}$	Velocity transformation for frame 'R' relative to '$\bar{R}$'
${}^{\bar{C}}\dot{\phi}_{C}$	Velocity transformation for frame 'C' relative to '$\bar{C}$'
${}^{R}T_{I}$	Transformation from the reference frame 'R' to the image frame 'I'

${}^{I}T_{P}$	Transformation from the image frame 'I' to the reference point frame 'P'
${}^{F}T_{\bar{P}}$	Transformation from the floor frame 'F' to the instantaneous reference point frame '$\bar{P}$'
${}^{\bar{R}}\dot{\Pi}_{R}$	Velocity transformation for frame 'R' relative to '$\bar{R}$'
s	Steering column offset between the steering axis and the axis of rotation of the steered wheel measured along the Y-direction of the steering column frame 's' (m)
L_a	Wheelbase distance between the contact point or patch of the front steered and driving wheel and the axis of rotation of the driven wheels. It is also the distance between a freewheeling caster and the axis of rotation of the driving wheels (m)
L_{ae}	Effective wheelbase distance between the contact point or patch of the front steered and driving wheel and the axis of rotation of the driven wheels (m) It is also the distance between a freewheeling caster and the axis of rotation of the driving wheels
L_b	Distance between the reference frame R and the contact point of the driving wheels measured along the Y-direction (m)
L_c	Distance between the reference frame 'R' and the floor measured along the Z-direction (m)
L_d	Distance between the reference frame 'R' and the longitudinal axis of the vehicle measured along the X-direction of the reference frame R (m)
L_f	Length of the inclined portion of the steering column (m)
r	Wheel radius (m)
L	Wheel span - distance between the contact points/patches of the two driving wheels for differentially driven AGV (m)
L_1	Distance between the contact points/patches of the left wheel from the longitudinal axis for differentially driven AGV (m)
L_2	Distance between the contact points/patches of the left wheel from the longitudinal axis for differentially driven AGV (m)

L_c	Distance between the vertical axis of the front camera to the axis of rotation of the driving wheels (m)
α	Steering column inclination in the fore and aft direction (rad)
θ_s	Steering angle - orientation of the XY-plane of the steering frame to the XY-plane of the hip frame (rad) This is the steered angle of the caster in the case of differentially driven AGV with camera vision
θ_{se}	Effective steering angle - yaw angle about the x-axis of a frame parallel to the x-axis of the reference frame 'R' (rad)
β	Roll angle about the y-axis of a frame parallel to the y-axis of the reference frame 'R' (rad)
γ	Pitch angle about the x-axis of a frame parallel to the x-axis of the reference frame 'R' (rad)
S_α	Short representation for $\sin(\alpha)$
C_α	Short representation for $\cos(\alpha)$
$\dot{\theta}_s$	Rate of change of steering angle - steering rate (rad/s)
$\dot{\psi}$	Angular velocity of the vehicle about the geometric center 'O' (rad/s)
$\dot{\psi}_1$	Angular velocity term of the vehicle due to inclined column steering (rad/s)
$\dot{\psi}_2$	Angular velocity of the vehicle due to driving and steering
$\dot{\lambda}$	Angular velocity about the X-axis of the reference frame 'R'
$\dot{\epsilon}$	Angular velocity about the Y-axis of the reference frame 'R'
$\dot{\theta}_r$	Angular velocity about the Z-axis of the reference frame 'R'
$\dot{\theta}_c$	Angular velocity of wheel slip
ω_x	Angular velocity of the driving wheel about the axis of rotation
V	Linear velocity of the vehicle at the geometric center 'O'
v_{rx}	Linear velocity of the vehicle along the X-axis of the reference frame 'R' (m/s)

v_{ry}	Linear velocity of the vehicle along the Y-axis of the reference frame 'R' (m/s)
v_{rz}	Linear velocity of the vehicle along the Z-axis of the reference frame 'R' (m/s)
v_{cx}	Linear velocity of the wheel along the X-axis of the contact point frame 'c' (m/s)
v_{cy}	Linear velocity of the wheel along the Y-axis of the contact point frame 'c' (m/s)
v_{cz}	Linear velocity of the wheel along the Z-axis of the contact point frame 'c' (m/s)
J	Jacobian matrix
$\hat{J}$	Reduced order Jacobian matrix
V_L	Linear velocity of the left wheel marked as #1 (m/s)
V_R	Linear velocity of the right wheel marked as #2 (m/s)
ε_d	Position offset (m)
ε_θ	Orientation offset (rad)
ε_{da}	Actual position offset (m)
$\varepsilon_{\theta a}$	Actual orientation offset (rad)
ε_{df}	Position offset (m)
$\varepsilon_{\theta f}$	Orientation offset (rad)
ε_{df}	Position offset from rear camera (m)
$\varepsilon_{\theta f}$	Orientation offset from rear camera (rad)
m	Slope of the equation of a line (y = mx + c) representing the track in the image window
c	Offset of the equation of a line (y = mx + c) representing the track in the image window (m)
G_1, G_2, G_3	Guidance controller gains

G_4, G_5	Guidance controller gains
δt	Sampling time for the LM628 Motion Controller Chip (341 μs)
ΔT	Sampling time for the overall control loop in camera mode (s)
K_p	Proportional Controller Gain for the LM628
K_i	Integral Controller Gain for the LM628
K_d	Derivative Controller Gain for the LM628
I_i	Integral Controller summing limit for the LM628
DP	Desired position of the motors in number of encoder counts (pulses)
SR	System resolution in number of pulses per encoder revolution (pulses/rev)
GR	Gear ratio between the motor and the wheel
ϕ_i	Host computer system clock rate
P	Moving reference point on the track
C	Center of the image window
ω_{x1}	Angular velocity of wheel-1 (rad/s)
ω_{x2}	Angular velocity of wheel-2 (rad/s)
n	Sample number
$\delta\theta_s[(n+1)\Delta T]$	Incremental steering angle at time $[(n+1)\Delta T]$
$\delta\varepsilon_d[(n+1)\Delta T]$	Deviation of the actual position offset from the desired position offset.
$\delta\varepsilon_\theta[(n+1)\Delta T]$	Deviation of the actual orientation offset from the desired orientation offset.
$\varepsilon_{dd}[(n+1)\Delta T]$	Desired position offset at time $(n+1)\Delta T$
$\varepsilon_{da}[(n)\Delta T]$	Actual (measured) position offset at time $(n)\Delta T$
$\varepsilon_{\theta d}[(n+1)\Delta T]$	Desired orientation offset at time $(n+1)\Delta T$

$\varepsilon_{\theta_a}[(n)\Delta T]$	Actual (measured) orientation offset at time $(n)\Delta T$
p_{rx}, p_{ry}	Position coordinates of the reference frame 'R' in the inertial coordinate frame
θ_r	Orientation of the reference frame in the XY-plane of the inertial frame
v_{rx}, v_{ry}	Instantaneous velocity of the reference frame 'R' in the inertial coordinate frame
$\dot{\theta}_r$	Angular velocity of the reference frame in the XY-plane of the inertial frame
R_1	Instantaneous radius of rotation
h, k	Center coordinates for the instantaneous circle of rotation
X_1, Y_1	Center coordinates for the instantaneous circle of rotation
x_p, y_p	Coordinates of the reference point **'P'**
a, b	Coordinates of the reference point **'P'** (another representation)
θ_p	Orientation of a vector at **'P'**
$p_{rx}(n\ \Delta T)$, $p_{ry}(n\ \Delta T)$	Position coordinates of the reference frame 'R' at time $(n\ \Delta T)$ in the inertial coordinate frame
$\theta_r(n\ \Delta T)$	Orientation of the reference frame in the XY-plane of the inertial frame
$v_{rx}(n\ \Delta T)$, $v_{ry}(n\ \Delta T)$	Instantaneous velocity of the reference frame 'R' at time $(n\ \Delta T)$ in the inertial coordinate frame
$\dot{\theta}_r(n\ \Delta T)$	Angular velocity of the reference frame in the XY-plane of the inertial frame
$f(x_p, y_p \mid \{\chi_0, \chi_1, \cdots \chi_l\})$	Function that best describes the geometric profile of the track in the x_p-y_p plane. χ_0, χ_1, $\cdots$ χ_l are the coefficients of the function.

$x_p = X(\theta_p \mid \{a_0, a_1, \ldots a_m)$	Function that best describes the geometric profile of the x-coordinates of point 'P'
$y_p = Y(\theta_p \mid \{b_0, b_1, \ldots b_m)$	Function that best describes the geometric profile of the y-coordinates of point 'P'
$f_x(x_p, y_p)$	Partial derivative of function $f(x_p, y_p)$ with respect to x_p
$f_y(x_p, y_p)$	Partial derivative of function $f(x_p, y_p)$ with respect to y_p
$f_{xx}(x_p, y_p)$	Partial derivative of function $f_x(x_p, y_p)$ with respect to x_p
$f_{xy}(x_p, y_p)$	Partial derivative of function $f_x(x_p, y_p)$ with respect to y_p
$f_{yy}(x_p, y_p)$	Partial derivative of function $f_y(x_p, y_p)$ with respect to y_p
dy/dx	First derivative of function $f(x_p, y_p)$
$\frac{d^2y}{dx^2}$	Second derivative of function $f(x_p, y_p)$
V_p	Velocity of the reference point 'P'
a_0, a_1, a_2	Coefficients of a function expressed in terms of sine and cosine of the orientation (θ_p) of a vector at 'P' for the position coordinate x_p. They are also the coefficients of a second order polynomial in ($t\ V_p$) for the position coordinate x_p
b_0, b_1, b_2	Coefficients of a function expressed in terms of sine and cosine of the orientation (θ_p) of a vector at 'P' for the position coordinate y_p They are also coefficients of a second order polynomial in ($t\ V_p$) for the position coordinate y_p

CHAPTER 1

INTRODUCTION

1.1 Introduction

One of the major concerns of most industries in modern times is to reduce the operating costs, while remaining competitive in the market. A major portion of the operating cost can be attributed to the material handling cost, whether it is in assembly, warehousing or component manufacture. Need for greater productivity and reducing labor costs are also factors of prime concern to most industries. Such pressing demands have led to an increased emphasis on automation, and therefore to the development of Autonomous Guided Vehicles. These are *driverless transportation systems* capable of intelligent motion and actions which allow a great deal of maneuverability. These vehicles are also referred in the literature as Mobile Robots, Wheeled Mobile Robots (WMRs), Automatic Guided Vehicles (AGVs) and Autonomous Vehicles.

Such vehicles may appear to be an expensive solution to the industrial problems but the long term benefits far outweigh the initial costs for developing such vehicles. It is much easier to quantify the intangible savings when employing such vehicles. To mention a few, there is less product damage, greater routing flexibility, greater control over material movement, ability to operate in hazardous environments, etc.

Industries adoption of AGVs is analogous to the transportation revolution that brought in trucks replacing the freight trains. A train passes each station in sequence, and facilities served by the train must

cluster near the rails. On the contrary, a truck goes wherever there are roads. It doesn't have to pass every station. It can bypass some and reach others in the order of priority. AGVs bring similar flexibility to factories.

1.2 AGV Applications

Interest in this subject has grown tremendously as the potential application of the autonomous vehicles has began to increase. AGVs bring flexibility to the factories. They can be easily reconfigured to meet change in production needs. In assembly lines, use of Autonomous Guided Vehicles provides enhanced job satisfaction and better product quality. Therefore conventional fork lift trucks and trailer carts used to transport raw materials from the warehouse to the shop floor, and finished products back to the warehouse, are being increasingly replaced by Automatic Guided Vehicles. Unlike a conveyor line, an AGV can be sent to any station in the system's route in any sequence and at any time. Thus flexible manufacturing has become a reality. AGVs allow the assembly lines to be split into parallel lines where identical operations are performed. This drastically increases the uptime. Apart from material handling, the classic areas where AGVs are used in the automotive industries are in motor assembly, body assembly, welding stations, door assembly and painting. A typical example for this is the truck assembly line in the General Motors plant at Oshawa, Canada, which employs nearly 500 AGVs.

The present day electronic industry is highly competitive requiring methods to reduce space and work-in-progress. The present trend is towards volume production of many different models which makes conventional conveying

methods difficult to implement. AGVs offer a flexible transporting systems to meet these industrial demands. Clean room operations, which are a must in the electronic industries further necessitates the use of AGVs. Other industries where such vehicles are increasingly being used include aerospace, food, paper, textile and pharmaceuticals industry.

Mobile robots can also be used in non-industrial environments. For example, they could be used in offices for document handling, in postal operations, in hospitals for transporting supplies, in agriculture for seed sowing etc. Autonomous vehicles could also be used for intelligent wheel chairs for the disabled. Some of the above mentioned applications are already a reality. To meet the specialized needs of different industries, AGVs may be fitted with a variety of fixtures for holding or transferring workpieces. These vehicles are currently being studied for usage as exploratory vehicles in land, and underwater applications. Their usage in planetary exploration include remote repair and maintenance. Significant research is underway for the development of autonomous vehicles for military applications.

There are many industrial and non-industrial application areas yet to be developed with the existing technology, apart from the fact that new markets would be generated with the rapid advances in technical know-how. However, this does not mean that the AGVs alleviate most of the industrial problems. The installation and the maintenance costs are high. The need to develop simple machines to operate in structured environment, with reliable guidance and error recovery capabilities together with reasonable overall construction costs imposes constraints on system design.

1.3 Historical Development of AGVs

The earliest AGV was developed in 1954 by Barrett Electronic Corporation, USA. The vehicle's controller was based on vacuum tube technology with wire guidance as the guidance scheme. With rapid advances in the field of electronics, the controllers were transistorized in the next decade. In the 1970s integrated circuit technology replaced the transistorized controllers. The controllers then became compact with more computing power. Mini-computers were used to communicate with vehicles and direct their movements. Integration with other automated systems such as conveyor systems became more popular because the computer technologies employed by all these devices were similar and could readily be interfaced with one another.

In the late 1970s microprocessors became popular in fixed equipment and onboard AGVs. The central minicomputer used software to control the overall AGV system operation, the microprocessors on each vehicle permitted it to be controlled by individual vehicle software. In systems using onboard vehicle microprocessors, software has eliminated a great deal of hardware within the system and onboard the vehicles. In addition, advanced control capabilities such as real-time communications with all vehicles, continuous location and status monitoring of all vehicles, and enhanced system control options became possible.

As microprocessors became increasingly popular, sophisticated control capabilities were incorporated without the previously required hardware. The AGV concept was first applied on a large scale to manufacturing in 1974, when Volvo Automated Systems installed a 260 carrier system at their plant in

Sweden. There are increasing trends in using stationary robot arms with AGVs so that they can load and unload by themselves thus eliminating the need for operators and other machinery at the assembly lines. Hybrids of AGVs with robots are developed by the Flexible Manufacturing Systems, USA, and are employed in electronic industries.

1.4 Components of an AGV

Figure. 1.1 illustrates a schematic of an AGV showing the essential components as described in references [1, 2]. The components of an AGV are

1) Mechanical structure with a driving/steering mechanism
2) Onboard power
3) Onboard computing facility
4) Feedback control system
5) Guidance system
6) Electronic components and interfaces, and electrical components
7) Operating system software
8) Safety features
9) Communication system

The mechanical structure of the vehicle houses the control components of the vehicles. The wheels to provide motion to the vehicle and steering arrangement in the case of steered vehicle, are the essential components of the mechanical system of the vehicle. The mechanical structure also provides the space for loading the workpieces. The onboard power is required for continuous and uninterrupted operation of the AGVs. This power is needed by the onboard computing facility as well as by the driving and steering motors.

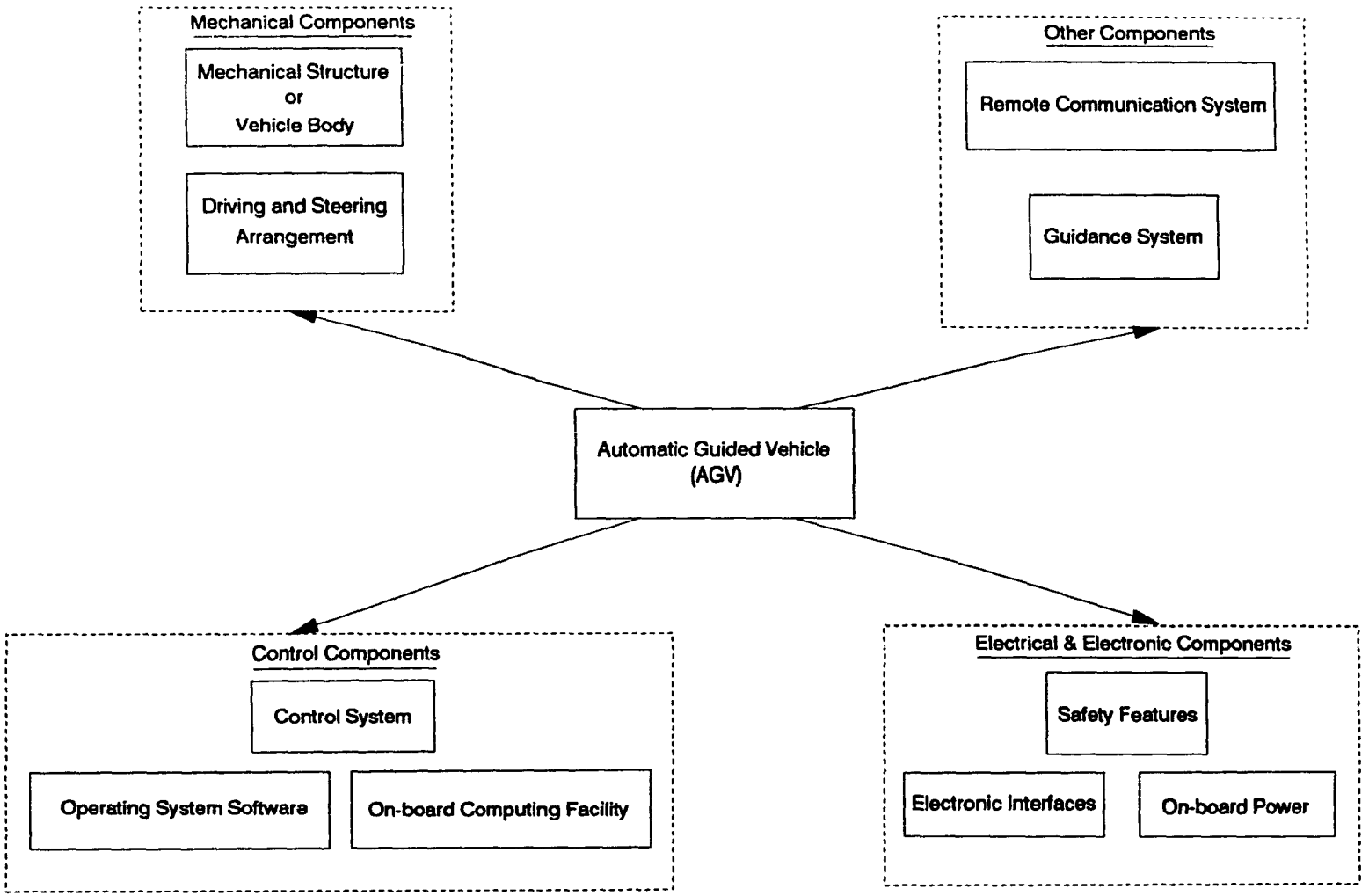

Fig. 1.1 Schematic of Components of an AGV

This is normally provided by two or more batteries. Most of the commercially available AGVs employ lead-acid batteries. The alternative is to use nickel-cadmium batteries. The advantage of the later is that they can be charged in a short time. However, these batteries need to be charged frequently.

A feedback control system is needed to monitor the driving and steering wheels. The elements of the feedback control system are, a motion controller, digital to analog converter, a servo amplifier and a feedback device that could provide motor speed/position. The host computer itself can be used as a motion controller if there is enough computing power to perform all the necessary controls and calculations. The usual practice is to allow the motion control to be performed by independent devices that can be interfaced with the host computer and with the other feedback control devices. Electronic components and interfaces are needed by the vehicle control systems. Electrical components such as relays, switches and LEDs are provided to enable ease of operation and trouble shooting of the vehicle.

The guidance system of the AGV depends on its application. A guidance system ensures that the AGV follows the desired track profile in order to perform the tasks that are assigned to the vehicle. The deviation of the vehicle from the desired track is measured by the guidance sensors and this information is passed onto the onboard computer. The guidance systems of the commercially available autonomous vehicles are, the wire guidance, the optical guidance, the inertial guidance, the infra-red guidance and dead-reckoning control. These systems are described in detail in chapter 2. An operating system software is needed for vehicle operation. The software

also checks for malfunctions in components and takes appropriate actions accordingly. The software is written in modular forms to enable easier integration of new features in the future.

Safety features are essential components for any automation and in this respect the AGVs are no exception to this requirement. The following are the various issues according to the Safety Standard established by the ASME [3] for Guided Industrial Vehicles.

- Contact sensors such as bumpers to protect the body of the vehicle
- Non-contact sensors such as ultrasonic or infrared sensors for obstacle detection and stopping
- Warning lights to indicate that the vehicle is moving
- Audible signals for blind corners
- Brakes-both software controlled and mechanical brakes should be present
- Emergency stop buttons should be provided all around the vehicle
- The software should be able to identify system malfunctions and should take appropriate actions
- The colour of the vehicle should be bright for easier visibility.
- A watch dog is required to monitor the onboard computer which controls the operation of the vehicle.

The above mentioned components are the basic components of an AGV and are mostly provided by the various manufacturers of AGVs. In a manufacturing environment employing a fleet of AGVs, it is necessary to provide a communication system between the onboard computer of the AGVs and the central main frame computer. The main frame computer monitors the movement of these vehicles and performs scheduling.

1.5 Summary

This chapter presents the definition for AGVs, and the various applications of AGVs in industrial and non-industrial environment. The historical development of AGVs is also discussed here. The essential components of an AGV are listed. AGVs provide flexibility in material handling and other industrial activities in with accurate tracking and parking capabilities. In industrial applications, AGVs replace the conventional conveying and transporting systems. AGVs are used in automobile industries, electronic industries, warehouses, hospitals, airports, industries involved in producing food products, paper, textile, pharmaceuticals, and in lawn mowing. Essential components of an AGV are, a mechanical structure or a vehicle body to house the control elements of the vehicle as well as to carry loads, driving and steering arrangements for vehicle movement, onboard power provided by rechargeable batteries for wireless and uninterrupted operation, onboard computing power for vehicle control, and feedback elements to ensure that the wheels of the vehicle are running at the desired speed. Electronic and electrical components are provided to facilitate control of the vehicle. A guidance scheme that enables the vehicle to follow the desired trajectory is an essential element of an AGV. Operating software, safety features and communication facilities to interact with an external supervisory computer are the other essential components of an AGV.

CHAPTER 2

BACKGROUND SURVEY AND DEFINITION OF PROBLEM

2.1 Introduction

Autonomous vehicles can be provided with a variety of wheelbase configurations. They can employ any one or more of the guidance schemes mentioned in section 1.4. The choice of wheelbase configuration and the guidance system depends on the task performed by the AGV and the environment in which the vehicle is used. In order to control the vehicle, controllers based on the kinematics and/or the dynamics of the vehicle are adopted. For this purpose, kinematic and/or dynamic models of the vehicle are developed. This model ranges from simple equations of motion based on the geometry of the vehicle to complicated sets of equations taking into account various physical characteristics of the vehicle body and the driving and steering mechanisms. Finally, in order to perform the overall position control of the vehicle to achieve accurate road following, a guidance control scheme is employed.

This chapter discusses the literature available in the above mentioned areas and identifies the areas of improvement. This chapter has been divided into three major sections. The first section summarizes the literature on kinematic (wheelbase) configuration, kinematic and dynamic modeling, guidance schemes, controllers for the guidance schemes and wheel level control schemes. The second section identifies the objective and the scope of the research addressed in this thesis. The third section provides a briefly describes the organization of the thesis.

2.2 Present State-of-the-Art

This section of the thesis describes the existing literature on autonomous vehicles in four parts. The first part is on the kinematic configurations of the autonomous vehicles. In this part, various wheelbase configurations adopted as well as special purpose wheels designed to provide certain features for the vehicle are described. The second part of this section details the kinematic and dynamic modeling aspects of AGVs. The third section is on the various guidance schemes adopted. The advantages and disadvantages of one scheme over the other are also described in this section. The last part of this section covers the control schemes proposed by the various researchers. This includes guidance in terms of overall position control and the wheel level control for low level feedback control of the driving and steering wheels.

2.2.1 Wheelbase Configuration and Types of Wheels

This section summarizes the various wheelbase configurations and the type of wheels employed in the AGVs developed by various researchers. This classification is to obtain a general idea about the wheelbase configuration that is mostly used in practice. The wheelbase configuration of most land vehicles can be classified as, two driving wheels and no steering wheels (differentially driven AGV), a steered wheel with two driving wheels, a steered wheel which is also driving and two idling wheels, multiple driving/steered wheels and special wheels.

2.2.1.1 Wheelbase Configuration with Two Driving Wheels

These AGVs employ two driving wheels on either side of the rear axle of the vehicle. In order to provide stability, these vehicles are provided

with one or more castors. In these vehicles steering is accomplished by driving the two wheels at different velocities. Fig. 2.1a shows a schematic diagram of an AGV with a differential drive. The driving wheels and the casters are indicated in this figure. An advantage of these vehicles is their ability to turn at zero radius. Also, the vehicle can move forwards and backwards. A limitation of these vehicles is that they cannot move side ways i.e. along the lateral axis. Examples of vehicles employing this kind of configuration (with or without a castor at the rear) are, the *Newt Robot* described by Hollis [6], and the vehicles considered by Julliere et al [7], Borenstein and Koren [8], and Hongo et al [9].

2.2.1.2 Wheelbase Configuration with a Driving and Steered Wheel

The other popular wheelbase configuration is the tricycle wheelbase configuration, a fixed rear axle provided with a driven wheel on either side of the axle. The front end of the vehicle has a driving wheel which is also steered. This configuration is illustrated in Fig. 2.1b. One of the limitations of this configuration is less maneuverability due to the absence of zero turning radius as compared to the differential drive arrangement. Further, it cannot travel backwards and may employ complicated mechanical structure to provide driving and steering of the same wheel. It has been demonstrated by Muir and Newman [10] that this arrangement is not desirable for kinematic control of AGVs. Examples of vehicles employing this kind of configuration are, the CONCIC-I AGV by Cheng et al [11], the Neptune vehicle [12], the Blanche vehicle from AT&T Bell Laboratories described by Miller [13], Nelson and Cox [14], Wilfong [15], and Cox [16].

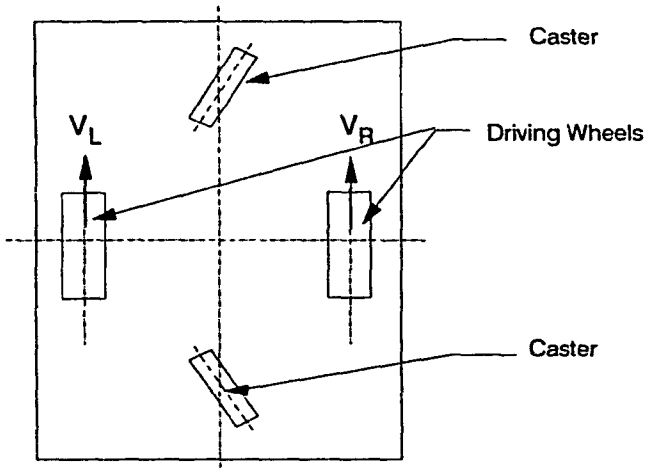

Fig. 2.1a An AGV With Differential Drive

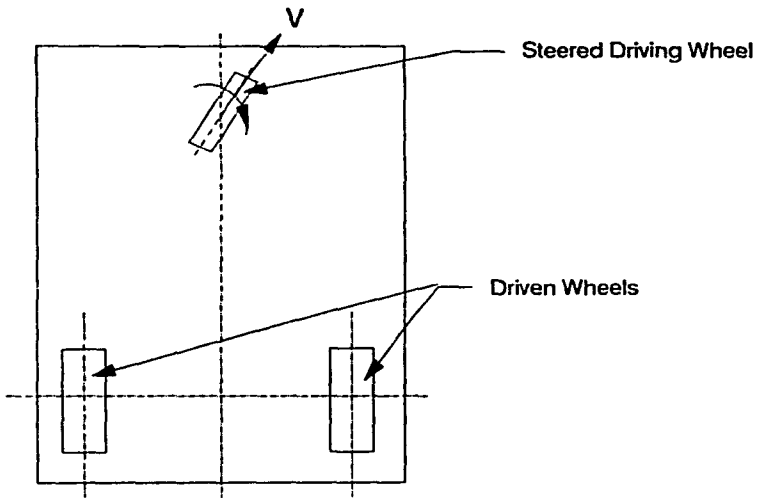

Fig. 2.1b An AGV With a Steered Driving Wheel

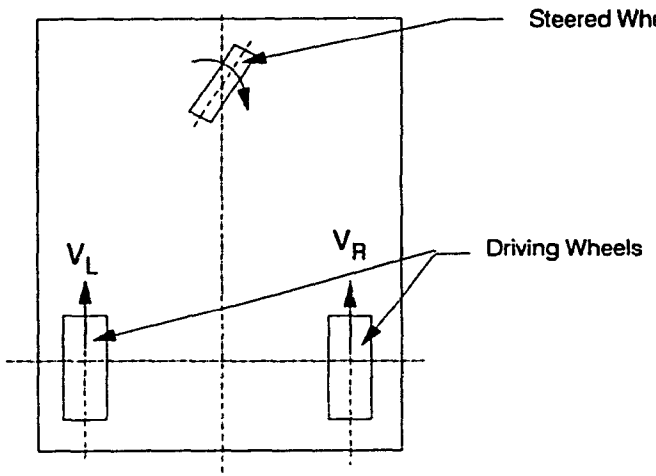

Fig. 2.1c An AGV With Two Driving Wheels and a Steered Wheel

2.2.1.3 Wheelbase Configuration with Two Driving Wheels and a Steered Wheel

This is a variation to the previously mentioned configuration. In this the front wheel is the steering wheel and the rear wheels are the driving ones and this arrangement is shown in Fig. 2.1c. This introduces a redundant degree of freedom in which there are two wheel speeds and a steering angle to control. This redundant degree of freedom aids in kinematic control of the vehicle. This phenomenon is demonstrated by Muir and Neuman [10].

2.2.1.4 Wheelbase Configuration with Multiple Driving and Steered Wheels

In the case of vehicles with four wheels, two wheels at the front are steerable and the remaining two wheels at the back are the driving ones. This configuration is similar to that of an automobile. The steering is performed by an Ackerman steering linkage. Schematic diagram of an AGV with four wheel configuration is shown in Fig. 2.1d. The two steered wheels can be replaced by an equivalent steered wheel at the center and this leads to the tricycle configuration. Examples of vehicles with this configuration are, the Stanford Cart described by Moravec [17] and the JPL Rover described by Muir and Neuman [10]. In the case of JPL Rover, the rear wheels are also steerable by a separate Ackerman linkage in addition to the front wheels that are steerable. All the four wheels are provided with independent driving arrangement. This arrangement is presented in Fig. 2.1e. *CMU Rover* explained by Moravec [17] also known as Pluto has three steered and driving wheels. There are three steering angles and three wheel speeds to control in order to achieve three degrees of freedom.

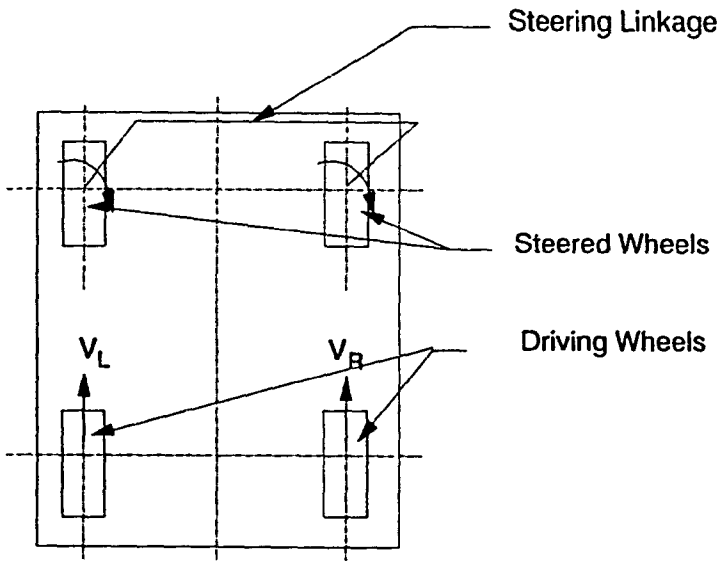

Fig. 2.1d An AGV With Two Driving and Two Steered Wheels

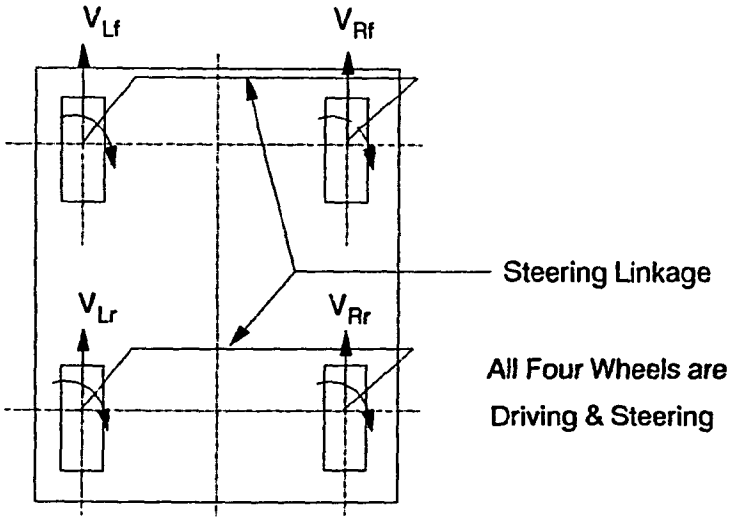

Fig. 2.1e An AGV With Four Driving and Steered Wheels

2.2.1.5 Special Wheels

Vehicles with more than two degrees-of-freedom are referred in the literature as omnidirectional vehicles. The *CMU Rover* mentioned earlier is an omnidirectional vehicle. The conventional configurations considered so far provide only two degrees of freedom. The conventional vehicles cannot move in the lateral or transverse direction. In order to provide an extra degree of freedom i.e. motion along the lateral direction, special wheelbase configurations and special wheels are considered in the literature.

The vehicles described by Jonsson [18] as reported by Hollier [4] and the Uranus Mobile Robot described by Podnar in the annual report from CMU edited by Moravec [19], employ special wheels which are known as Mccannum wheels. These wheels provide the vehicles the ability to move in any direction from 0 to 360 degrees, including a movement along the lateral axis (sideways - 90 degrees). This wheel shown in reference [4] is reproduced in Fig. 2.2. This wheel is made up of a number of free rolling rollers placed at an angle of 45 degrees on a rim. When viewed from the side, the end of each roller overlaps the beginning of the next, and due to the barrel shape of each roller, the wheel presents a circular profile. As the wheel rolls, its contact with the ground changes from one roller to the next smoothly. The AGV is provided with four wheels, one at each corner of the vehicle. By driving the wheels at different speeds and in different directions, movement along a variety of directions is possible. Sample movements using this wheel are discussed by Agullo et al. [20] and are shown in Fig. 2.3. For longitudinal movement, all the wheels are rotated in the same direction. The lateral movement (movement along the side, i.e. transverse), is obtained by rotating the wheels along one diagonal in one direction and those along the

Fig. 2.2 Schematic of the Mccannum Wheel
(Courtesy of International Trends in Manufacturing Technology by Hollier [4])

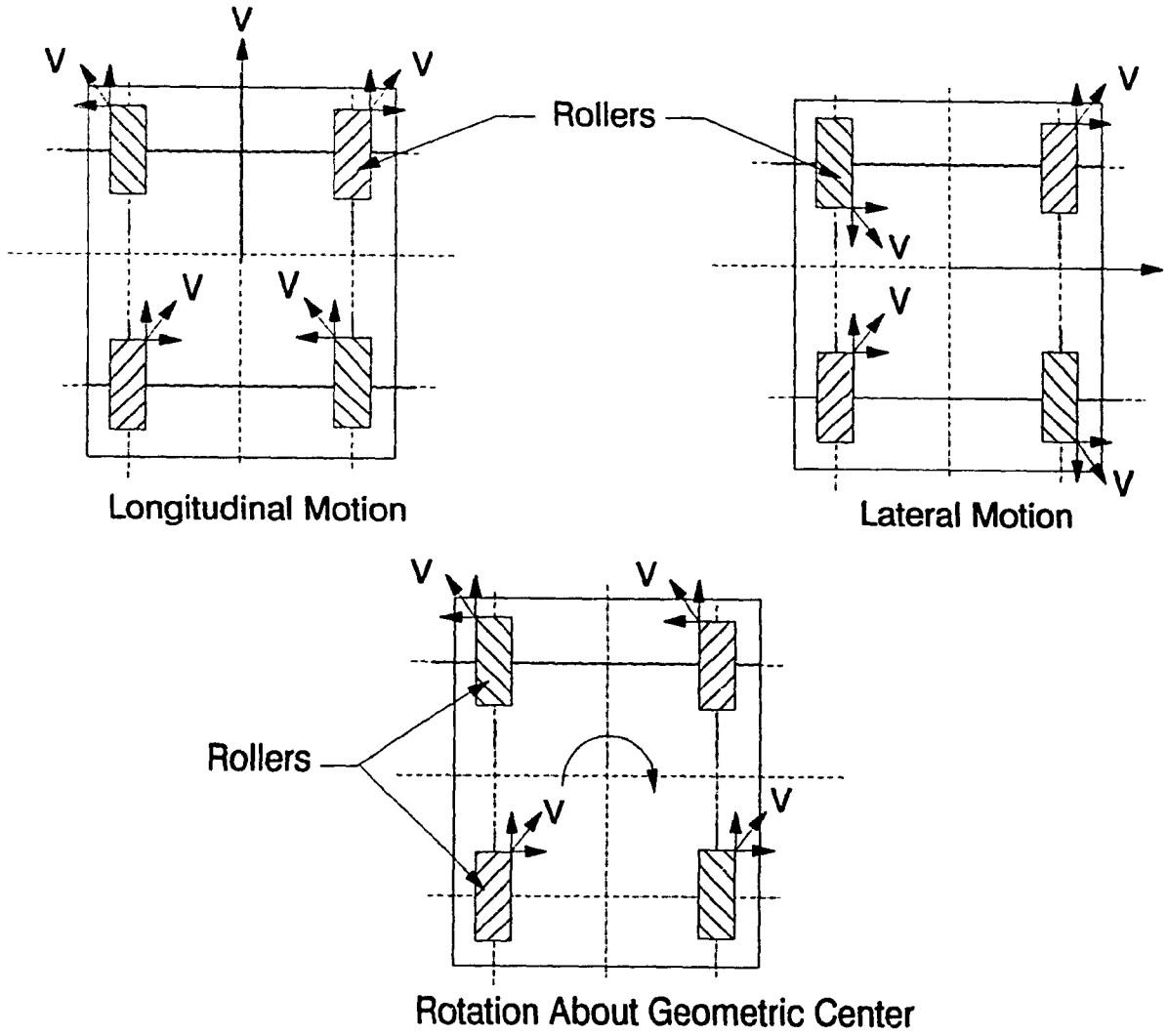

Fig. 2.3 Motion Modes of an AGV with Mccannum Wheels

other diagonal in the opposite direction. Spin motion is accomplished by rotating wheels on one side of the vehicle in a direction opposite to that of the wheels in the other side.

Hollier [4] reports a new type of driving mechanism to achieve omnidirectionality described by Fujiwara and Kawashima. A schematic of this vehicle from this reference is reproduced in Fig. 2.4. In this vehicle, there are two rotary discs to each of which are attached two driving wheels. The orientation of the rotary discs with respect to the chassis can be changed by controlling the revolving speeds of these four wheels. By rotating the two wheels attached to a rotary disc in opposite directions, the direction of the rotary disc can be changed without moving the chassis. Some of the motions achieved are shown in Fig. 2.5. This is equivalent to a system with differential drive and a steering mechanism to steer the wheels independently. This feature is provided in the motor-in-wheel-drive units developed by the Schabmuler Corporation, Germany [21]. A sample of this drive unit is shown in Fig. 2.6. This unit is compact from the mechanical structure point of view and is employed in several industrial AGVs. This is the wheel drive unit employed in the prototype AGV designed for experimentation in this thesis.

2.2.2 Kinematic Modelling

A kinematic model provides the equations of motion to compute the motion parameters of the AGV corresponding to the motion parameters of the wheels. A Jacobian matrix (J) relates these two sets of motion parameters. The motion parameters of the AGV are the linear and the angular velocities, and those of the wheels are the wheel speeds. The other parameters considered in

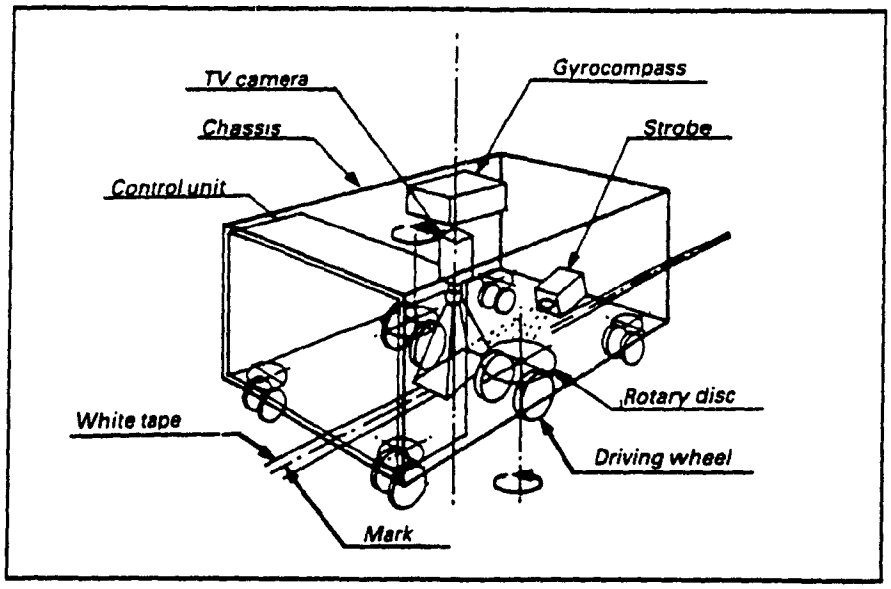

Fig. 2.4 Schematic of an AGV with Omnidirectional Motion (Courtesy of International Trends in Manufacturing Technology by Hollier [4])

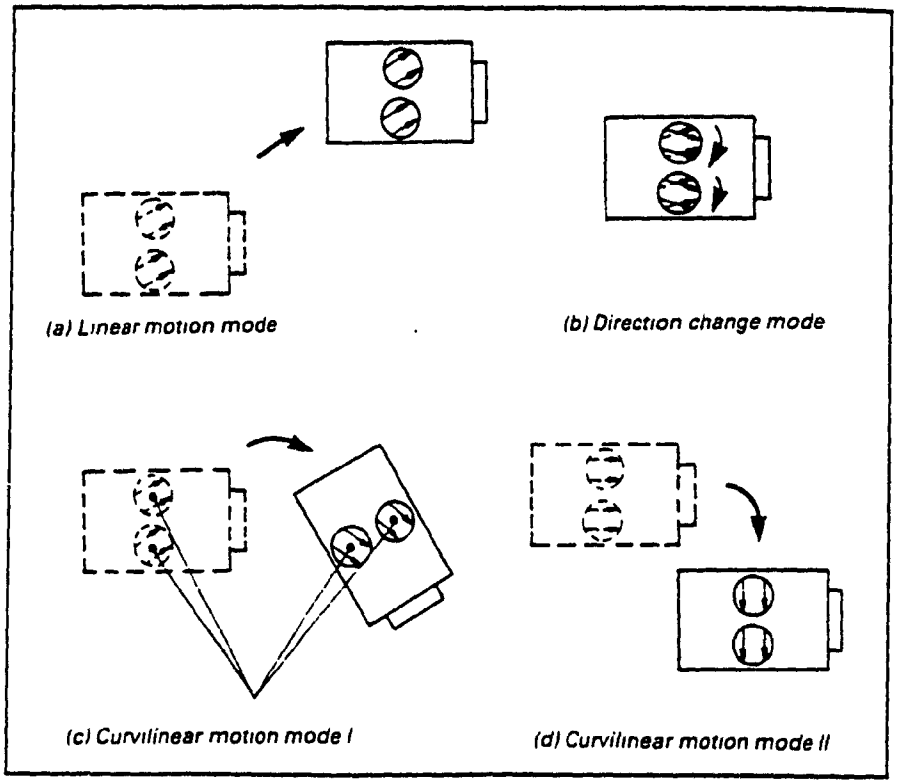

Fig. 2.5 Motion Modes with the Omnidirectional Vehicle (Courtesy of International Trends in Manufacturing Technology by Hollier [4])

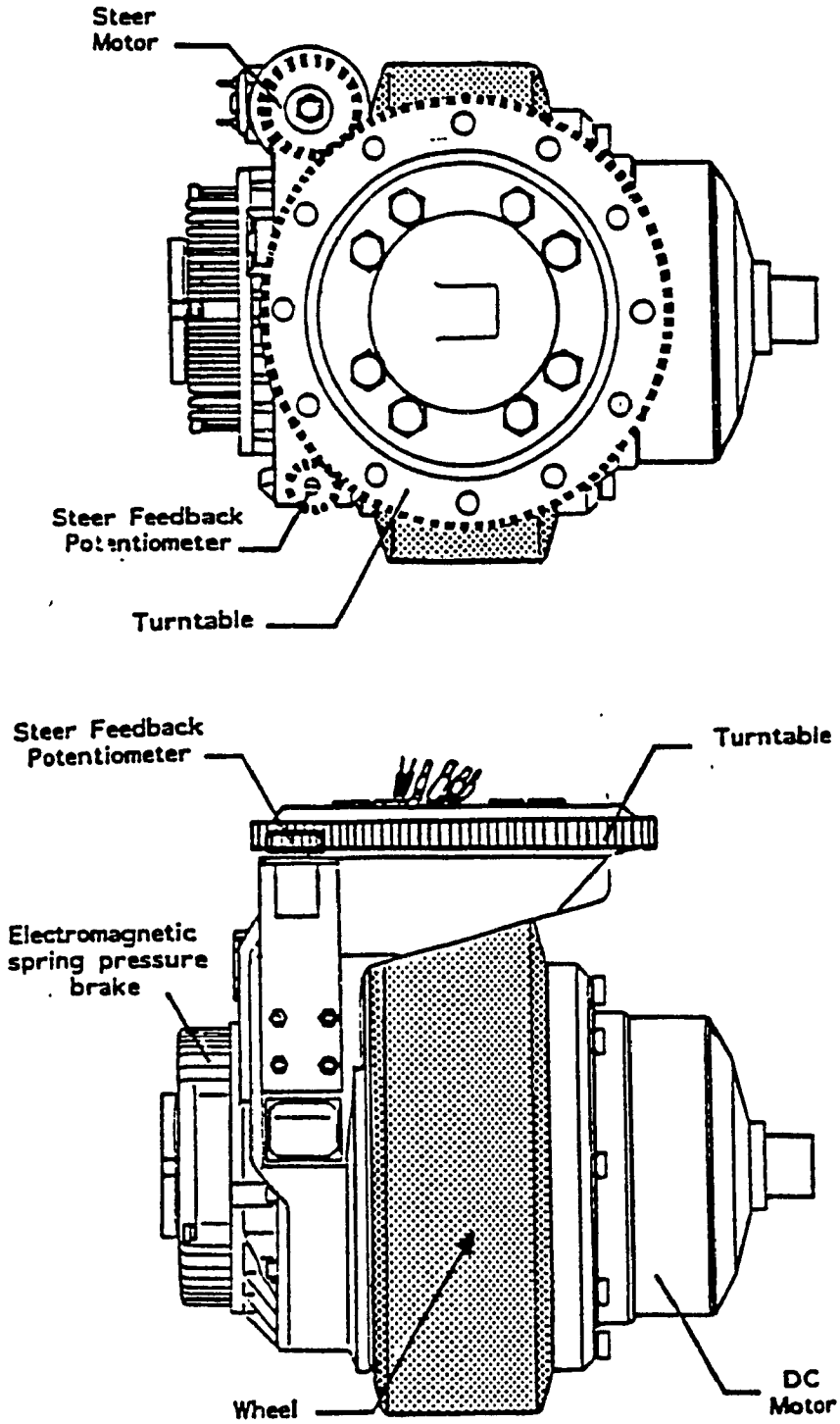

Fig. 2.6 Motor-in-wheel Drive Unit with Steering Arrangment (Courtesy of Schabmuller Corporation, West Germany [21])

the case of steerable wheels are, the steering angles and the steering rates. The process of computing the vehicle motion parameters from those of the wheels is the forward kinematic analysis. The inverse kinematic analysis computes the wheel motion parameters from those of the AGV. To compute the inverse kinematics the Jacobian matrix must be invertible.

To move the vehicle along a prescribed track, the wheel motion parameters are worked out from some mathematical description of the track. This technique is called dead reckoning control and is explained in section 2.2.3.7. To achieve this form of control, an accurate model of the vehicle is required to carry out the inverse kinematic analysis. This inverse operation for the AGV is similar to the process involved in computing the joint parameters of a robotic manipulator from a given set of world co-ordinates of the end effector. It will be shown in section 3.4 that this Jacobian is a function of the geometrical parameters of the vehicle (i.e. the wheel base, the inclination angle of the steering column, and the offset of the steering axis from the wheel axle) and the steering angle.

Since the inverse kinematic analysis is vital to the dead-reckoning control of an AGV, it becomes mandatory to determine whether the kinematic model of the vehicle is invertible or not well ahead of time. A criterion is worked out in this thesis to do so. This criterion is called "*path controllability*". Stated another way, a vehicle is said to be *path-controllable* if there exists a unique solution for the motion parameters of the wheels corresponding to the linear and angular velocities of the vehicle.

AGVs are different from the stationary robots in many respects [10]. These are listed below.

a) AGVs are closed-chain mechanisms.

b) In the case of AGVs, only some degrees of freedom can be actuated.

c) Both surface and point contacts are present in AGVs (hence the existence of higher pairs), but the stationary robot arms have only surface contacts (i.e. lower pairs).

Hence AGVs cannot be modeled using the Denavit-Hartenberg formulation [22] which is commonly used to model robot arms [23]. Muir and Neuman [10, 24, 25] present a kinematic modeling scheme for autonomous vehicles using transformation approach. To take into account the differences between robot arms and AGVs, Muir and Neuman adopt the Sheth-Uicker formulation [26] to model the kinematics of an AGV. It is believed that the approach of Muir and Neuman provides an elegant modeling technique, and presents itself as a counterpart to the transformation modeling approach that is popularly employed for robotic manipulators. The merits of this approach lie in its ability to generalize into any kind of wheelbase configuration with any number of wheels and various combinations of driving/driven and steerable/non-steerable wheels. Most of the other research work on kinematic modeling concentrated on tricycle configuration with vertical steering column and without offset [27, 28, 29]. These researchers adopted a simpler version of the tricycle configuration (straight steering column with and without offset) and the model is based on vector approach.

2.2.3 Dynamic Modelling

This thesis does not use the dynamic model of the AGV for control purposes. However, it uses a simulation package developed by Huang [35] for simulations studies. This package is based on a dynamic model of the CONCIC-II AGV. For this purpose and for the sake of completeness of the literature review, schemes for dynamic modelling of AGVs is presented in this section. Dynamic modeling can be accomplished using the classical techniques based on D'Alembert's principle used to model road and off-road vehicle dynamics [30, 31], extended form of Lagrangian and Newton-Euler formulations, the Newtonian dynamics with the transformation approach for kinematic modeling by Muir and Neuman [32], and the Hybrid Newton-Euler/Euler-Lagrangian formulation and natural orthogonal complement method by Saha and Angeles [27], and Cyril et al. [28]. The simulation package of Huang [34, 35] employs a dynamic model which is based on the classical method. This is not an elegant approach as is the transformation method and is not general in nature. However, Huang [35] presents a discussion on generalizing the dynamic modeling approach to include any kind of wheelbase configuration. The third approach is the orthogonal complement approach and is used by Saha and Angeles [27], and Cyril et al. [28]. Muir and Newman [32] present a modeling scheme that includes close-chains (non-holonomic systems), high-pair joints, friction, and unactuated and unsensed joints. According to the authors, the other dynamic modeling approaches did not address the problems of unactuated and unsensed joints, and do not have provisions to consider dry friction (stiction, Coulomb and rolling friction) and viscous friction. Further, it is shown that the model is general in nature to apply to any multibody robotic mechanism. Also it is claimed that the formulations are simple and computationally efficient and

allows parallel computations in multiprocessors due to the matrix-vector products.

2.2.4 Guidance Schemes

AGVs are usually driven by some guidance systems. The notable one is the use of an energized wire loop. Others use optical sensors, or beaconing together with onboard triangulation to compute the instantaneous position and orientation of the vehicle, inertial guidance, infra-red guidance, three dimensional imaging and laser range finding. The various guidance schemes for industrial path guidance schemes are described below.

2.2.4.1 Embedded Wire Guidance

Wire loops are embedded in the factory floor and are energized electrically. The AGV carries a matching antenna or coupler that detects the magnetic field surrounding the wire, and the vehicle is kept suitably straddled over the wire. There is a physical limitation to the magnetic field so generated. Consequently, there is a lower limit to the deviation between the vehicle and the wire. The highest speed attainable using this type of guidance is also limited. Moreover, in cases where the wire loops are either close to one another or overlap, they are energized at different frequencies to avoid confusion, resulting in having to change the tuning frequency of the on-board antenna depending on the zones of the shop-floor in which the vehicle is to operate effectively. This technology is the oldest and most widely used. Documented survey by Cheng et al. [11] of over 14 AGVs manufactured world wide shows that 11 of them rely on wire-guidance. It is also reported by Tsumura [38] that 90% of the guidance schemes in Japan adopt this technology.

2.2.4.2 Optical Guidance

Two schemes in optical guidance are, photosensing and camera vision. In the photosensing scheme, a photosensor tracks a fluorescent line on the floor. The AGV carries an ultra-violet light emitter to energize the guidepath that is previously prepared on the floor surface. The photosensor based control that is currently available suffers from limitations similar to the magnetic coupler in wire guidance. Consequently, AGVs of this type are more popular for slow-moving (less than 0.5 m/s) inter-office mail delivery carts. Besides, the fluorescent path requires extensive maintenance. Tsumura [32] reports that companies in Japan are employing this technology in offices and in machining small parts.

Cheng et al [10] presented a method of guiding autonomous vehicles using camera vision. In this scheme, a binary camera is focussed on a black tape or paint on the floor that describes the desired trajectory. The position and orientation of the vehicle relative to the tape are established and this information is used to navigate the vehicle. This vehicle has been named as **CONCIC-I** (**CON**cordia Center for Industrial Control-I). On-board data acquisition is also provided to evaluate the performance of the vehicle. The type of sensor adopted, the image processing scheme, the computing facility and the vehicle structure have limited the use of this AGV for serious research activities. Consequently, a second generation vehicle has been built to carry out experimental study, and has been named as **CONCIC-II**. In section 6.2, the features of **CONCIC-II AGV** which are absent in the **CONCIC-I** vehicle, are discussed.

Takeda et al. [39] describe a variation in the optical guidance using camera vision. The track to be followed is provided with discrete marks (10 mm diameter) which are optically detected. These marks are actually retro-reflective spots located at a distance of 1 m from each other. A CCD camera on the vehicle detects these marks which are illuminated by lights carried by the vehicle. Combinations of several spot marks are used for road signs (turning options). This guidance scheme is essentially an extension of the concept of following a tape or paint on the floor that describes the path to be followed by the vehicle. The scheme proposed by the authors may work well for straight line tracks but does not produce satisfactory result when the vehicle has to follow curved track profiles.

2.2.4.3 Road Following By Map Building

The vision scheme described above provides a fixed path for the vehicle to travel. In order that the vehicle travels freely without being constrained by the user provided path, road following based on map building is developed. CCD cameras are employed to provide three dimensional scene analysis. In this scheme, the image received is translated into a scene description by determining where objects and edges are in the image. There are number of methods employed for image processing, namely, color analysis, model fitting and high-level reasoning. In color analysis, the intensity and color of the image are used for analysis. Problems associated with this scheme are, illumination, shadow, and viewing angles. Vision schemes developed and implemented at the Carnegie Mellon University (CMU) in the early days were based on the gradient operator approach. In this scheme, a small window of the image is considered and this provides faster image processing. A thresholding is applied to get a binary image of the scene,

thereby obtaining the edges of the road. Problems associated with this scheme are, jaggered road edges and contrast. An alternative is to use the color of the image. In the conventional schemes the intensity or color of image processing is employed to achieve road map generation [40, 41, 42]. Herbert [43] provides a variation to the conventional method of road following. The author investigates the use of active sensing, laser range finding for both road following and map building. This provides stability with respect to illumination conditions and elimination of calibration process. The road following using map building is mostly applicable for field robots. Extensive research is underway using visual guidance at the Carnegie Mellon University [19]. Crisman et al. [44] presented a navigation scheme based on color vision in an unstructured environment. The environment considered by these authors are a road with no lane or road marks, poor lighting condition or presence of shadow and weather condition such as snow on the road.

2.2.4.4 Range Finding With Ultrasonic Sensors

The AGV is equipped with one or more ultrasonic sensors to prepare a map of the room. Transducers from Polaroid are commonly used due to their low cost, long range and good accuracy. The ultrasonic sensor has an emitter and a receiver. Sound waves are emitted at four different frequencies, and the time taken to receive the reflected wave is used to compute the distance between the AGV and the obstacle. Transmission of a pulse requires about 1 ms and a blanking time of 600 μs is provided to let the ringing die down. This is to ensure that the ringing does not interfere with the returning signal. It has been reported that as a result of the time spent on transmitting and blanking, the minimum distance that can be sensed is limited

to 27.5 cm and the maximum sensing range for the Polaroid sensor is 12 m. The sonars provide a good resolution in terms of measuring the distance of an object but they fail to do so in computing the angular position due to their wide beamwidth and this limits the application of sonars for AGV guidance. Reflections from smooth surfaces result in problems (distance measured is longer than the actual), and radiation patterns also pose problems due to the wide angle of the radiation pattern. Several schemes are discussed in the literature to alleviate these problems.

One such guidance approach is detailed by Elfes [12], and the vehicle has been named as Neptune in the Mobile Robotics Laboratory of the Carnegie Mellon University (CMU). The other mobile robot developed at CMU employing sonar is the Terragator, a field robot. Flynn [45] describes a sentry robot employing sonar and infrared sensors as the guidance system. Preciado et al. [46] presents an approach to compensate for the presence of sensor noise. The method is a geometric method and is not based on a statistical approach. The authors have considered noise from sonars to test the suitability of the compensation method.

Ultrasonic sensors are used more as a navigator than a guiding device. The material flow pattern in the industries is more or less fixed, and hence it is not necessary to generate the floor map, path planning etc, and this indicates that ultrasonic sensing is not for industrial guidance. However, the sonars can be employed in conjunction with other sensors in the shop floor to stop the AGV whenever they encounter obstacles or other AGVs in the circuit. One common application of sonars for guidance is for sentry robots as surveillance systems. The major advantage of the sonar is its

insensitivity to lighting conditions as in the case of camera/optical guidance schemes, and the information obtained is directly related to the environment in which the vehicle is operating. Tani et al. [47] present an AGV with multi-sensors. This AGV employs ultrasonic sensors and laser range finders for guidance control and CCD cameras for obstacle detection and avoidance.

2.2.4.5 Range Finding using Lasers

Nishide et al. [48] present a laser guidance scheme with a laser scanner on the vehicle and corner cubes on the ground. The initial coordinates of the cubes are provided as input to the host computer and this information is used in conjunction with the reflected beams received to compute the heading and position of the vehicle. Tsumura et al. [49] discuss a similar scheme as described by Nishide et al. [48]. The authors provide simulations and experimental study of the guidance methodology and mathematical formulations for error analysis. The positions and orientation computations have an error with a mean of 0.9 cm and a standard deviation of 1.6 cm and a mean of 0.64 deg and standard deviation of 0.17 deg respectively. Hoppen et al. [50] present a methodology of navigating a mobile robot using environment mapping and guidance using laser. The paper presents the guidance scheme for known or unknown indoor environments in the presence of moving obstacles.

2.2.4.6 Infrared Guidance

A transmitter/receiver mounted on the AGV emits an infrared signal, and utilizes its reflection to determine its current position and orientation relative to the surrounding reflectors. Position accuracy is inferior, since the reflectors are located at least 20 to 25 meters apart and there is a

practical limit on the number of reflectors that can be mounted on the ceiling or the walls of a given shop floor.

Miller and Wagner [13] present an optical rangefinder scheme. In this scheme, a 2mW 0.82 μ LED emits infra-red radiation. The system has been designed to assure safety for the eyes of the workers on the shop floor. This scheme has been tested on a prototype AGV "Blanche" at the AT & T Bell Laboratories. Flynn [45] discusses a multi-sensor system for mobile robot navigation combining sonars and infrared sensors. Giralt et al. [51] and Durrant-Whyte [52] present a multisensor based guidance. The infrared sensor does not provide an accurate estimate of the distance as the sonar, but provides good angular resolution. Hence, integrating the image data from these two sensors, an accurate estimate of the map of the room or place where the mobile robot is operating can be obtained. This is primarily for path planning applications involving sentry robots (surveillance) and does not find applications in industrial environment.

McGillem and Rappaport [53] detail vehicle locomotion using infrared beaconing. The paper presents relevant mathematical formulations to compute the vehicle location using different approaches to computing. The paper talks about lack of enough computing speed and hence devotes a section on finding the solutions sines and cosines of angles with less computation burden. The limitation on the computing speed can be easily overcome by replacing the Z80 processors with the current fast Intel 80286 or 80386 processors.

2.2.4.7 Dead-reckoning Control

Dead reckoning control of AGV is a method that does not depend on a sensor that detects the physical location of the AGV with respect to a desired track profile. The track profile is in the computer memory instead of being laid out physically. The distance and the direction travelled by the AGV are estimated from the wheel motion sensors such as encoders.

Dead-reckoning control is preferred to other types of guidance schemes [10, 54, 55, 56, 57, 58, 59, 60] for the following reasons :

1) Dead-reckoning control can provide higher operating speed for the AGVs as they are not constrained by the time needed for processing the data received from the physical sensors.

2) The AGV path can be easily modified by simply changing the user defined path in the computer memory and is under software control.

3) Since the dead-reckoning control scheme requires fewer components compared to the other guidance schemes, the unit price as well as the operating cost of the system are lower.

On the other hand the dead-reckoning control scheme has some disadvantages over the other schemes. Some of the limitations associated with this scheme are :

a) Since it relies on the information concerning the physical parameters of the AGV, any variation in those parameters from their nominal values will affect the tracking accuracy.

b) Accumulated errors due to errors in the wheel sensor measurements and

computational approximations.

c) Presence of wheel slip and floor unevenness provide misleading information concerning the distance travelled by the AGV.

Hongo et al. [9] present a different approach to compute the position and orientation of the vehicle based on the encoder measurements to minimize the effect of errors. Instead of mounting the encoders on the driving wheel shafts, these are attached to the measuring wheels which are mounted along the axis of rotation of the driving wheels but are actually driven wheels. Measurement errors are corrected periodically with the help of optical range finders in conjunction with a marker board. The location of the marker board is provided to the computer and the correction scheme corrects any deviation in the computed location using the optical range finder compared to that of the stored location. Several error terms are considered such as velocity error, position error and the direction error for guidance purpose. The introduction of velocity error is novel, and this is to study the effect of vehicle speed on the controllability of the system. Track following accuracy of few centimeters deviation from the desired course at low speeds upto 1.0 m/s reported. A stopping distance of 2 cm is mentioned. Position error of 20 cm is noticed while travelling a distance of 50 m (0.4%). The introduction of measuring wheels are not very well explained in the paper and a misalignment of the axis of rotation of these units with the driving wheel axis may be present and the model should account for this error. Errors in establishing the physical parameters of the vehicle need to be addressed.

Nakano et al. [55] discuss a prototype vehicle that employs dead-reckoning control for guidance and an optical range finder for error correction. All four wheels are driving wheels and are steerable thereby providing omni-directionality. The paper does not present enough experimental results to provide tracking accuracy.

Banta [56] reports a parameter estimation scheme for correcting modeling errors due to wear, misalignment or calibration degradation for dead-reckoning control. Simulations studies show considerable improvement in tracking accuracy using the estimation scheme.

Culley and Baldur [57] approach the problems of dead-reckoning control with a free wheel measurement technique. In this scheme, a free wheel is mounted along the longitudinal axis of the vehicle. In addition to the rolling motion, the wheel has two more degrees-of-freedom, namely, a move about its pivot point and a movement up and down with changes in terrain. The vehicle position and orientation are computed using the measurements taken from this wheel instead of the conventional practice of taking measurements from the driving and steering wheels.

2.2.4.8 Inertial Guidance

Devices such as linear accelerometers or gyroscopes provide information concerning the direction of travel, position and velocity of the vehicle without the use of external devices. These gyroscopes may be mechanical, ring laser, magnetic north seeker or fibre optic. Mechanical gyros have several disadvantages namely, low resistance to shock and vibration, warm-up time, and high cost. The magnetic north seekers are not useful in industrial

environments where metals are handled. The fibre optic scheme is preferred to the ring laser due to its longer life time, less precision required in manufacturing. Further, low cost and no additional mechanisms needed to lock them are the added features. The fiber-gyros use several turns of the fiber to generate lengthy paths. Kuritsky and Goldstein [63, 64] discuss a Ring Laser Gyro (RLG), a Vibration Beam Accelerometer (VBA), and developments in Fiber Optic Gyroscope (FOG) and Magnetic Resonance Gyroscopes (MRG's). The paper presents qualitative estimates of the guidance accuracy, alignment time, response to vibrations, shocks, and temperature. Bhanu et al. [65] elaborate a navigation scheme based on an inertial sensor. The inertial sensor information is used in conjunction with the information received from an optical sensor to achieve obstacle avoidance.

2.2.5 Control Schemes

Borenstein and Koren [8] present a cross coupled controller scheme for a differentially driven vehicle. This is to compensate for load or any other disturbance on one wheel which reflect on the other. This compensation prevents the vehicle from deviating from the resultant path. With this scheme, any error in one of the control loops affects both the loops. This is primarily useful for dead-reckoning control of AGVs and is not essential for vehicle control that employs an absolute referencing system. The introduction of cross coupling results in a lag. Due to the reduction in the wheel speeds, the vehicle will be running at a speed less than the desired speed and will not reach the destination at the prescribed time.

Hemami et al. [67, 68, 69] present a non-linear control scheme for a vehicle with a tricycled wheelbase configuration. In this scheme, the

steering angle is computed as a function of the position and orientation errors of the vehicle relative to the track. Small angle assumption is employed and this assumption is valid only for straight line tracks. The simulation results presented show that the vehicle travels along a straight line with zero position offset and a slowly varying orientation offset. This is impossible to realize in practice. The authors also present an optimal control law [68, 69] to minimize the square of the position and orientation errors. The authors have come up with values for the gains of the controller based on a minimization scheme. Hatwall and Milkulcik [70] present an optimal control strategy to achieve preview control for highway vehicles. In the case of highway driving, the driver looks at the track profile ahead of him and applies the correction at the steering wheel in order to maintain the vehicle on it's course of travel. This is similar to the track geometry identification and guidance of this thesis. Huang [35] discusses a simulation study to search for the optimal value for the controller gains.

Lin et al. [72] presented a trajectory planning scheme for robotic workcells employing robots, conveyors and a vision system. In this paper, the path profile traced by the component that is in motion with respect to the robot is established based on the visual information. The path profile is expressed in joint coordinates of the robot. A second order curve fitting is employed. This approach is similar to the guidance control based on the identified geometry of the track of this thesis.

2.3 Definition of Problem and Scope of the Thesis

From the discussions presented so far, it can be seen that there are a number of areas in which improvements can be made in order to improve the

ability of the AGV to function well in a given environment. The various areas identified are

- Path controllability and kinematic modeling of AGVs to identify a suitable non-redundant combination of driving and steered wheels and also a wheelbase configuration for kinematic control.
- Guidance scheme that is simpler and efficient.
- Guidance control schemes for accurate tracking.
- Prototype AGV development with a modular architecture.

2.3.1 Path Controllability and Kinematic Modeling of AGVs

From the literature review it has been observed that the most popular arrangement is the one in which the front wheel as the driving and steered wheel (tricycle wheelbase configuration). It has been mentioned earlier that Muir and Newman [10] reported that this arrangement is not suitable for kinematic control. Here the term suitability refers to the presence of kinematic singularity (loss of degrees-of-freedom and absence of a unique solution). The absence of kinematic singularity is termed as path controllability in this thesis. This is defined as the ability of the kinematic model to provide wheel speeds, steering angles and steering rates for all values of linear and angular velocities of the vehicle. Hence it is necessary to carry out a detailed analysis to verify mathematically the presence of path controllability for AGVs without redundancy in the driving/steering arrangement and with various combinations of driving and steered wheels for kinematic control. This can be accomplished by considering a vehicle with a driving and steered wheel at the front and rear ends of the vehicle. Since the transformation approach of Muir and

Neuman [10] is general in nature, this approach can be employed for modeling purposes.

2.3.2 Guidance System

From the literature review it can be seen that there is a need to develop a guidance system that has advantages over the conventional systems discussed in section 2.3. It can be inferred from reference [11] that a binary camera vision system employing low cost sensors is a suitable candidate. The binary camera vision employs a simple camera with optic ram chips and a black line (painted or taped) that describes the track to be followed. Light falling on the chips control the voltage level of the optic rams. By reading the voltage level of the ram chip, a black and white image of the track is obtained. Binary digitizing camera for guidance has the following advantages over the other schemes :

- Since the track to be followed by the vehicle can be easily modified, this scheme provides sufficient flexibility and hence the installation and the operating costs are minimal compared to the other schemes.

- Instead of a single point on the floor as seen by the other means of guidance (wire and optical guidances), the camera vision guidance provides a controllable width of view (large number of pixels) of the track to be followed. This facilitates better control of the vehicle and also aids in recognizing path features. This provides the ability to recognize the turning options on the floor.

- The image received for analysis from the binary camera is only two dimensional and does not contain any complex information. As a result of this, image filtering, smoothing and processing are relatively simple and are performed at a faster rate than the schemes employing complex imaging systems.

- The camera employed for guidance is simple in construction and hence the cost is minimal. This reduces the unit cost of AGV.

Owing to these considerations, it can be said that the binary digitizing camera vision technology can become a prime-alternative to the most popular method, the wire guidance approach. The wire guidance does not provide the flexibility for track modifications and imposes heavy demands on the infrastructure of the manufacturing plant and the maintenance crew. For instance, the floor has to be maintained to a level of 1/4", and the vehicles cannot be sprung for fear of losing the guiding signal. It costs as much as $100 per foot to repair or replace ground loops. Considering these operational expenses, the binary camera vision appears to be a better alternative for vehicle guidance.

The technology employed for guidance based on binary camera vision described by Cheng et al. [11] needs to be improved to achieve guidance control of the vehicle at higher speeds of the vehicle. The camera and the interface used in the study are based on an older technology and it takes 70 ms to transfer one frame of image to the memory. The frame rate of the CONCIC-I AGV [11] is 8 frames a second. This needs to be increased to 20 to 25 frames a second so that the vehicle can travel at high speeds. Moreover,

the image window size is fixed and it is not possible to transfer a few rows of the image instead of transferring the entire image data to computer memory. The image processing algorithm is slow and cannot identify road signs namely, left and right turns. Moreover, the camera controller allows interfacing of only one camera. In short, a fast imaging system and processing scheme are needed to identify the track and guide the AGV and also to recognize a set of road signs to take appropriate actions at road junctions.

2.3.3 Guidance Control Schemes to Follow Tracks Accurately

Control schemes that make use of the information concerning the position and orientation of the vehicle relative to the track has to be developed. The controllers for this purpose can take the form of a standard P or PI controller.

Further, it can be seen that the guidance control system of the conventional schemes employ a sensor at the front end and hence assures accurate track following of the front end or a small section of the vehicle. However, it does not assure road following of the rear end of the vehicle. In this, the rear end of the vehicle follows a path which is termed as the *TRACTRIX* in the literature [73]. The concept of tractrix is explained in section 5.1. In order to ensure accurate road following of the rear end of the vehicle as well, a sensor is needed at the rear end of the vehicle. Control laws that make use of the feedback information from the front and rear sensors need to be developed to achieve accurate track following of the front and rear ends of the vehicle (rather a large section of the vehicle) in a short time.

The control schemes mentioned above and available in the literature are feedback control schemes in which the error happens first and the corrective action takes place thereafter. These control schemes make use of the instantaneous position and orientation of the vehicle relative to the track and provide track following of either a small section of the vehicle at the front end or a large section composed of the front and rear ends of the vehicle. Neither do they provide the flexibility of defining track following of any other part of the vehicle nor do they have the intelligence to identify the track geometry.

To alleviate these problems one could employ a feed forward control scheme. The function of this control scheme is to identify the geometric nature of the track and guide the vehicle accordingly. Vehicle guidance can be carried out based on the requirement of the positioning of the AGV relative to the track profile. Hence it provides flexibility in terms of specifying which part of the AGV body has to follow the track. The track geometry can be identified using the sensor data (absolute position feedback from the camera and wheel speeds from shaft encoders) available upto that particular instant of time. It can be said that the vehicle adapts well with a large portion of the track profile rather than a small segment as seen by the camera. Since track profile ahead of the vehicle can be obtained by extrapolation, breaks in the track profile do not affect the performance of the vehicle.

2.3.4 Development of a Prototype AGV for Experiments

The vehicles developed by the other researchers listed in section 2.2 are fixed in nature without considerations for modularity. Since these are

for laboratory research activities, it is essential that the components of the vehicle be of modular form for easier appraisal since the technology is changing rapidly. This modularity is also needed in the architecture of the operating system software. A provision to change the wheelbase configuration is an interesting option as it allows the experimenter to evaluate the performance of one wheelbase configuration over the other for a particular application. Since the basic dimensions of the vehicle is maintained, the performance comparison provides reliable information. A data acquisition system to record the operational variables of the AGV in real time is also mandatory for experimental verification of the vehicle performance. Safety features for fault detection and for stopping the vehicle in case of malfunctions in the components of the vehicle or environmental problems are a prime requisite.

It is imperative to employ computer control in an hierarchical fashion in order to achieve the best tracking performance that is possible. The hierarchical computer control can have two or more stages depending on the type of application. The overall position control of the vehicle can be assigned to the host computer, the speed control of the wheel servos by independent motion controllers, and intensive computational aspects such as the identification of the track profile by a separate processor. This decentralization of tasks reduces the cycle time and therefore improves the tracking performance of the vehicle.

2.4 Layout of the Thesis

The thesis has been divided into three major sections in addition to Chapter 1 and Chapter 2 which describe the general concept of automated vehicles and the literature available in this area.

The first section is devoted to modeling and guidance to achieve accurate tracking. This section is sub-divided into Chapters 3, 4 and 5. The second section presented in Chapter 6, describes the development of an experimental vehicle to implement and test the models developed in the Chapters 3 to 5. The last section (Chapter 7) presents the results of simulations performed and the experimental validation of the mathematical models.

The approach to identify a combination of driving and steered wheels and a wheelbase configuration that is suitable for kinematic control of AGVs is described in Chapter 3. A generalized kinematic model for an AGV with a generic steering column configuration (without redundancy) is presented, and the presence or absence of kinematic singularity for various configurations are investigated. The kinematic model is based on a transformation approach which is preferred to the conventional vector approach. The results of the kinematic modelling scheme are used by the method to identify the geometry of the track described in section 5.4.

The guidance system of the vehicle is discussed in Chapter 4. This chapter describes an optical technique for AGV guidance employing a relatively inexpensive binary digitizing camera. The camera is continuously focussed on the track made by taping or painting the floor. This technique

offers a controllable width of view and flexibility in terms of installation as the track can be easily modified. A fast image processing scheme is used since the image received from the camera being simple in nature. In these respects this technique is superior to the conventional guidance schemes. The on-board computer samples the deviation of the vehicle relative to the track as sensed by the optical sensing means, and steers the vehicle so as to reduce the deviation (position and orientation) to desired values. This chapter also illustrates an algorithm to identify several primitive turn signals that are employed to build road signs.

Chapter 5 presents three guidance control schemes to achieve accurate track following. The first scheme is a conventional approach and it employs single camera guidance scheme with P and PI controllers. The second guidance scheme employs two cameras and controllers with variable gains, based on the track curvature and the instantaneous position of the front and rear ends of the vehicle relative to the track. The third approach is the track profile identification and guidance scheme. In this scheme, the geometric profile of the track on the floor is identified based on the motion parameters of the AGV and the parameters of steering control as obtained from the camera image. The term parameters of steering control is defined in this thesis as the instantaneous position and orientation of the longitudinal axis of the vehicle relative to an instantaneous reference point on the track. Based on the identified profile, the steering commands are computed in order to achieve the desired tracking strategy. The coefficients of the identified track profile are updated using the new set of motion parameters as the vehicle travels along. Different profiles such as polynomials, conic and straight line are considered and the relevant equations are presented. A

variety of driving criteria are defined and the necessary equations for track following are derived.

In order to test these models an experimental vehicle has been built at the Center for Industrial Control. The system design of this experimental vehicle is explained in Chapter 6. This chapter describes the development of the vehicle. The design philosophy and the features of the vehicle are discussed. The mechanical and the electrical components, the computer interfaces, the system software layout, and the safety features of the vehicle are described in detail. The master controller of the vehicle is based on an Intel-286 processor, and the low level servo control is provided by independent motion controllers. A data acquisition system is built into the vehicle to provide experimental data to verify theoretical predictions. The system also features a remote radio link for wireless control. Ultrasonic sensors are employed to avoid collision with any obstacles in the path. This is a unique research vehicle which offers simplicity in construction, flexibility to change over to other wheelbase configurations and facility for continuous enhancement.

Since there are a number of issues addressed in this thesis, the operating software must support a variety of options such as simple camera vision mode, road signs identification and guidance, dual camera mode, and track profile identification and guidance mode.

The results of a large number of simulations and experiments form the basis for Chapter 7. Component calibration experiments are carried out to study the elements of the control loop. Performance studies are conducted

while following a given track profile with and without load for various initial conditions. Experiments are also conducted to study the dynamic response of the guidance controller in response to a sudden change in the location of the track. Simulations are carried out to study the effectiveness of the guidance control scheme using two cameras over the single camera scheme. Simulations are performed using a computer model [35] of the experimental vehicle. The objective of the simulations are to test the correctness of the track profile identification model. Experiments in track following using the track identification scheme are not carried out due to the computational overheads.

Conclusions are presented in Chapter 8. This is followed by the recommendations for further study to improve tracking performance. This is Chapter 9. There are a total of 7 appendices in this thesis. Appendix-A discusses some useful mathematical formulations. The method of obtaining an inverse of a transformation matrix by Paul [23] is reproduced for completeness. Secondly, the method of least squared error solutions is presented. This is used by the image analysis scheme of Chapter 4 at the implementation stage. The least squared error solution is also employed by the track/path identification schemes. The mechanical design details are provided in Appendix-B. The components of the feedback control loop of the vehicle are detailed in Appendix-C. This appendix describes the LM628 precision motion controller chip, PWM servo amplifiers and the incremental encoders. The system diagnostics is explained in Appendix-D. A multiplexer circuit is designed to connect two binary digitizing cameras to a single camera controller. This interface and the software layout is presented in Appendix-E. The operating system software of the vehicle is described in

Appendix-F. Appendix-G summarizes the equations describing the CONCIC-II AGV system for simulation from the Masters thesis of Huang [35]. This is included as the simulation studies are carried out using the package developed by Huang.

2.5 Summary

This chapter discusses the literature available in vehicle design, modeling, guidance and control. The areas of improvements are identified and presented. The proposed guidance scheme and the experimental vehicle for testing are discussed. The layout of the thesis is detailed. The design aspects of the vehicle are based on the type of application. Tricycle wheelbase with a driving and steering wheel, diamond shaped wheelbase with differential drive, four wheel drive and steer are some of the wheelbase configurations in use. Some vehicles are provided with a special wheel called Mccannum wheel which provides three degrees of freedom movement.

The kinematic modeling of AGVs can be achieved using a transformation scheme and a vector approach. From the literature it has been established that the transformation scheme is more elegant and is general in nature. The various guidance schemes for AGVs in the literature are presented. This ranges from the conventional wire-guidance to the most recent laser and dead reckoning control schemes. Several control schemes are proposed in the literature ranging from cross coupled control loop to optimal and sub-optimal controls.

The scope of the thesis and the layout of the thesis are presented. In the scope of the thesis a number of areas of improvements are identified.

The presence of kinematic singularity is considered for the selection of proper combinations of driving and steering wheels for kinematic control. For this purpose development of a generic kinematic model of an AGV for a generic configuration is recommended. This thesis concentrates on an improved guidance scheme which is based on camera vision. A binary camera vision scheme that can identify the track and a set of primitives and road signs is suggested. A dual camera guidance scheme for accurate track following of the front and rear ends of the vehicle is recommended. A feed forward guidance scheme that is based on the identified geometry of the track is proposed. An experimental vehicle that is modular in structure to carry out tests to verify the models has been built.

CHAPTER 3

PATH CONTROLLABILITY AND KINEMATIC MODELING OF AGVs

3.1 Introduction

This chapter presents an approach to select a combination of driving and steered wheels and a wheelbase configuration for AGVs (without redundancy in the driving and steering arrangement) that is suitable for kinematic control. This suitability is termed as *path controllability* in this thesis. It is the absence of kinematic singularity. The concept of path controllability is explained in section 3.2. In order to arrive at the necessary conditions for *path controllability*, a generic non-redundant kinematic modeling scheme based on the transformation technique is presented. A kinematic model provides motion equations to compute the motion parameters of the AGV that corresponds to the motion parameters of the wheels. A Jacobian matrix (J) relates these two sets of motion parameters. The motion parameters of the AGV are the linear and the angular velocities, and those of the wheels are the wheel speeds. The other parameters considered for the motion parameters of the wheels in the case of steerable wheels are the steering angles and the steering rates. The process of computing the motion parameters of the AGV from those of the wheels is the forward kinematic analysis. The inverse kinematic analysis computes the wheel motion parameters from those of the AGV. To compute the inverse kinematics the Jacobian matrix must be invertible. At the points or zones where the Jacobian is non-invertible, kinematic singularities are present. At the singular point one or more degrees of freedom of the AGV cannot be used and it will not be possible to compute the motion parameters of the wheels that provide the desired motion parameters of the AGV.

It will be shown in section 3.3.7 that this Jacobian is a function of the geometrical parameters of the vehicle (i.e. the wheelbase, the inclination of the steering column, and the offset of the steering axis from the wheel axle) and the steering angle of the steerable wheel. Further, from the criteria for *path controllability*, derived in section 3.3.8, kinematic configurations of AGVs that have kinematic singularity for various values of the steering angle are discussed in section 3.4. Section 3.5 shows an arrangement with no kinematic singularity for all values of the steering angle. This is achieved by suitably arranging the steering column and wheelbase configuration. This is the differential drive configuration (no steered wheels) and is the configuration chosen for the experimental vehicle.

From these discussions the objectives of this chapter can be summarized as

(a) to identify a suitable combination of driving and steered wheels and also a wheelbase configuration for kinematic control of AGVs (without redundancy in the driving and steering arrangement) ;

(b) to provide a generic form of the kinematic equations that can be applied to most wheelbase configurations employed in AGVs.

To formulate the generic kinematic model, an AGV with a diamond shaped wheelbase configuration is considered. The front and rear ends of the AGV are provided with an inclined steering column and are attached to the wheel axle at some offset distance. On either side of the geometric center of the AGV, idling non-steerable wheels are provided. This is shown in Fig. 3.1.

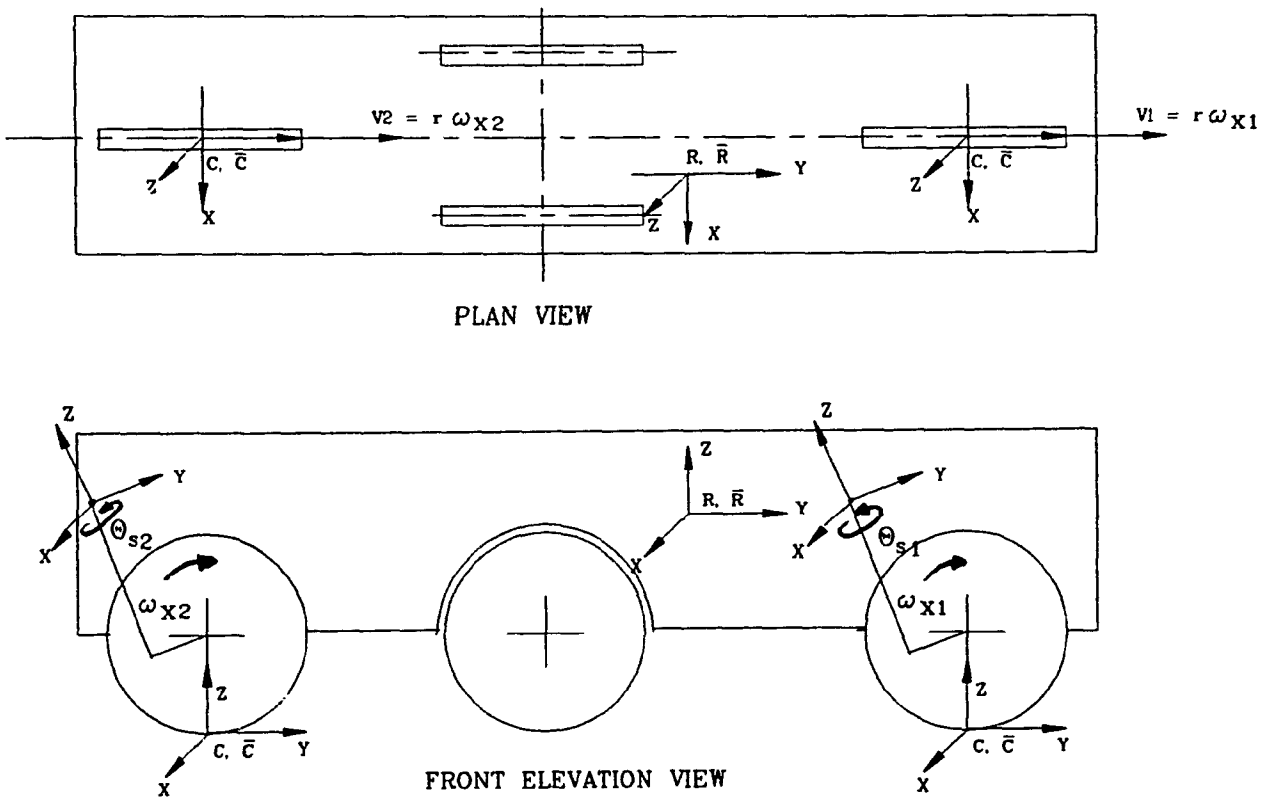

Fig. 3.1 AGV with a Generic Wheelbase Configuration

From the generic kinematic model, the kinematics of a differentially driven AGV is derived. Differentially driven AGVs are considered in this thesis as they provide *path controllability* in addition to the following

- the minimum radius of rotation of the vehicle is equal to one half of the wheel span.

3.2 Concept of Path Controllability

Since the inverse kinematic analysis is vital to kinematic control of an AGV, it becomes mandatory to determine whether the Jacobian is invertible or not before carrying out design and development. A criterion is worked out in this thesis to do so. This criterion is called "*non-redundant path controllability*". This criterion is valid only for vehicles without redundancy in their driving and steering arrangement and hence it is called *non-redundant path controllability.* For simplicity in the discussions this criterion is referred as *path controllability.* It has been mentioned in section 3.1 that this Jacobian relates the motion parameters of the wheels to those of the AGV. Hence invertibility of the Jacobian or the existence of *non-redundant path controllability* can be stated as, a vehicle is said to be *path controllable* if there exists a unique solution for the motion parameters of the wheels corresponding to a given value of linear and angular velocities of the vehicle.

3.3 Kinematic Analysis for Path Controllability

3.3.1 Introduction

The kinematic analysis discussed in the following sections considers only one half of the vehicle due to the symmetry of the configuration shown in Fig. 3.1. To derive the kinematics of the differentially driven AGV the

full configuration is considered. The kinematic formulations are carried out for an AGV with a generic configuration for the steering column. The generic configuration chosen has an inclination (α) in the fore and aft direction, and an offset (s) between the steering axis and the axis of rotation of the steered drive wheel. As a result of steering about an inclined column, velocity components are introduced in the YZ and XZ planes as well. The generalized model presented here includes the necessary equations to compute these additional degrees of freedom. The effect of inclined column steering on the location of the center of the contact patch (which is otherwise known as the contact point) will be detailed in section 3.3.3. Using the cumulative position transformation, an expression to evaluate the component of the angular velocity ($\dot{\psi}$) due to steering will be derived in section 3.3.6.

3.3.2 Coordinate Frame Assignment and Transformations

The coordinate frames assigned for the AGV under consideration are shown in Fig. 3.2. A floor frame 'F' is defined such that the motion parameters of the AGV can be referenced with respect to this frame. The XY-plane of this frame is chosen to be parallel to the floor surface and the Z-axis is perpendicular to the floor. A reference frame 'R' is chosen such that a general formulation is obtained in order to compute the position and orientation of any other point on the AGV relative to the floor frame. The Y-axis of this frame is parallel to the longitudinal axis of the vehicle, the X-axis is directed towards the right side and the Z-axis is parallel to the Z-axis of the floor frame. An instantaneous reference frame '$\bar{R}$' is chosen such that it is located at the same place as the frame 'R'. This frame has the following characteristics. The reference frame 'R' has a velocity relative to the frame '$\bar{R}$' but the position of the frame 'R' with respect to

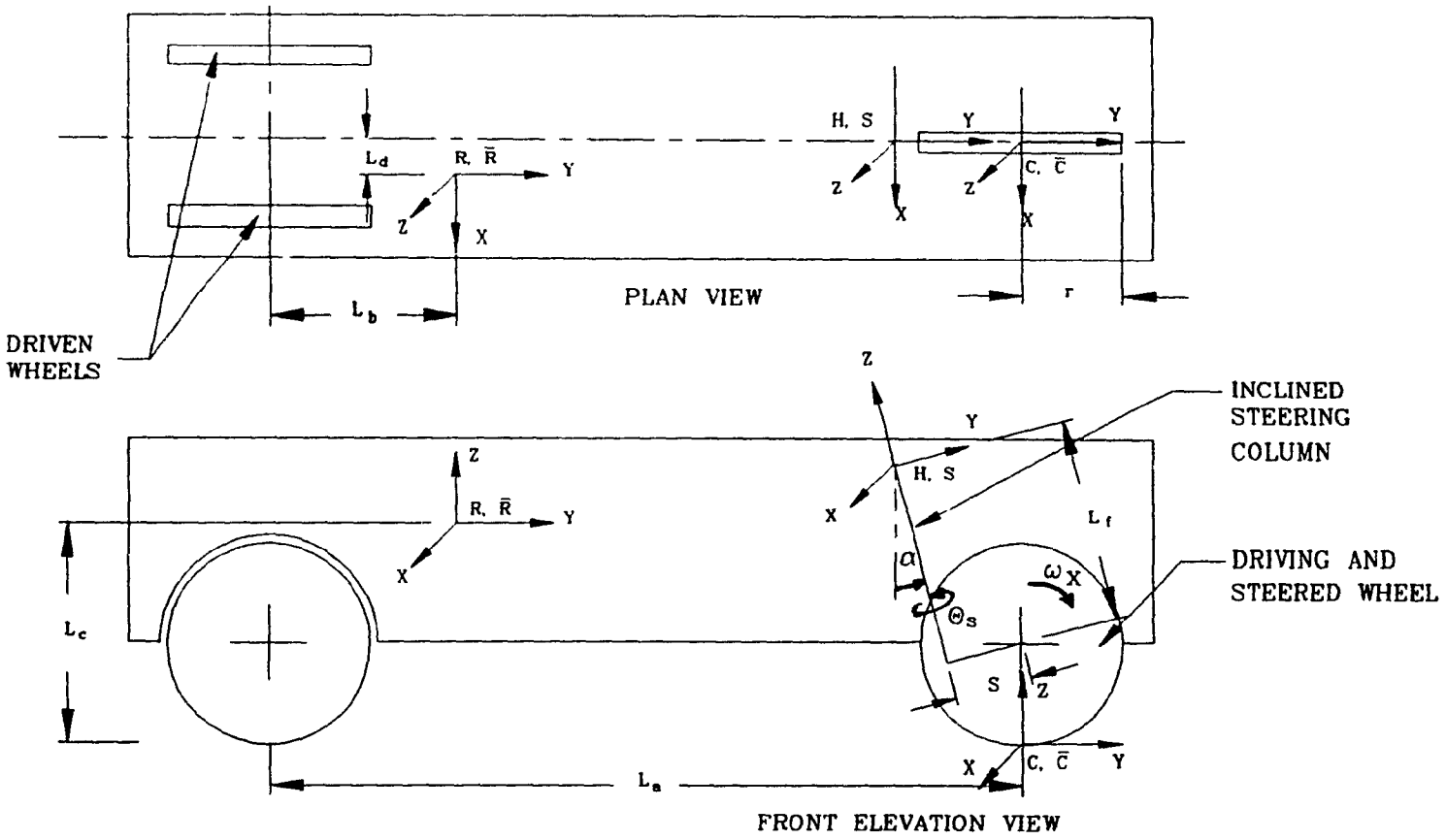

Fig. 3.2 AGV Parameters Definition and Coordinate Frames Assignment

the frame '$\bar{R}$' is zero. The velocity of the frame '$\bar{R}$' relative to the floor frame 'F' is zero.

An hip coordinate frame 'H' is chosen on the stationary portion of the steering column of the AGV. The rotating portion of the steering column houses a frame 'S' which is the steering coordinate frame. The Z-axis of these two frames coincide whereas the orientation of the XY plane of S with respect to H is given by the steering angle 'θ_s'. Coordinate frames 'C' and '$\bar{C}$' are defined for the wheel contact point. As in the case of inertial frame, here also we have an instantaneous coordinate frame '$\bar{C}$'. The Y-axis of the frame 'C' is directed along the direction of travel of the wheel, and the Z-axis is parallel to the wheel plane.

According to the definitions of Muir and Neuman [10,32], the transformations having only constant terms are represented as 'T' and those containing variables (such as the steering angles) are denoted as Φ. Each transformation (T or Φ) has a pre-superscript and a post-subscript such as ${}^{A}\Phi_{B}$, denoting that the transformation for the frame 'B' relative to the frame 'A' is given by the above notation. The inverse and the derivative (velocity transformation) of the transformation ${}^{A}\Phi_{B}$ are represented as $\left[{}^{A}\Phi_{B}\right]^{-1}$ and ${}^{A}\dot{\Phi}_{B}$ respectively. The inverse transformations are computed using the scheme outlined in the Appendix. A. In the following formulations it has been assumed that the contact area between the tire and ground is a point rather than a surface.

3.3.3 Contact Point Location of the Wheel with non-zero Steering Angle

The objective of this section is to provide the position transformation of the contact point of the wheel for non-zero steering angle relative to the reference frame. The relevant coordinate transformations are also presented.

The transformation ${}^{R}T_{H}$ is given by the following transformation equation

$$ {}^{R}T_{H} = \text{Trans}(-L_d,\ L_a - L_f S_\alpha - sC_\alpha - L_b,\ L_f C_\alpha + r - sS_\alpha - L_c)\ \text{Rotate}(X,\alpha) \quad (3.1) $$

Where L_a is the wheelbase distance between the contact points of the driving and driven wheels, L_b is the y-location of the reference frame relative to the driven wheel contact point, L_c is the z-location of the reference frame 'R' relative to the floor level, L_d is the x-location of the hip frame relative to the reference frame 'R', r is the steered wheel radius, L_f is the length of the straight portion of the steering column, s is the offset distance and α is the steering column inclination. These definitions are shown in Fig. 3.2.

Without loss of generality L_c is specifically chosen to be equal to 'r', the wheel radius. This greatly simplifies the final form of the mathematical expressions. The notations such as S_α and C_α refer to the sine and cosine of the angle 'α' respectively.

The transformation ${}^{H}\Phi_{S}$ is a rotational transformation about the Z-axis and is given as

$$ {}^{H}\Phi_{S} = \text{Rotate}(Z,\ \theta_s) \quad (3.2) $$

The transformation ${}^{S}T_{C}$ is computed from

$$ {}^{S}T_{C} = \text{Trans}(0,\ s,\ -L_f)\ \text{Rotate}(x,\ -\alpha)\ \text{Trans}(0,\ 0,\ -r) \tag{3.3} $$

Figure. 3.3 is a transformation graph for the equations (3.1) to (3.3). From this graph, the transformation for the location of the new contact point coordinate frame 'C' relative to the reference frame 'R' is

$$ {}^{R}\Phi_{C} = {}^{R}T_{H}\ {}^{H}\Phi_{S}\ {}^{S}T_{C} \tag{3.4} $$

Substituting the transformation equations (3.1) to (3.3) in (3.4), and rearranging the terms, one obtains

$$ {}^{R}\Phi_{C} = \left[\begin{array}{ccc|c} C_{\theta s} & -C_{\alpha} S_{\theta s} & -S_{\alpha} S_{\theta s} & x \\ C_{\alpha} S_{\theta s} & C_{\alpha} C_{\theta s} + S_{\alpha}^{2} & S_{\alpha} C_{\alpha} (1 - C_{\theta s}) & y \\ S_{\alpha} S_{\theta s} & -S_{\alpha} C_{\alpha} (1 - C_{\theta s}) & C_{\alpha}^{2} + S_{\alpha}^{2} C_{\theta s} & z \\ \hline 0 & 0 & 0 & 1 \end{array}\right] \tag{3.5} $$

$$ x = (r S_{\alpha} - s) S_{\theta s} - L_d \tag{3.6} $$

$$ y = (L_a - L_b) + (r S_{\alpha} - s) (1 - C_{\theta s}) C_{\alpha} \tag{3.7} $$

$$ z = -L_c + (r S_{\alpha} - s) (1 - C_{\theta s}) S_{\alpha} \tag{3.8} $$

The (3x3) matrix element in equation (3.5) is the rotational component and has the property of orthogonality. This means that the inverse and the

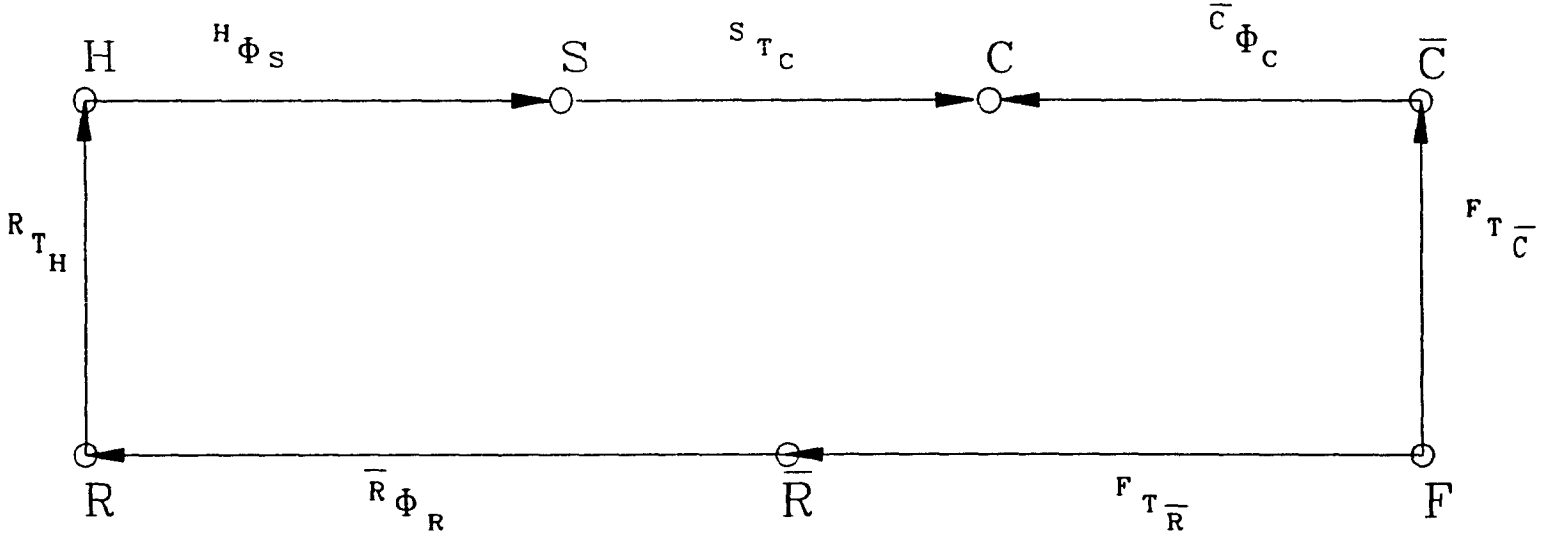

Fig. 3.3 Transformation Graph

transpose of the (3x3) matrix are one and the same and this simplifies the process of inversion. Equation (3.8) gives the location of the contact point in the vertical direction (z-axis) relative to the reference frame $\bar{R}$. Hence the change in the z-location of the contact point is Δz and is obtained from equation (3.8) as

$$\Delta z = - (r S_{\alpha} - s) C_{\theta_s} S_{\alpha} \qquad (3.9)$$

From this it can be inferred that due to steering about an inclined column, the front wheel drops by a distance Δz.

3.3.4 Effective Steering Angle

This sub-section is to provide an analytical expression to compute the effective steering angle (θ_{se}). The effective steering angle is the angle by which the steered wheel has actually turned in the XY-plane of the AGV as a result of the steering angle θ_s about the inclined steering column. For an AGV with a straight steering column, this angle is the same as the steering angle θ_s.

The (3x3) rotation matrix in equation (3.5) can also be obtained by performing rotations about the three principal axes located at the origin of the hip/steering coordinate frame as shown in Fig. 3.4. The x, y and z axes are parallel to that of the reference frame. First the yaw rotation (θ_{se}) is performed about the z-axis of the original coordinate frame. This is followed by a rotation (β) about the new (transformed) y-axis. Finally the rotation γ is carried out about the x-axis of the transformed coordinate frame. These operations are shown in Fig. 3.5. The overall transformation is

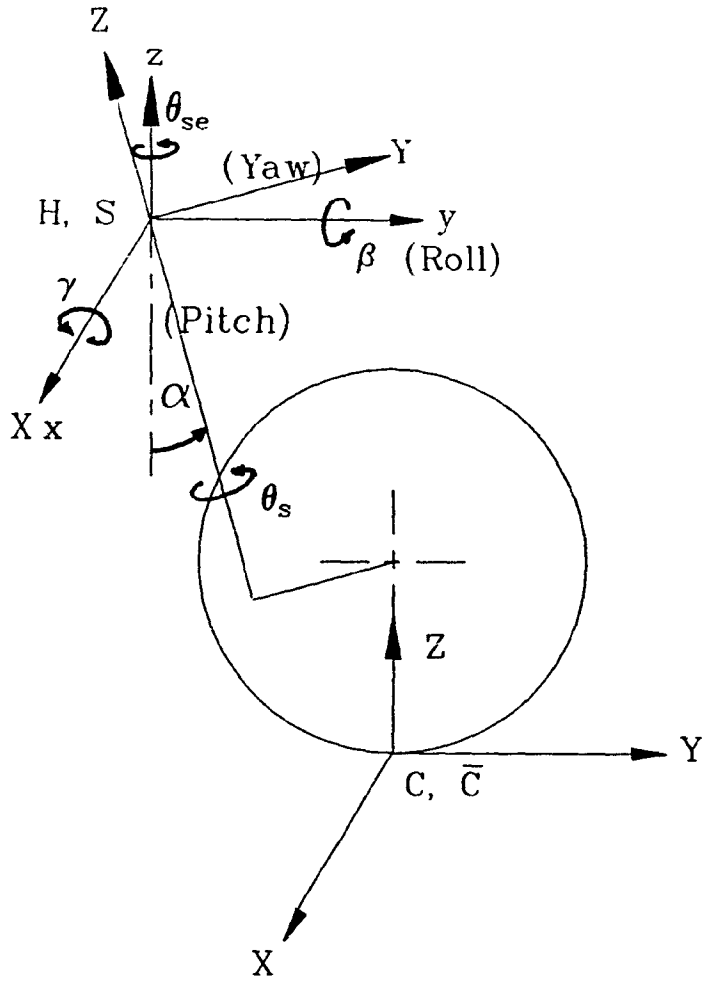

Fig. 3.4 Steered Wheel Oientation Definitions

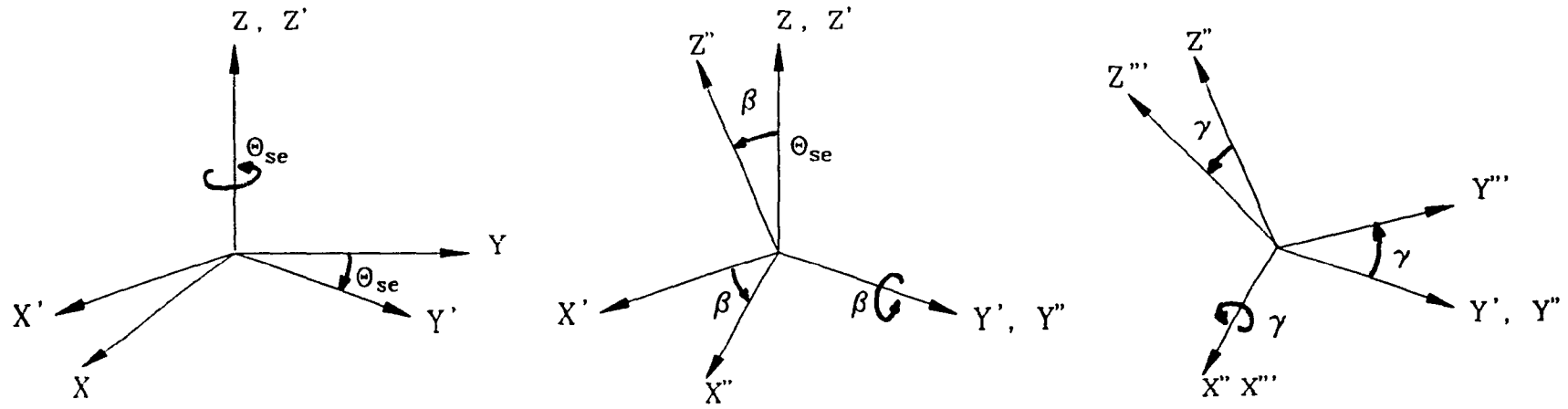

Fig 3.5 Yaw, Roll and Pitch Rotations and Transformations

$$\text{Rot}(\theta_{se}, \beta, \gamma) = \text{Rot}(z, \theta_{se})\ \text{Rot}(y', \beta)\ \text{Rot}(x'', \gamma)$$

$$= \begin{bmatrix} C_{\theta se}\, C_{\beta} & C_{\theta se} S_{\beta} S_{\gamma} - S_{\theta se} C_{\gamma} & C_{\theta se} S_{\beta} C_{\gamma} + S_{\theta se} S_{\gamma} \\ S_{\theta se}\, C_{\beta} & S_{\theta se} S_{\beta} S_{\gamma} + C_{\theta se} C_{\gamma} & S_{\theta se} S_{\beta} C_{\gamma} - C_{\theta se} S_{\gamma} \\ -S_{\beta} & C_{\beta} S_{\gamma} & C_{\beta}\, C_{\gamma} \end{bmatrix} \quad (3.10)$$

Comparing the elements (1,1), (1,2) and (1,3) of the two matrices given by the equations (3.5) and (3.10), the effective steering angle θ_{se} can be expressed as

$$\theta_{se} = \tan^{-1} \left[C_{\alpha} \tan \theta_{s} \right] \quad (3.11)$$

3.3.5 Effective Wheelbase Distance

From equation (3.7), it can be said that steering about an inclined column with an offset distance changes the wheelbase distance between the contact points of the steered driving wheel and the driven wheels. An expression to compute the effective wheel base distance L_{ae} can be derived from equation (3.7). Substituting L_b equal to zero, the resulting expression for L_{ae} is

$$L_{ae} = L_a + (r S_{\alpha} - s)(1 - C_{\theta s})\, C_{\alpha} \quad (3.12)$$

3.3.6 Angular Velocity term due to Steering

An analytical expression to compute the angular velocity of the reference frame ($\dot{\psi}_1$) due to steering is derived in this section. This parameter will be used in section 3.3.7 to compute the cumulative angular

velocity ($\dot{\psi} = \dot{\theta}_r$) of the reference frame due to driving and steering. The rate of change of x position of the contact point due to $\dot{\theta}_s$ is obtained by differentiating the expression in equation (3.6) with respect to time. The rate function $\dot{x}$ is given by

$$\dot{x} = (r S_\alpha - s) C_{\theta s} \dot{\theta}_s \tag{3.13}$$

The velocity term $\dot{x}$ produces an angular velocity $\dot{\psi}_1$ about the axle carrying the driven wheels. The distance between the contact point of the steered driving wheel and the driven wheel is given by the effective wheelbase distance L_{ae}. The angular velocity is

$$\dot{\psi}_1 = \frac{\dot{x}}{L_{ae}} = \frac{(r S_\alpha - s) C_{\theta s} \dot{\theta}_s}{L_a + (r S_\alpha - s)(1 - C_{\theta s}) C_\alpha} \tag{3.14}$$

3.3.7 Jacobian Matrix Formulation and Forward Kinematics

For the configuration chosen for the steering column, the motion parameters of the reference frame are the linear velocities v_{rx}, v_{ry} and v_{rz} along the X, Y and Z directions respectively, and the angular velocities $\dot{\lambda}$, $\dot{\epsilon}$ and $\dot{\theta}_r$ about the X, Y and Z axes respectively. The motion parameters of the wheel are the angular velocity ω_x about an axis passing through the wheel center and the steering rate $\dot{\theta}_s$ about the steering axis. This thesis considers one more parameter for the velocity formulation. This is the angular velocity of wheel slip $\dot{\theta}_c$ at the point of contact about the Z-axis of the contact point coordinate frame. This is not an independent variable and is a function of the steering rate $\dot{\theta}_s$ and the angular velocity $\dot{\theta}_r$ of the AGV. Initially the formulations are carried out with the assumption that $\dot{\theta}_c$ is an

independent variable, and subsequently appropriate substitutions are carried out to provide the expressions in terms of independent wheel variables.

Referring to the transformation graph of Fig. 3.3, the position transformation for the reference frame 'R' relative to the instantaneous reference frame '$\bar{R}$' can be expressed as

$$ {}^{\bar{R}}\Phi_{R} = \left[{}^{F}T_{\bar{R}} \right]^{-1} {}^{F}T_{\bar{C}} \, {}^{\bar{C}}\Phi_{C} \left[{}^{S}T_{C} \right]^{-1} \left[{}^{H}\Phi_{S} \right]^{-1} \left[{}^{R}T_{H} \right]^{-1} \tag{3.15} $$

Here the position transformation ${}^{\bar{R}}\Phi_{R}$ is an unity transformation as the two frames R and $\bar{R}$ are at the same location. Differentiating the expression for the position transformation in equation (3.15) with respect to time results in the velocity transformation

$$ \begin{aligned} {}^{\bar{R}}\dot{\Phi}_{R} = {} & \left[{}^{F}T_{\bar{R}} \right]^{-1} {}^{F}T_{\bar{C}} \, {}^{\bar{C}}\dot{\Phi}_{C} \left[{}^{S}T_{C} \right]^{-1} \left[{}^{H}\Phi_{S} \right]^{-1} \left[{}^{R}T_{H} \right]^{-1} + \\ & \left[{}^{F}T_{\bar{R}} \right]^{-1} {}^{F}T_{\bar{C}} \, {}^{\bar{C}}\Phi_{C} \left[{}^{S}T_{C} \right]^{-1} \left[{}^{H}\dot{\Phi}_{S} \right]^{-1} \left[{}^{R}T_{H} \right]^{-1} \end{aligned} \tag{3.16} $$

Here the elements of the transformation ${}^{F}T_{\bar{C}}$ are not available. Hence referring back to the transformation graph, the transformation ${}^{F}T_{\bar{C}}$ can be written in terms of other known transformations as

$$ {}^{F}T_{\bar{C}} = {}^{F}T_{\bar{R}} \, {}^{\bar{R}}\Phi_{R} \, {}^{R}T_{H} \, {}^{H}\Phi_{S} \, {}^{S}T_{C} \left[{}^{\bar{C}}\Phi_{C} \right]^{-1} \tag{3.17} $$

Substituting (3.17) in (3.16), eliminating the unity transformations ${}^{\bar{R}}\Phi_{R}$ and ${}^{\bar{C}}\Phi_{C}$, and after simplifying, one obtains

$$\bar{R}\dot{\Phi}_R = {}^R T_H \; {}^H\Phi_S \; {}^S T_C \; \bar{C}\dot{\Phi}_C \left[{}^S T_C \right]^{-1} \left[{}^H\Phi_S \right]^{-1} \left[{}^R T_H \right]^{-1} +$$

$$ {}^R T_H \; {}^H\Phi_S \left[{}^H\dot{\Phi}_S \right]^{-1} \left[{}^R T_H \right]^{-1} \qquad (3.18)$$

The transformation matrices ${}^R T_H$, ${}^H\Phi_S$ and ${}^S T_C$ are derived earlier and are given by equations (3.1), (3.2) and (3.3). The contact point velocity transformation $\bar{C}\dot{\Phi}_C$ is derived in the appendix. The quantity ${}^H\dot{\Phi}_S$ is evaluated by differentiating equation (3.2). Substituting the transformation values in the equation (3.18) and simplifying the following results are obtained. The transformation ${}^R T_H \; {}^H\Phi_S \; {}^S T_C \; \bar{C}\dot{\Phi}_C \left[{}^S T_C \right]^{-1} \left[{}^H\Phi_S \right]^{-1} \left[{}^R T_H \right]^{-1}$ has been computed to be of the following form

$$\begin{bmatrix} 0 & -(C_{\theta s} S_\alpha^2 + C_\alpha^2)\dot{\theta}_c - S_\alpha C_\alpha (1 - C_{\theta s})\dot{\theta}_s & b_{14} \\ (C_{\theta s} S_\alpha^2 + C_\alpha^2)\dot{\theta}_c & 0 & S_\alpha S_{\theta s} \dot{\theta}_c \quad b_{24} \\ S_\alpha C_\alpha (1 - C_{\theta s})\dot{\theta}_s & -S_\alpha S_{\theta s} \dot{\theta}_c & 0 \quad b_{34} \\ 0 & 0 & 0 \quad 0 \end{bmatrix} \qquad (3.19)$$

here

$$b_{14} = C_{\theta s} v_{cx} - C_\alpha S_{\theta s} v_{cy} + [(1 - C_{\theta s}) (r S_\alpha - s) C_\alpha - L_c S_\alpha C_\alpha (1 - C_{\theta s}) + (L_a - L_b) (C_\alpha^2 + C_{\theta s} S_\alpha^2)] \dot{\theta}_c$$

$$b_{24} = C_\alpha S_{\theta s} v_{cx} + (S_\alpha^2 + C_{\theta s} C_\alpha^2) v_{cy} + (s S_{\theta s} + L_d (C_{\theta s} S_\alpha^2 + C_\alpha^2)) \dot{\theta}_c - L_d C_\alpha \dot{\theta}_c$$

$$b_{34} = S_\alpha S_{\theta s} v_{cx} - (1 - C_{\theta s}) S_\alpha C_\alpha v_{cy} + [(L_a - L_b) S_\alpha S_{\theta s} +$$

$$L_d\, S_\alpha\, C_\alpha\, (1 - C_{\theta_s})\,]\,\dot{\theta}_c$$

The term ${}^{R}T_{H}\ {}^{H}\Phi_{S}\ \left[{}^{H}\dot{\Phi}_{S}\right]^{-1}\left[{}^{R}T_{H}\right]^{-1}$ of equation (3.18) after substitutions and simplifications yields

$$\begin{bmatrix} 0 & C_\alpha\,\dot{\theta}_s & S_\alpha\,\dot{\theta}_s & (s + (l_b - l_a)C_\alpha)\,\dot{\theta}_s \\ -C_\alpha\,\dot{\theta}_s & 0 & 0 & -l_d\,C_\alpha\,\dot{\theta}_s \\ -S_\alpha\,\dot{\theta}_s & 0 & 0 & -l_a\,S_\alpha\,\dot{\theta}_s \\ 0 & 0 & 0 & 0 \end{bmatrix} \qquad (3.20)$$

The overall transformation for the inertial frame velocity ${}^{\bar{R}}\dot{\Phi}_{R}$, which is the sum of the two matrix expressions (3.19) and (3.20) is given by

$$\begin{bmatrix} 0 & B_{12} & B_{13} & B_{14} \\ B_{21} & 0 & B_{23} & B_{24} \\ B_{31} & B_{32} & 0 & B_{34} \\ 0 & 0 & 0 & 0 \end{bmatrix} \qquad (3.21)$$

Where the elements of the matrix are

$$B_{12} = -(C_{\theta_s} S_\alpha^2 + C_\alpha^2)\,\dot{\theta}_c + C_\alpha\,\dot{\theta}_s \quad ; \quad B_{13} = -(1 - C_{\theta_s})\,S_\alpha\,C_\alpha\,\dot{\theta}_c + S_\alpha\,\dot{\theta}_s$$

$$B_{14} = C_{\theta_s} v_{cx} - C_\alpha\, S_{\theta_s}\, v_{cy} + [\,(1 - C_{\theta_s})(r\,S_\alpha - s)\,C_\alpha - L_c\,S_\alpha\,C_\alpha\,(1 - C_{\theta_s}) + (L_a - L_b)(C_\alpha^2 + C_{\theta_s} S_\alpha^2)\,]\,\dot{\theta}_c + \{\, s + (L_b - L_a)C_\alpha \,\}\,\dot{\theta}_s$$

$$B_{21} = (C_{\theta_s} S_\alpha^2 + C_\alpha^2)\,\dot{\theta}_c - C_\alpha\,\dot{\theta}_s \quad ; \quad B_{23} = S_{\theta_s} S_\alpha\,\dot{\theta}_c$$

$$B_{24} = C_\alpha S_{\theta s} v_{cx} + (S_\alpha^2 + C_{\theta s} C_\alpha^2) v_{cy} + \{ s S_{\theta s} + L_d (C_{\theta s} S_\alpha^2 + C_\alpha^2) \} \dot{\theta}_c - L_d C_\alpha \dot{\theta}_s$$

$$B_{31} = (1 - C_{\theta s}) S_\alpha C_\alpha \dot{\theta}_c - S_\alpha \dot{\theta}_s \quad ; \quad B_{32} = - S_{\theta s} S_\alpha \dot{\theta}_c$$

$$B_{34} = S_\alpha S_{\theta s} v_{cx} - (1 - C_{\theta s}) S_\alpha C_\alpha v_{cy} + [(L_a - L_b) S_\alpha S_{\theta s} + L_d S_\alpha C_\alpha (1 - C_{\theta s})] \dot{\theta}_c - L_a S_\alpha \dot{\theta}_s$$

The elements of this transformation and those in equation (A.59) in the appendix can be compared, and the AGV motion parameters $\{ v_{rx}, v_{ry}, v_{rz}, \dot{\theta}_r, \dot{\varepsilon}, \dot{\lambda} \}^t$ can be expressed in terms of the wheel velocities v_{cx}, v_{cy}, v_{cz}, $\dot{\theta}_c$ and $\dot{\theta}_s$ as

$$v_{rx} = B_{14} = C_{\theta s} v_{cx} - C_\alpha S_{\theta s} v_{cy} + [(1 - C_{\theta s}) (r S_\alpha - s) C_\alpha - L_c S_\alpha C_\alpha (1 - C_{\theta s}) + (L_a - L_b) (C_\alpha^2 + C_{\theta s} S_\alpha^2)] \dot{\theta}_c + \{ s + (L_b - L_a) C_\alpha \} \dot{\theta}_s \qquad (3.22)$$

$$v_{ry} = B_{24} = C_\alpha S_{\theta s} v_{cx} + (S_\alpha^2 + C_{\theta s} C_\alpha^2) v_{cy} + \{s S_{\theta s} + L_d (C_{\theta s} S_\alpha^2 + C_\alpha^2) \} \dot{\theta}_c - L_d C_\alpha \dot{\theta}_s \qquad (3.23)$$

$$v_{rz} = B_{34} = S_\alpha S_{\theta s} v_{cx} - (1 - C_{\theta s}) S_\alpha C_\alpha v_{cy} + [(L_a - L_b) S_\alpha S_{\theta s} + L_d S_\alpha C_\alpha (1 - C_{\theta s})] \dot{\theta}_c - L_a S_\alpha \dot{\theta}_s \qquad (3.24)$$

$$\dot{\theta}_r = B_{21} = (C_{\theta s} S_\alpha^2 + C_\alpha^2) \dot{\theta}_c - C_\alpha \dot{\theta}_s \qquad (3.25)$$

$$\dot{\varepsilon} = B_{31} = - (1 - C_{\theta s}) S_\alpha C_\alpha \dot{\theta}_c + S_\alpha \dot{\theta}_s \qquad (3.26)$$

$$\dot{\lambda} = B_{32} = S_{\theta s}\, S_{\alpha}\, \dot{\theta}_{s} \tag{3.27}$$

The linear and angular velocities of the wheel $\{v_{cx},\ v_{cy},\ v_{cz},\ \dot{\theta}_{c},\ \dot{\theta}_{s}\}^{t}$ in terms of the independent wheel variables are given below :

The linear velocity of the wheel v_{cx} along the x-direction is equal to zero. The linear velocity of the wheel (v_{cy}) in the direction of travel of the wheel is given by the product of the angular velocity of the wheel (ω_{x}) and the wheel radius (r), i.e.

$$v_{cz} = 0 \qquad v_{cy} = r\,\omega_{x} \quad \text{and} \quad v_{cx} = 0 \tag{3.28}$$

The steering rate ($\dot{\theta}_{s}$) is an independent variable. The angular velocity of the AGV is composed of components due to wheel speed and steering rate. The component due to wheel speed can be derived from Fig. 3.6 as below.

$$\dot{\psi}_{2} = \frac{r\,\omega_{x}\, S_{\theta se}}{L_{ae}} \tag{3.29}$$

The quantity θ_{se} is the effective steering angle given by equation (3.11). The distance L_{ae} is the effective wheelbase distance and is given by equation (3.12). The component ($\dot{\psi}_{1}$) due to the steering rate has been derived earlier as in equation (3.14). Hence the angular velocity $\dot{\theta}_{r}$ of the AGV about the reference frame is the sum of these two rates and is given as

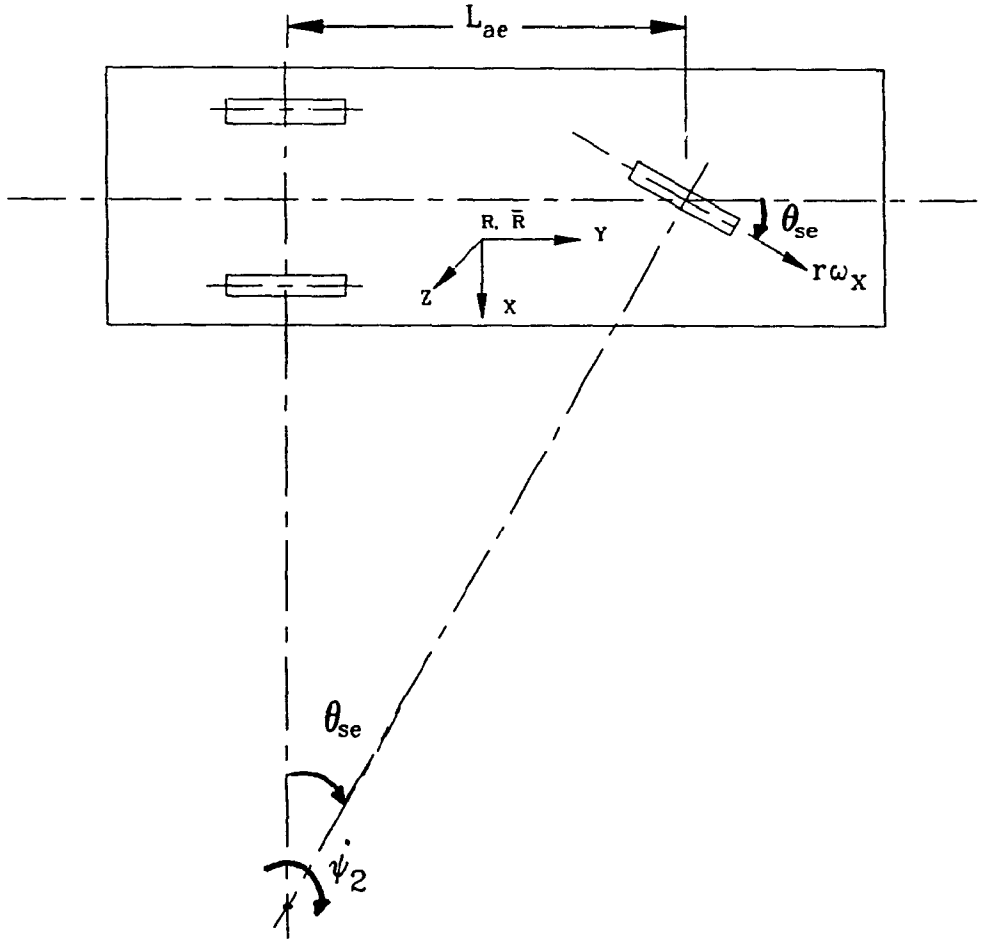

Fig. 3.6 AGV Motion Parameters Definition

$$\dot{\theta}_r = \dot{\psi}_2 + \dot{\psi}_1 = \left[\frac{r\ \omega_x\ S_{\theta se}}{L_{ae}} + \frac{(rS_\alpha - s)\ C_{\theta s}\ \dot{\theta}_s}{L_{ae}} \right] \tag{3.30}$$

Substituting the equation for $\dot{\theta}_r$ from (3.30) in equation (3.25), the angular velocity of the contact point in the XY-plane can be expressed as

$$\dot{\theta}_c = \frac{1}{(C_{\theta s}\ S_\alpha^2 + C_\alpha^2)} \left[\frac{r\ \omega_x\ S_{\theta se}}{L_{ae}} + \frac{(rS_\alpha - s)\ C_{\theta s}\ \dot{\theta}_s}{L_{ae}} + C_\alpha\ \dot{\theta}_s \right] \tag{3.31}$$

Equation (3.31) for $\dot{\theta}_c$ is substituted in equations (3.22) to (3.27). From this, the AGV velocity terms $\{ v_{rx},\ v_{ry},\ v_{rz},\ \dot{\theta}_r,\ \dot{\varepsilon},\ \dot{\lambda} \}^t$ can be expressed as a function of the independent variables of the wheels $\{\omega_x,\ \dot{\theta}_s\}^t$ in a matrix - form as below :

$$\begin{bmatrix} v_{rx} \\ v_{ry} \\ v_{rz} \\ \dot{\theta}_r \\ \dot{\varepsilon} \\ \dot{\lambda} \end{bmatrix} = \begin{bmatrix} d_{11} & d_{12} \\ d_{21} & d_{22} \\ d_{31} & d_{32} \\ d_{41} & d_{42} \\ d_{51} & d_{52} \\ 0 & d_{62} \end{bmatrix} \begin{bmatrix} \omega_x \\ \dot{\theta}_s \end{bmatrix} \tag{3.32}$$

i.e. $\{ v_{rx},\ v_{ry},\ v_{rz},\ \dot{\theta}_r,\ \dot{\varepsilon},\ \dot{\lambda} \}^t = [\ J\ ]\ \{ \omega_x,\ \dot{\theta}_s \}^t$ (3.33)

[J] is the Jacobian matrix of the steered driving wheel with an inclined steering column and an offset distance and is a (6 x 2) matrix, i.e. over determined system. The coefficients of the Jacobian matrix are

$$d_{11} = - C_\alpha S_{\theta s} r + \left[-s C_\alpha (1 - C_{\theta s}) + (L_a - L_b)(C_\alpha^2 + C_{\theta s} S_\alpha^2)\right] \frac{1}{(C_{\theta s} S_\alpha^2 + C_\alpha^2)} \left[\frac{r S_{\theta se}}{L_{ae}}\right] \tag{3.34}$$

$$d_{12} = \left[-s C_\alpha (1 - C_{\theta s}) + (L_a - L_b)(C_\alpha^2 + C_{\theta s} S_\alpha^2)\right] \frac{1}{(C_{\theta s} S_\alpha^2 + C_\alpha^2)} \left[\frac{(rS_\alpha - s) C_{\theta s}}{L_{ae}} + C_\alpha\right] + s + (L_b - L_a)C_\alpha \tag{3.35}$$

$$d_{21} = (S_\alpha^2 + C_{\theta s} C_\alpha^2) r + \left[s S_{\theta s} + L_d (C_{\theta s} S_\alpha^2 + C_\alpha^2)\right] \frac{1}{(C_{\theta s} S_\alpha^2 + C_\alpha^2)} \left[\frac{r S_{\theta se}}{L_{ae}}\right] \tag{3.36}$$

$$d_{22} = \left[s S_{\theta s} + L_d (C_{\theta s} S_\alpha^2 + C_\alpha^2)\right] \frac{1}{(C_{\theta s} S_\alpha^2 + C_\alpha^2)} \left[\frac{(rS_\alpha - s) C_{\theta s}}{L_{ae}} + C_\alpha\right] - L_d C_\alpha \tag{3.37}$$

$$d_{31} = - (1 - C_{\theta s}) S_\alpha C_\alpha r + \left[(L_a - L_b) S_\alpha S_{\theta s} + L_d S_\alpha C_\alpha (1 - C_{\theta s})\right] \frac{1}{(C_{\theta s} S_\alpha^2 + C_\alpha^2)} \left[\frac{r S_{\theta se}}{L_{ae}}\right] \tag{3.38}$$

$$d_{32} = \left[(L_a - L_b) S_\alpha S_{\theta s} + L_d S_\alpha C_\alpha (1 - C_{\theta s})\right] \frac{1}{(C_{\theta s} S_\alpha^2 + C_\alpha^2)} \left[\frac{(rS_\alpha - s) C_{\theta s}}{L_{ae}} + C_\alpha\right] - L_a S_\alpha \tag{3.39}$$

$$d_{41} = \frac{r\ S_{\theta se}}{L_{ae}} \qquad (3.40) \qquad ; \quad d_{42} = \frac{(rS_{\alpha} - s)\ C_{\theta s}}{L_{ae}} \qquad (3.41)$$

$$d_{51} = -(1 - C_{\theta s})\ S_{\alpha}\ C_{\alpha}\ \frac{1}{(C_{\theta s}\ S_{\alpha}^2 + C_{\alpha}^2)} \left[\frac{r\ S_{\theta se}}{L_{ae}} \right] \qquad (3.42)$$

$$d_{52} = -(1 - C_{\theta s})\ S_{\alpha}\ C_{\alpha}\ \frac{1}{(C_{\theta s}\ S_{\alpha}^2 + C_{\alpha}^2)} \left[\frac{(rS_{\alpha} - s)\ C_{\theta s}}{L_{ae}} + C_{\alpha} \right] + S_{\alpha} \qquad (3.43)$$

$$d_{62} = S_{\theta s}\ S_{\alpha} \qquad (3.44)$$

The above equations (3.32) to (3.44) are the necessary expressions to perform the forward kinematic analysis to compute the AGV motion parameters in terms of the wheel motion parameters.

3.3.8 Inverse Kinematic Analysis and Reduced Order Jacobian Matrix

For inverse kinematic analysis, it is necessary to compute the wheel motion parameters for the given AGV motion parameters. The inverse kinematic model of equation (3.33) can be written as

$$\{\ \omega_x,\ \dot{\theta}_s\ \}^t = [J^*]\ \{\ v_{rx},\ v_{ry},\ v_{rz},\ \dot{\theta}_r,\ \dot{\varepsilon},\ \dot{\lambda}\ \}^t \qquad (3.45)$$

where $[J^*]$ is the pseudo-inverse of [J].

This equation suggests that the two unknown motion parameters of the wheels are computed from the six velocity components of the AGV. Nevertheless, it should be noted that there are only two velocity terms associated with the AGV motion parameters that can be specified

independently. They are the linear velocity $\mathbf{v}_{ry}$ and the angular velocity $\dot{\theta}_r$. The order of equation (3.45) can be reduced to

$$\{ \omega_x, \dot{\theta}_s \}^t = [\hat{J}]^{-1} \{ \mathbf{v}_{ry}, \dot{\theta}_r \}^t \tag{3.46}$$

Where $\hat{J}$ is the reduced order Jacobian formed by the coefficients of the linear and angular velocity vectors $\mathbf{v}_{ry}$ and $\dot{\theta}_r$ respectively. The inverse model provides an unique solution if and only if the inverse of the reduced order Jacobian $\hat{J}$ exists. This requires that the determinant of the reduced order Jacobian should not be equal to zero. Equation (3.46) can be rewritten as

$$\begin{bmatrix} \omega_x \\ \dot{\theta}_s \end{bmatrix} = \frac{1}{det} \begin{bmatrix} d_{42} & -d_{22} \\ -d_{41} & d_{21} \end{bmatrix} \begin{bmatrix} \mathbf{v}_{ry} \\ \dot{\theta}_r \end{bmatrix} \tag{3.47}$$

Where d_{21}, d_{42}, d_{41} and d_{22} are given by equations (3.36) to (3.41), and *det* is the determinant of $\hat{J}$, and is

$$det = d_{21} * d_{42} - d_{41} * d_{22} \tag{3.48}$$

3.4 Criteria for Path Controllability of AGVs with Steering Column

In this section, criteria for *non-redundant path controllability* is investigated using the determinant of the reduced order Jacobian matrix (3.49) derived in the previous section. Substituting the values of d_{21}, d_{42}, d_{41} and d_{22} from (3.36) to (3.41) in the determinant equation (3.48) and rearranging the terms, the following decision equation is obtained

$$-L_{ae}\, r \left\{ C_\alpha^2 S_\alpha^2 (s - rS_\alpha)\, C_{\theta s}^3 - (s - rS_\alpha)\, C_{\theta s}^2 + S_\alpha^2\, C_\alpha^2 (s - rS_\alpha)\, C_{\theta s} + s\, C_\alpha\, S_{\theta s}\, S_{\theta se} \right\} = 0 \qquad (3.49)$$

The expression on the left side of equation (3.49) becomes zero while the polynomial function in θ_s tends to zero (providing a set of conditions) in addition to the two trivial conditions ($r = 0$ and $L_{ae} = 0$). If L_{ae} is zero and $r \neq 0$, then the vehicle is a mono-wheeled vehicle, i.e. a vehicle with only single wheel. A mono-wheeled vehicle has kinematic singularity and is uncontrollable. Considering the solution of equation (3.49) for different steering column configurations shown in Fig. 3.7, the following results are obtained.

3.4.1 Steering Column with Inclination and no Offset Distance

Substituting $s = 0$ in (3.49) and observing that S_α is non-zero, one obtains the following after simplifications:

i.e. $$r\, S_\alpha\, C_{\theta s} \left(C_\alpha^2 S_\alpha^2\, C_{\theta s}^2 - C_{\theta s} + S_\alpha^2\, C_\alpha^2 \right) = 0 \qquad (3.50)$$

The conditions for equation (3.50) to vanish are

i) $C_{\theta s} = 0 \quad ====> \quad \theta_s = \pi / 2$ and/or

ii) The solution for the quadratic expression in cosine of θ is

$$C_{\theta s} = \frac{1 \pm 1}{2\, S_\alpha^2\, C_\alpha^2} = \frac{2(1 \pm 1)}{\mathrm{Sin}^2 2\alpha}$$

In this expression, the denominator cannot be greater than one whereas the numerator can be either 0 or 4. The value 4 for the numerator is not valid

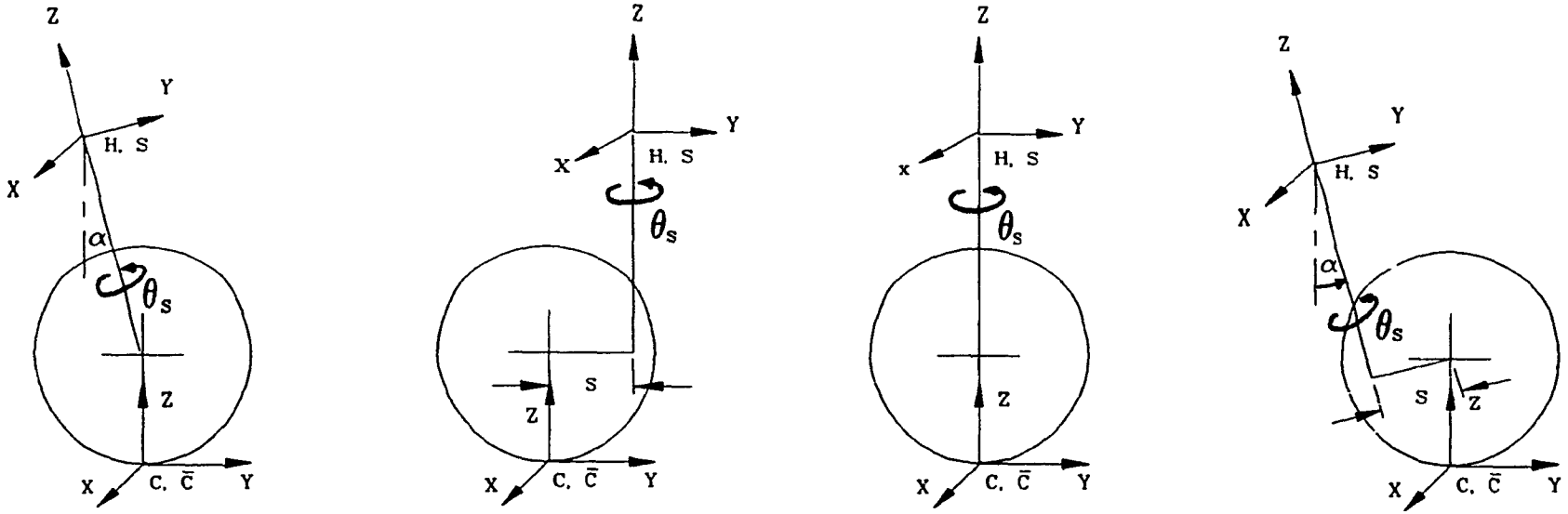

Case : 1	Case : 2	Case : 3	Case : 4
$\alpha \neq 0$	$\alpha = 0$	$\alpha = 0$	$\alpha \neq 0$
$s = 0$	$s \neq 0$	$s = 0$	$s \neq 0$

Fig. 3.7 Configurations of the Steering Column

as C_{θ_s} can never assume a value greater than one. Hence the valid solution is $C_{\theta_s} = 0$.

i.e. $$\theta_s = (2n + 1)\,\pi/2, \quad \text{where } n = 0, 1, 2, \ldots \tag{3.51}$$

Theorem - 3.1 : For an AGV with an inclined steering column, the *path controllability* exists at all steering angles except at $(2n+1)\pi/2$, where n = 0, 1, 2, ...

3.4.2 Steering Column with Offset Distance and no Inclination

The condition equation for an AGV with a straight steering column with only an offset distance (s) is obtained by substituting $\alpha = 0$ in equation (3.49) and is

$$s\,(\,2\,C^2_{\theta_s} - 1) = 0 \tag{3.52}$$

Conditions derived from this are

i) $s = 0$, which is never true for the case under consideration. (3.53)

ii) The solution for the second order polynomial in cosine of θ_s is

$$\theta_s = (2n + 1)\,\pi/4, \quad \text{and } n = 0, 1, 2, \ldots \tag{3.54}$$

Theorem - 3.2 : For an AGV having a straight steering column with an offset distance (s), the determinant is non-zero for all steering angles except for $(2n+1)\,\pi/4$, where n = 0, 1, 2, ...

3.4.3 Steering Column with no Offset Distance and no Inclination

This configuration is widely used in most of the AGVs. For this case, the criterion for the presence of singularity is obtained directly from equation (3.53). This equation suggests that if the offset distance s is

equal to zero, the determinant becomes zero for all values of the steering angle. This configuration should be avoided for kinematic control of AGVs.

Theorem - 3.3 : An AGV with a straight steering column ($\alpha = 0$) and no offset distance ($s = 0$) does not provide *path controllability* for all values of steering angles.

3.4.4 Steering Column with Inclination and Offset Distance

For this case no analytical solution exists due to the presence of the term ($s\, C_{\alpha}\, S_{\theta_s}\, S_{\theta_{se}}$) in equation (3.49). However one can make an observation that this is a combination of cases #1 and #2, and hence the presence of a zero determinant in one configuration is canceled by the other and vice versa. It was also numerically established that the determinant is non-zero for all values of steering angle.

Theorem - 3.4 : An AGV with an inclined steering column and a non-zero offset distance provides *path controllability* for all values of steering angles.

3.5 Path Controllability of AGVs with a Differential Drive

In this section, the path controllability of a differentially driven AGV is studied. The kinematic equations are derived from the generic kinematic model presented in section 3.3. The wheelbase configuration for the differential AGV is derived from the generic wheelbase considered in Fig. 3.1. A differentially driven AGV with two driving wheels on either side of the geometric center of the AGV and two casters one at the front and the other at the rear is shown in Fig. 3.8. The two driven wheels in Fig. 3.1 are replaced by two driving wheels. The front and rear driving and steered wheels of Fig. 3.1 are replaced by free wheeling casters. There is an offset distance between the point of contact of the casters and the pivot axis. The

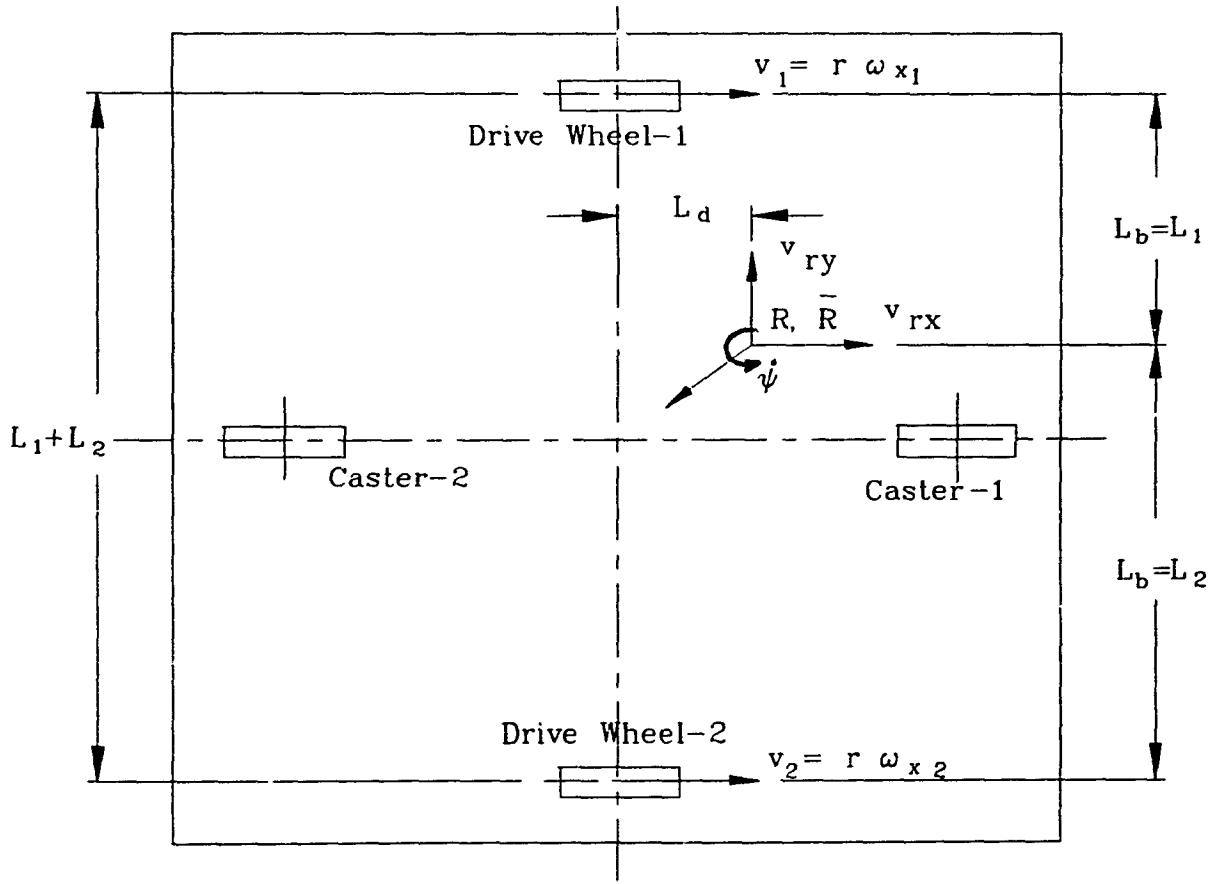

Fig. 3.8 AGV with Differential Drive (Diamond Shaped Wheelbase Configuration)

usefulness of this offset is explained in Appendix. A. The following formulations present the kinematic equations of motion and the criterion for path controllability.

From equation (3.21), the transformation $\bar{R}\dot{\Phi}_R$ for any driving and steered wheel can be written as

$$\bar{R}\dot{\Phi}_R = \begin{bmatrix} 0 & B_{12} & B_{13} & B_{14} \\ B_{21} & 0 & B_{23} & B_{24} \\ B_{31} & B_{32} & 0 & B_{34} \\ 0 & 0 & 0 & 0 \end{bmatrix} \qquad (3.55)$$

Where the elements of the matrix are

$$B_{12} = -(C_{\theta s} S_\alpha^2 + C_\alpha^2)\dot{\theta}_c + C_\alpha \dot{\theta}_s \quad ; \quad B_{13} = -(1 - C_{\theta s}) S_\alpha C_\alpha \dot{\theta}_c + S_\alpha \dot{\theta}_s$$

$$B_{14} = C_{\theta s} v_{cx} - C_\alpha S_{\theta s} v_{cy} + [(1 - C_{\theta s})(r S_\alpha - s) C_\alpha - L_c S_\alpha C_\alpha (1 - C_{\theta s}) + (L_a - L_b)(C_\alpha^2 + C_{\theta s} S_\alpha^2)]\dot{\theta}_c + \{s + (L_b - L_a)C_\alpha\}\dot{\theta}_s$$

$$B_{21} = (C_{\theta s} S_\alpha^2 + C_\alpha^2)\dot{\theta}_c - C_\alpha \dot{\theta}_s \quad ; \quad B_{23} = S_{\theta s} S_\alpha \dot{\theta}_c$$

$$B_{24} = C_\alpha S_{\theta s} v_{cx} + (S_\alpha^2 + C_{\theta s} C_\alpha^2) v_{cy} + \{s S_{\theta s} + L_d (C_{\theta s} S_\alpha^2 + C_\alpha^2)\}\dot{\theta}_c - L_d C_\alpha \dot{\theta}_s$$

$$B_{31} = (1 - C_{\theta s}) S_\alpha C_\alpha \dot{\theta}_c - S_\alpha \dot{\theta}_s \quad ; \quad B_{32} = -S_{\theta s} S_\alpha \dot{\theta}_c$$

$$B_{34} = S_\alpha S_{\theta s} v_{cx} - (1 - C_{\theta s}) S_\alpha C_\alpha v_{cy} + [(L_a - L_b) S_\alpha S_{\theta s} + L_d S_\alpha C_\alpha (1 - C_{\theta s})]\dot{\theta}_c - L_a S_\alpha \dot{\theta}_s$$

Referring to Fig. 3.8, the following conditions are derived from the geometry of the vehicle for an AGV with differential driving :

a) The steering angle θ_s = 90 degrees and is a constant value.

b) The steering rate $\dot{\theta}_s$ = 0

c) The offset s = 0

d) The inclination α = 0

e) The velocity terms $v_{cx} = v_{cz} = 0$

f) wheel # 1 : $L_b = L_1$; $L_a = (L_1 + L_2)$; $v_{cy} = r\,\omega_{x1}$

wheel # 2 : $L_b = -L_2$; $L_a = -(L_1 + L_2)$; $v_{cy} = r\,\omega_{x2}$

Substituting conditions (a) to (e) in the matrix equation (3.55), the resulting expression is

$$\begin{bmatrix} \dot{\bar{R}} \\ \dot{\Phi}_R \end{bmatrix} = \begin{bmatrix} 0 & -\dot{\theta}_c & 0 & -S_{\theta_s} v_{cy} + (L_a - L_b)\,\dot{\theta}_c \\ \dot{\theta}_c & 0 & 0 & C_{\theta_s} v_{cy} + L_d\,\dot{\theta}_c \\ 0 & 0 & 0 & 0 \\ 0 & 0 & 0 & 0 \end{bmatrix} \qquad (3.56)$$

From equation (3.55), the velocity transformation for the driving wheels 1 and 2 can be obtained by substituting the conditions presented in (f). The result of this substitutions is as follows. The velocity transformation for Wheel #1 is

$$\begin{bmatrix} {}^{\bar{R}1}\dot{\Phi}_{R1} \end{bmatrix} = \begin{bmatrix} 0 & -\dot{\theta}_{c1} & 0 & -r\,\omega_{x1} + L_2\, r\,\omega_{x1}/(L_1+L_2) \\ \dot{\theta}_{c1} & 0 & 0 & L_d\, r\,\omega_{x1}/(L_1+L_2) \\ 0 & 0 & 0 & 0 \\ 0 & 0 & 0 & 0 \end{bmatrix} \quad (3.57)$$

where the term $\dot{\theta}_{c1}$ is computed from equation (3.25). Substituting the conditions (a) to (f) for wheels #1 and #2, the angular velocities of the contact points for the two wheels are obtained as

$$\dot{\theta}_{c1} = \frac{r\,\omega_{x1}}{(L_1 + L_2)} \quad \text{and} \quad \dot{\theta}_{c2} = \frac{-r\,\omega_{x2}}{(L_1 + L_2)} \quad (3.58)$$

The velocity transformation for wheel #2 is

$$\begin{bmatrix} {}^{\bar{R}2}\dot{\Phi}_{R2} \end{bmatrix} = \begin{bmatrix} 0 & -\dot{\theta}_{c2} & 0 & -r\,\omega_{x2} + L_1\, r\,\omega_{x2}/(L_1+L_2) \\ \dot{\theta}_{c2} & 0 & 0 & -L_d\, r\,\omega_{x2}/(L_1+L_2) \\ 0 & 0 & 0 & 0 \\ 0 & 0 & 0 & 0 \end{bmatrix} \quad (3.59)$$

Since the vehicle is driven by two driving wheels, the resulting motion equations of the AGV is obtained by summing the motion equations for each wheel. The expression to compute the cumulative velocity transformation ${}^{\bar{R}}\dot{\Pi}_R$ is

$${}^{\bar{R}}\dot{\Pi}_R = {}^{\bar{R}1}\dot{\Phi}_{R1} + {}^{\bar{R}2}\dot{\Phi}_{R2} \quad (3.60)$$

The cumulative velocity transformation ${}^{\bar{R}}\dot{\Pi}_R$ is derived by summing the results presented in equations (3.56) and (3.57), and substituting (3.58). The general form of the motion equation for the differentially driven AGV is

found to be of the form

$$\bar{R}\dot{\Pi}_R = \begin{bmatrix} 0 & -\dot{\theta}_r & 0 & -r(\omega_{x1}+\omega_{x2}) + \frac{r}{(L_1+L_2)}(L_2\omega_{x1} + L_1\omega_{x2}) \\ \dot{\theta}_r & 0 & 0 & L_d\, r\, (\omega_{x1}-\omega_{x2})/(L_1+L_2) \\ 0 & 0 & 0 & 0 \\ 0 & 0 & 0 & 0 \end{bmatrix} \quad (3.61)$$

Here $\dot{\theta}_r$ is the angular velocity of the reference frame $\bar{R}$ relative to the frame R and is

$$\dot{\theta}_r = \dot{\theta}_{c1} + \dot{\theta}_{c2} = \frac{r}{(L_1+L_2)}(\omega_{x1} - \omega_{x2}) \quad (3.62)$$

The elements in the 4th column of the matrix in equation (3.61) are the linear velocities (v_{rx}, v_{ry}, v_{rz}) of the instantaneous reference frame $\bar{R}$ relative to the frame R. Rearranging the linear and angular velocity terms in a matrix form, the following form is obtained for the motion equations of the reference frame.

$$\begin{bmatrix} v_{rx} \\ v_{ry} \\ \dot{\theta}_r \end{bmatrix} = \frac{r}{(L_1+L_2)} \begin{bmatrix} L_1 & L_2 \\ L_d & -L_d \\ 1 & -1 \end{bmatrix} \begin{bmatrix} \omega_{x1} \\ \omega_{x2} \end{bmatrix} \quad (3.63)$$

The equation presented in (3.63) is the forward kinematic model to compute the motion parameters of the AGV in terms of the wheel motion parameters.

The inverse kinematic model computes the wheel speeds required to follow a desired velocity profile. The linear and angular velocities of the vehicle are provided as inputs to the system of equations. In order to compute the wheel speeds it is necessary to invert the matrix equation (3.63). Though there are three parameters on the left hand side of equation (3.63), it should be noted that there are only two independent variables v_{rx} and $\dot{\theta}_r$. The variable v_{ry} can be obtained by multiplying the equation for $\dot{\theta}_r$ by a constant L_d and hence it is a dependent variable. Eliminating the dependent variable, equation (3.63) can be expressed as

$$\begin{bmatrix} v_{rx} \\ \dot{\theta}_r \end{bmatrix} = \frac{r}{(L_1 + L_2)} \begin{bmatrix} L_1 & L_2 \\ 1 & -1 \end{bmatrix} \begin{bmatrix} \omega_{x1} \\ \omega_{x2} \end{bmatrix} \tag{3.64}$$

This equation (3.64) is in the standard form with a non zero determinant for all values of L_1 and L_2. The inverse model is given by

$$\begin{bmatrix} \omega_{x1} \\ \omega_{x2} \end{bmatrix} = \frac{1}{r} \begin{bmatrix} -1 & -L_2 \\ -1 & L_1 \end{bmatrix} \begin{bmatrix} v_{rx} \\ \dot{\theta}_r \end{bmatrix} \tag{3.65}$$

From equation (3.65), it can be concluded that a differentially driven AGV provides unique values for the wheel speeds in order to generate the required values of linear and angular velocities. It should be noted here that the distances L_1 and L_2 which are one half of the wheel span and are never equal to zero. Equation (3.65) is not a function of steering angles as the vehicle configuration chosen does not have steered wheels.

Theorem - 3.5 : An AGV with a differential drive provides *path controllability* for all values of the geometric parameters L_1 & L_2 (which are never equal to zero).

3.5 Summary

A criterion for *non-redundant path controllability* for kinematic control of AGVs is derived in this Chapter. The term *non-redundant path controllability* signifies the absence of kinematic singularity (Theorem-3.5). From the criterion it has been established that the differentially driven AGV does not exhibit kinematic singularity and hence is the preferred configuration in this thesis. Moreover, in the case of differentially driven AGVs, the mathematical expressions are simpler and the geometry of the vehicle is also simplified due to the absence of a steering mechanism. The other advantages are (1) the vehicle can spin about the geometric center at a minimum radius which is equal to one half of the wheel span and (2) the vehicle can travel in the forward and reverse direction. These features are absent if one considers a vehicle with a steered driving wheel at the front.

One could resort to a vehicle with front and rear drive and steer. The kinematic formulations in this case are complex and there will be four degrees of freedom to manipulate in order to achieve the motions provided by a differential drive. Vehicles with a vertical steering column without offset are not *path controllable* (Theorem-3.3). They are therefore not suitable for kinematic control. On the other hand, Theorem-3.1 has shown that vehicles with an inclined steering column but zero offset are *path controllable*, except when the steering angle happens to be $(2n+1)\pi/2$. And Theorem-3.2 has established that vehicles with a vertical steering column and a non-zero offset are *path controllable*, with the exception at a steering angle of $(2n+1)\pi/4$. It can be seen from Theorem-3.4 that AGVs with an inclined steering column and a non-zero offset are *path controllable* at all values of steering angles. From these discussions one may conclude that

vehicles with a differential drive and vehicle with a steering column offset and/or an inclined column are suitable for kinematic control purposes.

The analysis presented in this chapter further shows that other parameters need to be taken into account in choosing a particular wheel. For example, where the steering column is inclined at an angle, extra degrees of motion are introduced; motion in the vertical direction and roll of the steered wheel. In the case of non-zero offset, one has to drag the steered wheel to the side during steering, implying a larger steering torque.

The kinematic modeling approach presented in this chapter is sufficiently general to apply for any other wheel configuration. This is demonstrated in section 3.5 where the kinematics of a differentially driven AGV has been derived. A similar approach can be extended to analyze vehicles with multiple driving and steering columns. Although the transformation approach adopted in this thesis appears to be complicated, it has the definite advantage over, for instance, a vectorial approach, because it provides a systematic approach which can be converted into a generalized algorithm to generate a solution on a digital computer.

CHAPTER 4

GUIDANCE SYSTEM

4.1 Introduction

The guidance system adopted by the autonomous vehicles described in the literature are discussed in Chapter 2. An autonomous vehicle requires some kind of guidance system in order to move from one place to the other. The type of guidance scheme employed depends on a variety of factors. The factors that affect the selection of a guidance scheme are, the type of function performed, the environment in which the vehicle is functioning, the desired level of tracking accuracy, the volume of operation and the cost. The type of function performed may be a simple material transportation task from one place to the other or the most complicated task of carrying components from machine to machine in order to carry out assembly operations. The latter task requires accurate tracking and parking at low speeds near the machines. The environmental factors are whether the AGV is used in a shop floor, a dirty mine, a clean office floor and under water applications. The tracking and parking accuracies are dictated by the task that the vehicle is expected to perform. The volume of operation determines how much flexibility is required in changing the path in order to achieve maximum utilization with least down time. The cost also plays a significant role and in most cases, a trade off is set between cost and the performance.

The guidance scheme for implementation on the experimental vehicle is presented in this chapter. This thesis employs the binary digitizing camera vision as the guidance method. The track that describes the trajectory to be followed by an autonomous vehicle is prepared using a medium that provides

high contrast for the camera. The camera takes a picture of the floor and subsequently an image processing scheme analyzes the image. From this the instantaneous position and orientation of the vehicle (AGV) relative to the track are evaluated. This information is used to steer the vehicle in the proper direction in order to achieve the desired level of tracking.

It is believed that the employment of binary digitizing camera for guidance is a preferred choice for the following reasons :

- For this type of guidance, a track that is prepared by using a tape or painting the floor is quite sufficient. Hence the installation and maintenance costs are minimal compared to the other schemes.

- The camera vision scheme provides a wider field of view (consists of large number of picture elements) compared to the other schemes which rely on a single point (wire guidance) or a small confined area (optical guidance). This facilitates better control of the vehicle and also makes it possible to recognize complicated track features such as exits, cross junctions etc.

- The wire guidance monitors the intensity of a magnetic field as generated by the energized wire-loop. Since field intensity is inversely proportional to the square of the distance of the sensing device away from the wire, it is important to maintain the distance fairly constant for this distance. It is r orted that in such an installation, the floor has to be maintained within 1/4" of flatness over the length of the track of 20 feet. On the other hand, by using camera vision to monitor the track on the floor, the image generated is relatively unaffected by the distance

between the camera and the floor. The installation costs for the tape/paint in the case of camera vision guidance is insignificant compared to the wire guidance.

- A binary camera is preferred to a CCD camera that provides colored images or images with a large number of shades of gray. In the case of CCD camera, one has to perform extensive pre-processing (filtering and thresholding). A CCD camera is relatively more expensive than the binary camera that is being adopted in our vehicle.

One can resort to a simple technology for a binary camera, namely one that is based on the optical property of dynamic RAM chips (known as Optic-Rams). This technology is cheaper to implement and simpler image processing schemes are used as no threshold is required.

In section 4.2, image processing algorithm is presented. Section 4.2.1 describes a methodology to extract the valid track information from a frame of image taken by the camera. This provides the location of the center line of the track image in the camera window. From this track information, an image analysis algorithm computes the position and orientation of the longitudinal axis of the vehicle relative to the track. This is provided in section 4.2.2. This information is used by the control schemes described in Chapter 5 to ensure that the vehicle follows the desired trajectory. Section 4.3 details an algorithm to identify a set of primitives that are composed of left and right turns. From the primitives, road sign combinations are derived and are used to perform flow control of vehicle in a manufacturing environment. The experimental vehicle is provided with a track

layout consisting of a circle and two diagonal lines to demonstrate the ability of the algorithm to identify the road signs.

4.2 Image Processing Algorithm

4.2.1 Noise Filtering Technique

A camera frame contains noise signals in addition to the valid track information. Noise is caused by variations in the reflectivity of the floor, floor unevenness, presence of dirt particles and irregularities of the pixel characteristics. A noise filtering algorithm is used to extract the track information.

A sample image frame obtained using a binary digitizing camera is shown in Fig. 4.1. Each row is scanned from column-0 to column-15. Each column corresponds to 8 pixels (one byte). For each row, an image is defined as a dark area bounded by white pixels. Several such images may be present in a frame with one of them corresponding to the track. During the scanning process the number of pixels in each image encountered and its location in each and every row are recorded in an image data table. Thus, this table contains information about the starting location of all the images and the number of dark pixels in each image. Table. 4.1 illustrates an example of the image data table prepared using the algorithm described above for the sample image shown in Fig. 4.1.

The second phase of noise filtering is to extract the valid image data from the image data table. A minimum value is chosen for the number of pixels for an image to qualify as the track image. It is assumed that the number of pixels in noise is less than this minimum value. In the present

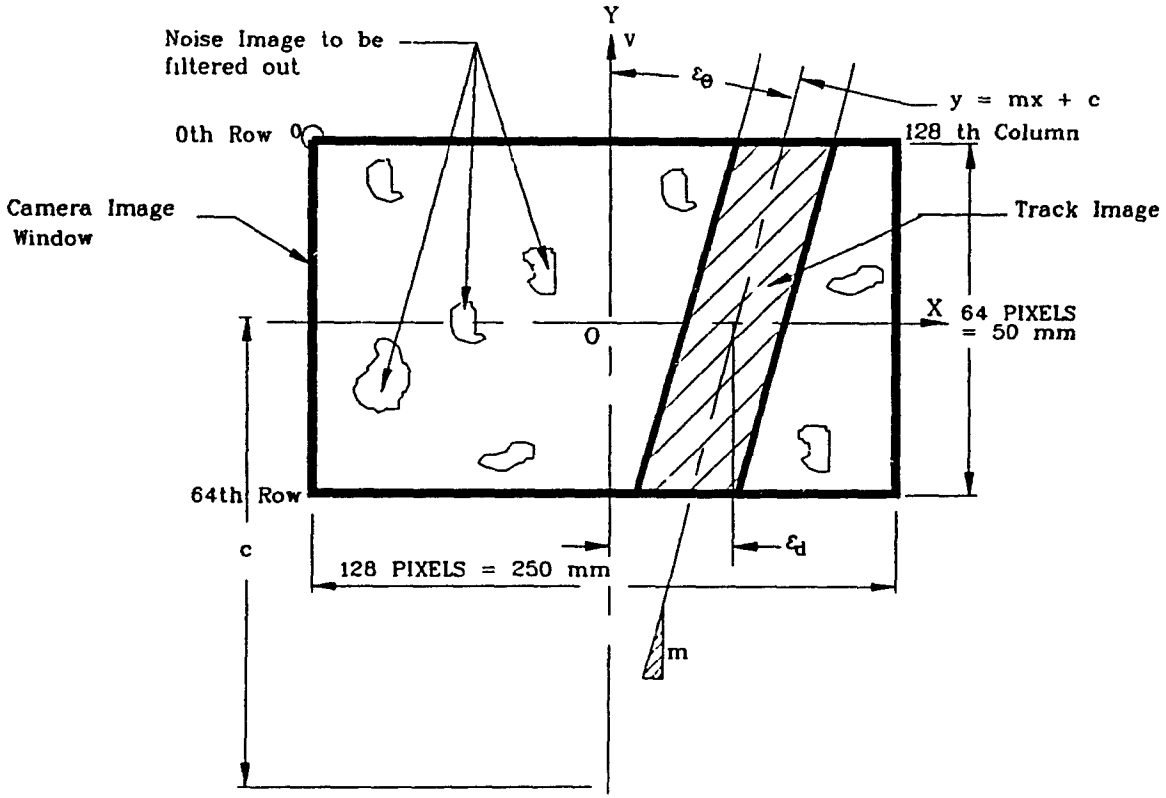

Fig 4 1 Camera Window and Track Parameters Definition

case, this minimum value is set at 2 bytes (16 bits). The image data in each row for that column is considered to be acceptable if the pixel count in that data exceeds a minimum prescribed value. For each row, only one image is accepted as the valid image. This results in a modified image data table as presented in Table. 4.2.

Row	Image - 1		Image - 2		Image - i	
	Count	Loc	Count	Loc	Count	Loc
1	5	20	25	40	25	84
2	4	21	26	38	24	84
.	..	...	...	...	...	...
.	..	...	...	...	...	...
m-1	25	32	0		5	106
m	24	30	0		10	105
m+1	26	28	0		7	107
.	..	...	...	...	...	...
.	..	...	...	...	...	...
.	..	...	...	...	...	...
k-2	24	22	0		3	60
k-1	25	20	0		6	62
k	26	18	0		15	61

Table. 4.1. Sample Image Table before Noise Filtering

Row	1	2	...	m-1	m	m+1	...	k-2	k-1	k
Counts, Loc	25,40	26,38	...	25,32	24,30	26,28	...	24,22	25,20	26,18

Table. 4.2. Sample Image Table after Noise filtering

4.2.2 Image Analysis

This section describes the image analysis scheme to extract the parameters of steering control for track following from the camera image.

These are the position offset (ε_d) and the orientation offset (ε_θ).

Position Offset (ε_d) : It is defined as the perpendicular distance between the center line of the track image and the center line of the camera image window.

Orientation Offset (ε_θ) : It is the angle between the direction of travel by the AGV and the direction pointed to by the track center line.

The equation of the center line of the track is of the form

$$y = m\,x + c \tag{4.1}$$

Where m is the slope of the track, and c is the offset from the center line of the camera window. Owing to noise problems the edges of the track image may not be clean and hence it is necessary to employ the method of least squares [74, 75] that provides the best line fit to a given set of data.

Equation (4.1) has two unknowns (m, c) and there are n equations due to n rows of image data. This is written as

$$\left\{ y_1\ y_2\ \ldots\ldots\ y_n \right\}^T = \begin{bmatrix} x_1 & 1 \\ x_2 & 1 \\ . & . \\ . & . \\ x_n & 1 \end{bmatrix} \begin{Bmatrix} m \\ c \end{Bmatrix} \tag{4.2}$$

Here y_1, y_2, ..., y_n represent the rows, x_1, x_2, ..., x_n are the corresponding column locations of the center line of the track. The superscript T is used to represent the transpose of a column vector. Using the method of least squares presented in references [74, 75], the solutions for the unknowns in equation (4.2) are presented below.

$$c = \frac{\sum x^2 \sum y - \sum x \sum xy}{n \sum x^2 - \left(\sum x\right)^2} \qquad m = \frac{n\sum xy - \sum x \sum y}{n \sum x^2 - \left(\sum x\right)^2} \quad (4.3)$$

Substituting $y = 0$ and $x = \varepsilon_d$ in equation (4.1), an expression for ε_d in terms of m and c is obtained. Referring to Fig. 4.1, an expression to compute the orientation offset ε_θ is derived. These are given below.

$$\varepsilon_d = - c / m \qquad \varepsilon_\theta = \tan^{-1} (1 / m) \quad (4.4)$$

Control laws that make use of these information for vehicle guidance are discussed in Chapter 5.

4.3 Algorithm to Identify Road Signs

One advantage of the camera vision described in this thesis over the other guidance schemes is that it can identify junctions on the floor. The image processing algorithm has been modified to identify junctions and take a left turn or a right turn or travel straight. The instructions concerning the turning options are either provided in a script file before starting the AGV or provided on-line with the help of a remote supervisory computer.

The algorithm presented here identifies a set of primitives. The primitives that are recognized by the AGV are shown in Fig. 4.2. There are two sets of primitives. The first set is composed of a left turn (P11) and a right turn (P12) primitive. The second set is a combination of straight travel option with a left (P21) or right turn (P22). The algorithm to identify a junction and the turn signs is described below.

The presence of a road sign is indicated by a sudden increase in the track width by two bytes. This change in the track width is sensed by the image analysis algorithm presented in section 4.2.2. This sets a flag called imageok_flag to -100. For normal running, this flag is set to 0. An intersection may consist of a left turn, right turn and combinations of these with/without a straight travel option. After the imageok_flag is set to -100, the corresponding image is further analyzed to identify the existence of the primitives. This process continues until the imageok_flag is set to 0 due to the normal track width or to 100 due to the absence of image. The following discussions are on the process of identifying the primitives.

The presence of a dark pixel in the zeroth pixel of the frame for at least ten rows indicates the presence of a left turn. A value of 1 is then assigned to the left turn flag. Similarly for the right turn, the pixel at the 128^{th} column is checked. If it is dark, then a right turn flag is set to one. Since the images received after detecting the presence of a turn signal are used to detect the existence of the left and right turns, the flag generation based on this scheme provides consistent results. This scheme has been implemented and has been found to be 100% successful.

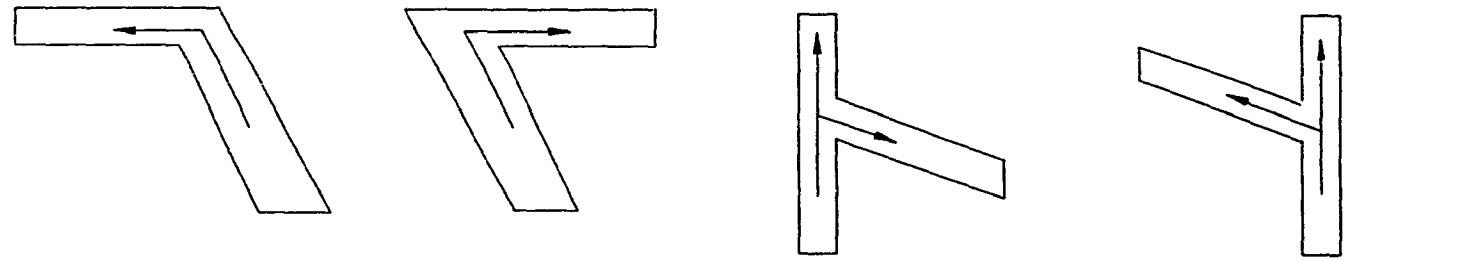

P12 – Left Turn

P11 – Left Turn

P21 – Right & Straight

P22 – Left & Straight

PRIMITIVES RECOGNIZED BY THE ALGORITHM

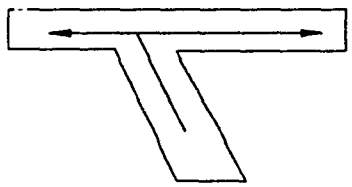

= P11 + P12
= R1

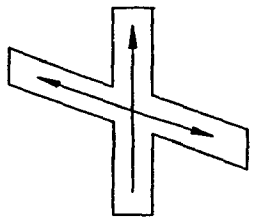

= P21 + P22
= R2

ROAD SIGN COMBINATIONS

Fig.4.2 Primitives and Road Signs Recognized by the Algorithm

The travel straight option is sensed by a change in the track width from large (45 pixels) to normal size (30 pixels) after detecting the turn signal. This results in the change of imageok_flag from -100 to 0. The presence of a straight travel sets up a flag called straight_flag to high (logic 1).

Based on the algorithm described above, a set of road signs can be recognized and are shown in Fig. 4.2. There are two sets of road signs. The first one is a combination of the first primitive set (P11 + P12 = R1) and has a left and a right turn sign on the floor. The second road sign is obtained by adding the second set of primitives (P21 + P22 = R2). This results in a left turn, a right turn and a straight travel option. Figure. 4.3 presents the turn flags generated for the road signs.

4.4 Summary

This chapter presents a guidance scheme for AGVs which has the advantage of being functionally effective and economical from the cost point of view. The binary camera vision scheme described in this chapter relies on a large number of pixel data on the floor and hence the position and orientation of the track relative to the vehicle can be extracted directly without having to use additional sensors and vehicle geometry. In addition to this, it also provides additional information concerning the track to be followed such as the road signs (turning options) on industrial highways to service several work stations. Since the images received from the camera are simple in nature, primitive image processing techniques are employed. Finally, the track can be easily modified and hence the provision of flexibility in terms of installation. This in turn reduces the installation and operating costs.

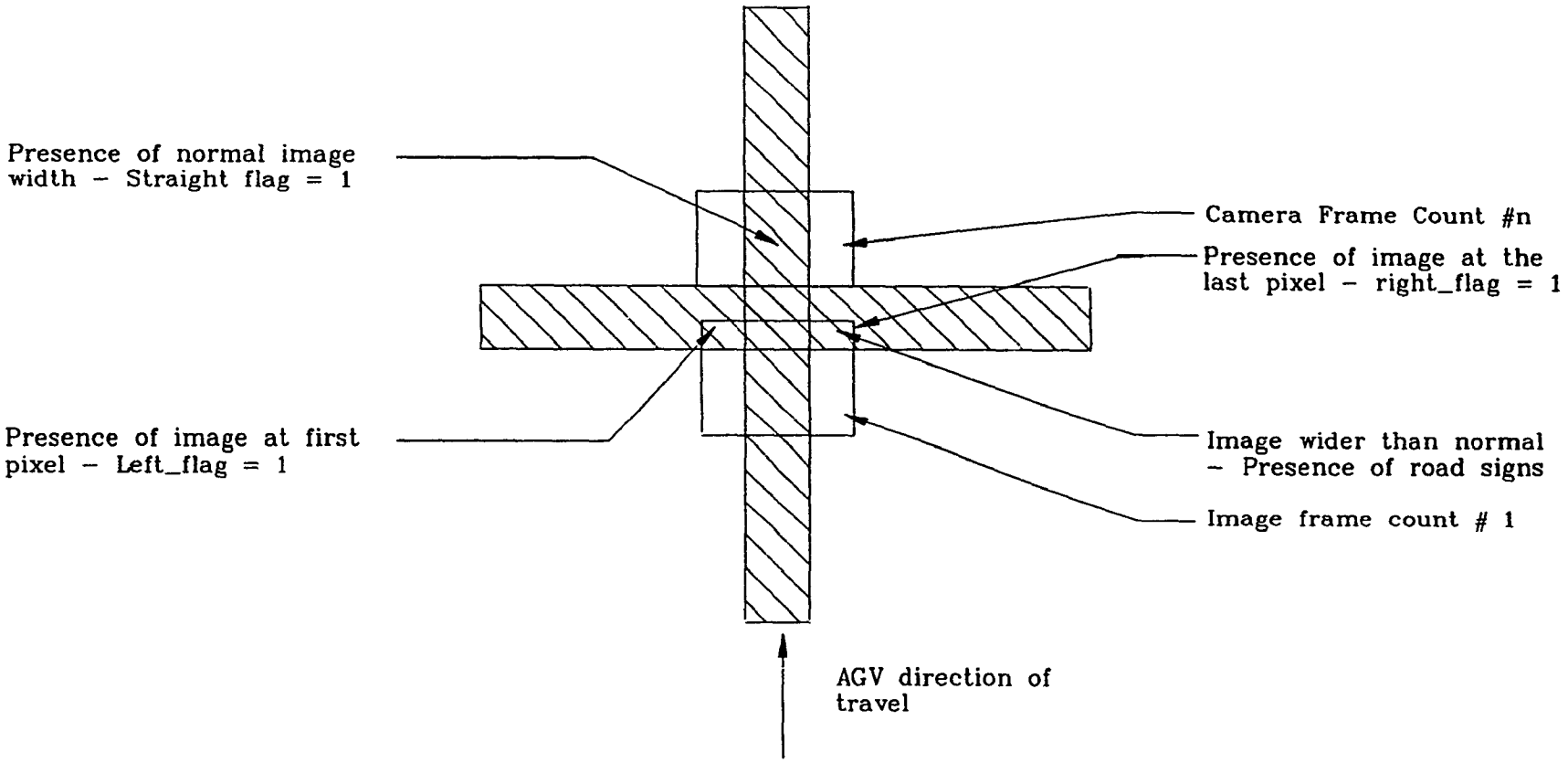

Fig. 4.3 Turn Flag Conditions for Road Signs

CHAPTER 5

GUIDANCE CONTROL SCHEMES TO FOLLOW TRACKS ACCURATELY

5.1 Introduction

This chapter presents three approaches for guidance control of the vehicle so that it follows the track accurately. The first approach is a conventional approach. In this approach, the vehicle follows the track profile based on the track information available at that instant. This is a feedback system where the guidance system identifies the deviation of the vehicle path from the track (error) and takes a corrective action thereafter. This control scheme assures track following of a small segment in the vicinity of the camera. In the present case, it is the front end of the vehicle. As a result of this, the rear end of the vehicle may not be aligned with the track all the time. Instead, it follows a path profile which is described in the literature as tracktrix [73]. The concept of tracktrix can be explained below. Two points A and E are chosen at the two ends of an inextensible string or a rod. According to the definition of tracktrix given by Yales [73], it is the path of the particle or point E pulled by the inextensible string whose end A moves along a line. Examples for tracktrix are, the path traced by a toy wagon pulled by a child and the path traced by the rear wheel of a bicycle. This approach is sufficient for applications requiring road following without much consideration for accuracy. This guidance control scheme is outlined in section 5.2.

If the application requires track following of the front and rear ends of the vehicle, the following approach is recommended for guidance control. An application requiring this criterion is the parking of the AGV close to

the workcell. This has to be accomplished in a short interval of time. In this scheme, an additional camera is employed at the rear end of the vehicle. A method to identify the geometric nature of the track is provided. Control laws that make use of the feedback information from the front and rear cameras are defined to achieve faster reduction in the deviation of the position and orientation offsets from the desired values with minimum overshoots and oscillations. The control laws are chosen based on the presence or absence of curvature and also based on relative location of the longitudinal axis of the vehicle relative to the track. The gains are modified on-line to achieve proper tracking. This scheme is explained in section 5.3.

The guidance control schemes mentioned so far do not make use of the track information available during the elapsed time interval nor do they predict the nature of the track and the parameters of steering control (ε_d and ε_θ) ahead of the vehicle. In addition to this, if there are breaks in the track profile, the vehicle cannot proceed and in most cases the vehicle is commanded to stop. For this purpose, a scheme that is intelligent to identify the geometry of the track and provide guidance control is recommended. This scheme is described in section 5.4. In this scheme, using the parameters of steering control (ε_d and ε_θ) during the elapsed time interval the motion parameters (ω_1 and ω_2) of the vehicle during the same interval, and a model of the vehicle, the geometric profile of the track on the floor is identified. From the identified track profile, the track profile ahead of the vehicle is obtained by extrapolation and information concerning the parameters of steering control for future travel is derived. The vehicle is steered based on this information and a driving criterion.

The criterion depends on the positioning of the AGV on the track. Several possible criteria are discussed. The criterion used in this thesis ensures that the contact patches of the front and rear casters are on the track. A control law is defined to steer the vehicle in the proper direction based on the difference between the desired and actual values of the parameters of steering control. Further, the coefficients of the computed geometric profile are adjusted using the most recent data.

5.2 Guidance Control Scheme Using Single Camera

5.2.1 Objective Function

In this scheme, the wheel speeds are computed by converting the parameters of steering control into steering angle command. The objective of the control scheme is to achieve proper tracking of the small segment of the vehicle. This is defined depending on the geometric nature of the track and the driving criterion. The term proper tracking is defined below for two track profiles.

Straight Line Tracks : The parameters ε_d and ε_θ of steering control should be minimized such that they become insignificant or within the limits set by the user for accurate tracking. The driving criteria is such that the longitudinal axis of the vehicle should coincide more or less with the track. Hence for straight line tracks the following conditions are defined for proper tracking :

$$\varepsilon_d \cong 0 \text{ and } \varepsilon_\theta \cong 0 \tag{5.1}$$

Tracks with Curvature: The deviations of the parameters ε_d and ε_θ from the desired value should be minimized for accurate tracking. In the case of tracks with curvatures it is necessary to define which point on the vehicle should be on the track. If the driving criterion is such that the camera center be on the track, the position offset (ε_d) should be equal to zero and the orientation offset (ε_θ) should approach a value which is characteristic of the track profile on the floor. The desired value of (ε_θ) is computed from the geometry of the track. The criterion for proper driving is given by

$$\varepsilon_d \cong 0 \text{ and } \varepsilon_\theta \neq 0 \tag{5.2}$$

The experimental vehicle has a diamond shaped wheelbase configuration with two driving wheels on either side of the geometric center and support casters at the front and rear. For this vehicle, another criterion can be defined and is that the front and rear casters should be on the track. For this criterion the position offset (ε_d) does not become zero and has a definite value in addition to the non-zero orientation offset (ε_θ). Again, from the geometry of the vehicle and the track, the desired values of the parameters are computed.

$$\varepsilon_d \neq 0 \text{ and } \varepsilon_\theta \neq 0 \tag{5.3}$$

A proportional controller which simply amplifies the deviations of these offsets from the desired value and providing a steering angle command to the wheels is presented below. A PI-Controller, i.e. proportional and integral controller is also proposed. In the implementation, the integral of the position offset alone is used. This is because of the fact that the

computational errors in evaluating the orientation offsets are larger compared to that of the position offsets due to the restricted camera window dimensions. This also suggests that the gain value for the orientation offset should be smaller than the gain for the position offset. A derivative term (i.e. PID) is not used as overshoots resulting from the integral are controller are necessary to achieve faster error reduction.

In the implementation, the curvature of the track is not checked (straight line or curved) to find out which objective function need to be used. Instead, in order to provide non-zero steering angle commands while following tracks with curvatures, the wheels are provided with only the incremental change in the wheel speeds.

5.2.2 Computation of Steering Angle Using a P-Controller

A control law to compute the steering angle θ_s is defined in terms of the position and orientation offsets as

$$\theta_s = G_1 \varepsilon_d + G_2 \varepsilon_\theta \tag{5.4}$$

Where G_1 and G_2 are gains to amplify the error signals. The magnitude of these gains have to be properly selected in order to avoid instabilities.

5.2.3 Computation of Steering Angle Using a PI Controller

A variation of the controller presented above is a PI (Proportional and Integral) Controller. A proportional controller reduces the steady state error to zero only asymptotically. Therefore a PI controller is a better choice. Addition of an integral term provides memory and overshoots. Memory

is required to follow track profiles with curvatures for which the track parameters should not be equal to zero. The track features should go to zero at steady state only in the case of straight line tracks. The overshoots resulting due to the integral term minimizes the deviation of the track parameters from the desired value at a faster rate.

The control law to compute the steering angle θ_s is defined as

$$\theta_s = G_1\varepsilon_\theta + G_2\varepsilon_d + G_3 \int \varepsilon_d \, dt \tag{5.5}$$

where G_1, G_2 and G_3 are gains for error amplification. The AGV control is based on discrete time functions and hence equation (5.5) can be rewritten as

$$\theta_s(n) = G_1 \, \varepsilon_\theta(n) + G_2 \, \varepsilon_d(n) + G_3 \sum_{i=1}^{n} \Delta T \, \varepsilon_d(i) \tag{5.6}$$

Here ΔT is the sampling time of the AGV control loop. From equation (5.6), the steering angle at time interval (n-1) can be written as

$$\theta_s(n-1) = G_1 \, \varepsilon_\theta(n-1) + G_2 \, \varepsilon_d(n-1) + G_3 \sum_{i=1}^{n-1} \Delta T \, \varepsilon_d(i) \tag{5.7}$$

Subtracting equation (5.7) from (5.6) we get

$$\theta_s(n) = \theta_s(n-1) + G_1 \left\{\varepsilon_\theta(n)-\varepsilon_\theta(n-1)\right\} + G_2 \left\{\varepsilon_d(n)-\varepsilon_d(n-1)\right\} + G_3 \, \varepsilon_d(n) \tag{5.8}$$

5.2.4 Computation of Wheel Speeds

For analysis, the wheelbase of the vehicle is considered to be diamond shaped with two drive wheels located on either side of the geometric center of the vehicle and supporting casters at the front and rear. Figure. 5.1 illustrates the schematic layout of the vehicle considered for implementation. By driving the left and right driving wheels at different velocities, an angular velocity $\dot{\psi}$ is produced about the location 'O'. This point 'O' is located at the intersection of the line joining the two driving wheel centers and the longitudinal axis of the vehicle. The magnitude of the angular velocity is equal to the ratio of the difference in the linear velocities of the two wheels and the wheel span L. Assuming small orientation angle, this is given by

$$\dot{\psi} = \frac{V_L - V_R}{L} \tag{5.9}$$

Referring to Fig. 5.1, the angular velocity $\dot{\psi}$ of the reference point 'O' on the AGV, assuming negligible side slip is written as

$$\dot{\psi} = \frac{V \tan\theta_s}{L_{ae}} \tag{5.10}$$

where L_{ae} is the effective wheelbase when the front caster is at an angle θ_s relative to the longitudinal axis of the vehicle. V is the linear velocity of the AGV. Since the casters employed in the AGV have an offset distance 's' relative to the pivot axis, the contact point (patch) of the caster trails the pivot axis when the AGV is in motion. As a result of this offset, the wheelbase distance between the caster and the driving wheels does not remain constant and varies with the steering angle. From the geometry of the

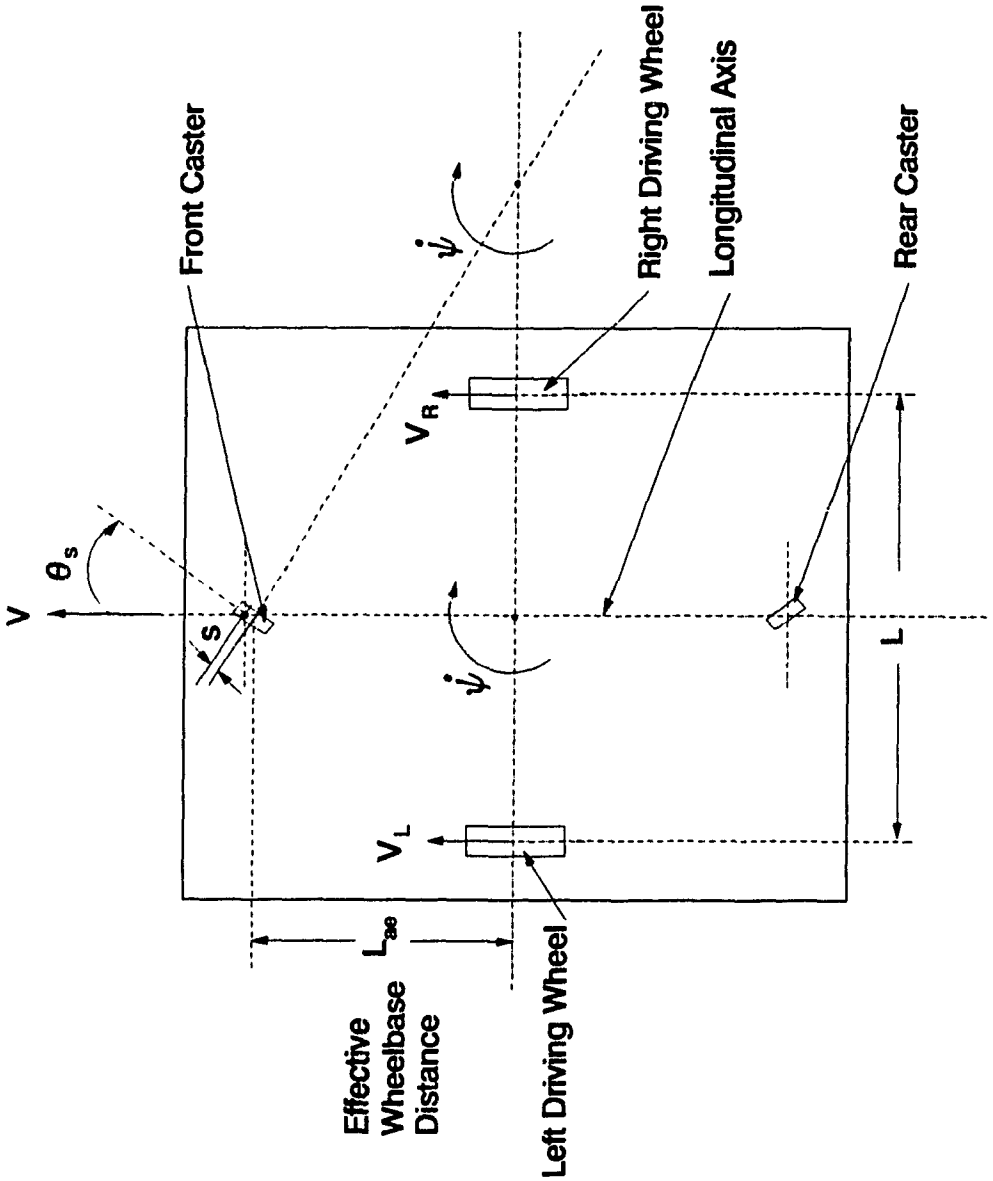

Fig. 5.1 Schematic Layout of the AGV

configuration, an expression to evaluate the effective wheelbase distance L_{ae} is obtained as

$$L_{ae} = L_a + s\,(1 - \cos\theta_s) \tag{5.11}$$

The parameter L_a is the wheelbase measured between the contact point of the caster and the rear driving wheels when the angle θ_s is equal to zero. The angle θ_s is the steering angle of the caster, the angle between the longitudinal axis of the vehicle and the direction of travel of the caster.

The expression provided to compute the angular velocity of the AGV is valid for any AGV with any kind of wheelbase configuration. But for the AGV under consideration, since there is no steered wheel and the caster is only a free wheeling caster, the two driving wheels need to be driven appropriately to result in an orientation θ_s for the caster. However, there is no feedback in this system to verify whether the caster has attained the desired steering angle or not.

Using the information provided above and also knowing the desired linear velocity of the AGV, one can compute the linear velocities of the two wheels that can provide the desired angular velocity. If the forward velocity of the AGV is V, the centers of the two wheels travel at this velocity, when the angular velocity $\dot{\psi}$ is zero. To result in a non-zero angular velocity $\dot{\psi}$, the driving wheels need to be driven at a differential velocity of, assuming yaw angle to be small,

$$\Delta V = \dot{\psi}\, L/2 \tag{5.12}$$

For a left turn condition, the sign of this velocity component is positive for the right wheel and is negative for the left wheel. Hence the resulting velocities of the two wheels can be expressed as

$$V_L = V - \dot{\psi} L / 2 \tag{5.13}$$

$$V_R = V + \dot{\psi} L / 2 \tag{5.14}$$

L_{ae} from equation (5.11) is substituted in (5.10). The resulting expression for $\dot{\psi}$ is substituted in equations (5.13) and (5.14) and after simplifications one obtains expressions to compute the wheel velocities for the left and right wheels as below.

$$V_L = V \left[1 - \frac{\tan\theta_s}{L_a + s(1 - \cos\theta_s)} \frac{L}{2} \right] \tag{5.15}$$

$$V_R = V \left[1 + \frac{\tan\theta_s}{L_a + s(1 - \cos\theta_s)} \frac{L}{2} \right] \tag{5.16}$$

5.3 Guidance Control Using Dual Cameras

5.3.1 Introduction

This section presents a guidance scheme that provides accurate tracking and faster minimization of deviation of the desired values of the offsets (position and orientation) of the rear end of the vehicle for parking purposes compared to the single camera approach described in section 5.2. The methodology proposed in this section employs sensors at the front and the rear end of the vehicle. The front and rear sensors provide the position and orientation of the front and rear of the vehicle relative to the track.

Control schemes have been devised to speedily achieve accurate tracking of the front and rear ends of the vehicle using this information.

5.3.2 Objective Functions

The objective is to align the longitudinal axis of the vehicle which connects the centers of the two cameras with a chord of the track profile. This chord is obtained by drawing a line connecting the intersection points of the track with the perpendicular lines drawn from the centers of the two cameras. While achieving this objective, it is also desired that the overshoots and the time taken to achieve the accurate tracking be kept minimum. While tracking straight lines, it is necessary that at steady state, the position and the orientation offsets become zero asymptotically. The objective function for straight line tracking can be defined as

$$\varepsilon_{\theta f} = \varepsilon_{\theta r} \cong 0; \qquad \varepsilon_{df} = \varepsilon_{dr} \cong 0 \tag{5.17}$$

In the case of tracks with curvature, at steady state, the centres of the front and rear camera windows be on the track so that the position offsets are zero while the orientation offsets are equal in magnitude and opposite in sign. The objective function for a track with curvature is defined as

$$\left.\begin{aligned} |\varepsilon_{\theta f}| &\cong |\varepsilon_{\theta r}| \cong k \\ \text{sign}(\varepsilon_{\theta f}) &= \text{sign}(\varepsilon_{\theta r}) \\ \varepsilon_{df} &\cong \varepsilon_{dr} \cong 0 \end{aligned}\right\} \tag{5.18}$$

5.3.3 Methodology to Identify Existence of Track Curvature

The sign of the orientation offsets received from the front and rear cameras are used to identify whether the track geometry has a curvature or not. This information is needed to meet the objective functions defined in section 5.3.2 for accurate tracking.

If the profile of the track is a straight line, the orientation offsets of the front and rear will be same in both magnitude and sign at all times, as shown in Fig. 5.2. This is characteristic of straight line track following. If the track profile has a curvature, the orientation offsets will have opposite signs and their magnitudes may or may not be the same. This condition is illustrated in Fig. 5.3. This is true for a given range of radii of curvature of the track and a fixed length of the vehicle. It is reasonable to assume that these conditions are satisfied by most of the AGVs and by the industrial tracks in the market.

5.3.4 Control Laws for Straight Line Tracks

The control laws defined in this section are based on the signs of the position offsets ε_{df} and ε_{dr} of the front and rear cameras. If the AGV is on one side of the track as in Fig. 5.2, the signs of the front and rear position offsets are opposite to each other. In order that the front end of the vehicle cross the track faster, the AGV needs to be steered towards the track profile. To achieve this objective, a control law of the following form is proposed.

$$\theta_s = G_1 \varepsilon_{df} + G_2 \varepsilon_{\theta f} + G_3 \left\{ |\varepsilon_{df}| + |\varepsilon_{dr}| \right\} \mathrm{sgn}(\varepsilon_{df}) \qquad (5.19)$$

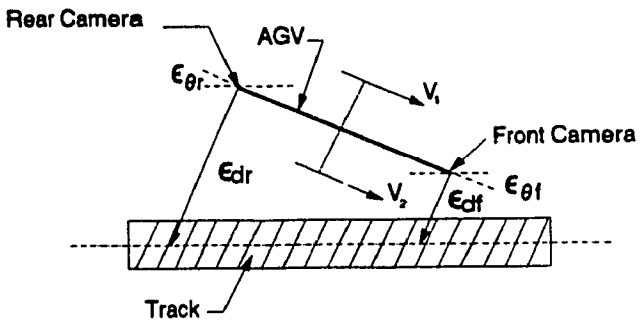

Conditions : $|\epsilon_{\theta f} = \epsilon_{\theta r}|$ $|\epsilon_{df}| \lesssim |\epsilon_{dr}|$ $\text{sgn}(\epsilon_{df}) = \text{sgn}(\epsilon_{dr})$

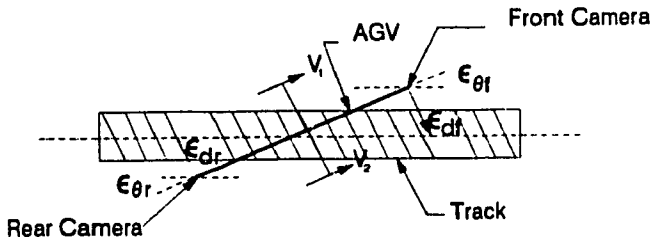

Conditions : $|\epsilon_{\theta f} = \epsilon_{\theta r}|$ $|\epsilon_{df}| \lesssim |\epsilon_{dr}|$ $\text{sgn}(\epsilon_{df}) = -\text{sgn}(\epsilon_{dr})$

Fig. 5.2 Definition of Parameters of Steering Control for Straight Line Tracks

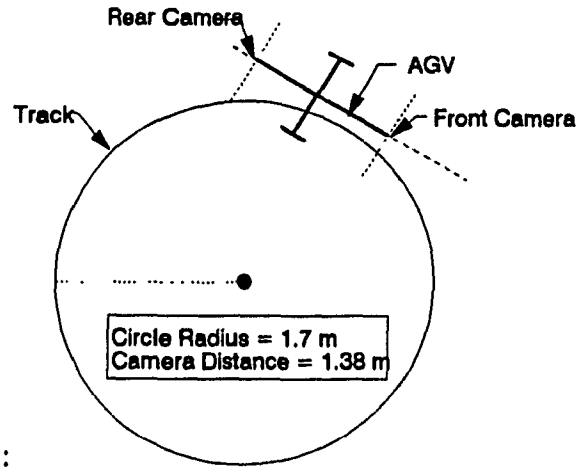

Conditions :

$\epsilon_{\theta f} \lesseqgtr \epsilon_{\theta r}$ $\quad \mathrm{sgn}(\epsilon_{\theta f}) = -\mathrm{sgn}(\epsilon_{\theta r})$ $\quad |\epsilon_{df}| \lesseqgtr |\epsilon_{dr}|$ $\quad \mathrm{sgn}(\epsilon_{df}) = \mathrm{sgn}(\epsilon_{dr})$

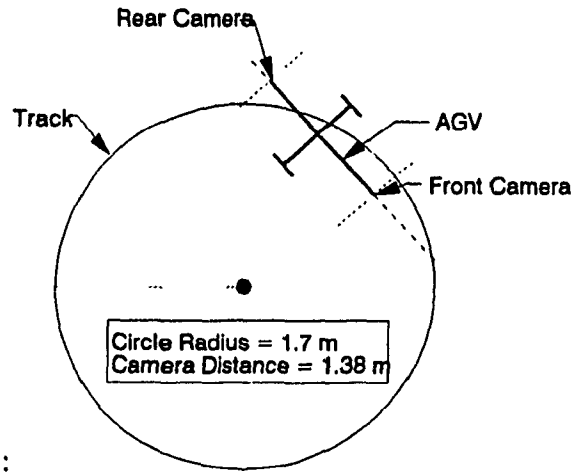

Conditions :

$\epsilon_{\theta f} \lesseqgtr \epsilon_{\theta r}$ $\quad \mathrm{sgn}(\epsilon_{\theta f}) = -\mathrm{sgn}(\epsilon_{\theta r})$ $\quad |\epsilon_{df}| \lesseqgtr |\epsilon_{dr}|$ $\quad \mathrm{sgn}(\epsilon_{df}) = -\mathrm{sgn}(\epsilon_{dr})$

Fig. 5.3 Definition for Parameters of Steering Control for a Circular Track

The term θ_s is the steering angle and the parameters G_1, G_2 and G_3 are the dc gains. The approach to select suitable values for these gains is discussed in section 5.3.6. In the equation presented above, there is an additional command signal term compared to the single camera guidance scheme. This is the sum of the absolute values of the front and rear position offsets. As a result of this a large steering angle command is generated and this makes the front end of the vehicle cross the track faster.

On the contrary, if the front and rear ends are on either side of the track as in Fig. 5.2, it is necessary to use a different control law that gradually brings the two ends of the vehicle as close to the track as possible. This is achieved by employing a controller of the following form

$$\theta_s = G_4 \ \varepsilon_{df} + G_2 \ \varepsilon_{\theta f} + G_5 \left| \left\{ |\varepsilon_{df}| - |\varepsilon_{dr}| \right\} \right| \text{sgn}(\varepsilon_{df}) \qquad (5.20)$$

The difference in the two position offsets is used to steer the vehicle in order to achieve error reduction gradually which will bring the front and the rear ends closer to the track with little or no overshoot. The value of gain G_4 dictates the stability of the control scheme. If gain G_4 is large, the front will cross the track once again and will be on the same side as the rear end. This results in controller switching which in turn results in cross over of the track by the rear end. This results in oscillatory performance.

In Chapter 9 discussions are presented for a further study which employs a reference point other than the front end. This is to achieve asymptotic

error correction after the reference point crosses the track for the first time. In the derivations presented so far only a proportional controller is considered. A proportional controller does not provide zero steady state error. It is necessary to include an integral component in the controller in order to achieve zero steady state error.

5.3.5 Control Laws for Tracks with Curvature

If the track has a constant curvature, the objective function defined in equation (5.18) needs to be satisfied, i.e. the orientation offsets $\varepsilon_{\theta f}$ and $\varepsilon_{\theta r}$ must be equal and non-zero in addition to the zero position offsets. Hence if the front and rear ends are on the same of the track, the control equation for straight line presented in (5.19) is modified as below :

$$\theta_s = G_1 \varepsilon_{df} + G_2 \left\{ \varepsilon_{\theta f} - \varepsilon_{\theta r} \right\} + G_3 \left\{ |\varepsilon_{df}| + |\varepsilon_{dr}| \right\} \mathrm{sgn}(\varepsilon_{df}) \qquad (5.21)$$

In the above equation, the difference in the orientation offsets is used instead of simply using the orientation offset of the front end only. Similarly, for the case in which the two ends of the AGV are on either side of the track, the control law of equation (5.20) is modified as below :

$$\theta_s = G_3 \varepsilon_{df} + G_2 \left\{ \varepsilon_{\theta f} - \varepsilon_{\theta r} \right\} + G_5 \left\{ |\varepsilon_{df}| - |\varepsilon_{dr}| \right\} \mathrm{sgn}(\varepsilon_{df}) \qquad (5.22)$$

5.3.6 Selection of Gain Values

The magnitude of the gains are selected based on the following three aspects :

1) presence or absence of curvature (curved track or a straight line

track);

2) the initial condition of the front and rear ends of the AGV, i.e. when the AGV is accelerating from rest, whether the front and rear ends are on the same side or on opposite sides of the track when the AGV is accelerating;
3) the relative location of the front and rear ends with respect to the track during motion after the front end of the AGV had crossed the track at least once.

For a straight line track, the orientation offset gain can be chosen to be zero as it is sufficient to use the position offsets for control purposes. This is because there will not be a situation where the vehicle will follow the track with a constant orientation offset and zero position offsets. On the otherhand, the converse of this situation is never true. In the case of tracks with constant curvature, the requirement of the objective function is that the orientation offsets at the front and rear ends be equal. In order to achieve this objective it is necessary to employ a non-zero value for gain G_2. The value of gain G_2 is chosen to be small as large values will result in oscillations in the vehicle response. This is particularly true when the difference in the orientation offsets itself is large.

During the acceleration stage of the AGV from rest, if the front and rear ends are on the same side of the track, the magnitude of gain G_1 in equations (5.19) & (5.21) is chosen to be as high as possible to result in faster crossover of the track. The magnitude of G_1 depends on the curvature of the track, and large values need to be selected for tracks with curvatures. Since the position offset increases due to the change in track

profile reduces the error correction performed by the control loop. This phenomenon is absent in the case of straight line tracks. As a result of this, gain values chosen for straight line tracks cannot be used as it will take longer time for the vehicle to approach the track.

Once the front end of the vehicle crosses the track, and as long as the front and rear ends are on opposite sides of the track, the magnitude of gains (G_3 and G_4) of the control law (5.20 or 5.22) are chosen to be as low as possible so that the error correction takes place asymptotically. Gain G_3 is approximately one half of gain G_1. After employing control equation (5.20), if the front and rear ends of the AGV once again be on the same side of the track, it is necessary to employ equation (5.19 or 5.21) with smaller value for gain G_1. This is to prevent the vehicle from hunting about the track.

On the contrary if the initial conditions are such that the front and rear ends are on opposite sides of the track, in order to make the front end to cross the track, the magnitude of gain G_4 of equation (5.20) is chosen high enough so that the front end crosses the track and overshoots. This in turn brings the rear end closer to the track. After the crossover, to achieve asymptotic reduction of the tracking offsets to the desired values, the magnitude of gain G_1 is chosen to be small. Simulations are carried out and the results indicate that this approach to variable controller gains results in excellent tracking performance. Gains are modified in real-time depending on whether the front and rear ends are on the same side of the track at least once or on the same side at least once.

5.4 Identification of Track Geometry and Guidance

5.4.1 Motion Equations and Position Transformations

The coordinate frames assigned for the AGV and the track image window are shown in Fig. 5.4 and are explained below. A moving reference point **P** is chosen on the track. A coordinate frame 'P' is chosen at this point. The location of the point **P** is obtained by drawing a line perpendicular to the longitudinal axis of the camera image window from the center of the image window (B) to the track line. The distance between points B and **P** is the position offset ε_d and the orientation between the longitudinal axis of the camera and the track line is the orientation offset ε_θ. In order to compute the location of this point **P** in the inertial coordinates, the following approach is adopted.

A transformation graph to compute the position of the point **P** from the position of the instantaneous reference frame $\bar{R}$ is shown in Fig. 5.5. From this transformation graph, and from Fig. 5.4, the following transformations are obtained. The transformation to the instantaneous reference frame 'R' from the floor frame 'F' is a translation and a rotation and is given by

$$ {}^{F}T_{\bar{R}} = \text{Trans}(X_r,\ Y_r,\ 0,\ 1)\ \text{Rot}(Z,\ \theta_r) \tag{5.23} $$

The transformation from the reference frame 'R' to the image window frame 'I' involves a translation. The transformation is

$$ {}^{R}T_{I} = \text{Trans}(X_I,\ Y_I,\ 0,\ 1) \tag{5.24} $$

The location of the reference point frame 'P' relative to the frame 'I' is

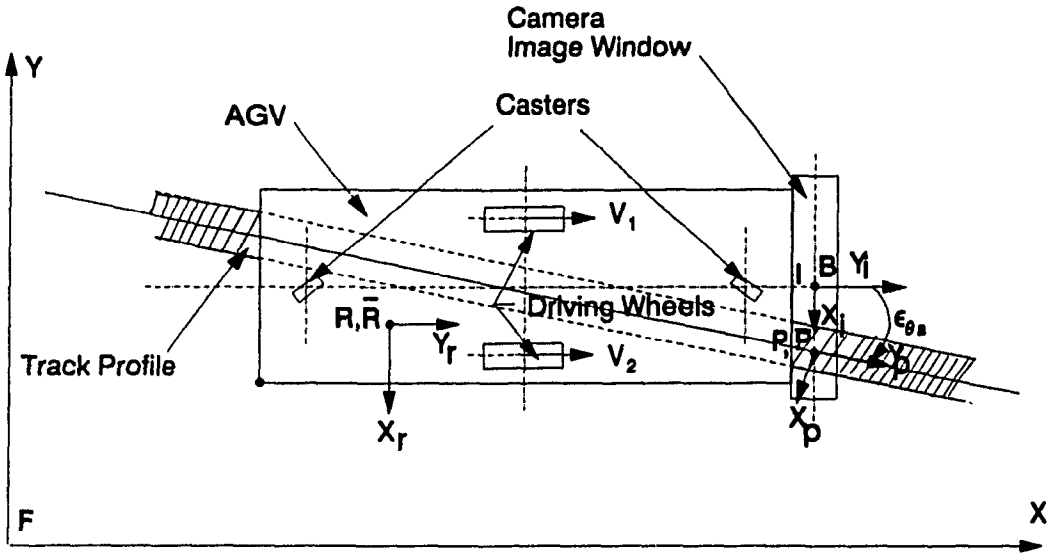

Fig. 5.4 Definition and Assignment of Coordinate Frames

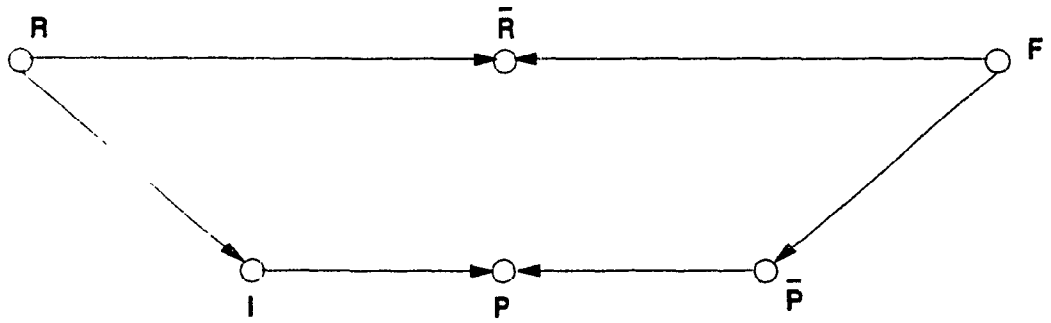

Fig. 5.5 Transformation Graph for Reference Point P

$$
{}^{I}T_{P} = \mathrm{Trans}(\varepsilon_{da},\ 0\ ,\ Z_{p},\ 1)\ \mathrm{Rot}(Z,\ -\varepsilon_{\theta a})
$$

$$
= \begin{bmatrix} \mathrm{Cos}(\varepsilon_{\theta a}) & \mathrm{Sin}(\varepsilon_{\theta a}) & 0 & \varepsilon_{da} \\ -\mathrm{Sin}(\varepsilon_{\theta a}) & \mathrm{Cos}(\varepsilon_{\theta a}) & 0 & 0 \\ 0 & 0 & 1 & Z_{p} \\ 0 & 0 & 0 & 1 \end{bmatrix} \qquad (5.25)
$$

Here the terms ε_{da} and $\varepsilon_{\theta a}$ are the measured or actual values of the position and orientation of the track relative to the longitudinal axis of the vehicle as provided by the camera image analysis described in section 4.4.

Referring to Fig. 5.5, the transformation for the frame 'P' from the floor frame in terms of the known transformations is

$$
{}^{F}T_{\bar{P}} = {}^{F}T_{\bar{R}}\ {}^{\bar{R}}\Pi_{R}\ {}^{R}T_{I}\ {}^{I}T_{P} \qquad (5.26)
$$

The transformation ${}^{\bar{R}}\Pi_{R}$ is the cumulative position transformation for an AGV with n-driving and steered wheels. In equation (5.26), position transformation ${}^{F}T_{R}$ replaces the term ${}^{F}T_{\bar{R}}\ {}^{\bar{R}}\Pi_{R}$ as ${}^{F}T_{R}$ can be derived from the position vector ${}^{F}p_{R} = \{p_{rx},\ p_{ry},\ \theta_{r}\}^{t}$ as a translation and rotation transformation. This is given by

$$
{}^{F}T_{R} = \begin{bmatrix} \cos\theta_{r} & \sin\theta_{r} & 0 & p_{rx} \\ -\sin\theta_{r} & \cos\theta_{r} & 0 & p_{ry} \\ 0 & 0 & 1 & 0 \\ 0 & 0 & 0 & 1 \end{bmatrix} \qquad (5.27)
$$

Similarly the transformation ${}^{F}T_{P}$ is written as

$$ {}^{F}T_{P} = \begin{bmatrix} \cos\theta_p & \sin\theta_p & 0 & p_{px} \\ -\sin\theta_p & \cos\theta_p & 0 & p_{py} \\ 0 & 0 & 1 & 0 \\ 0 & 0 & 0 & 1 \end{bmatrix} \qquad (5.28) $$

The right hand side of the position transformations for the point **P** on the track is obtained by substituting equations (5.27), (5.24) and (5.23) in equation (5.26). The resulting equations are expressed in terms of the position transformation of the reference frame R and are given as

$$ {}^{F}T_{P} = \begin{bmatrix} C_\theta C_\varepsilon + S_\theta S_\varepsilon & -C_\theta S_\varepsilon + S_\theta C_\varepsilon & 0 & w_{px} \\ C_\theta S_\varepsilon - S_\theta C_\varepsilon & S_\theta S_\varepsilon + C_\theta C_\varepsilon & 0 & w_{py} \\ 0 & 0 & 1 & 0 \\ 0 & 0 & 0 & 1 \end{bmatrix} \qquad (5.29) $$

Here the notations C_θ, S_ε represent the cosine and sine of the angles θ and ε respectively. Where w_{px} and w_{py} are given by

$$ w_{px} = p_{rx} + (\varepsilon_{da} + X_l)\cos\theta_r - Y_l \sin\theta_r $$
$$ w_{py} = p_{ry} + (\varepsilon_{da} + X_l)\sin\theta_r + Y_l \cos\theta_r $$

Comparing the elements of the two matrices given by (5.29) and (5.28), the expressions to compute the coordinates of x and y of the point **P** in the inertial frame are obtained as

$$\left.\begin{aligned} p_{px} &= p_{rx} + (\varepsilon_{da} + X_1)\cos\theta_r - Y_1 \sin\theta_r \\ p_{py} &= p_{ry} + (\varepsilon_{da} + X_1)\sin\theta_r + Y_1 \cos\theta_r \end{aligned}\right\} \tag{5.30}$$

And the orientation of a vector acting at **P** in the inertial frame is

$$\theta_p = \theta - \varepsilon \tag{5.31}$$

An AGV with a differential drive is considered for illustration. In order to compute the position coordinates ${}^{F}p_{R} = \{p_{rx},\ p_{ry},\ \theta_r\}^t$, the cumulative velocity transformation ${}^{\bar{R}}\dot{\Pi}_{R}$ derived in section 3.5 is considered. The final form of the equation is reproduced here for completeness.

$$\begin{bmatrix} 0 & -\dot{\theta}_{c1} - \dot{\theta}_{c2} & 0 & -r(\omega_{x1} + \omega_{x2}) + r\,(L_2\,\omega_{x1} + L_1\omega_{x2})/(L_1+L_2) \\ \dot{\theta}_{c1} + \dot{\theta}_{c2} & 0 & 0 & L_d\, r\,(\omega_{x1} - \omega_{x2})\,/(L_1 + L_2) \\ 0 & 0 & 0 & 0 \\ 0 & 0 & 0 & 0 \end{bmatrix} \tag{5.32}$$

From this equation the linear and the angular velocities of the AGV in terms of wheel velocities are derived and are presented in equation (3.60). This is reproduced below.

$$\begin{bmatrix} v_{rx} \\ v_{ry} \\ \dot{\theta}_r \end{bmatrix} = \frac{r}{(L_1 + L_2)} \begin{bmatrix} L_1 & L_2 \\ L_d & -L_d \\ 1 & -1 \end{bmatrix} \begin{bmatrix} \omega_{x1} \\ \omega_{x2} \end{bmatrix} \tag{5.33}$$

Here v_{rx} and v_{ry} are the linear velocities and $\dot{\theta}_r$ the angular velocity

of the AGV. ω_{x1} and ω_{x2} are the wheel speeds, L_1 and L_2 are the distances between the axis of rotation of the wheels and the geometric center of the AGV, L_d is the X-distance between the geometric center and the reference frame R.

To compute ${}^{F}T_{R}$ from the velocity transformations, two approximation schemes are considered, namely, the trapezoidal rule (2 points) and the Simpsons's parabolic rule (3 points) [76]. Simulations results are provided in Chapter 7 to compare the accuracy of the two schemes using a simulation package based on a dynamic model of the AGV [35]. If ΔT is the sampling interval of the overall system during which the track information (ε_{da} and $\varepsilon_{\theta a}$) is updated for computation, and n the sample count, the position transformation ${}^{F}\Phi_{R}(n\ \Delta T)$ at time $(n\ \Delta T)$ can be written as

Case 1 : Trapezoidal approximation.

$$ {}^{F}p_{R}\ (n\Delta T) = {}^{F}p_{R}\ ([n-1]\Delta T) + \frac{\Delta T}{2}\ V_{R}\ ([n-1]\Delta T) \left\{ \bar{R}\dot{\Pi}_{R}\ (n\Delta T) + \bar{R}\dot{\Pi}_{R}\ ([n-1]\Delta T) \right\} \tag{5.34} $$

Case 2 : Simpson's three point or parabolic approximation.

$$ {}^{F}p_{R}\ (n\Delta T) = {}^{F}p_{R}\ ([n-1]\Delta T) + \frac{\Delta T}{3}\ V_{R}\ ([n-1]\Delta T) \left\{ \bar{R}\dot{\Pi}_{R}\ (n\Delta T) + 4.0\ \bar{R}\dot{\Pi}_{R}\ ([n-1]\Delta T) + \bar{R}\dot{\Phi}([n-2]\Delta T) \right\} \tag{5.35} $$

Where ${}^{F}p_{R}\ (n\Delta T)$ is a position vector and is given by

$$ {}^{F}p_{R}\ (n\Delta T) = \{\ p_{rx},\ p_{ry},\ \theta_{r}\}^{t} \tag{5.36} $$

The term V_R ([n-1]ΔT) is the rotational transformation of the frame 'R' relative to 'F' at the time instant (n-1)ΔT and is given by

$$V_R([n-1]\Delta T) = \begin{bmatrix} \cos(\theta_r[n-1]\Delta T) & -\sin(\theta_r[n-1]\Delta T) & 0 & 0 \\ \sin(\theta_r[n-1]\Delta T) & \cos(\theta_r[n-1]\Delta T) & 0 & 0 \\ 0 & 0 & 1 & 0 \\ 0 & 0 & 0 & 1 \end{bmatrix} \quad (5.37)$$

The position vector ${}^F p_R$ (n ΔT) = $\{ p_{rx}, p_{ry}, \theta_r \}^t$ is obtained by substituting (5.37) in (5.34) and (5.35) and the resulting equations are presented below.

Case 1 : Position Transformations using rectangular approximation.

$$\left.\begin{aligned} p_{rx}(n\Delta T) &= p_{rx}([n-1]\Delta T) + \frac{\Delta T}{2}\left\{ v_{rx}(n\Delta T) + v_{rx}([n-1]\Delta T)\right\}\cos(\theta_r([n-1]\Delta T \\ &\quad - \frac{\Delta T}{2}\left\{ v_{ry}(n\Delta T) + v_{ry}([n-1]\Delta T)\right\} \sin(\theta_r([n-1]\Delta T) \\ p_{ry}(n\Delta T) &= p_{ry}([n-1]\Delta T) + \frac{\Delta T}{2}\left\{ v_{rx}(n\Delta T) + v_{rx}([n-1]\Delta T)\right\}\sin(\theta_r([n-1]\Delta T \\ &\quad + \frac{\Delta T}{2}\left\{ v_{ry}(n\Delta T) + v_{ry}([n-1]\Delta T)\right\} \cos(\theta_r([n-1]\Delta T) \\ \theta_r(n\Delta T) &= \theta_r([n-1]\Delta T) + \frac{\Delta T}{2}\left\{ \theta_r(n\Delta T) + \theta_r([n-1]\Delta T)\right\} \end{aligned}\right\} \quad (5.38)$$

Case 2 : Position transformation using Simpson's three point (parabolic) approximation.

$$
\left.
\begin{aligned}
p_{rx}(n\Delta T) &= p_{rx}([n-1]\Delta T) + \frac{\Delta T}{3}\left\{v_{rx}(n\Delta T) + 4.0\, v_{rx}([n-1]\Delta T)\right. \\
&\quad \left. + v_{rx}([n-2]\Delta T)\right\} \cos(\theta_r([n-1]\Delta T) - \frac{\Delta T}{3}\left\{v_{ry}(n\Delta T)\right. \\
&\quad \left. + 4.0\, v_{ry}([n-1]\Delta T) + v_{ry}([n-2]\Delta T)\right\} \sin(\theta_r([n-1]\Delta T) \\
p_{ry}(n\Delta T) &= p_{ry}([n-1]\Delta T) + \frac{\Delta T}{3}\left\{v_{rx}(n\Delta T) + 4.0\, v_{rx}([n-1]\Delta T)\right. \\
&\quad \left. + v_{rx}([n-2]\Delta T)\right\} \sin(\theta_r([n-1]\Delta T) - \frac{\Delta T}{3}\left\{v_{ry}(n\Delta T)\right. \\
&\quad \left. + 4.0\, v_{ry}([n-1]\Delta T) + v_{ry}([n-2]\Delta T)\right\} \cos(\theta_r([n-1]\Delta T) \\
\theta_r(n\Delta T) &= \theta_r([n-1]\Delta T) + \frac{\Delta T}{3}\left\{\theta_r(n\Delta T) + \theta_r([n-1]\Delta T) + \theta_r([n-2]\Delta T)\right\}
\end{aligned}
\right\} \quad (5.39)
$$

5.4.2 Identification of Track Geometry

5.4.2.1 Introduction

From the analysis presented in the previous section, one obtains the following :

a) x-position of point '**P**' relative to frame 'F' (n-samples).

b) y-position of point '**P**' relative to frame 'F' (n-samples).

These are shown in Fig. 5.6. This forms a set of data for the location of point **P** until the sampling time (n ΔT). Curve fitting technique is used to describe the geometric nature of the path that the point '**P**' has traced. This in turn is the profile of the track on the floor. The identified geometry of the track may take the following form

$$x_p = X\left(\theta_p \mid \{a_0, a_1, \ldots\ldots, a_m\}\right) \quad (5.40)$$

$$y_p = Y\left(\theta_p \mid \{b_0, b_1, \ldots\ldots, b_m\}\right) \quad (5.41)$$

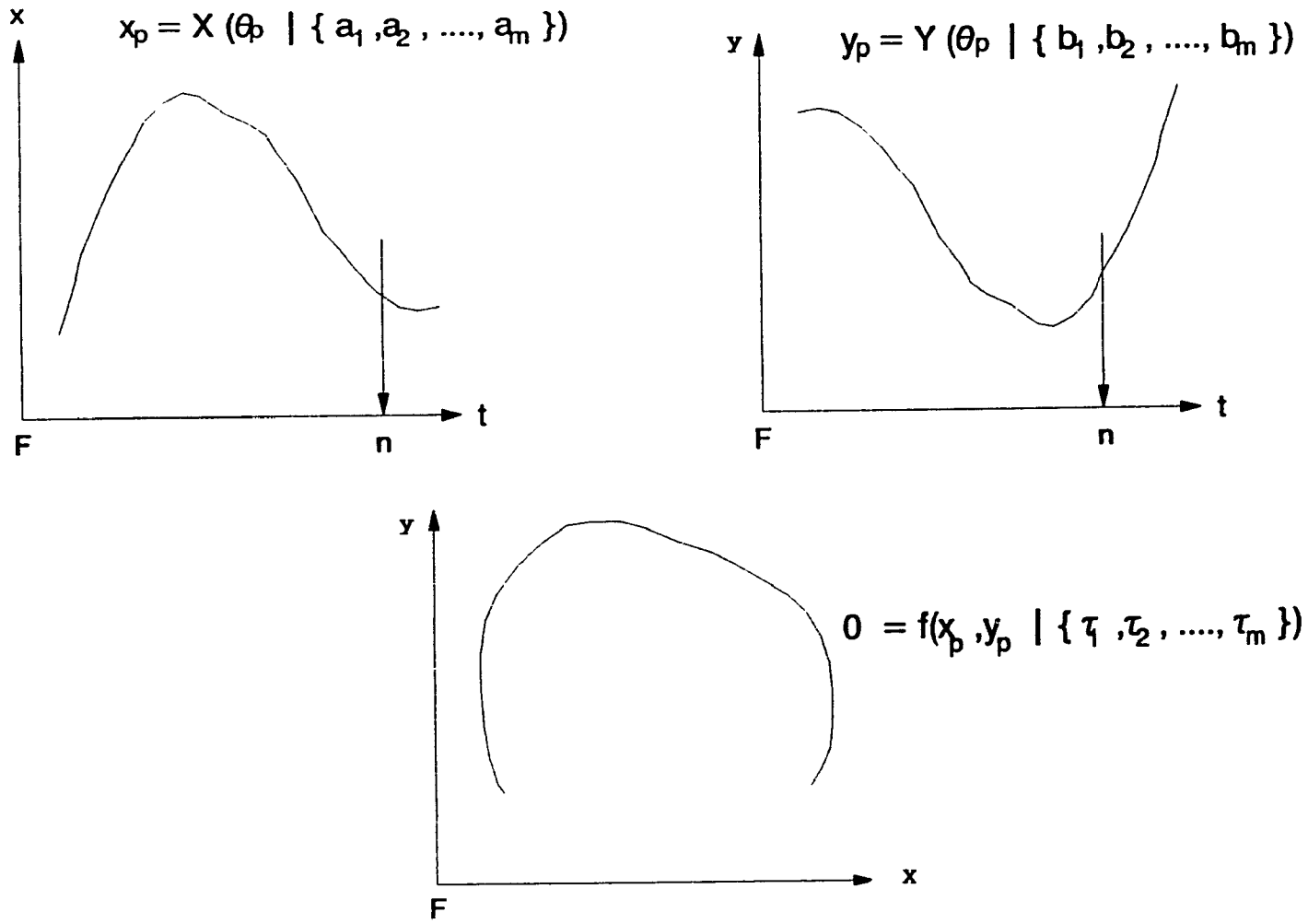

Fig. 5.6 Path Functions of Coordinates of Reference Point

Equations (5.40) and (5.41) respectively describe the path function for the x and y locations of the point 'P' relative to the floor frame 'F' as a function of the orientation of the vector at 'P' on the track. The coefficients of the polynomial functions are given by $\{a_0, a_1, \ldots a_m\}$ and $\{b_0, b_1, \ldots b_m\}$ respectively and the polynomial considered is of the order 'm'. The reason for expressing the functions for x_p and y_p positions of the point 'P' as a function of orientation is due to the fact that both the orientation and the coordinates (x_p, y_p) of P are functions of time and the linear velocity of the AGV.

The coefficients of the functions chosen are evaluated using the least sum of error square solution method described in the Appendix-A and reference [74]. The system of equations has m unknowns and there are n equations ($n >> m$). Though the coefficients can be evaluated when $n = m$, the values x_p, y_p, and θ_p are based on experimental results. Hence the evaluated values of the coefficients will not be the actual values.

From the computed path functions described above, the location (position and orientation) of the point P on the track from time $(n+1)\Delta T$ onwards is evaluated by extrapolation. The number of samples of data needed for geometry identification and the time intervals for which the extrapolation can be performed are influenced by the following factors :

1) Geometric nature of the track function

2) Linear velocity of the vehicle

3) Length and wheelbase of the vehicle

4) Sampling time (ΔT) of the AGV system

5) Window dimensions of the camera

The first factor, the geometric nature of the track function, depends on whether the function is a fast varying one or a slow varying one. In the case of a slow varying function, the convergence is slower as the identification requires sufficient data to identify the varying nature of the function. However, in this case, extrapolation of the function ahead of the AGV can be done for a very long distance. If the function is a fast varying one, the extrapolation can be done for a very short distance only.

If the vehicle is travelling fast, the parameters of steering feature information obtained is from sections of the track which are spaced widely apart, and this results in less samples for convergence for a given track profile. If the vehicle is travelling slow, the track features are obtained from sections of the track which are close to each other. As a result of this more samples are required. The velocity factor can be eliminated by considering the total distance travelled instead of the number of samples required for convergence.

The length and the wheelbase affect the convergence and extrapolation depending on the driving criterion chosen. Sampling time affects only the convergence. If the sampling of the parameters of steering control and the motion parameters of the vehicle are carried out at faster, then all the characteristics of the track function are obtained faster. This depends on the speed at which the vehicle is travelling and the rate of change of curvature of the track. If the vehicle is travelling slowly then faster

sampling not necessarily mean better results. The best sampling rate should be greater than twice the rate at which the function is varying. Window dimensions affect the convergence. In this case, the convergence depends on how much and how far the camera can see. The convergence of the coefficients of the identified geometry are tested for various conditions as specified above. The results are presented in Chapter 7.

The extrapolated track profile information is used to drive the AGV to achieve accurate tracking. The track functions computed are updated using the most recent values of the parameters. The discussions and the analysis presented in the following sections are to provide accurate tracking using the path functions computed above.

From the track equations (5.40) and (5.41) for the x and y positions of the point **P** with respect to time, the function that best describes the path of the point **P** in the XY-plane of the floor frame 'F' is derived. This is obtained by eliminating the orientation θ_p by simultaneously solving equations (5.40) and (5.41).

The analysis presented in this thesis addresses two sets of profiles for the track, namely, the conic profile and the polynomial profile. The method of obtaining the coefficients of these two functions are presented below.

5.4.2.2 Formulations for a Conic Function

It is assumed that the point **P** traces a path whose equations are of the following form. These equations are chosen to cover various profiles in conic functions namely, circles, ellipses, hyperbola and parabola.

$$x_p = a_0 + a_1 \cos\theta_p + a_2 \sin\theta_p \tag{5.42}$$

$$y_p = b_0 + b_1 \cos\theta_p + b_2 \sin\theta_p \tag{5.43}$$

If the function is strictly a conic, then the coefficients a_2 and b_1 should become zero. These are introduced to account for the presence of noise in the data received from the measuring devices. The general form of a conic is

$$\frac{(x_p - x_0)^2}{a^2} \pm \frac{(y_p - y_0)^2}{b^2} = 1 \tag{5.44}$$

In the ± sign, the plus is for ellipses and circles and the minus sign is for hyperbolas. The distances a and b are equal in the case of circles and is the radius of the circle. The distances x_0 and y_0 are the position coordinates of the center of the conic in the inertial frame.

Using the regression formulations presented in reference [74], expressions for the coefficients of equations (5.42) and (5.43) are obtained and are given as

$$a_1 = \frac{\sum x_p \cos\theta_p \sum \sin^2\theta_p - \sum \cos\theta_p \sin\theta_p \sum x_p \sin\theta_p}{\sum \cos^2\theta_p \sum \sin^2\theta_p - \left(\sum \cos\theta_p \sin\theta_p\right)^2}$$

$$a_2 = \frac{\sum x_p \sin\theta_p \sum \cos^2\theta_p - \sum \cos\theta_p \sin\theta_p \sum x_p \cos\theta_p}{\sum \cos^2\theta_p \sum \sin^2\theta_p - \left(\sum \cos\theta_p \sin\theta_p\right)^2}$$

$$a_0 = \frac{\sum x_p}{n} - \frac{a_1 \sum \cos\theta_p}{n} - \frac{a_2 \sum \sin\theta_p}{n}$$

$$b_1 = \frac{\sum y_p \cos\theta_p \sum \sin^2\theta_p - \sum \cos\theta_p \sin\theta_p \sum y_p \sin\theta_p}{\sum \cos^2\theta_p \sum \sin^2\theta_p - \left(\sum \cos\theta_p \sin\theta_p\right)^2}$$

$$b_2 = \frac{\sum y_p \sin\theta_p \sum \cos^2\theta_p - \sum \cos\theta_p \sin\theta_p \sum y_p \cos\theta_p}{\sum \cos^2\theta_p \sum \sin^2\theta_p - \left(\sum \cos\theta_p \sin\theta_p\right)^2}$$

$$b_0 = \frac{\sum y_p}{n} - \frac{b_1 \sum \cos\theta_p}{n} - \frac{b_2 \sum \sin\theta_p}{n}$$

Equations (5.42) and (5.43) are rewritten in the form $(x_p - x_0)$ and $(y_p - y_0)$ as in equation (5.44)

$$x_p - a_0 = a_1 \text{ Cos } \theta_p + a_2 \text{ Sin } \theta_p \qquad (5.45)$$

$$y_p - b_0 = b_1 \text{ Cos } \theta_p + b_2 \text{ Sin } \theta_p \qquad (5.46)$$

Multiplying (5.45) by b_1 and (5.46) by a_1, subtracting the first one from the second one and simplifying the result gives the following.

$$\text{Sin } \theta_p = \frac{b_1 (x_p - a_0) - a_1 (y_p - b_0)}{(b_1 a_2 - a_1 b_2)} \qquad (5.47)$$

Equation (5.46) is multiplied by a_2 and the result is subtracted from the product of b_2 and equation (5.45). The result is

$$\text{Cos } \theta_p = \frac{b_2 (x_p - a_0) - a_2 (y_p - b_0)}{(b_2 a_1 - a_2 b_1)} \qquad (5.48)$$

Squaring equations (5.47) and (5.48) and summing them results in

$$\left[\frac{b_1 (x_p - a_0) - a_1 (y_p - b_0)}{(b_1 a_2 - a_1 b_2)^2}\right]^2 + \left[\frac{b_2 (x_p - a_0) - a_2 (y_p - b_0)}{(b_2 a_1 - a_2 b_1)^2}\right]^2 = 1 \quad (5.49)$$

Equation (5.49) is expanded and the coefficients of like powers of x_p, y_p and constant terms are collected. The resulting equation is

$$x_p^2 (b_1 a_2 - a_1 b_2)^2 \left\{b_1^2 + b_2^2\right\} + y_p^2 (b_1 a_2 - a_1 b_2)^2 \left\{a_1^2 + a_2^2\right\} -$$
$$2 x_p y_p (b_1 a_2 - a_1 b_2)^2 \left\{a_1 b_1 + a_2 b_2\right\} - 2 x_p (b_1 a_2 - a_1 b_2)^2 \left\{\right.$$
$$b_1(a_0 b_1 - b_0 a_1) + b_2(a_0 b_2 - a_2 b_0)\left.\right\} - 2 y_p (b_1 a_2 - a_1 b_2)^2 \left\{\right.$$
$$- a_1(a_0 b_1 - b_0 a_1) - a_2(a_0 b_2 - a_2 b_0)\left.\right\} + (b_1 a_2 - a_1 b_2)^2 \left\{\right.$$
$$(a_0 b_1 - b_0 a_1)^2 + (a_0 b_2 - a_2 b_0)^2\left.\right\} - (b_1 a_2 - a_1 b_2)^4 = 0 \quad (5.50)$$

Equation (5.50) is the general form of the equation of a plane curve. This is of the following form

$$f(x_p, y_p \mid \chi_0, \chi_1, \ldots\ldots, \chi_1) = 0 \quad (5.51)$$

It has been mentioned earlier that if the profile of the track is strictly conic, then the coefficients a_2 and b_1 become zero. Substituting this condition in equation (5.50), the following equation is obtained.

$$x_p^2 a_1^2 b_2^4 + y_p^2 a_1^4 b_2^2 - 2 x_p a_1^2 b_2^4 a_0 - 2 y_p a_1^4 b_2^2 b_0 +$$
$$a_1^2 b_2^2 \left\{ b_0^2 a_1^2 + a_0^2 b_2^2 \right\} - a_1^4 b_2^4 = 0 \quad (5.52)$$

This is the general form of the equation of a conic. The value of the coefficients $\{a_0, a_1, a_2\}$ and $\{b_0, b_1, b_2\}$ are evaluated using the method of least sum of error square solution (LSES). These values are substituted in (5.50) and the equation of the plane curve is obtained. The correctness of these equations are tested using known equations of the track and the results are presented in Chapter 7.

5.4.2.3 Formulations for a Polynomial Function

To evaluate the coefficients of a polynomial function that closely resembles the track geometry, the following form of second order expressions are chosen to describe the path function traced by the reference point **P**.

$$x_p = a_0 + a_1 t V_p + a_2 t^2 V_p^2 \tag{5.53}$$

$$y_p = b_0 + b_1 t V_p + b_2 t^2 V_p^2 \tag{5.54}$$

Here t is the total elapsed time at which the process of identifying the track geometry is performed and V_p is the linear velocity of the point P. The linear velocity V_p is equal to the linear velocity V of the AGV. The product $t V_p$ is chosen as it provides the distance travelled at time t. Hence, the identification will provide consistent results irrespective of the linear velocity of the AGV. The coefficients of equations (5.53) and (5.54) are evaluated using the regression equations in the reference [74]. Final form of the equations are

$$a_1 = \frac{\sum x_p v_p^2 t^2 \sum v_p^2 t^2 - \sum v_p^3 t^3 \sum x_p v_p t}{\sum v_p^4 t^4 \sum v_p^2 t^2 - \left(\sum v_p^3 t^3 \right)^2}$$

$$a_2 = \frac{\sum x_p\, v_p\, t \;\; \sum v_p^4\, t^4 \;-\; \sum v_p^3\, t^3 \;\sum x_p\, v_p^2\, t^2}{\sum v_p^4\, t^4 \;\; \sum v_p^2\, t^2 \;-\; \left(\sum v_p^3\, t^3\right)^2}$$

$$a_0 = \frac{\sum x_p}{n} \;-\; \frac{a_1 \sum v_p^2\, t^2}{n} \;-\; \frac{a_2 \sum v_p\, t}{n}$$

$$b_1 = \frac{\sum y_p\, v_p^2\, t^2 \;\; \sum v_p^2\, t^2 \;-\; \sum v_p^3\, t^3 \;\sum y_p\, v_p\, t}{\sum v_p^4\, t^4 \;\; \sum v_p^2\, t^2 \;-\; \left(\sum v_p^3\, t^3\right)^2}$$

$$b_2 = \frac{\sum y_p\, v_p\, t \;\; \sum v_p^4\, t^4 \;-\; \sum v_p^3\, t^3 \;\sum y_p\, v_p^2\, t^2}{\sum v_p^4\, t^4 \;\; \sum v_p^2\, t^2 \;-\; \left(\sum v_p^3\, t^3\right)^2}$$

$$b_0 = \frac{\sum y_p}{n} \;-\; \frac{a_1 \sum v_p^2\, t^2}{n} \;-\; \frac{a_2 \sum v_p\, t}{n}$$

From (5.53) and (5.54) the product $t\, V_p$ can be expressed as

$$V_p\, t \;=\; \frac{1}{(a_1 b_2 - b_1 a_2)} \left\{(x_p b_2 - y_p a_2) - (a_0 b_2 - b_0 a_2)\right\} \tag{5.55}$$

Substituting (5.55) in (5.53), the following result is obtained.

$$x_p = a_0 + \frac{a_1}{(a_1 b_2 - b_1 a_2)} \left\{(x_p b_2 - y_p a_2) - (a_0 b_2 - b_0 a_2)\right\} + \frac{a_2}{(a_1 b_2 - b_1 a_2)^2} \left\{(x_p b_2 - y_p a_2) - (a_0 b_2 - b_0 a_2)\right\}^2 \tag{5.56}$$

Simplifying equation (5.56) and rearranging the terms, an expression in powers of x_p and y_p with some constant terms is obtained as below :

$$a_2b_2^2\,x_p^2 + a_2^3\,y_p^2 - 2\,a_2^2\,b_2\,x_p\,y_p + \Big\{\, b_1a_2\,(a_1b_2 - b_1a_2) - 2\,a_2b_2(a_0b_2 - b_0a_2) \,\Big\}x_p + \Big\{ - a_1a_2(a_1b_2 - b_1a_2) + 2\,a_2^2(a_0b_2 - a_2b_0) \Big\}\,y_p + (a_0b_2 - b_0a_2)\Big\{\, a_2(a_0b_2 - b_0a_2) - a_1\,(a_1b_2 - b_1a_2) \,\Big\} + a_0\,(a_1b_2 - b_1a_2)^2 = 0 \qquad (5.57)$$

$$f(x_p,\, y_p \mid \kappa_0,\, \kappa_1,\, \ldots\ldots,\, \kappa_6) = 0 \qquad (5.58)$$

where $\kappa_0,\ \kappa_1,\ \ldots\ldots,\ \kappa_6$ are the coefficients of the function expressed in x_p and y_p and $i = 0, 1, \ldots, 6$.

5.4.2.4 Formulations for a Straight Line Function

Equation (5.57) is of the same form as the function obtained in equation (5.50) but for the coefficients. Depending upon the type of function of the track profile, certain terms vanish. For example, if the geometric profile of the track is a straight line, the coefficients for the powers of x_p and y_p vanish and the resulting equation is of the following form

$$x_p = a_0 + a_1\,t\,V_p \qquad (5.59)$$

$$y_p = b_0 + b_1\,t\,V_p \qquad (5.60)$$

Eliminating $t\,V_p$ from equations (5.59) and (5.60), an expression for y_p in terms of x_p results in the standard $y = mx + c$ form. This is given by

$$y_p = \frac{b_1}{a_1}\,x_p - \frac{a_0b_1 - b_0a_1}{a_1} \qquad (5.61)$$

From equation (5.61) the slope m and the offset c of the straight line function are obtained. The equations for the straight line function can also be derived from the standard equation $y = mx + c$ instead of the polynomial function form as presented above. The least sum of error square (LSES) solution for the coefficients m and c in equation $y = mx + c$ is given in reference [75], and is given below.

$$c = \frac{\sum x^2 \sum y - \sum x \sum xy}{n \sum x^2 - \left(\sum x\right)^2} \qquad m = \frac{n\sum xy - \sum x \sum y}{n \sum x^2 - \left(\sum x\right)^2} \quad (5.62)$$

In Chapter 7 these equations are tested and coefficients convergence for straight line profiles using the polynomial and the straight line function are compared.

5.4.3 Driving Criterion for Accurate Tracking

In this section a driving criterion is defined in order to compute the desired values for the parameters of steering control for future travel of the AGV. The driving criterion provides the definition for accurate track following by stating which point(s) on the AGV has/have to be on the track. Many driving criteria are available for consideration some of which are

1) a criterion in which a reference point chosen on the AGV is on the track. In this, one may wish to have the center of the front camera or the geometric center of the AGV on the track;
2) a criterion in which multiple reference points chosen on the AGV are on the track, namely, the contact points (patchs) of the front and rear casters or the centers of the front and rear camera windows on the

track;

3) minimize the included area between the longitudinal axis of the AGV and the track.

Figures. 5.7a & 5.7b illustrate criterion (1), i.e. a single point on the track. These figures show the situation where the center of the front camera on the track and the geometric center of the AGV on the track respectively while following a track with a curvature. From Fig. 5.7a, it can be seen that for the criterion which requires the center of the camera window on the track, the position offset (ε_d) is equal to zero whereas the orientation offset (ε_θ) is not equal to zero. From Fig. 5.7b it can be inferred that for the criterion for geometric center of the AGV on the track, the position offset (ε_d) is non-zero in addition to the non-zero orientation offset (ε_θ).

Criterion (2) is presented in Figs. 5.7c & 5.7d. Fig. 5.7c shows that for the criterion that requires the casters on the track, the parameters of steering measured by the front and rear cameras are not equal to zero and are equal in magnitude. Their magnitudes depend on the track geometry.

The third criterion illustrated in Fig. 5.7e suggests that the driving and steering of the vehicle is performed so that the entire vehicle is within reasonable distance from the track.

Formulations are presented for criterion (2), i.e. multiple points on the track in section 5.4.4. Here the contact points (patches) of the casters on the track is considered. Section 5.4.4.3 presents the expressions to

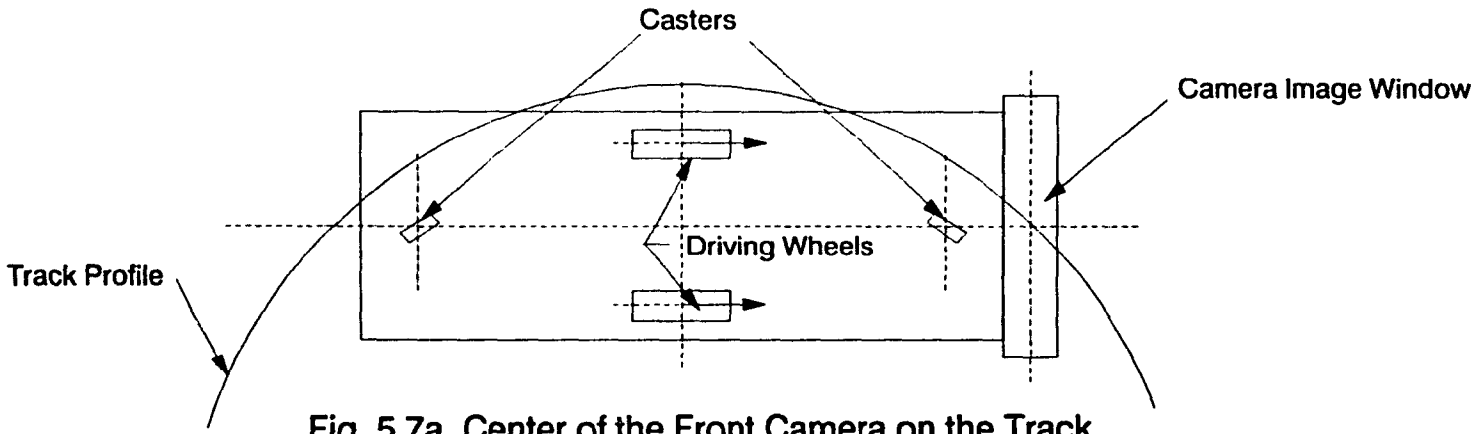

Fig. 5.7a Center of the Front Camera on the Track

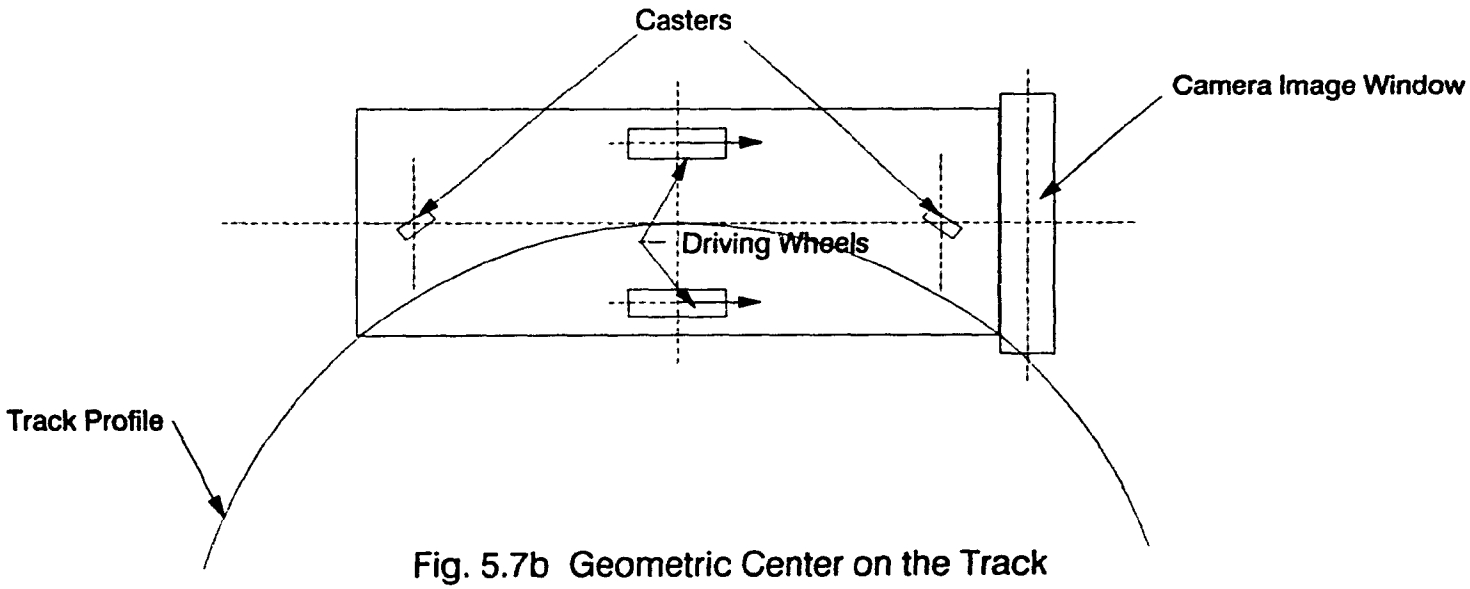

Fig. 5.7b Geometric Center on the Track

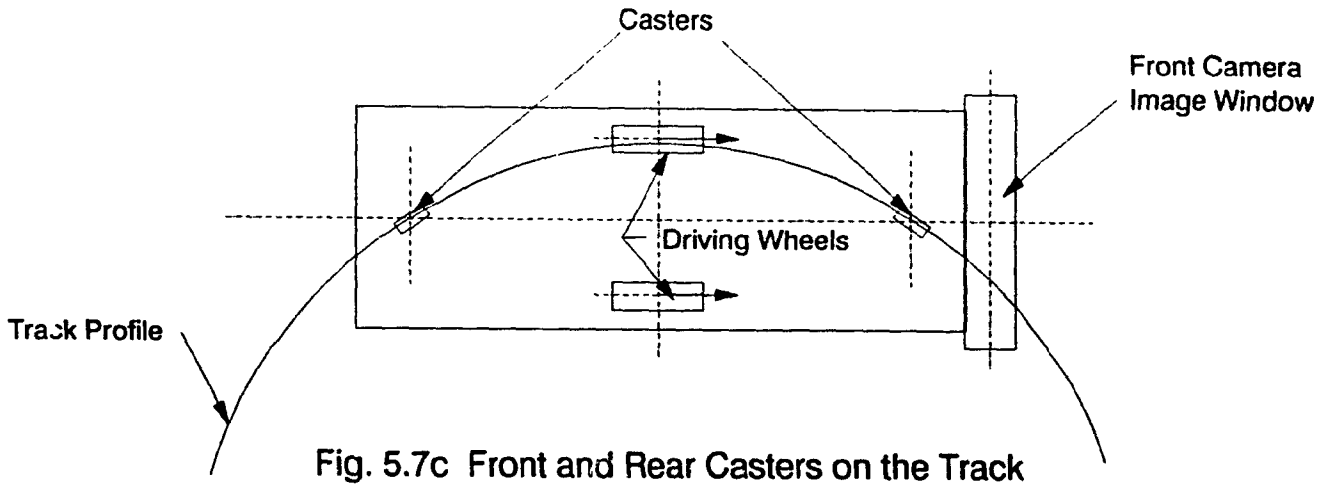

Fig. 5.7c Front and Rear Casters on the Track

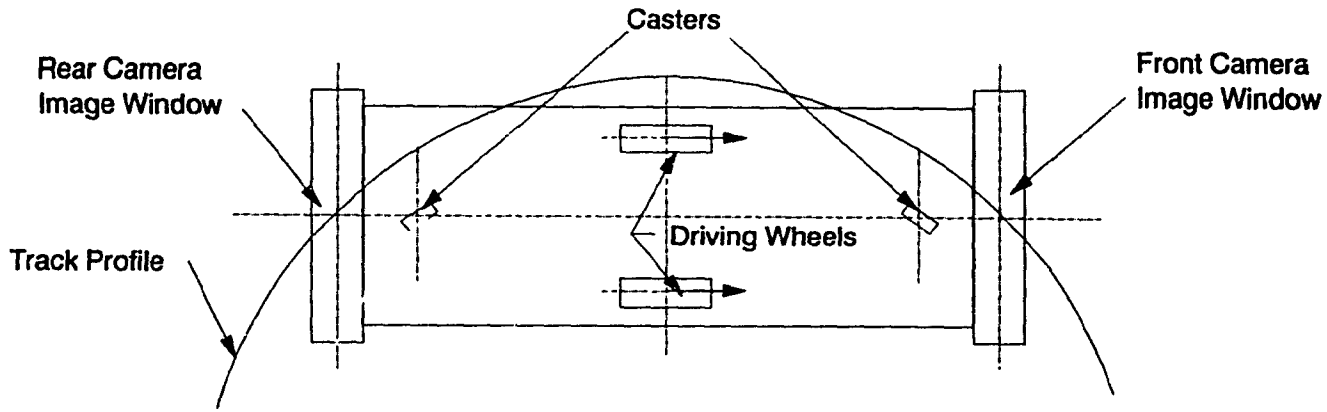

Fig. 5.7d Center of Both Cameras on the Track

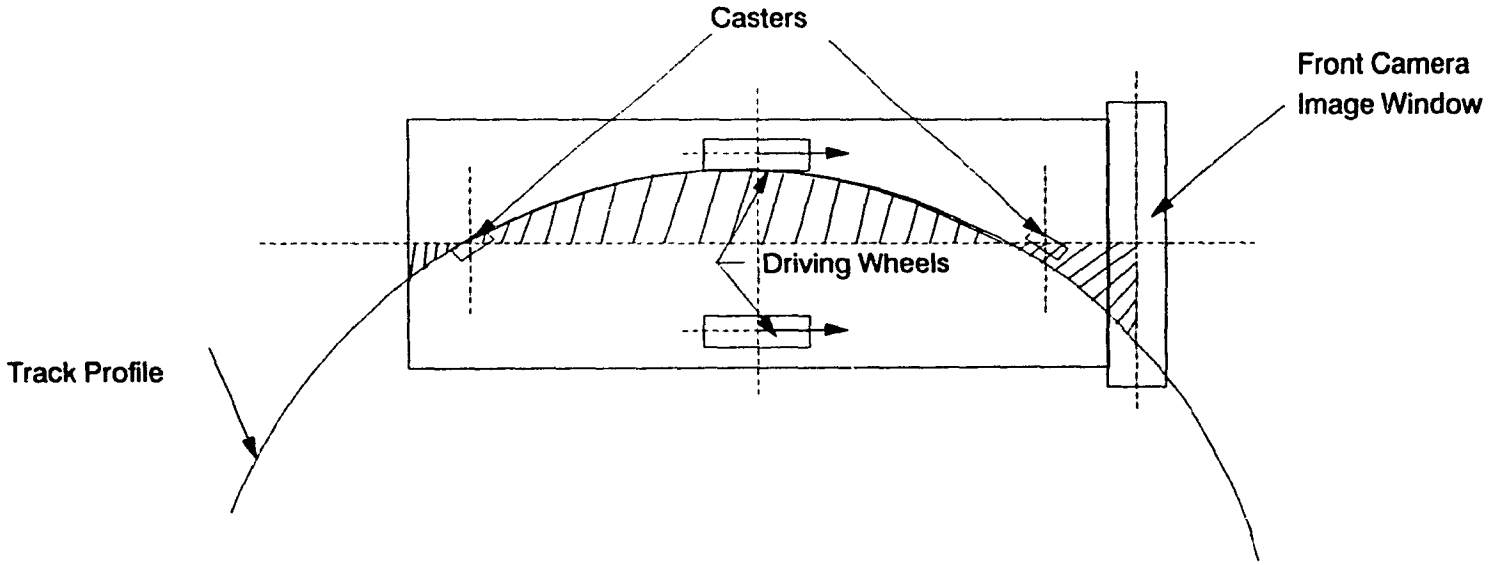

Fig. 5.7e Minimum Area Between the Track and the Longitudinal Axis of AGV

evaluate the desired values of the parameters of steering control based on the identified profile of the track and the methodology to derive these expressions.

5.4.4 Computation of Parameters of Steering Control

5.4.4.1 Coordinates of Instantaneously Coincident Circle

The steering angle or the required orientation of the caster at the time instant $(n+1)\Delta T$ is evaluated for accurate tracking using the analysis presented so far. Since the estimated equation of the track (5.36) may be a generic function, it is necessary to evaluate the coordinates of an instantaneously coincident circle. In this scheme the radius of rotation (R_1) of the point **P** as well as the center of the instantaneous circle $C(X_c, Y_c)$ at time $[(n+1)\Delta T]$ are evaluated. Figure. 5.8 shows the section of the track, identified geometry of the track and the instantaneously coincident circle. The following analysis is based on this figure. The following derivations are to obtain the equation of the closest circular approximation for $f(x_p, y_p \mid \chi \text{ or } \kappa)$ at the point **P** whose coordinates at the new expected location at time $[(n+1)\Delta T]$ is represented as (a, b). The equation of the instantaneously coincident circle is of the form [76]

$$(X - h)^2 + (Y - k)^2 = R_1^2 \tag{5.63}$$

The coordinates of the center of the instantaneous circle are given by (h, k). This equation should satisfy the following conditions :

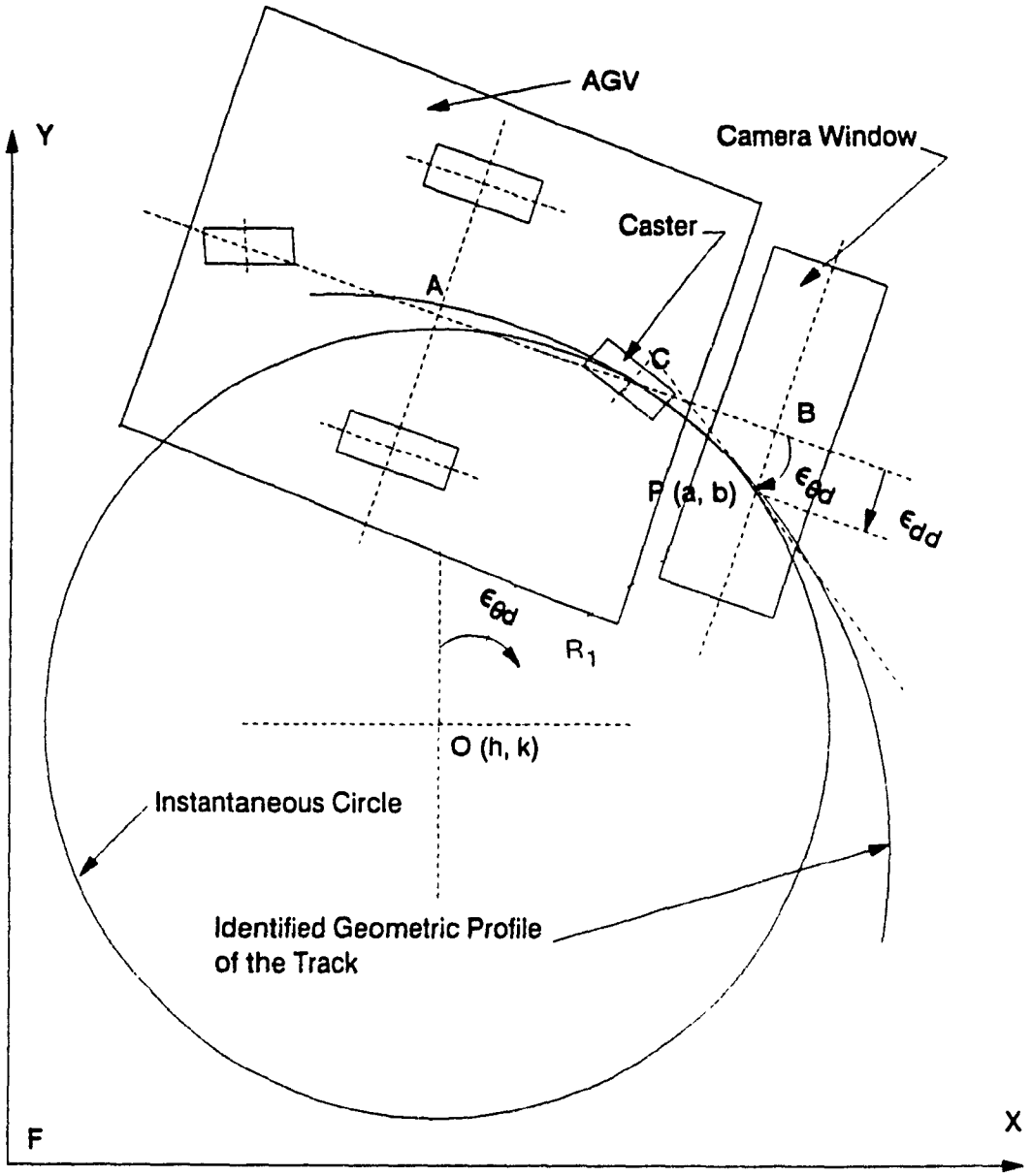

Fig. 5.8 Schematic for Instantaneously Coincident Circle

a) the circle is tangential to the graph of $f(x_p, y_p \mid \chi \text{ or } \kappa)$ function

b) $\dfrac{d^2Y}{dX^2} = f''(x_p, y_p)$ (5.64)

Considering a line normal to the tangent at (a, b) and passing through the center of the approximate circle, the slope of this line is given by

$$m = -\frac{1}{f'(a,b)} \tag{5.65}$$

The center of the circular approximation should be along the normal line, and is at a distance R_1 from (a, b). Differentitating (5.63) results in

$$\frac{dy}{dx} = -\frac{(X - h)}{(Y - k)} \tag{5.66}$$

Differentiating (5.66) one more time and simplifying one obtains

$$\frac{d^2Y}{dX^2} = \frac{\left[1 + \left(\frac{dY}{dX}\right)^2\right]}{Y - k} \tag{5.67}$$

Substituting (Y-k) from (5.66) in equation (5.67), the second derivative of the equation of the circle can be expressed in terms of the first derivative as

$$\frac{d^2Y}{dX^2} = - \frac{\frac{dY}{dX}\left[1 + \left(\frac{dY}{dX}\right)^2 \right]}{X - h} \qquad (5.68)$$

Since the circular approximation chosen is also tangential to the graph of f(x,y) at P(a, b), we have the following conditions :

$$\frac{dY}{dX} = f'(x_p, y_p) \qquad \text{at } (a,b) \qquad (5.69)$$

and

$$\frac{d^2Y}{dX^2} = f''(x_p, y_p) \qquad \text{at } (a,b) \qquad (5.70)$$

Substituting these conditions in equation (5.68) for d^2Y/dX^2, the second derivative is expressed in a different form as

$$f''(x_p, y_p) = - \frac{f'(a, b)(1 + [f'(a, b)]^2)}{a - h} \qquad (5.71)$$

From this the x-location of the center of the circular approximation is obtained as

$$h = a + \frac{f'(a, b)\ (1 + [f'(a, b)]^2)}{f''(a, b)} \qquad (5.72)$$

It has been shown in equation (5.65) that the normal at (a, b) has a slope $-1/f'(a,b)$ and passes through the center of the circle (h, k). Substituting this condition in equation (5.72), the equation to compute the Y-location of the center of the circular approximation is obtained as

$$k = b + \left[\frac{1}{f'(a,\ b)} \right](a - h) \qquad (5.73)$$

The radius of the circle is computed using equation (5.63). The first and second derivatives of the function f(x, y) are evaluated as below. For a function $f(x_p, y_p) = 0$, the first derivative is computed as

$$f_x(x_p, y_p) + f_y(x_p, y_p) \frac{dy}{dx} = 0 \qquad \text{i.e.} \qquad \frac{dy}{dx} = -\frac{f_x(x_p, y_p)}{f_y(x_p, y_p)} \qquad (5.74)$$

And taking the derivative of equation (5.74) one obtains

$$f_{xx}(x_p,y_p) + 2 f_{xy}(x_p,y_p) \frac{dy}{dx} + f_{yy}(x_p,y_p)\left(\frac{dy}{dx}\right)^2 + f_y(x_p,y_p) \frac{d^2y}{dx^2} = 0 \qquad (5.75)$$

From this, the expression to evaluate $\frac{d^2y}{dx^2}$ is obtained. The expressions to compute the coordinates of the center of the instantaneous circle for the two track profiles considered are discussed below.

5.4.4.1.1 Expressions for Conic Functions

The coordinates of the center of the instantaneous circle of rotation for the conic profile is derived below. Differentiating the expression for the conic profile given by equation (5.50) partially with respect to x_p yields

$$f_x(x_p, y_p) = 2 x_p (b_1a_2 - a_1b_2)^2 \left\{b_1^2 + b_2^2\right\} - 2 y_p (b_1a_2 - a_1b_2)^2 \left\{a_1b_2 + a_2b_2\right\} - 2 (b_1a_2 - a_1b_2)^2 \left\{b_1(a_0b_1 - b_0a_1) + b_2(a_0 b_2 - a_2b_2)\right\} \qquad (5.76)$$

Differentiating equation (5.76) with respect to x_p and y_p independently provides

$$f_{xx}(x_p, y_p) = 2 (b_1 a_2 - a_1 b_2)^2 \left\{ b_1^2 + b_2^2 \right\} \tag{5.77}$$

$$f_{xy}(x_p, y_p) = -2 (b_1 a_2 - a_1 b_2)^2 \left\{ a_1 b_2 + a_2 b_2 \right\} \tag{5.78}$$

Partially differentiating the function (5.50) with respect to y_p results in

$$\begin{aligned} f_y(x_p, y_p) = {} & 2 (b_1 a_2 - a_1 b_2)^2 \left[y_p \left\{ a_1^2 + a_2^2 \right\} - x_p \left\{ a_1 b_1 + a_2 b_2 \right\} \right] - \\ & 2 (b_1 a_2 - a_1 b_2)^2 \left\{ - a_1 (a_0 b_1 - b_0 a_1) - a_2 (a_0 b_2 - a_2 b_0) \right\} \end{aligned} \tag{5.79}$$

Partial differentiation of equation (5.79), an expression for $f_{yy}(x_p, y_p)$ results.

$$f_{yy}(x_p, y_p) = 2 (b_1 a_2 - a_1 b_2)^2 y_p \left\{ a_1^2 + a_2^2 \right\} \tag{5.80}$$

Substituting these results in equations (5.72) and (5.73), expressions to compute the coordinates of the circle center are obtained. From the coordinates of the circular approximation, the instantaneous radius of rotation is obtained from equation (5.59).

5.4.4.1.2 *Expressions for Polynomial Functions*

The procedure described before is followed in evaluating the coordinates of the center of the instantaneous circle of rotation for the polynomial function. Differentiating the function (5.57) partially with respect to x_p results in

$$f_x(x_p, y_p) = 2 a_2 b_2^2 x_p - 2 a_2^2 b_2 y_p + \left\{ b_1 a_2 (a_1 b_2 - b_1 a_2) - 2 a_2 b_2 (a_0 b_2 - b_0 a_2) \right\} \quad (5.81)$$

Differentiating equation (5.81) with respect to x_p and y_p independently provides

$$f_{xx}(x_p, y_p) = 2 a_2 b_2^2 \quad (5.82)$$

$$f_{xy}(x_p, y_p) = - 2 a_2^2 b_2 \quad (5.83)$$

Partially differentiating the function (5.81) with respect to y_p results in

$$f_y(x_p, y_p) = 2 a_2^3 y_p - 2 a_2^2 b_2 x_p - a_1 a_2 (a_1 b_2 - b_1 a_2) + 2 a_2^2 (a_0 b_2 - a_2 b_0) \quad (5.84)$$

Partial differentiation of equation (5.84) provides the following expression.

$$f_{yy}(x_p, y_p) = 2 a_2^3 \quad (5.85)$$

Substituting these results in equations (5.72) and (5.73), expressions to compute the coordinates of the center of the instantaneous circle are

obtained. From the coordinates of the circular approximation, the instantaneous radius of rotation is obtained from equation (5.59).

5.4.4.3 Computation of Parameters of Steering Control

In this section, mathematical formulations are presented to compute the steering parameters for proper driving as defined by the driving criterion chosen. The following computations are presented such that the contact points of the front and rear casters are on the track.

It has been mentioned in section 5.2.1, that in order to keep the contact points on the track, the track has to be located at a distance ε_{dd} from the longitudinal axis of the vehicle (which is also the center line of the camera image window) and should be oriented at an angle $\varepsilon_{\theta d}$. These are shown in Figs. 5.9 & 5.10. The objective of the following analysis is to compute these driving parameters (ε_{dd} and $\varepsilon_{\theta d}$) necessary to achieve the desired level of tracking.

The parameters $\varepsilon_{\theta d}$ and ε_{dd} are obtained from the geometry of the AGV as shown in Fig. 5.9 and are given below.

$$\varepsilon = \tan^{-1}\left[\frac{(b - k)}{(a - h)}\right] \tag{5.86}$$

$$\varepsilon_{\theta d} = \pi/2 - \theta_p + \varepsilon \tag{5.87}$$

$$\varepsilon_{dd} = R_1 \sin(\theta_p - \varepsilon) - R_1 \cos(\varepsilon_{\theta d}) \tag{5.88}$$

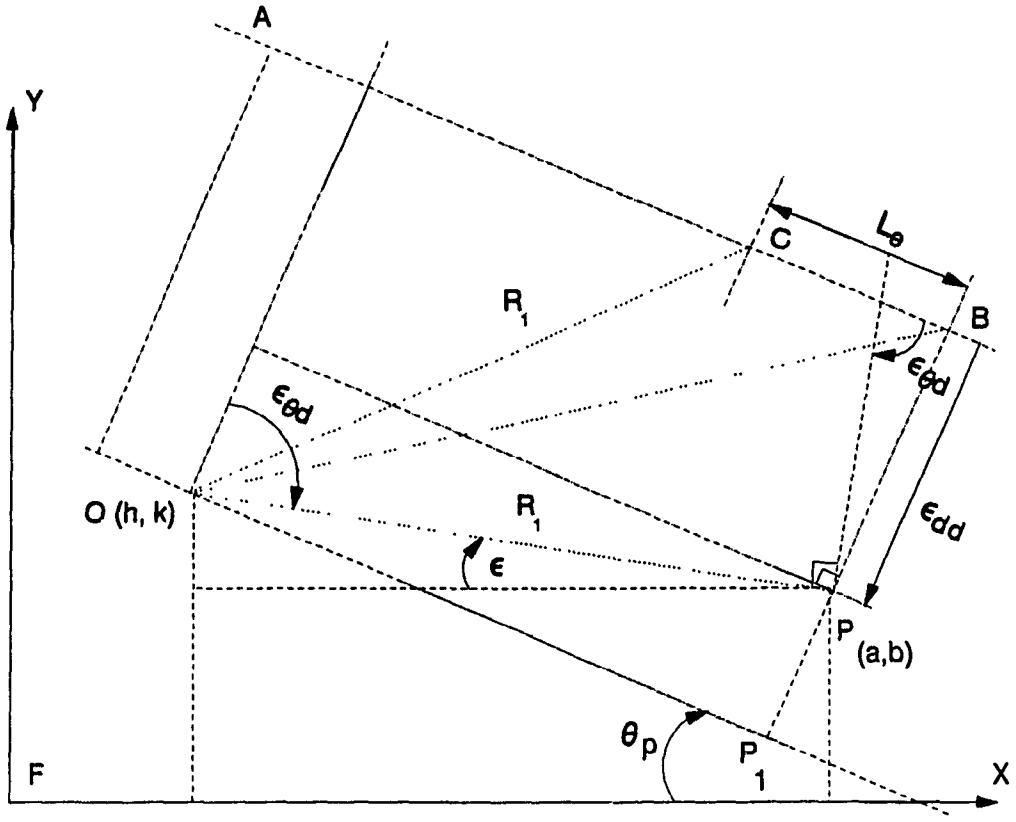

Fig. 5.9 Definitions for Computing Desired Parameters of Steering Control

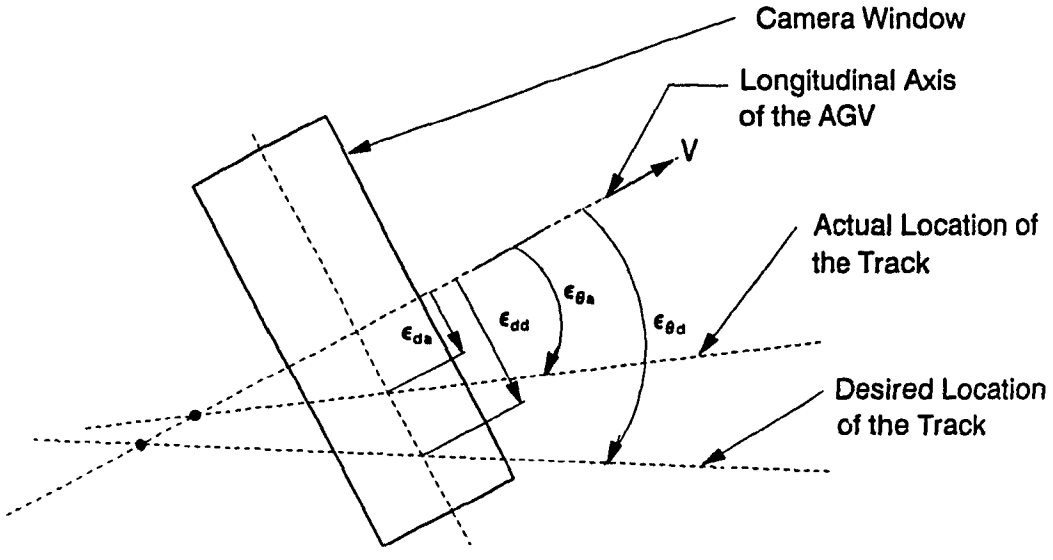

Fig. 5.10 Definition for Desired and Actual Parameters of Steering Control

5.4.5 Control Law for Tracking

The analysis presented in this section is to evaluate the wheel speeds required for the differentially driven AGV to perform accurate tracking as defined in the previous section. A control law of the following form is defined

$$\delta\theta_s(n+1)\Delta T = G_1\ \delta\varepsilon_d(n+1)\Delta T + G_2\ \delta\varepsilon_\theta(n+1)\Delta T + G_3 \sum_{i=0}^{n+1} \delta\varepsilon_d(i)\Delta T \qquad (5.89)$$

The angle $\delta\theta_s(n+1)\Delta T$ is the incremental steering angle at time [(n+1) ΔT] required by the caster(s) to achieve accurate tracking. The position and orientation offsets $\delta\varepsilon_d(n+1)\Delta T$ and $\delta\varepsilon_\theta(n+1)\Delta T$ are the difference between the desired values as computed by the equations (5.87) and (5.88) and the acutal measured values as provided by the image analysis. The deviation from the desired values are given by

$$\delta\varepsilon_d(n+1)\Delta T = \varepsilon_{dd}(n+1)\Delta T - \varepsilon_{da}(n)\Delta T \qquad (5.90)$$

$$\delta\varepsilon_\theta(n+1)\Delta T = \varepsilon_{\theta d}(n+1)\Delta T - \varepsilon_{\theta a}(n)\Delta T \qquad (5.91)$$

The constants G_1, G_2 and G_3 are the dc gains to provide appropriate corrective action to achieve the desired response. The summation is the integration of the position offset and provides a correction in order to achieve zero offset error at steady state. From this, the wheel speeds are computed.

5.4.6 Implementation Algorithm

1) At every time step store the following :

   The actual values of the position offset (ε_{da}) and the orientation offset($\varepsilon_{\theta a}$) of the track as computed by image analysis.

   The actual wheel speeds of the AGV as obtained from the feedback elements, i.e. ω_{x1} and ω_{x2} of wheels 1 and 2.

2) Compute the velocity components (v_{rx}, v_{ry}, $\dot{\theta}_r$) and the position coordinates (p_{rx}, p_{ry}, θ_r) of the reference frame (R) relative to the instantaneous frame ($\bar{R}$). Similarly compute the velocity components (v_{rfx}, v_{rfy}, $\dot{\theta}_{fr}$) and the position coordinates (p_{rfx}, p_{rfy}, θ_{rf}) of the reference frame (R) relative to the floor frame (F).

3) Similarly, compute the position coordinates of a coordinate frame at the point P (P) relative to the floor frame (F) at every time step.

   Position components are : p_{px}, p_{py}, θ_p, p_{pfx}, p_{pfy}, θ_{pf}

4) Use the least sum of error square solution (LSES) to solve for the coefficients of the polynomial functions.

   $x = X(\theta_P \mid \{ a_0, a_1, \ldots\ldots\ldots, a_m)$.

   $y = Y(\theta_P \mid \{ b_0, b_1, \ldots\ldots\ldots, b_m)$.

5) From step (5), eliminate the orientation θ_P and get an expression in terms of x and y alone, i.e. get the following function :

   $f(x, y \mid \alpha_0, \alpha_1, \ldots\ldots\ldots\ldots, \alpha_m) = 0$;

6) By extrapolation estimate the location of P at time [(n+1) ΔT] which is (a, b) using equations derived in step 5.

7) Calcluate the center (h, k) of instantaneous circle and it's radius R_1.

8) Compute the desired value of the position offset ε_{dd} and the desired value of the orientation offset $\varepsilon_{\theta d}$ required at time (n+1) ΔT.

9) Generate the deviations $\delta\varepsilon_d$ and $\delta\varepsilon_\theta$ as in equation (5.91).

10) Calculate the change in the steering angle $\Delta\theta_s$ using the control law.

11) Compute the change in the wheel speeds $\Delta\omega_{x1}$, and $\Delta\omega_{x2}$ respectively.

5.5 Summary

Three approaches for track following of AGVs using camera vision is discussed in this chapter. The first approach is based on single camera guidance, the second approach is based on a guidance scheme that employs two sensors (cameras) and the third approach employs a scheme to identify the track geometry and to provide vehicle guidance. In the case of the guidance scheme using a single camera, the vehicle is steered based on the track information available at that particular instant of time and employs a single sensor at the front end of the vehicle. Tnis scheme does not provide tracking of the entire body of the vehicle and assures track following of a small segment of the vehicle.

The second approach illustrated uses fore and aft sensing and provides track following of two segements of the vehicle, one at the front and the other at the rear. Hence this scheme is superio to the first and is the preferred arrangement for parking purposes. Objective functions for straight lines and tracks with curvature are defined to achieve accurate track following. The nature of the track profile is detected by checking the sign of the orientation offsets from the front and rear sensors. If the signs are the same, the track is a straight line, otherwise it is curved. This information is used by the control law in order to apply the proper objective function. Controllers proposed for this scheme are based on the position of the front and rear ends of the AGV relative to the track and also on the curvature of the track. Two controllers are proposed based on where the front and rear cameras are located with respect to the track. The function of the first controller is to make sure that the front end of the vehicle moves towards the track and crosses it fast. The second controller is used

to achieve asymptotic reduction in position offsets of the front and rear cameras. The gains of the controllers are changed in real-time to follow the track accurately.

The third method for guidance control presented in this chapter is based on a scheme to identify the geometry of the track. The coordinates of a point on the track at a particular instant as seen by the vehicle sensor (camera) are computed based on the track features and the wheel speed information available at that instant of time. The coordinates are computed by integrating the velocity information. Mathematical formulations for numerical integration using two point (trapezoidal) and three point (parabolic) approximation are presented.

The geometric profile of the reference point on the track at a particular time instant is identified based on the coordinate information available until that time instant. Mathematical formulations to identify the geometry of the track for polynomial, straight line and conic functions are presented. Least sum of error square solution (LSES) is adopted to evaluate the coefficients of these functions. For vehicle guidance, several driving criteria are proposed. Equations to compute the desired values of the parameters of steering control are derived for a criterion. This criterion assures that at least two points on the AGV be on the track. To compute the desired values of the parameters of steering control, the concept of the instantaneous circle of rotation is employed.

CHAPTER 6
DESIGN AND DEVELOPMENT OF THE PROTOTYPE AGV

6.1 Introduction

This chapter describes an experimental vehicle that was designed in order to implement and test the guidance control schemes described in the previous chapters. The experimental rig in this thesis is different from the experimental setup that is mostly used in other theses work in many respects. The experimental rig in this thesis is a prototype of an Automatic Guided Vehicle (AGV). The various aspects of building a vehicle are considered from design to actual prototyping of the vehicle. Hence a chapter is devoted in this thesis to describe the experimental vehicle. The areas that are dealt with are, the design of the mechanical structure of the vehicle, the selection of various components in order to provide power, motion, vision, feedback, computational power, electronic and electrical controls, and operating system software development.

6.2 Features of the AGV

The development of this vehicle addresses the following important aspects:

- design and fabrication of an autonomous vehicle that is suitable for site testing and for present and future research;
- to develop and implement an efficient image processing technique to identify and recognize path characteristics;
- provide means of establishing the vehicle performance.

These phases of development are laid out with the emphasis on the following features.

- Modifiable wheel-base configuration.
- Modular mechanical and electronic design.
- Modular architecture in operating system software.
- Low cost camera vision for guidance and simple pre-processing.
- Efficient image processing technique for guidance and to recognize road signs.
- Independent servo control for the motors using motion controllers.
- Controller algorithms based on vehicle kinematics.
- A multi-channel real-time data acquisition system.
- Ultrasonic sensors for obstacle detection and stopping.
- Wireless link for communication with external control systems.

The following discussion will dwell on the usefulness of these features and the details associated with the process of achieving these features.

6.3 *Components of the AGV*

Figure. 6.1 is a photograph of the prototype CONCIC-II AGV showing the overall configuration of the vehicle. The skirts at the front and back are to serve as bumpers to protect the vehicle from collisions. The space at the rear is for carrying payloads and the raised portion at the front end houses the computing facility. Ultrasonic sensors for obstacle detection are seen in the front end of the vehicle. Figure. 6.2 is a photograph of the stripped

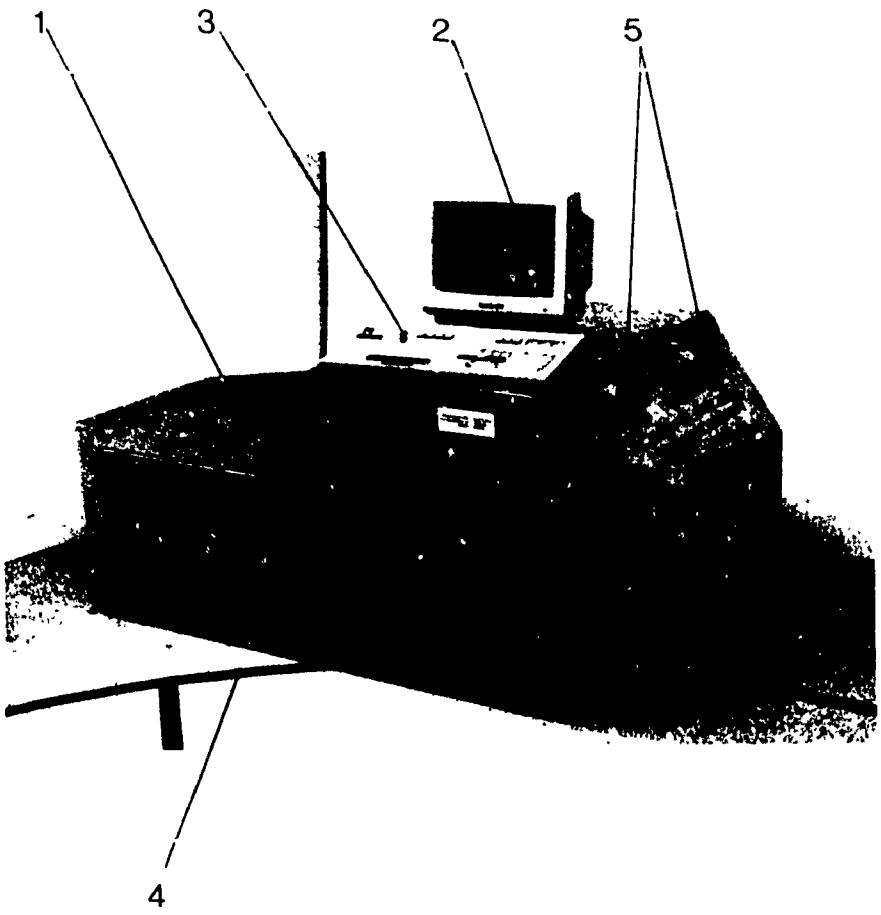

1. Prototype AGV
2. Terminal
3. Keyboard
3. Ultrasonic Sensors
4. Track with road signs

Fig. 6.1 Photograph of CONCIC-II AGV

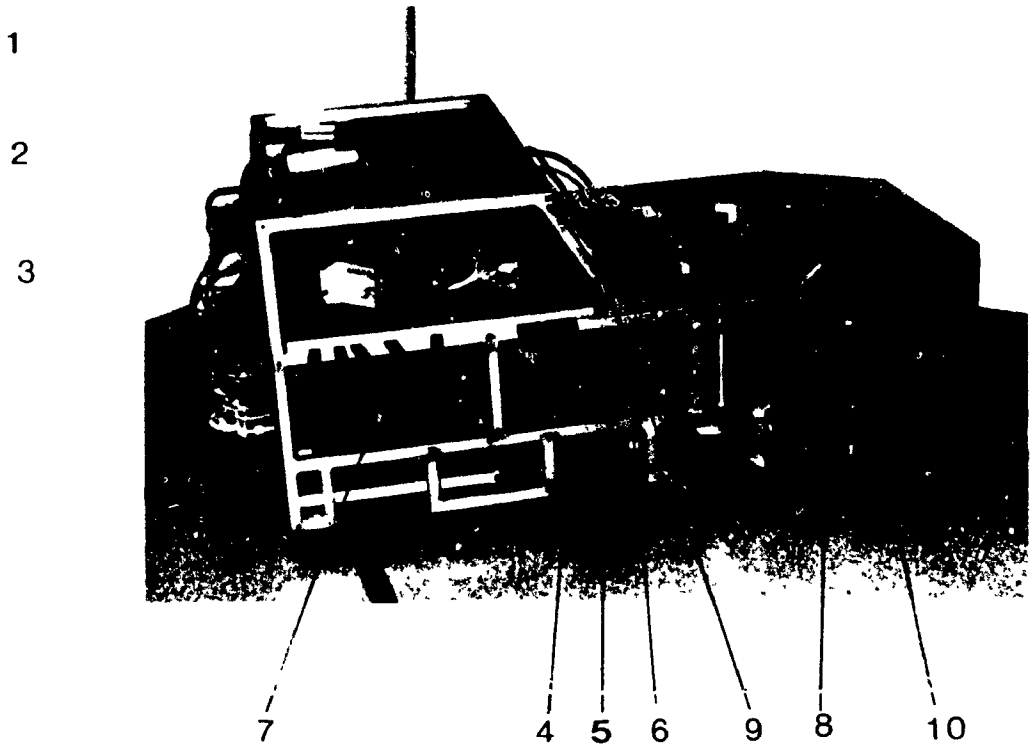

1. On-board Computer (80286)
2. Idetix Binary Camera
3. Lights
4. Motor-in-wheel drive Unit
5. Encoder Feedback
6. Wheel Mounting Bracket
7. On-board Power (12 V Battery)
8. DC to AC Inverter
9. Control Panel
10. Batteries Charging Facility

Fig. 6.2 Photograph of the Stripped Down AGV

down version of this vehicle showing the important components. From Fig. 6.2 it can be seen that the vehicle has a lower and an upper compartment. The upper compartment houses the computing units while the lower compartment is for the drive and power units of the vehicle. The system block diagram of the autonomous vehicle is shown in Fig. 6.3. This figure illustrates the interaction between the various components of the AGV. The essential components are the mechanical structure, the driving and the steering mechanisms including the actuators, the on-board computing facility, the servo controllers for wheel level feedback control, the feedback components, the servo amplifiers, the on-board power system and/or an absolute position referencing system for guidance as shown in Fig. 6.4. The system specification of the autonomous vehicle is presented in Table. 6.1. The dimensions of the vehicle, load carrying capacity, standard components used to provide power, motion and vision for the AGV, and the various modes of operation are listed in this table. The functions performed by the various components are described below.

6.3.1 Mechanical Structure and Driving Mechanism

The mechanical structure of the vehicle consists of a welded aluminium frame. This frame is partitioned into two levels. The lower level houses the driving arrangement and the power source. It is divided into 9 compartments. Wheel-sets may be mounted at any of the 9 locations using standard mounting brackets. This arrangement facilitates modification of the wheelbase configuration. This flexibility is an unique feature of this vehicle, enabling the researcher to evaluate the performance of a variety of wheelbase configurations. With most of the parameters of the vehicle remaining the same, one can compare the performance of different

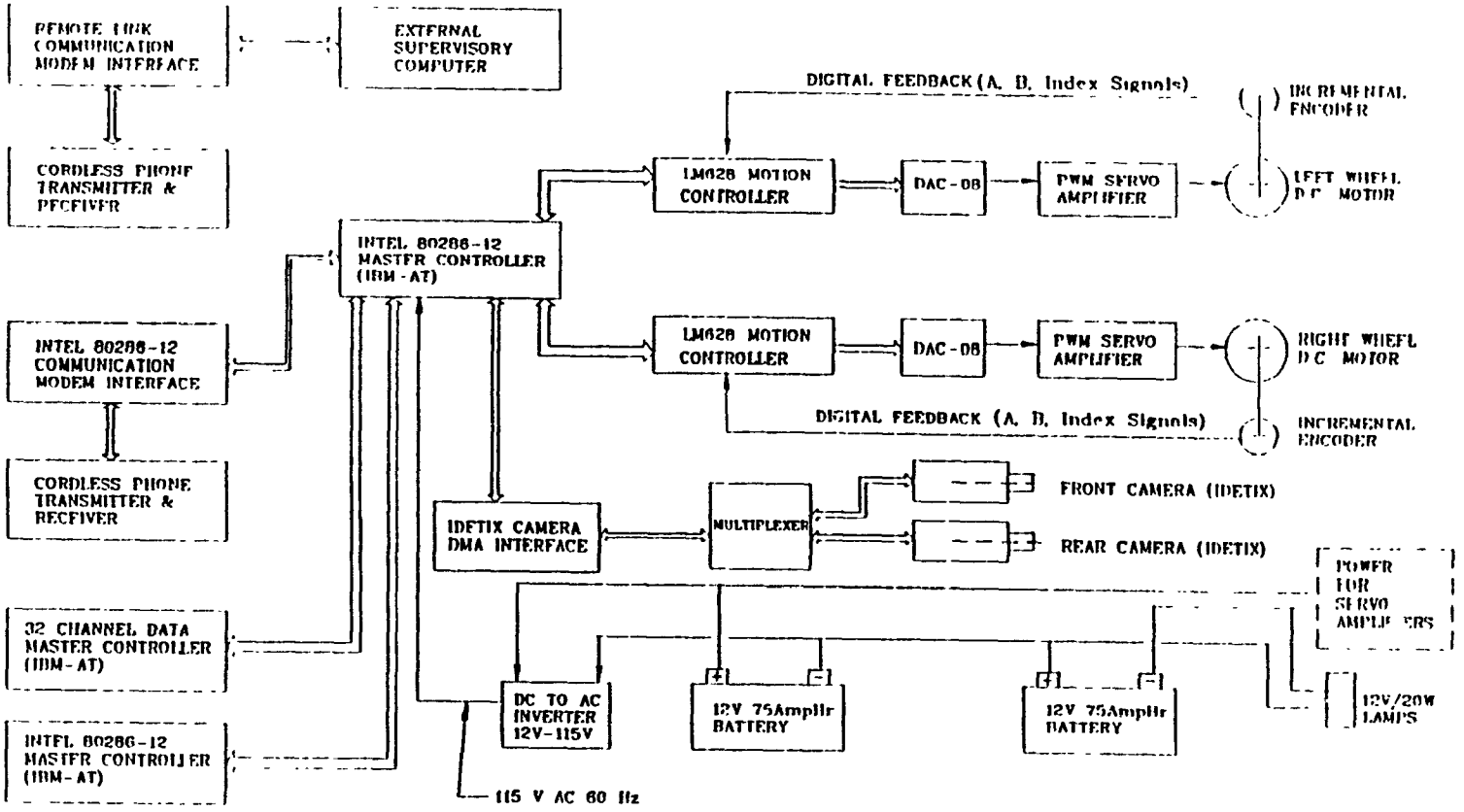

Fig 6.3 System Block Diagram of the CONCIC-II AGV

Components	Specification
Vehicle Design Aspects	
Length, Width and Height	1.57 m x 0.78 m x 0.63 m
Payload	650 lb
Dead Weight	275 lb
Wheelbase Configuration	Modifiable Diamond Shaped Wheelbase Differential Drive Casters at front and rear
Wheel Drive Units	Schabmuller motor-in-wheel drive Steerable; Motor - 24 V dc & 6 Amp.
Computing Facility	
System Main Computer	Intel 80286 @ 12 MHz with 80287 Operating System : DOS Parallel Processing with T800 Transputers for future use
Feedback Control System	
Low Level Servo Controller	LM628, National Semiconductor Corp. Digital PID Filter and Decoder.
Servo Amplifiers	PWM Amplifiers, Galil Motion Control 15V/75V, 9.0/38.0 Amp.
Feedback Arrangement	PMI Incremental Shaft Encoders Quadrature signal, 1024 pulses/rev.
Power System Design	
Power Source	Two 12 Volt Alkaline Batteries 75 Amp hr Capacity, 3 hrs power
Visual Navigation System	
Digitizing Camera	Idetix Camera - Micron Technology
Image Window Size	64 x 128 pixels (50 mm x 250 mm)
Operating Parameters	
Maximum Possible Speed	1.20 m/s (211 ft/min)
Max. Speed with Camera	0.93 m/s (Circular Track, R = 2.0 m)
Minimum Turning Radius	0.50 m (Circular Track)
Camera Mode Frame Rate	20 to 25 frames/s
Special Features	
Image Processing	Recognizes a Set of Road Signs
Communication	Remote Radio link at 300 baud
On-line Data Acquisition	32-Hardware & 10-Software Channels
Software	Modular, Default Setup Modifiable
Safety Features	Ultrasonic Sensor, Watch Dog Timer Component Malfunction Detection
Various Modes	Camera Vision Mode (Front/Rear/Turn) Dual Camera Mode (Front and Rear) Remote Radio Link Mode Track Reconstruction & Navigation

Table. 6.1 System Specification of the CONCIC-II AGV

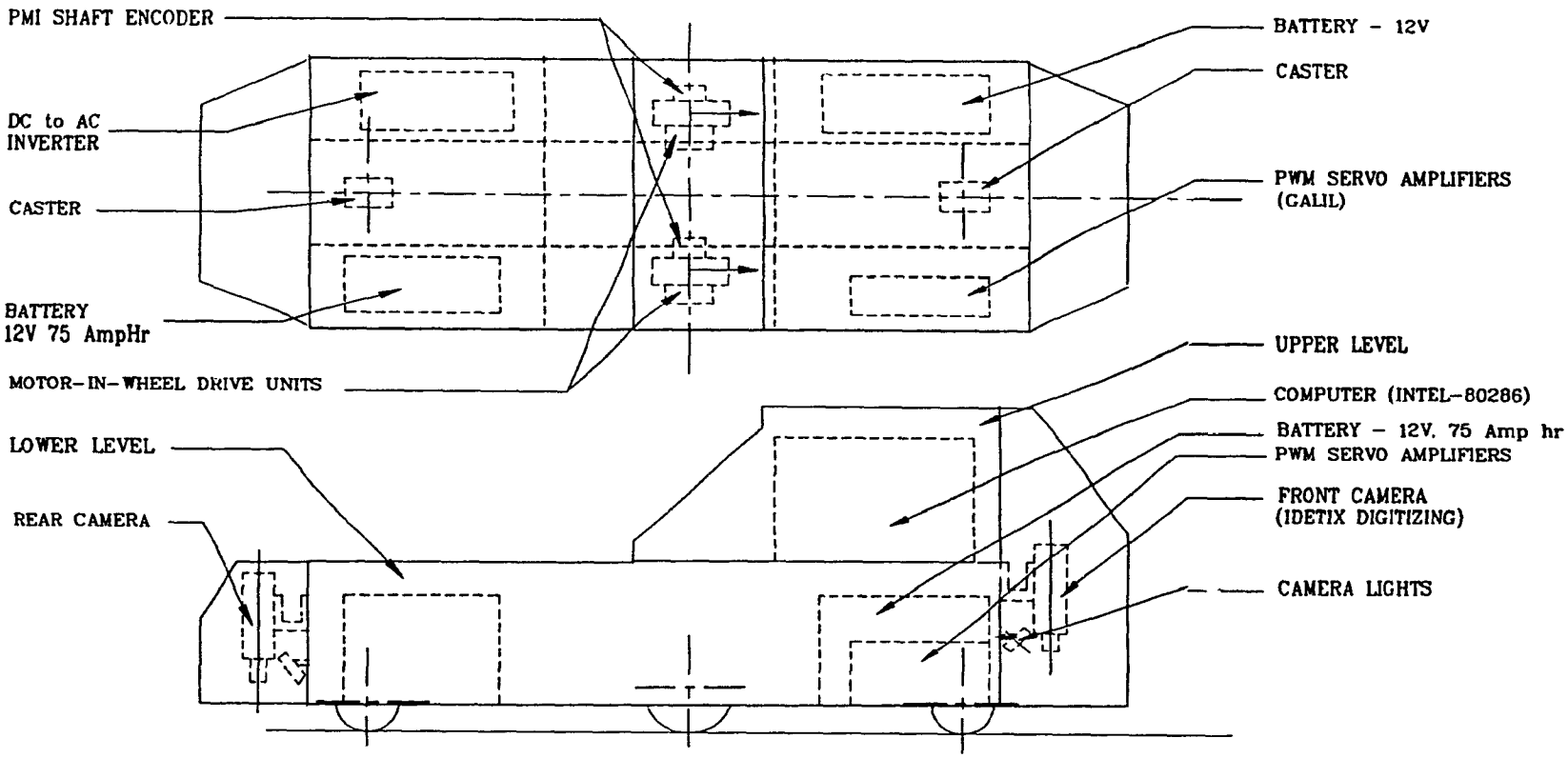

Fig. 6.4 Schematic Layout of the CONCIC-II AGV

configurations with credibility. The computing unit of the vehicle is housed in the upper level, where one also finds the operating console. Figures. 6.5 to 6.7 show the various possible wheel base configurations that can be achieved with this AGV structure and thus illustrate the flexibility of the vehicle.

In most of the industrial AGVs, power for the driving and steering wheels are provided by d.c. servo motors employing chain or belt drives or gear trains. These vehicles in general use a non-integral driving arrangement. This requires complex mechanical system, extensive design requirements and considerable space for mounting. To alleviate these problems, the AGV designed for experimentation in this thesis employs integral driving units from the Schabmuller Corporation, West Germany and is shown in Fig. 6.8. This unit has a driving motor, a speed reduction gearing arrangement, an hardened rubber wheel, a steering motor with a speed reducer, and feedback elements for the driving and steering motors. The armature of the driving motor houses a commutator and feedback elements on one end, and and a speed reduction unit at the other end. The gear ratio of the speed reducer is 1:9.9. The internal gear outer periphery houses the rubber wheel. The driving motor has a maximum speed of 1600 rpm and the wheel diameter is 0.075 m. The maximum speed that can be attained with this driving arrangement is 1.2 m/s (211 ft/min).

The driving motor is a permanent magnet (PM) brush type, 24 volts dc motor. The magnetic flux of the stator (permanent magnet) remains constant irrespective of the motor armature current and hence the speed torque characteristics of these motors exhibit linearity over an extended

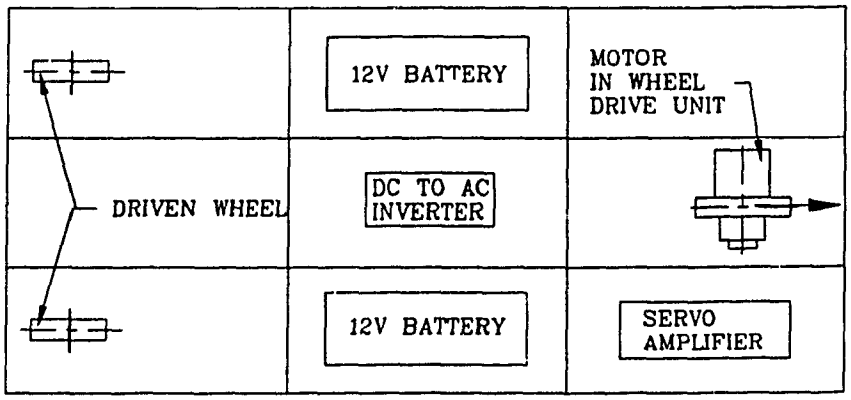

Fig. 6.5 Tricycle Wheelbase Configuration

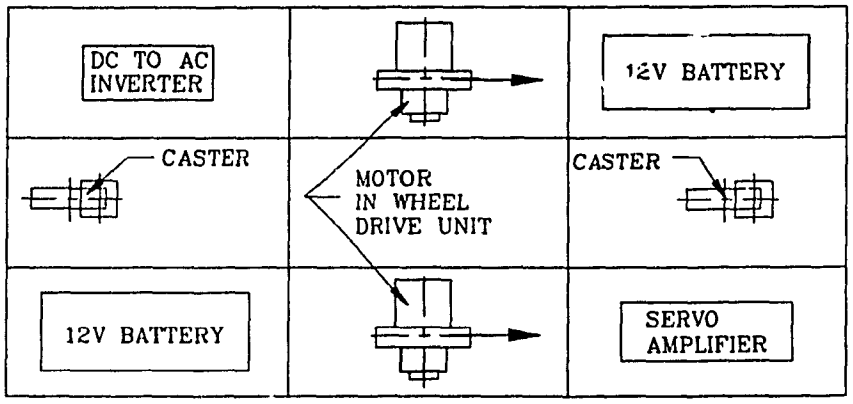

Fig 6 6 Differential Drive (Diamond Shaped) Wheelbase Configuration

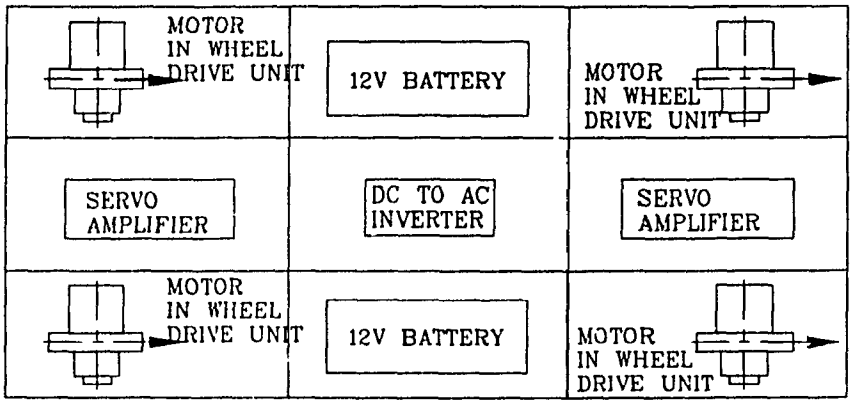

Fig 6 7 Four Wheel Drive and Steer Configuration

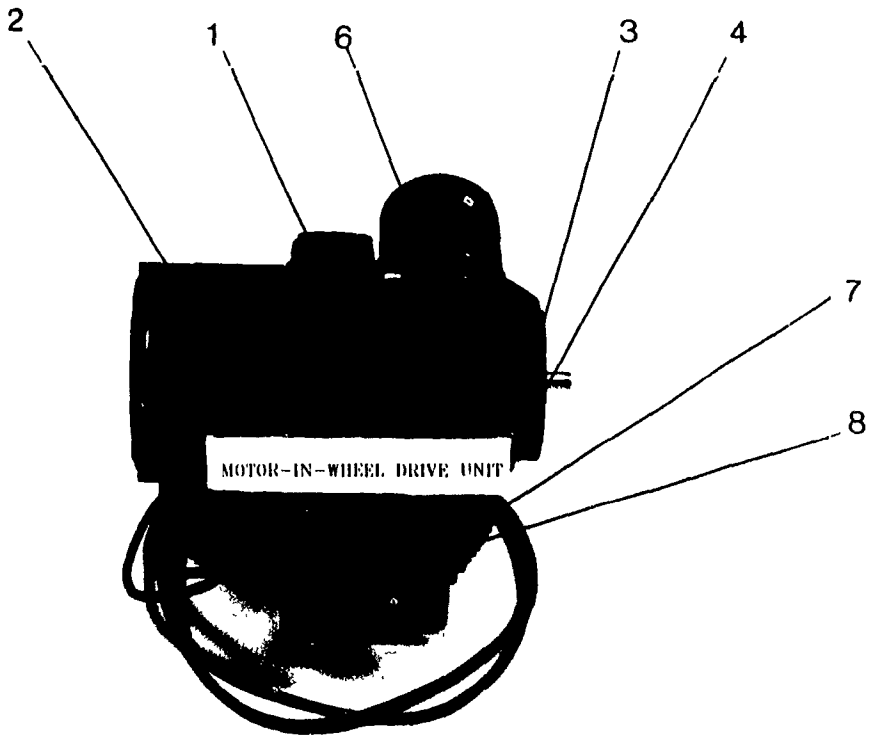

1. Driving Wheel
2. Driving Motor Speed Reducer
3. Driving Motor
4. Driving Motor Feedback Attachement
5. Steering Motor Feedback Arrangement
6. Steering Motor
7. Steering Motor Gearing
8. Wheel Mounting Ring

Fig. 6.8 Photograph of the Motor-in-Wheel Drive Unit

range [75, 76]. The reason for the complete linearity is that the armature reaction flux stays orthogonal to the magnetic flux of the magnets and the high coercive strength of the magnet resists any change in the flux whenever the armature reaction field enters. The stall torque generated by these motors is very high, and hence high accelerations can be achieved easily. PM motors do not require power to generate the magnetic flux compared to shunt or series wound motors. The power loss in these motors is only the I^2R loss in the armature (heat loss), and hence requires less or no cooling at all. Also use of permanent magnets provide high power output for a given air gap compared to other types of motors, and hence the power to weight ratio is high.

Presently the vehicle is driven by two motor-in-wheel-drive units located on either side of the geometric center of the vehicle. Linear motion is achieved by driving the two wheels at the same speed, while steering is accomplished by driving them at differential speeds. The vehicle is also provided with two supporting casters, one at the front and the other at the rear.

6.3.2 Control Components

The control system adopted here is based on the hierarchical control strategy. The main controller is an IBM-AT compatible (Intel-80286) operating at 12 MHz clock with an 80287 math co-processor. The reason for the selection of the IBM-AT is that most of the off-the-shelf components are interfaceable with the IBM-AT type computers. The various functions performed by this processor are shown in Fig. 6.9. Some of the functions listed in this figure are camera imaging and image analysis, computing wheel

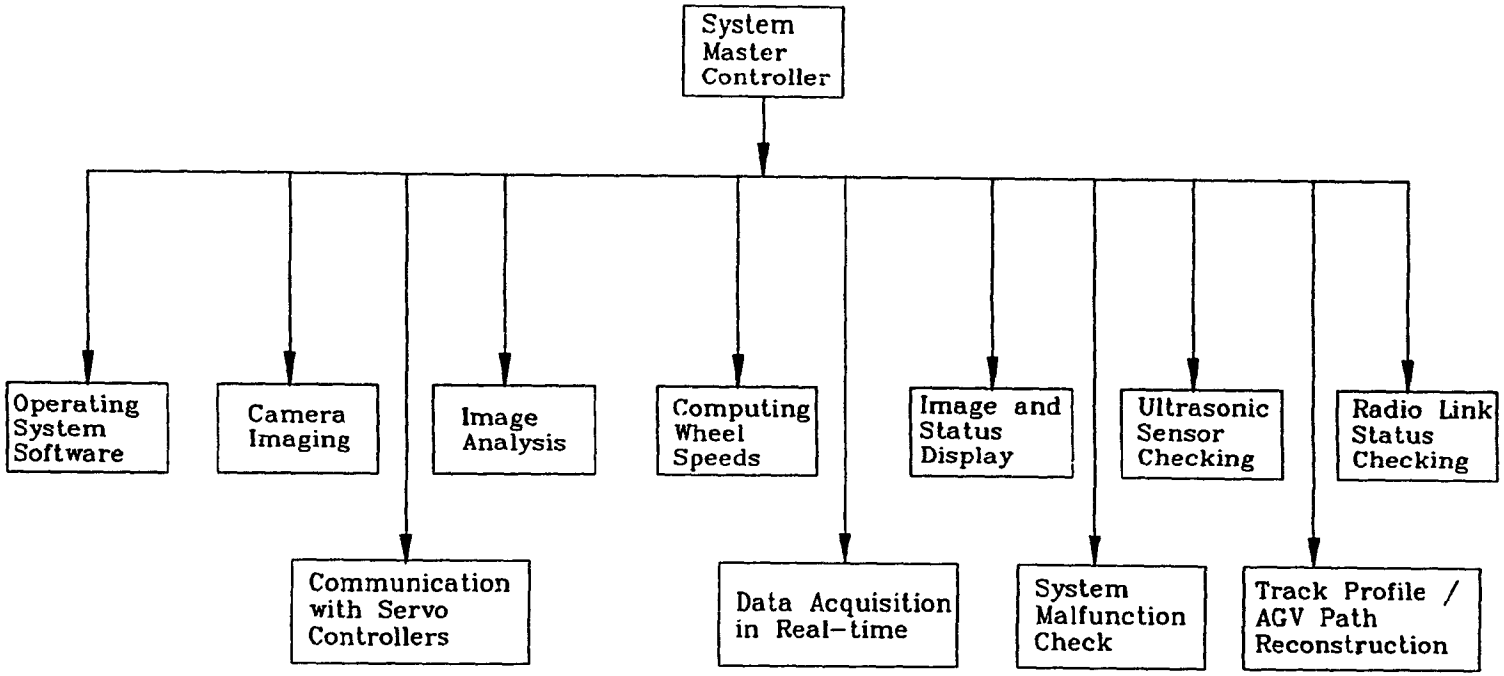

Fig. 6.5 Functions of the Master Controller

speeds, performing several operating system functions, data acquisition in real-time, etc. The low level controls are performed by independent motion controllers to perform the closed loop control of the motors.

The low level control loop employs LM628 precision motion controller chip from the National Semiconductor Corporation [79, 81, 82, 83]. One could employ a microprocessor or a microcontroller-IC for motor control. A microprocessor can handle a large number of data compared to a microcontroller. However, a microcontroller is a faster device than a microprocessor. Unlike a microprocessor, a microcontroller has on-chip memory and I/O circuitry, and can accept both analog and digital signals. As a result of this, need for separate circuitry to process the incoming signals is avoided. Rounding off errors in the case of microcontrollers is much smaller compared to that in a microprocessor. Standard off-the-shelf motion controller chips are microcontrollers with limited features and are much simpler than the conventional large scale microcontrollers. Hence in this thesis, motion controller chips are employed for servo control of dc motors. Our survey on motion controller chips showed that the LM628 motion controller is superior to the other motion controllers as it possess the following features :

- Digital PID Filter with 32 bit gains and are programmable while in motion. With this feature the controller gains can be tuned experimentally.

- Built in encoder decoding circuitry. Hence the need to build a counting circuitry is avoided.
- 32 bit position, velocity and acceleration commands. This results in

very good resolution for speed/position control.

- Feedback loop operates at 20 KHz rate thereby providing feedback information even at higher motor speeds without sacrificing the resolution.
- Ability to provide an easy interface with the pc.

Another motion controller chip possessing some of the characteristics of the LM628 is the HCT-1000 from Hewlett Packard [80]. In this chip, the position, velocity and acceleration input commands are only 16 bits long and this results in a loss of accuracy. The velocity information read from this chip is only 8 bits. However, the HCT-1000 chip permits the acceleration to be changed while in motion and has two velocity profiles to chose from namely, the trapezoidal and the parabolic. This feature is absent in the case LM628.

The operation of the LM628 chip does not affect the normal functioning of the host computer, i.e. once the host computer downloads the necessary control commands to the chip, the chip performs the closed loop control while the host computer does other functions. First, the chip is downloaded with a set of initializing commands. The first command is to reset the chip thereby clearing all the registers. This is followed by a command to inform the chip that the digital to analog converter (DAC) employed is 16 bits long, if such a DAC is employed. Then the coefficients of the digital PID filter, the mode of operation (position or velocity), the trajectory data (acceleration, the velocity and position - if in position mode) are provided. New values for these data (except the acceleration) can be downloaded while the chip is executing a previous trajectory command with the exception of the

acceleration. The position/velocity values loaded can be either an absolute or a relative value. A full description of this chip and the functions performed are described in detail in the Appendix. C. The various elements of the LM628 motion controller chip are shown in Fig. 6.10. From this figure it can be seen that the chip has a velocity profile generator, interface for communication with the host computer, digital PID filter, provisions to connect encoder lines and a digital to analog converter, and encoder pulse decoding circuitry.

Commands are written to the LM628 by the host computer using the I/O ports. The status of the LM628 needs to be checked from the host computer before attempting to write a command and/or data, as well as reading a data. This is achieved by checking the last bit *(busy bit)* in the status byte read from the LM628. The maximum duration of the *busy bit* is 100 μs. The busy bit goes high as soon as a command is written or data is either read or written.

The LM628 motion controller is provided with a digital PID filter as a controller. The discrete time equation which is representative of the algorithm implemented is given by the National Semiconductor Corporation [79]

$$u(n\ \delta t) = K_p\ e(n\ \delta t) + K_i \sum_{j=0}^{n} e(j\ \delta t) + K_d\ [e(k\ \delta t) - e(k-1)\delta t] \qquad (6.1)$$

Where $u(n\ \delta t)$ is the digital command to the digital to analog converter and is the command signal to the servo-amplifier. The terms K_p, K_i and K_d are the gains of the proportional, integral and the derivative terms. These

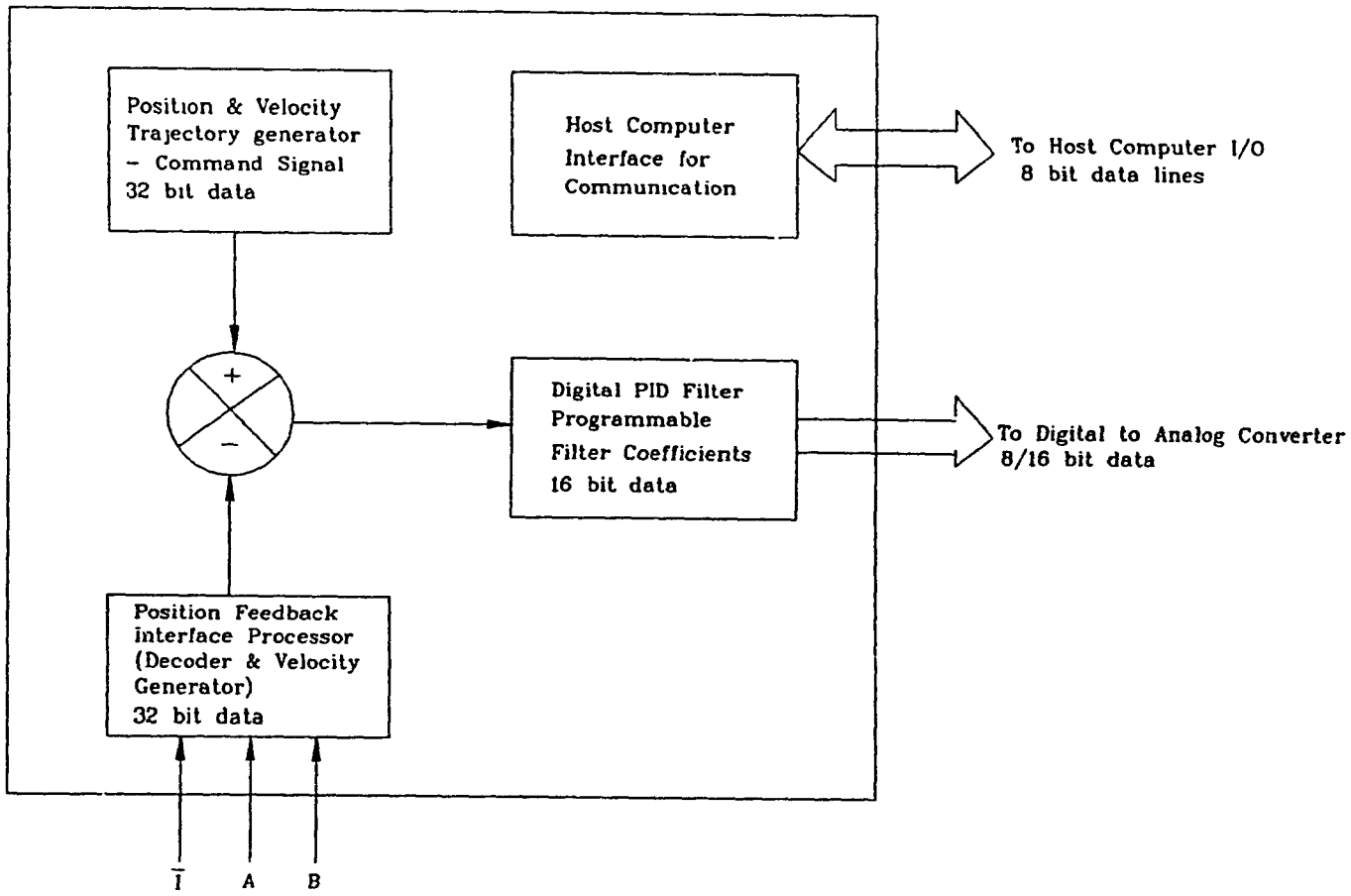

Fig. 6.10 Elements of the LM628 Precision Motion Controller Chip

values are programmable and can be altered while the motion is being executed. The parameter n is the motion controller sampling time and is given by $2048/f_{CLK}$. The parameter (k δt) is the sampling time interval for the derivative controller. The value of (k δt) ranges from $2048/f_{CLK}$ to $65536/f_{CLK}$. This time may or may not be equal to the motion controller sampling time (n δt) and is also programmable on fly. The proportional and integral terms have a sampling time of $2048/f_{CLK}$, where f_{CLK} is the operating frequency of the LM628. For the CONCIC-II AGV, the value of f_{CLK} is 6 MHz, and hence the sampling time is 341 μs. The term e(n δt) is the position/velocity error and is a function of the desired position/velocity d(n δt) and actual position/velocity a(n δt) at the sampling time (n δt), and is defined as

$$e(n\ \delta t) = d(n\ \delta t) - a(n\ \delta t) \tag{6.2}$$

The integration sum limit is represented as I_1. This is given by

$$I_1\ (n\ \delta t) = K_1\ e(j\ \delta t) \tag{6.3}$$

The user can set a magnitude for I_1. The controller then makes sure that the sum of the integral terms does not exceed this value. This is necessary to prevent overshooting of the output signal compared to the desired value due to integration.

The LM628 chip accepts 5V TTL quadrature signals (A and B) from an incremental encoder. Index pulse (I) can also be directly connected to the chip. The chip has a built-in encoder decoding circuitry. The timing

diagram for the quadrature encoders is shown in Fig. 6.11. From this figure it can be inferred that because of the quadrature signal, the resolution of the counting is multiplied by a factor of four compared to the number of pulses per revolution of the encoder disc. The position and velocity information (desired/actual) can be read directly from the LM628 chip. Here the velocity is computed from the number of encoder pulses received. The chip has an internal velocity profile generator. The profile generated is a trapezoidal function with an acceleration period, a constant velocity period and a deceleration period. This is illustrated in Fig. 6.12.

All trajectory parameters are 32-bit values. The position value has a sign bit as well. Velocity and acceleration are only positive values. The first 16 bits signify the integer and the lower 16 bits is the fractional value. The code value of the position count that has to be loaded to the LM628 is

$$DP = SR * \text{Desired wheel revolutions} * GR \qquad (6.4)$$

Where,

DP - Desired position in number of encoder counts

SR - System Resolution = Encoder Resolution * 4; here the factor 4 is due to the quadrature signal output.

GR - Gear Ratio between the motor and the wheel

For CONCIC-2 AGV, the equations to compute the positions for the driving and steering motors are

Encoder resolution = 1024 counts per encoder revolution (drive motor).
= 256 counts per encoder revolution (steer motor).

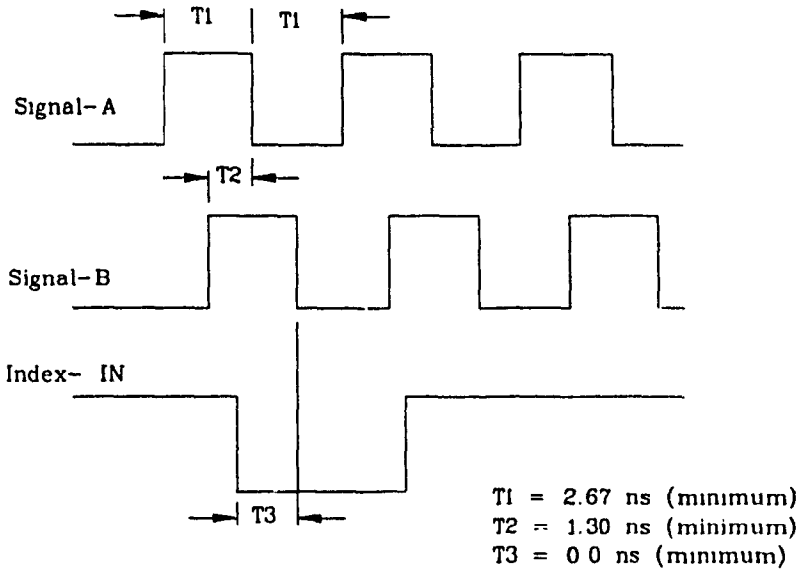

Fig. 6 11 Quadrature Signal Output of an Incremental Encoder

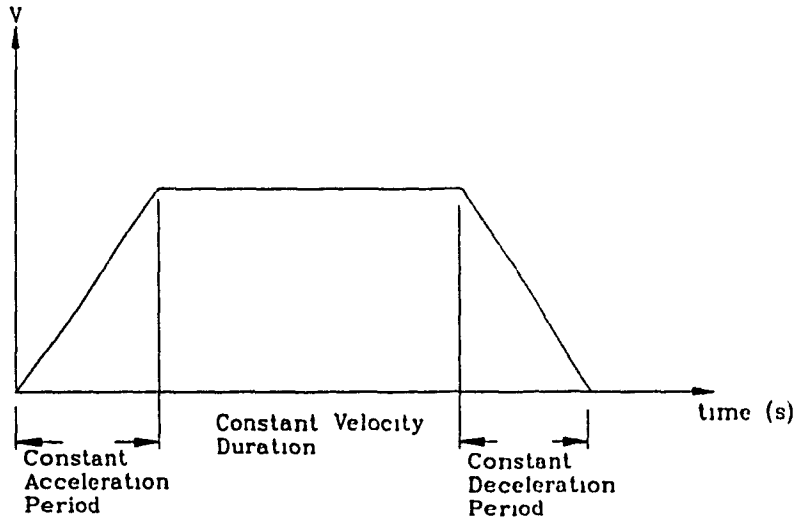

Fig. 6.12 LM628 Trajectory Generator Velocity Profile

SR - System resolution = 4096 counts per encoder revolution (drive motor).
= 1024 counts per encoder revolution (steer motor).

GR - Gear Ratio = 9.9 for driving motor.
= 0.0317 for steering motor.

Hence the coded value of DP to be loaded is

$$DP = 4096 * 9.9 * \text{Driving wheel revolutions} \quad (6.5)$$

$$DP = 1024 * 0.037 * \text{Steering wheel angular position} \quad (6.6)$$

Since the range of value for the position count is -2^{30} to $[2^{30}] - 1$, the maximum number of driving wheel revolution counts that can be counted is 26479 revolutions. Position values are signed bits.

The operating clock rate (ϕ_1) of the motion controller is 6 MHz. At this rate, the sampling time δt is computed as

$$\delta t = 2^{11} / \phi_1 = 2048 / (6 * 10^6) = 341.0\ \mu s \quad (6.7)$$

The coded value of velocity V(coded) is given by the expression

$$V(coded) = SR * \delta t * CF * GR * \text{desired wheel rpm} * 65536 \quad (6.8)$$

Here CF is the conversion factor from minutes to second, which is equal to 1/60. The factor 65536 is to adjust for the fractional part the velocity data after conversion to counts per sample. For CONCIC-2, the value of V(coded) is given by

$$V(drive) = 4096 * 9.9 * 341 * 10^{-6} * 65536 * \text{desired rpm}/60.0 \quad (6.9)$$

$$V(steer) = 1024 * 0.317 * 341 * 10^{-6} * 65536 * \text{desired rpm}/60.0 \quad (6.10)$$

The acceleration is computed from

$$A = SR * \delta t * \delta t * \text{desired acceleration} * GR \quad (6.11)$$

The acceleration equation for CONCIC-2 is given by

$$A(drive) = 4096 * 9.9 * 341 * 10^{-6} * 341 * 10^{-6} * 9.9 * \text{acceleration} \quad (6.12)$$

$$A(steer) = 1024 * 0.317 * 341 * 10^{-6} * 341 * 10^{-6} * 9.9 * \text{acceleration} \quad (6.13)$$

One of the limitations of this chip is that the acceleration value cannot be changed while the motion is being executed. The acceleration can be changed only after a motor off command is executed and the trajectory command that was issued before is completed. Owing to constant acceleration, whenever the AGV is commanded to stop while following a track with a curvature, the vehicle will move towards the inside of the curvature. This happens when the two wheels are loaded with the same acceleration values. This is because the outer wheel that is running faster than the inner wheel takes longer time to come to a stop due to constant deceleration value. Another limitation is that the velocity profile is trapezoidal and this is the only profile available. The third limitation is that the actual velocity of the motor read from the chip by executing the actual velocity command is only 16 bits and this corresponds to a wheel speed of ±4.2 rpm for the experimental AGV discussed in this chapter.

6.3.3 Servo Amplifiers

The second important element of the servo control loop is the servo-amplifier. A servo amplifier provides the power as required by the motor depending upon the load driven by the motor and the desired speed set by the user. Figure. 6.13 shows the circuit diagram of the servo amplifier. The off-the-shelf servo amplifiers from Galil Motion Control [84] employed in the AGV are pulse width modulation amplifiers with H-type output circuitry, operating in current mode with armature current feedback. Figure. 6.14 shows an amplifier with an H-type circuitry and this provides bi-directional control. This amplifier is a four quadrant amplifier thereby providing a full bi-directional control of motors. The input voltage is 24 volts dc, the continuous and the peak currents are set at 9 amps and 37 amps respectively. The switching frequency is 20 KHz. The input to the amplifier is an analog signal in the ±7.5 volt range. The amplifier is provided with a power stage as well as a logic stage. The power stage has the pulse width modulation unit and the power transistors to drive the motor. The logic stage generates the error signals for the power stage depending upon the load requirements and performs a variety of logic functions. The logic stage has provisions to switch off the amplifier or inhibit the motor in either or both directions, provisions to set the continuous and peak currents, provide self diagnostics for trouble shooting purposes, etc. Fig. 6.15 is a photograph of the servo amplifier showing the two stages and the terminals for connections.

The servo amplifiers have been set to operate in current mode with current feedback and the current amplifier operates as an inverting amplifier. There is no other feedback connection to the amplifier as digital feedback is employed with the LM628 motion controllers. The current loop

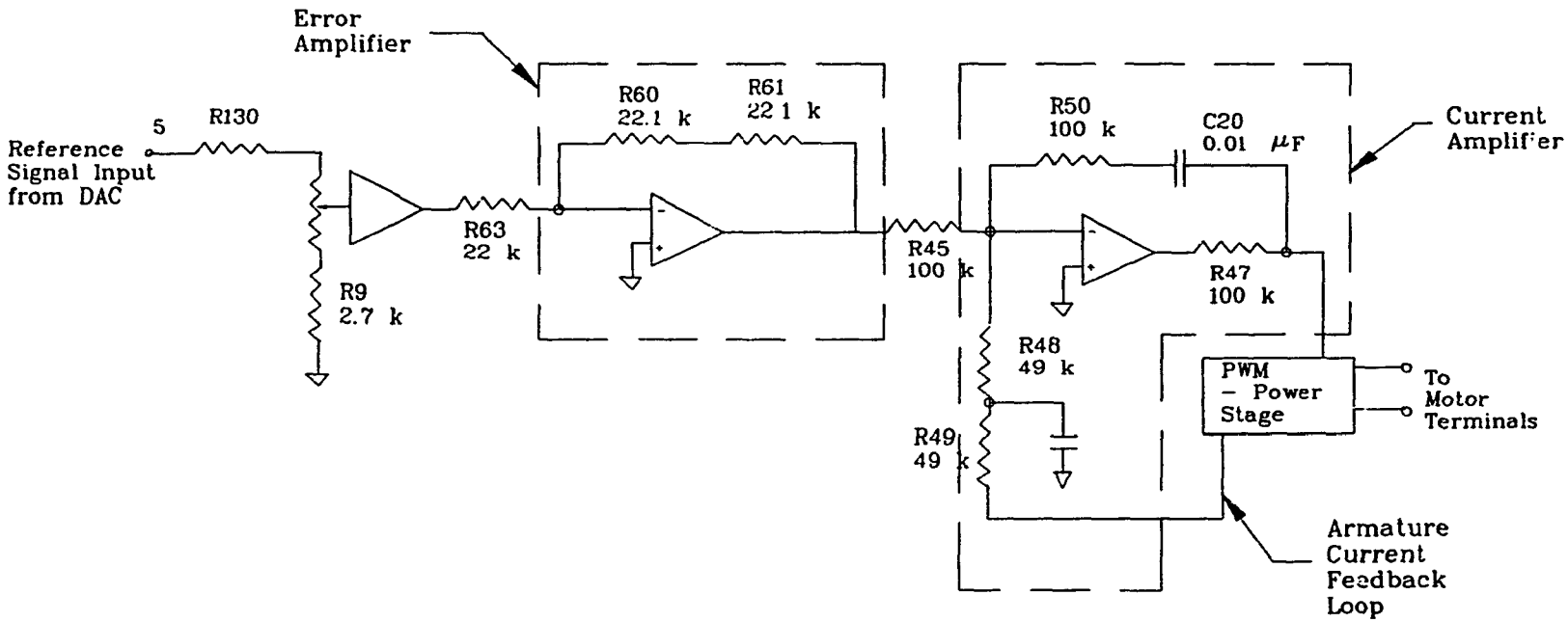

Fig. 6.13 PWM Servo Amplifier Circuit Diagram

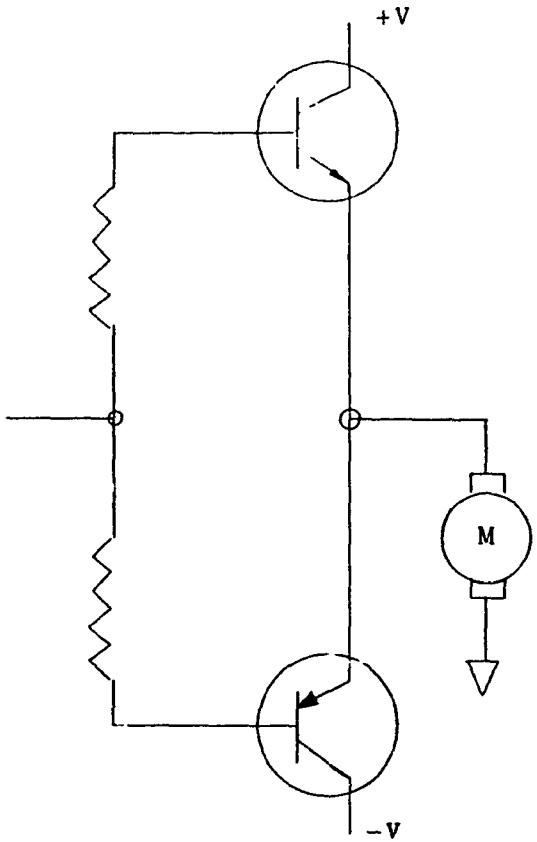

T – Type PWM Amplifier

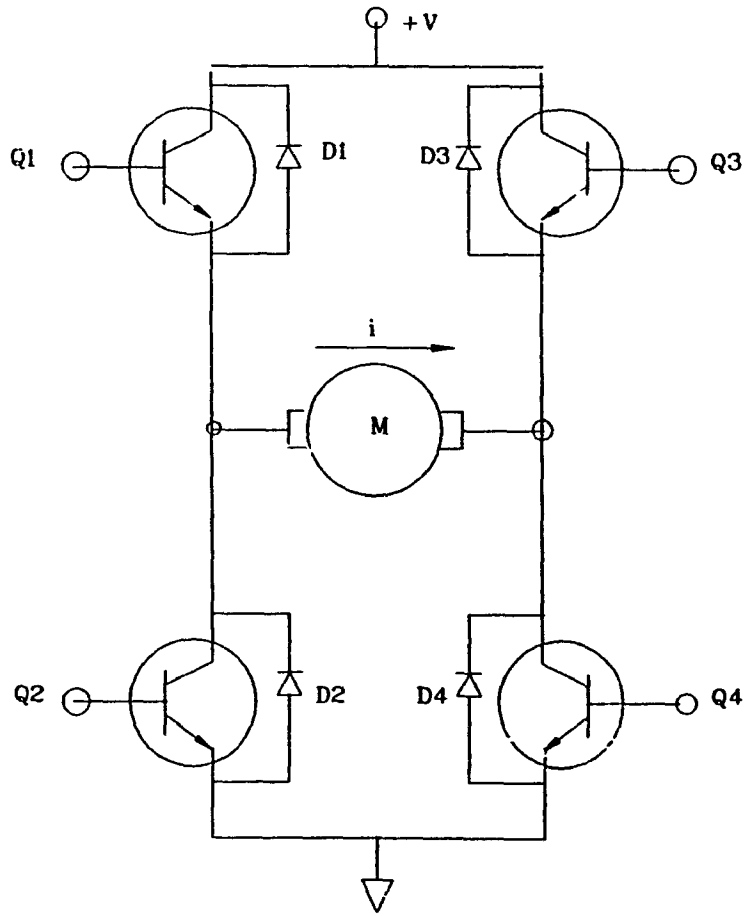

H – Type PWM Amplifier

Fig. 6.14 T and H Type PWM Servo Amplifiers

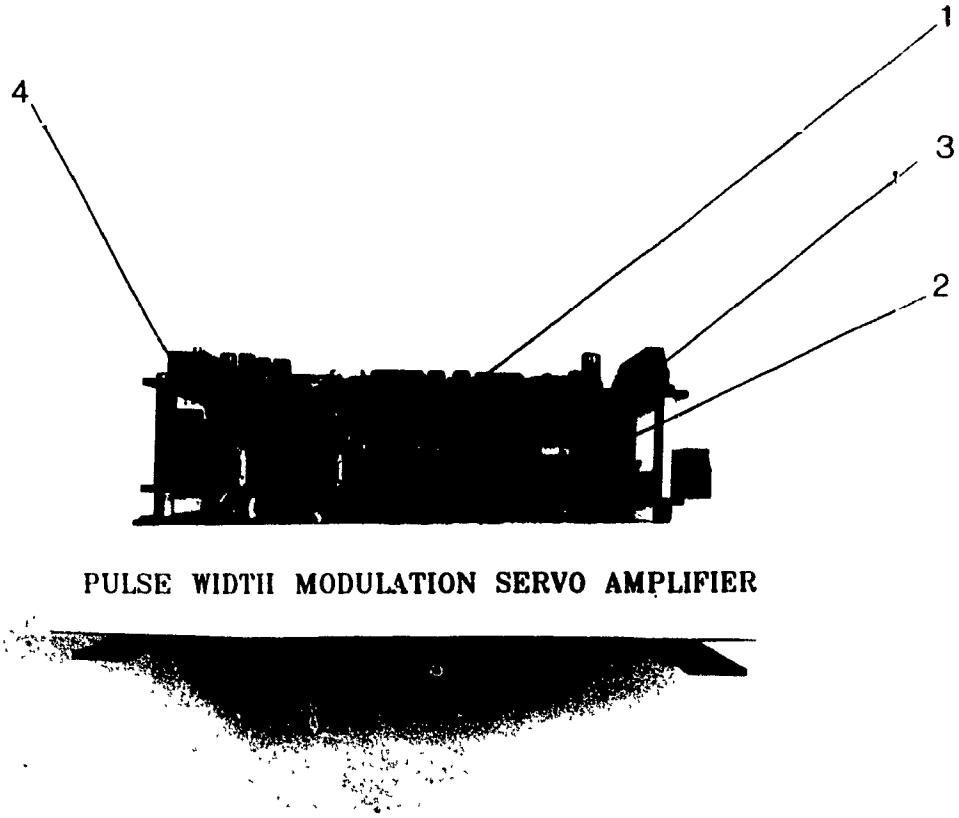

1. Logic Stage
2. Power Stage
3. Gain Potentiometers
4. Terminals

Fig. 6.15 Photograph of Galil Servo Amplifier

compares the load current with the desired current as computed by the error amplifier based on the feedback information. The current amplifier also ensures that the current input to the power stage does not exceed the current limits set by the user.

6.3.4 Guidance System

An optical technique using a relatively inexpensive camera vision technique is employed for guidance. An on-board computer processes frames of the image of the track as captured by the camera. The instantaneous position and orientation of the vehicle relative to the track is determined and is used to steer the vehicle so as to reduce the deviation.

It has been mentioned in section 2.3.2 that the use of a binary camera with optic rams is more suitable compared to the existing means of guidance. One camera which embodies the optic-ram is the IDETIX digitizing camera from the Micron Technology [85]. A camera interface board transfers the image information to the host computer memory by the Direct Memory Access (DMA) mechanism. A photograph of the camera and the interface are shown in Fig. 6.16. This camera has been chosen for the following reasons :

- The time taken to transfer a byte of image from the camera to the pc memory is 6.5 μs. This fast data transfer rate is desirable for real-time control.

- Ability to access the pixels of the image window randomly. This feature is useful to analyze only a small portion of the image window. This results in greater saving in processing time.

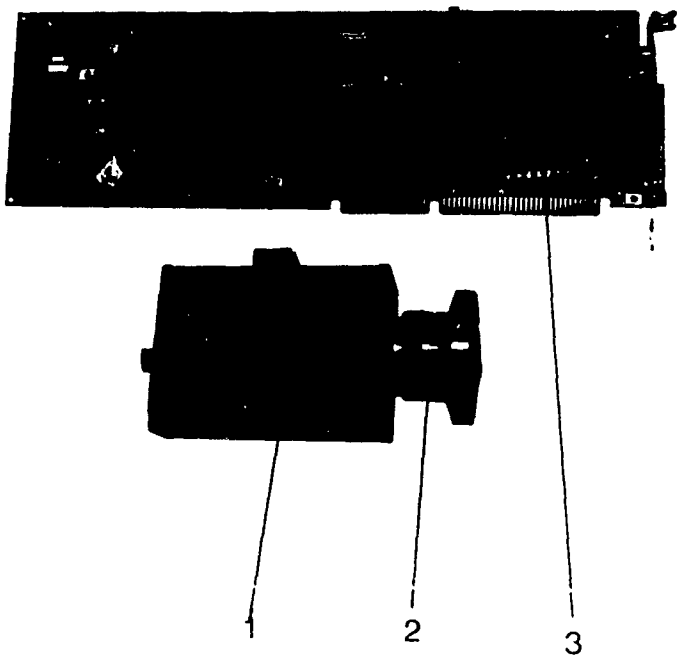

1. Camera Head
2. Lens (4.2 mm)
3. Camera Controller Interface Card

Fig. 6.16 Photograph of the IDETIX Digitizing Camera System

- The operating window size is modifiable by software. This also provides the same flexibility as in the previous case. The only difference is that the image data received from the camera can be made much smaller instead of the entire window. This reduces the time taken for image transfer.

- It supports two types of optic ram chips namely, IS32 (128 x 256) and IS256 (256 x 512) thereby providing a wide range of resolution.

- Multiple camera heads can be connected to the interface board with an external hardware to select the camera for image transfer. The experimental AGV has a camera at the front and at the rear. These two are connected to the same controller. A multiplexer is designed to receive one Kbyte of image from one camera and another Kbyte of image from the second camera subsequently.

Important factors to be considered while employing camera vision for guidance are, the type of lens and the location of the camera. If the camera is too close to the floor, then the accuracy with which the track is read by the camera improves. However in this situation the window size becomes very small and this limits the maximum speed at which the vehicle can operate. This is because the small window dimension limits the maximum overshoot (deviation from the desired track) the vehicle can tolerate without losing the track image. 16 mm lens provides high resolution images but the window is small and are not suitable candidate when the vehicle is to operate at high velocity. In the present design, we have chosen a 4.2 mm lens and the distance between the lens and the ground is adjusted to be approximately 200 mm. This provides an image window size that is 50 mm deep and 250 mm

wide. The track width is typically 30 mm wide. These dimensions result in a reasonably good image and the vehicle can have a maximum overshoot of 0.125 m on either side of the track. For this size of the viewing window the track image may be approximated by a straight line, the parameters of which may change from frame to frame. From the experimental results it was observed that the maximum speed that can be achieved is 0.95 m/s for a circular track of 2.0 m diameter. The parameters of the camera and the track image are defined in Fig. 6.17. This image shows the camera image window resolution distance in mm per pixel, the track image and the noise, the equation that best describes the track and the parameters of steering control.

The optic ram chip employed has 65,536 elements arranged in 128 rows and 256 columns. There are provisions to use a subset of this array (e.g. 64 by 128). Each element is connected to a capacitor, precharged to 5 volts at each refresh cycle. When the reflected light from an object falls on a particular element, the corresponding capacitor is discharged. A threshold charge-level is suitably chosen so that the light intensity of the image may be digitized into two levels. Capacitors with less than the threshold level of charge are regarded as white pixels, and are assigned the logic level 0. The black pixels on the other hand are assigned the logic value 1. The values (0 or 1) of the image are transferred from the camera interface board to the computer memory. The average time taken to transfer 1 K byte of pixel information is 6.5 ms for the CONCIC-II AGV, corresponding to a window of 64x128 pixels.

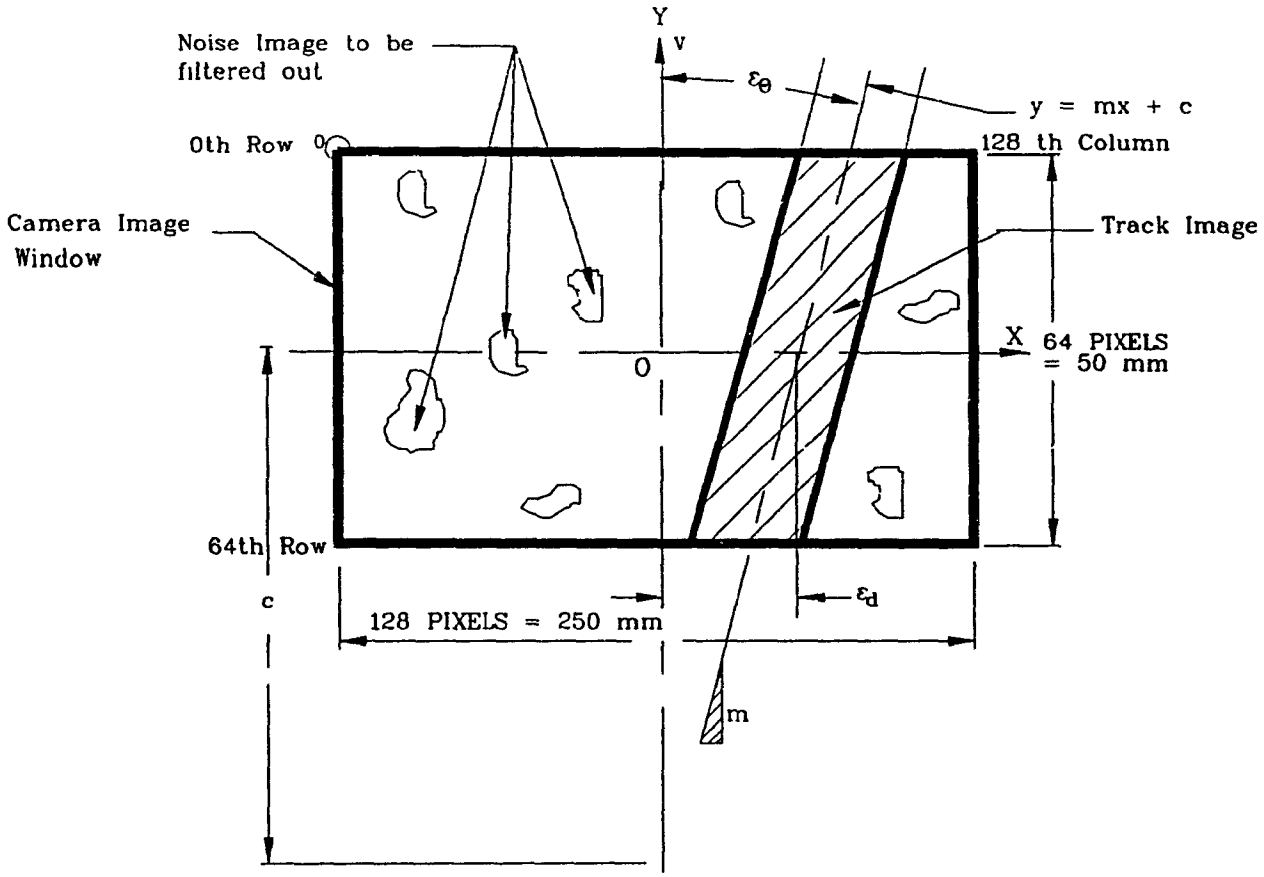

Fig. 6.17 Camera Window and Track Parameters Definition

6.3.5 Power System

The layout of the power system of the vehicle is shown in Fig. 6.18. This figure shows the components of the power system, and the necessary connections to perform a variety of functions. The power system of the AGV consists of a dc to ac inverter providing ac power for the host computer and lights for the cameras. The power system also provides power for the servo amplifiers. Power for these units are derived from two 12 Volt dc batteries rated at 75 Amp hrs. Relays are (shown only in the safety circuit board - Fig. C.12) provided to control the power to the motors and amplifiers. Some of these relays are activated by the computer in order to make sure that the components of the vehicle are functioning properly before powering the motors. There is also provision in the power system to charge the batteries as and when required. Push buttons (marked as RED and GREEN) are provided to shut the motor power (emergency stop) and to power the motors. Switches (SW1 to SW5) are the main power switch (SW2), switch on the computer and monitor power (SW4), set the power for the computer and monitor as internal or external (SW5), power for the front and rear lights (SW1 and SW3).

6.3.6 Overall Feedback Control Loop

The control loop of the AGV is presented in Fig. 6.19. The binary digitizing camera provides a visual feedback of the absolute position of the AGV (section 4.6) and the steering angle is computed using the methodology described in section 5.2. This information is used to compute the changes in the wheel speeds required to follow the track on the floor. Using equations (4.7) and (4.8) the wheel speeds are computed. These values are the command signals to the trajectory generator of the LM628 chip. The output of the trajectory generator of the LM628 is the instantaneous velocity command and

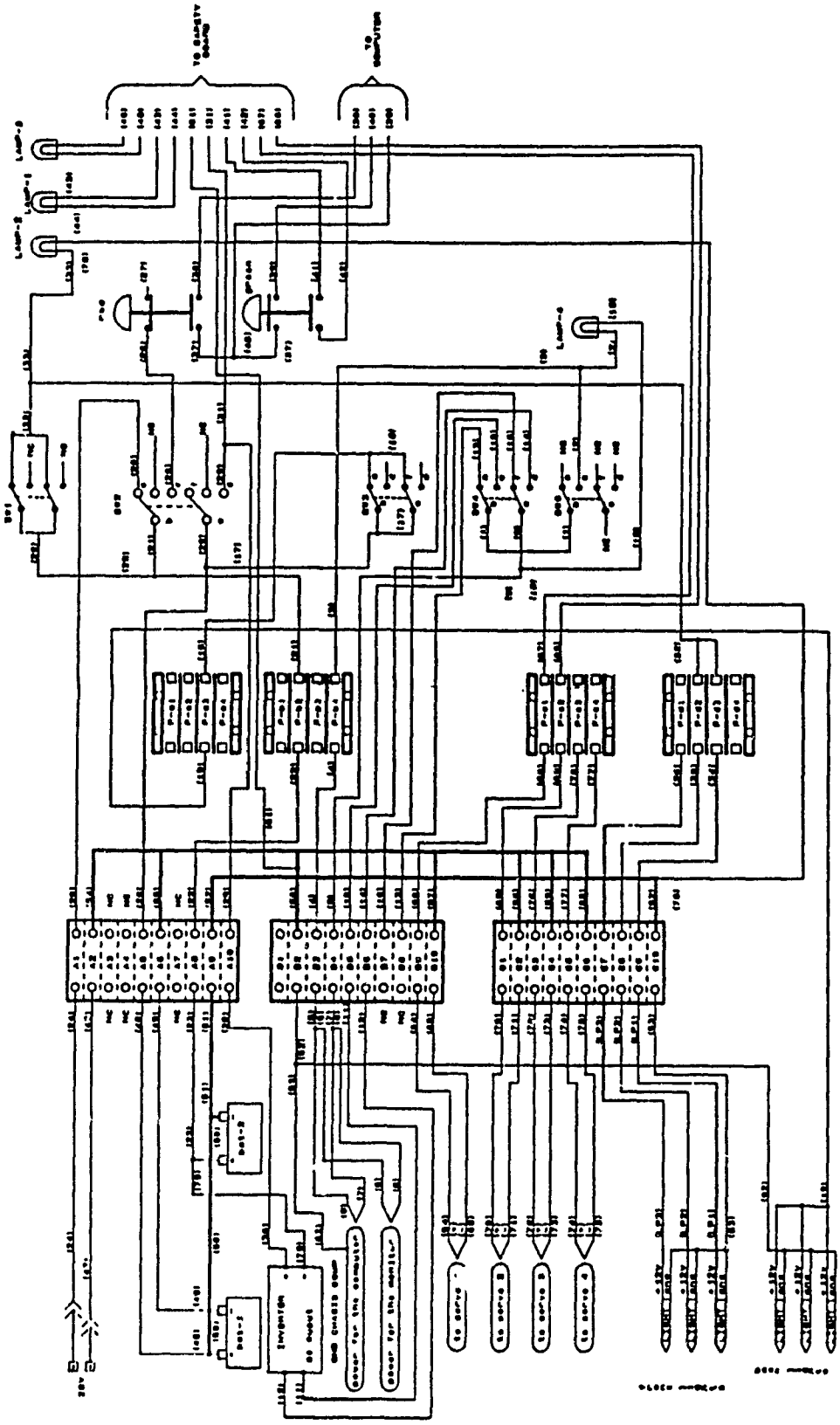

Fig. 6.18 Layout of the Power System of the AGV

is available at every 341 μs intervals. The summation block shown compares the instantaneous values of the desired speed and the actual speed of the motor and generates the error signal. The actual motor speed information is provided by the incremental optical encoders with quadrature output signals. The output of the summation loops is then passed through the PID filter. A digital to analog converter (DAC-08) converts the filter output to an analog signal for the PWM amplifier.

The output of the DAC is connected to a gain potentiometer with a dc gain of 10.0. This amplified signal is then sent through an inverting amplifier whose dc gain is 2.0. The output of this amplifier is connected to the current amplifier and then to the PWM power stage. The power stage of the amplifier uses pulse width modulation (PWM) to provide the desired power to the motor depending upon the error signal generated. The PWM section of the amplifier is connected to the motor terminal.

6.3.7 Radio Link

A radio link has been incorporated [85, 86] as an optional feature for communication between the host computer of the AGV and an external computer. It should be noted here that this facility is not essential to test the control schemes. A block diagram of the radio link is presented in Fig. 6.20. This figure shows the components of the radio link and the connections between them. The remote link facility consists of a special purpose modem which can translate computer signals from an RS-232 serial port into FM-radio signals for the transmitter/receiver of a cordless telephone. An external computer is connected to the modem using the serial port. The host computer of the AGV communicates with another modem with similar characteristics.

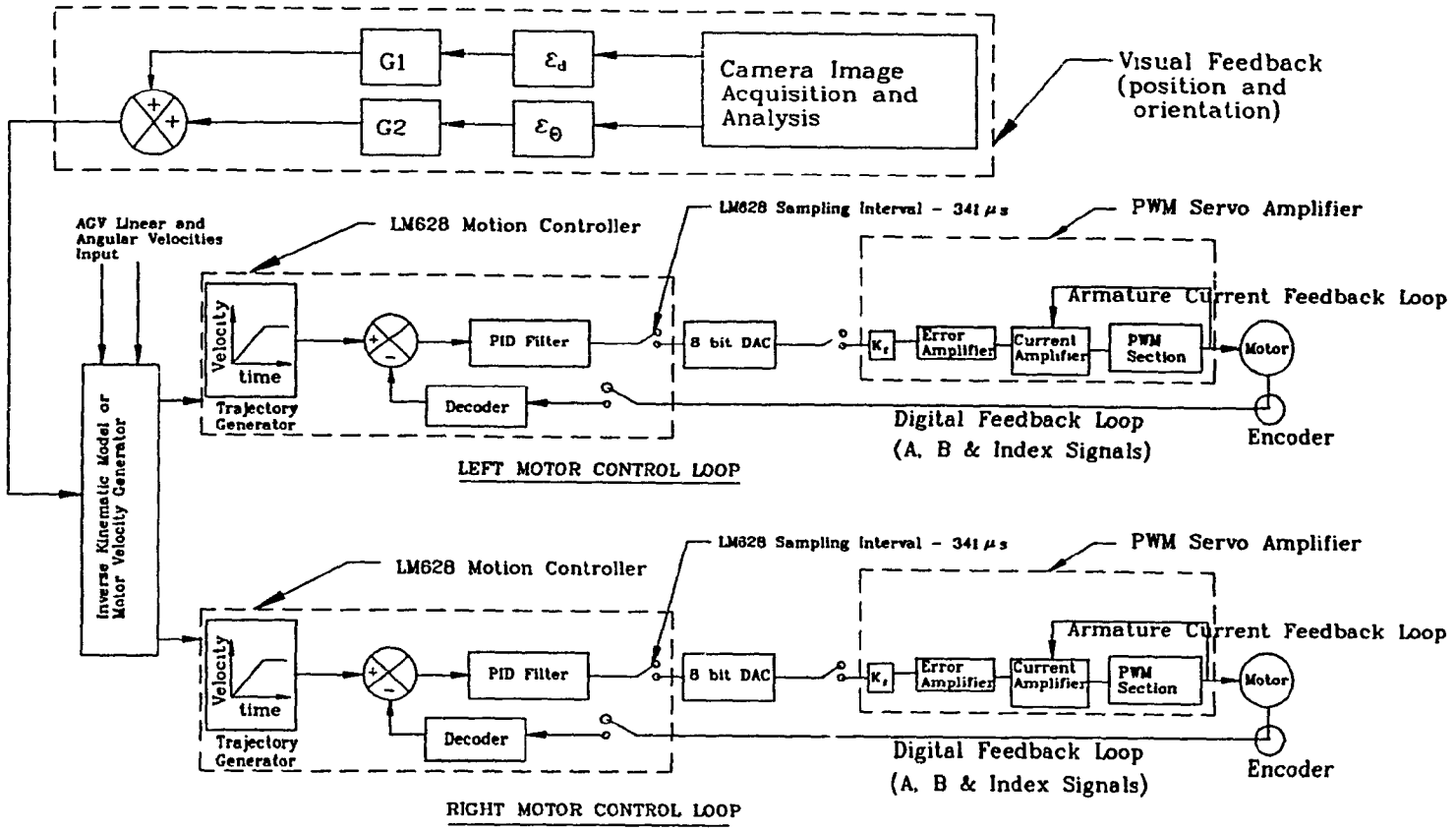

Fig. 6.19 Control Loop with Visual Feedback

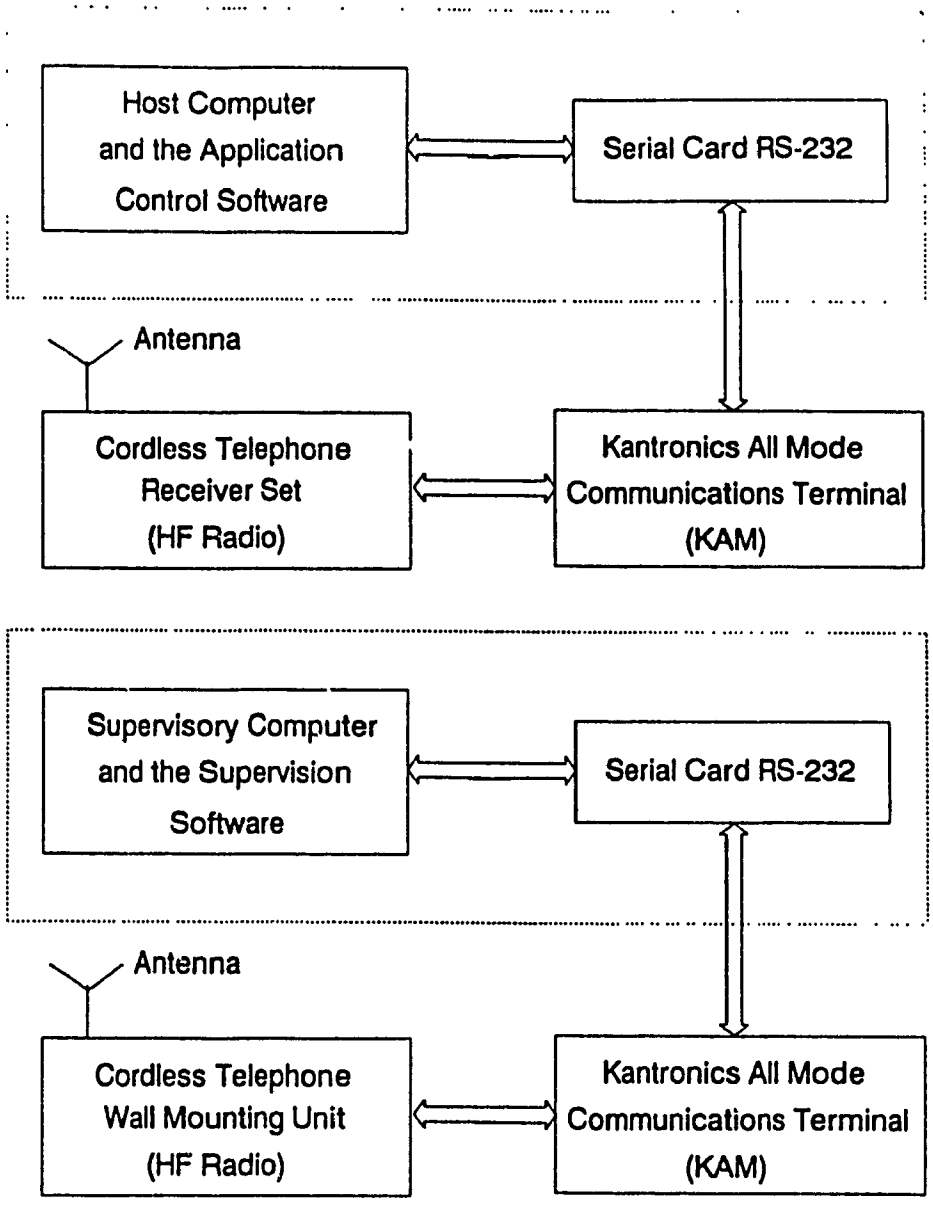

Fig. 6.20 Block Diagram of the Radio Link

This modem is connected to the transmitter/receiver of the cordless telephone. A communication software is executed in both computers to establish a link. After establishing the links, data transfer between the computers can take place as and when desired. The application software decodes the data that is being received and takes the appropriate action. The current system operates at 300 baud. This matches well with the system frame rate and hence the low baud rate of the modem does not degrade the performance of the AGV system.

6.3.8 Data Acquisition System

An on-board data acquisition system has been designed and implemented in the autonomous vehicle. This system is necessary to study the behavior of the AGV under varying operating conditions and controller settings. The data acquisition system is provided with hardware and software channels. There are 32 hardware channels out of which 12 are used currently and the remaining 20 are for future development. The hardware channels are provided to maintain a time history of the following:

- Motor terminal voltages from both motors
- Peak and continuous currents of the motor (load/no load)
- Command signal input to the servo amplifiers
- Battery voltages

From the motor voltages and currents the power consumption and the motor torques are evaluated. The continuous currents is measured in two channels. One is to record the low currents when the AGV is not carrying any payload and the other is to record the higher value of the current when the AGV is

loaded. The peak current channel records the starting current required by the motors. The input to the servo-amplifier and its output to the motor are useful in obtaining the characteristics of the amplifier and DAC. This information is needed for the dynamic modeling of AGVs for simulation and to implement controllers based on the dynamics of AGVs as well as for simulating the controllers for AGVs. The battery voltage indicates whether the batteries are in good condition for the normal functioning of the AGV.

There are a total of 12 software channels. The operating system software has provisions for inclusion of more software channels. The name software channel is given to these as these channels store only the data that is computed and not by direct measurement. The data recorded by the software channels are

- Desired wheel speeds read from the motion controllers.
- Actual wheel speeds read from the motion controllers.
- Actual speed of the wheels.
- Position and orientation offsets from the front camera (ε_{df} and $\varepsilon_{\theta f}$).
- Position and orientation offsets from the rear camera (ε_{dr} and $\varepsilon_{\theta r}$).
- Steering angle command based on camera information.
- Control law in operation in dual camera mode.

This information is used by the scheme to identify the track geometry scheme described in Chapter 5. Fig. 6.21 is a block diagram of the data acquisition system showing the hardware structure of the implementation for hardware data acquisition. Referring to this figure it can be seen that the data acquisition system is interrupt driven, multiplexed and demultiplexed. The multiplexer is provided at the analog side where the external analog

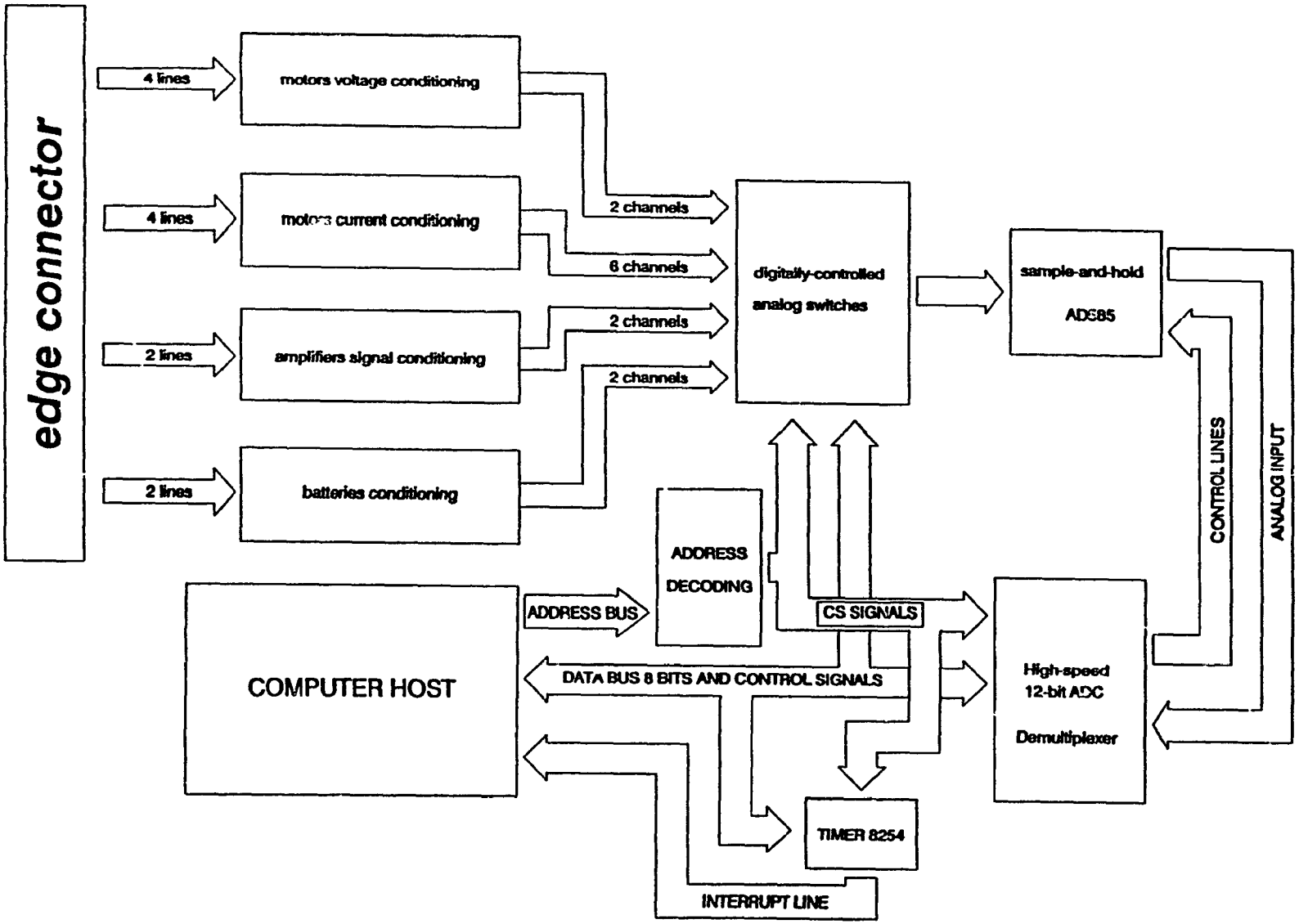

Fig. 6.21 Block Diagram of the Data Acquisition System

components are connected through conditioning circuits. This multiplexer is digitally controlled so that the channels selection for sampling can be carried out by software. The conditioning circuits are to filter out any noise that may be present in the analog signals, and also to amplify the valid signals. The multiplexer is to select the channels whose signal has to be sampled by the sample and hold circuit and is converted to digital by the A to D converter which is the demultiplexer. Interrupt 3 of the host computer is used to control the timing of the sampling. The timer is started by the control software after the completion of the image acquisition. Timer chip 8254 is programmed to generate an interrupt at every 16 ms which is the time available between minimum value of the time taken for computations between two consecutive imaging. This is done such that the voltages and currents of the motors are read before issuing a new command to the motors by the control software. Hence the data read from the data acquisition system is more or less (not fully) the supposed to be the steady state value available. It is very difficult to wait for the steady state values as the cycle time is one quarter of the time constant of the servo loop. The time constant of the servo loop has been established experimentally in section 7.2.4.

6.3.9 System Software Layout

The system software of the AGV is a top-down design, and is modular in architecture to facilitate software maintenance and continual enhancement. The control codes are developed using the Borland Turbo-C compiler. It contains several include files (parameter definitions), and about 50 major sub functions/sub function groups besides the main supervisory subroutine, as shown in Table 6.2. This table also shows the functions performed by each

Main.c - Main Supervisory Module
Functions Referred by MAIN.C
keybd.c - Joystick operation
camera.c - Camera vision mode guidance
dual.c - Turn at junctions random/defined
drc.c - Dead reckoning control mode
radio.c - Radio link mode - calls the
camcalib.c- Camera image & window calibration
modify.c - Alter the system default settings
default.c - Display the system default setup
menu.c — Display menu for various modules
LM628 Motion Controller Utilities
utility.c - LM628 Motion Controller utilities write & read words, bytes, check busy, write simultaneously, stop motor
filter.c - PID Filter gains
traj.c - Trajectory downloading
Data Acquisition System Routines
datacq.c - Interrupt driven data acquisition
datasel.c - Select data acquisition channels
dac_acq.c - Select channel for calibration
data_chk.c- Get data from selected channel
disksave.c- Save the data acquired to disk
Camera Vision Routines
initcam.c - Camera controller initialization
cdrive.c - Camera controller utility functions
continuo.c- Set the camera in continuous imaging
single.c - Set the camera in single frame mode
movescr.c - Display the camera image on monitor
stopidx.c - Stop the camera
intime.c - Increase exposure time
detime.c - Decrease exposure time
analyze.c - Function to process & analyze image
timer.c - Function to start and stop 8254 timer
invkin.c - Compute wheel speeds (kinematics)
dualcam.c - Front and rear camera guidance
Track Geometry Identification
path.c — Identify track geometry in real-time
navigate.c— Guidance using geometry identification
drawpath.c— Sketch track and AGV profile-real-time
Optional Utilities
agvhost.c — Communication with the host computer
sonar.c — Ultrasonic sensor functions
safety.c - Vehicle safety feature functions

Table. 6.2 Operating Software Modules and Their Functions

module. These sub functions range from system validation and calibration, equipment calibration (camera, motors and data acquisition system), system default setup and modification of the default values, image data filtering and processing, and the driving and steering of the vehicle. The architecture of the operating system software is presented in Fig. 6.22. This figure shows the sub function modules and the interaction between various modules in providing a overall control of the vehicle. The functions performed by the various modes detailed in Appendix H.

In all the modes of operation, the software has provisions to start/stop (function keys F1/F2) the data acquisition if the data channels have been chosen previously, switch on/off (F3/F4) the ultrasonic sensors, trace the profile of the track or the path of the AGV on the floor in real-time (F5, F6, F7, F8), continuously check for hardware and software problems (safety circuit), smooth stop of the AGV using the deceleration value chosen (key S/s), normal stop by issuing a zero voltage to the signal input of the amplifiers (Space Bar), and perform a panic stop by reversing the polarity of the input command (<ESC> key and <enter> key), provide a status report, and either issue a stop command to the AGV or switch off the relays in order to stop the power to the amplifiers. The vehicle is provided with only one interrupt circuitry feature. As a result of this, either the ultrasonic sensors or the data acquisition can be used as they both use the same interrupt for control.

6.3.10. Timing Considerations

Since the real-time control of a mechanical system is considered in this thesis, the time taken by the various functions performed is very important

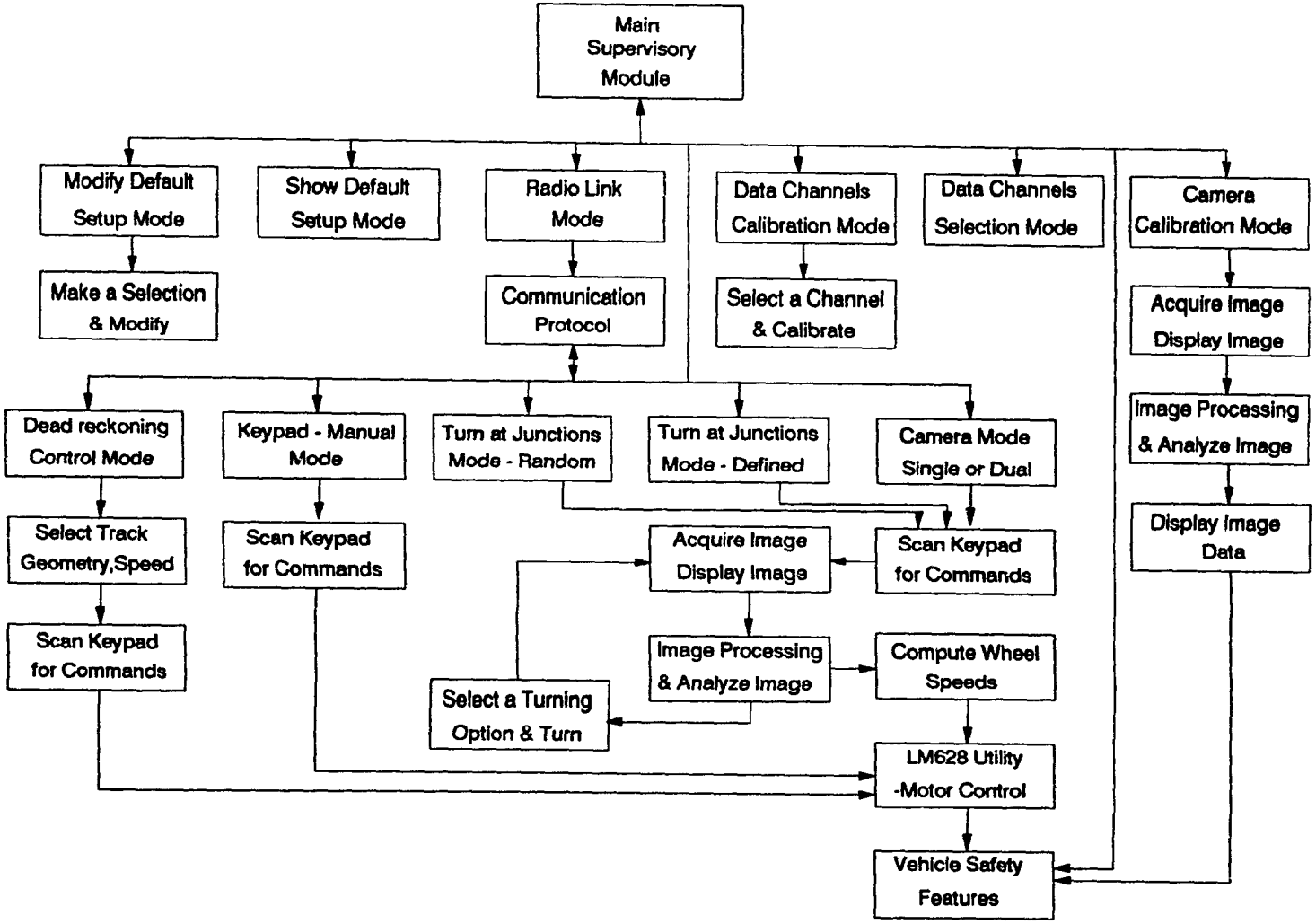

Fig. 6.22 Operating System Software Layout

in order to attain a satisfactory performance. To evaluate the time taken by various programming steps in the software, a hardware timer using 8254 chip is built into the vehicle circuitry. This timer is also used to obtain the sampling interval time for the PI controller in the camera vision mode. Using this timer, the time taken by various modules in the camera vision mode is evaluated and is provided in Table. 6.3. From this table it can be seen that the system provides a frame rate of 16 to 25 frames a second depending upon the features that are in use. The maximum time count is set at 200 ms and is programmable.

Task Description	Time (ms)
Camera Exposure Time	4.0
Image Acquisition & Transfer to Memory (1 Kbyte)	18.9
Image Processing and Analysis	9.0
Image Display in Real-time	6.5
Computing Wheel Speed Commands, Downloading Data to Motion Controllers & Logical Functions	1.9
Data Acquisition for 8 Hardware Channels	2.2
Data Acquisition for 8 Software Channels	2.7
Total Time for One Cycle	44.3

Table. 6.3 Timing Information for the Autonomous Vehicle

It can be seen that there is a discrepancy in the time presented here to take one frame of image and transfer it to the computer memory compared to the timing of 6.5 ms reported in the section 6.3.4, as wel. as in the IDETIX camera users technical manual. The reason for this is due to the manner in

which the camera is employed in the camera vision mode. The time 6.0 ms is valid if and only if the camera is set to operate in continuous mode in which the camera takes pictures continuously and transfers the image to the memory without waiting for the image analysis to finish. This method also makes the CPU busy, all the time working only with the camera controller. Another problem associated with continuous imaging is that it will not be possible to judge whether the image in the memory belongs to one single frame or it is composed off two or more frames. To alleviate these problems, the camera has been to set to operate in single frame mode. With this mode of operation, as soon as the camera controller completes the task of transferring one frame of image to the computer memory, a stop command is issued to the camera to disable the picture taking process. The image processing and analysis are performed thereafter. After completing one set of computations, the camera is enabled to take another picture and this process continues. As a result of this, the camera needs parameter downloading while it is being stopped, and this takes more time than 6.5 ms as reported.

6.3.11 Safety Features

The operating system of the vehicle has been provided with facilities for self diagnosis in order to detect malfunctions in the various components. Once a problem is noticed, the vehicle is commanded to stop either by the operating software or by the hardware. The various aspects of safety one need to consider for AGVs are identified and listed below.

1) Hardware should power the servo amplifiers only after the reset signal from the PC is received and the servo controllers are checked by the software.

2) Emergency stop feature to shut the motor powers.

3) Provision to identify the signal input voltage level of the servo amplifier exceeding the preset maximum voltage for full motor speed.

4) Provision to isolate the amplifiers from the motors.

5) A watch dog timer to monitor the computer for system hang ups due to hardware and/or software problems when the vehicle is in motion.

6) Motion controllers should be checked for possible malfunctions at the beginning before the amplifiers are powered as well as while the vehicle is in motion.

7) Encoders must be checked for malfunctions when the system is started as well as while the vehicle is in motion.

8) Ultrasonic sensors for obstacle detection and stopping.

9) The amplifier powers should be turned on and off by the software.

10) Presence of valid image data should be checked.

11) Sufficient battery voltage for normal functioning of the system.

Fig. 6.23 shows the state diagram of the safety circuit and Fig. 6.24 is the flow chart of the control software for the safety circuit. When the computer performs a cold boot, the safety system may be in any one of the several states indicated. On receiving a reset from the computer, the safety circuit comes back to state-1 which is the initial state. This is indicated by the route code CO-O. This is the stage where the emergency stop is not activated, there is no over voltage to the servo amplifiers, motion controllers received an hardware reset (input signal indicated by the letter H) and the encoders are not tested yet. The letters XYZ in the state block diagram represents the output display (LEDs) on the interface board indicating the status of the safety system. ON condition of the red light on

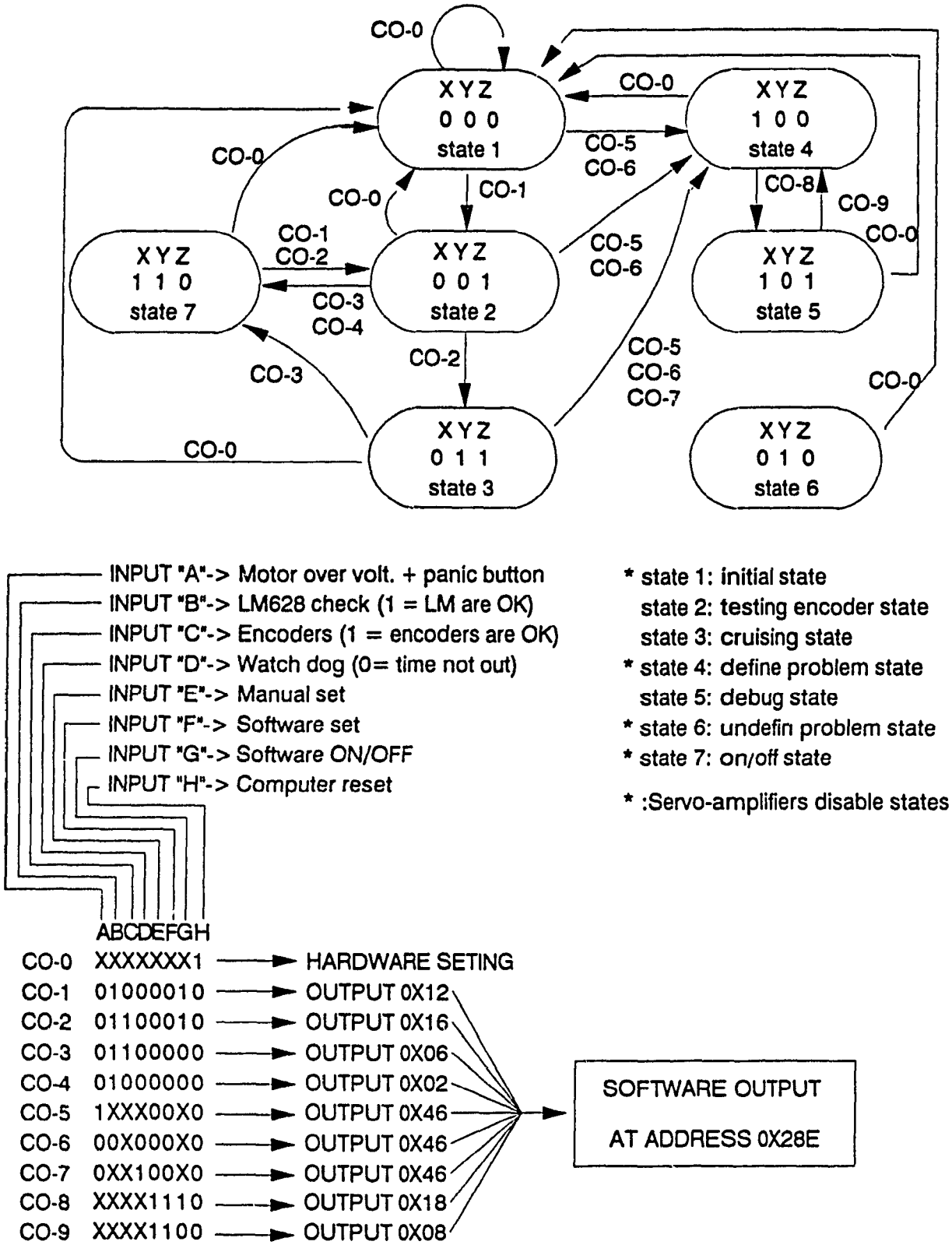

Fig. 6.23 State Diagram of Safety Circuit Control Software

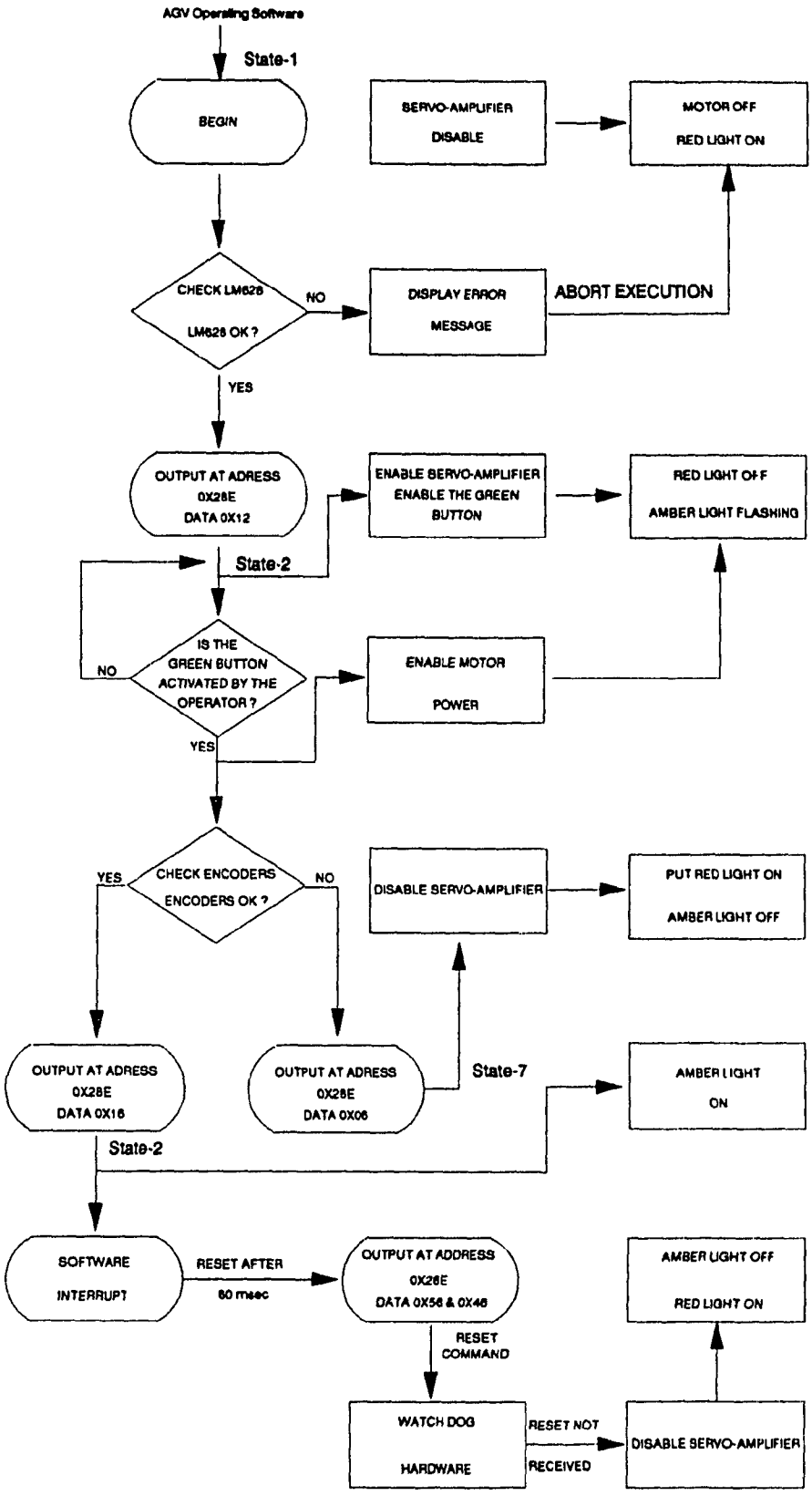

Fig.6.24 Flow Chart of Safety Circuit Control Software

the system panel indicates this status.

When the letter Z is assigned a value of 1 or LED Z is ON (logic 1), then it means that the motion controllers have been tested and are found to be functioning normally. This is indicated by the route code CO-1 where the LM628s are checked and are found to be functioning normally. Referring to the flow chart shown in Fig. 6.24, the software sends data 0x12 to the address 0x28E to indicate the successful testing of LM628 chips. As a result of this, the hardware switches on the relays supply power to the amplifiers. The motor power can be turned on by activating the power button manually. A software polling is performed to check whether the green button is activated or not. During this stage the red light is off and an amber light flashes indicating the motor power is not activated. Once the computer detects the green button being activated, it sends a control signal to energize the relays.

When a value of 1 is assigned to the letter Y (LED-Y ON state) it indicates that the encoders are tested and are functioning properly. This is state-3 and the route code is CO-2. After this, the vehicle can be operated with the main operating software. The letter Z or the LED-Z when the LED-Z is ON it indicates problems with the system and this cuts off the power to the amplifiers. State-5 is the manual debugging state and this can be reached from state-4 by sending an output value of 0x18 to address 0x28E. State-6 indicates the situations that are not covered in the safety feature. This is an undefined problem state. State-7 is provided to switch OFF the safety features or bypass the safety features using the system software.

An emergency stop button is provided to stop the vehicle manually for safety reasons. When this button is activated, all the relays are deenergized thereby cutting off the power to the motors. Once this button is activated, the vehicle can be restarted only by hardware reset to the computer. Activation of this button sets bit 0 to low and this status is read by the software. There is no route code associated with the emergency stop button. The software periodically checks for this condition and a status message *Emergency Stop Button Activated* appears.

It is necessary to identify the situation wherein the control signal to the amplifier exceeds a preset value which corresponds to a maximum motor speed. In the current implementation, the wheels attain the maximum speed when 6 bits of the DAC-08 are used and this corresponds to a control voltage of 4.2 V to the servo amplifiers. If the motion controller generates a large output command which would use more than the necessary 6 bits of the DAC, this is an indication of problems with the control system. This condition is detected by the hardware safety circuit and this sets bit-5 to logic 1 in the PAL. This is indicated by the route code C0-5 and this takes the system to state-4. The hardware safety disables the amplifiers and a *DAC Output Voltage Too High* message is generated. The provision for isolating the motors from the amplifiers is to make sure that the back e.m.f of the motors does not damage the amplifiers when the AGV is pushed manually. This is accomplished by activating the emergency stop button.

A watch dog timer ensures that the host computer does not hang up while the AGV is in motion. Without this feature, the computer control will not be

functioning and the motors will be rotating at the last specified command velocity. Once the computer control is lost, the AGV can be stopped only by switching off the power to the amplifiers. To bypass this condition, an external timing circuit with a software interrupt is designed which requires a reset counter signal from the master computer before a preset time duration is attained. Currently this time has been set at 60 ms arbitrarily . If the reset signal is not received before this 60 ms duration, a signal is generated by this watch dog circuit to set bit 7 of the PAL to a logic value 0 as in the state diagram Fig. 6.23. This is indicated by the route code CO-7 and state-4 is reached. This condition switches off the control relays that are controlling the power to the amplifiers and hence the motor power is cut off. Once the vehicle is stopped by the watch dog timer, the vehicle can be restarted only by performing a hardware reset of the computer.

Initially, before the vehicle moves, the motion controllers are checked by the software for the presence of the LM628 motion controller chip and possible malfunctions. The absence of the motion controller is detected when the data read from the status register address is 0xFF. Once this condition is noticed, the execution of the software is aborted. System diagnostics provide a status report as *LM628 Motion Controllers Missing*. If the motion controllers are present the following checks are performed to identify malfunctioning of the chips.

During the entire execution of the software, malfunctions can be noticed whenever the busy bit of the status register of the LM628 does not appear within 100 ms. This condition terminates the software execution and the diagnostic message *LM628 not responding* appears. If the busy bit checking is

passed, then a further check is carried out to check whether the registers of the chip are functioning properly.

After the busy bit check is passed and before entering the main menu of the operating software, a known data (speed or position) is written to the registers of the motion controller and is read back to check the write/read registers. Discrepancies in the data comparison results in the termination of the software execution and the diagnostic message *LM628 Malfunctioning* appears. When the vehicle is in motion, this check is implemented in a different way. Since a speed or position data is always written to the motion controllers only data read has to be performed to establish the status of the read/write registers. The malfunctioning of the LM628 cuts off power to the motors and state-4 is reached and the route is indicated by CO-6.

The encoders are monitored by checking the validity of the data received from them. Initially, before displaying the operating menu, a small position or velocity command is issued to the motion controllers and the actual position or velocity of the wheels are checked. Before issuing this a command to the motion controllers, the software checks the status of the green button explained earlier is performed. If the feedback data read is not valid, bit 2 in the safety circuit of the PAL is set to logic 0 as in the state diagram of Fig. 6.24. The execution of the software terminates on detecting this error. If the encoder check is not successful when the vehicle is moving, the vehicle is commanded to stop by using the software motor off command of the LM628 motion controller chip. This command is used as it does not use the feedback information while stopping. A message *Encoders Malfunctioning in Servo Loop* is generated by the diagnostic software

along with the servo loop number where the problem is noticed..

The provision of ultrasonic sensors is for obstacle detection and collision avoidance. In this, the ultrasonic sensors are provided at the front of the vehicle. These devices are turned on and off by software control. When an obstacle is detected, a software interrupt is generated and the vehicle is brought to a halt using the *motor off* command which results in a fairly smooth stop. The diagnostic software produces a message *Obstacle detected.* Once the obstacle is removed, the vehicle accelerates to the original speed.

The image analysis function checks continuously the validity of the image as received by the camera. This sets a flag called imageok_flag. If the image is valid, i.e., track image with a normal predefined width (35 mm in the case of CONCIC-II AGV), then the flag is set to 0. If the image is mostly white, the flag is set to -100 and for a mostly black/dark condition, the flag is set to 100. While in camera mode (continuous running mode with no turning option), if the flag generated is -100 for four continuous frames, then the AGV is commanded to perform a *motor off* stop. If the flag is 100, then the current image data is ignored and the vehicle proceeds based on the previous data. The system messages window displays *Invalid Image Data.*

The data acquisition system of the AGV provides the actual battery voltage and this information is used by the operating system software to decide whether the vehicle is in condition for normal functioning or not. If the batteries voltages are low, then a *Battery Voltage Insufficient* message appears on the status window.

It should be noted that in all the cases described in the safety features section, the vehicle is commanded to stop whenever a problem is detected. If the vehicle has been stopped by a software error detection, one could restart the AGV by reloading the software. On the contrary if the stopping is due to hardware problems, it is necessary to restart the entire computing system.

6.4 Summary

In this chapter, the design philosophy and system architecture of an autonomous vehicle are presented. The present design facilitates a versatile research vehicle with which performance studies of various wheelbase configurations can be carried out. The modular design concept in selecting the various components provides easier system upgrading with the technological advancement. The employment of low cost vision technique coupled with an efficient image processing technique obviates the necessity to employ a complicated and sophisticated guidance system. Employment of special purpose motion controller chip LM628 simplifies the controller design and also offers concurrent control of multiple motors as these chips can operate without having to use the bus of the host computer. Provision of on-line data acquisition system is useful for system validation. The dual camera guidance concept provides forward and backward travel as well as accurate tracking capability. A complete investigation on the safety features required for the AGV is carried out and has been implemented. The operating software is modular in nature and has variety of features. Operating parameters of the system can be modified on-line.

From Table. 6.1 it can be inferred that the operating system provides images of the track at a rate of 20 to 25 frames/s. As a result of this very high frame rate and a stable performance are expected at higher velocities and with tracks having smaller radii of curvature. Referring to Table 6.1, it can be seen that the vehicle has a payload of 600 lb in addition to its dead weight of 275 lb. In camera mode a maximum speed of 0.93 m/s on a circular track of 1.7 m radius is achieved.

CHAPTER 7
VALIDATION OF GUIDANCE CONTROL BY SIMULATION AND EXPERIMENTATION

7.1 Introduction

This chapter presents results on simulations and experiments performed to study the effectiveness of the guidance and control schemes proposed in the previous chapters. This chapter has been divided into four sections. The first section presents results obtained from calibrating the control components of the prototype AGV. The objective of these tests are to establish the linearity and the operating limits of these components for control purposes. The second section (7.2) discusses the experimental results obtained with the control scheme that uses the parameters of steering obtained from a single camera at the front end of the vehicle. Track profiles considered are, straight line, straight line track with an offset, circular profile and elliptic profile. These results illustrate the ability of the control scheme to provide accurate track following of the vehicle.

The third section (7.4) of this chapter is on vehicle guidance using two cameras, one at the front and the other at the rear end of the vehicle. Here, simulation studies and experimental results in following a straight line track and a circular track are provided. A simulation package based on a dynamic model of the CONCIC-II AGV developed by Huang [35] is used to provide simulations. This package has been developed for a guidance scheme employing camera at the front end of the vehicle. Appropriate modifications are thus made to the package to include the guidance scheme that employs the rear camera as well. An abridged version of the dynamic model equations is

presented in Appendix G. Program listing of the simulation package is also included in this appendix.

The fourth section (section 7 5) presents the results of identifying the geometry of the track profile and the desired values of the position and the orientation offsets for accurate tracking. For this purpose simulations and experimental data are used. In this section experimental results for guidance control are not provided as they are not carried out. This is because the computational requirements of this scheme is beyond the scope of the prototype AGV. Nonetheless, research is underway to use parallel processing hardwares for this purpose.

Simulation studies are to verify the equations as these data are free of noise. Simulations are carried out with a known track profile. Offline calculations are performed with data from an experimental vehicle. These calculations provide the identified geometry of the track, the coefficients of a function that closely describe the track profile, and the desired values of the parameters of steering control for accurate driving.

7.2 Component Calibration

Components of the servo loop of the vehicle, namely, the digital to analog converter (DAC), the servo amplifier, and the motor are calibrated here. Calibration experiments are carried out to study the effect of a number of rows of image considered for the LSES. The results indicated a marginal improvement (less than 1%) when the number of rows is increased from 3 to 30. Hence these results are not provided here. Some experiments are carried out to provide exact model of the components of the AGV for modeling

and simulation purposes. Huang [35] has used this information to model the AGV and to carry out simulation studies. Some of the experiments carried out and not discussed in this thesis are, calibration of the data acquisition channels and estimating the servo delay of the motor-amplifier set. Using the results of data acquisition from the AGV, Huang [35] verified the correctness of the simulations model and the software package to simulate the CONCIC-II AGV. It has been mentioned earlier that this model and the software package have been used to carry out simulation studies on the guidance scheme that employs two cameras.

7.2.1 DAC-08 Calibration

This experiment is to establish the linearity of the digital to analog converter (DAC) and then to evaluate the gain of the DAC for modeling purposes. The gain is expressed in voltage output per unit variation in the data input to the DAC. The results are shown in Figs. 7.1a & 7.1b for the DACs in the control loops of motors A & B respectively. A regression equation is also presented. From the results, for motor-A, it can be observed that the output voltage is zero when the input is 127 (0111 1111 in binary form), the positive maximum is attained at 164 (0100 1100) and the negative maximum is at 80 (1101 0000). Here the most significant bit (bit 7) is the sign bit (+/-). It can be seen that of the 8 bits available, only six bits are used to cover the entire operating speed range of the motor. Similarly for motor-B, the positive maximum is at 72 (0100 1000), the negative maximum is at 176 (1011 0000) and the zero output is at 127 (0111 1111). The outputs of DACs for the motors A & B are reversed as they are mounted to rotate in opposite directions. This is due to operating constraints posed by the structure of the AGV.

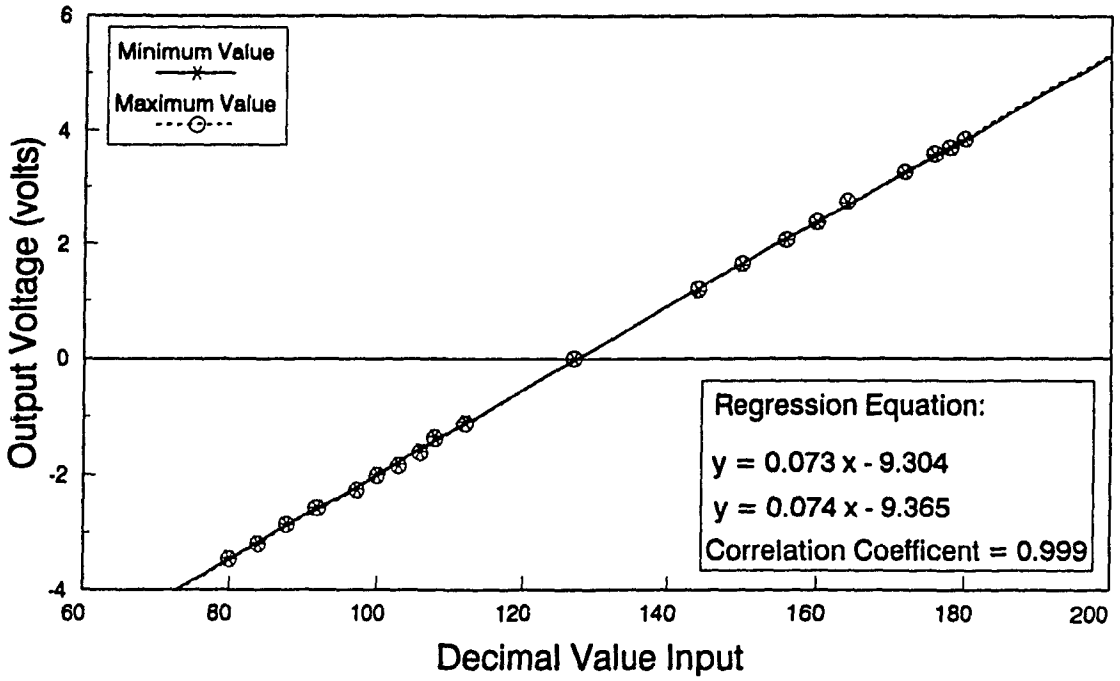

Fig. 7.1a DAC - 08 Calibration Curve for Motor-A

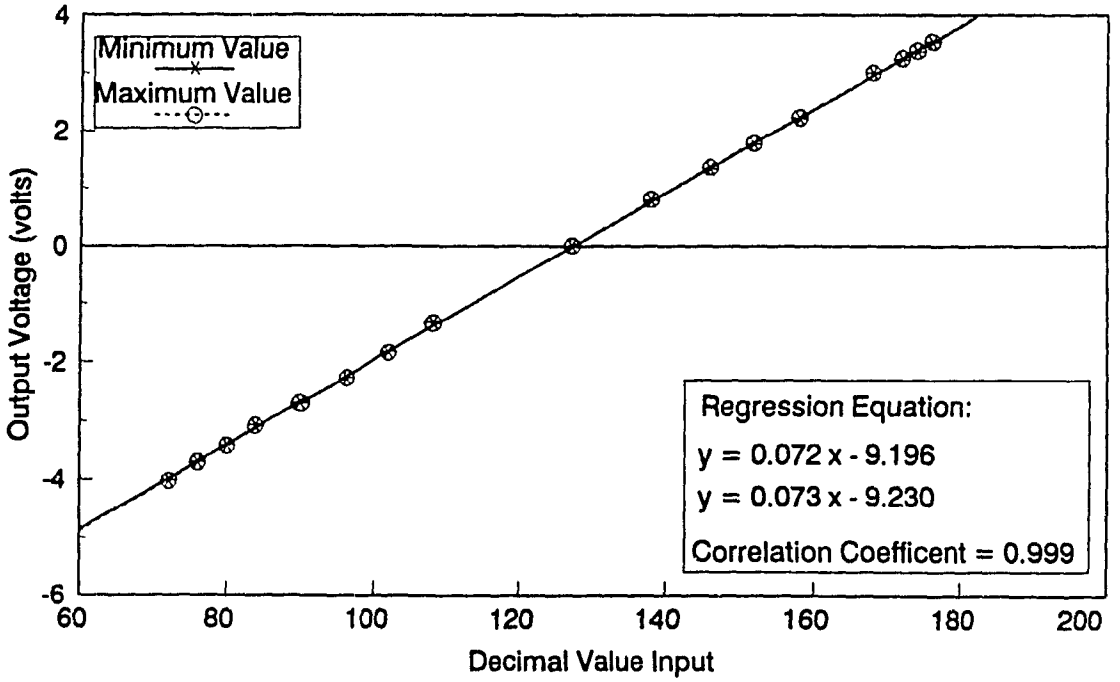

Fig. 7.1b DAC - 08 Calibration Curve for Motor-B

7.2.2 Servo Amplifier Calibration

The output signal of the DAC is the input signal to the servo amplifier. This input is the command signal for the amplifier which controls the terminal voltage of the motor which in turn decides the motor speed. Experiments are designed to test the linearity of the servo amplifier with the motor and to compute the amplifier gain. The results are presented in Figs. 7.2a & 7.2b. The result is not linear and a power series expression is present for the response. This shows the presence of some non-linear component in the amplifier.

7.2.3 Motor Calibration

Experiments are carried out to obtain the relationship between the desired and the actual speed of the motor, and the motor terminal voltage. The results for motors A and B are illustrated in Fig. 7.3a to 7.3b. A linear relationship exists between the speed values and the terminal voltages. This establishes that the motor speed can be varied by changing the terminal voltage linearly.

7.3 Experimental Results in Track Following

The magnitude of the vehicle acceleration has been established experimentally and the recommended value is 0.024 m/s^2. The value of the PID gains are also experimentally evaluated and are 225, 100, 50 and 30 for K_p, K_i, K_d and I_i respectively. Results showing the effect of controller gains of the P & PI controllers of the camera feedback loop are presented. The transient and steady state response of the vehicle to variations in track geometry are investigated. Some results pertaining to following a straight line track, circular and elliptic tracks are provided.

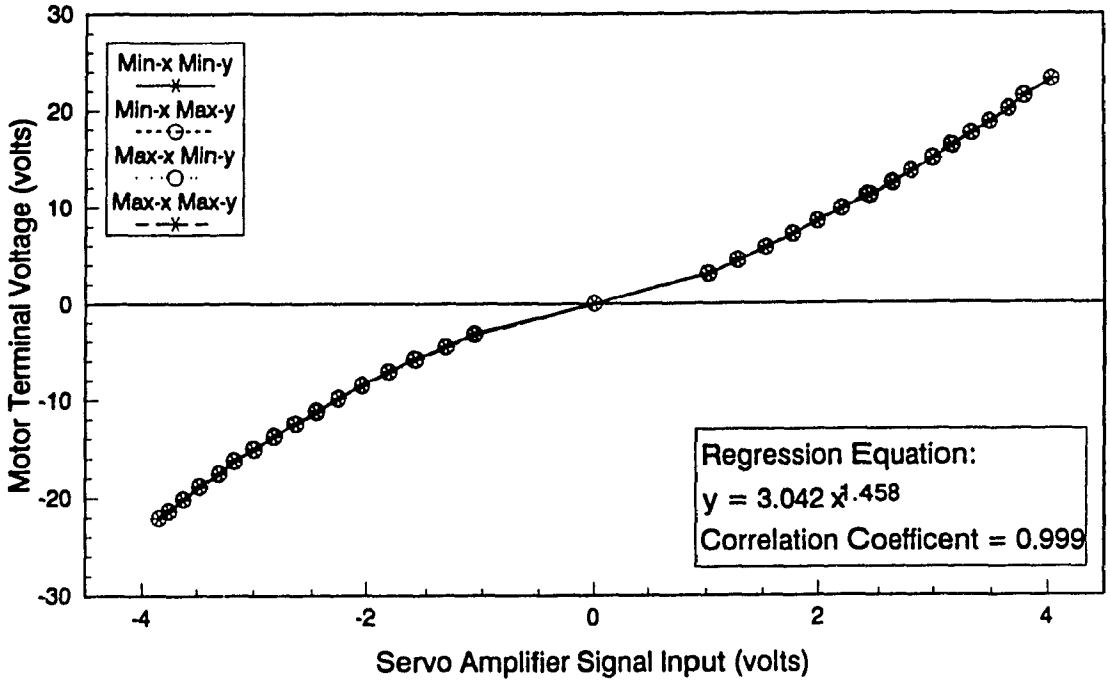

Fig. 7.2a Servo Amplifier Gain Curve for Motor-A

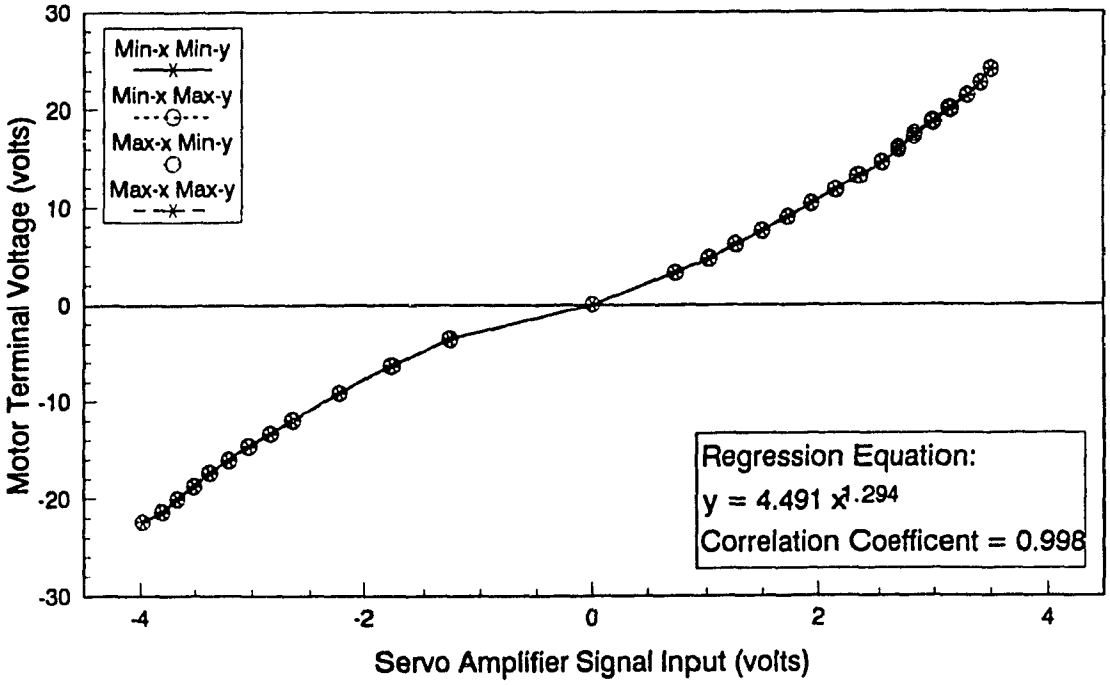

Fig. 7.2b Servo Amplifier Gain Curve for Motor-B

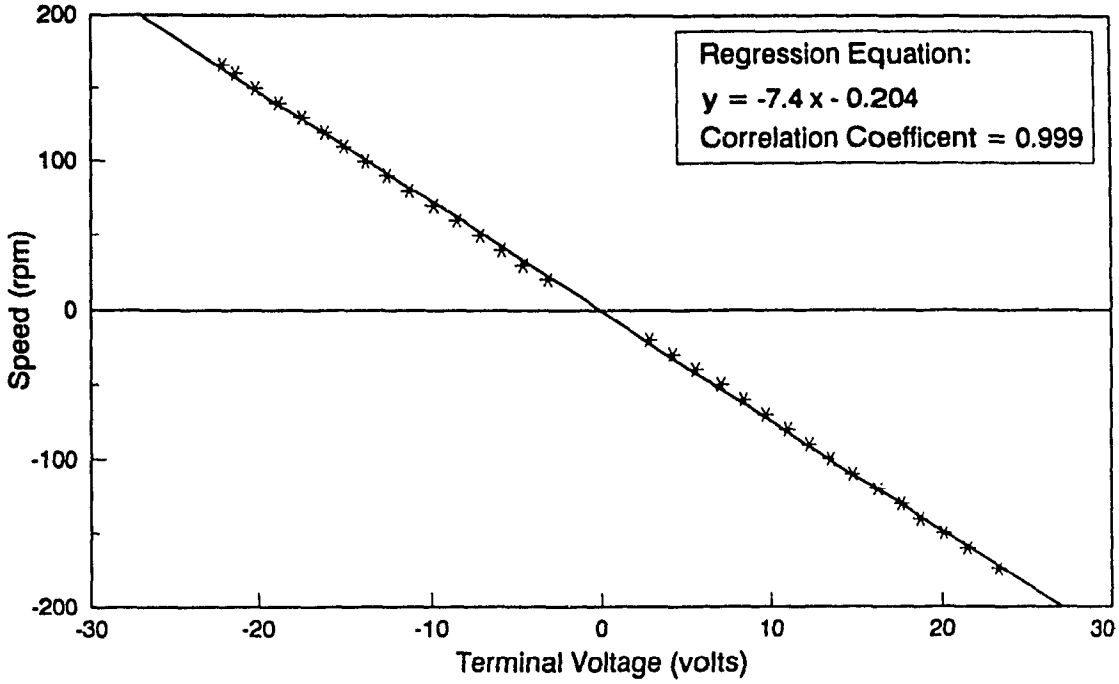

Fig. 7.3a Motor Terminal Voltage Versus Desired Speed for Motor-A

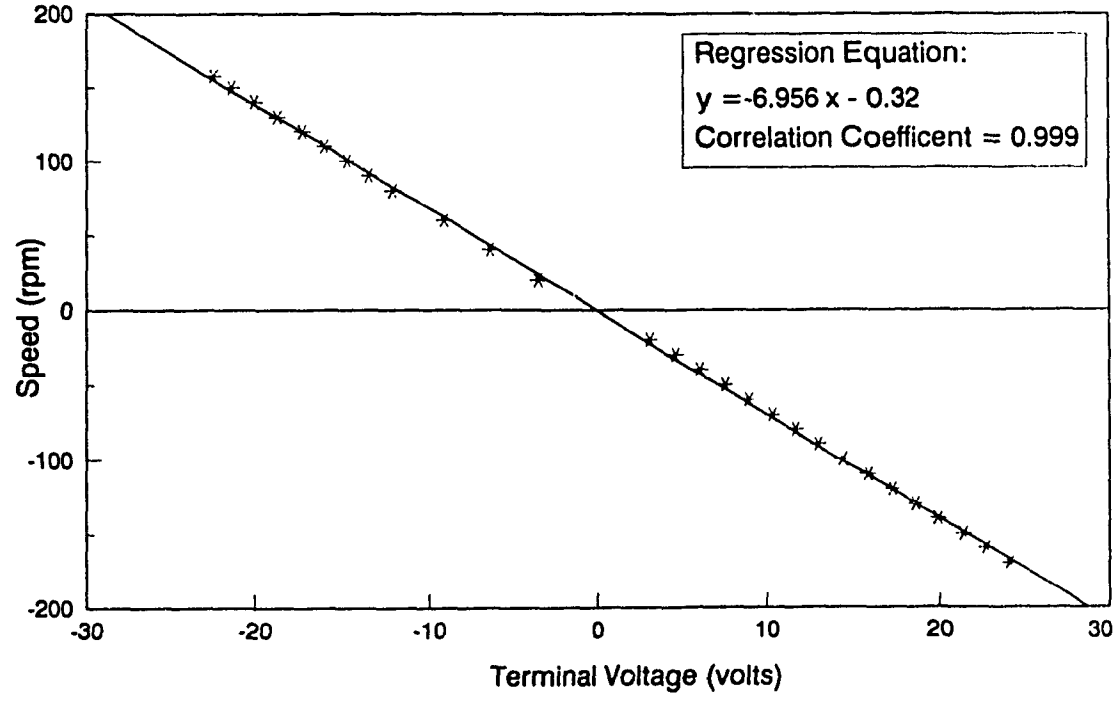

Fig. 7.3b Motor Terminal Voltage Versus Desired Speed for Motor-B

7.3.1 Effect of P and PI Controller Gains on Performance

The results of using a proportional controller in the camera feedback loop for various gain settings are compared in Fig. 7.4. The performance of a PI controller is also included. For a P-controller a suitable gain is in the vicinity of 2.5. This controller compares favorably with the PI controller (P = 2.5 & I = 0.07). However the latter exhibits better steady state performance compared to that of a P-controller, and is preferred for the vehicle. It was also established by Huang [35] by simulations, that the gain settings chosen experimentally are the best values that results in a satisfactory performance of the vehicle.

7.3.2 Track Following Performance at Various Speeds for Straight Line Tracks

Tests are conducted for various values of linear velocity (step input) of the AGV with no payload and the results are shown in Fig. 7.5a. During the initial transient period (0 to 4 s), the vehicle tends to build up its speed while allowing the magnitude of the position offset to grow. Rapid corrective action takes place after this, resulting in an overshoot, followed by a satisfactory tracking performance. This initial behavior is due to the design characteristics of the motion controller chip LM628. It has been mentioned in section 6.3.2 that while the acceleration value for the trajectory profile is programmable, it remains in force until a stop command is issued to the chip.

Servo loop continues the speed build-up with the said constant acceleration, until the instantaneous speed error is zero. This performance

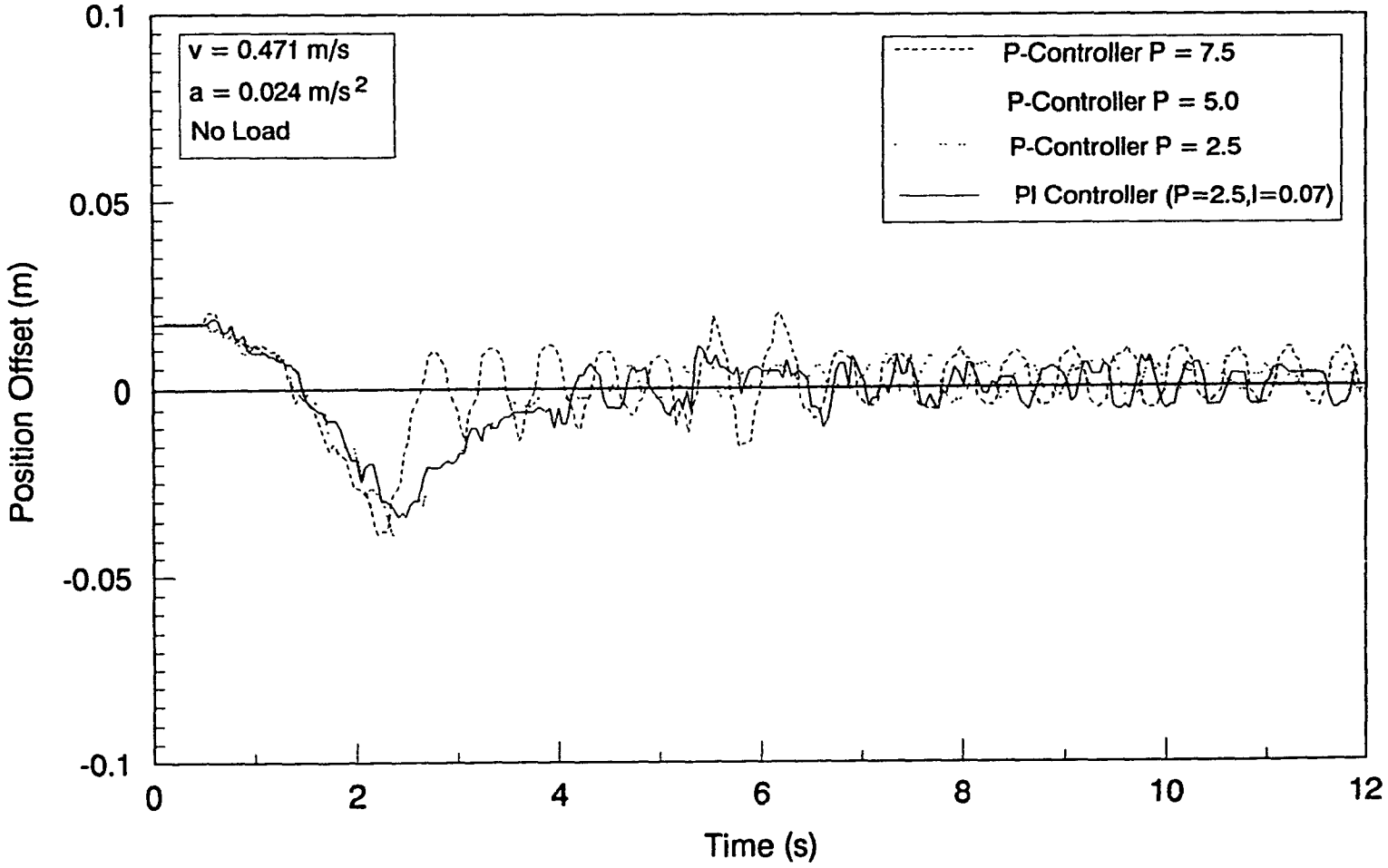

Fig. 7.4 Performance Comparison of P and PI Controllers on Straight Line Track

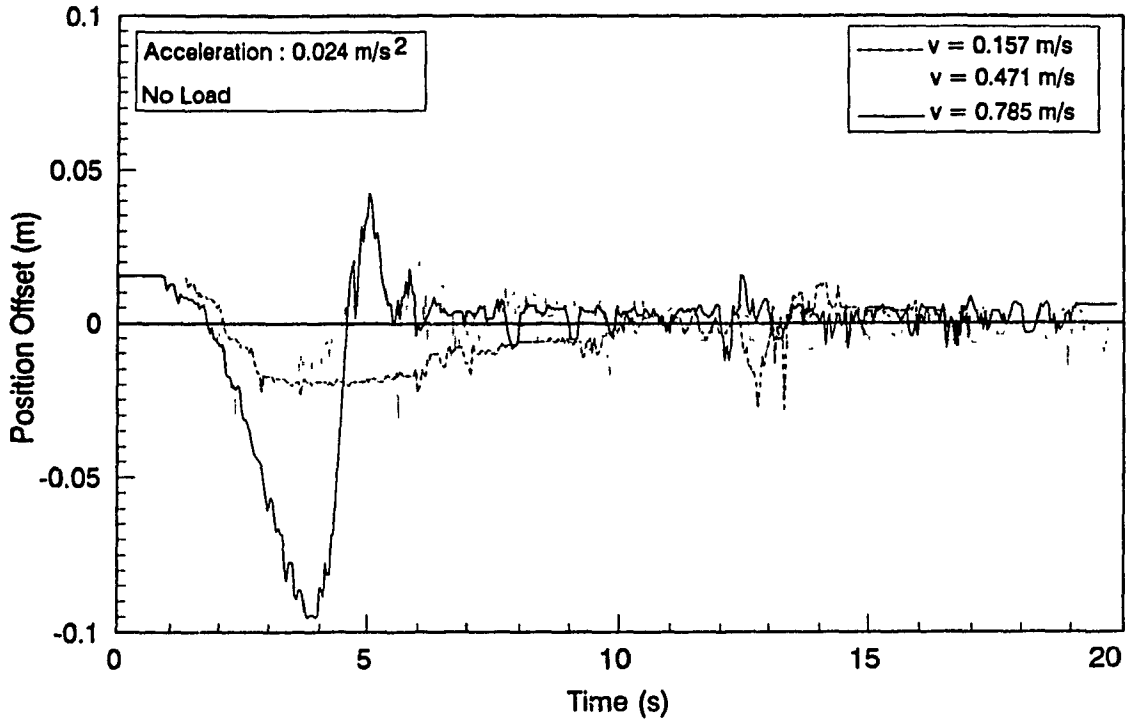

Fig. 7.5a Tracking Performance at Various Linear Speeds Under Same Initial Condition for a Straight Line Track

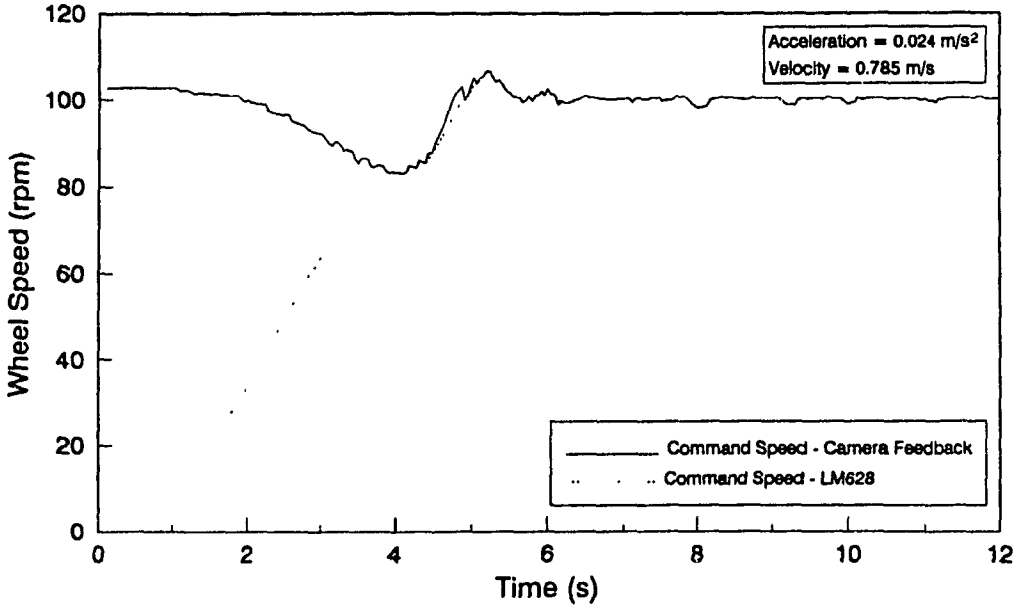

Fig. 7.5b Command Speeds Comparison - LM628 and Camera Feedback

is very well illustrated in Fig. 7.5b, which shows the speed response for one of the two wheels. Again, the response as obtained from the LM628 speed is shown with the response computed by the control software. The magnitude of the initial position error because of this behavior of the controller chip is still within 0.1 m. The transient period from stop to full speed is less than 7 s even for 0.8 m/s.

Performance study results for the vehicle travelling with and without a payload are presented in Fig. 7.6 with identical initial conditions. The maximum offset with a payload is 33% less. The steady state performance for the two cases show little difference. Tests are carried out with different initial conditions at the normal operating speed of the vehicle. This test is to establish the maximum initial offsets that the guidance scheme can tolerate. The results of this test are provided in Fig. 7.7. The behavior is the same for positive and negative position offsets, and even an initial position offset of -0.08 m (8 cm), which is 80% of the maximum value of the window dimension of the camera, provided a satisfactory response.

7.3.3 Dynamic Response for a Sudden Change in the Location of the Track

Figure. 7.8a shows the dynamic response of the AGV to a sudden change in the location of the geometry of the track, a situation designed to study the robustness of the guidance control of the vehicle. The straight-line track is offset by 0.065 m, and it occurs at a point the vehicle has attained the desired speed. In the upper portion of Fig. 7.8a, the actual track condition is presented. This figure also shows the transient and steady state responses. The test is conducted at vehicle speeds 0.79 m/s, 0.63 m/s, 0.47 m/s and 0.31 m/s. A 10% overshoot is observed, providing satisfactory recovery of the vehicle after a sudden geometric change in the track. The

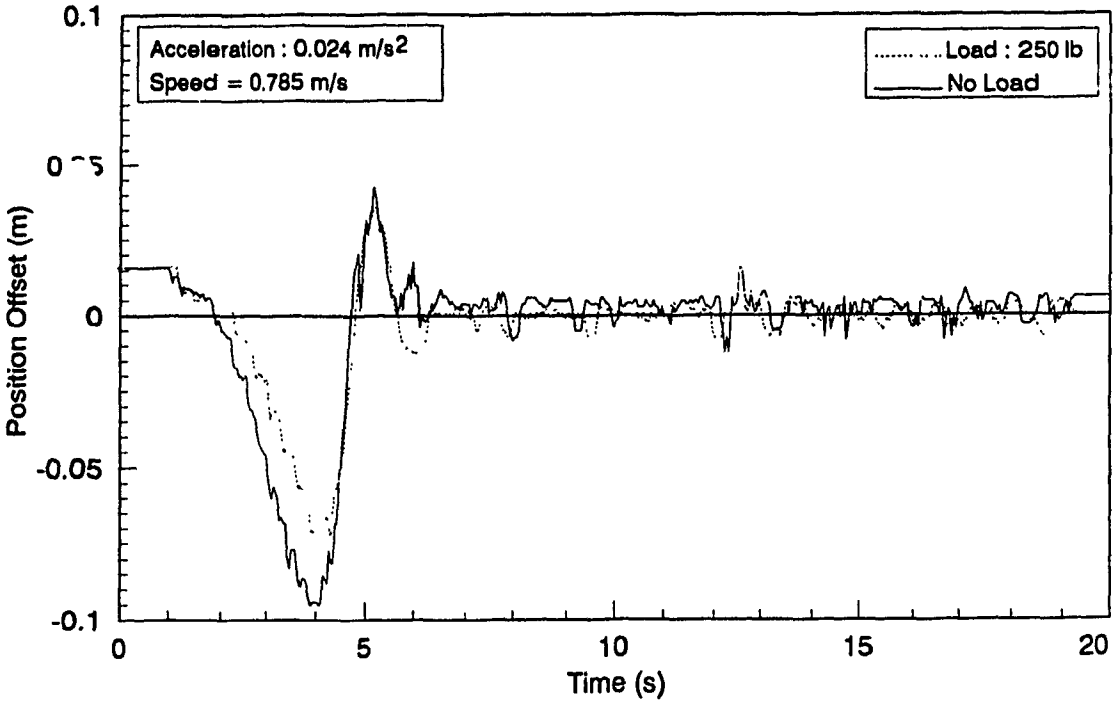

Fig. 7.6 Comparison of Tracking Performance on a Straight Line Track with and without load under Same Initial Condition

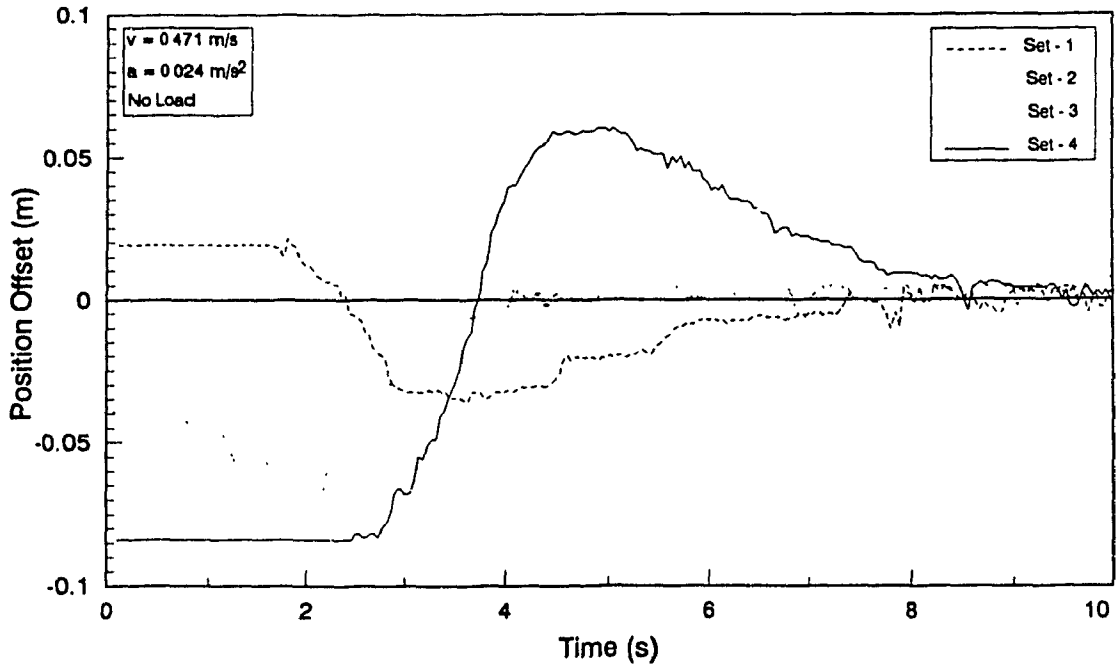

Fig. 7.7 Comparison of Tracking Performance on a Straight Line Track at Various Initial Condition

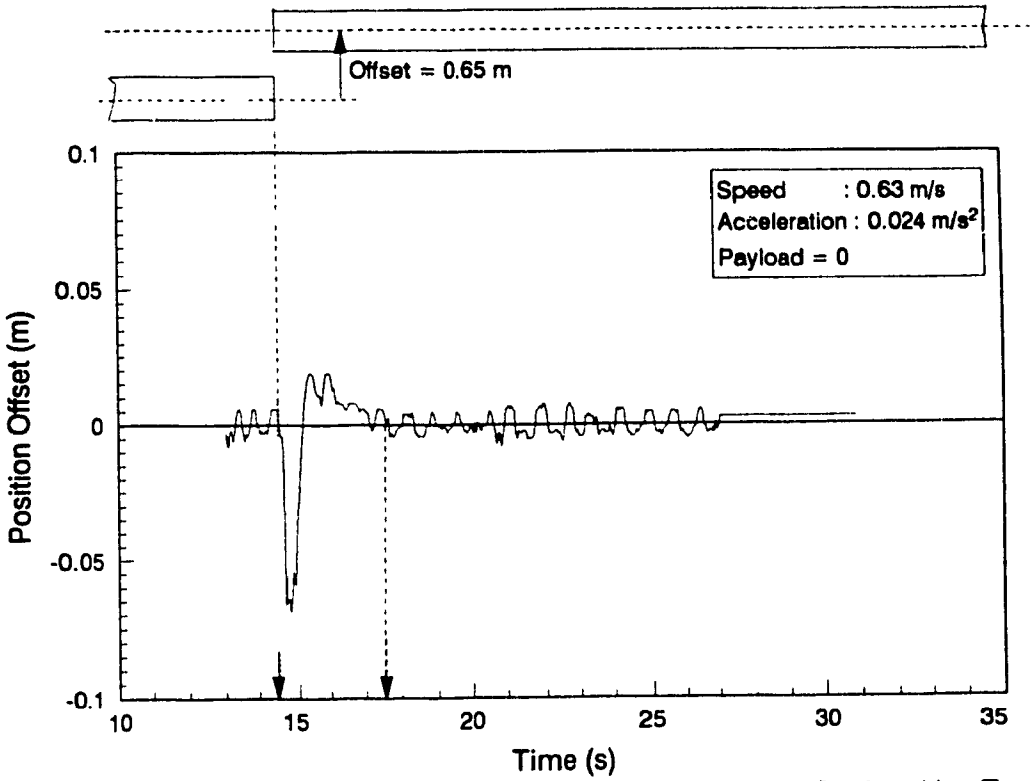

Fig. 7.8a Dynamic Response of the AGV on an Offsetted Straight Line Track

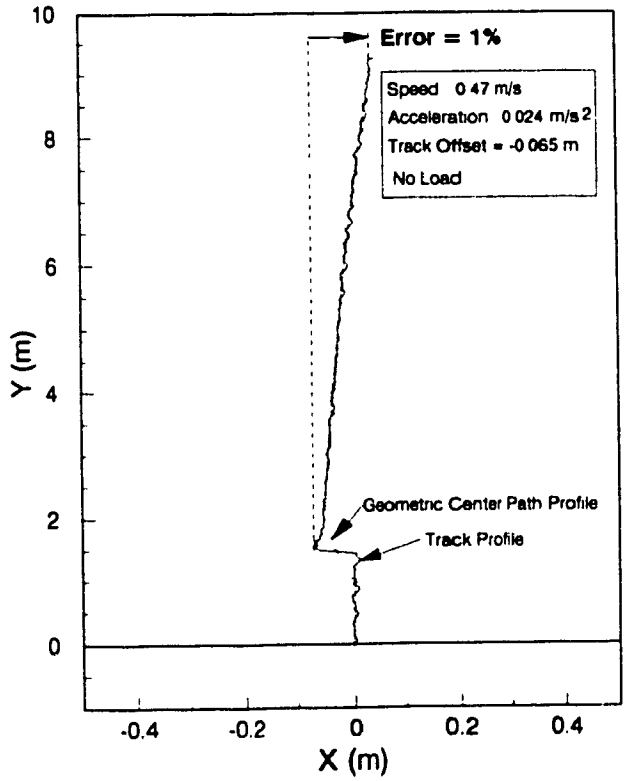

Fig. 7.8b Profile of the Track & the Geometric Center of the AGV

measured value of the offset by the image processing scheme is 0.70 m and the error is approximately 8%. A transient period of 3.0 s (approximately) is observed for a vehicle speed of 0.63 m/s.

For the track with an offset shown in Fig. 7.8a, the track profile and the vehicle response curve are presented Fig. 7.8b. The coordinates of the track and the vehicle at various time instants are computed using the schemes described in section 5.4.1. The computed track profile has an error of 1% (0.1 m over a distance of 10 m). This is attributed to errors in computing the wheel speeds, errors in evaluating the physical parameters of the vehicle, errors in establishing the position offset (ε_d) and accumulated errors of computations. The computed track profile shows overshoots at higher velocities due to vibrations resulting from the camera mounting.

7.3.4 Minimum Stopping Distance on Straight Line Tracks

This experiment is to establish the distance travelled by the AGV before coming to a full stop after a stop command is issued to the motors by means of the motor off feature of the LM628 motion controller. This information is useful for parking purposes where it is necessary to know at what speed the vehicle should be running in order to make sure the vehicle stops with minimum overshoots. The motor off command is issued in the experiment by the operating software when it detects the absence of the track image on the floor. When the motor off command is issued, a zero voltage is given as an output to the motors and the motor is allowed to come to a stop by itself. Figure. 7.9 presents the results at various linear speeds of the vehicle. The minimum stopping distance of 5 mm is observed when the vehicle is operated at a speed of 0.16 m/s and is the recommended speed for parking.

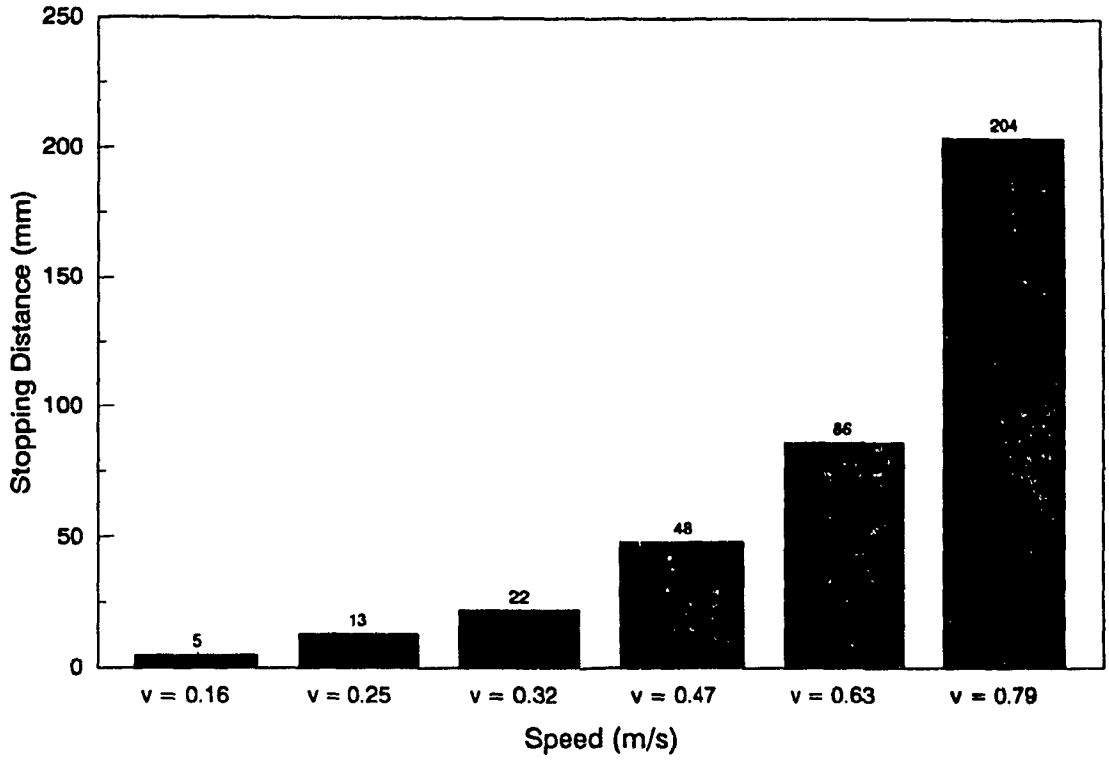

Fig. 7.9 Stopping Distance of AGV at Various Speeds on Straight Line Track

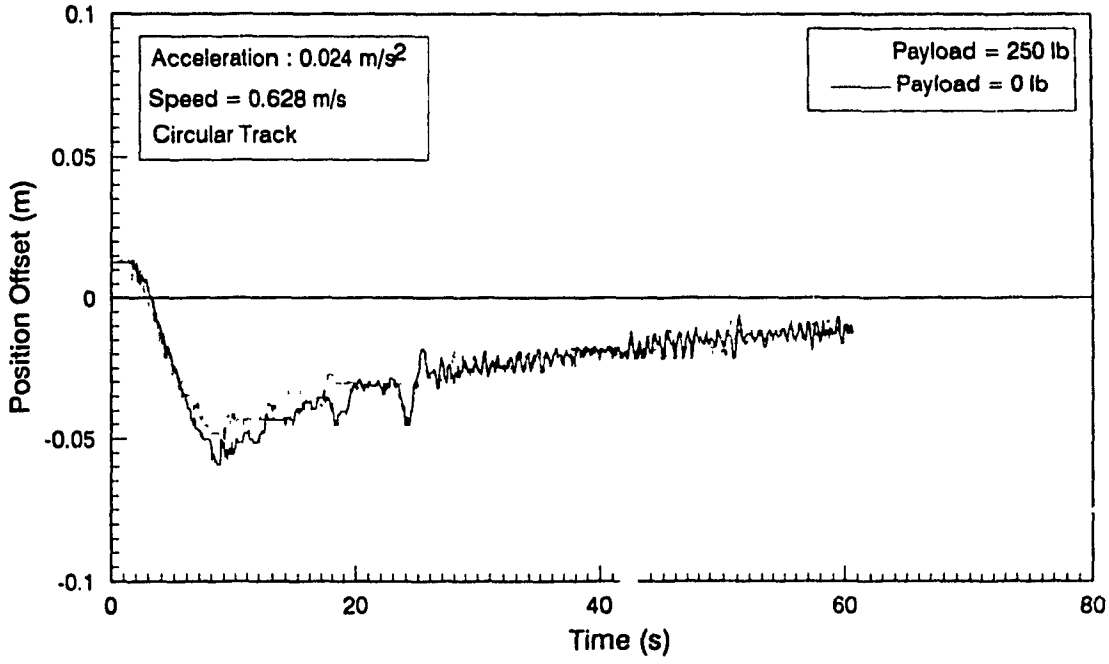

Fig. 7.10 Comparison of Tracking Performance with and without Loadon a Circular Track

The results have an error of 1%.

7.3.5 Conic Profiles

Conic profiles considered are circles and ellipses. It has been mentioned in section 7.3.2 that the LM628 follows a linear velocity profile and the acceleration value cannot be changed while the vehicle is in motion. As a result of this, the transient response of the vehicle for step input cannot be obtained while following a conic track profile and the speed commands are given to the LM628 in small increments.

Figure. 7.10 presents results from experiments carried out on a circular track of radius 2.95 m with and without a payload. It can be seen that the results do not present degradation of performance with payload compared to the case without the payload.

As in straight line tracks, here also the dynamic response of the AGV to a sudden change in the track position is studied. Fig. 7.11 shows that a portion of the tape of the circular track has been shifted radially outwards. This figure shows the position offset as measured by the front end of the vehicle. This shows the position error or the offset in the track location as measured by the camera and the time taken for the vehicle to follow the track in the new location. The position offset measured has an error 8% and the time taken for the vehicle to follow the track at the new location is 3 seconds.

Position offsets while following an elliptic track at various speeds is shown in Fig. 7.12. Since the curvature of the track changes constantly, the

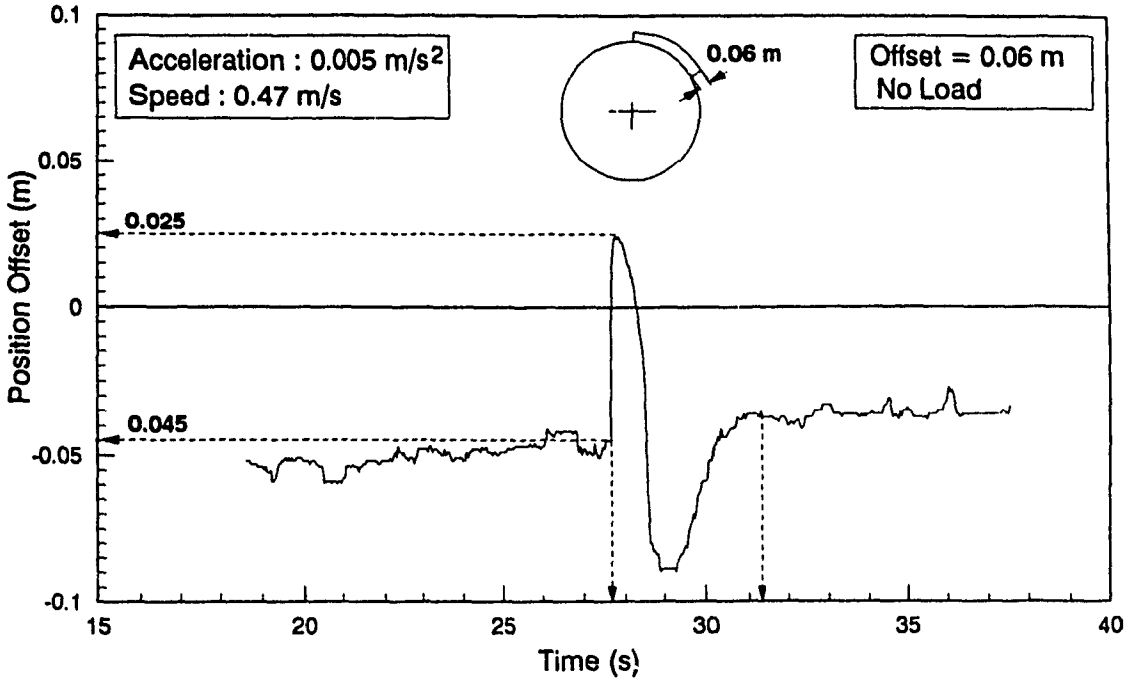

Fig. 7.11 Performance of the Guidance Scheme for Sudden Change in the Track Location for a Circular Track

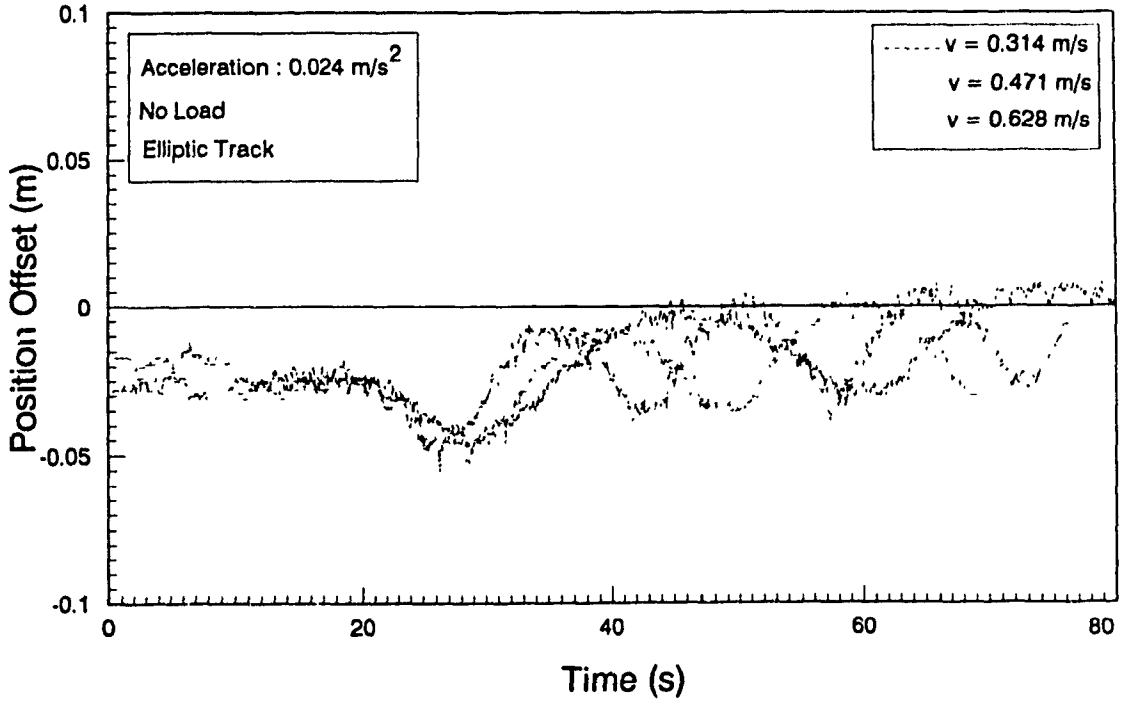

Fig. 7.12 Comparison of Tracking Performace at Various Linear Speeds under Same Initial Condition for an Elliptic Track

position offset various cyclically. The magnitude of the peaks at various speeds are more or less the same.

7.4 Performance Comparison of Dual and Single Camera Guidance - Simulation Results

Simulations are carried out to study the effectiveness of the guidance scheme based on the dual camera in providing accurate track following of the front and rear ends of the vehicle. Two sets of results are provided for track following of a straight line track and a circular track. The initial condition of the AGV for these sets are chosen such that for one set, the front and rear ends are on one side of the track, and for the other they are on opposite sides of the track. In order to clearly identify the improvement in tracking during the transient and steady states, it is necessary to eliminate the effect of constant acceleration problem of the LM628 motion controller chips. For this purpose the following approach is employed.

Figures. 7.13a & 7.13b are for following a straight line track with the two initial conditions mentioned above. The gain of the controllers are provided in the figures. The magnitude of these gains are arrived by trial and error. Large gain values are employed initially so that the front end of the AGV crosses the track faster, and thereafter smaller gain values to achieve asymptotic error correction. From the results it can be seen that in both (single and dual) guidance schemes the tracking position offsets at the front and rear ends of the vehicle become zero eventually, and in the results presented, the time taken is approximately 10 s. The interesting aspect of the dual camera guidance is that it reduces the total time taken to attain close to zero tracking position offset. Figure. 7.13a is for the initial condition in which the front and rear ends are on the same side of the track.

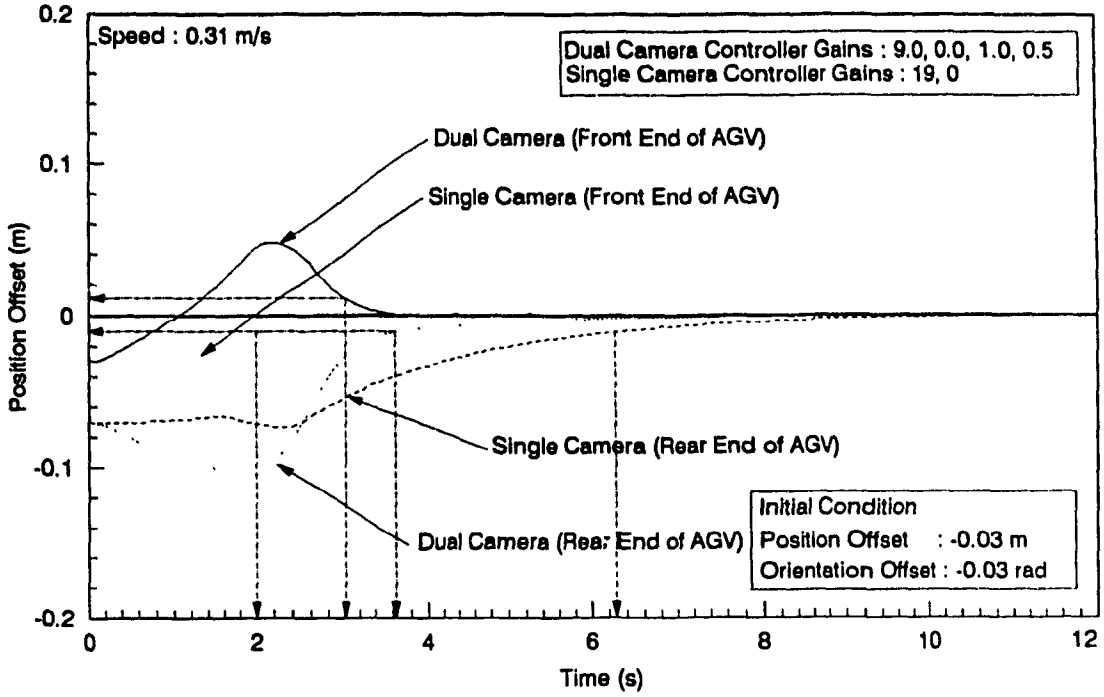

Fig. 7.13a Performance Comparison of Single and Dual Camera Guidance Schemes on a Straight Line Track

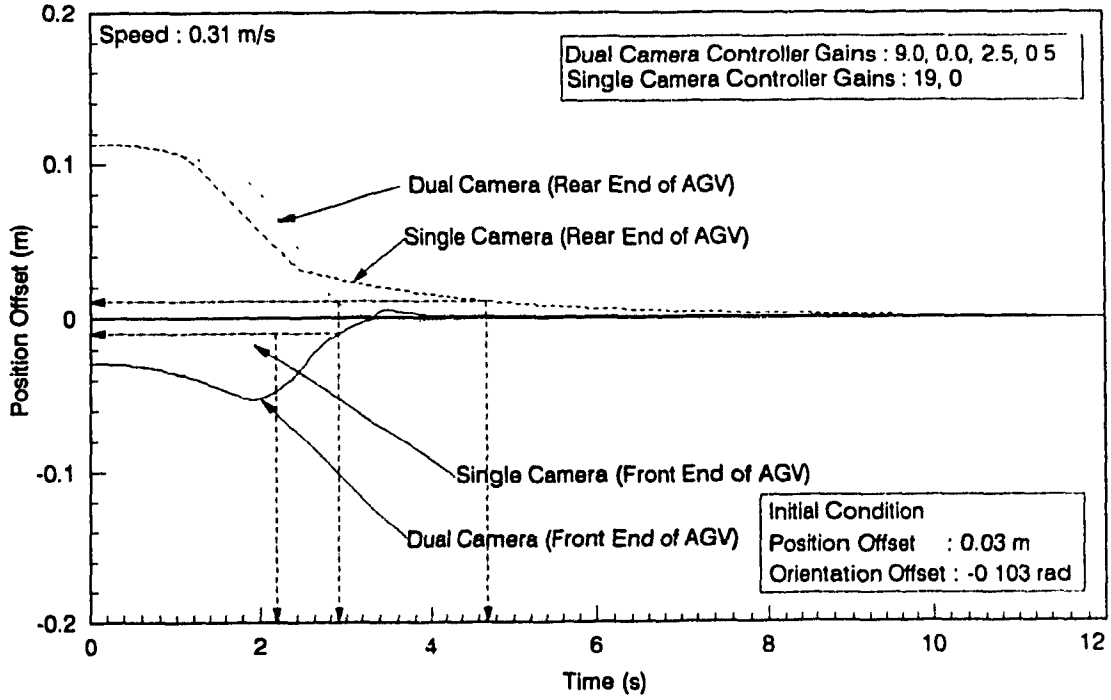

Fig. 7.13b Performance Comparison of Single and Dual Camera Guidance Schemes on a Straight Line Track

This figure shows that the time taken to reduce the front and rear tracking offsets to 0.01 m (5% of the window dimension). In the case of single camera guidance, the rear end offset is reduced in 6.3 s whereas the front offset is reduced in about 2 s. On the contrary, the dual camera reduces front and rear offsets in about 3.0 s and 3.6 s respectively, thereby resulting in a faster reduction in tracking offset for the rear end (44% reduction in time). Similarly, Fig. 7.13b shows the performance improvement with dual camera for the initial condition in which the front and the rear ends of the AGV are on opposite sides of the track. As mentioned in Chapter 5, the value of the gain-G3 is not the same in Figures. 7.13a & 7.13b and hence demonstrates the use of variable gains in the control loop.

A circular track of radius 3.0 m is chosen for simulation. The results of following this circular track are shown in Figs. 7.14 to 7.16. It can be inferred from Fig. 7.14a that the single camera guidance requires 7.8 s and 2.4 s to reduce the position offsets of the rear and the front ends of the AGV to 5% of the camera window dimension (0.01 m). As in the case of straight lines, here also, the guidance scheme using dual cameras requires slightly more time for the front end (3.3 s) and much less time for the rear end (4.6 s). This demonstrates the suitability of the guidance scheme employing dual cameras for circular tracks. Figure. 7.14b is for situation where the front and rear ends are on opposite sides of the track. In this, though the total time taken by both scheme to reduce the position offsets to within 5% of the window dimension is the same, the dual camera exhibits better performance as there are less or no oscillations. Both schemes exhibit steady state errors of 5% and 2.5% respectively for the two cases considered. This is due to the absence of an integral controller. The

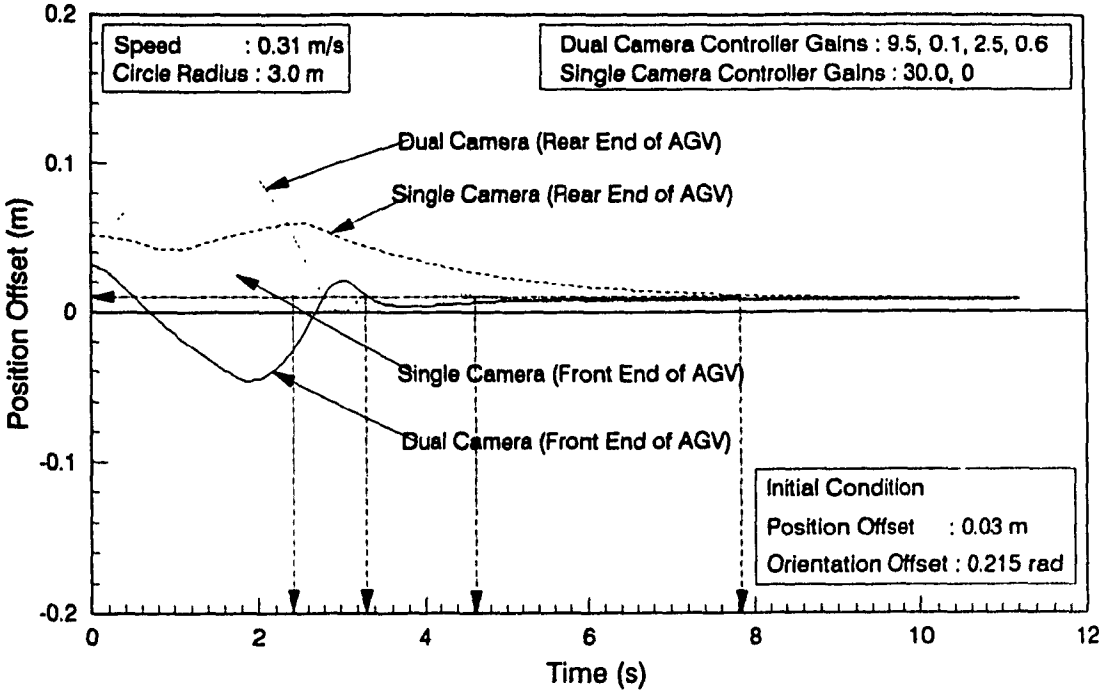

Fig. 7.14a Performance Comparison of Single and Dual Camera Guidance Schemes on a Circular Track

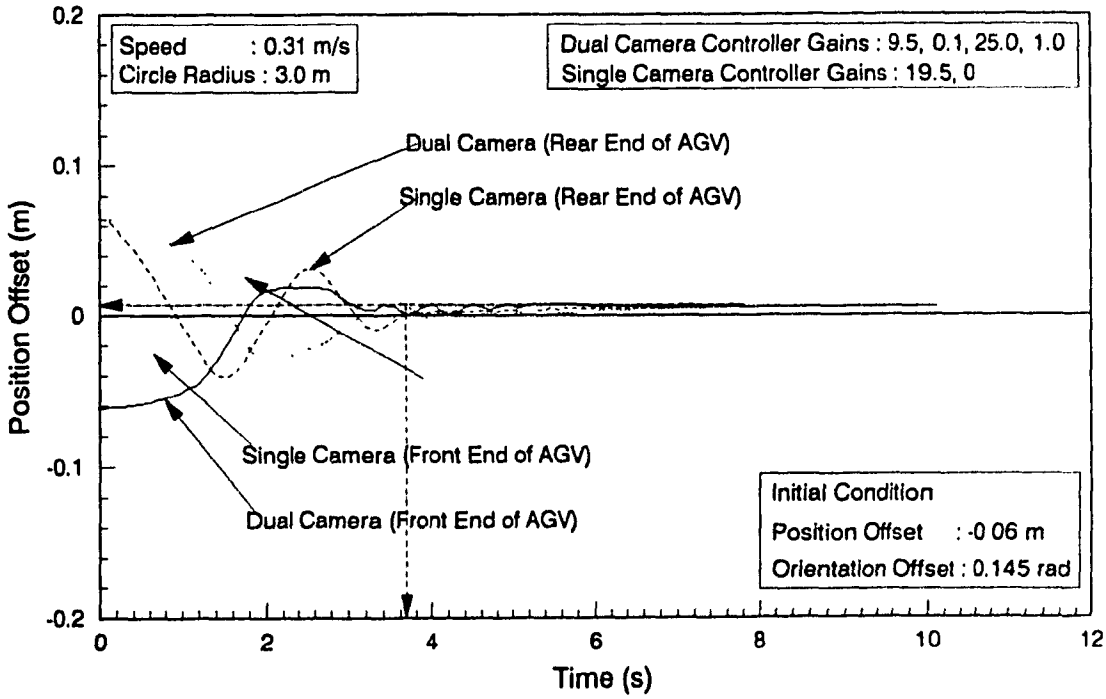

Fig. 7.14b Performance Comparison of Single and Dual Camera Guidance Schemes on a Circular Track

variation of the orientation offset of the vehicle is presented in Figs. 7.15 and 7.16. The dual camera guidance shows marginal improvement in terms of time taken to attain the same orientation for the front and rear ends. Better performance results from the use of dual camera guidance due to the absence of oscillations. These results illustrate the suitability of the guidance scheme based on dual cameras to park the AGV accurately within a short span of time.

7.5 Identification of Track Geometry

7.5.1 Simulation Results

It has been mentioned in section 5.4.1 that there are two schemes, namely, the trapezoidal and the Simpson's parabolic approximations to compute the position coordinates of the vehicle from the wheel speeds information. Simulation results are presented in this section to show the effectiveness of one scheme over the other. For this purpose, the wheel speed information is obtained from the simulation package of Huang [35]. For the scheme on identifying the track geometry, illustrations are provided to show the correctness of the formulations. The input data for these illustrations are obtained from assumed track functions. The identified profile is compared with the assumed function. The parameters of steering control are generated and are provided.

7.5.1.1 Comparison of Integration Approximation Schemes

Figure. 7.17 presents the results of computing the distances travelled by the AGV along the X and Y axes of an inertial frame. The computations are performed using the trapezoidal and Simpson's formulations presented in Chapter 5. The X-distance is the offset distance between the track and the

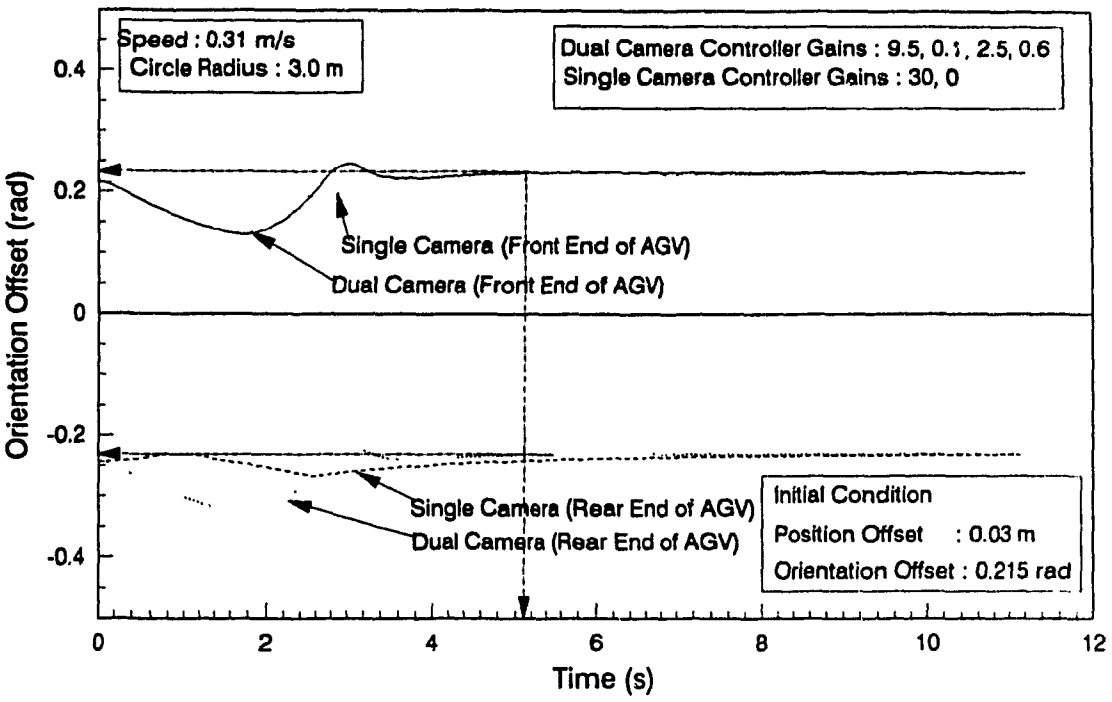

Fig. 7.15 Performance comparison of Single and Dual Camera Guidance on a Circular Track

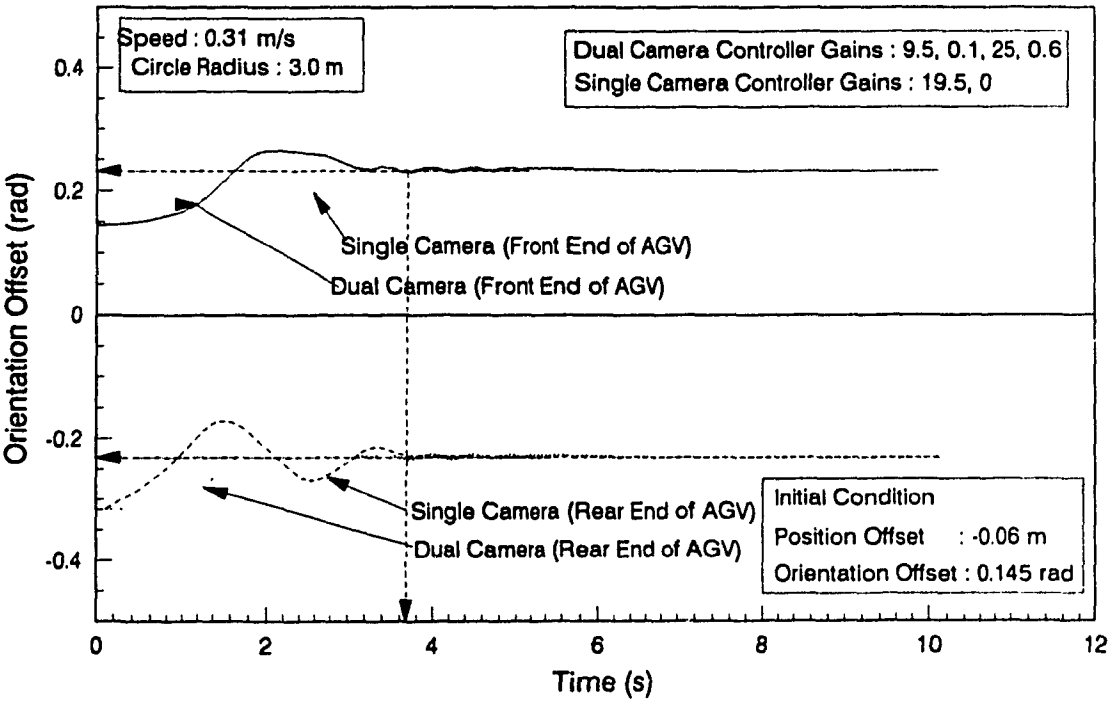

Fig. 7.16 Performance comparison of Single and Dual Camera Guidance on a Circular Track

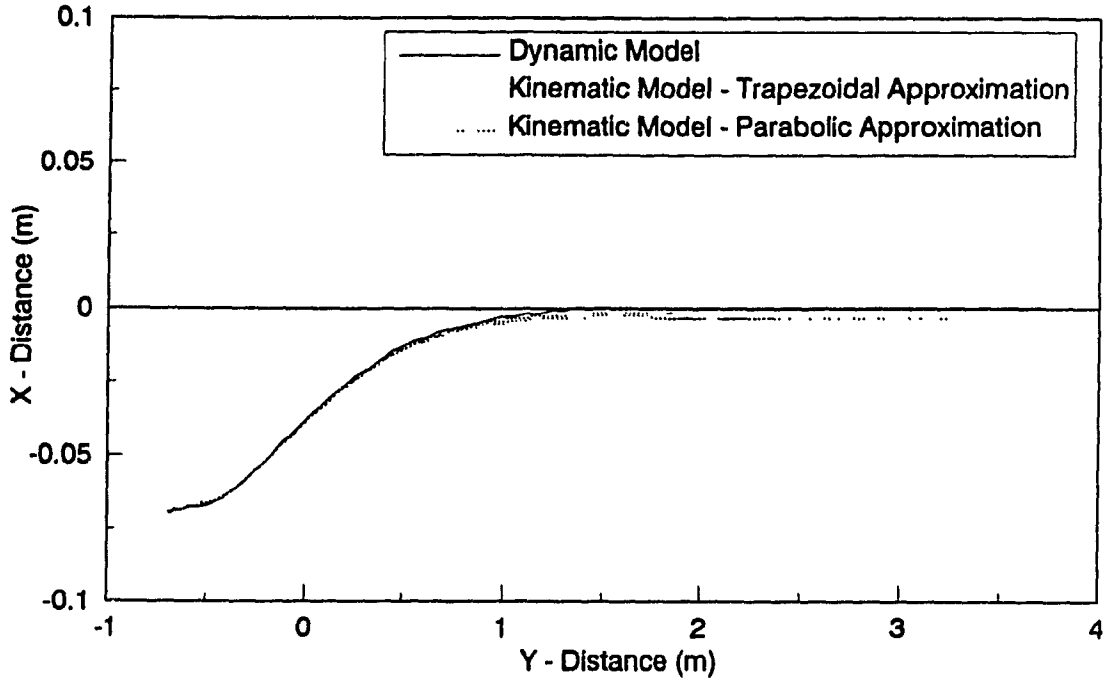

Fig. 7.17 Comparison of Schemes for Integration

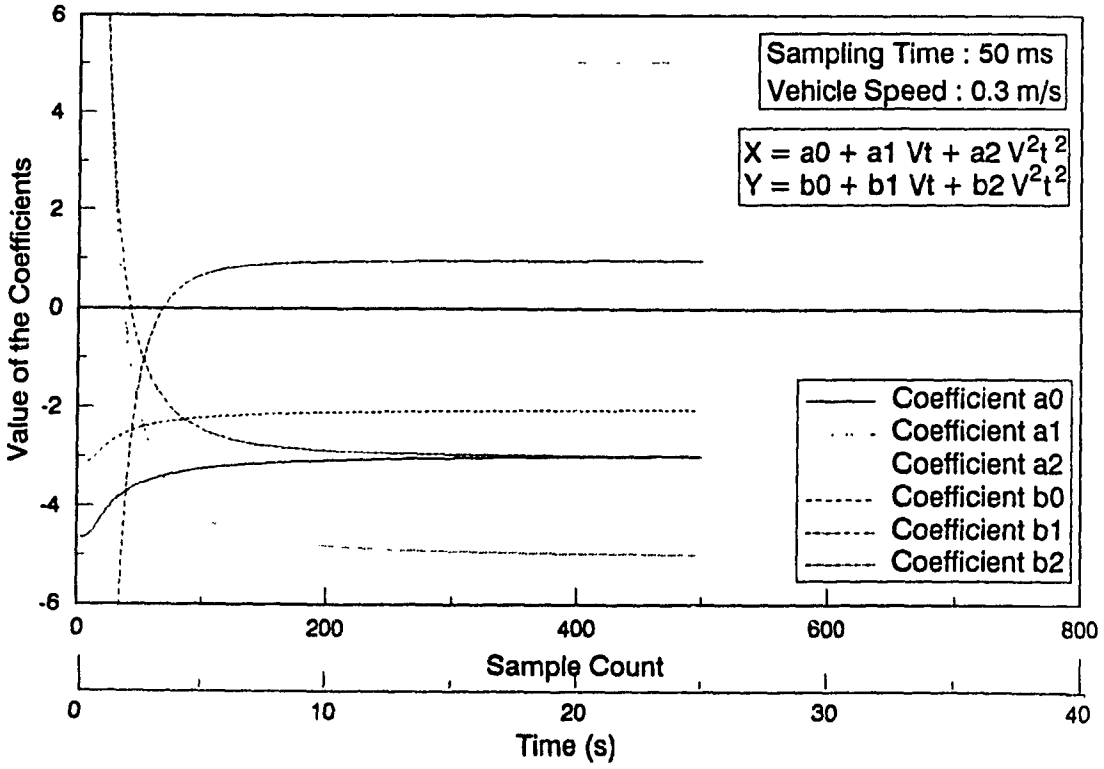

Fig. 7.18 Convergence of Coefficients of a Polynomial Function

geometric center of the AGV. The Y-distance is the total distance travelled along/parallel to the Y-axis of the inertial frame. In this figure the solid lines show the response computed using the simulation package based on a dynamic model of the vehicle [75]. Using equations (5.34) and (5.35), the coordinates of the geometric center of the AGV at various time instants are computed. It can be seen from the figure that after a travel of 1.5 m along the Y-direction, for the simulations based on the dynamic model, the X-distance approaches zero, whereas in the case of computations based on the trapezoidal and parabolic approximation schemes, offsets of 3 mm and 6 mm are noticed. Though this difference is insignificant, the trajectory obtained using the trapezoidal approximation is closer to the dynamic model profile and hence is the preferred choice. This result also indicates that it is not necessary to use a dynamic model of the vehicle to describe the path of the geometric center and a kinematic model is sufficient.

7.5.1.2 Identifying Polynomial Profiles

A polynomial function of the following form is chosen to provide the X and Y position values as a function of the total time elapsed and the vehicle speed.

$$X = a_0 + a_1 V t + a_2 V^2 t^2$$

$$Y = b_0 + b_1 V t + b_2 V^2 t^2$$

The coefficients are chosen to be $a_0 = -3.0$; $a_1 = -5.0$; $a_2 = 5.0$; $b_0 = -2.0$; $b_1 = -3.0$; $b_2 = 1.0$. The sampling time and the vehicle speed are chosen as 50 ms and 0.3 m/s respectively. The convergence of the coefficients (a's and b's) are shown in Fig. 7.18. Referring to this figure, it can be seen that, the magnitudes of all the coefficients with the

exception of a_0 and b_0 are large for the first 50 samples. This is due to the fact that the data available during this stage are not sufficiently far apart to describe the geometry. Very close convergence to the actual value is observed at around 200 samples or 10 seconds. Total convergence is observed after 400 samples, i.e. 20 seconds. This is equivalent to a distance travel of 6 m along the polynomial profile. The deviation between the estimated and the actual value of the coefficients are 2.6%, 1%, 0.1%, 2.5%, 1%, and 0.1% for a_0, a_1, a_2, b_0, b_1, and b_2 respectively.

7.5.1.3 Polynomial and Straight Line Forms for Straight Line Tracks

It has been mentioned in section 5.4.2.4 that the polynomial approximation can be extended to compute the coefficients of a straight line track function without an explicit formulation. This section presents the results of convergence using the polynomial approximation and the straight line approximation (y=mx+c form). The results of convergence of the coefficients m and c of the straight line track are presented in Figs. 7.19a & 7.19b. The assumed equation is of the form $y = 1.333\ x + 2.0$. From the results it can be seen that the straight line function provides faster convergence than the polynomial form. However, the initial values of the coefficients obtained are very large in the former case. Hence during the beginning stages of the identification scheme upto a distance travel of 1.5 m (which is 100 samples or 5 seconds in the present case), it is advisable to use the polynomial formulation and then switch to the straight line formulation thereafter.

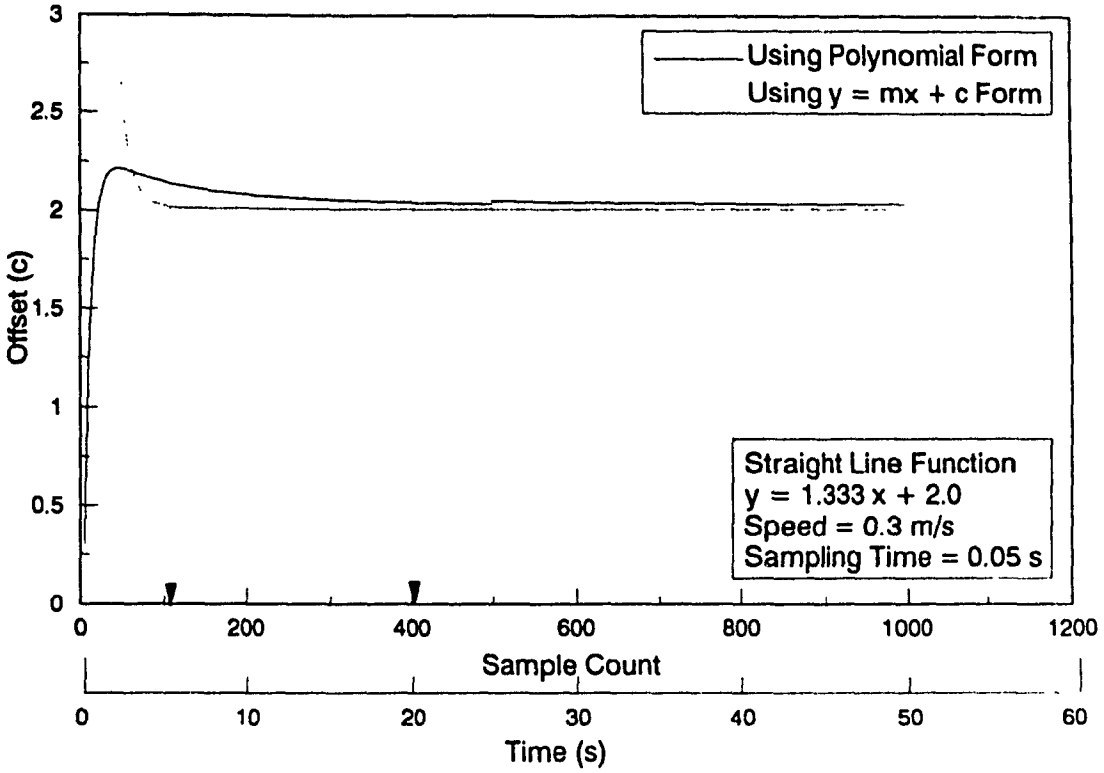

Fig. 7.19a Comparison of Coefficient Convergence for a Straight Line Track

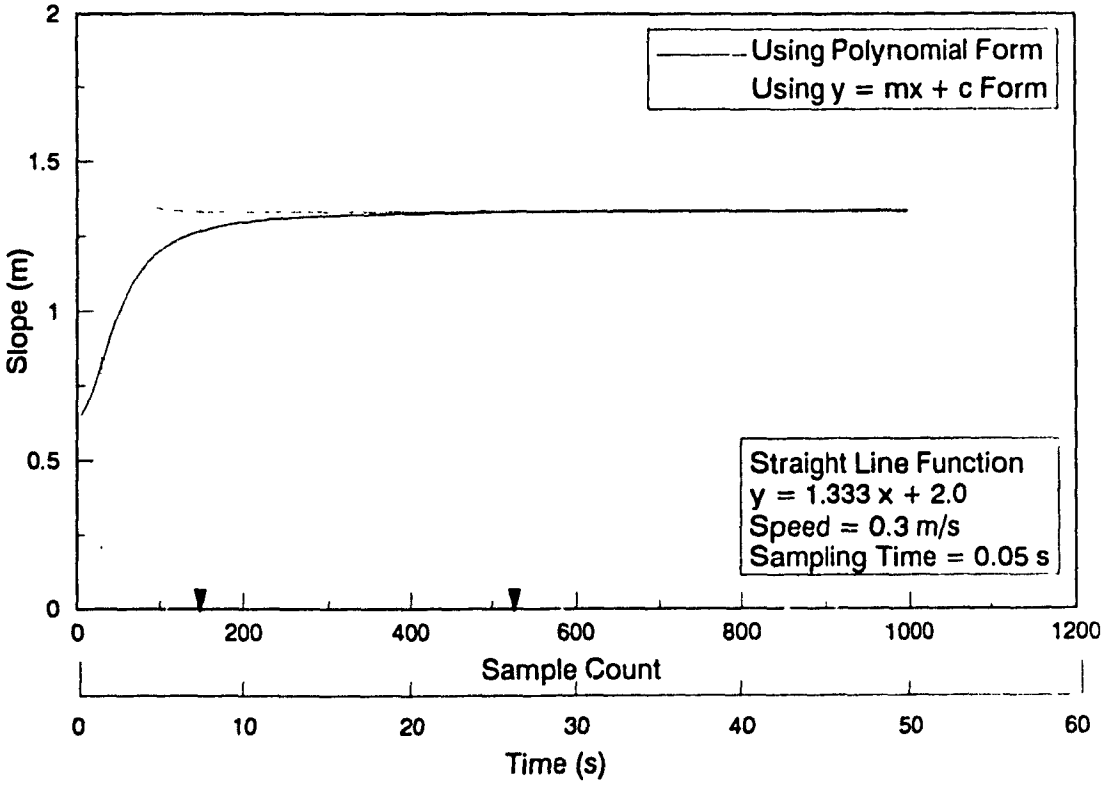

Fig. 7.19b Comparison of Coefficient Convergence for a Straight Line Track

7.5.1.4 Identification of Conic Profiles - Circular Track Function

A circular function of the form $3.0^2 = X^2 + Y^2$ is used as a reference to generate the X, Y coordinates and the orientation θ. Figures. 7.20a and 7.20b illustrate the convergence of the coefficients (a's and b's) and the parameters of the circle (radius-R, x and y coordinates of the center). From these figures, it can inferred that the coefficients converged after 600 samples or after covering one half of the circle (of radius 3 m). The value of the circle parameters are 0.01 m, 0.01 m and 2.995 m respectively and is a 1% deviation from the actual values. We can also infer from the figures that the circle parameters have a meaningful value after the initial 400 samples, i.e. after one third of the circle is traversed.

7.5.1.5 Identification of Conic Profile - Elliptic Track Function

An elliptic function with the parameters a and b as 1.5 and 0.75 with the coordinates of the center as $x_0=0$, and $y_0=0$ is chosen as the reference input. The convergence of the coefficients a's and b's of the generic conic function are shown in Fig. 7.21. As in the case of circular track, here also convergence is noticed only after 400 samples.

7.5.1.6 Influence of Sampling Time and Vehicle Speed on Convergence

In section 5.4.2.1, discussions are presented on the factors that affect the rate of convergence of the coefficients of the track function. In this section, simulations results are presented on the effect of two of the various factors discussed. Figure. 7.22 shows the convergence for the one of the coefficients (slope,m) of a straight line function for three sampling intervals. The minimum sampling time considered here is the average sampling

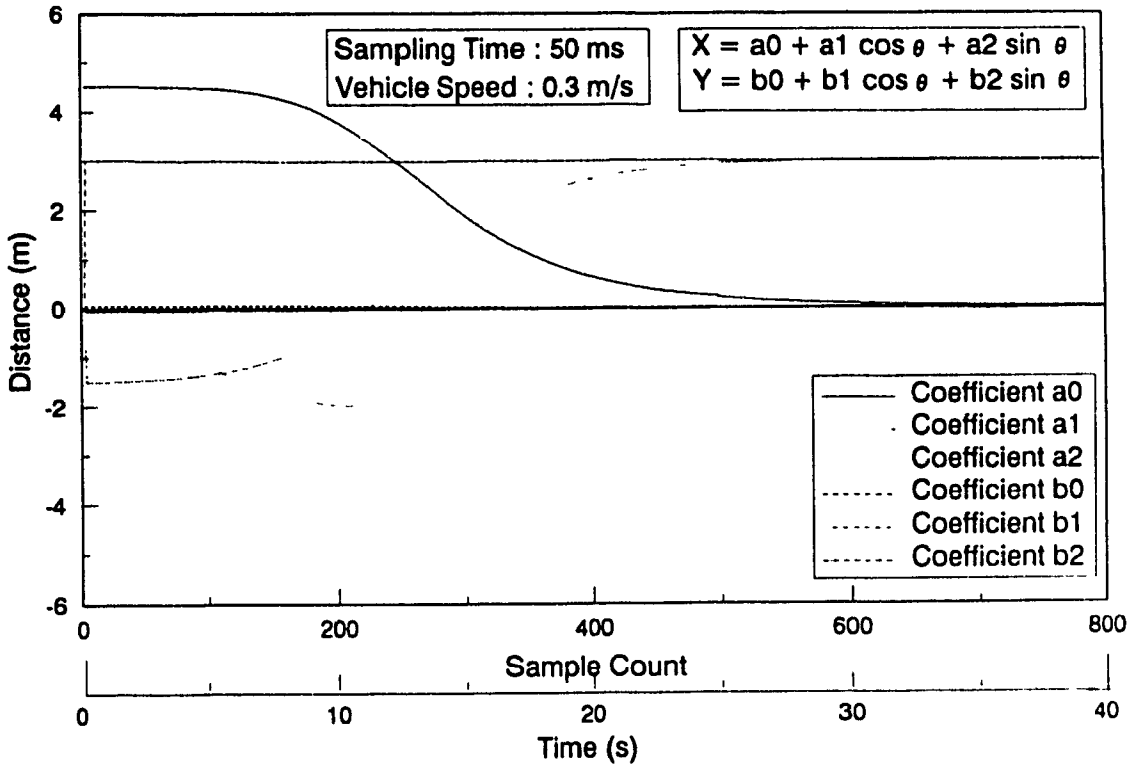

Fig. 7.20a Convergence of Coefficients of Conic Profile for a Circular Track

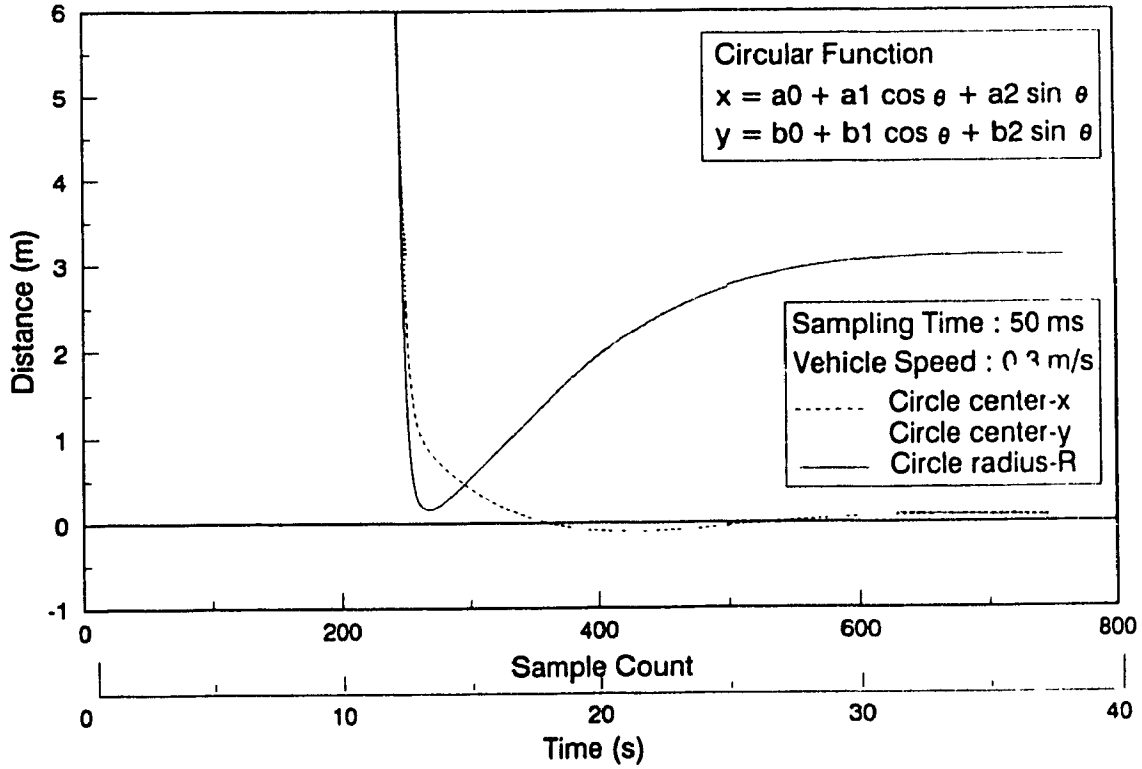

Fig. 7.20b Convergence of Circular Function Parameters using Conic Profile

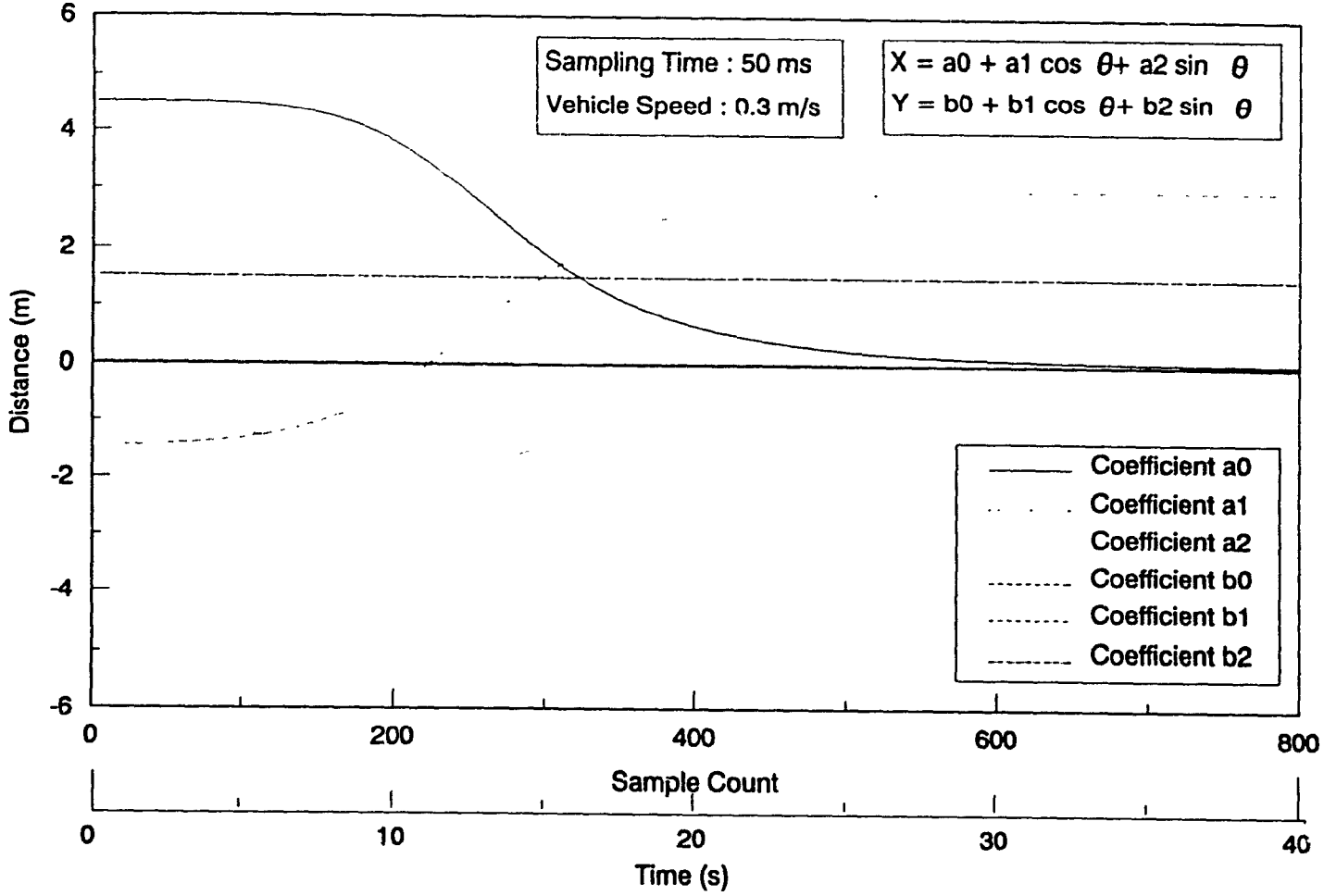

Fig. 7.21 Convergence of Coefficients of an Elliptic Function

time of the guidance system of the AGV which is approximately 50 ms. This value is chosen as the sampling time of the prototype AGV varies from 40 ms to 60 ms. From Fig. 7.22 it can be summarized that the increase in the sampling time (at a particular speed) for the identification scheme decreases the number of samples required for convergence at the expense of increase in the total time for convergence. The convergence time for sampling times 50 ms, 100 ms and 150 ms, are 7 s, 7.5 s and 8.25 s respectively. Hence it can be concluded that the increase in the sampling time of the identification scheme increases the convergence time while providing a reduction in computer memory required for storage due to less data required for convergence.

Figure. 7.23 shows the effect of vehicle speed on the convergence presented for a parameter of a straight line track. This illustrates that at higher vehicle speeds at a particular sampling time, the convergence takes place faster. This is due to the fact that the data are obtained from a larger section of the track profile within the same interval compared to slow speeds. The time taken for convergence at 0.3 m/s, 0.6 m/s and 0.9 m/s are 125 s, 70 s and 45 s respectively. From this it can be concluded that doubling the speed reduces the convergence time by 40% and tripling the speed reduces the time by 60%. Hence, a linear relation exists between the vehicle speed and the convergence time at a particular sampling time.

7.5.2 Experimental Results

7.5.2.1 Calibration of Software Data Acquisition Channels

The scheme to identify the track geometry uses the actual value of the wheel speeds to evaluate the position and the orientation of the vehicle in inertial coordinates. This actual wheel speed information can be obtained

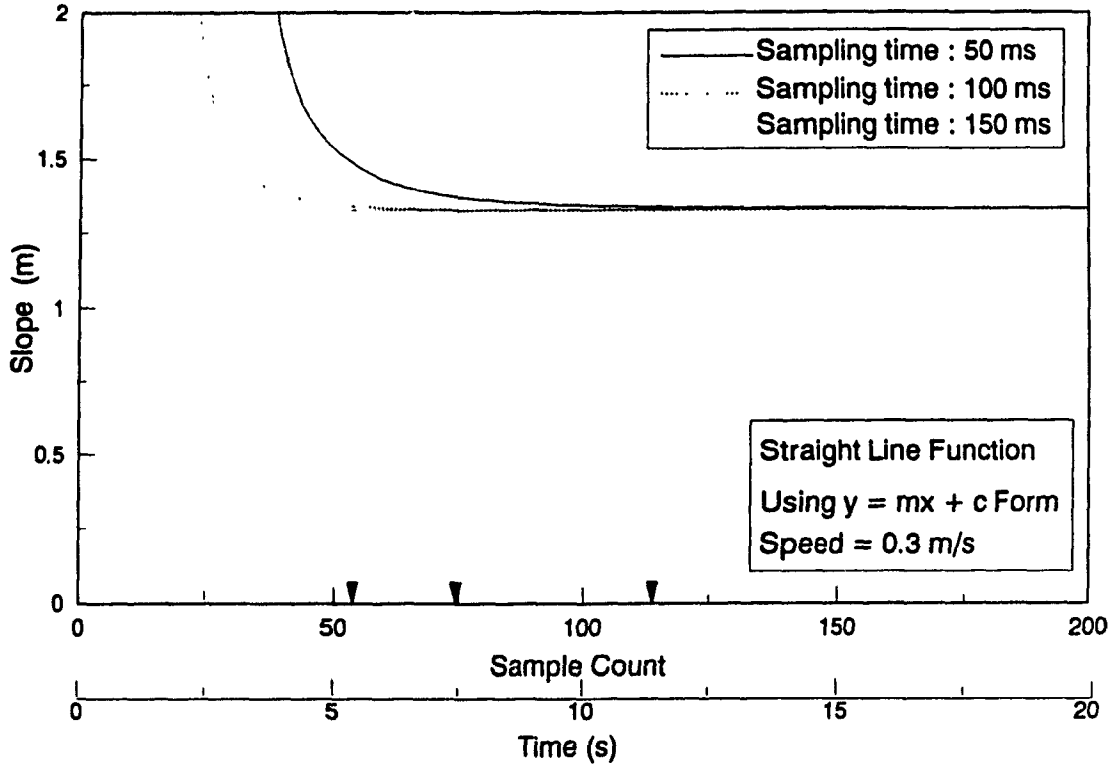

Fig. 7.22 Effect of Sampling Time on Convergence Rate for Straight Line

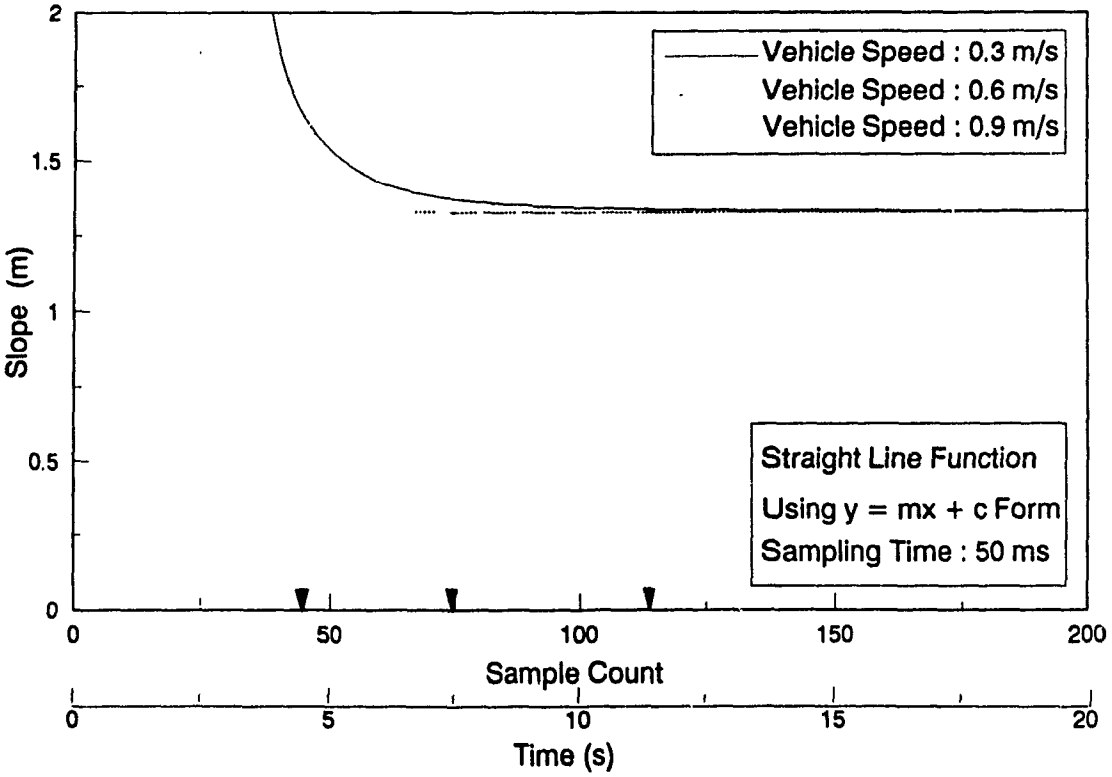

Fig. 7.23 Effect of Vehicle Speed on Convergence Rate for Straight Line

from the LM628 motion controller chip. The following discussions are on the accuracy with which the actual wheel speed data can be obtained. Subsequently a method to improve the reading accuracy of the actual wheel speed is presented.

The actual velocity information from the motion controller is 16 bits long and this corresponds to a resolution of ± 4.2 rpm for the CONCIC-II AGV. This is the accuracy with which the actual wheel speed data can be obtained from the LM628 chip. In order to obtain the actual wheel speed with better accuracy the following scheme is adopted. In this scheme, the position count (number of pulses counted) information from the LM628 is used. The position count registers are 32 bits long. Then the cycle time information from the 8254 timer (which is used by the data acquisition system) is used to compute the velocity. The simple slope method of computing the velocity (derivative of the position) is employed. This approach is employed since the position counts and the cycle time information are available every 40 ms and this is sufficiently small to compute the velocity accurately.

Figures. 7.24a & 7.24b present the desired wheel velocity and the wheel velocity read from the LM628. It does gives the actual wheel velocity computed using the scheme described above for the left and right wheels respectively. The deviation between the actual wheel speed and the desired speed is ± 0.5 rpm. Other information obtained from this figure are, during speed build up an overshoot of 1% exists, the time taken to reach the desired acceleration of 0.024 m/s^2 is 1.95 seconds and the actual wheel speed does not remain constant during steady state.

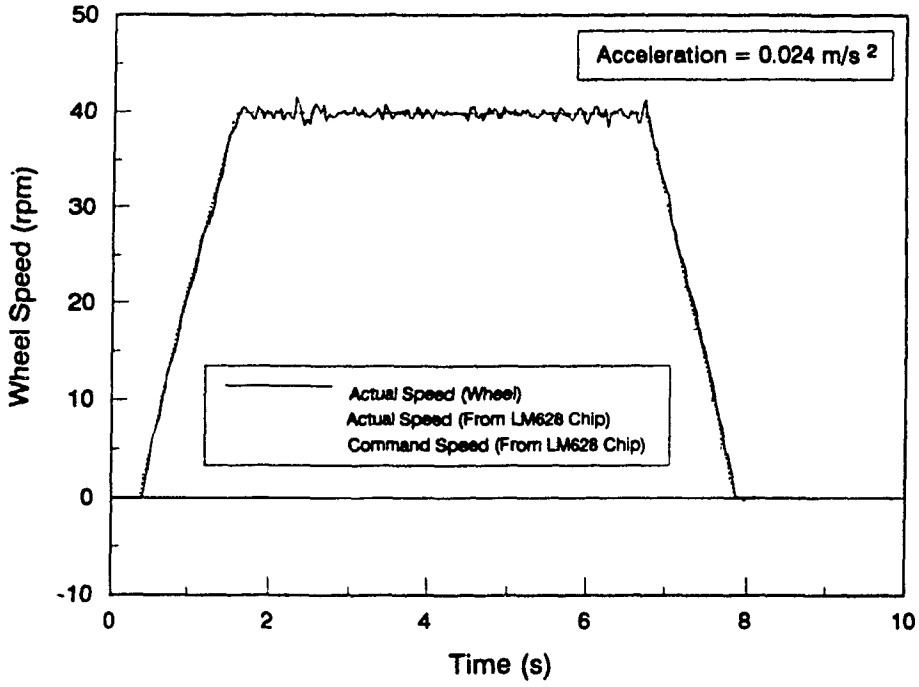

Fig. 7.24a Comparison of Wheel Speeds for Wheel-A

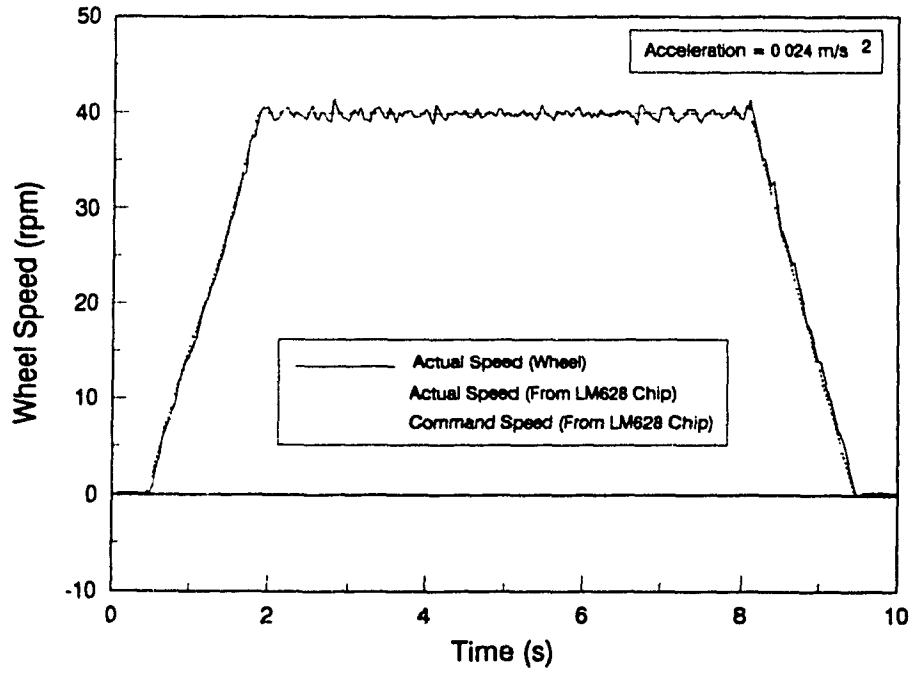

Fig. 7.24b Comparison of Wheel Speeds for Wheel-B

7.5.2.2 Tests for Ability of the Vehicle to Travel Straight

This test is necessary to establish whether the AGV travels along a straight line when the two wheels are commanded to run at the same velocity. This is also to ascertain the correction factor to be added to the actual wheel speeds using the scheme described above. This correction factor is to make sure the trajectory of the AGV computed from the actual wheel speeds using the schemes described in section 5.4.1 is the same as the actual trajectory followed by the AGV on the floor obtained by actual measurements.

The AGV was positioned on a straight line track in such a manner that at least the orientation offset is equal to zero. The initial offset distance of the longitudinal axis of the vehicle from the track was measured to be 0.020 m. The two driving wheels are commanded to run at the same velocity at a given time. The camera mode is employed for this purpose. In this mode the gains for the steering control are chosen to be zero (G1 = G2 = G3 = 0). This is to make sure that the steering angle is zero and there are no additional velocity inputs to the servo loops from the camera feedback loop.

After the AGV had reached a reasonable distance, the vehicle was commanded to make a normal stop following the predefined deceleration profile. From measurements it was observed that the vehicle was travelling straight. The actual profile traced by the geometric center of the AGV was computed based on the kinematics of the vehicle and the computed value of the actual wheel speeds. The results are shown in Fig. 7.25. From this it can be seen that the computed profile bends to the left. The offset of the final position from the starting position is 0.07 m. Since the computed path of the vehicle goes to the left, a compensation (ω_2 = 1.0018 ω_2, an empirical

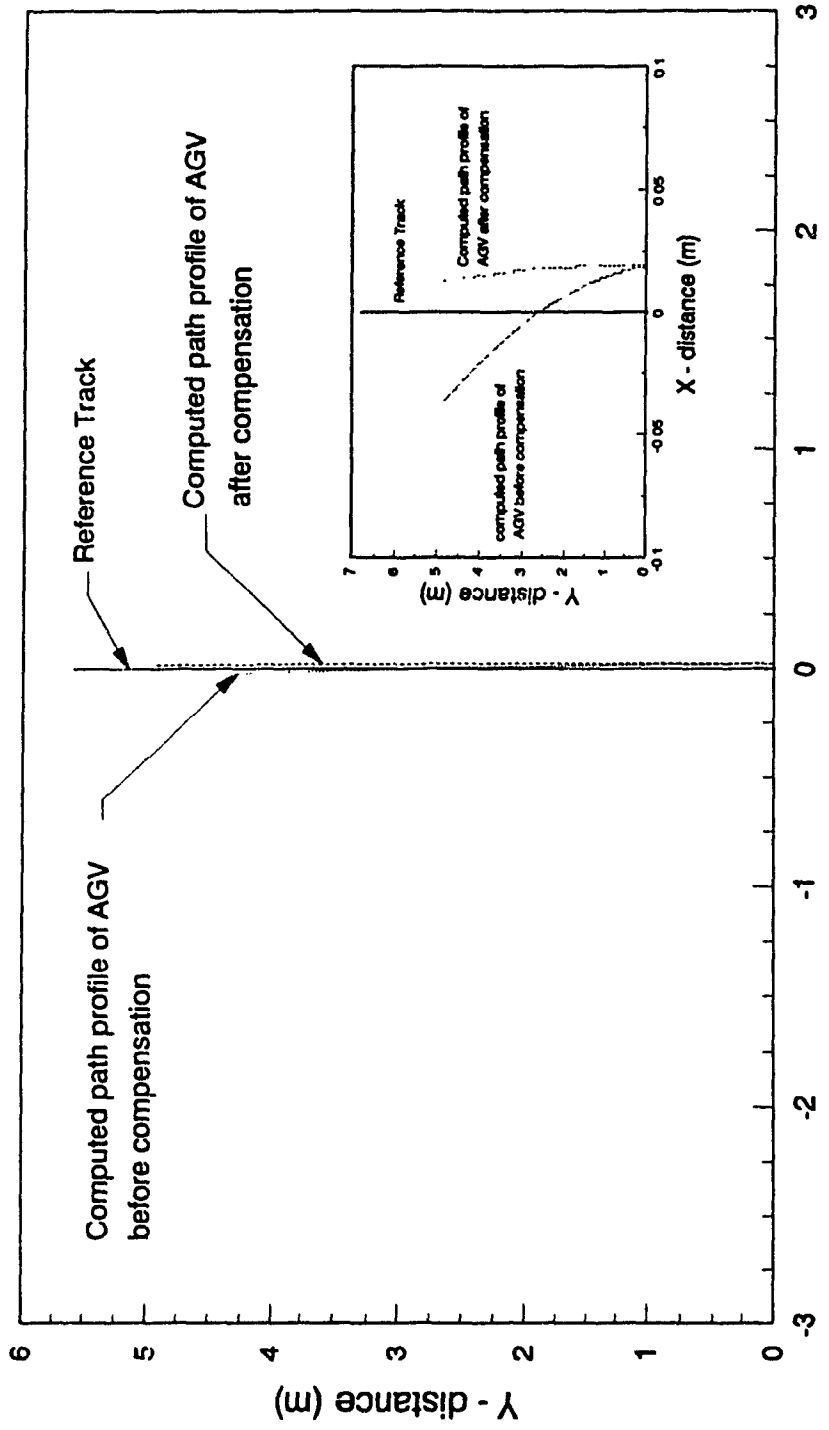

Fig. 7.25 Path Traced by the AGV for the Same Speed Command to Wheels

formula) is provided to the left wheel to increase the magnitude of the actual wheel speed. This makes the computed path almost a straight line matching the path on the floor.

7.5.2.3 Construction of Profile of the Track and the Path of the AGV

The profile of the track and the path traced by the geometric center of the AGV were constructed. This result is also presented in section 7.3.3. In this section, results are complied for various speeds and are presented in Figs. 7.26a and 7.26b. Though the actual track was straight, due to computational errors in estimating the position offset (ε_d), the constructed profile of the track deviates from the actual profile. The deviation is 0.6% for a track length of 9 m and can be regarded as negligible. This deviation is a function of the vehicle speed and is observed to be 0.03 m error for every 0.16 m/s change in the vehicle speed. This error is due to the resolution with which the position and the orientation offsets are computed, errors in computing the actual wheel speeds and errors introduced due to vibrations in the camera mounting, lighting and floor conditions. The track offset value obtained at various speeds were more or less the same with an overall error of 8% from the actual value.

7.5.2.4 Identifying Coefficients of a Straight Line Profile

This section presents the results of computing the coefficients of a straight line function using the experimental data while following a straight line track. It is assumed that initially the track is orientated at an angle of 0.6 rad in the inertial frame. This is introduced in order to obtain at least one non-zero coefficient for the track function, i.e. $m \neq 0$ in the equation $y = mx + c$. The results of computing m and c are provided in

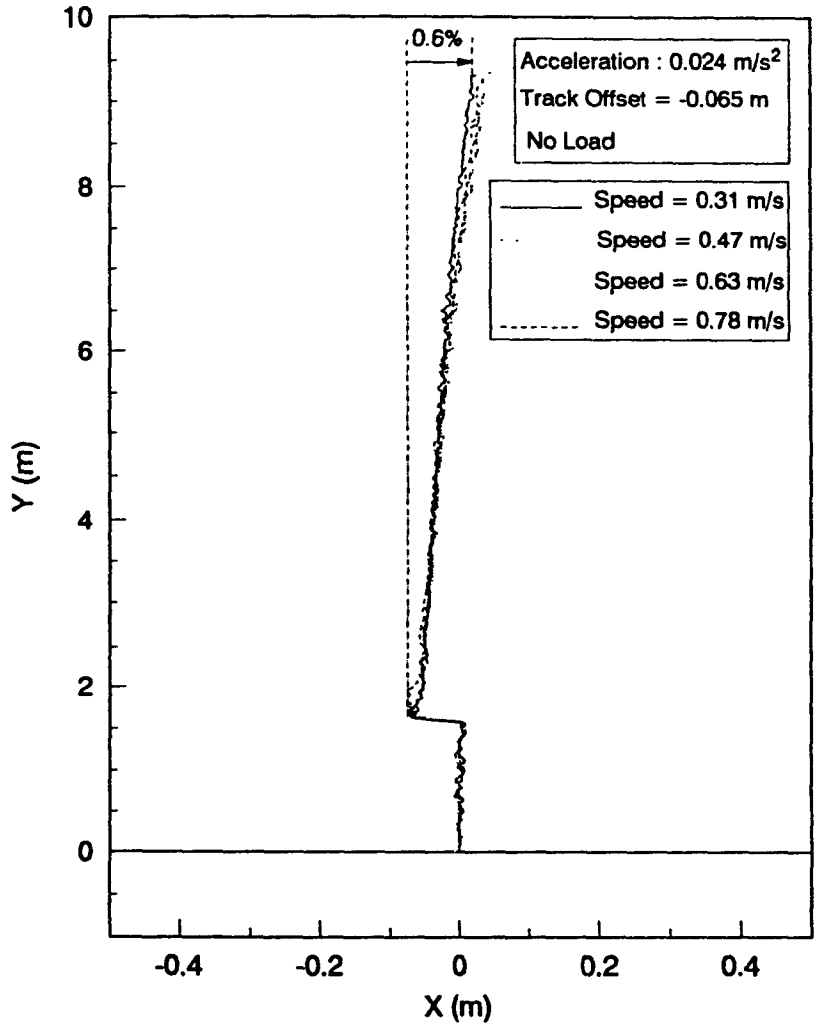

Fig. 7.26a Reconstructed Profile of a Straight Line Track with Offset

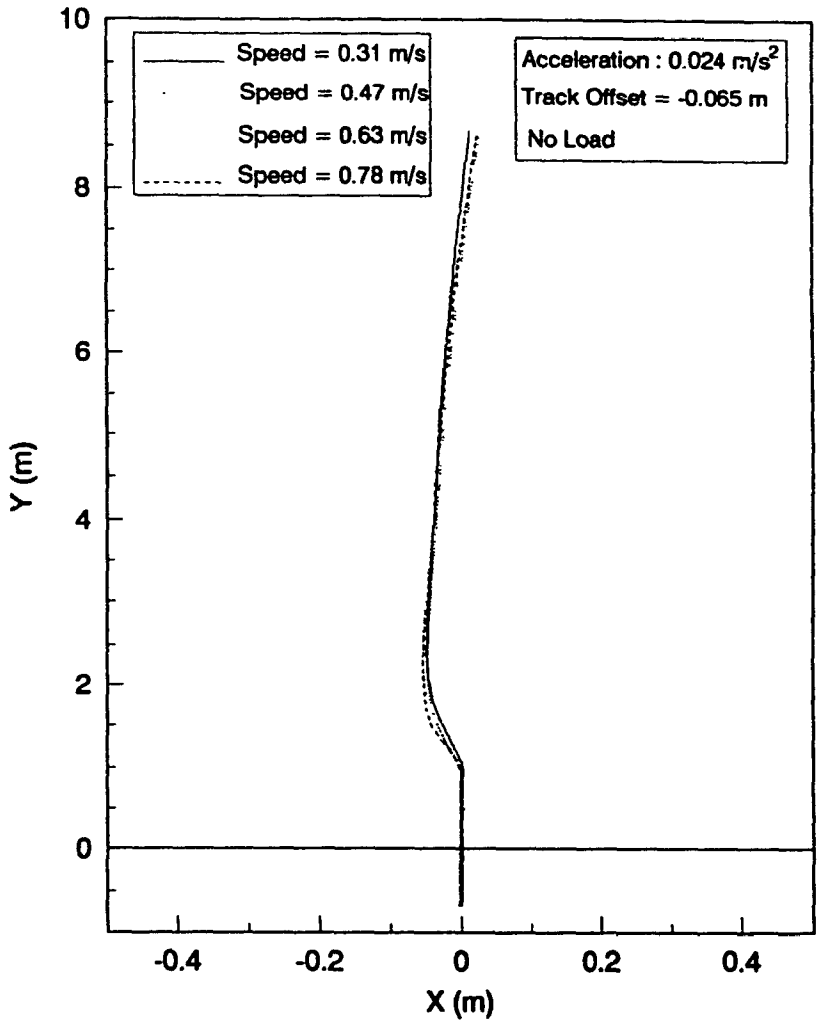

Fig. 7.26b Profile of the Path of geometric center of AGV

Figs. 7.27a & 7.27b. The error in computing m is 11% and the coefficient c has an error of 8 mm as against the input value of zero. The coefficients converged within 200 samples which is equivalent to a distance travel of 2.29 m.

7.5.2.5 Identifying the Coefficients of a Conic Profile - Circular Function

The results of track profile identification while following a circular track profile are presented in Figs. 7.28, 7.29a, 7.29b for a vehicle speed 0.63 m/s. From Fig. 7.28 it can be seen that the computed profile of the track resembles the actual track on the floor with an error of 5.5% (17 cm error in 295 cm). This figure also shows the computed track profile when the vehicle made more than one full turn. This is to show the effect of accumulated error. The computed path for the second turn is slightly inside and the deviation from the first turn is insignificant.

The convergence of the coefficients of the conic profile and the parameters of the circle are presented in Figs. 7.29a and 7.29b. Convergence is attained after 600 samples (after tracing one half of the circle of radius 2.95 m). The magnitudes of the parameters of the circle before 500 samples are very large and hence are not shown in Fig. 7.29b. The radius of the circle from the identification scheme is 3.2 (9% error) after 800 samples and 3.12 after 900 samples (5.5% error). Recalling the discussions presented for the simulations results in section 7.5.1, the convergence performance observed for the experimental results are the same as those in the simulation indicating that the effect of noise in the actual data from the experimental AGV are not appreciable and does not degrade the performance of the identification scheme.

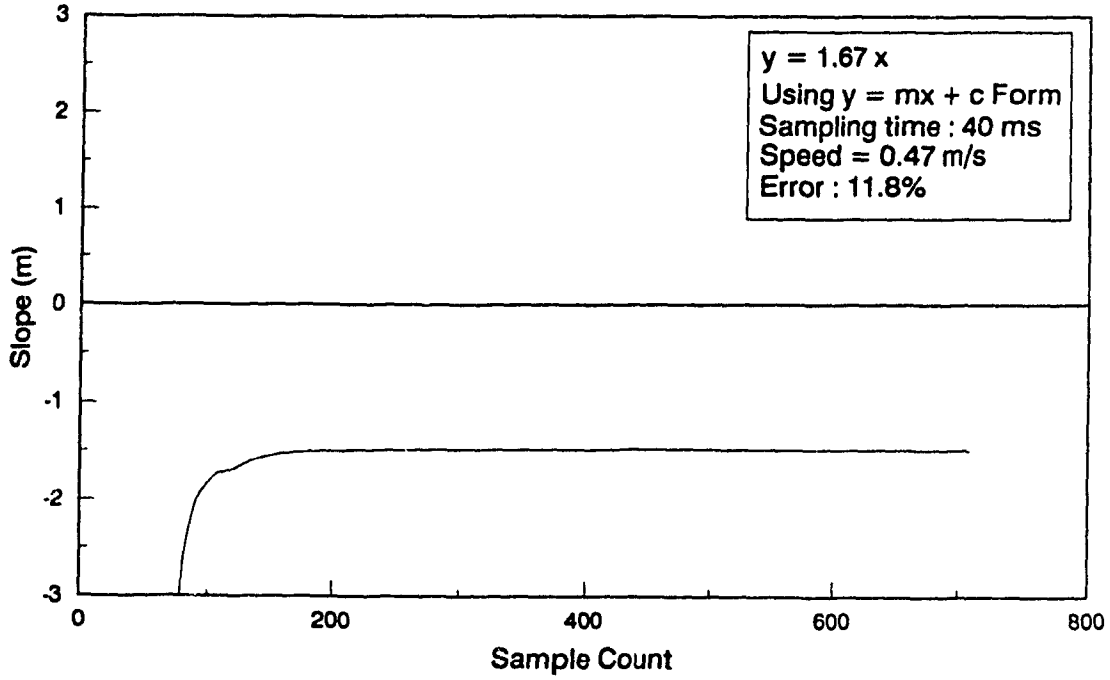

Fig. 7.27a Convergence of Coefficient of a Straight Line Track

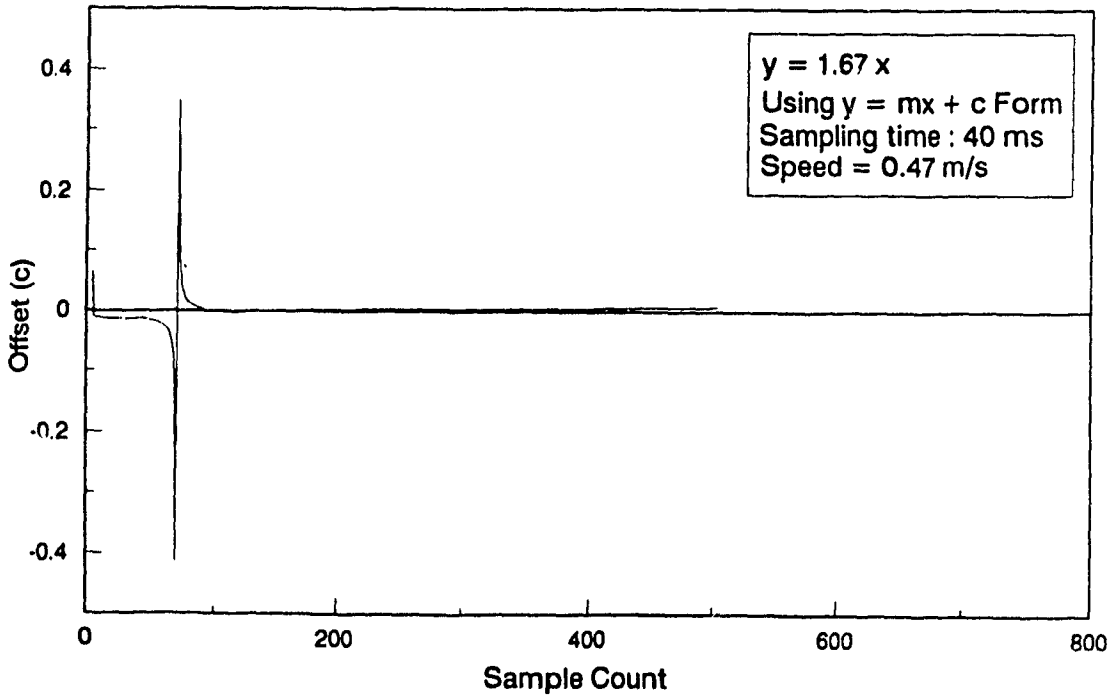

Fig. 7.27b Convergence of Coefficient of a Straight Line Track

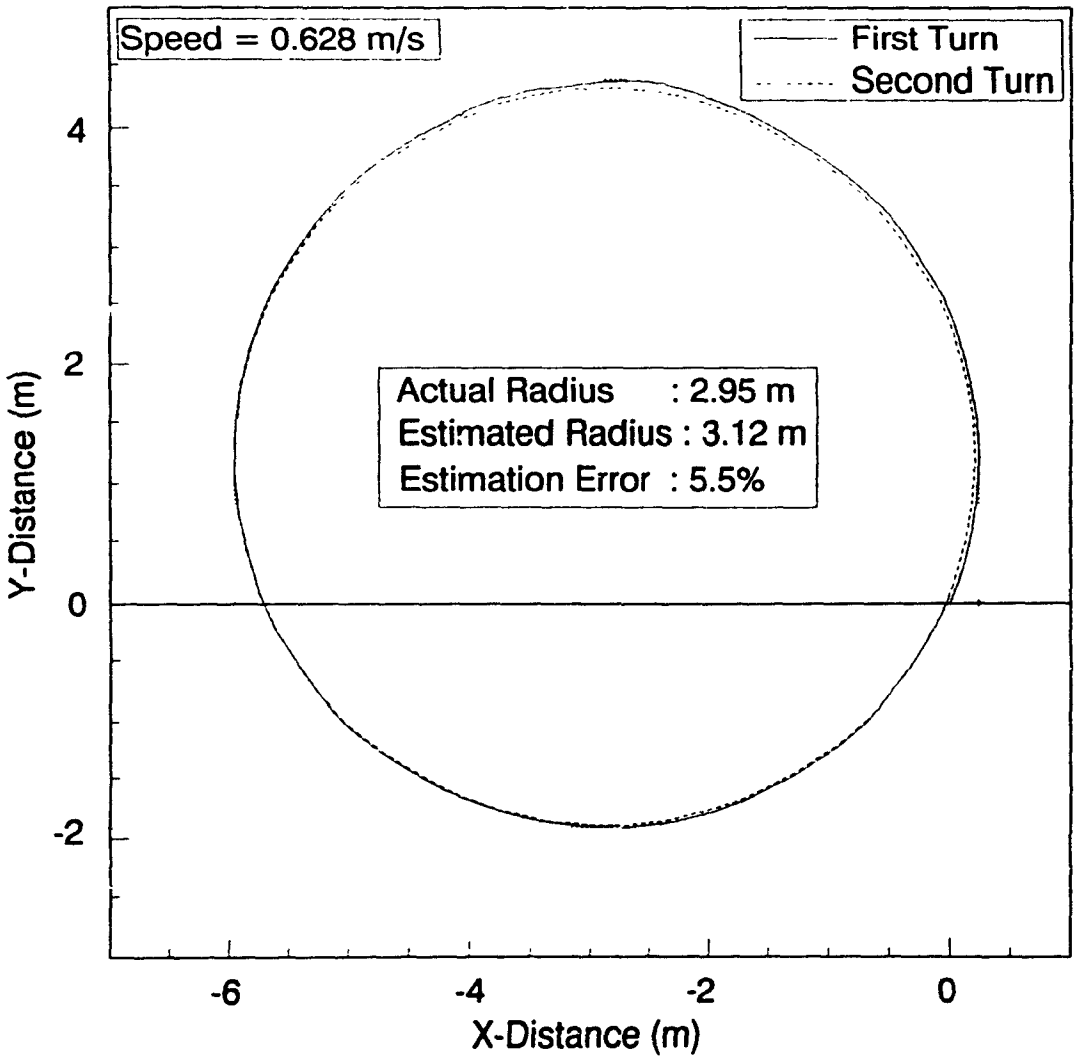

Fig. 7.28 Computed Profile of a Circular Track Based on Sensor Data

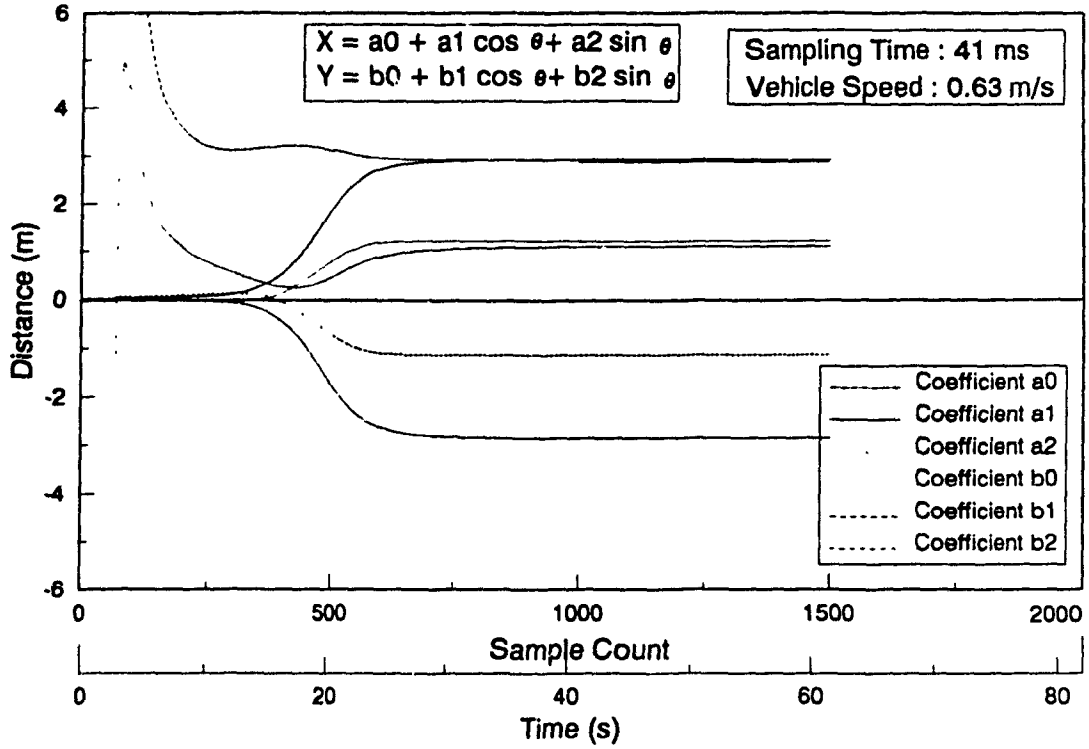

Fig. 7.29a Convergence of Coefficients of a Circular Track

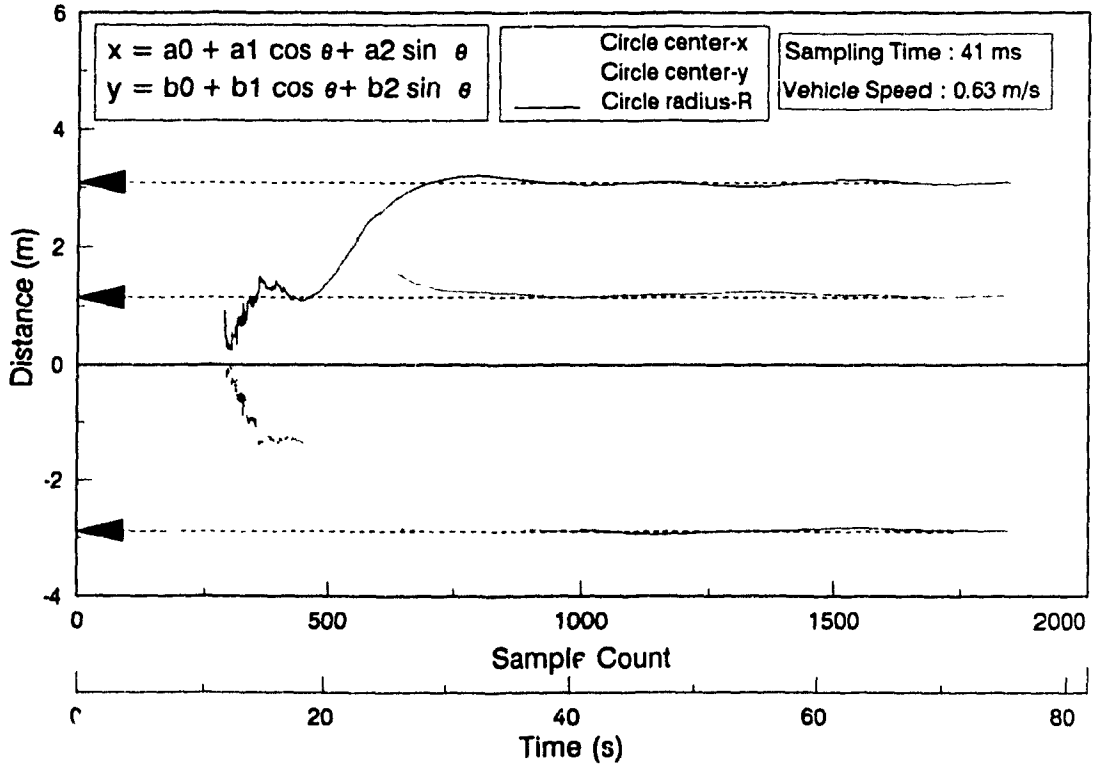

Fig. 7.29b Convergence of Parameters of a Circular Track

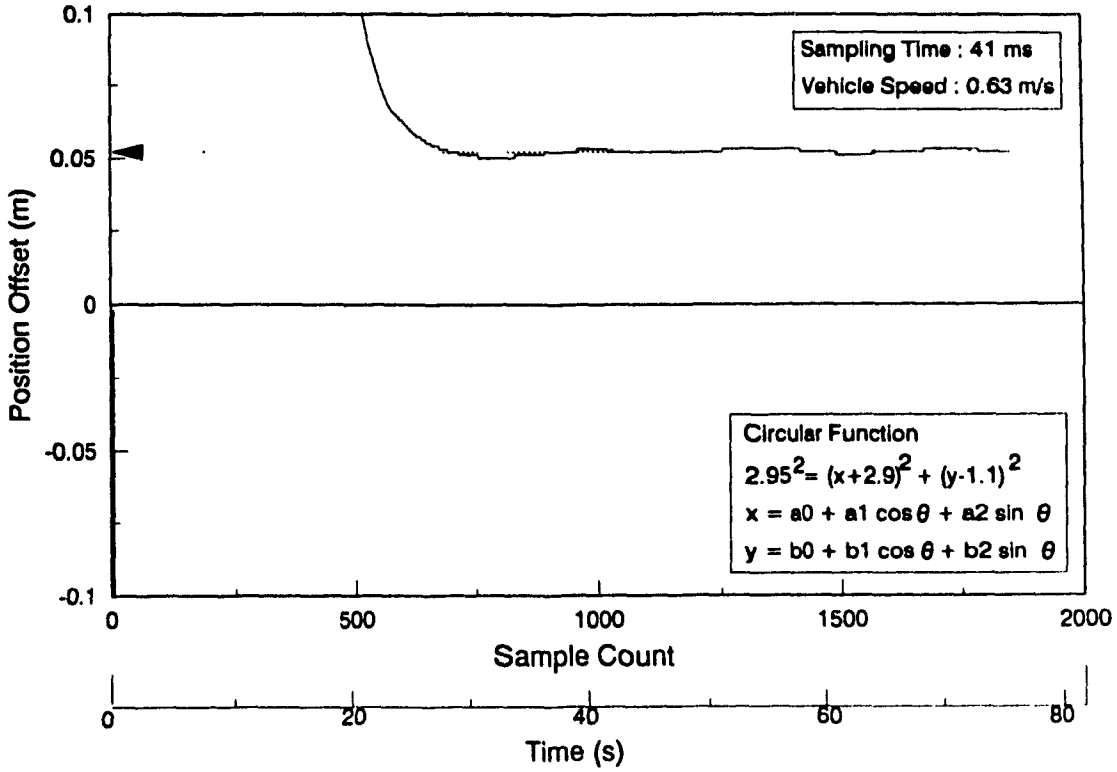

Fig. 7.30a Convergence of Position Offset for Circular Track

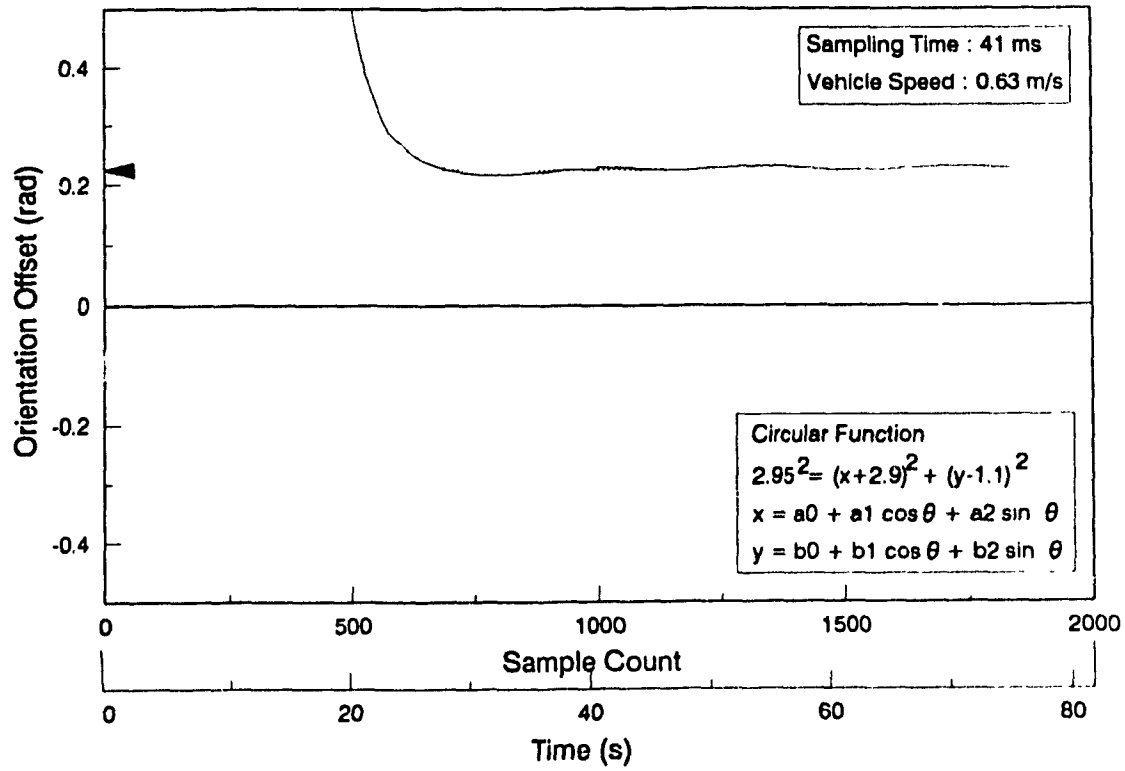

Fig. 7.30b Convergence of Orientation Offset for Circular Track

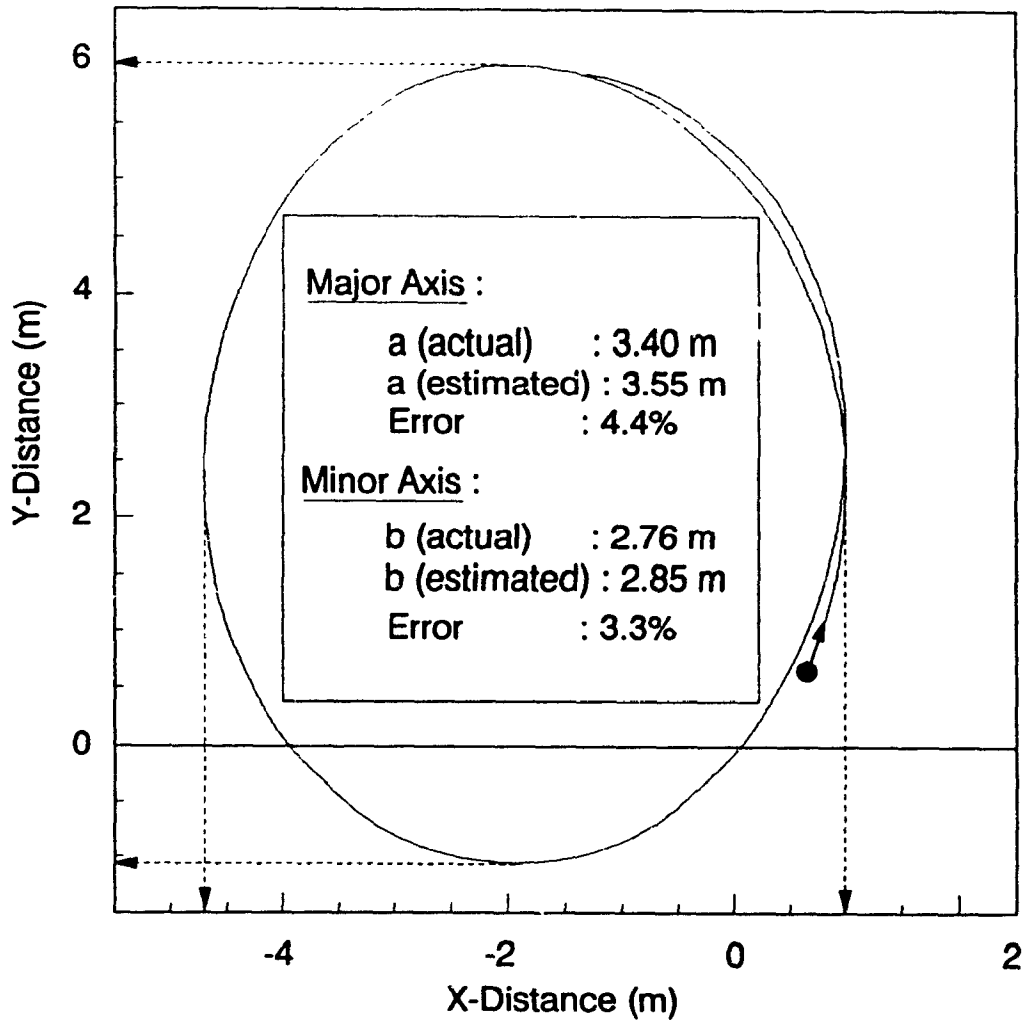

Fig. 7.31 Computed Profile of an Eliiptic Track

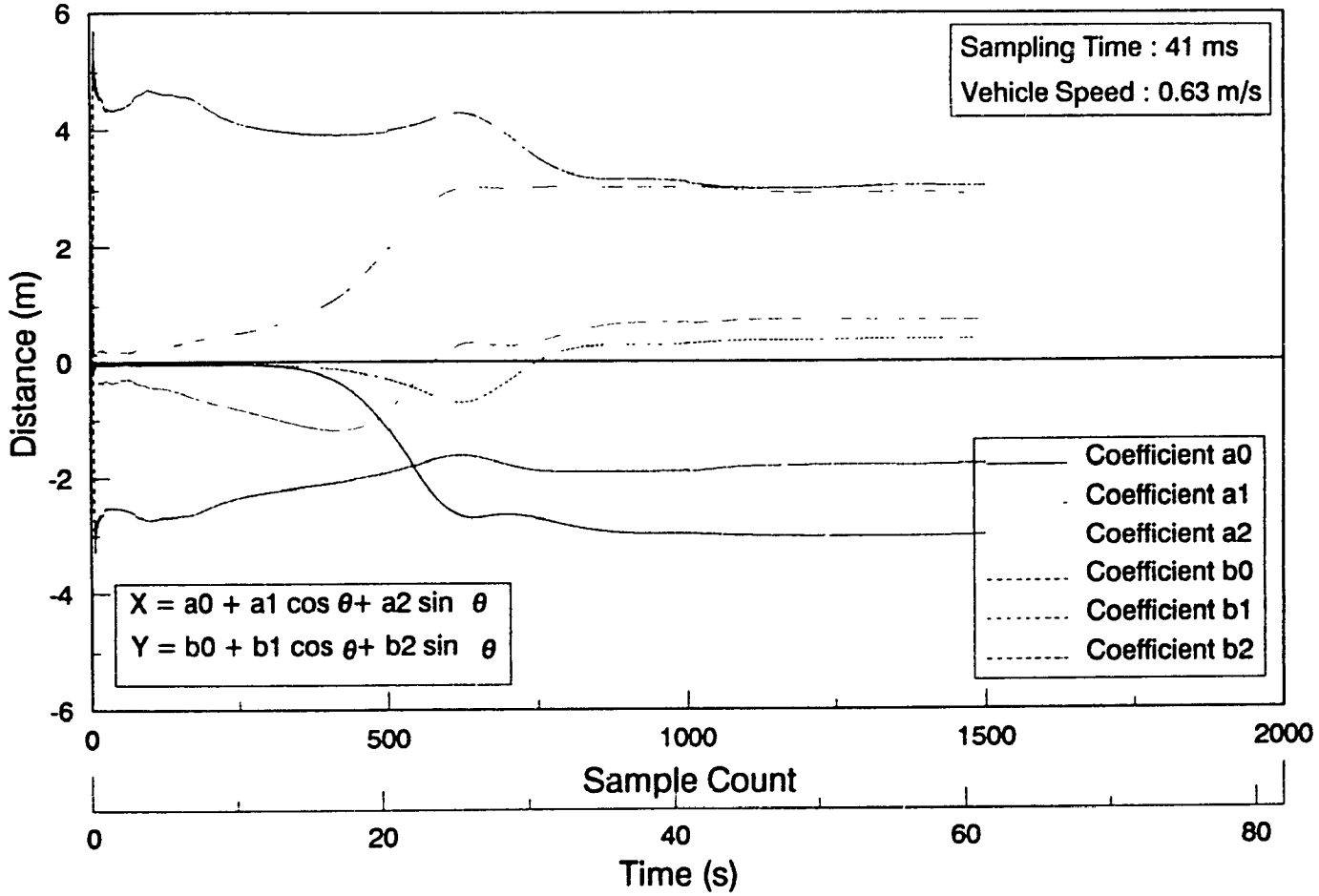

Fig. 7.32 Convergence of Coefficients of an Elliptic Track

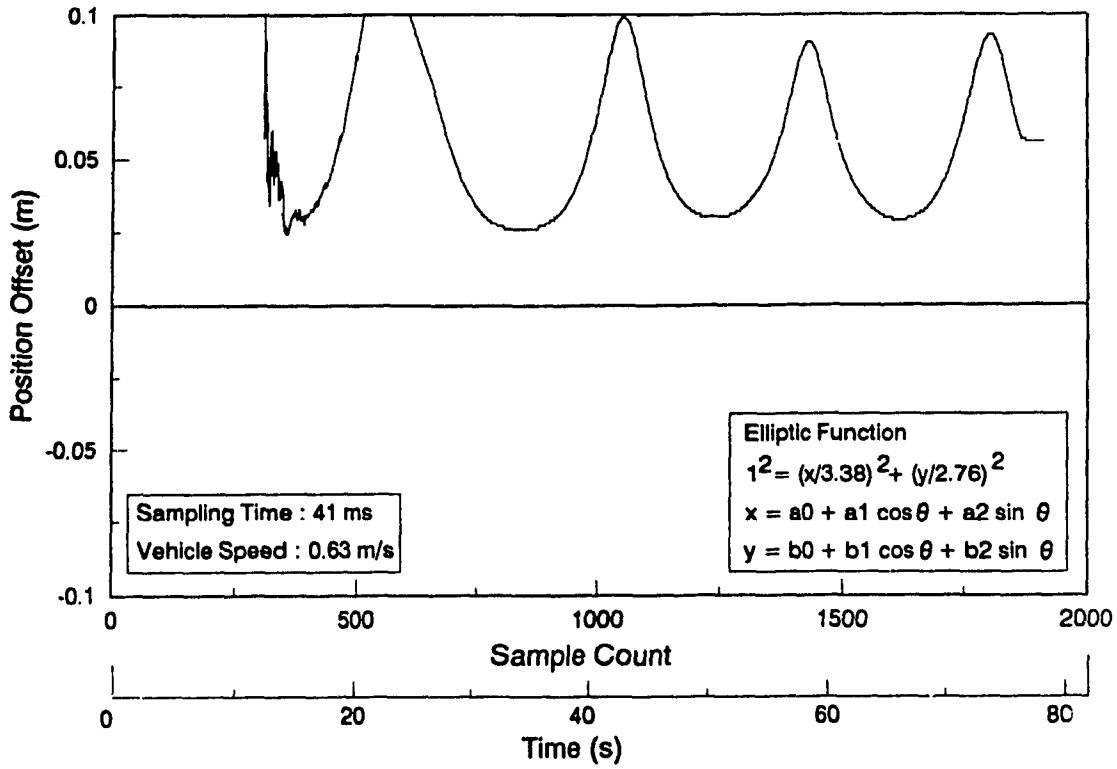

Fig. 7.33a Convergence of Position Offset for an Elliptic Track

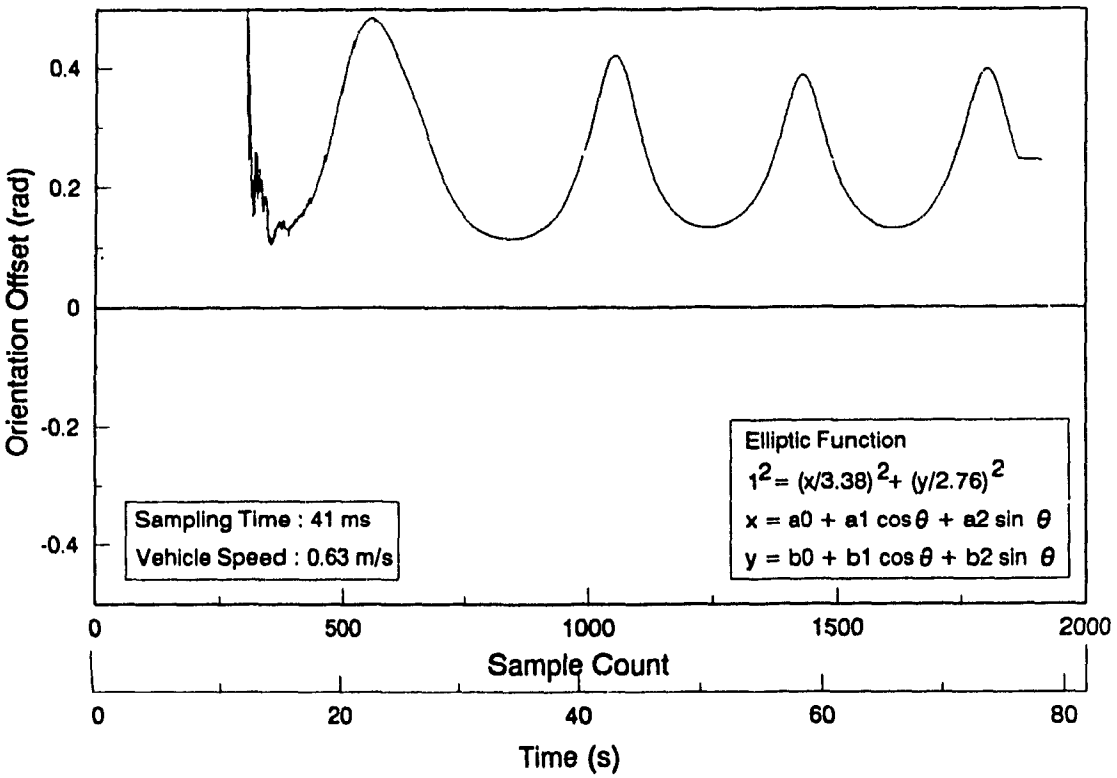

Fig. 7.33b Convergence of Orientation Offset for an Elliptic Track

The desired values of the parameters ε_d and ε_θ are computed using the results of identification of the track geometry presented above are illustrated in Figs. 7.30a & 7.30b. The control scheme should check the actual value of these parameters with these desired values and provide corrective action accordingly. The magnitude of the desired values are ε_d = 0.055 m and ε_θ = 0.22 rad to ensure that the front and rear casters on the track.

7.5.2.6 Identifying the Coefficients of a Conic Profile - Elliptic Function

As in the case of circular track, experiments are carried out with an elliptic track whose major and minor axes are 3.40 m and 2.76 m respectively. The comptued profile of the track at a vehicle speed of 0.63 m/s is shown in Fig. 7.31. The errors in the estimated values of the major and minor axis are 4.4% and 3.3% respectively.

Figure 7.32 illustrates the convergence of the coefficients of the conic profile. The convergence is achieved after 800 samples which is higher than the number of samples required for convergence in the case of simulation results presented in section 7.5.1.5. The desired values of the parameters ε_d and ε_θ are comprised of peaks and valleys and are shown in Figs 7.33a & 7.33b.

7.6 Summary

Simulation studies and experimentations are carried out to study the effectiveness of the guidance schemes presented in Chapter 5. The results are classified under four major sections. The components of the overall position control loop are calibrated and are presented in the first section.

The objective of component calibration is to establish the operating characteristics of the components for control purposes. From the results it can be concluded that the components with the exception of servo amplifiers exhibit complete linearity. The servo amplifiers exhibit nonlinearity at very low motor speeds.

The second set of results are presented for vehicle guidance using a single camera at the front end of the vehicle. An acceleration value of 0.024 m/s^2 for straight lines and 0.005 m/s^2 for tracks with curvature are arrived experimentally as the recommended settings. Experiments are carried out to select a controller for the guidance system. From the results it is established that a PI controller with the gains P=2.5 and I=0.07 provides a satisfactory response for straight line tracks. For tracks with curvature, P=1.0 and I=0.07 is the recommended setting. Results of track following with the same initial condition at various vehicle speeds are provided. These results illustrate that a satisfactory tracking performance results even at a higher speed of 0.785 m/s. Effect of payload on tracking performance indicates that the transient overshoots are much smaller (33%) in magnitude with load and no change in the steady state performance.

Tests are conducted to study the effect of changing the initial errors of the vehicle on tracking at a constant speed of 0.471 m/s. This is the speed at which most of the industrial AGVs are operated. The results show that the vehicle recovers from the initial error quickly even at an initial orientation offset of 40 degrees and a position offset of -0.08 m. Dynamic response of the AGV for sudden change in the track location is studied at various speeds. The difference between the actual displacement in the track

location and that measured by the image analysis is 5 mm for a displacement of 65 mm. The vehicle recovers from this disturbance in 3 seconds and attains a steady state tracking error of 5 mm.

Performance tests are conducted while following circular and elliptic tracks. It is not possible to obtain transient response of the vehicle due to the constant acceleration of the LM628 motion controller chips. As a result of this, extensive performance studies are not carried out. Tracking performance with and without a payload on circular tracks are more or less the same. Dynamic response for a sudden increase in the radius of the circular track illustrates that the performance is satisfactory not only for straight line tracks but also for tracks with curvature.

The third set of results are on simulations to study the effectiveness of the dual camera guidance over the single camera guidance. Considerable improvement in terms of reduction in time taken (40%) to reduce the tracking errors (position and orientation offsets) at the front and rear ends are observed. Guidance control using dual camera also showed less oscillations while tracking circular tracks.

The fourth set of results are the simulation studies to identify the geometry of the track. Guidance control simulations and experiments are not carried out and hence are not provided. To verify the correctness of the equations the simulations are carried out. Thereafter, calculations are carried out with the actual data from the experimental AGV. The process of computing the vehicle position from the wheel speeds indicates that the simple trapezoidal rule is the proper choice for integration. Simulations on

the convergence of coefficients of the polynomial function using polynomial profile equations show that convergence is achieved after a travel of 3 m on the polynomial track. Tests are carried out to identify the track profile equations (polynomial or straight line) to compute the coefficients of a straight line track function. Tests on the suitability of polynomial and straight line forms to describe a straight line function show that the time taken by the polynomial form to converge is twice that of the straight line form. However, the initial values of the coefficients are very large in the straight line case.

A known circular track (radius = 3.0 m) is used as an input to the conic profile equation described in Chapter 5. For this track, convergence of coefficients of a conic profile equation and the parameters of the circle are obtained. Convergence is observed after the vehicle travels one half of the circle. Similar tests are carried out with an elliptic track function input. Convergence of coefficients is noticed after travelling along one half of the ellipse.

Tests are conducted to study the effect of sampling time and the vehicle speed on the speed of convergence of the coefficients of the track profiles. The results show that lower the sampling time or higher the sampling rate, faster is the convergence in terms of distance travelled. The effect of speed shows faster convergence at a higher velocity in terms of number of samples required. Convergence of coefficients are tested with the actual data from the experimental vehicle while following a variety of track profiles and are observed to be the same as the simulations. The identified track profiles exhibit a maximum error of 10%.

CHAPTER 8

CONCLUSIONS

8.1 Introduction

This thesis deals with a guidance control scheme based on binary camera vision and control schemes to achieve accurate track following of AGVs. In order to achieve the above mentioned objective, research and development activities are carried out in the following aspects :

- Development of a methodology and a criterion to select the suitable combination of driving and steered wheels (without redundant) and also the wheelbase configuration for kinematic control. Suitability here means *non-redundant path controllability*.
- Guidance system based on binary camera vision and a fast image processing techinque that identifies the track and a set of road signs.
- Guidance control to follow the track accurately using schemes employing single camera, dual camera and identification of track geometry and guidance.
- Design and development of a prototype AGV.

Section 8.2 presents the summary of the methodology and the results for non-redundant path controllability. A summary of the binary camera vision and the results are detailed in section 8.4. Section 8.5 has three sub-sections to summarize the methodology and the results of guidance control. The features of the prototype AGV are summarized in section 8.6. Applications of the guidance control schemes, the camera vision scheme and the prototype AGV

are discussed in section 8.7. The last section (section 8.8) of this chapter presents an abridged version of the summary presented in sections 8.1 to 8.6 and highlights the contributions of this thesis.

8.2 Path Controllability and Kinematic Modeling of AGVs

Existence of kinematic singularity is used as the basis for the selection of a suitable combination of driving and steering wheels (without redundancy) and wheelbase configuration for the kinematic control of the vehicle. This suitability is termed as path controllability in this thesis. At the singular points there is loss of degrees of freedom and it will not be possible to compute a unique solution for the wheel speeds or steering angles or steering rates for given linear and angular velocities of the AGV. For this purpose a kinematic modeling scheme for AGVs is presented. Modeling is accomplished using the transformation scheme described by Muir and Newman [10]. A generic configuration with a diamond shaped wheelbase configuration with a wheel that is driving and steered at the front and rear is considered. The steering axis has an inclination in the fore and aft direction and an offset with respect to the contact point of the wheel. From the generic form of the equations, a criterion for path controllability, i.e. ability of the kinematic model to provide a unique solution for the wheel speeds, steering angles and steering rates for a given position and orientation of the vehicle. The kinematic modeling approach presented in this thesis is sufficiently general to apply for any other wheel configuration. The following conclusions are arrived at from the non-redundant path controllability criterion

- Vehicles with differential drive with no steered wheels offer path controllability for all values of the linear and angular velocities

of the AGV, i.e. kinematic singularity is not present.

- Vehicles with inclined steering column and with an offset distance are path controllable at all values of the steering angle.
- Vehicles with an inclined steering column and with zero offset are path controllable, except when the steering angle is $(2n+1)\pi/2$.
- Vehicles with a vertical steering column and a non-zero offset are path controllable, except when the steering angle is $(2n+1)\pi/4$.
- Vehicles with a vertical steering column without offset are not path controllable.

The analysis presented further illustrates that other parameters need to be taken into account in choosing a particular wheel configuration. For example, when the steering column is inclined at an angle, extra degrees of motion are introduced; motion in the vertical direction and roll of the steered wheel. In the case of non-zero offset, one has to drag the steered wheel to the side during steering, implying a larger steering torque.

The preferred arrangement for kinematic control is the differentially driven AGV with no steered wheels. In this case in addition to the absence of kinematic singularity, the expressions are simpler. Moreover, the geometry of the vehicle is also simplified with the absence of a steering mechanism. The other advantages are (1) the vehicle can spin about the geometric center at a minimum radius which is equal to one half of the wheel span and (2) the vehicle can travel in the forward and reverse direction.

8.3 Guidance System Based on Binary Camera Vision

Binary camera vision employing a simple camera with optic ram chips and a black line (painted or taped) that describes the track to be followed is considered. A fast image processing scheme is described to identify the track and guide the AGV as well as to recognize a set of primitives. Hence the image processing scheme recognizes road signs to take appropriate actions at road junctions. The time taken to acquire 1 K byte of image data is 18.9 ms and for analysis a duration of 9.0 ms is required. Since the image is acquired and processed rapidly, the track is followed by the vehicle very accurately even at high speeds (0.8 m/s), even if the track has variable curvatures. It is believed that the employment of binary digitizing camera for guidance is a preferred choice for the following reasons :

- The track can be modified easily and hence the flexibility in installation and maintenance;
- Camera vision provides a controllable width of view of the track to be followed. This provides position and orientation of the vehicle relative to the track. Further, it has the ability to recognize road signs;
- Simple image processing scheme is employed since the image received for analysis is two dimensional and does not contain any complex information.
- Camera employed is simple in construction and inexpensive.

From the experiments performed to ascertain the number of rows of image required for image analysis it was established that analyzing only three rows (4^{th}, 30^{th} and 56^{th} rows) out of the possible 64 rows of image data results

in a error of 3 mm while evaluating the position offsets. Increasing the number of rows of image considered for analysis showed marginal improvement at the cost of computing time.

8.4 Guidance Control to Follow the Track Accurately

8.4.1 Guidance Scheme Using Single Camera

The steering command is computed based on the instantaneous position and orientation of the vehicle relative to the track. This information is obtained from the image analysis performed on the image from a camera located at the front end of the vehicle. Experiments on the effect of controllers (P and PI) and their gains indicate that a PI controller with P=2.5 and I=0.07 provides satisfactory performance on straight line tracks. For tracks with curvatures a gain setting of P=1.0 and I=0.07 is recommended. It has been noticed that due to the presence of constant acceleration of the LM628 motion controller chip, there is a 'speed' until which the feedback from the camera will not have any effect on the overall positional control of the vehicle. This 'speed' is a function of the command speed of the wheels. The time taken to reach this 'speed' depends on the acceleration of the vehicle. Hence in all the experiments, a monotonic increase in the position offset of the vehicle is noticed during the transient stage. It has been noticed that this monotonic increase in the position error has not exceeded 0.10 m, the limits of the camera window dimensions. Even at a vehicle speed of 0.79 m/s the guidance system recovered from this error in 3 seconds and a steady state error of 0.005 m is attained thereafter. The guidance scheme exhibited less overshoots and oscillations with a payload of 250 lb compared to a situation with no payload indicating that the controllers are tuned well for the vehicle to carry loads. Tests on the effect of initial condition on the

tracking ability of the guidance scheme on straight lines show that a satisfactory performance results even at the maximum possible position and orientation offsets of 0.08 m and 40 degrees respectively at the maximum speed of 0.785 m/s.

From the results on vehicle stopping distances at various speeds on straight line tracks, it can be concluded that a minimum stopping distance of 5 mm is achieved at a linear velocity of 0.16 m/s and is the recommended operating speed for parking purposes. Experiments on dynamic response of the guidance control scheme show that for an offset of 65 mm in the track location (one quarter of width of image window) recovery is achieved within 3 seconds even at a speed of 0.785 m/s. Results on circular and elliptic track profiles show satisfactory steady state performances. Tests on the ability of the image processing scheme to identify road signs indicate that the algorithm developed for this purpose function well.

8.4.2 Guidance Scheme Using Dual Cameras

An approach for accurate track following of a small section at the front and a small section at the rear end of the vehicle is presented here. On the contrary, only the small section at the front end of the vehicle follows the track accurately when the single camera approach is used. Using dual cameras results in faster minimization of tracking errors with minimum overshoots and oscillations. In this approach, a camera is employed at the rear end of the vehicle in addition to the camera at the front end. Vehicle guidance is achieved using the instantaneous position and orientation offsets obtained from the image analysis performed on the track image obtained from both sensors. From the sign of the orientation offsets obtained, it is possible

to decide whether the track has a curvature or not. If the sign of the orientation offsets obtained from the front and rear camera are the same, the track is a straight line, otherwise is curved. Objective functions are defined based on the track curvature. In the case of straight line tracks, the objective of the control scheme is to reduce the position and the orientation offsets to zero. On curved tracks with constant curvature such as a circular track, the position and the orientation offsets at the front and rear ends should be equal in magnitude and non-zero, and the position offsets may or may not be equal to zero depending on which part of the AGV needs to be following the track. The controller gains are changed in real-time depending on the position of the front and rear ends of the vehicle relative to the track and the existence of track curvature.

Simulations and experimentations are carried out on straight line and circular tracks. From the results it is established that the dual camera guidance achieves faster reduction (40% less time) in the tracking errors (position and orientation offsets) of the rear end compared to the single camera guidance. Moreover, there are less number of oscillations in the transient response.

8.4.3 Guidance Scheme using Track Geometry Identification

This is a feed forward control scheme unlike the single and dual camera schemes which are feedback systems. The feed forward scheme is an intelligent method as the vehicle guidance is based on the identified geometry of the track. Guidance is performed using the extrapolated track ahead of the vehicle and the instantanoues data that are available. The knowledge of the geometry of the track provides the desired values of

position and orientation offsets for a particular driving criterion to achieve accurate tracking. The driving criterion defines which part(s) of the AGV needs to be following the track accurately. The driving criterion chosen for analysis is that the contact points/patches of the front and rear casters be on the track. Two schemes are proposed to identify the geometry of the track, one is using a generic conic function and the other is a second order polynomial function.

From the results obtained using a large number of simulations and experimental data, it has been established that the track geometry is identified in a reasonable time. In the case of circular tracks, an error of 6% is noticed (radius = 3.0 m) in the computed radius using the kinematic equations and estimated using the identification scheme. In the case of an elliptic track, the computed values of the length of the major and minor axis have an error 5% and 10% respectively. These results are obtained using experimental data. Only simulations are performed for the polynomial functions. Convergence of the coefficients for all geometric profiles considered is achieved within a travel of 3 m along the periphery of the profile.

Performance data using the guidance scheme are not available for comparison as experiments are not carried out using this scheme. This is because the computational overheads increases the cycle time from 41 ms to 200 ms. Hence proper identification of the track geometry is not feasible. To maintain the cycle time less than 60 ms (required for proper identification of the track geometry), it is necessary to perform the computations of the identification scheme in a separate processor, i.e.

parallel processing. In Chapter 9, an approach to achieve this parallel computation is presented.

8.5 Vehicle Design and Development

The present design facilitates a versatile research vehicle with a modifiable wheelbase configuration with which performance studies of various wheelbase configurations can be carried out. Since most of the components employed are off-the-shelf components, easier system upgrading with the technological advancement is feasible. Employment of low cost camera vision technique coupled with an efficient image processing technique obviates the necessity to employ a complicated and sophisticated guidance system for vehicle guidance. Special purpose motion controller chips LM628 for motion control simplify the controller design and also offer concurrent control of multiple motors as these chips can function without using the host computer bus for motor control. Provision of on-line data acquisition system is provided to record the operating parameters of the vehicle in real-time in order to validate the theoretical findings. The system also features a dual camera guidance scheme with a camera at the front and rear with variable controller gains. A scheme to identify the geometry of the track has been implemented. A complete investigation on the safety features required for the AGV has been carried out and has been implemented. The operating software is modular in form in order to facilitate addition of new features for future development and is written using the Borland Turbo-C. The software also supports communication with an external supervisory computer. The vehicles uses ultrasonic sensors for obstacle detection. The operating parameters of the vehicle can be modified in real-time.

In camera vision mode an imaging rate of 20 to 25 frames/s is obtained depending on the features of the AGV that are in use. As a result of this very high frame rate a stable performance is achieved even at higher velocities (> 0.5 m/s) and with tracks having smaller radii of curvature. The vehicle has a payload of 600 lb in addition to its dead weight of 275 lb. Experiments on trackability of the vehicle with payloads indicate satisfactory performance. As far as the maximum speed is concerned, a maximum speed of 0.93 m/s on a circular track of 1.7 m radius is achieved. On straight line tracks a step input command of 1.03 m/s was feasible. The theoretical maximum speed that the vehicle can attain is 1.2 m/s which is the maximum speed provided by the driving wheels.

Experiments are performed on various components in the control loops indicate that there exists a linear relation between the input and the output of these components. The results from the DAC-08 show that the wheels/motors attain the maximum speed when 6 bits of the available 8 bits are used. The servo amplifier exhibits non-linearity and the relation between the control signal voltage and the motor terminal voltage is a power series. From the experiments on the effect of vehicle acceleration on the ability to follow the track accurately, it has been established that suitable values for the wheel acceleration for straight line tracks and for tracks with curvatures are 0.024 m/s and 0.005 m/s respectively.

8.6 Applications

Of the three control schemes described, the single camera scheme is preferred for applications that do not require accurate tracking of the rear end of the vehicle, namely, moving from one work station to the other.

The guidance control scheme using dual cameras is suitable for applications requiring accurate track following and faster alignment of the front and rear ends of the vehicle with the track, such as, parking the vehicle beside a work station or for operating the vehicle in narrow spaces with track profiles of varying curvature or geometry.

The intelligent guidance control scheme (track geometry identification and guidance) is suitable for applications where the requirement is to accurately follow a track whose curvature changes slowly, i.e. the changes in coefficients take place change gradually.

The binary camera vision technique is suitable for applications where the environment provides contrast between the track and the floor. The prototype AGV is useful for experimental research to study the effectiveness of various wheelbase configurations consisting of combinations of driving and steered wheels. It also allows testing of a variety of control schemes and other guidance schemes using CCD cameras and ultrasonic sensors.

8.7 Summary

The contributions of this thesis can be grouped as major and minor in nature. Major contributions are, (1) methodology to select the suitable combination of driving and steered wheels (without redundancy) and also the wheelbase configuration for kinematic control, (2) a supe ior method for guidance control based on dual cameras (front and rear) to achieve faster reduction in tracking errors of a large segement of the vehicle consisting of two small sections one at the front and the other at the rear and (3) an approach for intelligent guidance control that could provide accuracy in

track following as it is based on the identified geometry of the track and not simply on the instantaneous position and orientation of the AGV relative to the track. Minor contributions are (1) binary camera vision for guidance and a fast image processing scheme that identifies the track as well as road signs and (2) design and development of a prototype vehicle that is modular in structure (mechanical, control components and software).

It can be concluded that the differential drive arrangement does not exhibit kinematic singularity and is the preferred configuration. From the experimental results it can be inferred that the single camera guidance performs well as the transient overshoots are less than the image window dimension (±0.1 m) even at a linear speed of 0.79 m/s and the steady state errors are less than 5% of the image window. This is within the accuracy value set by the industries for automation using AGVs. Tests on dynamic response of the camera guidance indicate that the vehicle recovers from a sudden change in the track location in 3 seconds. The guidance scheme performed well with a payload of 250 lb. From the simulation results it can be concluded that the dual camera guidance minimizes the tracking error of the rear end in a time that is 40% less than in single camera guidance. It also exhibits less oscillations and the overshoots are minimum. Results from the intelligent guidance control scheme illustrates that the scheme can identify the geometry (within 10% error) of the track within 3 m travel along the periphery of the track. It also provides the desired value of the position and the orientation offset for control purposes. Though the results for the guidance control part are not provided (neither simulated nor experimented), it is believed that the control scheme will provide excellent tracking performance as the geometry identified is within 10% error.

CHAPTER 9

RECOMMENDATIONS FOR FUTURE WORK

9.1 Image Processing

There are two areas in which work need to be carried out in order to enhance image processing and analysis. The first one is incremental image processing and the second is the method of computing the orientation offset. The image analysis scheme described in Chapter 4 considers every frame of image data received as a new data and analyzes the image from left to right (every column in a row of image data). Since a priori information on the column location of the track image is not available, it is not be possible to analyze a small column window to extract the necessary parameters.

Since the track image appears as a straight line in the image window and the imaging rate is in the order of 16 to 25 frames a second, the cumulative track profile obtained by assembling two consecutive frames can be considered to be a straight line. With this assumption, and knowing the wheel speeds, the location of the track in the next frame can be estimated. Knowing the approximate location of the track in the image data received, a small image window can be defined for analysis. Nevertheless, this kind of selective analysis is valid only if the track is continuous.

Secondly, it has been established experimentally that the approach employed to evaluate the orientation offset from the image data obtained does not provide consistent results, particularly when the orientation offset is less than 20 degrees. In some cases the sign of the error is wrong as well. One reason attributed to this is the fact that the window dimensions are so

small that variation of a few pixels in one or many rows of the track image results in a large error in the computed orientation. As a result of this, the orientation offset is not considered by the control loop, in the experiments carried out. The method of computing the orientation needs to be modified in order to compute the orientation offset accurately.

9.2 Wheel Level Control Scheme

The control loop used in this thesis is based on a scheme where each wheel is provided with an independent control loop with no interaction between them. Stated in another way, feedback errors from one wheel do not affect the other. Since the vehicle is driven by more than one driving wheel, errors in one of the wheels affect the trajectory or the path traced by the vehicle. Sources of errors in guidance control fall under two major groups and are

I) Environmental Factors.

II) System Errors.

I. Environmental Factors

a) Variations in the floor roughness factor (coefficient of friction) resulting in non-equal wheel speeds for the right and left wheels.

b) Load distribution between wheels being unequal.

c) Variations in the floor gradient levels (ups and downs).

These errors can be modelled as a time varying external disturbance in the control loop.

II. System Errors

a) Errors resulting from the system gains for the control loops for each wheel (loop gain, amplifier gains, and encoder resolutions).

b) Encoder tracking errors.

c) Wheel Alignment errors.

d) Wheel slippage.

e) Wheel diameter variations.

f) Servo-lag

These errors cannot be quantified directly in the control loop for simulation and implementation. The errors in the system gains involving the loops for the wheels can be compensated by using a cross coupled control scheme described below. In this scheme, the error from one wheel is fed to the other and vice versa. The encoder tracking error also gets corrected using this scheme. The wheel alignment error cannot be compensated directly. This can be measured experimentally, and a correction factor can be included in the control loop. Wheel slippage can be sensed only by providing a sensor on the driven wheels. Wheel diameter variation can also be estimated experimentally, and a correction factor need to be included in the control loop. The servo-lag is contributed by the motor time constant. As a result of this, the total time taken by the AGV to travel a given section of the track is more than the desired value.

In summary, two control loops are proposed to account for the effect of errors. They are the cross coupled control loop, and the cartesian control loop. The cross coupled control loop is to provide better handling characteristics to minimize the effect of disturbances on the path traced by the AGV. The cartesian control loop is to compensates for the servo-lag which also results due to the presence of the coupled control loop. The coupled control loop is used widely for numerical control machines and is proposed for AGV control by Borenstein and Koren [8].

9.2.1 Cross Coupled Control Loop

Figure. 9.1 shows the schematic layout of the cross coupled control loop to minimize the effect of disturbances. It can be seen from the layout of the control loop that there is an additional error input to the servo loop of each motor. The error from wheel-2 is fed to the wheel-1 loop, and vice versa. This additiona' feedback minimizes the tracking error and this alters the linear velocity of the vehicle and hence the vehicle will be lagging in cartesian coordinates.

9.2.2 Cartesian Control Loop

It was established in the previous section that the *coupled control loop* contributes additional lag in addition to the servo-lag. A direct consequence of *servo-lag* is that the vehicle will be trailing behind a fictitious reference point that has virtual motion along the reference track. This point depicts the location at which the AGV is expected to be at a given instant. In order to compensate for the lags, an additional feedback loop is introduced as shown in Fig. 9.2. This feedback loop computes the wheel speeds based on the absolute position error of the AGV. The actual location

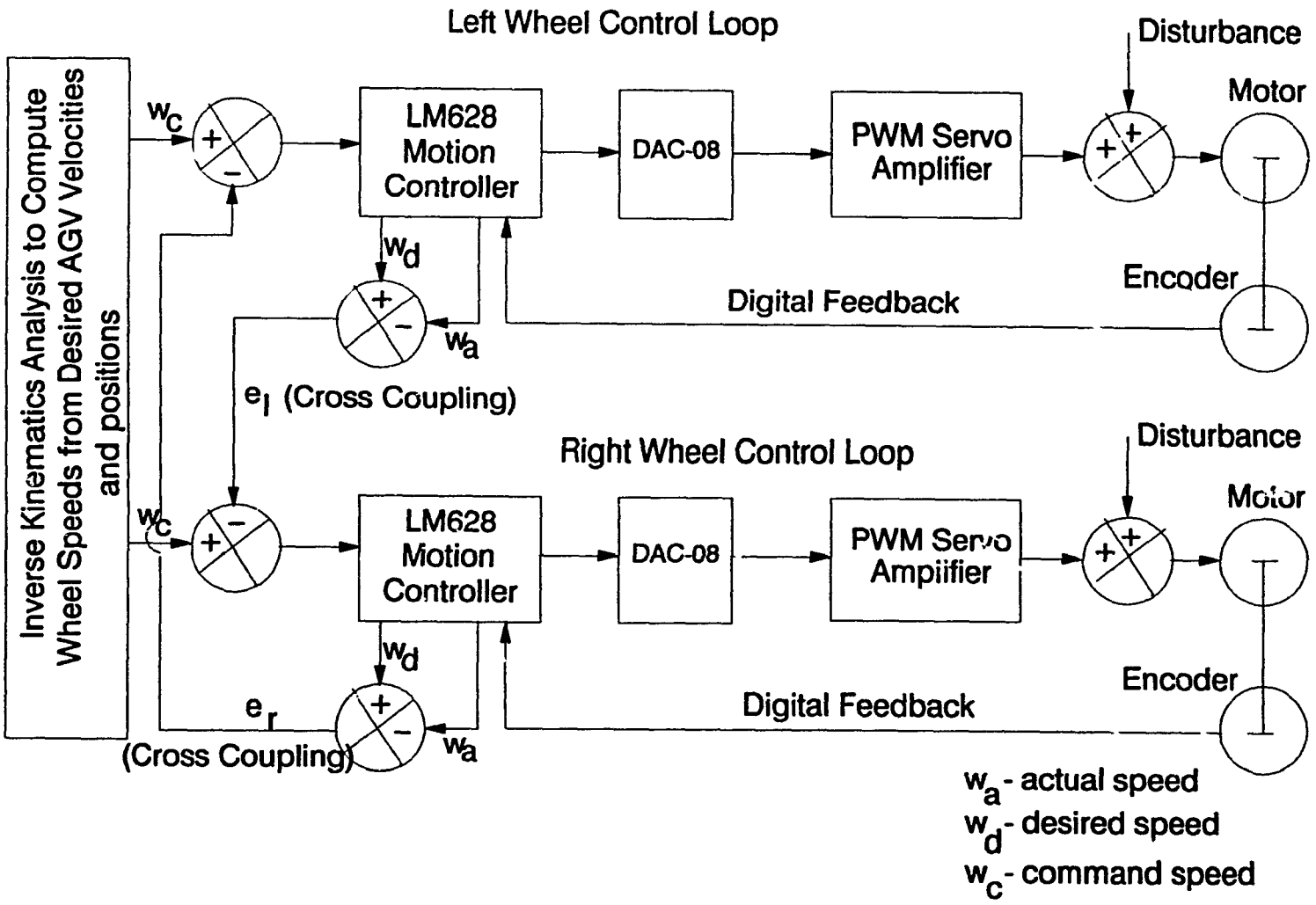

Fig. 9.1 Cross Coupled Control Loop with LM628 Motion Controllers

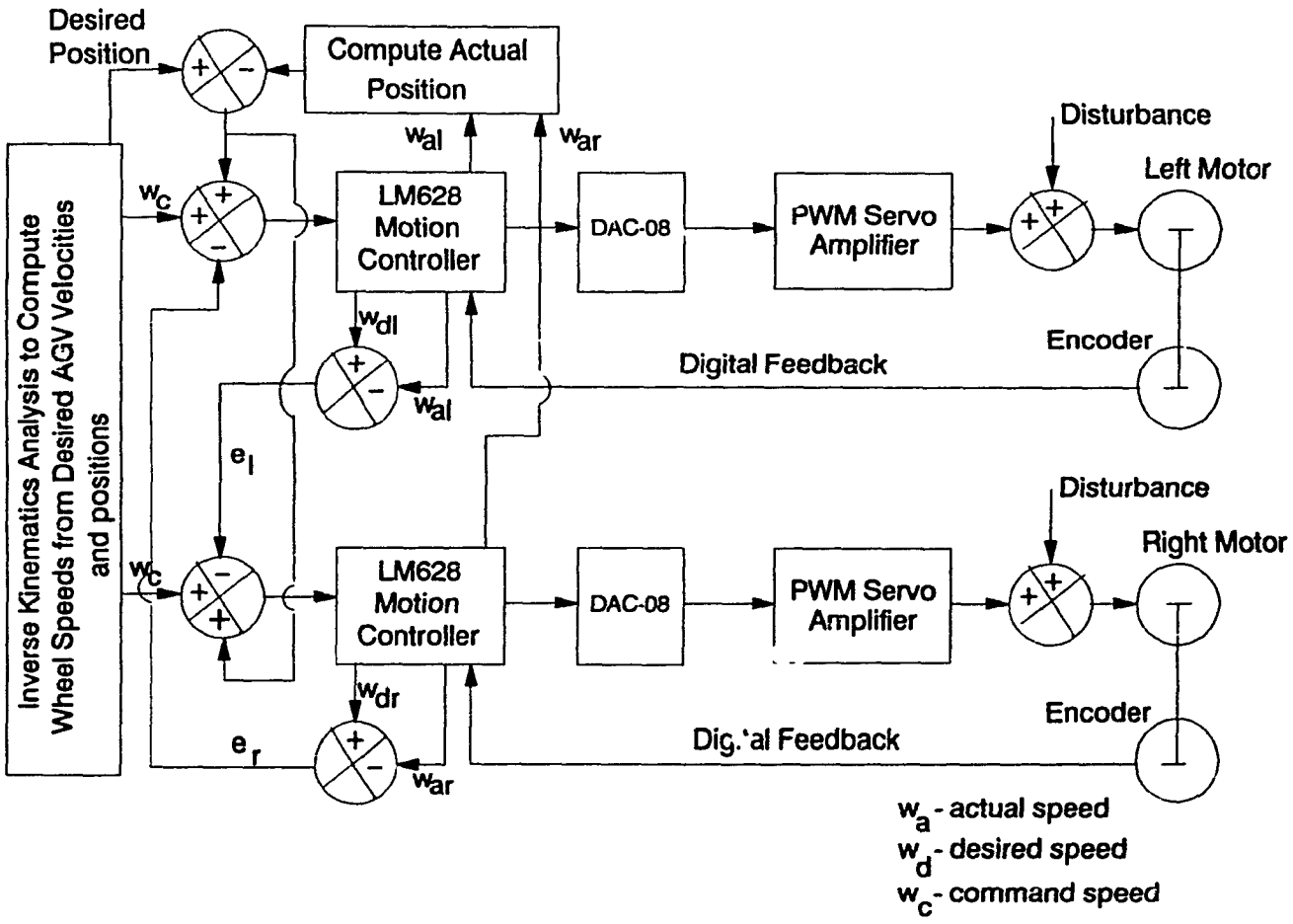

Fig. 9.2 Control Loop with Cartesian Feedback and Cross Coupling

(position and orientation) of the AGV is computed using the actual wheel speeds, and is compared with the desired location.

9.3 Modified Control Equations for Tracking

The control equations presented in (5.4) and (5.8) are independent of the vehicle speed and hence will not provide faster corrective action at higher speeds which is necessary. To provide a variable corrective action as a function of speed, the following approach is proposed.

Considering the equation for the proportional only controller presented in equation (5.4), differentiation of this equation with respect to time results in an expression for the rate of change of steering angle as

$$\Delta\dot{\theta}_s = G_1 \Delta\dot{\varepsilon}_d + G_2 \Delta\dot{\varepsilon}_\theta \tag{9.1}$$

From Fig. 5.10, it can be seen that the parameter $\Delta\dot{\varepsilon}_d$ is a function of the vehicle speed (V), desired orientation offset ($\varepsilon_{\theta d}$) and the current orientation offset ($\varepsilon_{\theta a}$). The parameter $\Delta\dot{\varepsilon}_\theta$ is equal to the incremental value of the rate of change of angular position of the AGV, which is $\Delta\dot{\theta}_r$. Referring to Fig. 5.10, $\Delta\dot{\varepsilon}_d$ is given by

$$\Delta\dot{\varepsilon}_d = V \left\{ \frac{1}{\sin \varepsilon_{\theta d}} - \frac{1}{\cos \varepsilon_{\theta a}} \right\} \tag{9.2}$$

The angular velocity $\Delta\dot{\theta}_r$ about the reference frame 'R' produces a velocity v_x at the pivot axis of the caster along the x-direction. The magnitude of v_x is

$$v_x = \Delta\dot{\theta}_r (L_a - s) \tag{9.3}$$

Where L_a is the wheelbase distance between the contact points of the driving wheels (wheelbase) and the casters, while the steering angle θ_s is equal to zero, i.e. the casters are straight and are aligned with the longitudinal axis of the vehicle. An equal and opposite force will be sensed at the contact point of the caster. This force and v_x constitutes a couple ($s\,\Delta\dot{\theta}_s$). Hence the term $\Delta\dot{\theta}_s$ is also computed from

$$\Delta\dot{\theta}_s = \frac{\Delta\dot{\theta}_r (La - s)}{s} \tag{9.4}$$

Equating (9.1) and (9.4) and substituting equation (9.3), and replacing $\Delta\dot{\varepsilon}_\theta$ by $\Delta\dot{\theta}$, the following result is obtained.

$$\frac{\Delta\dot{\theta}_r (La - s)}{s} = V G_1 \left\{ \frac{1}{\sin \varepsilon_{\theta d}} - \frac{1}{\cos \varepsilon_{\theta a}} \right\} + G_2 \Delta\dot{\theta}_r$$

$$\text{i.e.} \qquad \Delta\dot{\theta}_r \left\{ \frac{La - s}{s} - G_2 \right\} = V G_1 \left\{ \frac{1}{\sin \varepsilon_{\theta d}} - \frac{1}{\cos \varepsilon_{\theta a}} \right\} \tag{9.5}$$

But from the inverse kinematic analysis presented in section 3.4, the value of $\Delta\dot{\theta}_r$ in terms of incremental angular velocity of the wheels is given by

$$\Delta\dot{\theta}_r = \frac{r}{L_1 + L_2} \left\{ \Delta\omega_{x1} - \Delta\omega_{x2} \right\} \tag{9.6}$$

Substituting (9.6) in (9.5), and rearranging the terms

$$(\Delta\omega_{x1} - \Delta\omega_{x2}) = \frac{(L_1 + L_2)\, V\, G_1}{r\left[\frac{La - s}{s} + G_2\right]}\left\{\frac{1}{\sin \varepsilon_{\theta d}} - \frac{1}{\cos \varepsilon_{\theta a}}\right\} \qquad (9.7)$$

The effect of steering does not change the linear velocity of the AGV and affects only the angular velocity and hence the following relation is obtained

$$L_1\, \Delta\omega_{x1} + L_2\, \Delta\omega_{x2} = 0 \qquad (9.8)$$

Solving equations (9.7) and (9.8) simultaneously, the expressions to compute the change in the wheel angular velocity of the wheels required are obtained and are presented below.

$$\Delta\omega_{x1} = \frac{G_1\, L_2\, V}{r\left[\frac{La - s}{s} + G_2\right]}\left\{\frac{1}{\sin \varepsilon_{\theta d}} - \frac{1}{\cos \varepsilon_{\theta a}}\right\} \qquad (9.9)$$

$$\Delta\omega_{x1} = \frac{G_1\, L_1\, V}{r\left[\frac{La - s}{s} + G_2\right]}\left\{\frac{1}{\sin \varepsilon_{\theta d}} - \frac{1}{\cos \varepsilon_{\theta a}}\right\} \qquad (9.10)$$

Implementation of this scheme has not been carried out due to problems in obtaining a good estimate of the orientation offset (ε_θ).

9.4 Alternate Approach to Identifying Track Geometry

In this scheme, the coordinates of the reference point P is computed based on the velocity transformations of P. A reference frame is chosen at P

and is P. An instantaneously coincident reference frame is chosen at $\bar{P}$. The coordinate frames are shown in Fig. 5.4.

A transformation graph describing the kinematic relationship between the reference frame 'R' and the frame 'P' is shown in Fig. 5.4. Referring to Fig. 5.4, the transformation for the frame 'P' from the instantaneous frame '$\bar{P}$' is

$$ {}^{\bar{P}}\Phi_{P} = \left[{}^{F}T_{\bar{P}} \right]^{-1} {}^{F}T_{\bar{R}} \; {}^{\bar{R}}\Pi_{R} \; {}^{R}T_{I} \; {}^{I}T_{P} \qquad (9.11) $$

Differentiating equation (9.11) with respect to time, the velocity transformation ${}^{\bar{P}}\dot{\Phi}_{P}$ is obtained as below :

$$ {}^{\bar{P}}\dot{\Phi}_{P} = \left[{}^{F}T_{\bar{P}} \right]^{-1} {}^{F}T_{\bar{R}} \; {}^{\bar{R}}\dot{\Pi}_{R} \; {}^{R}T_{I} \; {}^{I}T_{P} \qquad (9.12) $$

Here the term ${}^{F}T_{\bar{R}}$ can be expressed as a function of other transformation terms as below.

$$ {}^{F}T_{\bar{R}} = {}^{F}T_{\bar{P}} \; {}^{\bar{P}}\Phi_{P} \left[{}^{I}T_{P} \right]^{-1} \left[{}^{R}T_{I} \right]^{-1} \left[{}^{\bar{R}}\Pi_{R} \right]^{-1} \qquad (9.13) $$

It should be noted here that the transformations such as ${}^{\bar{P}}\Phi_{P}$ and ${}^{\bar{R}}\Pi_{R}$ are unity transformations. Substituting equation (9.13) in (9.12) and after simplifications, the following result is obtained for the reference point velocity transformation,

$$\bar{P}_{\dot{\Phi}_P} = \left[{}^{1}T_P \right]^{-1} \left[{}^{R}T_I \right]^{-1} \bar{R}_{\dot{\Pi}_R} {}^{R}T_I \; {}^{I}T_P \qquad (9.14)$$

From this velocity transformation, the position transformation can be obtained using the schemes described in Chapter 5.

9.5 Methodology to Identify Point of Inflexion

The scheme to identify the geometry of the track described in Chapter 5 cannot distinguish whether the track is composed of more than one geometric profile or not. One way of achieving this is to identify the point of inflexion of two geometric profiles. The point of inflexion is identified based on the concavity of the track profile at a given instant. Figure. 9.3 illustrates two possible concavity situations for a function 'f'. The graph of 'f' at $x = x_1$ to $x = x_2$ is said to be

i) Concave Upwards if the first derivative of 'f' (f') is increasing on the interval (x_1, x_2).

ii) Concave Downwards if the first derivative of 'f' (f') is decreasing on the interval (x_1, x_2).

To evaluate the concavity at a particular point (x = a, y = b) i.e., at the contact point of the caster, the second derivative of f is considered and the following conditions are tested for the nature of concavity.

i) if $f''(x, y) > 0$ (+ve) at (a, b), then it is concave upwards.

ii) if $f''(x, y) < 0$ (-ve) at (a, b), then it is concave downwards.

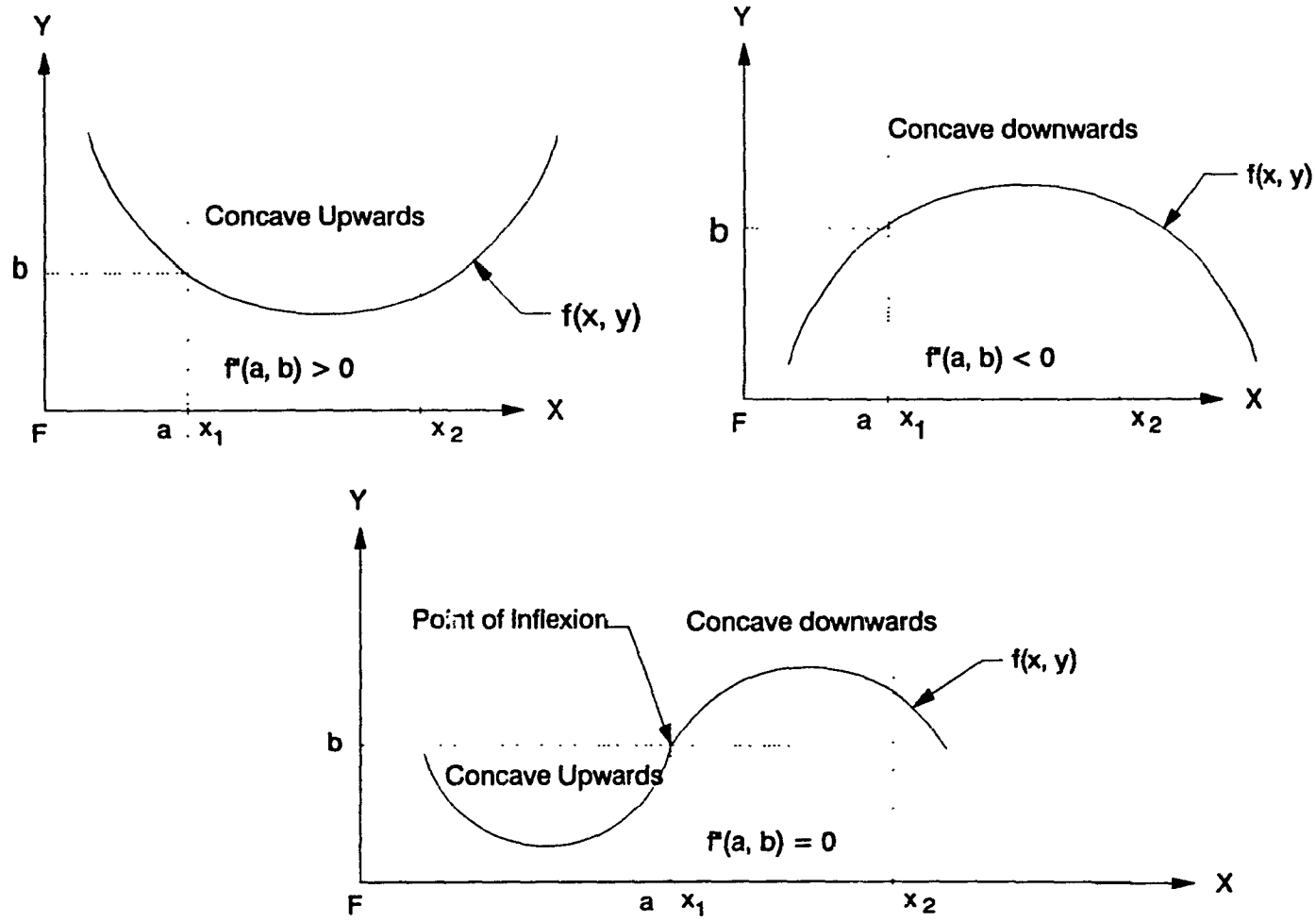

Fig. 9.4 Definition for Concavity

The second derivative conditions presented is also useful to determine the point of inflexion wherein the concavity changes from upward to downward or vice versa. The point of inflexion is normally located at the value of x and y for which f"(x, y) becomes zero. This information is useful for the track identification technique to construct track profiles with varying concavity. However, this condition is not the sufficient condition to identify the point of inflexion as there are functions for which the second derivative becomes zero at points which are local minima and not the point of inflexion.

9.6 Dual Camera Guidance Based On a Reference Point

The dual camera guidance scheme described in Chapter 5 uses the front end of the AGV as a reference point to switch from high gain to low gain controllers. Though this approach provides excellent performance, it is preferable to study the effect of choosing some other reference point along the longitudinal axis. This study will provide information on the optimum location of the reference point that will result in faster error correction. In order to perform this control scheme, it is necessary to compute the distance y_c of the reference point **c** and is shown in Figs. 9.4. The reference point has been chosen to be at a distance L_1 from the front camera and is at a distance L_2 from the rear camera. The distance y_c is the distance obtained by drawing a line at **c** and perpendicular to the longitudinal axis of the vehicle to the track. This line is parallel to the lines drawn to establish the parameters ε_{df} and ε_{dr}. A line is drawn perpendicular to the longitudinal axis at the reference point to the track. From the geometry of the vehicle, an expression to compute the distance y_c is

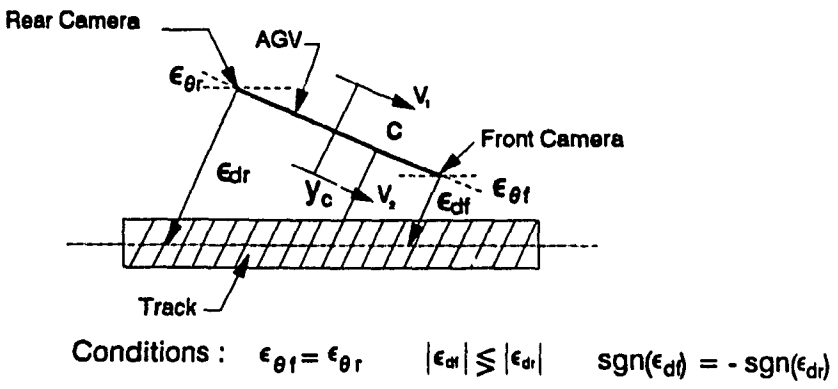

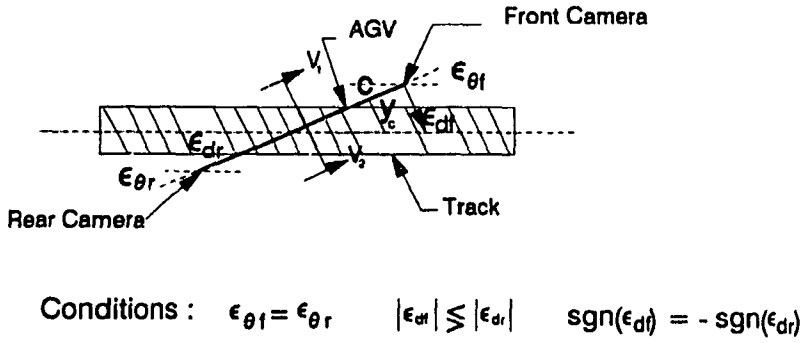

Fig. 9.4 Definition of Parameters of Steering Control Using a Reference Point for Straight Line Tracks

established as

$$y_c = \left[\frac{| \varepsilon_{df} + \varepsilon_{dr} |}{(L_1 + L_2)} L_1 + \min \left\{ |\varepsilon_{df}|, |-\varepsilon_{dr}| \right\} \right] \text{sgn } (\varepsilon_{df}) \qquad (9.15)$$

This equation is valid if and only if the parameters ε_{df} and ε_{dr} have the same sign. This indicates that the AGV is on one side of the track and is shown in Fig. 9.4.

If the signs are opposite, the front and rear ends of the track must be on either side of the track. The reference point c may or may not be on the same side as the front end. Figure. 9.4 presents this situation. The distance y_c is computed from

$$y_c = \frac{| \varepsilon_{df} + \varepsilon_{dr} |}{(L_1 + L_2)} L_1 \text{ sgn}(\varepsilon_{df}) - \varepsilon_{dr} \qquad (9.16)$$

Control laws can be defined based on the signs and magnitudes of ε_{df}, ε_{dr} and y_c.

9.7 Optimization of Controller Gains for Dual Camera

The value of the controller gains for the dual camera scheme are obtained by trial and error. A technique to search for the best values for the controller gains can be developed to provide the best performance.

9.8 Implementation of Scheme to Identify the Track Geometry

The control scheme based on the identified geometry of the track profile has not been implemented. It has been mentioned in section 8.6 that to

perform these computations using 80286-12 it requires 150 ms per calculation. This reduces the frame rate from 25 to 5. These computations can be carried out using a parallel processing hardware in PC environment such as an INMOS transputer T-800 and Parallel-C [93, 94]. Though the calculations are carried out in parallel using this hardware, one need to take into account of the time taken for data transfer from the host computer (80286) to the T-800 and vice versa. Currently it requires to transfer one floating point value 9.6 ms, and for the present calculations, it is necessary to transfer 6 floating point values from PC to T-800 and two floating points from T-800 to PC. The total time taken for this operation is 96.8 ms. Hence the use of a transputer will result in a 33% reduction in processing time. To achieve the cycle time of 60 ms (maximum time per frame of image taken by the prototype AGV in camera mode with all the options in use), it is necessary to device a scheme to speedup the data transfer rate between the PC and the transputer. One approach is to use the DMA (direct memory access) mechanism with OCCAM and Parallel-C [95]. Preliminary results of this work indicated data transfer time of 0.05 ms per byte and this corresponds to a time of 0.4 ms for an 8-bit floating point value. This work is still in progress.

REFERENCES

1. J. Zygmont, "Guided Vehicles Set Manufacturing in Motion," High Technology, pp. 16-21, Dec. 1986.

2. J.M. Holland : "Basic Robotics Concepts," Howard W. Sams & Co., Indianapolis, USA, 1983.

3. G. Hammord : "Automated Guided Vehicle Systems (AGVs) at Work," IFS Publications Ltd, Bedford, England, 1986.

4. R.H. Hollier : "International Trends in Manufacturing Technology - Automated Guided Vehicle Systems," IFS Publications Ltd, UK, Springer-Verlag, New York, USA, 1987.

5. The American Society of Mechanical Engineers : "Safety Standards for Guided Industrial Vehicles," ASME/ANSI B56.5-1988, USA, 1988.

6. R. Hollis, "Newt : A Mobile, Cognitive Robot," *Byte Magazine*, Vol. 2, No. 6, pp. 30-45, June 1977.

7. Julliere, M., L. Marce, and H. Place, "A Guidance System for a Mobile Robots," *13th ISIR/Robots 7 Conference*, Chicago, pp. 13-58, 1983.

8. Borenstein, J. and Y. Koren, "Motion Control Analysis of a Mobile Robot," ASME *Journal of Dynamic Systems, Measurement and Control*, Vol.109, pp. 73-79, 1987.

9. Hongo, T., H. Arakawa, G. Sugimoto, K. Tange, and Y. Yamamoto, "An Automatic Guidance System of a Self-Controlled Vehicle," *IEEE Transactions on Industrial Electronics*, Vol. IE-34, No. 1, pp. 5-10, 1987.

10. Muir, P.F. and C.P. Neuman, "Kinematic Modeling of Automated Guided Vehicles," Technical Report No. CMU-RI-TR-86-12, The Robotic Institute, Carnegie-Mellon University, PA, 1986.

11. Cheng, R.M.H., Y. Courbet, M. Surpaceanu, P. Favreau and A. Fahim, "Investigation of an Automatic Guided Vehicle (AGV) Driven by Camera Vision," *Proceedings of the International Conference on Intelligent Autonomous Systems,* pp. 162-167, Amsterdam, The Netherlands, 1986.

12. A. Elfes, "Sonar Based Real-World Mapping and Navigation", *IEEE Journal of Robotics and Automation*, Vol. RA-3, No. 3, pp. 249-265, 1987.

13. Miller, G.L. and E.R. Wagner, "An Optical Rangefinder for Autonomous Robot Cart Navigation," *Proceedings of the IEEE Robotics and Automation*, Vol. RA-3, No.3, pp. 239-248, Raleigh, North Carolina, 1987.

14. Nelson, W.L. and I.J. Cox, "Local Path Control for an Automatic Vehicle," *Proceedings of the IEEE International Journal of Robotics and Automation,* pp. 1504-1510, Philadelphia, PA, 1988.

15. G.T. Wilfong, "Motion Planning for an Autonomous Vehicle," *Proceedings of the IEEE International Journal of Robotics and Automation*, pp. 529-533, Philadelphia, 1988.

16. I.J. Cox, "Blanche: Position Estimation for an Autonomous Robot Vehicle," *Proceedings of the IEEE/RSJ International Workshop on Robots and Systems (IORS)*, pp. 423-439, 1989.

17. H.P. Moravec, "The Stanford Cart and the CMU Rover," *Proceedings of the IEEE*, Vol. 71, No. 7, pp. 872-884, 1983.

18. S. Jonsson, "New AGV With Revolutionary Movement," *3rd International Conference on Automated Guided Vehicle Systems*, Stockholm, Sweden, 1985.

19. H.P. Moravec, "Autonomous Mobile Robots Annual Report - 1985," Robotics Institute Technical Report No. CMU-RI-MRL-86-1, Carnegie Mellon University, Pittsburgh, PA, 1986.

20. Agullo, J., S. Cardona, and J. Vivancos, "Kinematics of Vehicles With Directional Sliding Wheels", *Mechanisms and Machine Theory*, Vol. 22, No. 4, pp. 295-301, 1987.

21. Data Sheets on Motor-in-wheel Drive Units, Schabmuler Elektromotoren, Feldkirchen, West Germany and NDC Automation, Charlotte, North Carolina.

22. Denavit, J. and R.S. Hartenberg, "A Kinematic Notation for Lower-pair Mechanisms Based on Matrices," ASME *Journal of Applied Mechanics*, pp. 215-221, 1955.

23. R.P. Paul, "Robot Manipulators: Mathematics, Programming, and Control," The MIT Press, Cambridge, MA, 1981.

24. Muir, P.F. and C.P. Neuman, "Kinematic Modeling for Feedback Control of an Omnidirectional Mobile Robot," *Proceedings of the IEEE International Conference on Robotics and Automation*, Vol. 3, pp. 1772-1778, Raleigh, North Carolina, 1987.

25. Muir, P.F. and C.P. Neuman, "Kinematic Modeling of Wheeled Mobile Robots," *Journal of Robotic Systems*, Vol. 4, No. 2, pp. 281-340, 1987.

26. Sheth, P.N. and J.J. Uicker Jr., "A Generalized Symbolic Notation for Mechanisms," ASME *Journal of Engineering for Industry*, Series: B, Vol. 93, No.70, pp. 102-112, 1971.

27. Saha, S.K. and J. Angeles, "Kinematics and Dynamics of a Three-Wheeled 2-DOF AGV," *Proceedings of the IEEE International Conference on Robotics and Automation*, Vol. 3, pp. 1572-1577, Scottsdale, Arizona, 1989.

28. Cyril, X., R.M.H. Cheng and T.S. Sankar, "On the Dynamics of AGVs," *Proceed. of the 4th International Conference on CAD/CAM, Robotics and Factories of the Future*, Vol.2, pp. 264-273, India, 1989.

29. Alexander, J.C. and J.H. Maddocks, "On the Kinematics of Wheeled Mobile Robots," *The International Journal of Robotics Research*, Vol. 8, No. 5, Dec 1989.

30. J.R. Ellis, "vehicle Dynamics," Business Books, London, 1969.

31. J.Y. Wong, "Theory of Ground Vehicles," John Wiley & Sons, New York, USA, 1978.

32. Muir, P.F. and C.P. Neuman, "Dynamic Modeling of Multibody Robotic Mechanisms: Incorporating Closed-Chains, Friction, High-Pair Joints, and Unactuated and Unsensed Joints," *Proceedings of the IEEE International Conference on Robotics and Automation*, Vol. 3, pp. 1546-1551, Philadelphia, PA, 1988.

33. Feng, D. and B.H. Krogh, "Dynamic Steering Control of Conventionally-Steered Mobile Robots," *Proceedings of the IEEE International Conference on Robotics and Automation Conference*, Vol. 1, pp. 390-395, Cincinnati, Ohio, 1990.

34. Cheng, R.M.H. and M. Huang, "Dynamic Modelling of an AGV System," *Proceedings of the IASTED Conference*, Santa Clara, California, 1990.

35. M. Huang, "Dynamic Modeling and Simulation of an AGV (CONCIC-II)," Masters Thesis, Concordia University, Montreal, Canada, March 1991.

36. d'Andrea-Novel, B., G. Bastin and G. Camion, "Modelling and Control of Non Holonomic Wheeled Mobile Robots," *Proceedings of the IEEE International Conference on Robotics and Automation Conference*, Vol. 2, pp. 1130-1135, Sacramento, California, 1991.

37. K.J. Dowling, "Sensing and Guidance Techonologies for Autonomous Vehicles," *Japan-U.S.A. Symposium on Flexible Automation*, Osaka, Japan, pp. 317-320, July 14-18, 1986.

38. T. Tsumura, "Survey of Automated Guided Vehicle in Japanese Factory," *Proceedings of the IEEE International Conference on Robotics and Automation Conference*, pp. 1329-1334, 1986.

39. Takeda, T., A. Kato, T. Suzuki and M. Hosoi, "Automated Vehicle Guidance Using Spotmark," *Proceedings of the International Conference on IEEE Robotics and Automation Conference*, pp. 1349-1353, 1986.

40. Turk, M., D. Morgenthaler, K. Gremban, M. Marra, "Video Road-Following for the Autonomous Land Vehicle," *Proceedings of the IEEE International Conference on Robotics and Automation Conference*, Vol. 1, pp. 273-280, Raleigh, North Carolina, 1987.

41. Waxman, A.M., J.J. LeMoigne, L.S. Davis, B. Srinivasan, T.R. Kushner, E. Liang, T. Siddalingaiah, "A Visual Navigation System for Autonomous Land Vehicle," *IEEE Transactions on Robotics and Automation*, Vol. RA-3, No. 2, pp. 124-141, 1987.

42. Thorpe, C., M. Herbert, T. Kanade, S. Shafer, "Vision and Navigation for the Carnegie-Mellon Navlab," *IEEE Transactions on Pattern Analysis and Machine Intelligence*, Vol. 10, No. 3, pp. 362-373, 1988.

43. M. Herbert, "Building and Navigating Maps of Road Scenes Using an Active Sensor," *Proceedings of the IEEE International Conference on Robotics and Automation Conference*, pp. 1136-1142, Scottsdale, Arizona, 1989.

44. Crisman, J.D. and C.E. Thorpe, "UNSCARF, A Color Vision System for the Detection of Unstructured Roads," *Proceedings of the IEEE International Conference on Robotics and Automation Conference*, Vol. 3, pp. 2496-2501, Sacramento, California, 1991.

45. A.M. Flynn, "Combining Sonar and Infrared Sensors for Mobile Robot Navigation," *The International Journal of Robotics Research*, Vol. 7, No. 6, pp. 5-14, 1988.

46. Preciado, A., D. Meizel, A. Segovia, M. Rombaut, "Fusion of Multi-Sensor Data : A Geometric Approach," *Proceedings of the IEEE International Conference on Robotics and Automation Conference*, Vol.3, pp. 2806-2811, Sacramento, California, 1991.

47. Tani, K., N. Shirai, O. Matsumoto, K. Komoriya, "Autonomous Control of Mobile Robots," *Proceedings of the ISART*, pp. 317-324, 1991.

48. Nishide, K., M. Hanawa and T. Kondo, "Vehicle Position and Heading Measurement System Using Laser and Corner Cubes," *Japan-U.S.A. Symposium*

on Flexible Automation, Osaka, Japan, pp. 343-347, July 14-18, 1986.

49. Tsumura, T., M. Hashimoto, N. Fujiwara and K. Tanizawa, "Position and Heading Compensations for a Self-contained Measuring System of a Vehicle Travelling on Roadway," *Japan-U.S.A. Symposium on Flexible Automation*, Osaka, Japan, pp. 353-358, July 14-18, 1986.

50. Hoppen, P., T. Knieriemen and E. Puttkamer, "Laser-Radar based Mapping and Navigation for an Autonomous Mobile Robot," *Proceedings of the IEEE International Conference on Robotics and Automation*, Vol. 2, No. 948-953, Cincinnati, Ohio, 1990.

51. Giralt, G., R. Chatila, and M. Vaisset, "An Integrated Navigation and Motion Control System for Autonomous Multisensory Mobile Robots," *First International Symposium on Robotics Research*, MIT Press, pp. 191-214, 1984.

52. H.F. Durrant-Whyte, "Sensor Models and Multisensor Integration," *The International Journal of Robotics Research*, Vol. 7, No. 6, pp. 97-113, 1988.

53. McGillem, C.D. and T.S. Rappaport, "Infra-red Location system for Navigation of Autonomous Vehicles," *Proceedings of the IEEE International Conference on Robotics and Automation Conference*, pp. 1236-1238, Philadelphia, PA, 1988.

54. Julliere, M., L. Marce and H. Perrichot, "A Guidance Scheme for a

Vehicle Which has to Follow a Memorized Path," *Proceedings, the 2nd International Conference on Automated Guided Vehicle Systems, and 16th IRA Conference,* pp. 211-221, Chicago, 1983.

55. Nakano, E., N. Koyachi, Y. Agari and S. Hirooka, "Sensor System of a Guideless Autonomous Vehicle in a Flexible Manufacturing System," *Proceedings of the 15th International Symposium on Industrial Robots,* pp. 305-312, 1985.

56. L.E. Banta, "Advanced Dead Reckoning Navigation for Mobile Robots," Ph.D Dissertation, Georgia Institute of Technology, Atlanta, 1987.

57. G. Culley and R. Baldur, "Experiments with a Free Wheel Approach to AGV Navigation," *ASME Computers in Engineering Conference and Exhibit,* San Francisco, California, Aug. 1988.

58. C. Ming Wang, "Location Estimation and Uncertainty Analysis for Mobile Robots," *Proceedings of the IEEE International Journal of Robotics and Automation,* pp. 1230-1235, Philadelphia, PA, 1988.

59. Kanayama, Y., Y. Kimura, F. Miyazaki, and T. Noguchi, "A Stable Tracking Control Method for an Autonomous Mobile Robot," *Proceedings of the IEEE International Conference on Robotics and Automation Conference,* Cincinnati, Ohio, pp. 384-389, Cincinnati, Ohio, 1990.

60. L. E. Banta, " Self Tuning Navigation Algorithm," *Proceedings of the IEEE International Conference on Robotics and Automation Conference,* pp.

1313-1314, Philadelphia, PA, 1988.

61. Okazaki, M., H. Tomikawa, M. Sudare and K. Terada, "New Guidance System for Automated Navigational Vehicle," *Japan-U.S.A. Symposium on Flexible Automation*, Osaka, Japan, pp. 321-329, July 14-18, 1986.

61. O. Amidi, "Integrated Mobile Robot Control," Robotics Institute Technical Report No. CMU-RI-TR-90-17, Carnegie Mellon University, Pittsburgh, PA, May 1990.

63. Kuritsky, M.M. and M.S. Goldstein, "Inertial Navigation," *Proceedings of the IEEE*, Vol. 71, No. 10, pp. 1156-1176, 1983.

64. Cox, I.J. and G.T. Wilfong : "Autonomous Robot Vehicles," Springer-Verlag, U.S.A, 1990.

65. Bhanu, B., B. Roberts and J. Ming, "Inertial Navigation Sensor Integrated Motion Analysis for Obstacle Detection," *Proceedings of the IEEE International Conference on Robotics and Automation*, Vol. 2, No. 936-941, Sacramento, California, 1990.

66. Kanayama, Y., Y. Kimura, F. Miyazaki and T. Noguchi, "A Stable Tracking Control Method for an Autonomous Mobile Robot," *Proceedings of the IEEE International Conference on Robotics and Automation Conference*, Vol. 1, pp. 384-389, Sacramento, California, 1990.

67. Hemami, A., M.G. Mehrabi, and R.M.H. Cheng, "A New Control Strategy for Tracking in Mobile Robots and AGV's," *Proceedings of the IEEE International Conference on Robotics and Automation*, Ohio, pp. 1122-1127, Sacramento, California, 1990.

68. Hemami, A., M.G. Mehrabi, and R.M.H. Cheng, "Synthesis of an Optimal Control Law for Path Tracking in Mobile Robotics," Internal Report, Center for Industrial Control, Concordia University, 1990.

69. Hemami, A., M.G. Mehrabi, and R.M.H. Cheng, "Steering Control in Mobile Robots with Left and Right Independent Traction Wheels," Internal Report, Center for Industrial Control, Concordia University, 1990.

70. Hatwal, H. and E.C. Milkulcik, "An Optimal Control Approach to the Path Tracking Problem for an Automobile," *Transactions of the CSME*, Vol. 10, No. 4, pp. 233-241, 1986.

71. Wessell, D.E., M. Chow and R.K. Cavin III, "The Trajectory Problem for a Mobile Robot with Bounded Input," *IASTED Conference on Adaptive Control and Signal Processing*, New York, U.S.A, pp. 90-92, Oct. 10-12, 1990.

72. Lin, Z., V. Zeman and R.V. Patel, "On-line Robot Trajectory Planning for Catching a Moving Object," *Proceedings of the IEEE International Conference on Robotics and Automation Conference*, pp. 1726-1731, Scottsdale, Arizona, 1989.

73. Robert C. Yates : "Curves and Their Properties," The National Council of Teachers Mathematics, 1974.

74. Kennedy, J.B. and Adam M. Neville : "Basic Statistical Methods for Engineers & Scientists," Harper & Row Publishers, pp. 225-318, 1976.

75. B.K. Paul Horn : "Robot Vision," The MIT Press, McGraw-Hill Company, U.S.A, pp. 461-462, 1986.

76. Larson, R.E. and R.P. Hostetler, "Calculus With Analytical Geometry," D.C. Heath and Company, U.S.A, pp. 177-181, 196-200, & 477-486, 1979.

77. DC Motors Speed Controls Servo Systems, An Engineering Handbook by Electro-Craft Corporation, Minneapolis, U.S.A, Fifth Edition, 1980.

78. Handbook for Applying Low Inertia PM DC Motors, Pacific Scientific, Illinois, U.S.A, 1984.

79. The LM628 Precision Motion Controller Chip Data Sheets, The National Semiconductor, U.S.A, 1988.

80. General Purpose Motion Control IC HCT-1000, Opto-Electronics Designers Catalog, Hewlett Packard Company, pp. 443-446, 1988-89.

81. G.L. Kmetz, "Program a Motion Controller with a PC-based Evaluator," Electronic Design, pp. 107-111, May 1988.

82. Steven Hunt, "LM628 Programming Guide," Application Note No. 693, National Semiconductor, April 1990.

83. David Dale, "LM628/Lm629 User Guide," Application Note No. 706, National Semiconductor, August 1990.

84. PWM Servo Amplifiers Users and Operating Manual, Galil Motion Control, California, U.S.A, 1988.

85. Idetix Digital Vision System, Operator's Manual, Micron Technology Incorporated, Idahom U.S.A, 1986.

86. L.C. Eggebrecht : Interfacing to the IBM Personal Computer, Howard W. Sams & Co, A Division of Mcmillan Inc., 1987.

87. Axelson, J. and J.Hughes, "A Wireless Data Link," Modern Electronics, pp. 18-27, & 91, Sept. 1988.

88. Kantronics All Mode Communicator Users Manual, Kantronics RF Data Communication Specialists, Kansas, U.S.A, October 1987.

89. Sonar Ranging Module, Data Sheets from Texas Instruments, Texas, U.S.A, 1983.

90. S. Ciarcia, "An Ultrasonic Ranging System," Byte Magazine, pp. 113-123, Oct. 1984.

91. Ramesh Rajagopalan and G. Huard, "System Report on CONCIC-2 AGV : Design, Control and Theory of Operation," Internal Report No. CIC-0024, Centre for Industrial Control, Concordia University, Montreal, Canada, June 1989.

92. Ramesh Rajagopalan and G. Huard, "Final Report on CONCIC-II AGV Employing Binary Camera Vision and Hierarchical Steering Control : Design, Theory, Control and Results," Internal Report No. CIC-0038, Centre for Industrial Control, Concordia University, Montreal, Canada, Jan. 1991.

93. Ramesh Rajagopalan, R.M.H. Cheng and S.C.L. Poon, "Parallel Computation of Robot Dynamics using Transputers", ISMM International Conference on Parallel and Distributed Computing and Systems, New York, Oct. 1990.

94. Poon, S.C.L., R.M.H. Cheng and Ramesh Rajagopalan, "Interrupt Driven File Server for Transputers", North American Transputer Users Group Meeting-4, Ithaca, Oct. 1990.

95. Jayashree Rajagopalan, "Data Transfer from PC to Transputer (T-800) using DMA Mechanism and OCCAM," Internal Report, Center for Industrial Control, Concordia University, 1991 (in preparation).

96. Cheng, R.M.H. and Ramesh Rajagopalan, "Kinematics of an Automatic Guided Vehicle with an Inclined Steering Column", *ASME Computers in Engineering Conference and Exhibit*, San Francisco, California, Aug. 1988.

97. Cheng, R.M.H., Ramesh Rajagopalan and T.S. Sankar, "System Architecture of an Automatic Guided Vehicle", *Fourth International Conference on CAD, CAM, Robotics and Factories of the Future, ISPE*, India, Dec. 1989.

98. Cheng, R.M.H. and Ramesh Rajagopalan, "Ambidextrous Automatic Guided Vehicle", *submitted to the Canadian Patents Office*, 1989.

99. Cheng, R.M.H. and Ramesh Rajagopalan, "Criteria for Kinematic Control of AGVs with Steered Driving Wheels", *submitted to the Journal of Robotic Systems*, 1990.

100. Ramesh Rajagopalan and R.M.H. Cheng, "An Autonomous Vehicle Using Binary Digitizing Camera Vision : Design and Experiments", *submitted to the IEEE Transactions on Industrial Electronics*, 1991.

101. Ramesh Rajagopalan and R.M.H. Cheng, "Architecture of Operating System Software of an Autonomous Vehicle", *ASME Computers in Engineering Conference and Exhibit*, Santa Clara, California, Aug. 1991.

102. Ramesh Rajagopalan, R.M.H. Cheng and G. Huard, "Multi-axis Motion Controller for AGVs and Robots", *ASME Computers in Engineering Conference and Exhibit*, Santa Clara, California, Aug. 1991.

103. Ramesh Rajagopalan and R.M.H. Cheng, "Binary Camera Vision for AGV Navigation", *Fourth World Conference on Robotics Research, RI of the SME*, Pittsburgh, Sept. 17-19, 1991.

APPENDIX - A

MATHEMATICAL FORMULATIONS AND DISCUSSIONS

APPENDIX - A

MATHEMATICAL FORMULATIONS AND DISCUSSIONS

A.1 Procedure to Compute Inverse Transformations

Since the transformations are homogeneous, the inverse transformations can be computed using the scheme described by Paul [23], and is presented below.

$$ {}^{A}T_{B} = \left[\begin{array}{cccc} n_x & o_x & a_x & p_x \\ n_y & o_y & a_y & p_y \\ n_z & o_z & a_z & p_z \\ \hline 0 & 0 & 0 & 1 \end{array}\right] \qquad \text{(A.1.1)} $$

And the inverse of this transformation is

$$ \left[{}^{A}T_{B}\right]^{-1} = \left[\begin{array}{cccc} n_x & n_y & n_z & -(p.n) \\ o_x & o_y & o_z & -(p.o) \\ a_x & a_y & a_z & -(p.a) \\ 0 & 0 & 0 & 1 \end{array}\right] \qquad \text{(A.1.2)} $$

Reference Frame and Contact Point Transformations

It should be noted that the orientation of the frame R relative to $\bar{R}$ is given by the angles λ, ε and $\dot{\theta}_r$ about the X, Y and Z axes respectively. The position transformation for ${}^{\bar{R}}\Phi_{R}$ is given by

$$ {}^{\bar{R}}\Phi_{R} = \mathrm{Rot}(\theta_r, \varepsilon, \lambda) = \mathrm{Trans}(r_x, r_y, r_z)\ \mathrm{Rot}(Z, \theta_r)\ \mathrm{Rot}(Y', \varepsilon)\ \mathrm{Rot}(X'', \lambda) $$

$$\begin{bmatrix} C_{\theta r}\, C_{\varepsilon} & C_{\theta r} S_{\varepsilon} S_{\lambda} - S_{\theta r} C_{\lambda} & C_{\theta r} S_{\varepsilon} C_{\lambda} + S_{\theta r} S_{\lambda} & r_x \\ S_{\theta r}\, S_{\varepsilon} & S_{\theta r} S_{\varepsilon} S_{\lambda} + C_{\theta r} C_{\lambda} & S_{\theta r} S_{\varepsilon} C_{\lambda} - C_{\theta r} S_{\lambda} & r_y \\ -S_{\varepsilon} & C_{\varepsilon} S_{\lambda} & C_{\varepsilon}\, C_{\lambda} & r_z \\ 0 & 0 & 0 & 1 \end{bmatrix} \qquad \text{(A.1.3)}$$

Where r_X, r_Y and r_Z are equal to zero since the two coordinate frames are located at the same origin.

The position transformation $\bar{c}_{\Phi_c}$ for the contact point is given by a rotational transformation as below.

$$\bar{c}_{\Phi_c} = \begin{bmatrix} C_{\theta} & -S_{\theta} & 0 & c_x \\ S_{\theta} & C_{\theta} & 0 & c_y \\ 0 & 0 & 1 & c_z \\ 0 & 0 & 0 & 1 \end{bmatrix} \qquad \text{(A.1.4)}$$

As in the previous case here also c_X, c_Y and c_Z are equal to zero. Differentiating the position transformation of equation (A.1.3) with respect to time and applying the initial condition $\theta_r = \varepsilon = \lambda = 0$, results in the velocity transformation $\bar{R}\dot{\Phi}_R$

$$\bar{R}\dot{\Phi}_R = \begin{bmatrix} 0 & -\dot{\theta}_r & -\dot{\varepsilon} & v_{rx} \\ \dot{\theta}_r & 0 & -\dot{\lambda} & v_{ry} \\ \dot{\varepsilon} & \dot{\lambda} & 0 & v_{rz} \\ 0 & 0 & 0 & 0 \end{bmatrix} \qquad \text{(A.1.5)}$$

The velocity transformation for the contact point transformation $\bar{c}_{\dot{\Phi}_c}$ is obtained by differentiating the position transformation of equation (A.1.4). Substituting $\theta_c = 0$ results in

$$\bar{c}_{\dot{\Phi}_c} = \begin{bmatrix} 0 & -\dot{\theta}_c & 0 & v_{cx} \\ \dot{\theta}_c & 0 & 0 & v_{cy} \\ 0 & 0 & 0 & v_{cz} \\ 0 & 0 & 0 & 0 \end{bmatrix} \qquad \text{(A.1.6)}$$

A.2 Effect of Castor Angle

The steering columns of some vehicles are inclined in the fore and aft direction. This angle is referred to as the castor angle in the literature. This agnle is given to provide directional stability for the steered wheel if in case of any external distrurbances while the castor is in motion. This external disturbance may be due to wheel steering or side forces due to uneven road conditions. Under these situations, it is necessary that the wheel plabe be maintained to be parallel to the direction of motion. The castor angle is termed as leading or trailing one depending upon whether the angle is positive or negative. This choice (positive or negative) is based on whether the front wheel or the rear wheel is powered or driving. The CONCIC-II AGV considered in this thesis is of this type. In the case of rear wheel driven vehicles, the castor angle is negative, i.e. the point of intersection of the pivot axis of the castor with the ground lies ahead of the contact point of the castor. This gives negative trail. On the otherhand, if the front wheel is both driving and steered, the castor angle is positive, and the trail is positive. In this case the point of

intersection of the pivot axis trails the wheel contact point.

Figure. A.1a shows the situation when the rear wheel is driving and the front wheel is either a steering wheel or a caster, with an offset between the point of contact and the pivot axis. In this figure, b is the contact point/patch center and a is the steering axis/pivot axis intersection point. The motion along the ground is indicated by the velocity vector V whereas the reaction force opposing the motion is represented by R. Figure. A.1b illustrates the free body diagram of the system under no disturbances. Figure. A.1c is for the case when the wheel is disturbed and the wheel makes an angle θ with respect to the direction of travel. At this time, the intersection point remains at the same location a, whereas the contact moves and is shown by $\bar{b}$. The reaction force R acts through the new contact point $\bar{b}$, but still parallel to the direction of travel. Since the points a and $\bar{b}$ are separated by a distance x, the force R creates a moment (M) in the clockwise direction. The magnitude of this couple is given by Rx. This moment brings back the wheel to be parallel to the direction of travel. Hence, it can be concluded that if the castor angle was not provided, the steered wheel will be wandering in response to any disturbance that acts on it, and could alter the path the vehicle is expected travel along.

A.3 Method of Least Sum of Error Square Solution

In this appendix, mathematical formulations to compute the elements of the equation of the track are presented. The equation of the track considered in chapter 5 for analysis is of the form

$$y = m\,x + c \qquad \text{(A.3.1)}$$

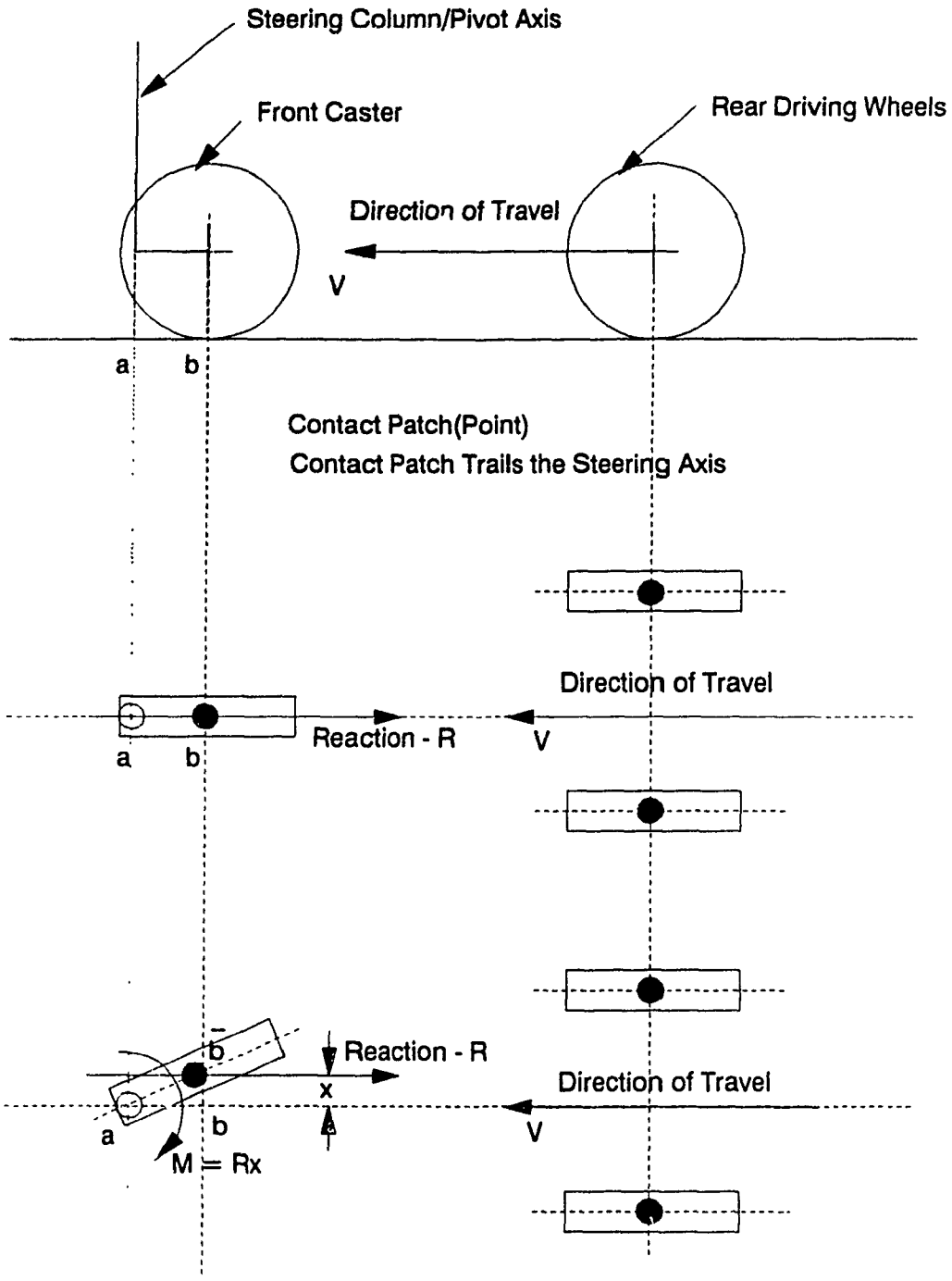

Figs. A.1a,b,c Caster Action for Vehicles with Rear Wheel Driving

In this equation, m is the slope of the line and c is the offset, y is the image row and x is the column location of the image. Since the camera image is composed of more than two rows of image, there will be more number of y and x values than the number of unknown parameters. The edges of the image of the track received from the camera may not be a true straight line due to noise and resolution of the pixels to distance ratio. Consequently, it is necessary to consider more number of rows of image data to compute the unknowns and a least sqaured error solution method has to be applied to solve the system of equations with more equations and less unknowns. The general form of the equation is

$$\left\{ y_1 \;\; y_2 \;\; \ldots\ldots\ldots \;\; y_n \right\}^T = \begin{bmatrix} x_1 & 1 \\ x_2 & 1 \\ . & . \\ . & . \\ x_n & 1 \end{bmatrix} \begin{Bmatrix} m \\ c \end{Bmatrix} \qquad \text{(A.3.2)}$$

i.e. $$\vec{Y} = \vec{X}[A] \qquad \text{(A.3.3)}$$

Here y_1, y_2, ..., y_n represent the rows, x_1, x_2, ..., x_n are the corresponding column locations of the image center. The superscript T is used to represent the transpose of the column vector. The Least Sum of Error Square Solution (LSES) can be derived using equation (A.3.3) as

$$\vec{Y} = \vec{X}[A] = A^T X^T = M B \qquad \text{(A.3.4)}$$

Here $M = A^T$ and $B = X^T$. Since the objective is to compute the matrix M, it

is given by

$$M = y\ B^{-1} \tag{A.3.5}$$

Equation (A.3.5) results in an unique solution if and only if B is a square matrix. Since the matrix B is a non-square matrix, it is necessary to compute the error E as

$$E = y - M\ B \tag{A.3.6}$$

The objective function is to minimize the error E. The sum of the square of the errors is

$$\Sigma\ |\ e_1\ |^2 = \Sigma\ e_1^T\ e_1 \tag{A.3.7}$$

i.e. Trace $(E^T\ E)$ = Trace $(\ (y-MB)^T\ (y-MB)\ )$

$$= \text{Trace}\ (y^Ty - B^TM^Ty - y^TMB + B^TM^TMB) \tag{A.3.8}$$

Differentiating equation (A.3.8) with respect to M, results in

$$\frac{d}{d\bar{M}}(\text{Trace}\ (E^TE)) = -yB^T - yB^T + (B^TM^T)^T\ B^T + (B^TM^T)^TB^T \tag{A.3.9}$$

From this equation it can be inferred that the left hand side of the equation (A.3.9) is zero, if $yB^T = MBB^T$, i.e.

$$M = yB^T(BB^T)^{-1} = y\ \left[B^T(BB^T)^{-1}\right] = y\ \Delta(B) \tag{A.3.10}$$

Where $\Delta(B)$ is the pseudo-inverse of B. Substituting M and B from equation (A.3.4), expression for A is obtained as

$$A^T = y\,\Delta(X^T) = y(X^T)^T\,(X^T(X^T)^T)^{-1} = y\,X\,(X^TX)^{-1}$$

i.e.
$$A = (X^TX)^{-1}\,X^T\,y \qquad \text{(A.3.11)}$$

Hence the unknowns m and c can be computed by solving the equation (A.3.11) after making the appropriate substitutions. Substituting the matrix X and the column vector y from equation (A.3.1) and simplifying, the unknowns c and m are computed from

$$c = \frac{\sum x^2 \sum y - \sum x \sum xy}{n\sum x^2 - \left(\sum x\right)^2} \qquad \text{(A.3.12)}$$

$$m = \frac{n\sum xy - \sum x \sum y}{n\sum x^2 - \left(\sum x\right)^2} \qquad \text{(A.3.13)}$$

APPENDIX - B

MECHANICAL COMPONENTS DESIGN DETAILS

APPENDIX - B

MECHANICAL COMPONENTS DESIGN DETAILS

B.1 Introduction

It has been mentioned in Chapter 6 that the AGV has been designed to provide maximum flexibility in order to change the wheel base configuration as and when desired. The objective of this feature is to experimentally verify the best possible wheel base configuration that can perform a particular industrial task.

Referring to Fig. 6.3, it can be seen that the structure of the AGV has been divided into two levels. The lower level houses the wheel drive units, the batteries, the dc to ac inverter and the servo amplifiers. The front end of the upper level has the system computer and the control panel. The rear half of the upper level is left empty so that materials can be transported for testing the load carrying capacity of the AGV. The camera and the lights are located at the front end of the vehicle.

B.2 Lower Level Frame Weldment

The lower level of the weldment has been divided into 3 compartments along the longitudinal and lateral directions respectively, thereby providing 9 equal cells. Figure. B.1 shows plan and elevation views of the lower level showing the cells. The circles shown in the top view indicates the maximum limit reached when the steering arrangment is used. These cells have provision for mounting a wheel mounting bracket. These are the brackets to which the motor-in-wheel drive units (described in chapter 6) are attached. One such bracket is presented in Fig. B.2. There are two kinds of brackets,

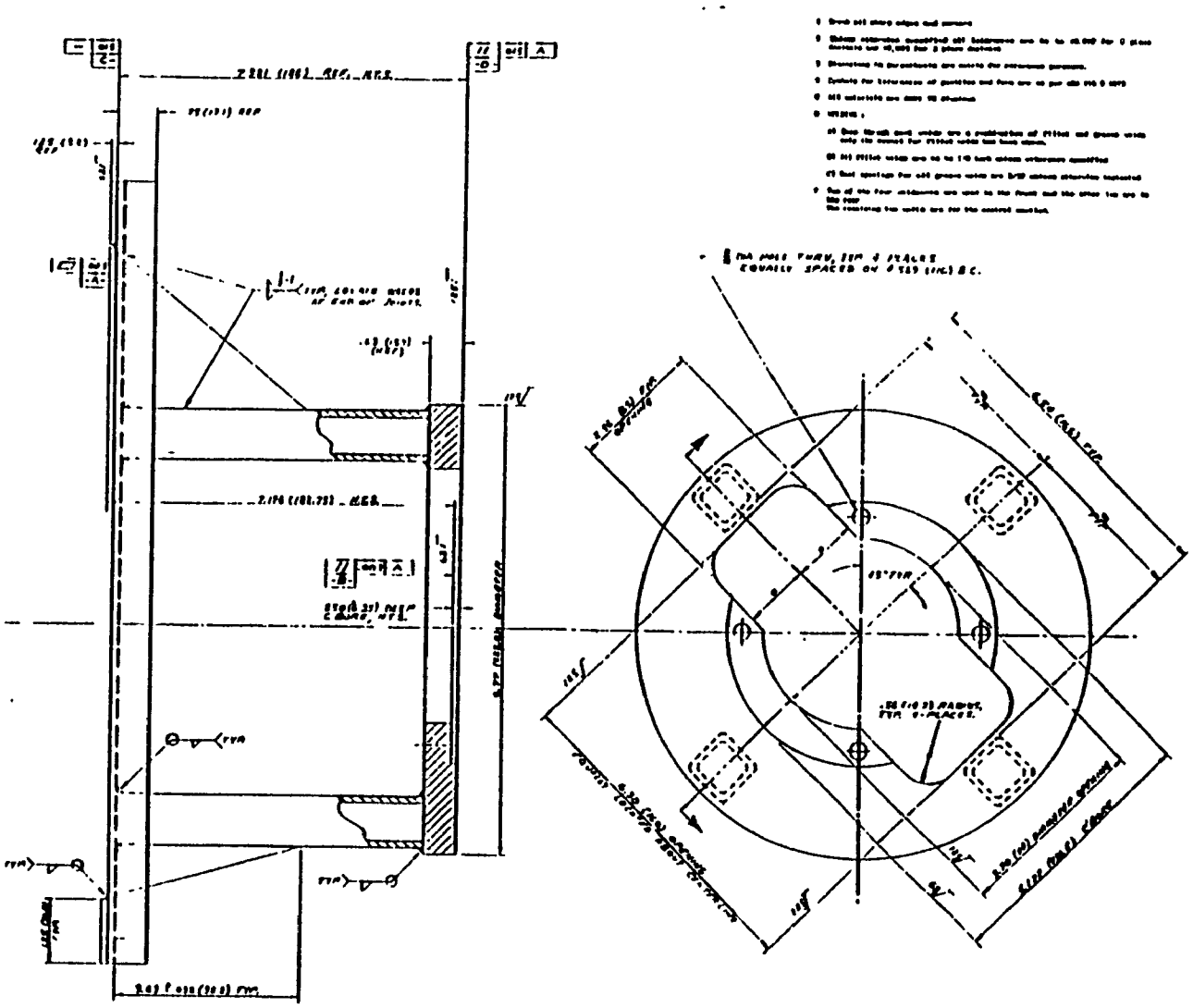

Fig. B.1 Lower Level Weldment (Plan and Elevation Views)

centered and offsetted wheel mounting area with respect to the top ends of the bracket that attaches with the lower level frame. The centered brackets are for mounting the wheels at the middle compartment and those with the offsets are for the extreme compartments. An assembly view with driving wheel sets is shown in Fig. B.3. Idling casters can also be attached with these brackets. Caster mounting arrangement is illustrated in Fig. B.4.

B.3 Mass Center Calculation

Since the distribution of loads in the vehicle is not totally balanced, the mass center does not coincide with the geometric center. As a result of this, some wheels are loaded more heavily than others. Hence, it is necessary to compute the actual load distribution on each wheel using the layout of the AGV and rearrange the components of the AGV in order to achieve equal distribution of loads on wheels.

The location of various components of the AGV is shown in Fig. B.5. With this arrangement, the mass center location is calculated as follows. The overall dimension of the AGV is 1115 mm long, 781 mm wide and 600 mm high. The geometric center (x, y) is at (557.5, 390.5) mm. The mass centers of various components relative to the origin are given below. The origin is chosen at the left hand bottom corner of the AGV and is shown in Fig. B.5. The mass centers are

Mass center of battery-1 is $(x_1, y_1) = (182.5, 125)$

Mass center of battery-2 is $(x_2, y_2) = (932.5, 656)$

Mass center of computer is $(x_3, y_3) = (830.0, 230)$

Mass center of servo-amplifier $(x_4, y_4) = (932.5, 125)$

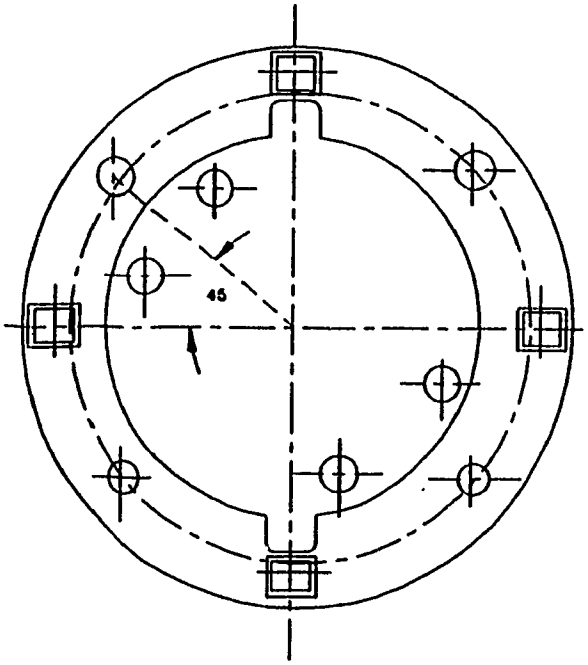

Fig. B.2 Wheel Mouting Brackets for the Motor-in-wheel Drive Units

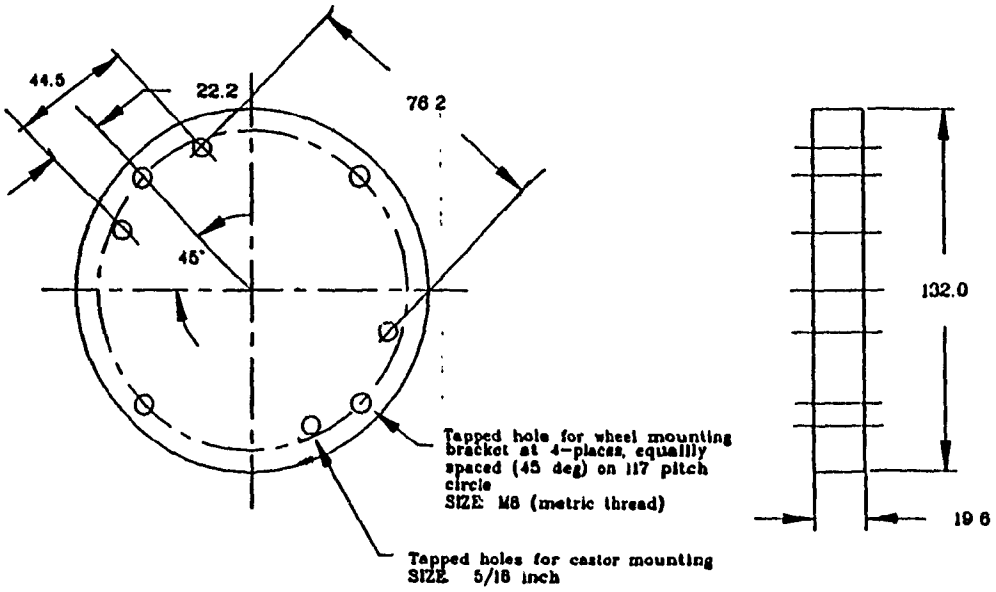

Fig. B.3 Lower Level Weldment with Motor-in-wheel Drive Units

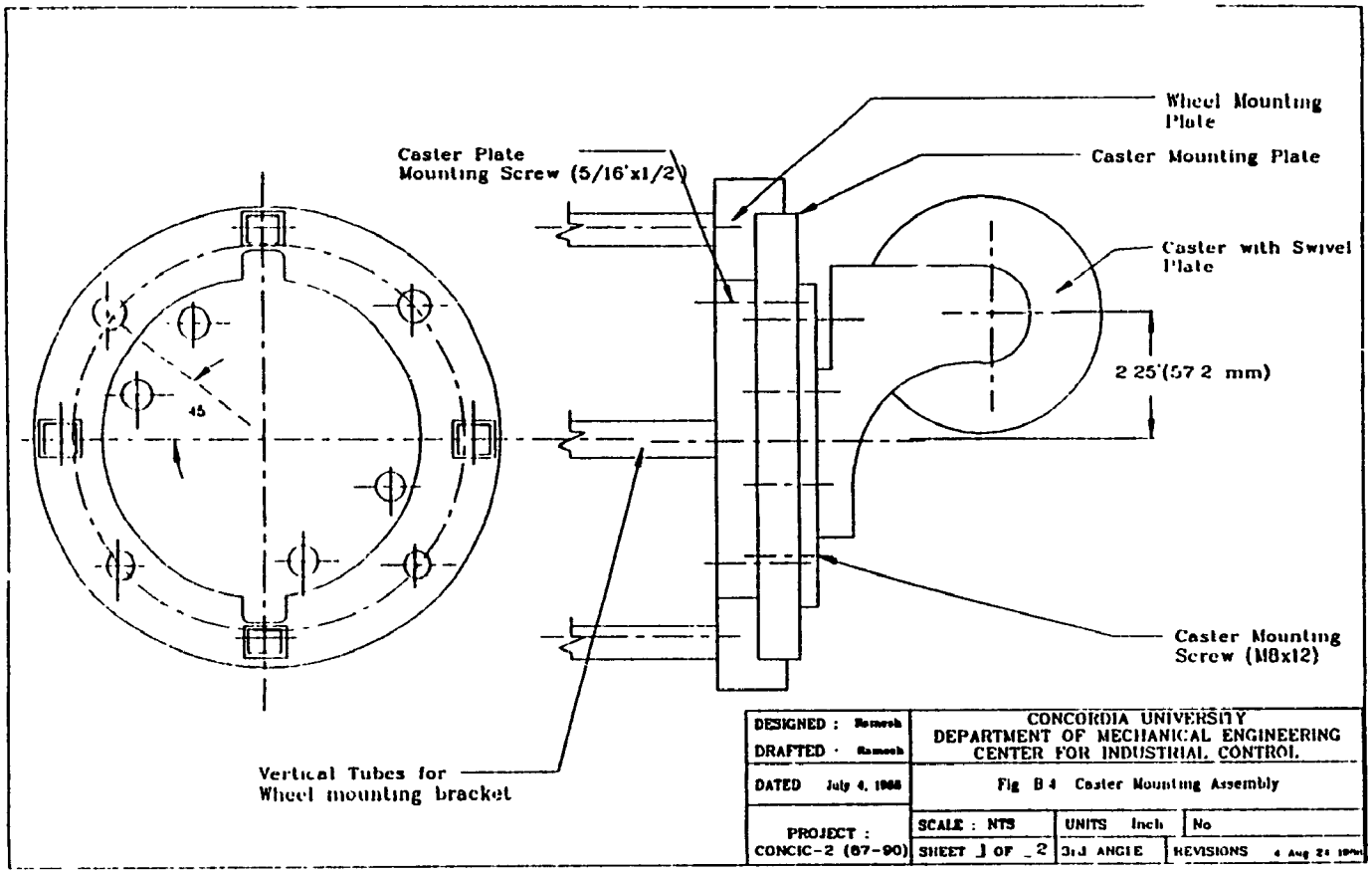

Fig. B.4 Caster Mounting Arrangement

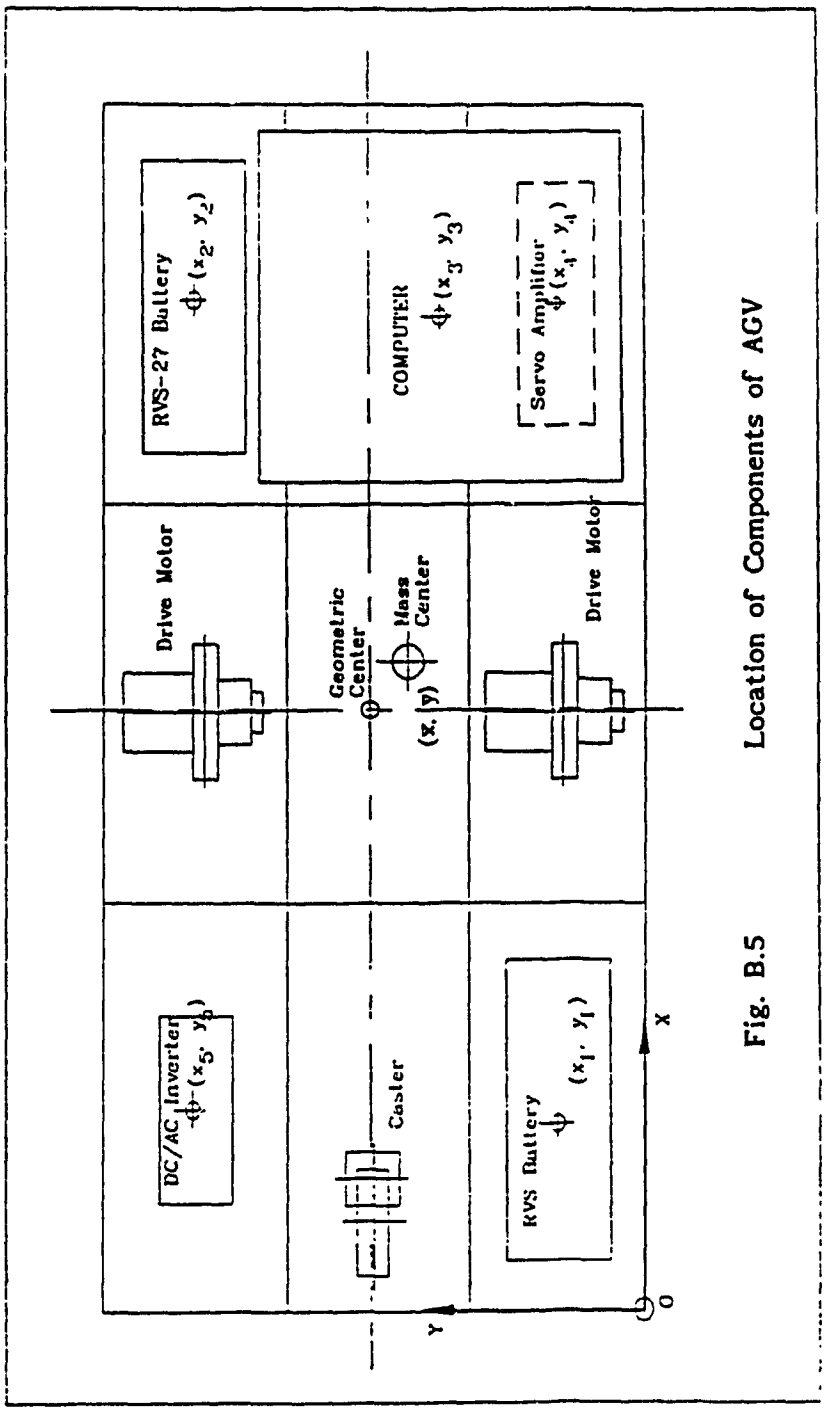

Fig. B.5 Location of Components of AGV

Mass center of UPS unit $(x_5, y_5) = (182.5, 656)$

Taking moments about the origin results in

$$W \bar{x} = \sum_{i=1}^{5} w_i x_i \tag{B.1}$$

$$W \bar{y} = \sum_{i=1}^{5} w_i y_i \tag{B.2}$$

And W is the total mass acting at the mass center $(\bar{x}, \bar{y})$ and is given by

$$W = \sum_{i=1}^{5} w_i \tag{B.3}$$

Substituting the values of (x_i, y_i) and w_i for i = 1, 2,..,5, the computed mass centers are

$$\bar{x} = 587.8 \text{ mm} \quad \text{and } \bar{y} = 376.0 \text{ mm} \tag{B.4}$$

Though the geometric center and the mass center do not coincide, the mass distribution chosen here provides a mass center which is very close to the geometric center.

B.4 Driving Arrangement

The driving motor is a permanent magnet (PM) brush type 24 volts dc motor. The armature houses a commutator and feedback elements on one end, and and a speed reduction unit at the other end. The specifications of the driving arrangement is presented in Table B.3. The motor-in-wheel drive unit from the manufacturer does not have provisions to attach an encoder and it

Lower level frame	1 unit	28.5 lb
Upper level frame	1 unit	12.0 lb
Batteries with the holders	2 units	120.0 lb
Wheel-drive units	2 units	38.0 lb
Wheel Mounting brackets	4 units	24.0 lb
Computer (IBM-AT)	1 unit	30.0 lb
Servo-amplifiers	2 units	6.0 lb
UPS- power supply	1 units	15.0 lb
Total Weight		273.5 lb

Table B.1 Overall System Weight Analysis

Standard tube size used : 1" x 1" rounded sq. tube: 1/8" thick
Tube Material : Aluminum (T6061)
Tube weight : 10 pounds for 20 ft length.

a)	78.1 cm long tube	8 units	624.8 cm
b)	111.8 cm long tube	4 units	447.2 cm
c)	29.0 cm long tube	12 units	348.0 cm
d)	31.0 cm long tube	4 units	164.0 cm
e)	14.5 cm long tube	4 units	58.0 cm
f)	17.5 cm long tube	4 units	70.0 cm
	Total length used		1710.0 cm

Tube length used = 1710 cm = 56.102'
Total weight of lower level = 28.05 lb.

Table B.2 Lower Level Frame Weight Estimation

Gear ratio of the speed reducer	1:9.9
Maximum motor speed	1350 rpm
Maximum wheel speed	145 rpm
Maximum linear speed	1.2 m/s
Wheel diameter	150 mm
Tire width	25 mm
Maximum axial load on tire	200 Kg
Tire material	rubber
Tire static friction coefficient	0.02 Kg/ton

Table B.3 Driving Arrangement Specification

Rated Voltage	V	24 Volts
Maximum Power Input	P_{in}	198 Watts
Maximum Power Output	P_{out}	130 Watts
Continuous current	I_c	9.00 Amp
Starting (peak) current	I_p	45.5 Amp
Armature Inductance	L_a	4.7 mH
Armature Resistance	R_a	0.602 Ω

Table B.4 Electrical Characteristics of the Driving Motor

provides only for a tachometer. Hence a collar and an attachment are designed for providing an encoder feedback. This assembly is shown in Fig. B.6.

B.5 Drive Motor Parameters Calculations

From the motor characteristic curves shown in Fig. B.7, the motor torque constant (K_t) is computed.

$$\text{Torque Constant } K_t = \frac{3 - 1.35 \text{ Nm}}{26.5 - 12 \text{ A}} = 0.114 \text{ Nm / A} \qquad \text{(B.5)}$$

The relationships between the motor torque and the voltage, and speed are given by

$$\frac{22.5 - 0 \text{ V}}{0 - 3.2 \text{ Nm}} = -7.031 \text{ Volts / Nm} \qquad \text{(B.6)}$$

$$\frac{1250 - 500 \text{ rpm}}{1 - 2.82 \text{ Nm}} = -412.088 \text{ rpm / Nm} \qquad \text{(B.7)}$$

From these relations the velocity constant K_e has been estimated to be

$$K_e = \frac{7.031 \text{ V/Nm}}{-412.088 \text{ rpm/Nm}} = 0.0171 \text{ Volt/rpm} = 0.163 \frac{\text{Volt}}{\text{rad/s}} \qquad \text{(B.8)}$$

The stall torque (T_s), static friction torque (T_f) and the no load speed (N_f) of the motor are obtained from Fig. B.7 and are

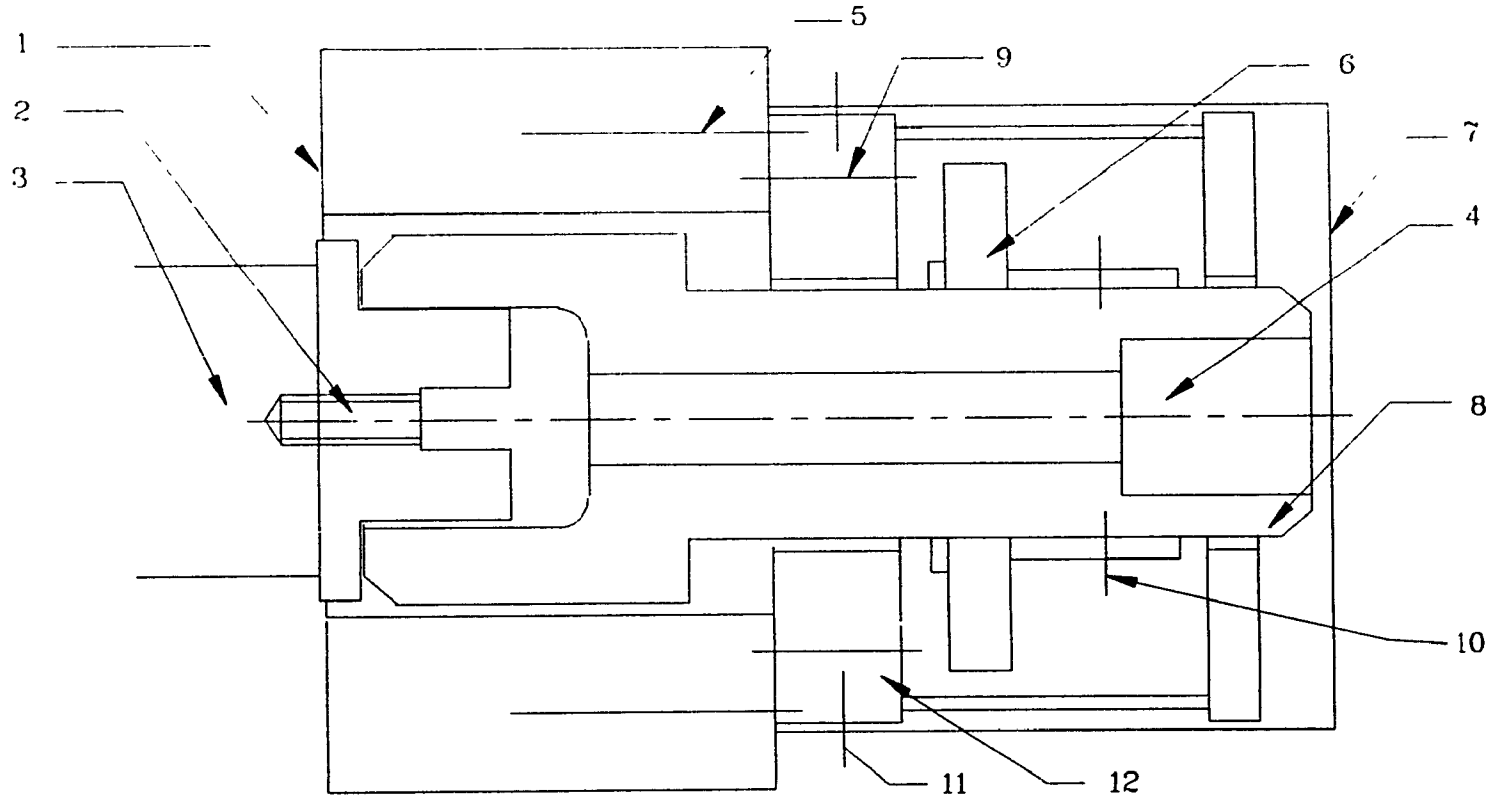

1) Drive Motor End Plate (New one-Part No
2) Tapped Hole on the Armature Shaft
3) Motor Armature Shaft
4) Encoder Mounting Adaptor -lock screw
5) Base plate_Encoder Assembly
6) Encoder Disc
7) Encoder Outer Casing (cover)
8) Sleeve for Encoder Mounting
9) 3/16" Screw for Encoder
10) Encoder Mounting Screw
11) Casing Mounting Screw
12) Encoder Led Assembly

DESIGNED BY RR & WF DRAFTED BY RAMESH	CONCORDIA UNIVERSITY DEPARTMENT OF MECHANICAL ENGINEERING CENTER FOR INDUSTRIAL CONTROL		
DATED 11-10-1988 Material	Fig B 6 Drive Motor Encoder Mounting Arrangement		
PROJECT NAME & PERIOD CONCIC-2 (1987-90)	SCALE 4 · 1 UNITS MM	SHEET OF	Drg. No REVISIONS 2 on June 20, 1989

Fig B.6 Drive Motor Encoder Mounting Arrangement

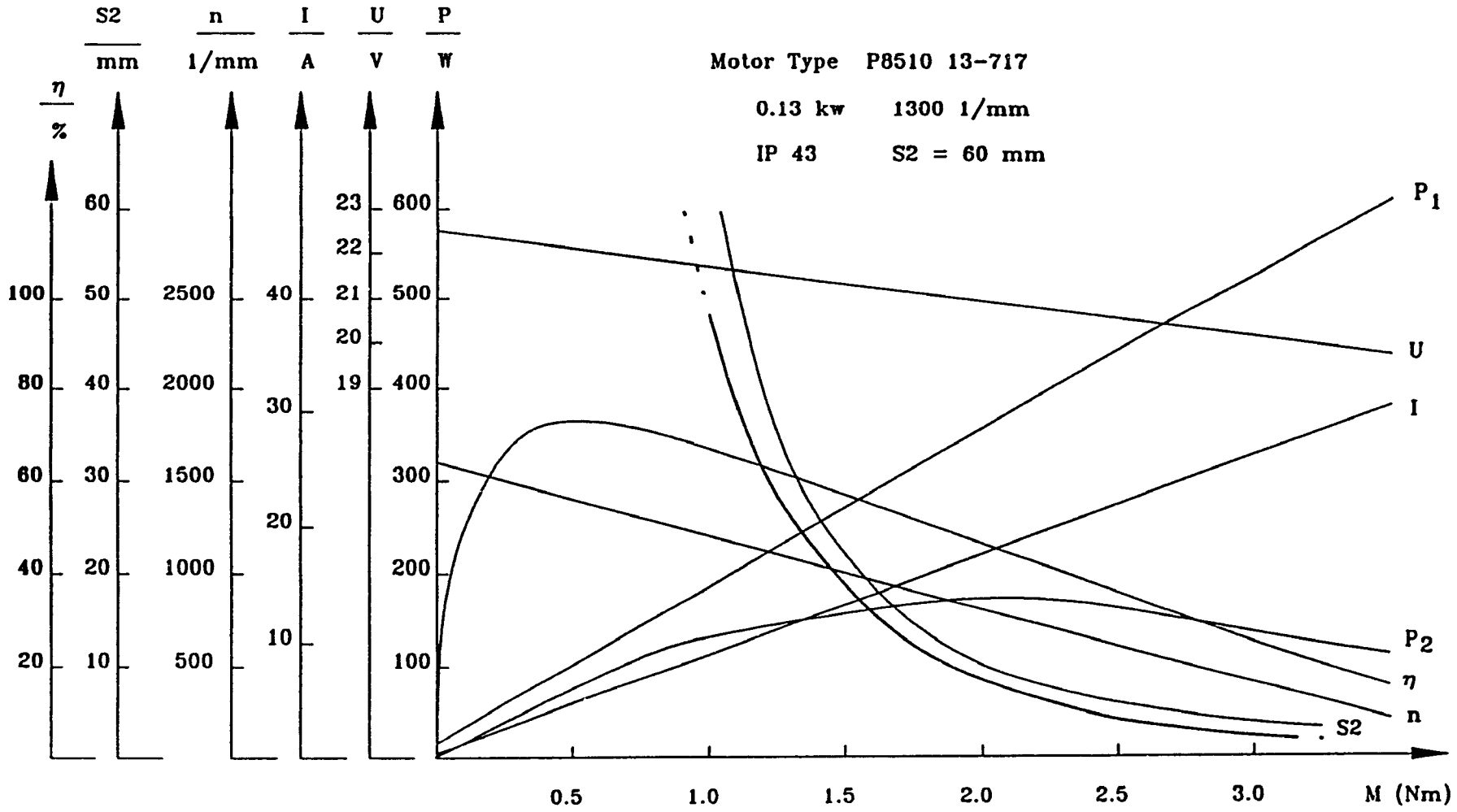

Fig. B.7 Drive Motor Characteristic Curves
(Courtesy of Schabmuller Corporation [21])

$$\text{Stall torque} = T_s = 4.05 \text{ Nm} = 4.05 \ \frac{\text{Kg. m}^2}{\text{sec}^2} \tag{B.9}$$

$$\text{Static friction torque} = T_f = 8.2 \text{ Nm} = 8.20 \ \frac{\text{Kg. m}^2}{\text{sec}^2} \tag{B.10}$$

$$\text{No load speed} = N_f = 1700 \text{ rpm} = 178.03 \text{ rad/s} \tag{B.11}$$

From the manufacturers specifications, the rotor inertia is J_m is

$$\text{Rotor inertia} = J_m = 0.002 \text{ Kg.m}^2 \tag{B.12}$$

The mechanical damping coefficient (D_s) and the time constant (τ_m) are evaluated from the mechanical parameters of the motor as below.

$$\text{Damping } D_s = \frac{T_s}{N_f} = \frac{4.05 \text{ Nm}}{178.03 \text{ rad/sec}} = 0.0228 \ \frac{\text{Kg-m}^2}{\text{sec}} \tag{B.13}$$

$$\text{Mechanical time constant } \tau_m = \frac{J_m}{D_m} = \frac{0.002}{0.0228} = 0.088 \text{ s} \tag{B.14}$$

The electrical parameters of the motor are provided in Table B.4. The electrical time constant τ_e is given by

$$\text{Electrical time constant} = \tau_e = \frac{L_a}{R_a} = \frac{4.7 \text{ mH}}{0.602 \ \Omega} = 0.0078 \text{ s} \tag{B.15}$$

B.6 Steering Arrangement

The overall assembly of the integral drive unit with a steer motor is presented in Fig. 6.8. It can be seen that an aluminum bracket in the shape

of an inverted L houses a bearing for the steering unit. One end of the aluminum bracket is attached to the stator casing of the drive motor. The inner race of the bearing is attached to the bracket. A lock plate is also attached to the inner race to prevent any axial movement of the bearing. The outer race of the bearing is fixed in position by a lock ring. The lock ring also locks a large speed reduction gear. The lock ring with the gear forms the stationary components of the steering unit. The lock ring can be attached to a fixed body in the system (vehicle body). The power for the steering is provided by a permanent magnet dc motors. The steer motor is a self contained unit with a speed reduction gear unit. This motor is fixed to the body of the aluminum L-bracket mentioned above. The speed reducer shaft of the steer motor carries a plastic gear which engages with a stationary large gear. Hence whenever the steer motor rotates, this pinion also rotates as the large gear is stationary, the wheel body along with the steer and drive motor turns (to the left or right). The gear ratio is 1:62.7.

B.7 Steer Motor Parameters Calculations

The characteristic curves and specification of the steering motor are provided in Fig. B.8, and in Table. B.5 respectively. Only the speed torque and current torque curves are available for this motor from the manufacturer. From the motor characteristic curves, the motor torque constant (K_t) is computed as

$$\text{Torque Constant } K_t = \frac{8 - 2 \text{ Nm}}{3 - 1 \text{ A}} = 3 \text{ Nm / A} \qquad \text{(B.16)}$$

The relationships between the motor torque and the speed is given by

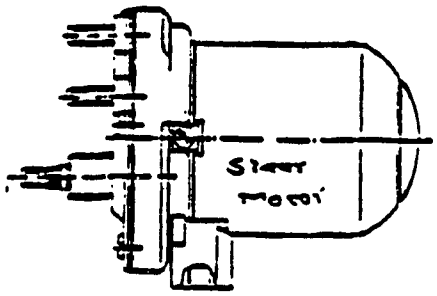

Typ	U [V]	M_H [Ncm]	M_A [Ncm]	n [min⁻¹]		P_1 [W]	P_2 [W]		Welle Shaft Arbre	Schaltbild Wiring diagram Schema électrique	Anschluß Connection Connexion	
12734	12	2	10	45	60.4	42	13		W12	S9	K23	360°
403 040	12	2	10	45	60.4	42	13		W12	S11	K23	360°
402 825	24	2.5	10	45	42.7	42	13		W12	S3	K23	continuous
402 901	24	2.5	10	45	42.7	42	13		W25	S3	K23	
402 916	24	2.5	10	45	42.7	42	13		W28	S3	K23	
402 981	24	2.5	10	45	60.4	42	13		W12	S10	K23	360°
403 042	24	2.5	10	45	60.4	42	13		W12	S11	K23	360°

Parameters of Steering Motor
(Courtesy of Schabmuller Corporation [21])

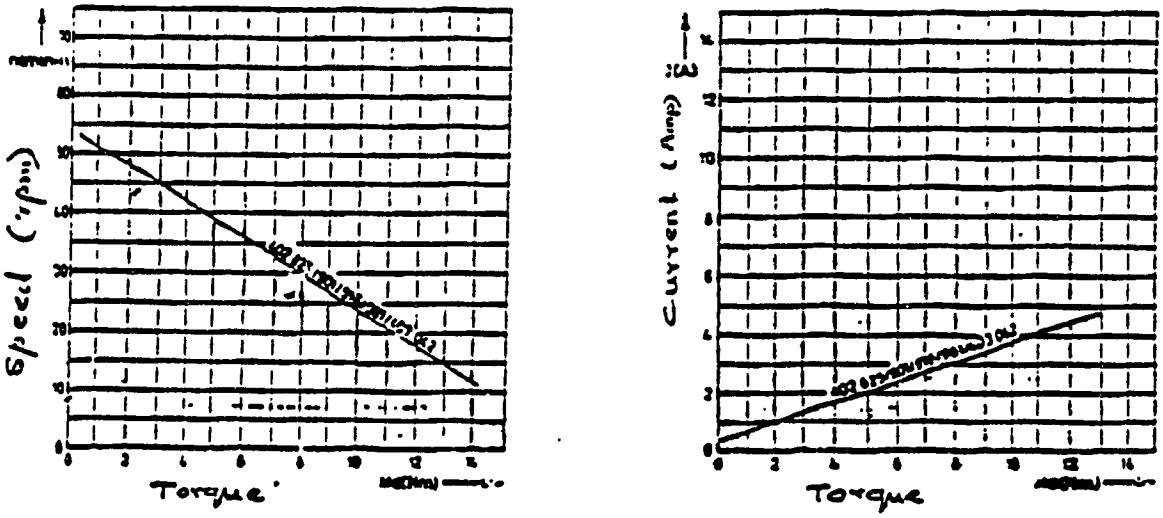

Fig. B.8 Characteristic Curves for Steering Motor
(Courtesy of Schabmuller Corporation [21])

$$\frac{15 - 47.5 \text{ rpm}}{13 - 2 \quad \text{Nm}} = -2.955 \text{ rpm / Nm} \tag{B.17}$$

The stall torque (T_s), and the no load speed (N_f) of the motor are deduced from the graph (Fig. B.8) and are

$$\text{Stall torque} = T_s = 18.0 \text{ Nm} = 18.0 \frac{\text{Kg. m}^2}{\text{sec}^2} \tag{B.18}$$

$$\text{No load speed} = N_f = 45 \text{ rpm} \tag{B.19}$$

The rotor inertia, and the motor mechanical time constant data are not available from the manufacturer. Hence it will not be possible to compute the mechanical time constant of the motor. The electrical parameters of the steering motor are given in the Table B.5. From these parameters, the electrical time constant τ_e is given by

$$\text{Electrical time constant} = \tau_e = \frac{L_a}{R_a} = \frac{4.1 \text{ mH}}{10.9 \ \Omega} = 0.376 \text{ s} \tag{B.20}$$

Rated Voltage	V	24 Volts
Maximum Power Input	P_{in}	42 Watts
Maximum Power Output	P_{out}	13 Watts
Continuous current	I	1.75 Amp
Starting (peak) current	I	8.8 Amp
Armature Inductance	L	4.135 mH
Armature Resistance	R	10.9 Ω

Table B.5 Electrical Characteristics of the Steering Motor

APPENDIX - C

COMPONENTS OF THE FEEDBACK CONTROL SYSTEM

AND

DATA ACQUISITION SYSTEM INTERFACE

APPENDIX - C

COMPONENTS OF THE FEEDBACK CONTROL SYSTEM AND DATA ACQUISITION SYSTEM INTERFACE

C.1 LM628 Motion Controller Interface

This section of the thesis describes the components and operation of the servo-controller chip LM628. The LM628 is a precision motion controller chip from the National Semiconductor laboratory intended for servo control of dc servo motors. This motion controller can be used if and only if the feedback is of a quadrature signal from an incremental encoder. The host computer downloads the necessary motion parameters that are described in section C.6, and then issues the appropriate command to the chip to start the motion. After this, it is not necessary for the host computer to interact with the motion controller. The host computer can perform other tasks during this time. The motion controller chip performs the closed loop control to drive the motor to the desired position or to run the motor at the desired velocity. The motion controller can also issue an interrupt to the host processor to indicate the completion of the task. The data downloaded can be either in decimal or hexadecimal format. The components of the chip are shown in Fig. 6.12.

Fig. C.1 illustrates the pin layout of LM628 motion controller. The bi-directional data lines D0 to D7 (pins 4 to 11) are connected to the host computer data lines. These lines are used to write commands and data, and also to read data from the LM628. They are also used to read the status byte from the LM628 before writing data or command to the chip. Pins 1, 2, and 3 are the encoder input signals I, A and B respectively. Pin 26 is the system

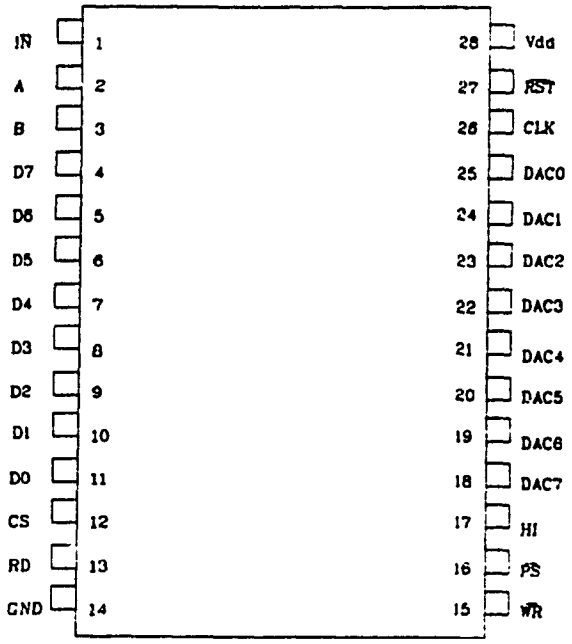

Fig C 1 Pin Layout of the LM628 Motion Controller

clock input (CLK). There is a RESET input pin (27) to initialize the LM628 chip internal registers. This is done while the computer is being powered up. and is an hardware reset. There are two other pins performing important function of reading and writing data from and to the chip. They are the Chip Select (CS) of pin 12, and the Port Select (PS) f pin 16. When PS is low, command port is selected, and data port if high. The following modes are controlled by PS :

Commands are written to the command port (PS low)

Status byte is read from the command port (PS low)

Data is written and read via the data port (PS high)

C.1.2 Position Feedback Interface

The LM628 servo-controller accepts 5V TTL quadrature signals (A and B) from an incremental encoder. Index pulse (I) can also be directly connected to the chip. The chip has a built in encoder decoding circuit. Because of the quadrature signal, the resolution of the counting is multiplied by a factor of four compared to the number of pulses per revolution of the encoder disc. It is possible to read the actual position based on the encoder counts, as well as the velocity. Here the velocity is computed directly from the encoder pulses and no external velocity measuring device needed. The time interval between two pulses is used to compute the velocity. The encoder signal inputs are synchronized with the LM628 clock. The maximum clock rate of the LM628 is 6 MHz. The maximum capture rate for the encoder counting circuit is 1 MHz. If noise is present in the encoder signals and if it disappears before the next encoder signal arrives, then the LM628 decoder will ignore the noise. It is necessary to filter out the noises that may

mimic the quadrature counts or persists through encoder transitions.

C.1.3 Velocity Profile Generator

The LM628 motion controller has an internal velocity profile generator. The profile generated is a trapezoidal function with an acceleration period, a constant velocity period and a deceleration period. The duration of the acceleration and the decelerations are one and the same. This profile is not programmable and it can not be modified by the user. However, one can change the velocity and position command while the LM628 is executing a motion command. The acceleration can not be changed while the motion is in operation, and hence either the motor has to be brought to rest or the previous trajectory command should have been completed before altering the acceleration value.

C.1.4 Sampling Interval

Since the controller is digital, the rate at which the data in/out are performed will affect the performance of the control system. The proportional and integral terms have a sampling time of $2048/f_{CLK}$, where f_{CLK} is the operating frequency of the LM628. In our case, the value of f_{CLK} is 6 MHz, and hence the sampling time is 341 μs. The sampling time of the derivative term in the PID filter is programmable. This time ranges from $2048/f_{CLK}$ to $(256 * 2048/f_{CLK})$ in steps of $2048/f_{CLK}$. For CONCIC-2 AGV, the range is from 341 μs to 87,381 μs.

C.1.5 Command and Data Read-Write Operations

Commands are written to the motion controller by the host computer using the I/O ports Figure. C.2 shows the LM628 command write operation. This is

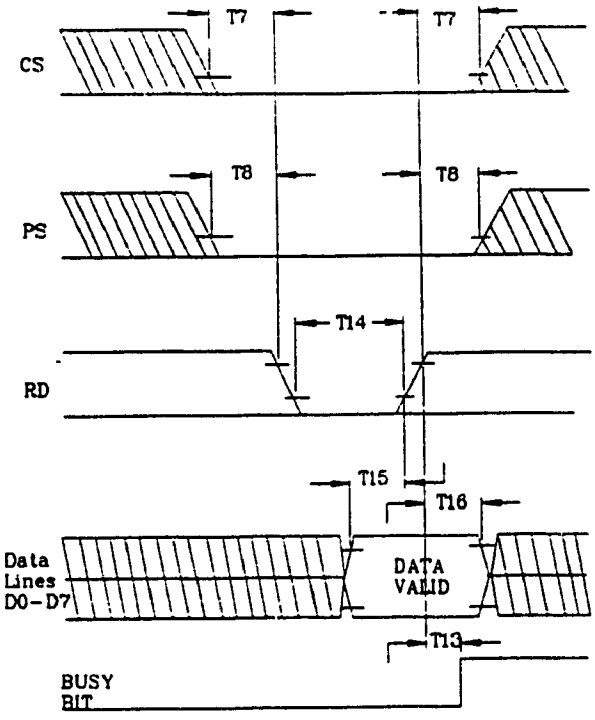

T7 = 0 0 ns
T8 = 30 0 ns
T13=
T14= 100 0 ns
T15= 50 0 ns
T16= 100 0 ns

Fig C 2 Command Byte Write OPeration Timing Diagram

done while the Port Select ($\overline{PS}$) input is logic low. The desired command code is written to the parallel port line and the write ($\overline{WR}$) input pin is strobed. The command byte is latched into the LM628 on the rising edge of the $\overline{WR}$ input.

It is important to check the status of the LM628 from the host computer before attempting to write a command and/or data, as well reading a data. This can be achieved by checking the last bit *(busy bit)* in the status byte read from the LM628. This read operation is accomplished by strobing the Read ($\overline{RD}$) input when $\overline{PS}$ is low. The status information is valid as long as the $\overline{RD}$ is low. Figure. C.3 illustrates the status byte read operation. The *busy bit* is never longer than 100 μs, and is anywhere from 15 μs to 25 μs. The busy bit goes high as soon as the write a command byte or read or write a data operation is completed.

The data read and write operations (Figs. C.4 & C.5) are done with the $\overline{PS}$ logic high. Each byte requires a Write ($\overline{WR}$) or Read ($\overline{RD}$) strobe. The motion controller has two addresses, one for writing control commands, and the other for writing and reading data. All write and read operations need to be performed only when the busy bit is logic zero (not busy). All commands and data written with the busy bit high will be ignored. For writing commands, it is necessary to check the busy bit first, and if found low, the command is written to the LM628. For data write or read, for 32 bit data, it is necessary to check the busy bit before writing or reading every 16 bits (2 bytes) of data.

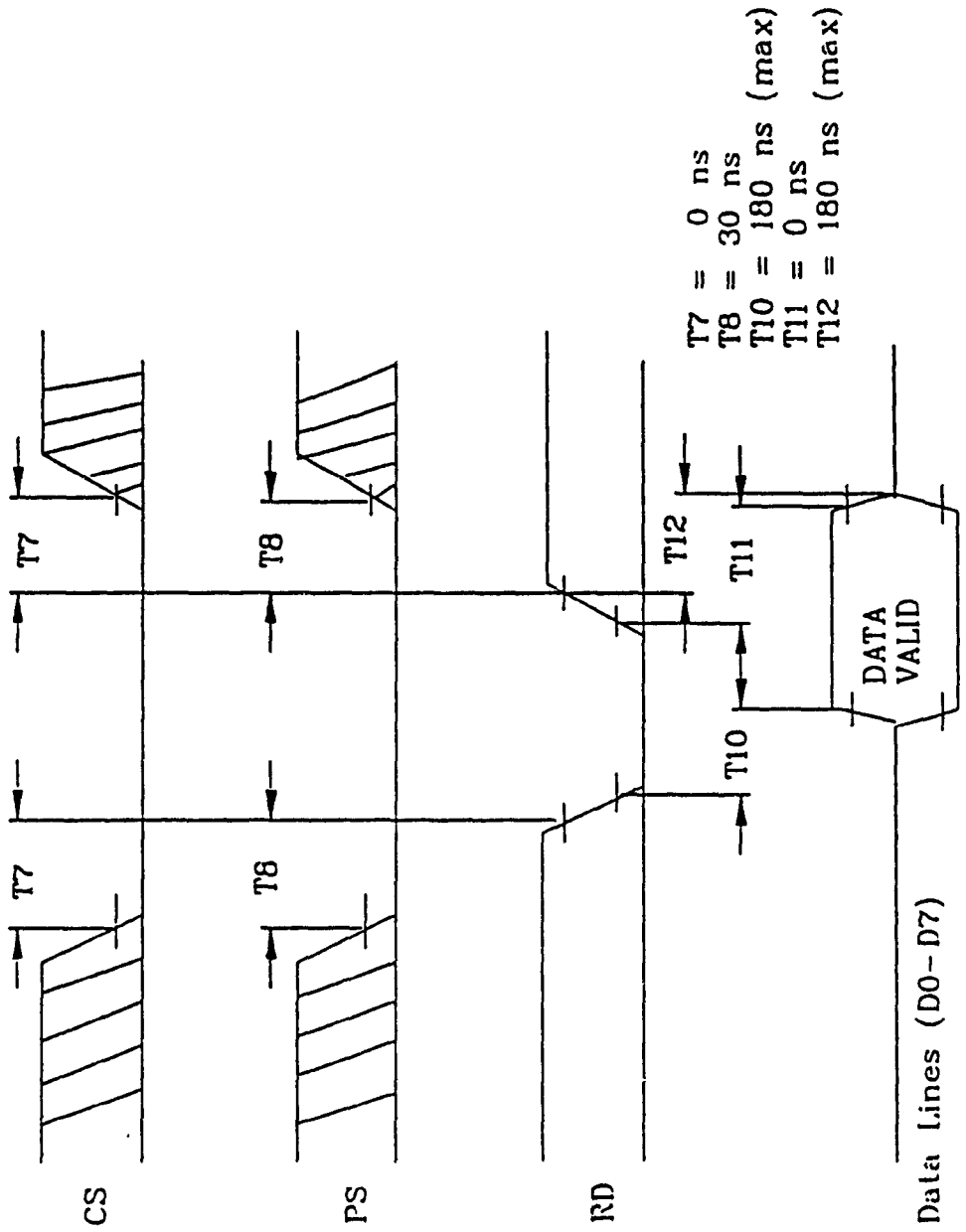

Fig. C.3 Status Byte Read Operation Timing Diagram

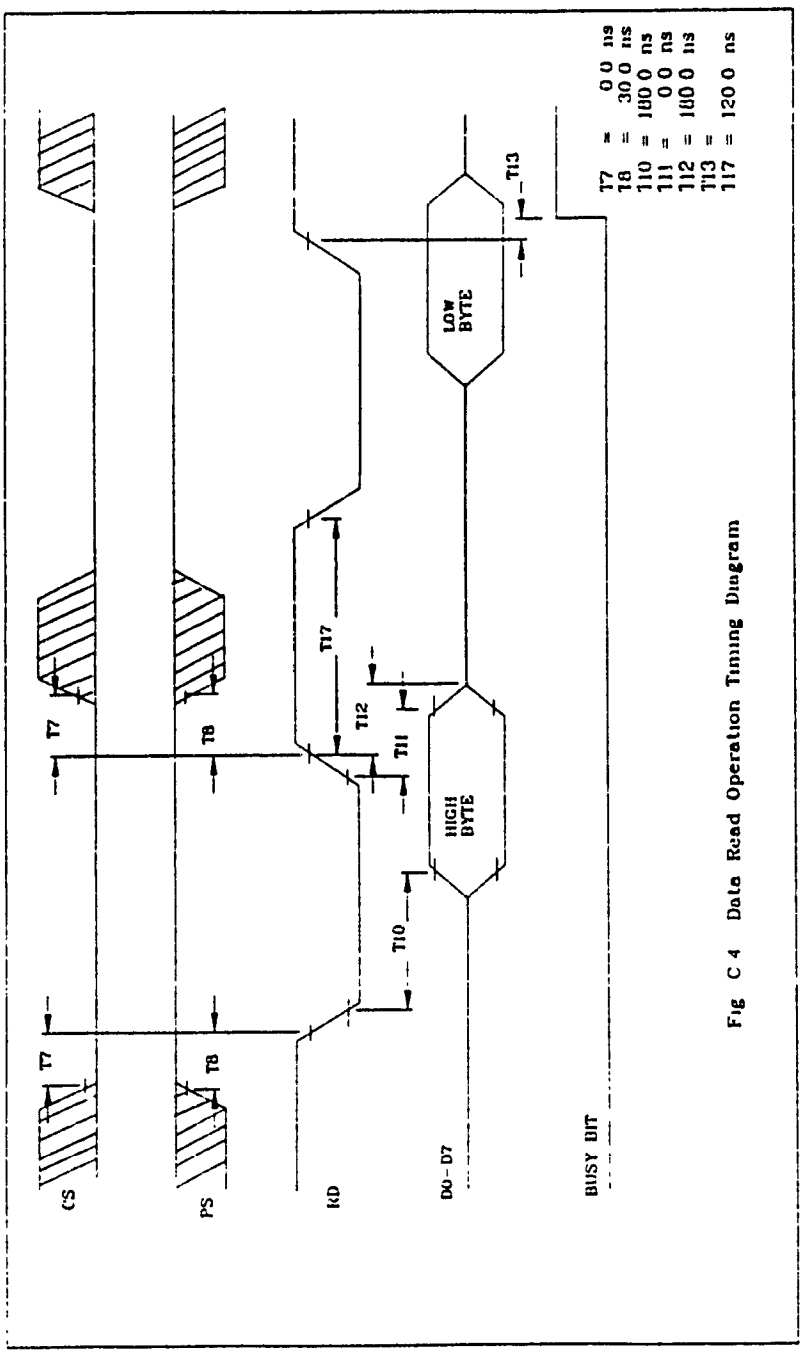

Fig C 4 Data Read Operation Timing Diagram

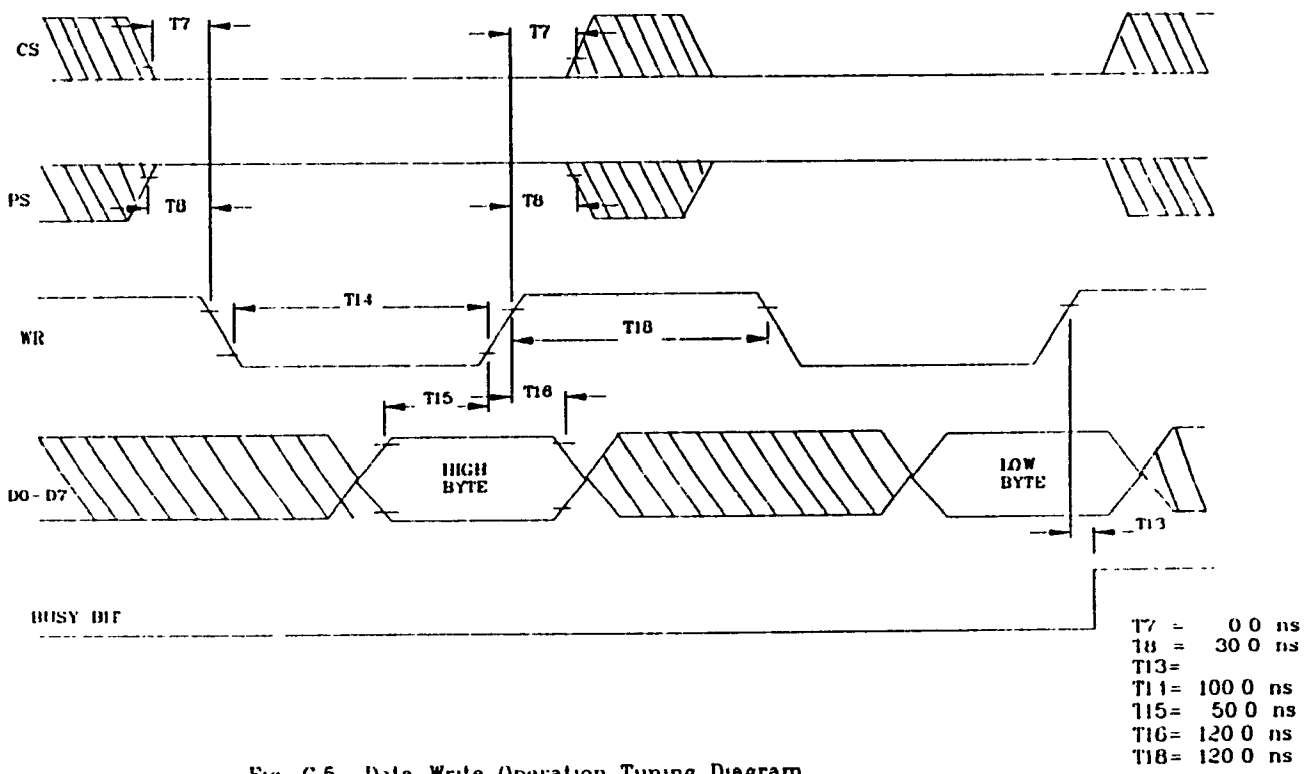

Fig C 5 Data Write Operation Timing Diagram

C.1.6 Motion Controller Commands

The LM628 has a set of internal commands to perform various functions. Table. C.1 illustrates the various commands of the LM628 and the corresponding data value to be downloaded to execute those commands. These functions can be categorized as

a) Initialization Commands

b) Filter Control Commands

c) Trajectory Control Commands

d) Interrupt Control Commands

e) Data Reporting Commands

C.1.6.1 Initialization Commands

There are four initialization commands namely RESET the LM628, set the output port to PORT8, set the output port to PORT12 and Define Home. The hexadecimal values to be loaded to the LM628 to execute these commands are 00 Hex, 05 Hex, 06 Hex and 02 Hex respectively. If the DAC used is of 8 bits, then it is not necessary to execute the set output port to PORT8. The command RESET the LM628 is equivalent to the hardware reset discussed in section C.1. The command DEFINE HOME provides an absolute zero position.

C.1.6.2 Filter Control Commands

There are two filter control commands. They are load filter parameters and update filter. The corresponding hexadecimal values for these are 1E Hex, and 04 Hex respectively. Table C.2 shows the filter control word bit allocation. Bits 15 to 8 are used to set the derivative sampling time. In Table C.3 derivative sampling time selection is presented by changing the value of the bits 15 thru 8. Bits 7 to 4 are not used. A logic high on bits

Type	Description	Hex Value	Data Bytes
Initialize	Reset LM628	00	0
Initialize	8 bit output	05	0
Initialize	12 bit output	06	0
Initialize	Define home	02	0
Filter	Load filter para.	1E	2 to 10
Filter	Update filter	04	0
Trajectory	Load trajectory	1F	2 to 14
Trajectory	Start motion	01	0
Interrupt	Set index pos.	03	0
Report	Read status byte	None	2
Report	Read signal regs.	0C	2
Report	Read index pos.	09	4
Report	Read desired pos.	08	4
Report	Read real pos.	0A	4
Report	Read desired vel.	07	4
Report	Read real vel.	0B	2
Report	Read int. sum.	0D	2

Table C.1 LM628 Command Summary

Bit Position	Function
Bit 15	Derivative sampling interval bit 7
Bit 14	Derivative sampling interval bit 6
Bit 13	Derivative sampling interval bit 5
Bit 12	Derivative sampling interval bit 4
Bit 11	Derivative sampling interval bit 3
Bit 10	Derivative sampling interval bit 2
Bit 9	Derivative sampling interval bit 1
Bit 8	Derivative sampling interval bit 0
Bit 7	Not used
Bit 6	Not used
Bit 5	Not used
Bit 4	Not used
Bit 3	Loading Kp (Proportional) data
Bit 2	Loading Ki (Integral) data
Bit 1	Loading Kd (Derivative) data
Bit 0	Loading Il (Integral limit) data

Table C.2 Filter Control Word Bit Allocation

Bit Position								Sampling Interval μs
15	14	13	12	11	10	9	8	
0	0	0	0	0	0	0	0	341.00
0	0	0	0	0	0	0	1	682.67
0	0	0	0	0	0	1	0	1024.67
0	0	0	0	0	0	0	1	1365.33
.	.	.	.	.	.	.	.	.....
.	.	.	.	.	.	.	.	.....
1	1	1	1	1	1	1	1	87381.33

Table C.3 Derivative Term Sampling Interval Selection Code

3 to 0 indicates that the data downloaded are K_p, K_i, K_d and I_1 respectively. The order of loading is the same as that shown above. The filter coefficients downloaded to the LM628 are of 16 bit words.

The downloaded filter coefficients are written to a primary buffer. A set of secondary buffers form the working register. The data from the primary register is moved to the secondary registers if and only if the filter update command is executed. This command is done by writing a command 04 Hex to the LM628 after checking the busy bit. As a result of this feature, the primary buffer can be loaded with a large set of filter coefficients in advance, and updating the filter can be done at regular intervals to save execution time for real time systems. There is no information in the LM628 literature concerning the maximum number of data sets that can be loaded and the buffer size.

C.1.6.3 Trajectory Control Commands

As in the case of filter control commands, the trajectory control commands also have two commands. They are load trajectory parameters and start motion and the corresponding hexadecimal values to be downloaded are 1F Hex, and 01 Hex. The trajectory control word bit allocation is shown in Table. C.4. Bits 15 to 13 are not used. A logic high on bit 12 indicates that the direction of rotation is forward (clockwise) and is valid only in the velocity mode. Bit 11 is to set the mode of operation as velocity or position. Bits 10 thru 8 are to stop the motor. Bit 10 is for *smooth stop* of the motor and uses the programmed acceleration (deceleration) value. Bit 9 is the *panic stop* as the motor is stopped at the maximum possible acceleration. This is accomplished by setting the desired position to the

Bit Position	Function
Bit 15	Not used
Bit 14	Not used
Bit 13	Not used
Bit 12	Forward direction - velocity mode only
Bit 11	Velocity mode selection
Bit 10	Smooth stop - use selected deceleration value
Bit 9	Stop abruptly - use maximum acceleration value
Bit 8	Turn off - zero output to the DAC, no feedback
Bit 7	Not used
Bit 6	Not used
Bit 5	Acceleration will be loaded (absolute)
Bit 4	Acceleration will be loaded (relative)
Bit 3	Velocity will be loaded (absolute)
Bit 2	Velocity will be loaded (relative)
Bit 1	Position will be loaded (absolute)
Bit 0	Position will be loaded (relative)

Table C.4 Trajectory Control Word Bit Allocation

Bit Position	Function
Bit 7	Motor Off
Bit 6	Breakpoint Reached (Interrupt)
Bit 5	Excessive Position Error (Interrupt)
Bit 4	Wraparound Occured (Interrupt)
Bit 3	Index Pulse Observed (Interrupt)
Bit 2	Trajectory Complete (Interrupt)
Bit 1	Command Error (Interrupt)
Bit 0	Busy Bit

Table C.5 Status Byte Bit Allocation

Bit Position	Function
Bit 15	Host Interrupt
Bit 14	Acceleration Loaded (not updated)
Bit 13	Trajectory Update Executed (filter not updated)
Bit 12	Forward Direction
Bit 11	Velocity Mode
Bit 10	On Target
Bit 9	Turn off - excessive position error
Bit 8	Eight Bit Output Mode
Bit 7	Motor Off
Bit 6	Breakpoint Reached (Interrupt)
Bit 5	Excessive Position Error (Interrupt)
Bit 4	Wraparound Occured (Interrupt)
Bit 3	Index Pulse Acquired
Bit 2	Trajectory Complete (Interrupt)
Bit 1	Command Error (Interrupt)
Bit 0	Acquire Next Index Puise (Set Index Executed)

Table C.6 Signal Register Bit Allocation

current position. This is the dynamic breaking of motor and is achieved by reversing the direction of rotation of the motors. Bit 8 is to stop the motor by applying a zero output to the DAC. This is equivalent to turning off the motor. During this kind of stopping, the LM628 does not check the feedback signals coming from the encoders. It permits the motor to come to a dead stop due to it's own inertia.

Bits 5 through 0 are to inform the nature of the data that is being downloaded to the LM628. This ranges from absolute acceleration, relative acceleration, absolute velocity, relative velocity, absolute position and relative position. A high on these bits indicates the data is being loaded. The order of loading is the same as the way it is mentioned above. All data values contain 32 bits (two 16 bit words). The position and velocity can be downloaded at any time while the motion is in progress, whereas the acceleration cannot be changed unless either the motor is in the off bit condition or the current trajectory command is completed.

As in the case of filter commands, here also the data are written to a primary buffer. On execution of the start motion command, the data is moved to the working secondary registers. This feature allows downloading of multiple data values to the LM628 in advance. No information is available concerning the size of the buffer to hold the data.

C.1.6.4 Data Reporting Commands

The data reporting commands consist of read status byte, read real and desired positions, velocity, read signal register, read index signal position and read integration sum limit. The status byte read operation has no

command byte, and is performed by simply reading the command port. The other read operations mentioned above requires the following commands to be written to the command port before reading the data from the data port. The command bytes are 08 Hex, 0A Hex, 07 Hex, 0B Hex, 09 Hex and 0D Hex respectively. The real velocity read is only 16 bit wide. The bytes are read from most to the least significant bytes.

C.1.6.5 Interrupt Control Commands

CONCIC-2 does not use these commands and hence are not described here.

C.1.7 LM628 Motion Controller Interface Card

The motion controller card has the LM628 motion controller chips and the necessary hardware to provide communication with the host computer and the outside world. The outside world for the LM628 includes the incremental encoders from where the chip receives input pulses, and the DAC and servo amplifiers to which the control signal is sent. Opto-couplers are provided in the system to prevent component damages due to short circuits. The couplers are provided between the LM628, IBM bus, servo amplifiers and encoders. Figure. C.6 shows the location of the components on the interface board. The motion controller card has been designed and wire-wrapped to control four motors independently. For this purpose, the interface card can be divided into three segments. They are :

a) Interface with the IBM BUS

b) Motion Controller and DAC-08

c) Conditioning for the servo amplifiers

d) Conditioning for encoder signals

e) Safety Features

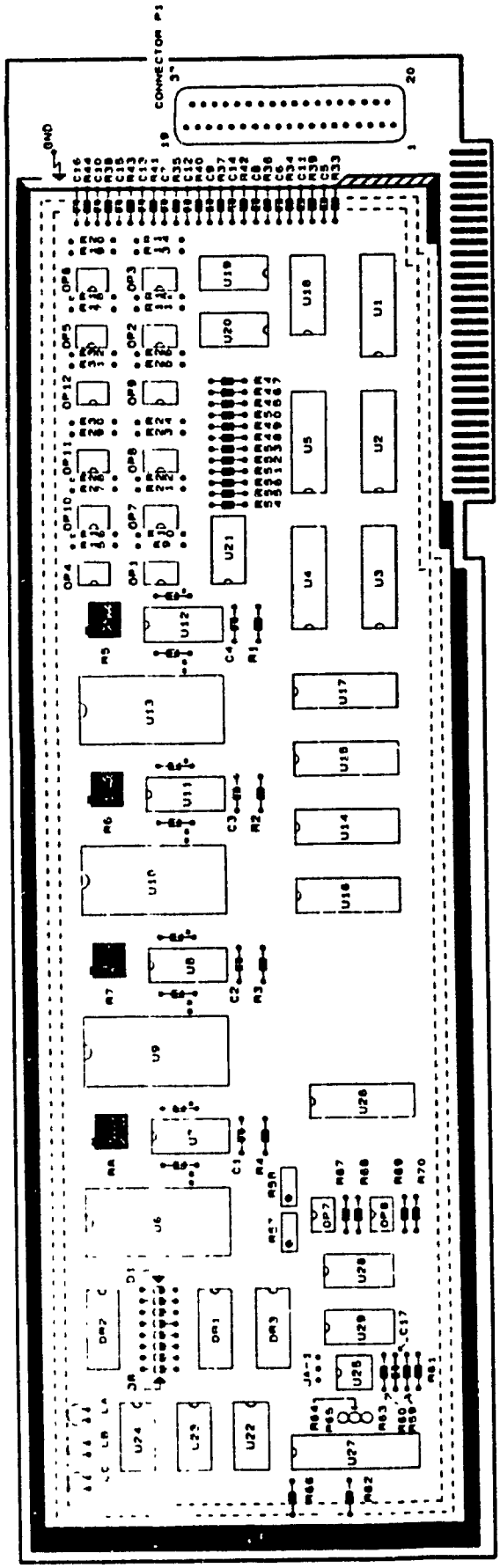

Fig. C.6 Layout of LM628 Motion Controller Interface Board

C.1.7.1 Interface with the IBM Bus

Figure C.7 illustrates the circuit diagram of this interface. Bus drivers 74LS245 and 74LS244 are used to drive all the IBM BUS signals to the LM card. The maximum clock rate of the LM628 motion controller chip used is 6 MHz. The Intel-286 processor used in CONCIC-2 is operating at 12 MHz. Hence it is necessary to divide the clock signal of the 286 processor by a factor of 2. This is done by the flip-flop 74LS76. The host computer resets while booting with a reset signal going high from low, whereas the LM628 resets on low from high. An inversion of the computer reset signal has been carried out to meet this requirement. Decoding the address is performed by the use of two PAL16L8 (programmable array logic). The various addresses available for the control of the four motors are provided in Table C.7. There are a total of 12 addresses for chip selection of all LM628. These 12 addresses are, one command and data address to control each motor (total of 8), and two common command and data addresses for each pairs (A & B, C & D) of motors. It is assumed that the motors A & B are used for driving and C & D are for steering. These common addresses are provided to issue update or start a trajectory command. This facilitates simultaneous starting and stopping of pairs of motors.

C.1.7.2 Motion Controller and the DAC-08

The interface circuit is shown in Fig. C.7. The DAC employed is an 8 bit DAC. Pin 17 on LM628 which is the HI pin is only for future development and is not connected. Of the 8 bits available with the DAC-08, only 4 bits are used by the driving motors. These four bits cover the entire speed range of the motors.

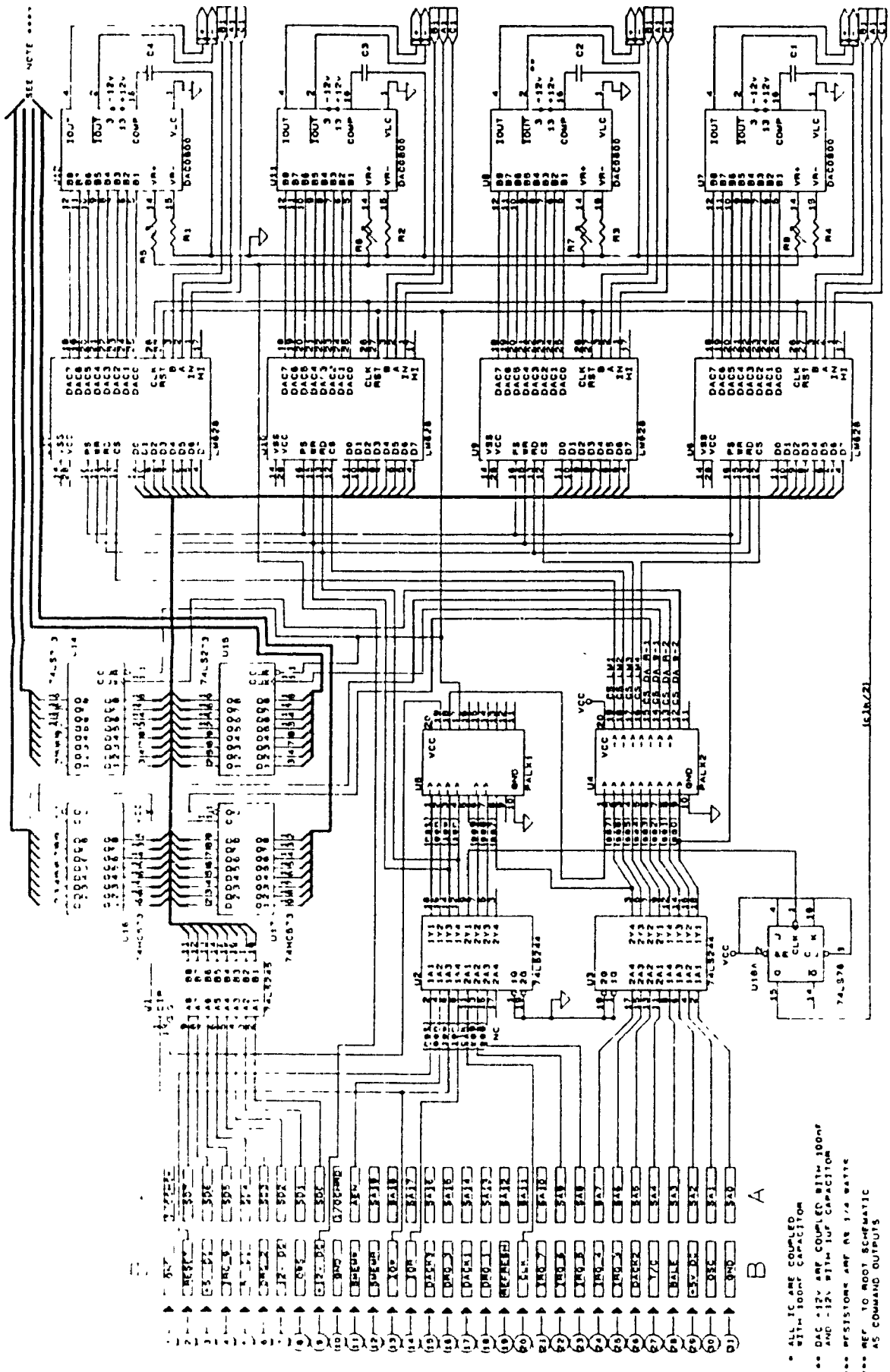

Fig. C.7 Interface With the IBM Bus

C.1.7.3 Conditioning for the Servo Amplifiers

The signal conditioning circuit of the servo amplifiers interface is presented in Fig. C.8. Two operational amplifiers are used for each output signal going to the servo amplifiers. The first operational amplifier is to convert the current signal coming out of the DAC-08 to a voltage signal. The second operational amplifier is needed to attenuate the signal from the first one in order to generate an output voltage in the range of -7.0 to 7.0 Volts. This is the input voltage range as required by the servo amplifiers from Galil Motion Control employed in the AGV. A current limiting resistor of 100 kW is added at the input terminal of the servo amplifier.

C.1.7.3 Conditioning for the Encoders Signals and Safety Features

The encoder interface with the LM628 is shown in Fig. C.9. The LM628 has provisions for direct connection of the encoder signal output lines. However, there is a problem associated with this arrangement. The encoder signals do contain some element of noise and hence a simple filtering need to be added. This is the function of this conditioning circuit. A RC-filter with a Schmidt trigger is added to remove the unwanted spikes. Figures C.10, C.11, C.12 shows the hardware interfacing for the safety features.

C.2 Servo Amplifier

A servo amplifier provides the power as required by the motor depending upon the load carried by the motor and the desired speed/position set by the user. A servo amplifier is at the down stream of the control loop after the servo-controller and before the motor. Most of the commercially available

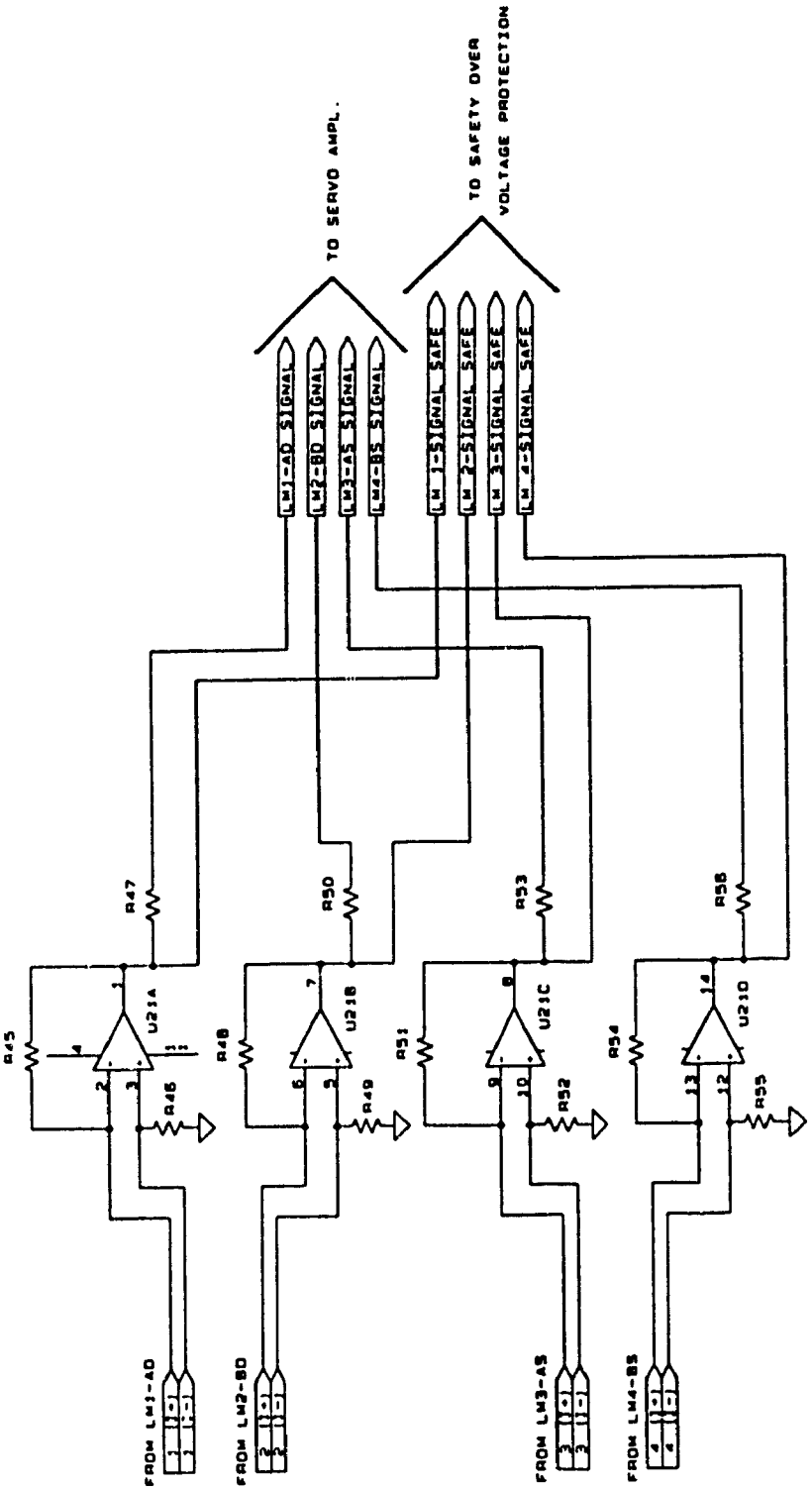

Fig. C.8 Interface With the Servo Amplifier

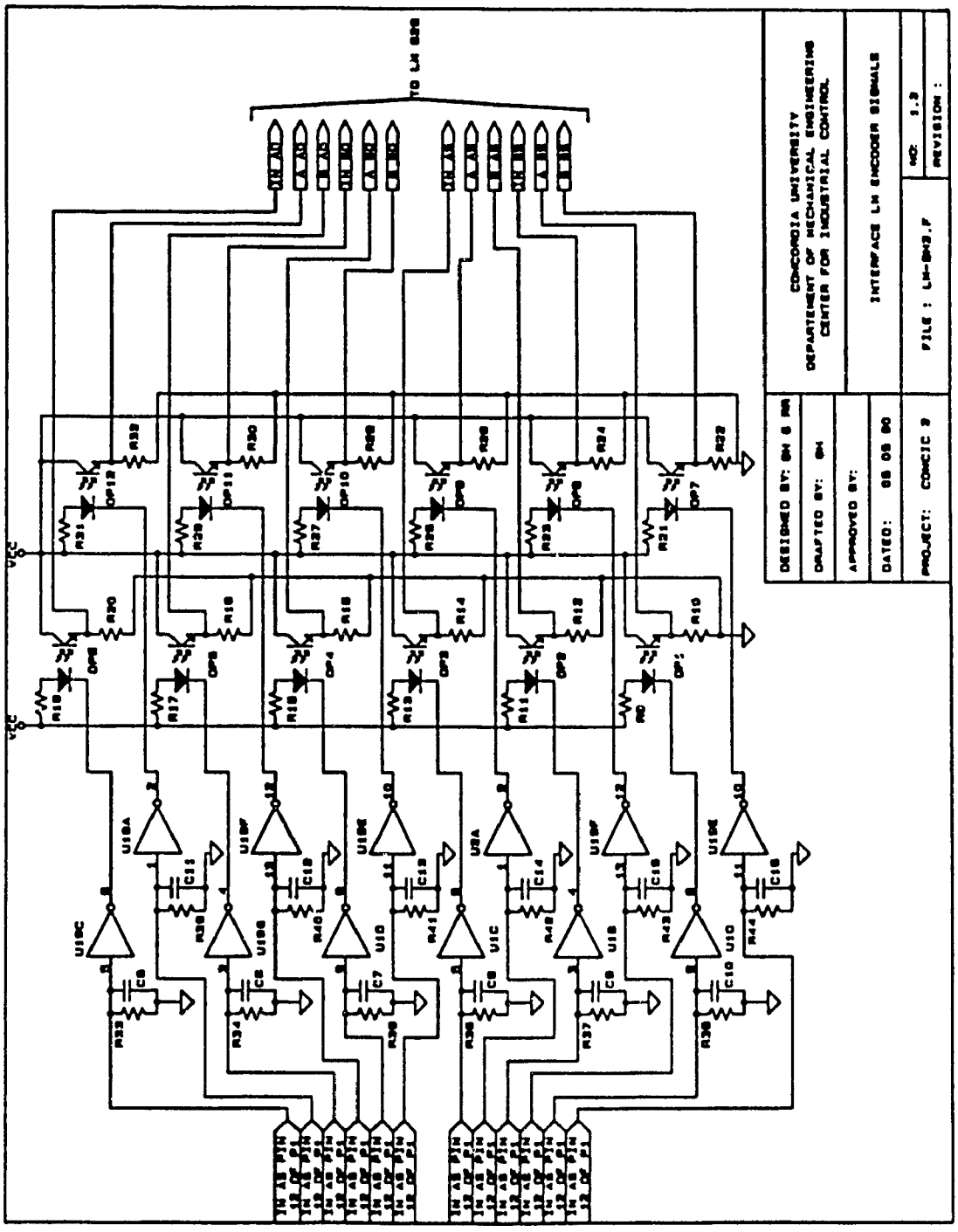

Fig. C.9 Interface With the Incremental Encoder

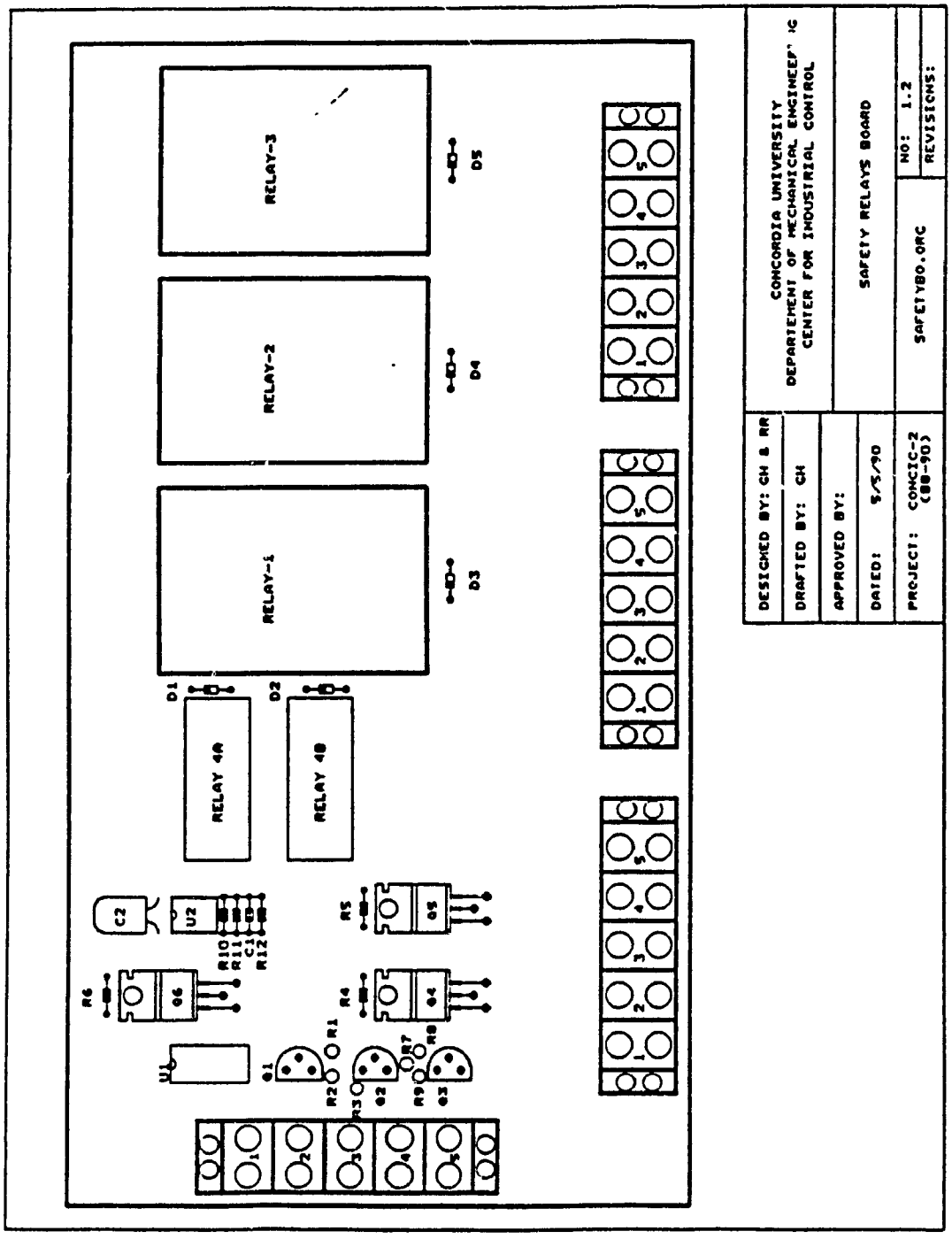

Fig. C.10 Layout of the Safety Relays Board

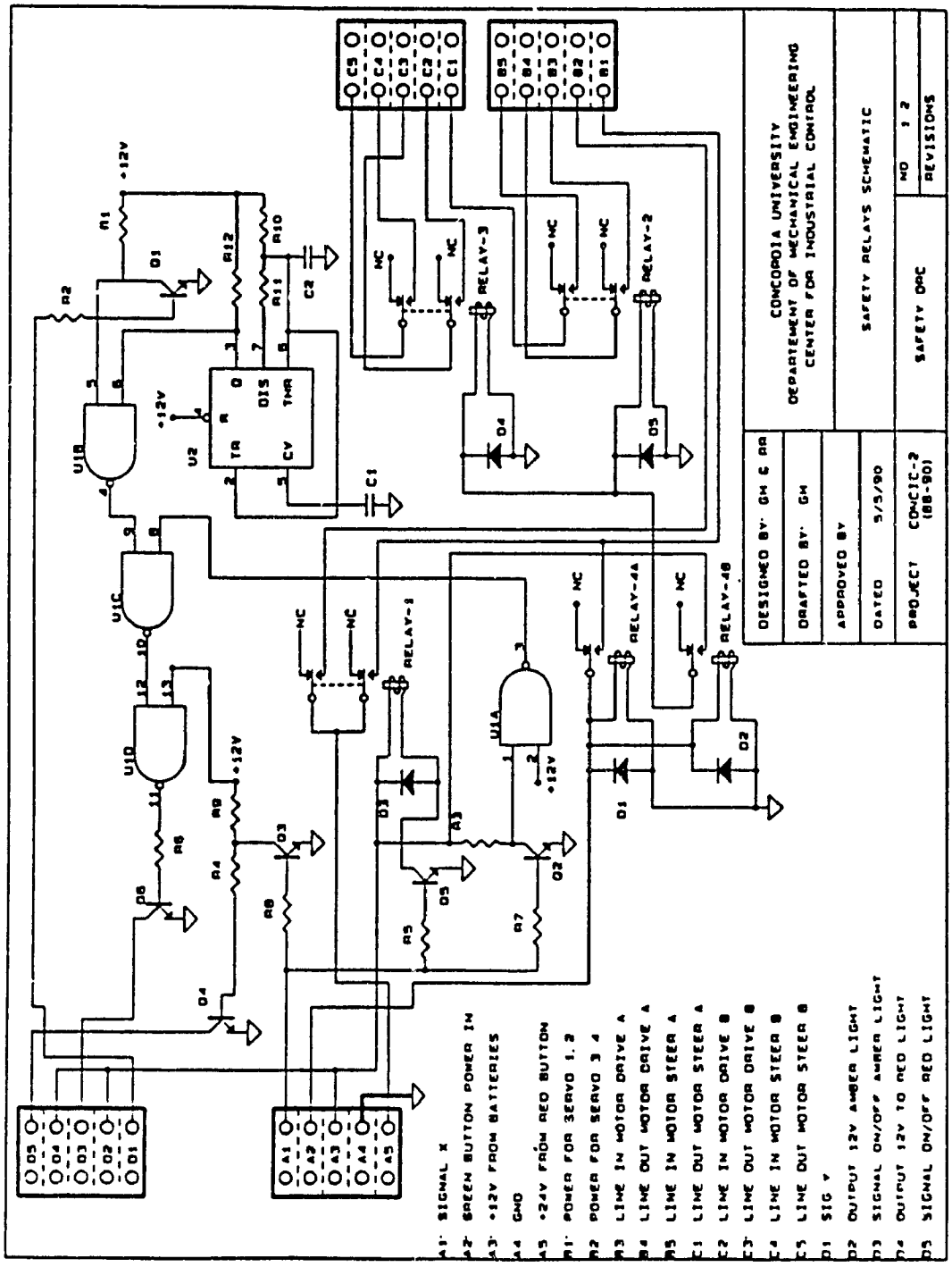

Fig. C.11 Schematic of Safety Relays

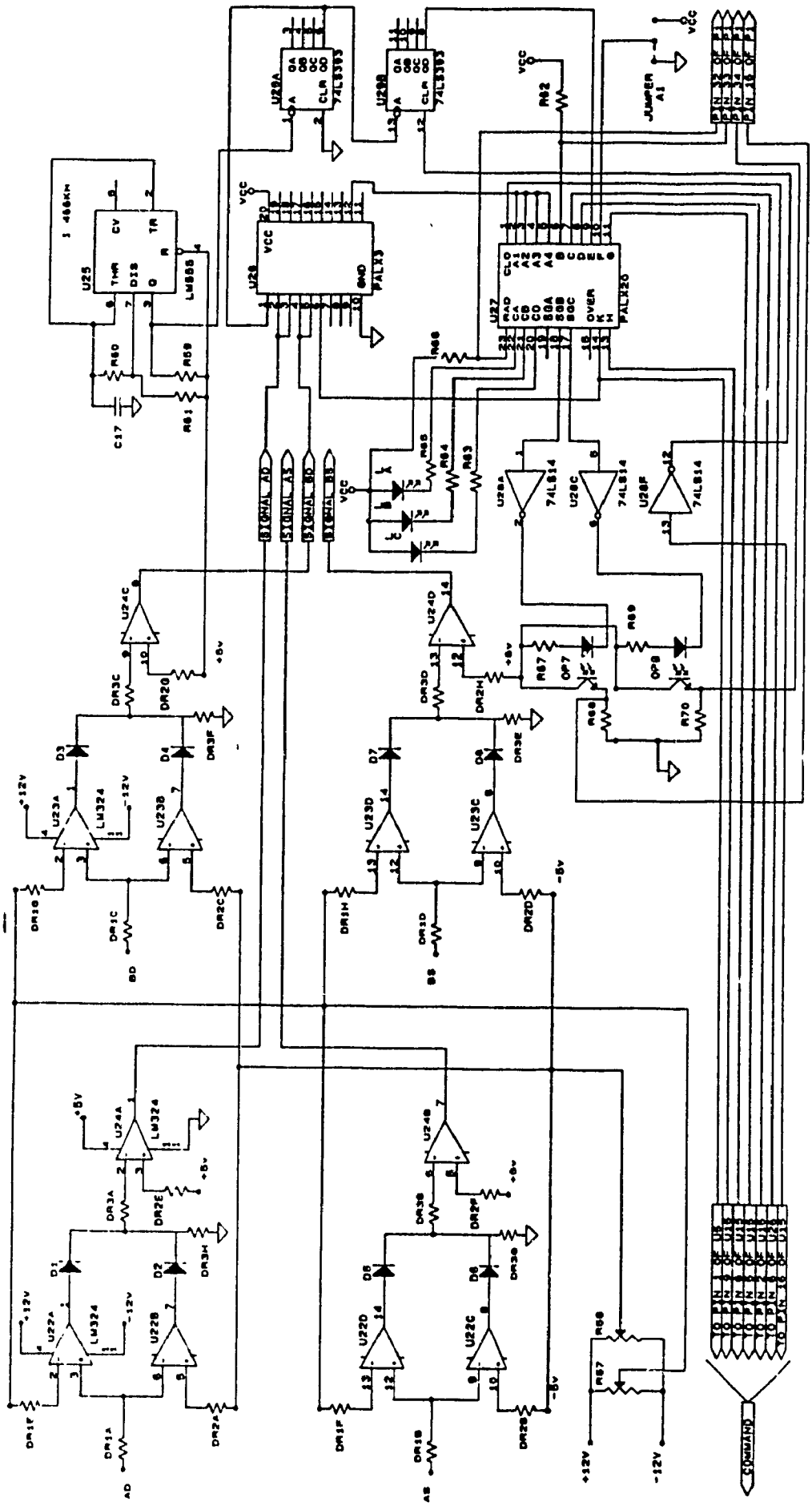

Fig. C.12 Motion Controller Interface with the Safety Relays

servo amplifiers have a logic stage in addition to the power stage. The logic stage provides feedback arrangement in order to connect the output of a tachometer or the motor voltage to provide an analog feedback system. The logic stage has provisions to set the continuous and peak current limits and inhibit the motor in both directions if necessary. The off-the-shelf servo amplifiers employed in the AGV are pulse width modulation amplifiers from Galil Motion Control.

Servo amplifiers provide uni-directional and bi-directional control of motors. These amplifiers are used to control small motors compared to the conventional speed control devices which are employed to operate the huge industrial motors. Servo amplifiers can be classified into two types based on the type of feedback that has been employed as current and voltage amplifiers. The amplifiers are further classified based on the mode in which they are used. This classification provides the following : linear amplifiers, SCR amplifiers, and the switching amplifiers. These three amplifiers provide a full bi-directional control. The amplifiers are further classified as H and T types depending upon the type of output circuit employed.

C.2.1 Pulse Width Modulation of Servo Amplifier

Amplifiers employing pulse width modulation are energy efficient compared to the linear amplifiers. As a result of this the efficiency of these amplifiers remain high at all load requirements. This is because in the case of linear amplifiers, a constant dc voltage is applied continuously, and hence at low loads, the power is lost in heat. This can be avoided if one can control the power input to the amplifier depending on the load

requirements. This is achieved with the use of switching amplifiers. Amplifier switching can be done by varying the pulse width depending on the load and hence the name pulse width modulation. A minimum duty cycle of 50% is present in PWM amplifiers. By varying the pulse width (duty cycle), the average value of the output voltage is modified and hence power saving is achieved.

As mentioned in the section 6.1, T and H-type are the two other classifications based on the type of output. The H-type needs only one power source, whereas the T-type requires two power sources. One undesirable characteristic of the H-type is that it is not easy to sense the motor current as the motor voltage is floating. The H-type with bipolar drive is employed in the servo-amplifiers used in the AGV. In the bipolar drive system, the transistors are turned on in pairs. For positive rotation of the motor, the power transistors Q_1 and Q_4 are turned on. The pair Q_2 and Q_3 are used for the counter clockwise rotation of the motor. This provides a motor voltage to vary from positive maximum (rated value) to the negative maximum (rated value). There is a disadvantage in using the bipolar drive in that there is a switching time to turn the transistors on and off. As a result of this a delay has to be introduced in the hardware between turning off one pair and turning on the other set. This delay is approximately 5 μs. As a result of this, the switching frequency is limited to 20 kHz.

The concept of four quadrant control is to provide a bidirectional servo control system. This can provide positive and negative torques as well as rotation of the motor in both directions possible. The H-type amplifiers provide this kind of control.

C.2.2 Servo Amplifier as a Current Amplifier

The servo amplifier employed in the AGV has been set to operate as a current amplifier and is shown in Fig. C.12. The armature current is obtained by measuring the voltage drop across a resistor. This is compared with the output of an error amplifier and the error is processed by the current amplifier to provide a voltage command to the pulse width modulation section of the amplifier. The current amplifier is a lag-lead network. The transfer function of the current amplifier is given by

$$\frac{I_{out}(s)}{V_{error}} = \frac{A_1}{s\tau_a + 1} \qquad (C.1)$$

Here A_1 is the gain of the current amplifier, τ_a is the time constant of the current amplifier and is given by

$$\tau_a = R_{50}\, C_{20} = 100\text{x}10^{-3} \text{ x } 0.01 \text{ x } 10^{-6} = 1 \text{ ms} \qquad (C.2)$$

And V_{error} is represented as

$$V_{error} = V_{eamp} - V_{m} \qquad (C.3)$$

And A_1 is the dc gain given by -R50/R45 = -10. V_{eamp} is the output voltage of the error amplifier, and I_m is the current corresponding to the current measured by the current sensing resistors.

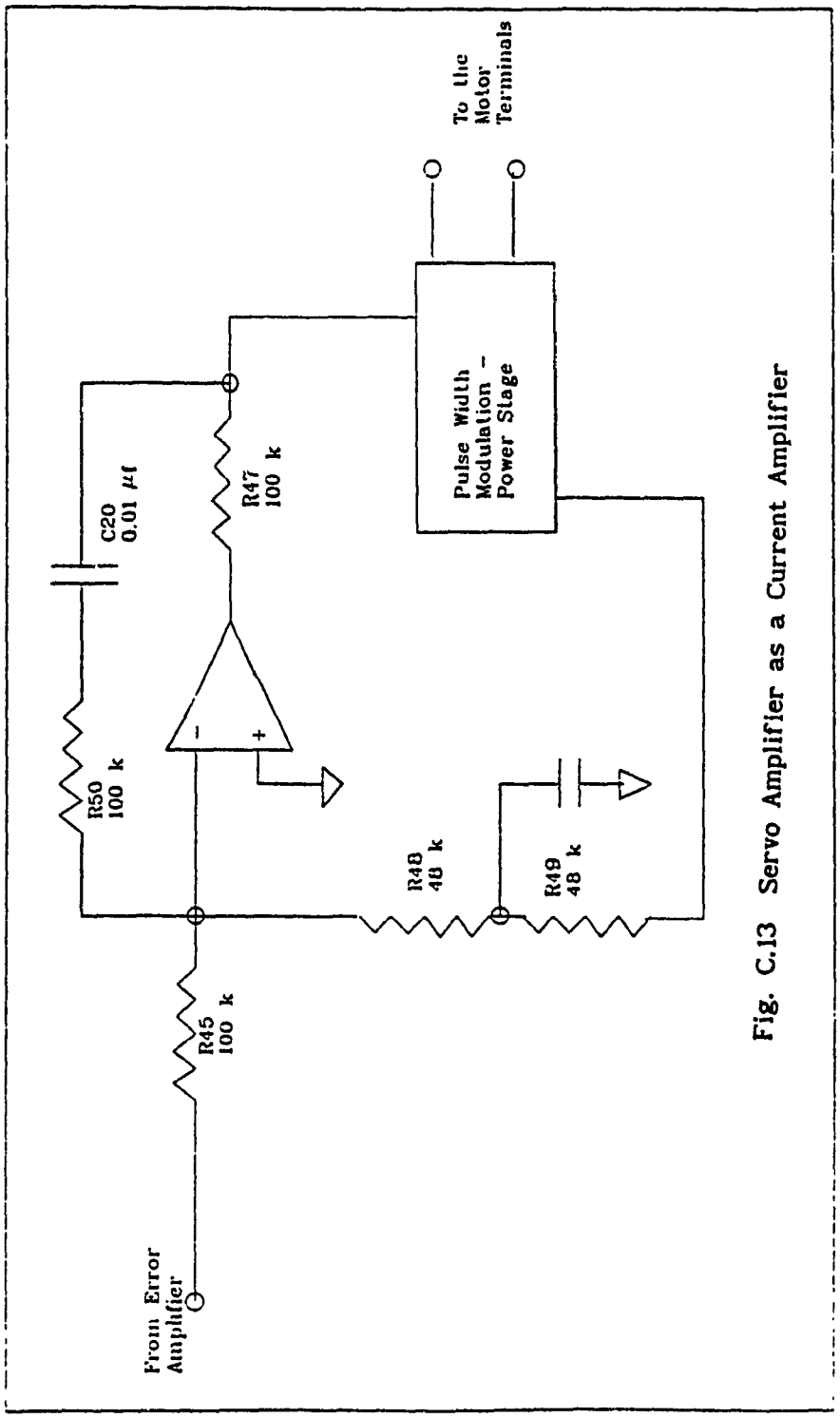

Fig. C.13 Servo Amplifier as a Current Amplifier

Motor Combinations	Control Port Address	Data Port Address
A	0x280	0x281
B	0x282	0x283
C	0x284	0x285
D	0x286	0x287
A & B	0x290	0x291
C & D	0x28A	0x28B
A B C D	0x28C	0x28D

Table. C.7 Motor Combinations and Control Addresses

	1	2	3	4	5	6	7
Ic				X	X		
Sh			X			X	
In	X	X	X		X	X	X
Pr		X				X	
Vs	X	X	X	X	X	X	

X - Illuminated LED

1. External inhibit.
2. Under / over voltage protection.
3. Short protection.
4. Cntinuous current limit.
5. Insufficient load inductance or loss of tacho feedback.
6. Over temperature.
7. Internal power supply is loaded

Table. C.8 LED Diagnostics for Galil PWM Servo Amplifier

C.2.3 Galil PWM Servo Amplifier Features

The servo amplifiers employed in the AGV are from the Galil Motion Control Incorporation. The amplifier type number is ESA 15/75H. This means that the amplifier can deliver a maximum continuous current of 15A and the maximum operating voltage is 75 Volts. The letter H implies that it is horizontally mounted. The minimum supply voltage to the amplifier is 20 Volts. The maximum peak current delivered by the amplifier is 37 amps. The amplifier employs power mosfet bridge drive and is of four quadrant type. The efficiency of the system is 95% with a switching frequency of 20 KHz. The amplifier has zero deadband. The input to the amplifier is an analog signal in the ±10 volt range. The amplifier has a power and logic stages. The power stage contains the pulse width modulation unit and the power transistors to drive the motor. The logic stage generates the error signals for the power stage depending upon the load requirements, and also performs few logic functions. Motor rotation can be inhibited in one or both directions. The amplifier can be either set in the current or voltage mode. For the CONCIC-2 AGV, the amplifiers are set in the current mode with the armature voltage feedback as well.

The logic stage of the amplifier has a differential amplifier (pins 11 to 13). This is useful for signal buffering and eliminates common-mode signals. A motor inhibit input (pin 15) is provided to turn off the power and the logic stages of the amplifier by pulling this input to a low state. During normal operations, this pin is left in tri-state. One half of the amplifier can be disabled in the clockwise or counter clockwise direction by applying a zero input to the pins 17 and 18 respectively. To monitor the motor current, pin 8 is provided. This pin is also used to set the

continuous and peak currents of the amplifier. The amplifier is also provided with LEDs to indicate under/over voltage, terminals shorting, wrong supply connection, insufficient inductance, current limits, temperature sensing and loss of feedback signals. Table C.8 shows the LED diagnostics.

C.2.3.1 Peak Current Duration

The duration of the peak current is computed from the following equation

$$t_p = -2.2 \ln \frac{I_p + I_{op} - I_c}{I_p} \qquad (C.4)$$

I_{op} is the actual operating current, I_p and I_c are the rated peak and continuous currents of the amplifier and t_p is the time in seconds for which the peak current of I_p is available. The values of I_{op}, I_p and I_c for the AGV discussed in this thesis are 9 amps, 37 amps and 15 amps respectively. Substituting these values in the equation (6.4), the value of t_p obtained is 0.39 seconds.

C.2.3.2 Input Terminals and Amplifier Characteristics

The amplifier is provided with three input terminals with different adjustable gains. Each output is buffered by a voltage follower having high impedance to isolate the inputs from the rest of the circuit. These terminals are marked as 5, 6 and 7. The maximum voltage that can be applied at each terminal is computed from

$$V_{in} \leq \frac{5.5 + 43 \times R_{s1} \times 10^{-5}}{K_1} \qquad (C.5)$$

The impedance of each input is

$$R_{in} = 12.7 \times 10^3 + R_{sl} \quad \Omega \qquad (C.6)$$

The amplifier of the AGV is working in current mode and hence the current gain of each input in current mode

$$G_c = \frac{18 \times 10^3 \times I_c \times K_l}{12.7 \times 10^3 + R_{sl}} \quad \text{(Amp/Volt)} \qquad (C.7)$$

C.2.3.3 CONCIC-2 AGV Settings

The value of R_{sl} is = 100 Ohms. The wiper of the trimming potentiometer T6 is fully clockwise, and hence the value of K_l is 1.0. The continuous current value is 15.0 amps. Substituting these values in the equations (6.5) to (6.7), the following values are arrived for the CONCIC-2 AGV.

Maximum voltage input-5 is V_{5in} = 7.5 Volts

Impedance of the input-5 is R_{5in} = 22.7 Kohm

Current gain of the input-5 is G_{5c} = 11.8 Amp/Volt

Maximum voltage input-7 is V_{7in} = 41.0 Volts

Impedance of the input-7 is R_{7in} = 52.9 Kohm

Current gain of the input-7 is G_{7c} = 2.5 Amp/Volt

C.2.3.4 Load Inductance

It is necessary that the motor should have enough load inductance to minimize the current ripples within 10% of the rated current value. The inductance required to keep the ripples within 10% of the rated current is computed from

$$L = 0.1 \times 2.5 \times 10^{-3} \times V_s / I_c \qquad (C.8)$$

Where L is the total inductance required in mH and V_s is the input voltage of the amplifier. If the motor armature inductance L_{arm} is less than this value, a choke must be added on the motor circuit. The value of the choke inductance in mH is

$$L_{ch} = L - L_{arm} \qquad (C.9)$$

In the CONCIC-2 AGV, for the drive motor, the value of L_{arm} is 4.7 mH, V_s is 22 Volts and the L computed is 0.67 mH. For the steer motor L_{arm} is 4.15 mH, V_s is 24 Volts, and L computed is 3.3 mH. Since the inductances of the drive and steer motors of the AGV are greater than the computed inductance using equation (6.8), a choke is not required.

C.2.3.5 Amplifier in Current Mode with Armature Voltage Feedback

The servo amplifiers from the Galil motion control can be set to operate in current mode with armature voltage feedback as in the Fig. C.13. It has been mentioned earlier that the amplifier has three input terminals (5 to 7). These inputs can be connected to a reference signal and voltage output of a tachometer or armature voltage measured across the motor terminals. The amplifier is shipped with the factory setting such that a feedback connection has to be made at the input terminals either 6 or 7. Since the impedance of these terminals are higher than that of the pin 5, these are used for feedback connection. The reference signal is connected to the pin 5. This kind of analog feedback arrangement is useful if it is desired to control the motor with and without the use of an external control system. If an external

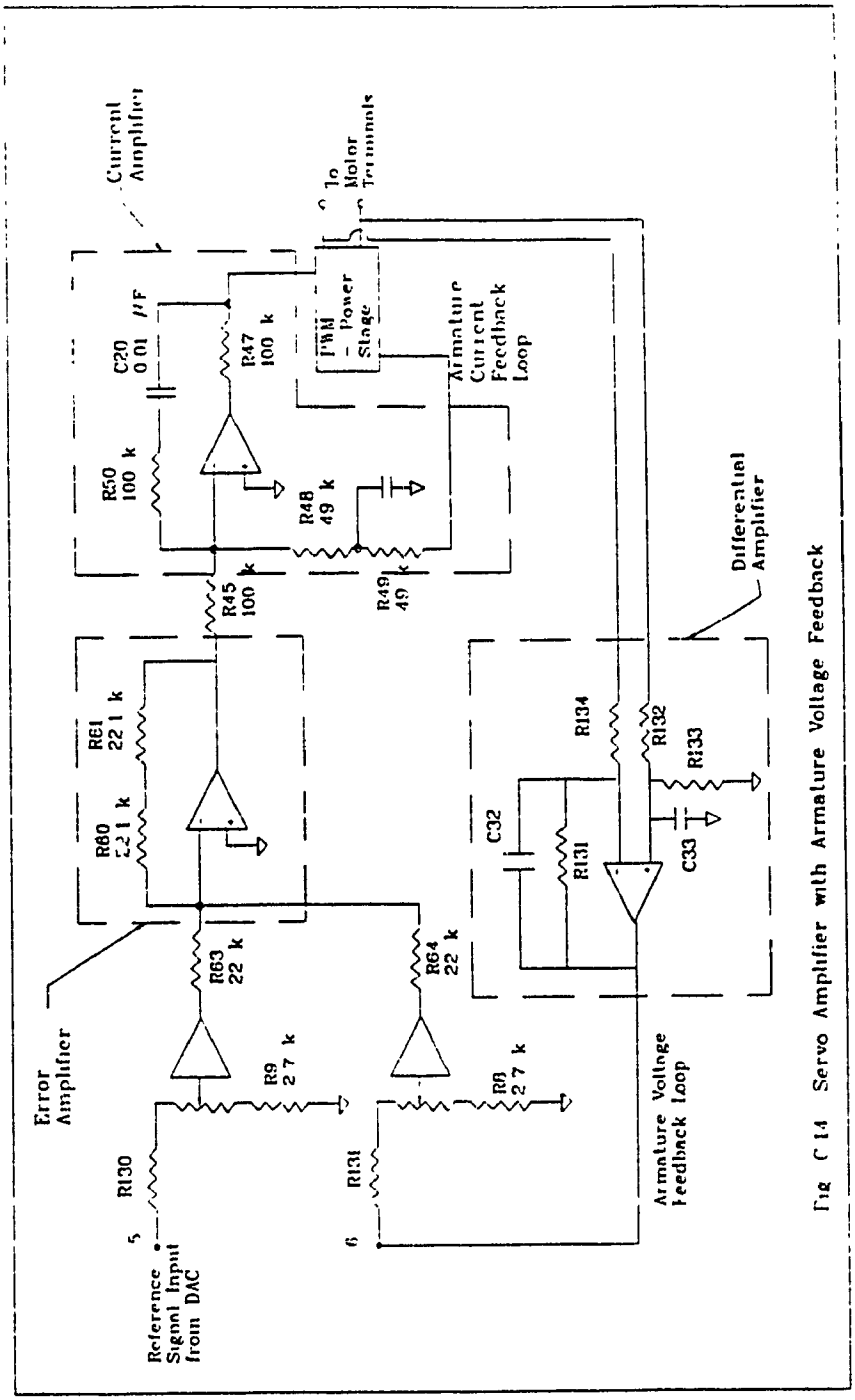

Fig. C.14 Servo Amplifier with Armature Voltage Feedback

control system is not available then a system consisting of a reference signal and a tachometer attached to the motor is suffice to perform the closed loop control of the motor.

If it is desired to use an external control system such as digital control using micro-computers and sophisticated motion controllers, then a digital loop can be used as the main control loop. The analog loop may or may not be needed in such cases. To disconnect the analog feedback loop, it is necessary to change the current amplifier to a linear inverting amplifier rather than a lag-lead network. The servo amplifier is shipped with the current amplifier as a lag-lead amplifier. This conversion can be achieved by disconnecting the capacitor C45. A jumper is provided to connect the two terminals. With this arrangement the amplifier will not be having a feedback loop except the current feedback. The current loop compares the load current with the desired current as computed by the error amplifier based on the feedback information. The error amplifier also limits the desired current values to be within the current limits set by the user.

The differential amplifier (U7) is used for armature voltage feedback. Since the output of the amplifier to the motor is a pulse width modulated signal, the motor voltage is not a simple dc signal. It is necessary to pass the motor output voltage through a differential amplifier to obtain an average dc signal. This differential amplifier also eliminates common mode signals. The output of the amplifier is connected to the input terminal 7 of the amplifier. These connections are shown in Fig. C.13. This is actually a velocity feedback loop. The velocity loop is c by connecting the following terminals :

Terminal 1 (18,20) to terminal 11 (14c)

Terminal 4 (30,32) to terminal 12 (2a)

Terminal 13 (2c) to terminal 5 (10a)

Terminal 6 (10c) is used for the input command.

The value of the resistors and capacitors are

$$R_{132} = R_{134} \quad ; \quad R_{131} = R_{133} \quad ; \quad C_{32} = C_{33} = 0.1 \text{ to } 0.47\ \mu F \tag{C.10}$$

The output of the differential amplifier is computed from

$$V_o = \frac{V_{12}\, R_{133}}{R_{133} + R_{132}} \left[1 + \frac{R_{131}}{R_{134}} \right] - \frac{V_{11}\, R_{131}}{R_{134}} \tag{C.11}$$

Where V_{11} and V_{12} are the voltage inputs at the terminals 11 and 12 respectively. The value of these two input voltages should be in the range of -6V to +6V. This gives rise to a condition shown below.

$$V_{11} \leq \frac{6\, R_{131}}{R_{134}} \qquad \text{and} \qquad V_{12} \leq \frac{6\, (R_{133} + R_{132})}{R_{133}} \tag{C.12}$$

The following constraints should also be met,

$$\frac{R_{133}}{R_{132}} < \frac{5}{V_s} \quad ; \quad R_{132} = R_{134} \geq 10\, V_s^2 \tag{C.13}$$

V_s is the input voltage of the amplifier. For CONCIC-2 the value of these resistors and capacitors are

$$R_{132} = R_{134} = 6.2\ k\Omega\ ;\quad R_{131} = R_{133} = 1\ k\Omega\ ;\quad C_{32} = C_{33} = 0.10\ \mu F \qquad (C.14)$$

In order to set the gains of the trimmer pots, it is necessary to use the motor in position mode with an external position feedback. In this mode, a digital feedback loop providing position feedback is employed. For setting the amplifiers for the AGV, the motion controller chip with an encoder feedback is used. With the gains of the motion controller being kept at a nominal value, the velocity feedback gain of the amplifier is adjusted while the trimmer pot (terminal 5) is kept at a fully clockwise (maximum) position. This setting of 5 provides maximum forward gain, and hence the speed of response is at the maximum attainable value. The trimmer pot (terminal 7) is adjusted until the motor response is critically damped. This means that there is a 5% overshoot.

C.2.3.6 Procedure to Set the Galil Servo Amplifiers

Before using the servo amplifiers to control the motors, it is necessary to set the continuous and peak current limits of the amplifier based on the motor ratings. The current amplifier (U4) makes sure that the continuous current supplied to the motor does not exceed the continuous current limit. The peak current limit is useful while starting the motor from rest during which the motor has to accelerate to overcome the load inertia. To adjust the current limits, jumper J2 is arranged such that the connection A-B is closed and A-C is open. The currents can be adjusted by monitoring the voltage output at pin #8. The voltage at pin #8 (V_8) can be computed from the motor rated current values as below :

$$V_8 = 0.125 * I \qquad (C.15)$$

Where I is the continuous or peak current of the motor. For CONCIC-2 AGV, these values are 9 amps and 36 amps respectively. The corresponding voltages at pin #8 are 1.125 V and 4.5 V respectively. Pin #5 is provided with the maximum input voltage (7.5 V) through a current limiting resistor R21 of value 100 kΩ. The input gain trimmer pots are kept at a fully clockwise position. The terminals #2 and #3 are connected to the 24 volt dc source. It is not necessary to connect the motor to set the current limits. To set the continuous current (I_c), the trimmer pot T3 is turned counter clockwise such that the voltage read from pin #8 is more or less equal to the continuous current value. At this stage, pot T3 is given a few more turns. Trimmer pot T2 (I_c) is adjusted to the required continuous current value while monitoring the voltage output at pin #8. The peak current is set by turning the pot T3 clockwise until the required voltage is read from pin #8. After setting the limiting currents, jumper J2 is connected such that A-B is open and A-C is closed so that the current feedback loop is closed.

C.3 Position/Velocity Feedback Components

A feedback device is necessary for the closed loop position and/or velocity control of motors. Analog feedback of the motor velocity can be obtained by the use of a tachometer or using the armature voltage feedback. A potentiometer can also be employed to provide position feedback. For digital feedback, an encoder is employed. An encoder feedback provides a pulse train whose frequency depends on the motor speed. A decoder circuit is needed to count the pulses and convert it to a corresponding speed or position information. Encoder feedback does not require an analog to digital converter as in the case of analog feedback.

C.1.7.1 Interface with the IBM Bus

Figure C.7 illustrates the circuit diagram of this interface. Bus drivers 74LS245 and 74LS244 are used to drive all the IBM BUS signals to the LM card. The maximum clock rate of the LM628 motion controller chip used is 6 MHz. The Intel-286 processor used in CONCIC-2 is operating at 12 MHz. Hence it is necessary to divide the clock signal of the 286 processor by a factor of 2. This is done by the flip-flop 74LS76. The host computer resets while booting with a reset signal going high from low, whereas the LM628 resets on low from high. An inversion of the computer reset signal has been carried out to meet this requirement. Decoding the address is performed by the use of two PAL16L8 (programmable array logic). The various addresses available for the control of the four motors are provided in Table C.7. There are a total of 12 addresses for chip selection of all LM628. These 12 addresses are, one command and data address to control each motor (total of 8), and two common command and data addresses for each pairs (A & B, C & D) of motors. It is assumed that the motors A & B are used for driving and C & D are for steering. These common addresses are provided to issue update or start a trajectory command. This facilitates simultaneous starting and stopping of pairs of motors.

C.1.7.2 Motion Controller and the DAC-08

The interface circuit is shown in Fig. C.7. The DAC employed is an 8 bit DAC. Pin 17 on LM628 which is the HI pin is only for future development and is not connected. Of the 8 bits available with the DAC-08, only 4 bits are used by the driving motors. These four bits cover the entire speed range of the motors.

Encoder feedback can be either incremental or absolute. An incremental encoder generates pulses as the motor rotates. The shape of the pulses may be square, trapezoidal or sinusoidal. The absolute encoders are superior in performance compared to that of the incremental encoders as they provide the analog information of the position without the need for a decoder. They are bulky in order to meet the entire range of operation, expensive and sensitive to the working environment. On the other hand, the incremental encoders are relatively simple, compact in design and are 3 to 5 times cheaper than the absolute encoders.

The drive motors employ incremental encoders with quadrature output signals A and B which are at a phase difference of 90 degrees. The driving motors are provided with encoders from PMI motion technologies whose specification is provided in Table C.9. The quadrature signal provides bi-directional control of motors. Another usefulness of the quadrature signal is that it improves the accuracy with which the feedback measurements can be made. From Fig. 6.11, it can be seen that we can count 4 times (00, 10, 11, 01) for one cycle of the encoder signals A and B. This feature permits the use of encoders with smaller number of lines per revolution to achieve four times the resolution of the encoder.

The minimum speed increment that can be sensed by the feedback system of the driving motor is computed to be

$$N_{min} = \frac{1}{1024} * \frac{1}{4} = 0.000244 \text{ rev/min/pulse} \qquad (C.16)$$

This speed value in terms of linear velocity of the wheel is given by

Encoder Specification for Drive Motors	
Company	PMI Motors
Type	Incremental Encoders with ABI signals
Model Type	M23
Output Waveform	Square wave ; 5Volt TTL Standard signal
Input Voltage	5 Volt ±5%
Resolution	1024 pulses per revolution
Hub Size	0.3750 inch diameter
Color Coding	
Output - A	White
Output - B	Blue
Index - I	Green
Ground	Black
Supply Voltage	Red
Specification	M23 - 1024 - ABI - 5 - S - C - .3750

Encoder Specification for Steer Motors	
Company	BEI Motors
Type	Incremental Encoders with ABI signals
Model Type	M23
Output Waveform	Square wave ; 5Volt TTL Standard signal
Input Voltage	5 Volt ±5%
Resolution	256 pulses per revolution
Hub Size	0.25 inch diameter
Color Coding	Terminals are marked on the enocder
Specifications	M23 - 256 - ABI - 5 - S - C - .2500

Table C.9 Encoders Specification

$$V_{min} = p * d * N_{min} * GR / 60 \quad m/s \qquad (C.17)$$

Where d is the wheel diameter which is 0.05 m, GR is the gear ratio between the motor and the wheel and is 9.9. The factor 60 is to convert minutes to seconds. Substituting the values in (C.17), the minimum linear velocity increment that can be measured is

$$V_{min}\,(\text{driving wheel}) = 6.328 \times 1 \text{ m/s} \qquad (C.18)$$

In the case of motor-in-wheel drive units, the feedback element(s) can be attached only at the motor end instead of at the output shaft end. Due to this, any error in the transmission system will not be sensed by the feedback controller. This results in transmission errors which may play a role in the accuracy of the feedback control.

C.6 Data Acquisition System Interface

It has been mentioned in Chapter 6 that the CONCIC-II AGV is provided with a data acquisition system to record voltages and currents of the motors and other accessories in real-time. For this purpose, an interrupt driven data acquisition system has been designed and the functionality of this system has been discussed earlier in section 6.3.8. Also in section 6.3.9.10 the software layout is explained. In this section, the circuit diagrams of this interface is provided. Figure. C.15 is the layout of the components on the data acquisition board. Figure. C.16 is the circuit diagram for interfacing it with the host computer. This board also features the analog to digital converter (ADC). Of the 16 bits available, only 12 bits are

employed in the current design. This board also houses the 8254-timer which is used to compute the system cycle time, actual wheel velocity and for integration by the integral controller of the navigation system. The second set of figures provided are the signal conditioning circuits which are interfaced with the outside world which consists of the motors, amplifiers and the batteries. This board consists of conditioning circuits to filter noise and to amplify signals when necessary. Figure. C.17 is the component layout of the signal conditioning board and Fig. C.18 is the circuit diagram of the multiplexing arrangement. Figures C.19 - C.22 are the circuit diagrames for the motor voltage conditioning, motor current conditioning, battery voltage conditioning and the DAC-08 voltage conditioning circuits.

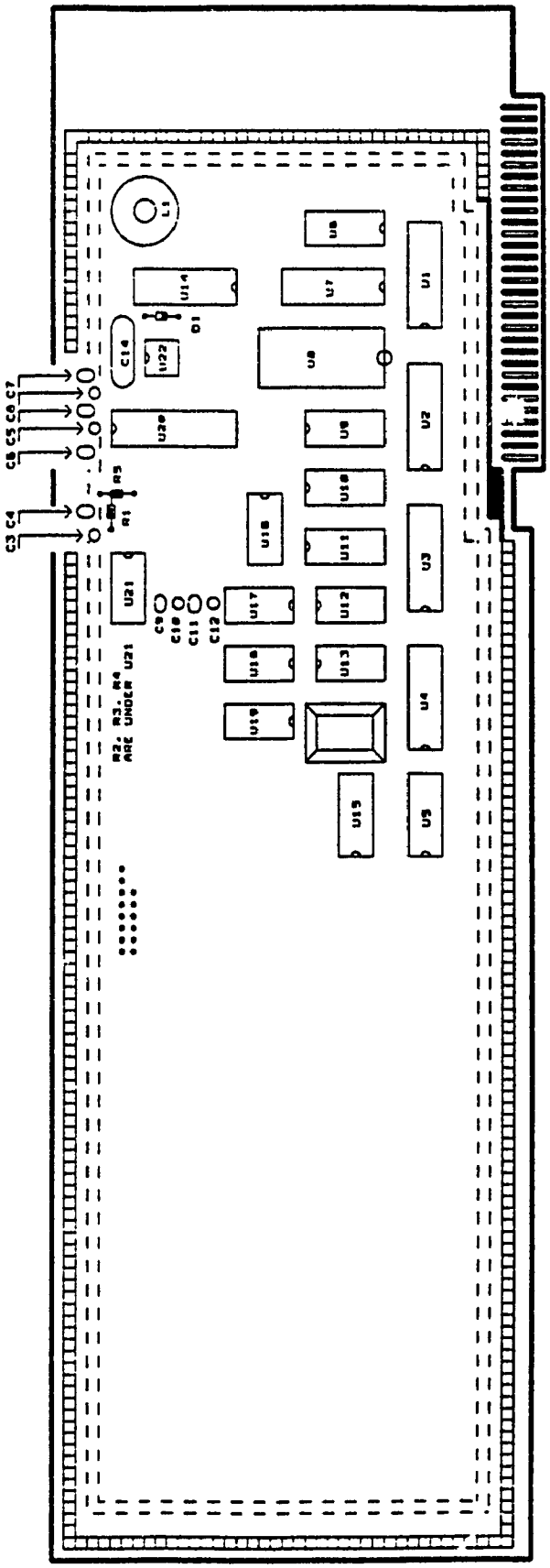

Fig. C.15 Component Layout of the Data Acquisition Board Interface

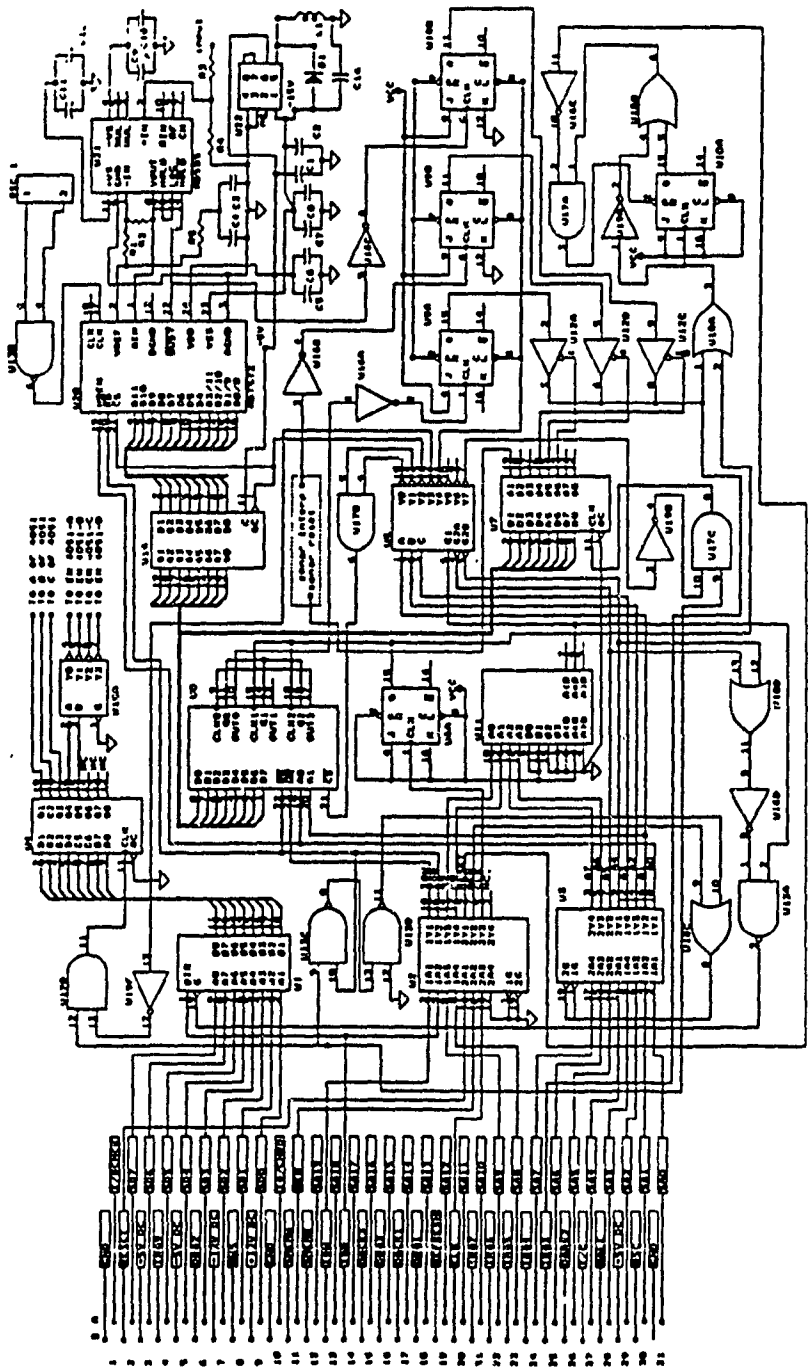

Fig. C.16 Circuit Diagram of the Data Acquisition Board

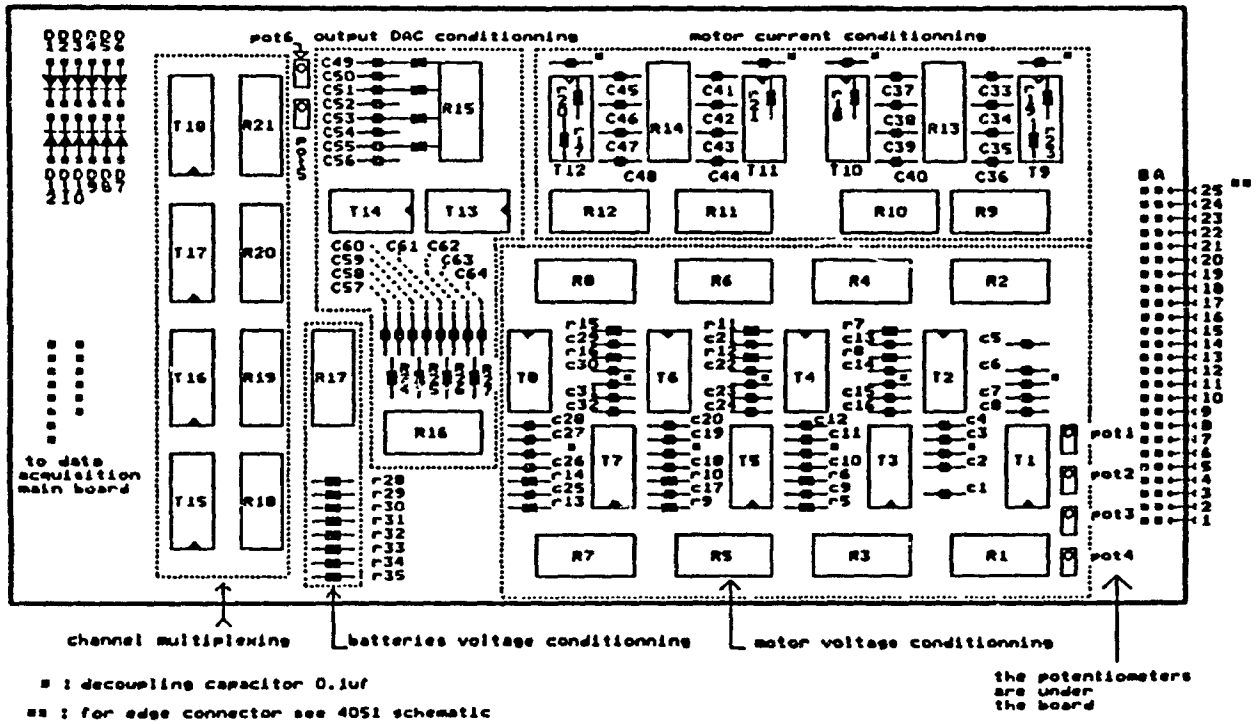

Fig. C.17 Component Layout of the Signal Conditioning Circuit Board

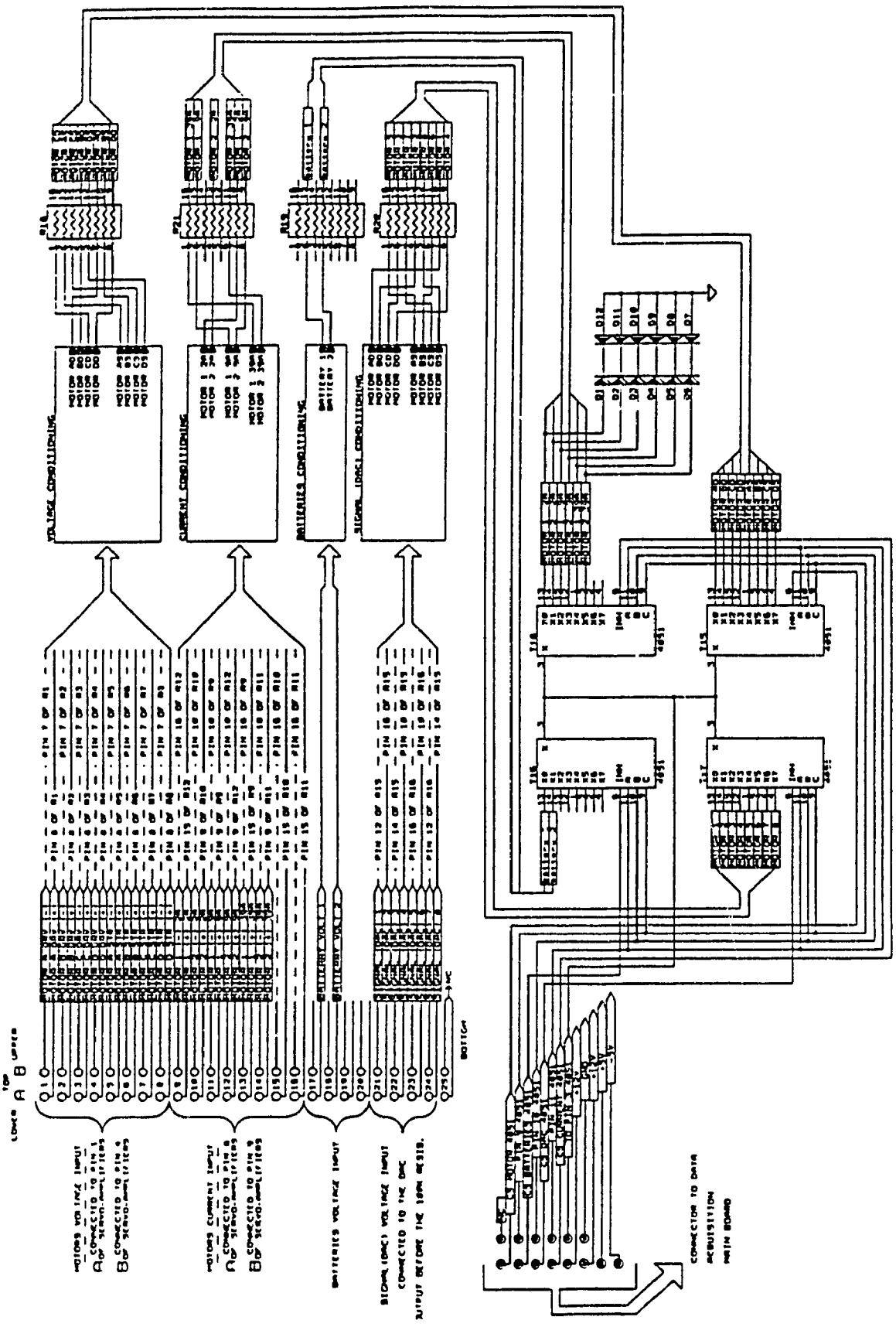

Fig. C.18 Data Acquisition Multiplexing Interface

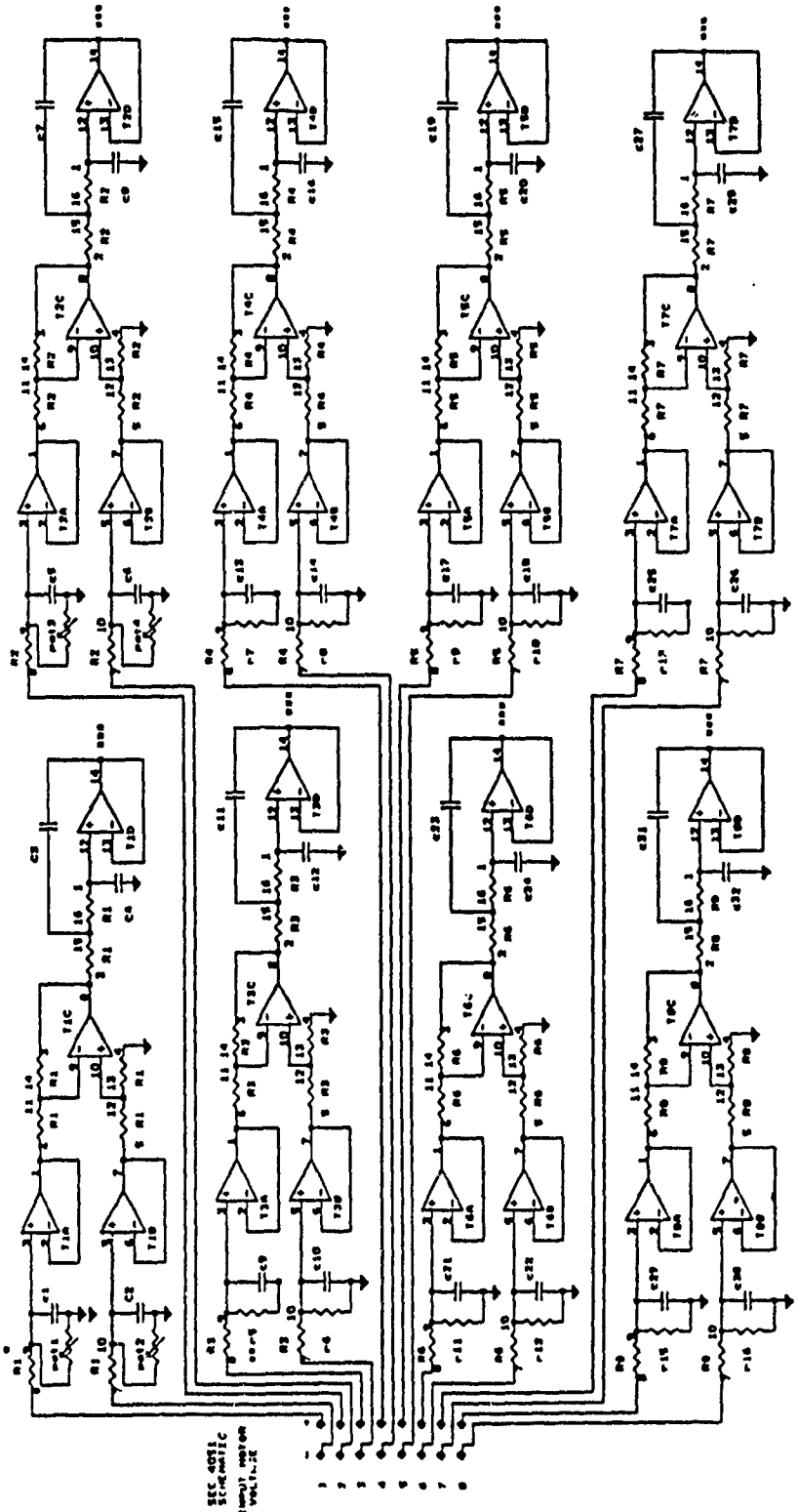

Fig. C.19 Data Acquisition Motor Voltage Conditioning Interface

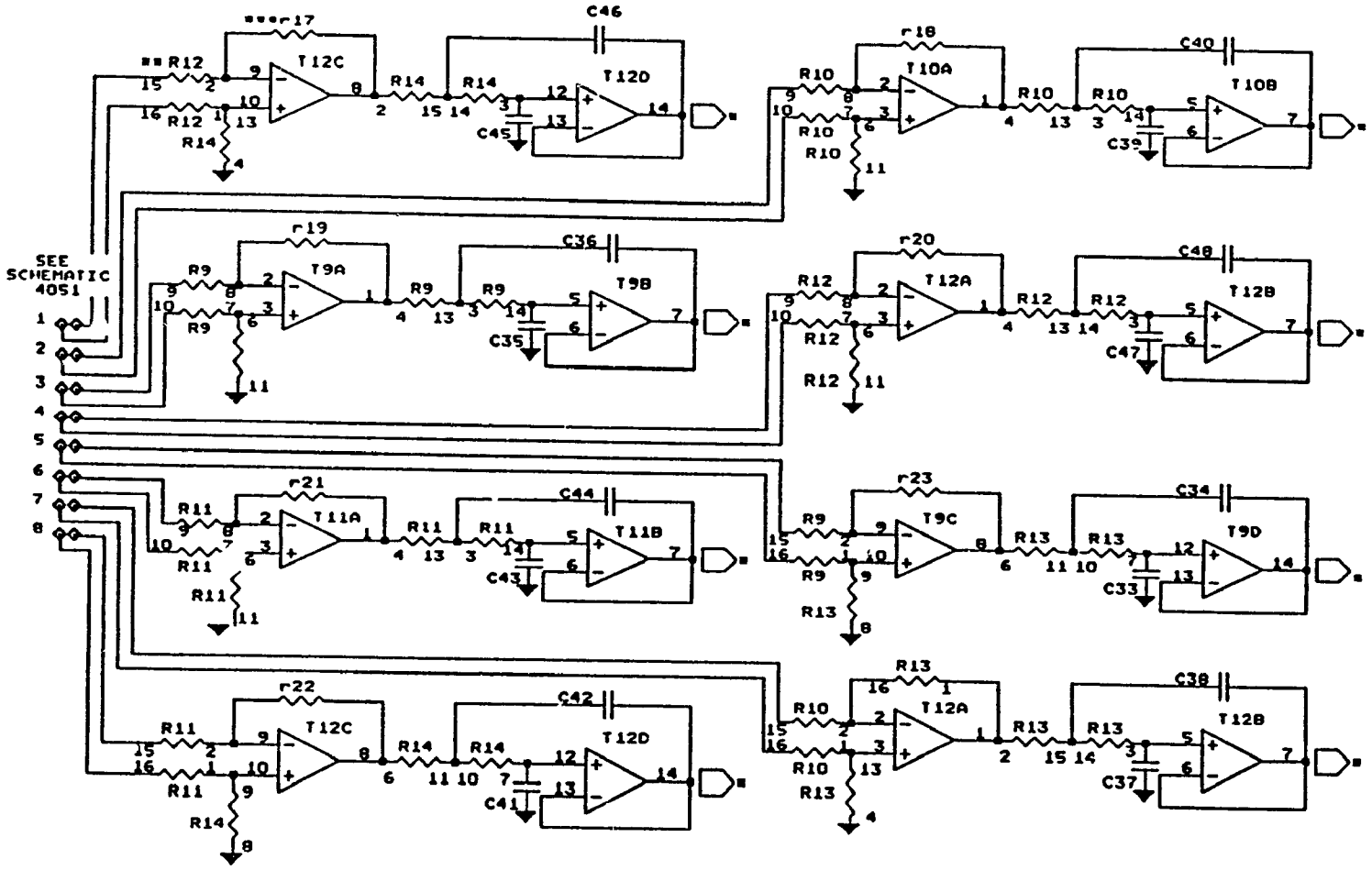

■ : SEE SCHEMATIC 4051

■■ : CAPITAL R = RESISTOR ARRAY

■■■ : NORMAL r = SINGLE RESISTOR

Fig. C.20 Data Acquisition Motor Current Conditioning Interface

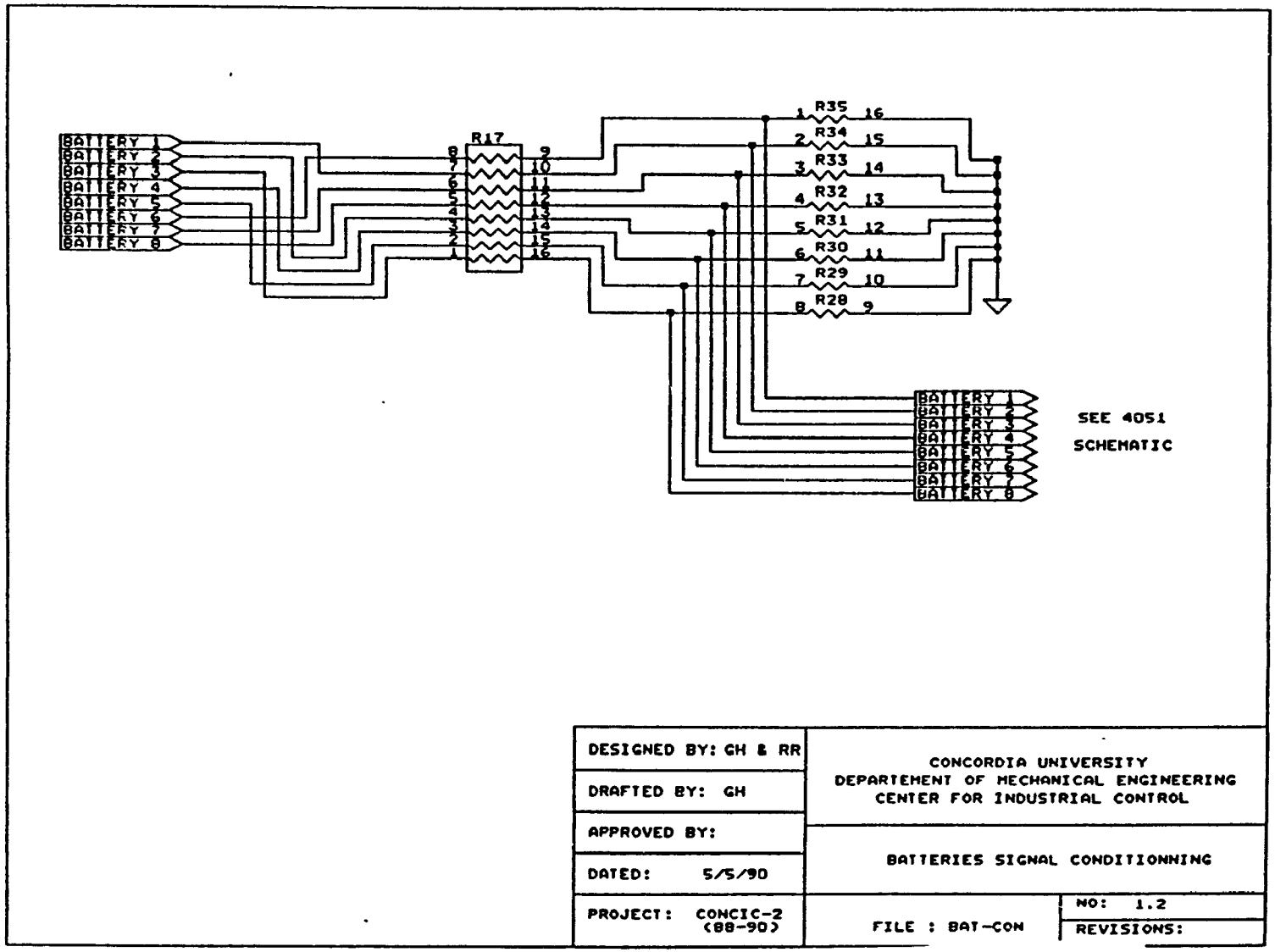

Fig. C.21 Data Acquisition Battery Voltage Conditioning Interface

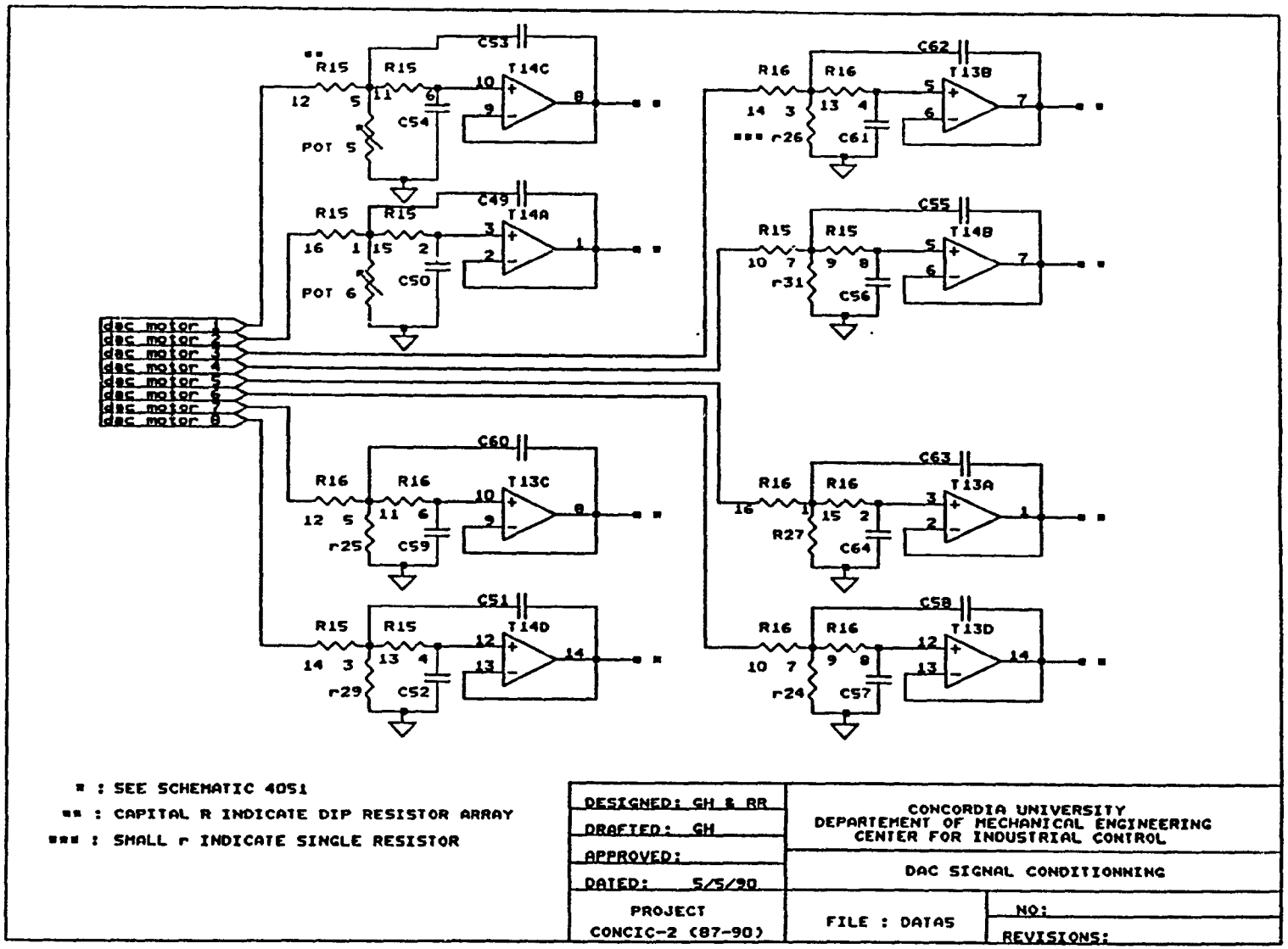

Fig. C.22 Data Acquisition DAC-08 Voltage Conditioning Interface

APPENDIX - D

CAMERA MULTIPLEXER INTERFACE DESCRIPTION

APPENDIX - D

CAMERA MULTIPLEXER INTERFACE DESCRIPTION

D.1 Introduction

The purpose of the camera multiplexer circuit is to allow two Idetix cameras to be connected to one Idetix camera controller board. Both cameras are connected to the interface board in parallel, with the exception of one signal - the data sent from the optic rams to the controller board. The most significant address bit sent from the controller board to the cameras decides which camera will have its data sent to the interface board when a picture is taken. This division takes place at the address location that corresponds to 1 K byte. The parameters to be downloaded to the camera controller for single and double cameras are provided in Table. D.1. This table shows a situation wherein it is desired to receive only 512 bytes of data from each camera. The row increment has been set to be twice that for the 1 K byte situation.

Parameter	Front Only	Rear Only	Both Cameras
Starting Row Address	0x0080	0x00fe	0x0080
Row Increment	0x02	0x02	0x04
Last Row	0x00fe	0x17c	0x017c
Number of Bytes	1 K Bytes	1 K Bytes	1 K Bytes

Table. D.1 Camera Controller Parameters for Downloading

With this interface, as far as the camera controller board is concerned only one camera is connected and is referred as a *virtual camera* in this

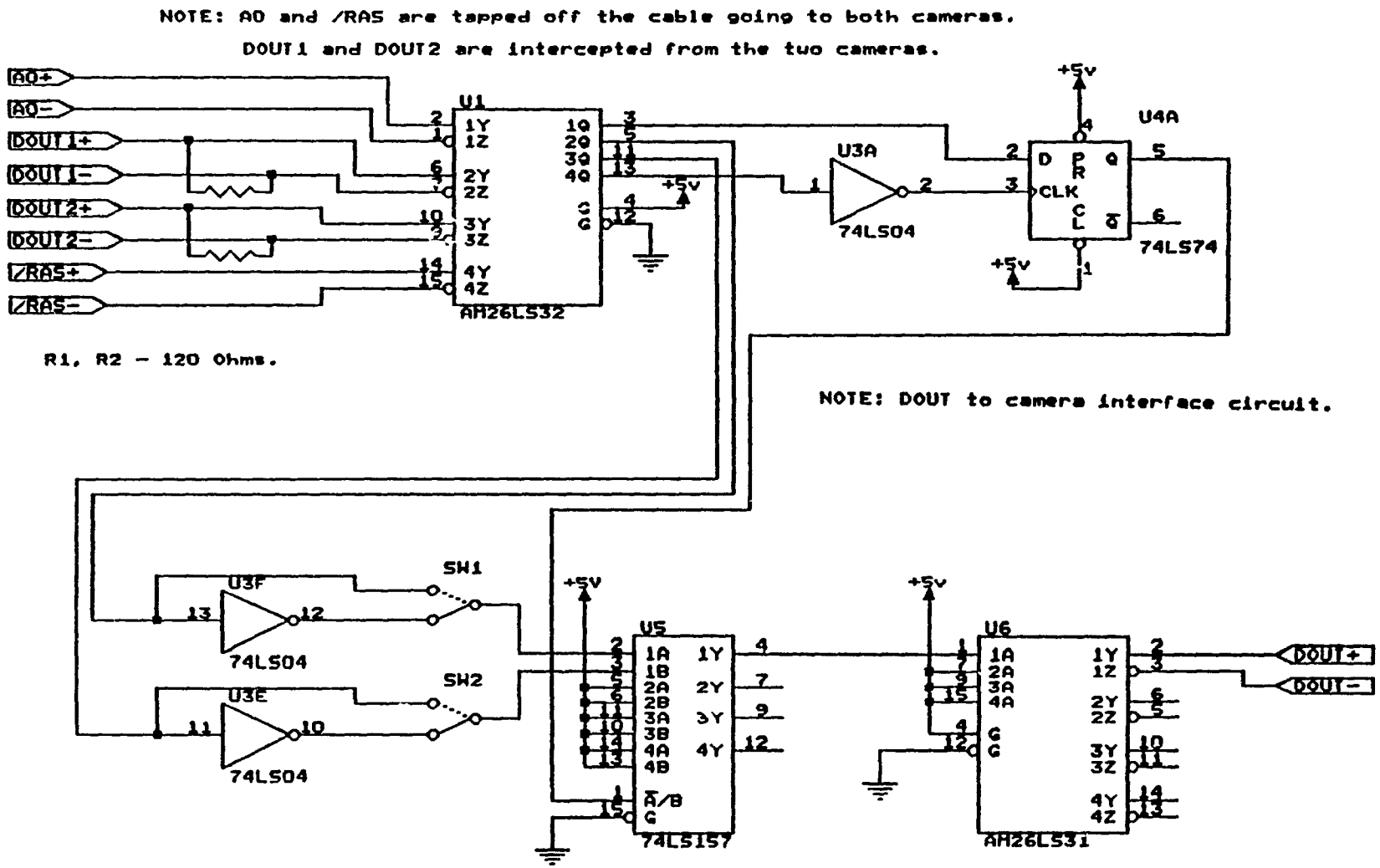

Fig. D.1 Camera Multiplexing Circuit Interface

thesis. When the interface board tries to read the first half of the image from the *virtual camera*, it will receive the image from the first camera. When it tries to read the second half of the image from the *virtual camera*, the image data from the second camera is received by the camera controller. The main benefit of this approach is that only one interface board is required, and the time required to obtain two pictures is the same as for one full picture.

D.2 Circuit Description

The interface circuit for two cameras using one controller is presented in Fig. D.1. This interface has three ports of which two are incoming and the other is outgoing. The incoming ports are connected to the camera heads while the outgoing one is connected to the camera controller board. In this setup, there are two switches to select single or double cameras for data transfer and to reverse the image. The image reversal is useful for white tape/paint on the floor instead of the black tape/paint that is used normally.

All the signals from the interface board are connected to both cameras, with the exception of the DOUT signals which are intercepted by the circuit. An AM26LS32 quad differential line receiver taps the A0 (input 1) and $\overline{RAS}$ (input 4) signals from the cable which connects the two cameras to the interface board. The data out (DOUT) signals from each camera are intercepted by the receiver chip (inputs 2 & 3), with 120 Ohm terminating resistors on the inputs. Output 4 ($\overline{RAS}$) of the Am26LS32 is inverted and is used to clock a 74LS74 flip-flop. Output 1 (A0) of the Am26LS32 is presented as the data

input to the flip-flop. When $\overline{RAS}$ makes a high to low transition, it indicates a valid row address. A0 is the most significant bit of the address byte, which is used to indicate which half of the image is being read from the cameras. After A0 is clocked into the flip-flop by $\overline{RAS}$, it is sent to the $\overline{A}/B$ input of the 74LS157 quadruple 2-line to 1-line data selector/multiplexer which selects which camera's data is to be sent to the interface board. Outputs 2 and 3 of the AM26LS32 (DOUT1 and DOUT2, respectively) are connected to a 74LS04 hex inverter, and to SPDT switches S1 and S2. The switches determine whether a positive or a negative image will be sent to the camera interface board. The 74LS157 will present on its output the data from camera 1 or camera 2, depending on whether A0 is low or high. The output data is sent to an AM26LS31 quad differential line driver, whose output is connected to the DOUT input of the camera interface board. The circuit derives its power from the +5V and GND lines coming from the camera interface board.

APPENDIX - E

SYSTEM DIAGNOSTICS

APPENDIX - E

SYSTEM DIAGNOSTICS

Symptom	Probable Cause
The motors start turning continuously as soon as the power is turned on and software loading is completed.	Check the feedback connections. Loss of feedback signal.
The motors change directions rapidly and seems to oscillate while the main menu is displayed.	1) Defective LM628 chip. 2) Chips and the controller board may not be properly secured in place. Push the chips and the board.
LM628 Motion Controller not responding message displayed on the screen while in some modes.	This is because the motion controller chip is not communicating with the host computer. Stop the system, push the chips If the problem persists, change the chips
Full motor speed is attained as soon as the speed request key is depressed. NO RESPONSE for PANIC stop keys and the MOTOR STOPS only for NORMAL stop.	Feedback is not operational. If only one motor gives this problem interchange the snap-on connector with the other motor working properly. If the problem is still present then, check the encoder signals by rotating the motor by hand. Check the wiring. If the motor behaves properly after interchanging, check the LM628 connections to the snap-on connector as well as the DB-37 connector on the board. Also interchange the LM628 chips to check for a defective chip.
Graphics card not initialized message appears on the screen.	Motion Controller Board Missing. Address decoding is absent. Decoder is defective. Hercules graphics card missing. Graphics functions used without initializing the hercules card by software.
Screen is blank in graphics mode but is working well for text mode.	Hercules graphics card missing.

The image is white completely.	Camera head not connected. The interface in the camera head is defective.
Dark screen image with a white line running on the screen in camera mode.	Camera controller defective Disconnect the camera from the controller and check for a fully white (bright) image If the problem persists, then the controller is defective. Otherwise the interface board in the camera malfunctioning.
No camera image on screen	Check the lights. May be off. Check the aperture opening. Check the floor for dark patches. Exposure time may be too small.
Computer and the monitor are not working properly.	Power for the computer is low. Check the battery connected to the computer.
Monitor and the computer seem to be functioning, but the AGV slows down gradually.	Computer power is too low. Not enough power for the servo amplifiers. Check the amplifier indicator LEDs for power low condition. Charge the batteries.
One of the motors turn too fast all of sudden and gets back to normal speed.	Feedback connections loose. Servo controller chips are not secured in place properly.

APPENDIX - F

OPERATING SYSTEM SOFTWARE DESCRIPTION

APPENDIX - F

OPERATING SYSTEM SOFTWARE DESCRIPTION

F.1 Show the Default Setup

This option allows one to check the default or chosen options of the vehicle. The console display shows the number of servo controllers employed, gain values for the PID filters, step change in velocity and the acceleration value, number of cameras employed and the camera that is being used for control, the type of controller used by the camera vision mode and the gains for this controller, and indicates whether the vehicle is travelling in the forward or reverse direction. The camera window dimensions (number of pixels converted to distances in mm) and shows whether the wheels are lifted off the ground or not are also displayed.

F.2 Modification of the Default Setup

The various options provided are discussed below.

(1) Wheels lifted up condition - The PID gains for the wheels lifted up condition should be very much smaller than the normal running condition. This is due to the fact that when the wheels are lifted off the floor, the motors have to overcome only their inertia and no external loading exists. Experimentally the gains values have been determined and are provided as a default condition.

(2) Number of servo controllers onboard - The servo controller board has provisions to accommodate upto 4 motion controllers. As a result of this, the vehicle structure can be modified to accommodate more than two driving wheels or a maximum of two driving and steered wheels.

(3) Controller Gains - The gains for the PID filter of the motion controller can be modified in order to study their effect on the vehicle performance.

(4) AGV cruising speed and acceleration - This option provides step changes in the cruising speed of the vehicle and the desired acceleration value. These options are useful for experimental verification of the vehicle performance.

(5) Controller selection in the camera mode - Various controller options are provided. Proportional, Proportional and Integral, Non-linear or dual camera are the possible options. If the dual camera mode is selected, the gains for the camera mode and the number of cameras are preset automatically to a particular value unless they are modified using the appropriate option.

(6) Controller gains in the camera mode - The gains G1 and G2 for the orientation offset and the position offset respectively as well as G3, the gain for the Integral controller can be modified to study the effect of these gains on the tracking performance of the vehicle.

(7) Camera for guidance - This option is to choose the front or rear camera for guidance in the single camera mode.

(8) Number of cameras in use - To study the effectiveness of the dual and single camera modes, this mode is provided. In single camera mode, only one camera is used for guidance, but the parameters from the other camera can be stored using the data acquisition system of the AGV.

(9) Provision to enter the calibrated values of the camera window dimension - This provides the window dimensions in order to convert the pixel count information to a corresponding distance in mm.

(10) The number of rows of the image used for image analysis - This can be changed in order to evaluate the accuracy with which the camera image analysis can be performed.

F.3 Camera Calibration Mode

This mode is provided to calibrate the camera vision setup used for vehicle guidance. Upon entering this mode, the focus, the aperture opening of the lens, the exposure time and the lights for track illumination can be adjusted in order to get a clear picture of the track image. The window size is measured in order to provide a calibration that converts the number of pixels to a corresponding value in mm. The console display shows the track width, position and orientation of the center of the track image relative to the center line of the image window. This information is used to check the accuracy of the parameters measured using the camera compared to known values of the position and orientation. This calibration process needs to be carried out periodically in order to make sure that the camera and the lighting arrangement have not been disturbed.

F.4 Keypad Mode

This is a semi-manual mode in which the vehicle is driven by manipulating the arrow keys on the keypad of the host computer. This is equivalent to driving the vehicle using a joy stick. This feature is

provided to bring the vehicle to the desired location. This feature is also used to check the proper functioning of the vehicle controllers, the servo amplifiers, the motors and the encoders. The UP/DOWN and the LEFT/RIGHT arrow keys are assigned to drive the left and right wheels of the vehicle. The UP/LEFT and the DOWN/RIGHT keys are used to rotate the wheels in the clockwise and counter clockwise directions respectively. The menu shows the camera image, the desired and the actual wheel speeds and the operating menu to perform a variety of control are shown. Provisions to start and stop the data acquisition option, and the ultrasonic sensors are also included.

F.5 Camera Vision Mode

This mode uses the binary camera vision for guidance. In this mode of operation, the cruising speed of the vehicle is altered by operating the UP/DOWN arrow keys. This mode uses the noise filtering, image analysis and the inverse kinematic analysis to compute the wheel speeds using the command cruising speed and the parameters obtained from the camera presented in chapter 5 for vehicle control. The AGV simply follows the track on the floor and ignores any junctions that may be present in the track. The vehicle can use the front camera or rear camera or both cameras for guidance or guidance based on track profile identification which is described in chapter 5. The screen displays the vehicle status such as data acquisition started, sonar on, obstacle detected and so on are displayed in the status window. The various options that are available are shown in the lower part of the window. The option of using (f)ront, (r)ear or (b)oth cameras for guidance is achieved by operating the keys that are shown in parenthesis. The vehicle is commanded to stop if the track image is absent for 4 consecutive frames if the track profile identification and guidance mode is not requested.

F.6 Dual Mode - Random Turning Options

A special demonstration mode is implemented to confine the vehicle to run in a circuit consisting of a circular path with two diametrically opposite straight line segments. Thus the vehicle can continuously demonstrate its versatility to negotiate curvature and take appropriate actions at several common road signs (crosses, T junctions and branches). By allowing the vehicle to make its own decision as to which direction to take at the road sign, one achieves a continuous demonstration in which the coasting speed alone needs to be specified. The primitives and the road signs identification scheme described in section 5.5 is implemented in this mode.

Here the screen window is the same as in the previous mode (camera vision mode) but the status window reports about the turn junction being identified and the turning option selected randomly. A random number generator is used and is initialized with the time of the day in order to avoid the pseudo-random generation. At a cross junction as in Fig. 6.31, a random number is generated first to decide whether the AGV should continue to travel along the original direction of travel or make a turn. The vehicle turns if the random number is even otherwise travels straight. Once the decision is to turn, then the random number is generated once again, and based on the odd or even nature of the number the AGV is commanded to turn left or right. Once the decision is to turn, the AGV reduces the speed gradually and comes to a dead stop as soon as the geometric center of the vehicle is aligned with the intersection. During this slowing down process, the distance travelled by each wheel is used to compute the distance

travelled by the AGV. This distance is then compared with the actual distance between the camera center line and the geometric center of the AGV.

F.7 Dual Mode - Defined Turning Options

The system is also provided with a user defined turning options mode. In this mode, a script file is provided to the operating program of the AGV. This file contains information concerning turning (left/right/straight) at a particular junction as well as information whether the vehicle has to wait for a certain duration in order to complete machining operations on the component that is being carried. A sample script file is shown in Fig. 6.32. In this figure, the first column is the junction number, the second one is the decision and the third column is the waiting time. This mode uses the same module as used by the previous mode but also checks for the turning option that is read from the file. The validity of the turning option defined in the file with the option available on the floor is also checked. If the defined option is invalid then the vehicle is commanded to stop and a message is displayed in the status window of the vehicle.

F.8 Remote Radio Link Mode

The operation of the radio link mode has been described in section 6.3.9. The remote radio link option has two sub-modes of operatio, the keypad and the camera vision. The difference between the operation of these sub-modes compared to the normal usage is that it checks the serial port of the pc for data at the end of every cycle of operation and puts data on the serial link concerning the status of the AGV. The data on the serial port read by the pc is the command received via the radio link from an external supervisory computer. The data available on the serial port has two

parts. One is the actual data and the other is the carriage return which indicates the termination of the data.

F.9 Dead-reckoning Control Mode

This mode is provided to drive the AGV through a known trajectory without the use of camera vision feedback. There are three sub-modes available based on the geometric profile of the trajectory to be followed by the AGV. They are the straight line functions, the conic functions and the polynomial functions. The cruising speed of the vehicle is specified before starting the motion and this can be changed while the vehicle is in motion.

F.10 Data Acquisition Channels Selection Mode

This mode enables the selection of the number of samples per channel. The data from the channels that need to be stored are provided. This mode also has options to store the junction signs while in dual mode, specify the nature of the track profile for identification scheme, and it also has the option to store the sampled data in a file. While allocating memory for data storage, the availability of memory space is also checked. For the host computer of the AGV, the total available memory space is 640 K bytes. The DOS and the operating program of the AGV occupy 64 K bytes and 146 K bytes (approximately) respectively. This leaves 430 K bytes of memory for data storage. Since the data stored are floating points (4 bytes each), a total of 107 K bytes of data can be stored. The maximum number of channels currently used are 22 and hence the maximum value of the total data per channel is 4800 (approximately). The sampling interval is 50 ms and this indicates that the data storage duration is 250 seconds.

F.11 Data Acquisition Channels Calibration Mode

This is provided to calibrate the data acquisition channels. In the case of hardware channels, the data received from the analog to digital converter of the data acquisition system is a number which has to be converted to a corresponding voltage or current value. In order to perform this, each channel is connected to an external power supply and the potentiometers are adjusted to get a full scale reading of the digital value corresponding to the maximum voltage/current the channel is expected to measure. The software channel readings can also be obtained. This is to get a relationship between the motor terminal voltage, duty cycle of the pulse width and the motor speed.

APPENDIX - G

DYNAMIC MODEL OF CONCIC-II AGV

APPENDIX - G

DYNAMIC MODEL OF CONCIC-II AGV

G.1 Introduction

The objective of this appendix is to provide an abridged version of the dynamic model of the CONCIC-II AGV system presented by Huang [35]. The dynamic model and the simulation package developed by Huang [35] has been used to perform some of the simulations to study the behavior of the CONCIC-II AGV with single and dual camera guidance. Changes are incorporated in the simulation package in the control scheme for dual camera guidance discussed in Chapter 5 & 7.

G.2 Modeling of the Vehicle

The various components of the CONCIC-II AGV considered for modeling are, the mechanical structure, the driving units (motor-in-wheel-drive units), LM628 motion controller chips, digitial to analog converter, servo amplifier, the encoder feedback and the binary camera vision system. The following analysis are on the modeling aspects of the above mentioned components.

G.2.1 Assumptions

In the following modeling formulations, the vehicle is considered as a collection of 3 interconnected rigid bodies, i.e. the AGV body (plus the two motorized wheels which are rigidly mounted to it) and the two casters. Since it has been assumed that there are no side slips, the vehicle body can be considered as a rigid body with two degrees of freedom -- the forward translation and the yaw rotation. The casters have one more degree of freedom since it can rotate freely about the pivot axis.

For each of the rigid bodies, resistance (friction) forces act at the contact patch between this rigid body and the floor, and reaction forces between adjacent rigid bodies. In the case of motorized wheel, the tractive force also exists between the wheel and the floor. The resistance (friction) is dependent on the characteristics of the tires and the condition of the floor. The reaction forces are the links between the rigid bodies. The tractive forces are dependent on the characteristics of the motor in the motorized wheel. A detailed discussion of these forces is presented in section G.3. The assumptions are summarized into three groups and are

i. Vehicle Body

- the vehicle body is considered to be a two degrees of freedom system
- the vehicle has a symmetrical structure about the fore-and-aft plane of the vehicle
- the location of the center of the mass coincides with the geometrical center of the vehicle

ii. Driving Wheels, Casters and the Servo System

- the two motor-wheel units and their servo systems are considered to be identical
- the weight support of the vehicle is equally distributed to all the wheels and casters
- the wheels and casters roll without longitudinal or side slip
- the casters take about 1% of the total mass, therefore their mass is considered negligible
- two casters are considered to have the same characteristics
- no friction in the bearings of the casters
- the working surface offers sufficient friction to prevent side slip or

longitudinal slip at the wheels. This assumption is valid since the AGV is used mostly for indoor applications and the maximum operating speed is limited to 1.2 m/s.

iii. Visual Feedback System

- the camera image window is assumed to have no limit

G.2.2 Mechanical Structure Load Distribution

The location of the components of the AGV are shown in Fig. B.5. This arrangement facilitates that the mass center to coincide more or less with the geometric center. As a result of this, the normal force endured by the four wheels can be assumed to be the same. The normal reaction at the wheels and floor is calculated by

$$N_i = \frac{\text{weight of the vehicle body}}{4} + \text{Weight of the wheel (i)} \qquad \text{(G.1)}$$

where the subscript i presents the location of the wheels:

i = 1 for the left motorized wheel;

i = 2 for the right motorized wheel;

i = f for the front caster;

i = r for the rear caster.

G.3 Review of Vehicle Dynamics

Fig. G.1 represents a body-centered system XYZ of a rigid body. Consider a typical point P(x, y, z) within the system moving with linear velocities u, v, w, in the X, Y, Z direction respectively. Let U, V, W be the instantaneous velocities of the origin in direction X, Y, Z and p, q, r be the rotational velocities about X, Y, Z. The direction of the angular velocities are defined

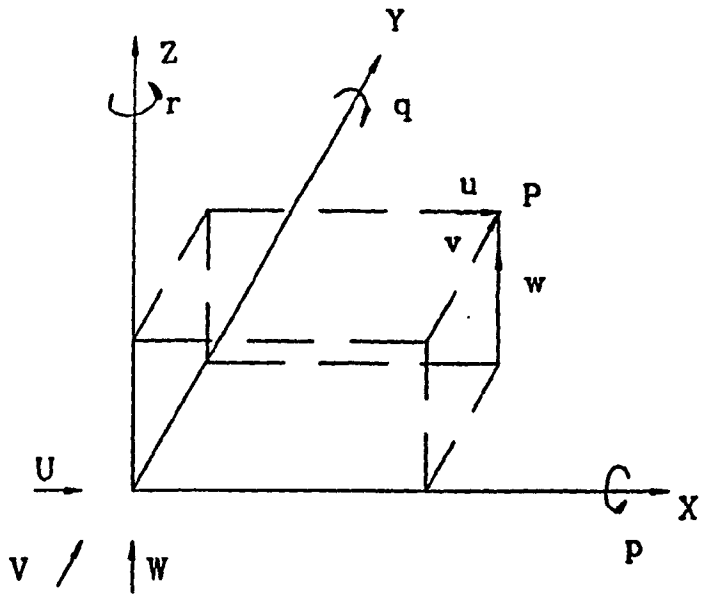

Fig. G.1 Body Centered System

by the right-hand rule.

The velocities of the point P can be presented as follows [30]:

$$\left.\begin{aligned} u &= U - r\cdot y + q\cdot z \\ v &= V - p\cdot z + r\cdot x \\ w &= W - q\cdot x + p\cdot y \end{aligned}\right\} \qquad (G.1)$$

Differentiating equations (G.1) with time, the acceleration $\dot{u}$, $\dot{v}$, and $\dot{w}$ are :

$$\left.\begin{aligned} \dot{u} &= {}^{du}/_{dt} = \dot{U} - \dot{r}\cdot y - r\cdot\dot{y} + \dot{q}\cdot z + q\cdot\dot{z} \\ \dot{v} &= {}^{dv}/_{dt} = \dot{V} - \dot{p}\cdot z - p\cdot\dot{z} + \dot{r}\cdot x + r\cdot\dot{x} \\ \dot{w} &= {}^{dw}/_{dt} = \dot{W} - \dot{q}\cdot x - q\cdot\dot{x} + \dot{p}\cdot y + p\cdot\dot{y} \end{aligned}\right\} \qquad (G.2)$$

Substituting equations (G.2) with $\dot{x} = u$, $\dot{y} = v$, $\dot{z} = w$,

$$\left.\begin{aligned} \dot{u} &= \dot{U} - \dot{r}\cdot y - r\cdot v + \dot{q}\cdot z + q\cdot w \\ \dot{v} &= \dot{V} - \dot{p}\cdot z - p\cdot w + \dot{r}\cdot x + r\cdot u \\ \dot{w} &= \dot{W} - \dot{q}\cdot x - q\cdot u + \dot{p}\cdot y + p\cdot v \end{aligned}\right\} \qquad (G.3)$$

Replacing u, v, w in the equation of $\dot{u}$ by equations (G.1):

$$\left.\begin{aligned} \dot{u} &= \dot{U} - r\cdot(V - p\cdot z + r\cdot x) - \dot{r}\cdot y + q\cdot(W - q\cdot x + p\cdot y) + \dot{q}\cdot z \\ &= \dot{U} - r\cdot V + q\cdot W + r\cdot p\cdot z - r^2\cdot x - \dot{r}\cdot y - q^2\cdot x + p\cdot q\cdot y + \dot{q}\cdot z \\ &= \dot{U} - r\cdot V + q\cdot W - (r^2 + q^2)\cdot x + (p\cdot q - \dot{r})\cdot y + (r\cdot p + \dot{q})\cdot z \end{aligned}\right\} \qquad (G.4)$$

Hence equations (G.3) can be shown to be as follows:

$$\left.\begin{aligned} \dot{u} &= \dot{U} - r\cdot V + q\cdot W - (q + r)\cdot x + (q\cdot p - r)\cdot y + (r\cdot p + q)\cdot z \\ \dot{v} &= \dot{V} - p\cdot W + r\cdot U - (p^2 + r^2)\cdot y + (r\cdot q - p)\cdot z + (p\cdot q + r)\cdot x \end{aligned}\right\} \quad (G.5)$$

Equations (G.5) defines the accelerations of the point P(x,y,z) in a rigid body in terms of the accelerations and velocities of the origin of the body-centered system. Applying D'Alembert's principle, the equations of motion of the rigid body are:

$$\left.\begin{aligned} \textstyle\sum \delta\, m\ \dot{u} &= \textstyle\sum X, \text{ the total external force in X direction} \\ \textstyle\sum \delta\, m\ \dot{v} &= \textstyle\sum Y, \text{ the total external force in Y direction} \\ \textstyle\sum \delta\, m\ \dot{w} &= \textstyle\sum Z, \text{ the total external force in Z direction} \\ \textstyle\sum \delta m\ (y\cdot \dot{w} - z\cdot \dot{v}) &= \textstyle\sum L, \text{ the total external moment about x axis} \\ \textstyle\sum \delta m\ (z\cdot \dot{u} - x\cdot \dot{w}) &= \textstyle\sum M, \text{ the total external moment about y axis} \\ \textstyle\sum \delta m\ (x\cdot \dot{v} - y\cdot \dot{u}) &= \textstyle\sum Z, \text{ the total external moment about z axis} \end{aligned}\right\} \quad (G.6)$$

The moments and products of the inertia of rigid body are defined as

$$\left.\begin{aligned} I_x &= \textstyle\sum[\delta m(y^2 + z^2)] = \text{moment of inertia about OX} \\ I_y &= \textstyle\sum[\delta m(x^2 + z^2)] = \text{moment of inertia about OY} \\ I_z &= \textstyle\sum[\delta m(y^2 + x^2)] = \text{moment of inertia about OZ} \\ P_{yz} &= \textstyle\sum(\delta myz) = \text{product of inertia about OY and OZ} \\ P_{xz} &= \textstyle\sum(\delta mxz) = \text{product of inertia about OY and OZ} \\ P_{xy} &= \textstyle\sum(\delta mxy) = \text{product of inertia about OX and OY} \end{aligned}\right\} \quad (G.7)$$

If the origin of the body-centered system is defined to be at the center of the body, then

$$\sum(\delta mx) = \sum(\delta my) = \sum(\delta mz) = 0 \tag{G.8}$$

Substituting the equation of $\sum M$ in equations (G.6) by (G.5):

$$\sum M = \sum[\delta m(z\cdot\dot{u} - x\cdot\dot{w})]$$

$$\sum M = \sum\Big(\delta m\{z\cdot[\dot{U} - r\cdot V + q\cdot W - (q^2 + r^2)\cdot x + (q\cdot p - \dot{r})\cdot y + (r\cdot p + \dot{q})\cdot z] - x\cdot[\dot{W} - q\cdot U + p\cdot V - (p^2 + q^2)\, z + (p\cdot r - \dot{q})\cdot x + (q\cdot r + \dot{p})y]\}\Big)$$

$$\sum M = \sum(\delta mz)\cdot\dot{U} - \sum(\delta mz)\cdot r\cdot V - \sum(\delta mz)\cdot q\cdot W - (q^2 + r^2)\sum(\delta mxz) + (q\cdot p - \dot{r})\sum(\delta mzy) + (r\cdot p + \dot{q})\sum(\delta mz^2) - \sum(\delta mx)\dot{W} + \sum(\delta mx)\cdot q\cdot U - \sum(\delta mx)\cdot p\cdot V + (p^2 + q^2)\sum(\delta mzx) - (p\cdot r - \dot{q})\sum(\delta mx^2) - (q\cdot r + \dot{p})\sum(\delta mxy)$$

Collecting the terms in (G.7), and using equation (G.8), the external moment of a rigid body about Y axis $\sum M$ with a body-centered system located at its mass center can be written as:

$$\begin{aligned}\sum M &= -(q^2 + r^2)P_{xz} + (q\cdot p - r)P_{zy} + (r\cdot p + q)\sum(\delta mz^2) + (p^2 + q^2)P_{xz} - (p\cdot r - q)\sum(\delta mx^2) - (q\cdot r - p)P_{xy} \\ &= I_y\dot{q} - (I_z - I_x)p\cdot r + (p^2 - r^2)P_{xz} - (q\cdot r + \dot{p})I_{xy} + (q\cdot p - \dot{r})P_{zy}\end{aligned} \tag{G.9}$$

By following the same procedure, all the external forces and moments of a rigid body with a body-centered system located at its mass center can be obtained as:

$$\left.\begin{aligned}
\sum X &= m(\dot{U} - r\cdot V + q\cdot W)\\
\sum Y &= m(\dot{V} - p\cdot W + r\cdot U)\\
\sum Z &= m(\dot{W} - q\cdot U + p\cdot V)\\
\sum L &= I_x\dot{p} - (I_y - I_z)q\cdot r + (r^2 - q^2)P_{yz} - (p\cdot q + \dot{r})P_{xz} + (p\cdot r - \dot{q})P_{xy}\\
\sum M &= I_y\dot{q} - (I_z - I_x)p\cdot r + (p^2 - r^2)P_{xz} - (q\cdot r + \dot{p})P_{xy} + (q\cdot p - \dot{r})P_{zy}\\
\sum N &= I_z\dot{r} - (I_x - I_y)q\cdot p + (q^2 - p^2)P_{xy} - (r\cdot p + \dot{q})P_{yz} + (r\cdot q - \dot{p})P_{xz}
\end{aligned}\right\} \quad (G.10)$$

When there is no overhead in the z axis, $W = \dot{W} = 0$. Equation (G.10) becomes:

$$\left.\begin{aligned}
\sum X &= m(\dot{U} - r\cdot V)\\
\sum Y &= m(\dot{V} + r\cdot U)\\
\sum L &= I_x\dot{p} - (I_y - I_z)q\cdot r + (r^2 - q^2)P_{yz} - (p\cdot q + \dot{r})P_{xz} + (p\cdot r - \dot{q})P_{xy}\\
\sum M &= I_y\dot{q} - (I_z - I_x)p\cdot r + (p^2 - r^2)P_{xz} - (q\cdot r + \dot{p})P_{xy} + (q\cdot p - \dot{r})P_{zy}\\
\sum N &= I_z\dot{r} - (I_x - I_y)q\cdot p + (q^2 - p^2)P_{xy} - (r\cdot p + \dot{q})P_{yz} + (r\cdot q - \dot{p})P_{xz}
\end{aligned}\right\} \quad (G.11)$$

Furthermore, for a 3 d-o-f rigid body moving along x, y, and rotating about z, then the moments about x, and y axis are also considered to be balanced. Correspondingly $p = \dot{p} = 0$, $q = \dot{q} = 0$. The motion equations are:

$$\left.\begin{aligned} \sum X &= m(\dot{U} - r \cdot V) \\ \sum Y &= m(\dot{V} + r \cdot U) \\ \sum N &= I_z \dot{r} \end{aligned}\right\} \qquad \text{(G.12)}$$

Similarly for a 2 d-o-f rigid body moving along y and rotating about z, then $U=\dot{U}=0$. From equations (G.12), the equation for 2 d-o-f are:

$$\left.\begin{aligned} \sum Y &= m \cdot \dot{V} \\ \sum N &= I_z \cdot \dot{r} \end{aligned}\right\} \qquad \text{(G.13)}$$

G.4 Equations of Motion for the CONCIC-2 AGV

The equations of motion are derived by applying the vehicle dynamics in section G.2 to the three independent rigid bodies, the AGV body with two motorized wheels mounted on it rigidly, and two casters which can rotate freely about the pivot axis. For the convenience, the following definitions are used in the later discussion. Main body of the vehicle is defined as the AGV without the four wheels. AGV body is referred to the main body of the vehicle with two motorized wheels.

Fig. G.2 presents the entire AGV subject to all the external forces. These forces act at the contact patch of the two motorized wheels and the two casters. The forces can be grouped under three categories:

- friction forces including rolling resistance and lateral forces;
- tractive forces;
- normal reaction forces.

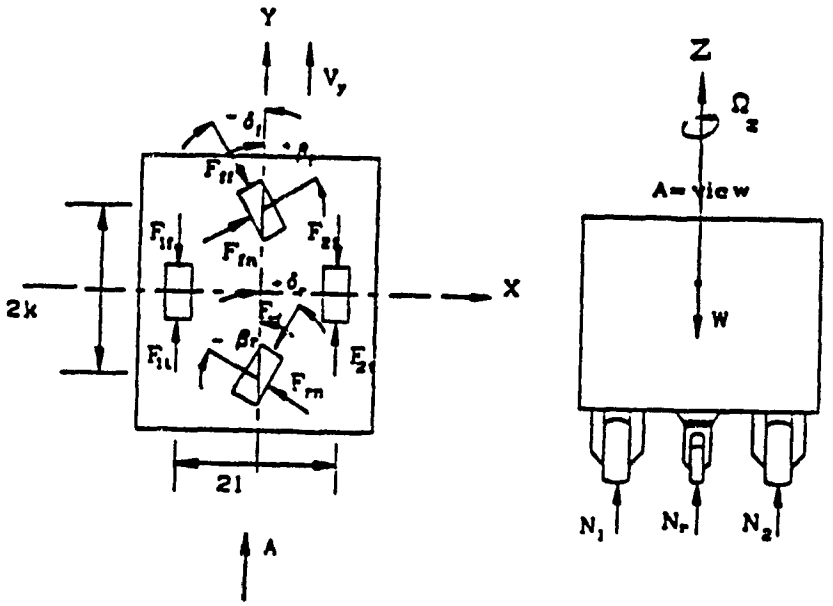

Fig. G.2 Schematic of Body Centered System and External Forces for CONCIC-II AGV

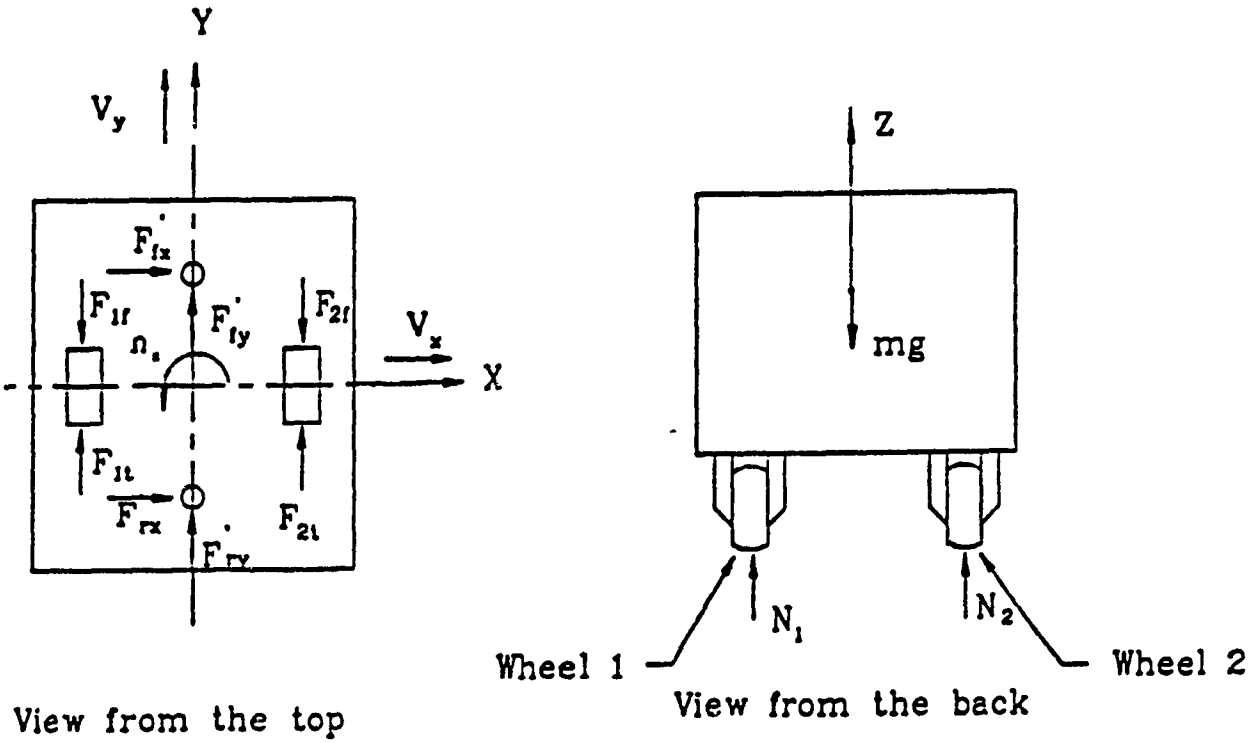

Fig. G.3 AGV Body with All the External Forces

The notation for the first two categories is F_{ij}, where the first subscript i stands for the location of the wheels or casters:

1 for the left motorized wheel;

2 for the right motorized wheel;

f for the front caster;

r for the rear cater.

Where second subscript j stands for the type of force:

f for the rolling resistance;

n for the lateral force;

t for the tractive force.

For the normal reaction forces, the following notation is used:

N_1 for the left motorized wheel;

N_2 for the right motorized wheel;

N_f for the front caster;

N_r for the rear caster.

A more detail discussion about the location of the forces and the reaction forces between the rigid bodies is presented in the following sections.

G.4.1 Equations of Motion for the AGV Body

Fig. G.3 presents the AGV body with the 2 casters replaced by reaction forces at their pivot points. A body-centered system xyz is located at the center of mass of the AGV body which is coincident with its geometric center. The y axis of the system is defined along the longitudinal axis of the

vehicle body, and it is also the direction of AGV's travel at the mass center. The z axis is normal to the floor (Fig. G.3), and the x axis is obtained by the right hand rule. V_y is linear velocity along y axis, and Ω_z is the angular velocity about Z axis. The direction of the angular velocity is also defined by the right hand rule.

For a 2 d-o-f rigid body, using equations (G.13), the equations of motion for AGV body are:

$$\left.\begin{aligned} m\,\dot{V}_y &= \sum Y \\ I_z \cdot \dot{\Omega}_z &= \sum N \end{aligned}\right\} \qquad (G.14)$$

Where $\sum Y$ is the total force at the direction of travel of AGV, $\sum M$ is the total moment of the AGV body about the vertical axis z passing through the mass center. m is the mass of the main body of the vehicle with the two motorized wheels (the AGV body), and the I_z is the inertia of it about the z - axis.

G.4.2 Forces Acting on the AGV Body

The forces on the AGV body act on:

- the 2 locations of which casters are pivoted on the AGV body;
- the contact patch between the motorized wheels and the floor.

Since the friction at the bearing is negligible, the reaction forces at caster pivot are transferred from the casters to the AGV body. The reaction forces include the normal reaction between the body and the casters, and the

forces caused by the rolling resistance and the lateral forces at the caster. The normal reaction N'_{fv}, N'_{rv} at front and rear casters respectively, are equal to quarter of the weight of the main body of the vehicle. The reaction of the rolling resistance and lateral forces of the caster are presented in two forces vectors F'_{ix}, F'_{iy} along x and y axis respectively (i=f for front caster, and i=r for rear caster).

At the contact patch of each motorized wheel, two kinds of forces are in action. A tractive force (F_{it}) is generated by the motor. It provides the driving and steering motion. This force acts in the direction of the wheel heading. Resistance force F_{if} and F_{2f} are caused by the friction and the deformation of the wheels at the contact patch. It happens in the opposite direction of the wheel heading (Fig. G.3).

From the external forces described above, the total external forces along the y-axis and the total moment about the z-axis can be obtained as:

$$\left.\begin{aligned} \sum Y &= F_{1t} + F_{2t} - F_{1f} - F_{2f} + F'_{fy} + F'_{ry} \\ \sum M &= (F_{2t} - F_{1t})1 + (F_{1f} - F_{2f})\,1 + (F'_{rx} - F'_{fx})k \end{aligned}\right\} \qquad (G.15)$$

where the 1 is the wheel-span of the vehicle, and k is the wheel-base. Substituting equations (G.14) by (G.15), the equations of motion of the AGV body are obtained as:

$$\left.\begin{aligned} m\cdot\dot{V}_y &= F_{1t} + F_{2t} - F_{1f} - F_{2f} + F'_{fy} + F'_{ry} \\ I_z\cdot\dot{\Omega}_z &= (F_{2t} - F_{1t})l + (F_{1f} - F_{2f})\,l + (F'_{rx} - F'_{fx})k \end{aligned}\right\} \qquad (G.16)$$

G.4.3 Equations of Motion for the Casters

The casters have 3 d-o-f motion: the translation along x and y axis, and the rotation about z axis corresponding to the body-centered system at the AGV body. As shown in Fig. G.4, a caster moves by following the pivot-point (the center of the axle which moves with the AGV body) and a rotation about the pivot-point.

Consider the case of the caster at the front, a system $x_f y_f z_f$ which is parallel to the system at AGV body is located in the center of mass of the front caster ($x_r y_r z_r$ for the rear caster). The center of mass is usually located somewhere between the center of the caster and pivot point. Let Δ be the distance between the origin of the system and the pivot point. Let the linear velocities along x_f and y_f be V_{xf}, V_{yf}, and the angular velocity of the caster about z_f be $\dot{\delta}_f$. The equations of motion of the front caster is derived from equation (G.12):

$$\left.\begin{aligned} \sum X_f &= m_f(\dot{V}_{xf} - \dot{\delta}_f\cdot V_{yf}) \\ \sum Y_f &= m_f(\dot{V}_{yf} + \dot{\delta}_f\cdot V_{xf}) \\ \sum N_f &= I_{zf}\ddot{\delta}_f \end{aligned}\right\} \qquad (G.17)$$

where m_f is the mass of the caster, and I_{zf} is the moment of inertia of the caster about z_f. $\sum X_f$ is the total force along x_f, $\sum Y_f$ is the total force

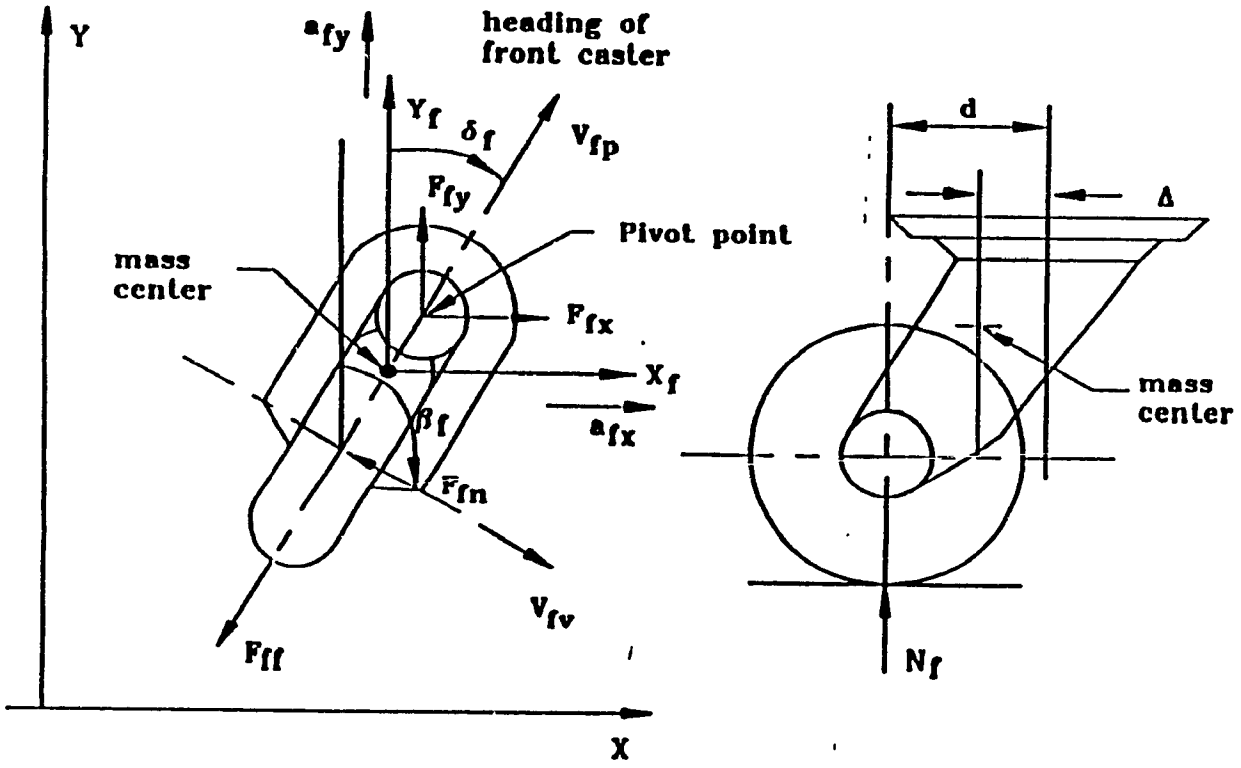

Fig. G.4 Schematic of Body Centered System and External Forces for the Caster

along the y_f, and the $\sum N_f$ is the total moment about the z_f axis.

Similarly at the rear caster, let the linear velocities along x_r and y_r be V_{xr}, V_{yr}, and the angular velocity of the caster about z_r be $\dot{\delta}_r$. The equations of motion of rear caster are:

$$\left.\begin{aligned} \sum X_r &= m_r(\dot{V}_{xr} - \dot{\delta}_r \cdot V_{yr}) \\ \sum Y_r &= m_r(\dot{V}_{yr} + \dot{\delta}_r \cdot V_{xr}) \\ \sum N_r &= I_{zr}\ddot{\delta}_r \end{aligned}\right\} \qquad (G.18)$$

where m_r is the mass of the front caster, and the I_{zr} is the moment of inertia of the front caster about z_r. $\sum X_r$ is the total force along x_r, $\sum Y_r$ is the total force along the y_r, and the $\sum N_r$ is the total moment about the z_r axis.

G.4.4 Forces Acting on the Casters

The forces on the caster act at

- the pivot point which is connected to the AGV body through the pivot axle.
- the contact patch between the caster and floor.

The reaction between the caster and the AGV body at pivot point is in three components and are,

N'_{fv}: the normal reaction from the AGV body to the front caster;

F'_{fx}: the reaction force at x_f direction;

F'_{fy}: the reaction force at y_f direction.

Similarly for the rear caster,

N'_{vr}: the normal reaction from the AGV body to the front caster;

F'_{xr}: the reaction force at x_r direction;

F'_{yr}: the reaction force at y_r direction.

Friction forces act at the contact patch between the caster and the floor. In the case of the front caster, the patch has two degrees of motion at the level plane. The linear velocity at the contact patch is presented by two velocity vectors, V_{fp} is the vector along the direction of the caster heading, and the vector V_{fv} is the vector vertical to it. When the direction of the caster heading is parallel to the velocity of pivot point, V_{fv} is zero, and there will be no lateral friction along this direction. Otherwise friction F_{fn} occurs in the direction against V_{fv} vector. The rolling friction F_{ff} lies in the opposite direction of V_{rp}.

The angle between y_f axis and the caster heading is defined as δ_f, the positive sign of the angle is defined as the clockwise. (Fig. G.4). The angle between the y_f axis and force F_{fn} is presented by β_f, and

$$\beta_f = \delta_f + \pi/2 \tag{G.19}$$

Thus, for the caster:

$$\left.\begin{aligned} \sum X_f &= -F_{ff}\sin(\delta_f) - F'_{fx} + F_{fn}\sin(\beta_f) \\ \sum Y_f &= -F_{ff}\cos(\delta_f) + F_{fn}\cos(\beta_f) - F'_{fy} \\ \sum N_{cf} &= F_{fn}\cdot(d-\Delta) + [F'_{xf}\cos(\delta_f) - F'_{yf}\sin(\delta_f)]\cdot\Delta \end{aligned}\right\} \tag{G.20}$$

Substituting equations (G.20) into (G.17), the equations of motion of front caster are:

$$m_f(\dot{V}_{xf} - \dot{\delta}_f \cdot V_{yf}) = - F_{ff} \sin(\delta_f) - F'_{fx} + F_{fn} \sin(\beta_f) \quad \text{(G.21a)}$$

$$m_f(\dot{V}_{yf} + \dot{\delta}_f \cdot V_{xf}) = - F_{ff} \cos(\delta_f) + F_{fn} \cos(\beta_f) - F'_{fy} \quad \text{(G.21b)}$$

$$I_{fz} \ddot{\delta}_f = F_{fn} \cdot (d - \Delta) + [F'_{xf} \cos(\delta_f) - F'_{yf} \sin(\delta_f)] \cdot \Delta \quad \text{(G.21c)}$$

For the rear caster, the equations of motion can be obtained similarly as:

$$m_r(\dot{V}_{xr} - \dot{\delta}_r \cdot V_{yr}) = - F_{rf} \sin(\delta_r) - F'_{rx} + F_{rn} \sin(\beta_r) \quad \text{(G.22a)}$$

$$m_r(\dot{V}_{yr} + \dot{\delta}_r \cdot V_{xr}) = - F_{rf} \cos(\delta_r) + F_{rn} \cos(\beta_r) - F'_{ry} \quad \text{(G.22b)}$$

$$I_{rz} \ddot{\delta}_r = F_{rn} \cdot (d - \Delta) + [F'_{xr} \cos(\delta_r) - F'_{yr} \sin(\delta_r)] \cdot \Delta \quad \text{(G.22c)}$$

The mass of caster is considered to be negligible in this analysis. $m_f = m_r = 0$. The left hand of (G.21a, b), and (G.22a, b) are all zero. Therefore the reaction forces between these bodies are as follows

$$\left.\begin{aligned} F'_{fx} &= -F_{ff}\sin(\delta_f) + F_{fn}\sin(\beta_f) \\ F'_{fy} &= -F_{ff}\cos(\delta_f) + F_{fn}\cos(\beta_f) \\ F'_{rx} &= -F_{rf}\sin(\delta_r) + F_{rn}\sin(\beta_r) \\ F'_{ry} &= -F_{rf}\cos(\delta_r) + F_{rn}\cos(\beta_r) \end{aligned}\right\} \quad \text{(G.23)}$$

Substitute equations(G.23) into (G.21c)

$$\begin{aligned} I_{fz} \ddot{\delta}_f &= F_{fn}(d - \Delta) + [F'_{xf} \cos(\delta_f) - F'_{yf} \sin(\delta_f)] \cdot \Delta \\ &= F_{fn}(d - \Delta) + [- F_{ff}\sin(\delta_f)\cos(\delta_f) + F_{rn} \sin(\beta_f)\cos(\delta_f) \\ &\quad + F_{ff} \cos(\delta_f)\sin(\delta_f) - F_{rn} \cos(\beta_f)\sin(\delta_f)] \cdot \Delta \end{aligned}$$

Thus

$$I_{fz} \ddot{\delta}_f = F_{fn}(d - \Delta) + F_{rn}[\sin(\beta_f)\cos(\delta_f) - \cos(\beta_f)\sin(\delta_f)] \cdot \Delta \quad \text{(G.24)}$$

Substituting the equation (G.19) into (G.25) becomes

$$I_{fz}\ddot{\delta}_f = F_{fn}(d - \Delta) + F_{rn}[\cos(\delta_f)\cos(\delta_f) + \sin(\delta_f)\sin(\delta_f)]\cdot\Delta$$
$$= F_{fn}(d - \Delta) + F_{fn}\Delta$$

$$I_{fz}\ddot{\delta}_f = F_{fn}\cdot d \qquad \text{(G.25)}$$

Similarly to the rear caster, the equation for the rotation about z_r axis is

$$I_{rz}\ddot{\delta}_r = F_{rn}\cdot d \qquad \text{(G.26)}$$

G.5 Equation of Motion of the AGV

Substituting the reaction forces F'_{fx}, F'_{fy}, F'_{rx}, and F'_{ry} of equations (G.23) into equations (G.16), the motion equations of the AGV main body can be obtained in terms of all the external forces acting on the vehicle.

$$\left.\begin{aligned} m(\dot{V}_y + \Omega_z \cdot V_x) &= F_{1t} + F_{2t} - F_{1f} - F_{2f} - F_{ff}\cos(\delta_f) + \\ &\quad F_{fn}\cos(\beta_f) - F_{rf}\cos(\delta_r) + F_{rn}\cos(\beta_r) \\ I_z\dot{\Omega}_z &= (F_{2t} - F_{1t})\cdot \quad + (F_{1f} - F_{2f})\cdot \quad + (F_{rn}\sin(\beta_r) - \\ &\quad F_{ff}\sin(\delta_r) - F_{fn}\sin(\beta_f) + F_{ff}\sin(\delta_f))\cdot k \end{aligned}\right\} \qquad \text{(G.27)}$$

Where δ_f, δ_r may be determined by the following equations.

$$\left.\begin{aligned} I_{fz}\ddot{\delta}_f &= F_{fn}\cdot d \\ I_{rz}\ddot{\delta}_r &= F_{rn}\cdot d \end{aligned}\right\} \qquad \text{(G.28)}$$

And the angles β_f and β_r are calculated by

$$\left.\begin{aligned} \beta_f &= \delta_f + \pi/2 \\ \beta_r &= \delta_r + \pi/2 \end{aligned}\right\} \qquad \text{(G.29)}$$

For a base reference system which is shown in Fig. G.5, the coordinate of the AGV within it, is presented as

$$\left.\begin{aligned} \overline{X} &= \overline{X}_0 + \int_0^t [V_x\cdot \cos(\theta - 90^\circ) + V_y\cdot \cos(\theta)]dt \\ \overline{Y} &= \overline{Y}_0 + \int_0^t [V_x\cdot \sin(\theta - 90^\circ) + V_x\cdot \sin(\theta)]dt \\ \theta &= \theta_0 + \int_0^t \Omega_z dt \end{aligned}\right\} \qquad \text{(G.30)}$$

G.6 Formulation of External Forces

To generate analytical formulae to those external forces of vehicle may be the most difficult work for the dynamic modeling. As it was mentioned before, many external forces are dependent on the characteristics of wheels and floor. The formulae for these forces varies according to the wheels. All the external forces contributing in the motion equation of CONCIC-2 AGV are in three categories: **tractive forces, lateral forces (cornering force and side-friction), rolling resistance.** The following sections will give a detailed investigation of these three forces.

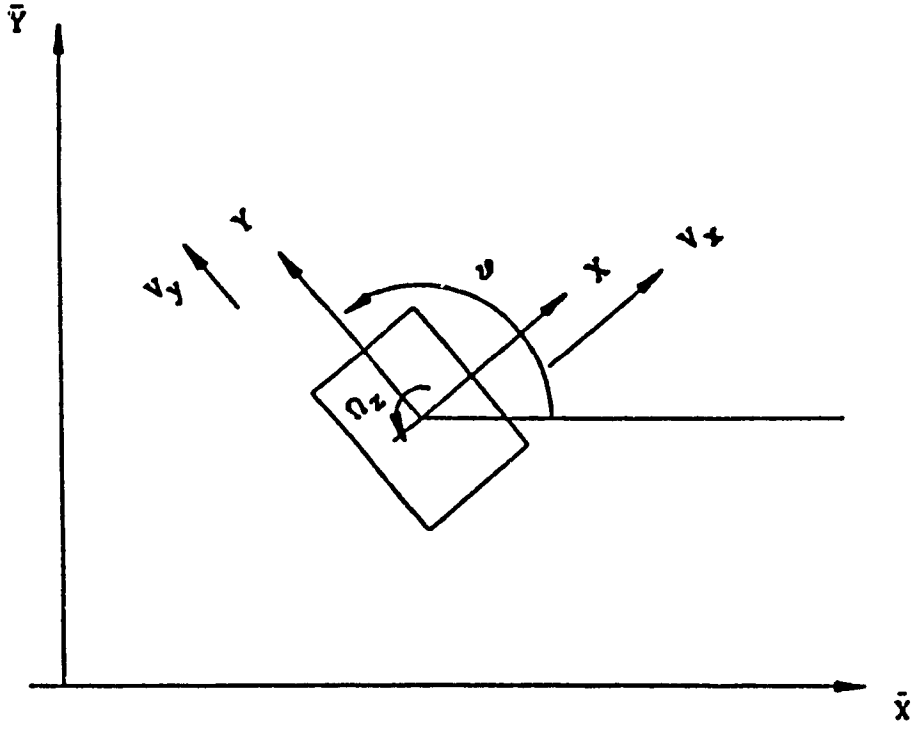

Fig. G.5 Base Coordinate System and Body Centered System of AGV

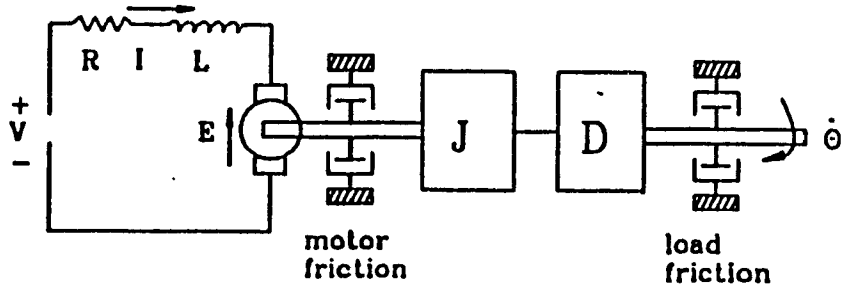

Fig. G.6 Model of Motor and Load System

G.6.1 Tractive force

G.6.1.1 Formulation of tractive force

According to the configuration of differential drive-steering, the whole effort of the motion is provided by the forces between the two driving wheels and the working surface. The tractive force is the force which the motor can provide to the vehicle. And it is the only force which depends on the motor characteristic, but not the characteristics of the wheel and the floor.

The dc motor in the motor-wheel unit is a permanent magnet dc motor. From the torque-current curve of the motor supplied by the manufacturer the torque generated by the motor T_g can be calculated in the following formula:

$$T_g = k_t I \tag{G.31}$$

Where I is the motor current, and k_t is defined as torque constant.

Fig. G.6 gives a motor and load system. Where J is the moment of inertia of motor referred to the motor shaft (with the wheel as the load in the case of CONCIC-2), D is viscous damping factor, T_f is the static friction torque, T_m is the load torque from the motor shaft, and θ is the angular displacement of the motor rotation.

The dynamic equation of this system is written as

$$T_g = J \frac{d^2\theta}{d^2t} + D \frac{d\theta}{dt} + T_f + T_m \tag{G.32}$$

Substituting T_g in equation (G.31) into equation (G.32)

$$T_m = k_t I - J \frac{d^2\theta}{d^2t} - D \frac{d\theta}{dt} T_f \qquad \text{(G.33)}$$

The torque transferred to the wheel from the motor shaft is

$$T_t = nT_m$$

Where, n is gear ratio. And the tractive force at wheel and floor will be

$$\left.\begin{aligned} F_t &= T_t / r_d = \frac{nT_m}{r_d} \\ &= \frac{n}{r_d}(k_t I - J \frac{d^2\theta}{d^2t} - D\frac{d\theta}{dt} - T_f) \end{aligned}\right\} \qquad \text{(G.34)}$$

Where r_d is the radius of the motorized wheel.

G.6.1.2 Tractive forces of CONCIC-2 AGV

For CONCIC-2 AGV, the tractive forces at the left motorized wheel (wheel 1) is obtained from equation (G.34)

$$F_{1t} = \frac{n_1}{r_{1d}} (k_{1t} I_1 - J_1 \frac{d^2\theta_1}{d^2t} - D_1 \frac{d\theta_1}{dt} - T_{1f})$$

Where n_1 is the gear ratio, r_{1d} the radius of the wheel, J_1 the moment of inertia of the motor and wheel about the motor shaft, D_1 is the viscous

damping factor, and the T_{1f} is the friction torque for the left motor-wheel unit.

Similarly for the right wheel (wheel 2), the tractive force is

$$F_{2t} = \frac{n_2}{r_{2d}} \left(k_{2t} I_2 - J_2 \frac{d^2\theta_2}{d^2t} - D_2 \frac{d\theta_2}{dt} - T_{2f}\right)$$

Where n_2, r_{2d}, k_{2t}, J_2, D_2, and T_{2f} are defined as same as above, but for wheel 2.

Since the two motor-wheel units are assumed to have the same characteristics. Let

$$n_1 = n_2 = n;$$
$$r_{1d} = r_{2d} = r_d;$$
$$k_{1t} = k_{2t} = k_t;$$
$$J_1 = J_2 = J;$$
$$T_{1f} = T_{2f} = T_f.$$

Therefore

$$\left.\begin{aligned} F_{1t} &= \frac{n}{r_d} \left(k_t I_1 - J \frac{d^2\theta_1}{d_2^2t} - D \frac{d\theta_1}{dt} - T_f\right) \\ F_{2t} &= \frac{n}{r_d} \left(k_t I_2 - J \frac{d^2\theta_2}{d^2t} - D \frac{d\theta_2}{dt} - T_f\right) \end{aligned}\right\} \quad (G.35)$$

Let V_1 and V_2 be the linear velocity at the contact point of motorized wheel 1 and wheel 2. Then

$$\frac{d\theta_i}{dt} = n \frac{V_i}{r_d} \qquad (i = 1,2) \qquad \text{(G.36)}$$

The accelerations are

$$\frac{d^2 \theta_i}{dt^2} = \frac{ndV_i}{r_d dt} \qquad \text{(G.37)}$$

From the geometry of the vehicle

$$\left.\begin{aligned} V_1 &= V_y - l\,\Omega_z \\ V_2 &= V_y + l\,\Omega_z \end{aligned}\right\} \qquad \text{(G.38)}$$

Where l is the one half the wheel-span of CONCIC-2 AGV. Then

$$\left.\begin{aligned} \frac{d^2\theta_1}{dt^2} &= \frac{n}{r_d}(\dot{V}_y - l\dot{\Omega}_z) \\ \frac{d^2\theta_2}{dt^2} &= \frac{n}{r_d}(\dot{V}_y + l\dot{\Omega}_z) \end{aligned}\right\} \qquad \text{(G.39)}$$

Substituting equations (G.39)and (G.38) into (G.35), the tractive force of are

$$\left.\begin{aligned} F_{1t} &= \frac{n}{r_d}\left[k_t I_1 - \frac{Jn}{r_d}(\dot{V}_y - l\dot{\Omega}_z) - \frac{Dn}{r_d}(V_y - l\Omega_z) - T_f\right] \\ F_{2t} &= \frac{n}{r_d}\left[k_t I_2 - \frac{Jn}{r_d}(\dot{V}_y + l\dot{\Omega}_z) - \frac{Dn}{r_d}(V_y + l\Omega_z) - T_f\right] \end{aligned}\right\} \quad (G.40)$$

G.6.2 Rolling resistance

A perfect solid wheel has a point-contact with the hard floor at any given instant. The contact point has no relative motion with respect to the floor, the wheel eliminates the large friction which would arise if the load were in direct contact with the ground. In practice, however, it is not always the case. The contact of the wheel with the floor is rather a patch than a point because of the deformation at the wheel and the floor. Some resistance to the motion of the wheel exits. This resistance has two distinct causes. It is due

(1) to the fact that the wheel and ground may deform, with the result that the contact between wheel and ground takes place not at a single point, but over a certain patch,

(2) to a combined effect of bearing friction.

The rolling resistance is the friction caused by the second reason.

Rolling resistance is a force highly dependent upon the characteristics of the wheel and the condition of the floor. For a wheel with a rubber or pneumatic tire, the rolling resistance of tires on hard floor is primarily caused by the hysteresis in tire material due to the deflection of the

carcass while rolling. Friction between the tire and the road caused by sliding, the resistance due to air circulating inside the tire in the case of pneumatic tire, and the fan effect of the rotating tire on the outside air also contribute to the rolling resistance of the tire, but they are secondary importance. For a solid wheel on a hard and smooth floor, the rolling resistance is caused by the displacement of the point of instantaneous rolling of the wheel because of the deformation of the wheel and the floor.

The ratio of the rolling resistance and the downward force at the wheel is usually defined as the coefficient of rolling resistance k_r.

$$k_r = \frac{R}{W}$$

The following gives more details for the three different types of wheels on the hard floor.

G.6.2.1 Rolling resistance of CONCIC-2 AGV

The case for CONCIC-2 AGV is that four hard rubber wheels run on a hard, smooth concrete surface. Referring to the discussion above, the coefficients of rolling resistance of the wheels may take the form of

$$k_r = k_1(1 + k_2 V) \qquad \text{(G.44)}$$

The coefficient of rolling resistance of motorized wheels and casters of CONCIC-2 are not available from the manufacturer. For this thesis, these figures are estimated from the knowledge to reduce the deviation between the simulation and experiment results. As a wheel with hard rubber tire, k_1 is

chosen to be the average value as 0.007, and k_2 is taken as 0.01. The value of k_1 and k_2 effects the motor voltage and current of the drive-motor at steady state. Higher k_1 and k_2 required higher current and voltage.

It is assumed that the four wheels of CONCIC-2 AGV have the same characteristics of rolling resistance, thus the formula of rolling resistance of the wheels of CONCIC-2 AGV is

$$F_{1f} = 0.007(1 + 0.01V_1)\cdot N_1 \tag{G.45}$$

And the notations are referred as the definition before.

Substituting V_1 and V_2 of equation (G.38) into equation (G.45), The rolling resistance for the motorized wheels are

$$\left.\begin{aligned} F_{1f} &= k_1(1 + k_2V_y - k_2\cdot\cdot\Omega_z)\cdot N_1 \\ F_{2f} &= k_1(1 + k_2V_y + k_2\cdot\cdot\Omega_z)\cdot N_2 \end{aligned}\right\} \tag{G.46}$$

G.6.3 Lateral force

Lateral force is a force which acts perpendicularly to the wheel plane. It is created when the wheel tends to slip sideways (side-slip) or when the wheel is steered. The lateral force which is caused by the side-slip is also called side-friction, and that caused by the steer-action is usually called the cornering force. Lateral force is caused by friction and deformation at the contact patch between the wheel and the floor. Thus, as in the case of rolling resistance, lateral force also varies with different type of wheels.

G.6.3.1 Side-friction force

When a vehicle negotiates with a relatively high speed or is subjected to other side disturbances, a horizontal force F_n is exerted on the wheels to prevent the vehicle sliding sideways. The force acts at the direction perpendicular to the wheel plane. When F_n is smaller than the active force F_a, the vehicle will slip sideways. This slipping is often experienced in greasy asphalt and smooth concrete at high speed.

The side-friction depends on the downward force on the wheel and the coefficient of friction k_n between the wheel and the floor. It is calculated by the following formula:

$$F_n = k_n \cdot N \tag{G.47}$$

where N is normal reaction at the wheel. The coefficient of friction k_n varies with the material of wheels (or tires), the condition of the floor and the wheel (or tire), and other factors such as the downward load, etc.

The side-friction affects the lateral stability of the vehicle. For example, on a hard, smooth, concrete surface, because of the greater deformation at the contact patch of the pneumatic tire, it provides greater side-friction than solid tires and hard rubber tires, thus the vehicle exhibits more lateral stability. But on soft mud roads, the pressure per square inch on the larger surface of a pneumatic tire in contact with the ground being much smaller, the tire is unable to force the mud from beneath it. It has no *actual* contact with the ground, but floats on a very thin layer

of mud. the coefficient of friction at this case is very small, a sharp turn may cause side slip.

G.6.3.2 Cornering force

The cornering force is caused by the steering action of the wheels. In the case of a solid tire on a hard surface, the cornering force is very small because of the small contact area (point contact). The resistance of the steering action is in the form of a small friction moment, and it is considered to be negligible.

When the plane of a wheel with a pneumatic tire is steered not to be in line with the path of motion, a deformation and displacement of the contact patch occurs which gives a lateral force and a moment which attempt to realign the wheel in the direction of wheel heading. And the front portion of the contact patch is parallel to the direction of motion and eventually slides to the center line of the wheel and at rear portion of the patch. For a small steering angle, the whole contact patch is substantially parallel to the direction of rolling, but as the angle increases that portion moves forward until at an angle of 12° to 15° the whole area is sliding and the lateral force reaches the maximum. It is seen that the lateral force increases from the front to the rear of the contact length for some angles, and the offset of the resultant lateral force produces the aligning torque about the vertical axis. The offset is called the pneumatic trail, and the resultant lateral force is defined as cornering force. The product of cornering force and pneumatic trail determines the aligning torque. The aligning torque helps the steered tire return to the original position after negotiating a turn. At large angles of steer the lateral forces are

progressively limited by the sliding which occurs at the rear part of the contact path.

The relationship between the slip angle and the cornering force of various types of tires under a variety of operation conditions have been investigated quite extensively. It is seen that for slip angle below certain value, such as 4°, the cornering force is approximately proportional to the slip angle. Beyond the angle, the cornering force increases at a lower rate and reaches the maximum value where the tire begins sliding laterally. That angle (as 4° in the example) is defined as **limit-angle** in this thesis. In order to compare the cornering behavior of different tires, a parameter called cornering stiffness C_α is used, which is defined as the derivative of the cornering force F_c with respect to the slip angle α.

$$C_\alpha = \frac{\partial F_c}{\partial \alpha}$$

or

$$F_c \cong C_\alpha \cdot \alpha \qquad 0 < \alpha < \text{limit-angle} \qquad \text{(G.48)}$$

A number of factors affect the cornering behavior of pneumatic tires. The most important are the normal load and the inflation pressure of the tire. The cornering stiffness is obtained through experimental data.

Rubber tires have properties that lies between the solid wheels and the wheels with pneumatic tires. When the tire is made of hard rubber, it behaves like a solid tire with a greater friction. But a softer rubber under relatively more load also exhibits deformation at the contact patch. It has similar characteristics to a pneumatic tire, and the cornering force can be

calculated by the formula (G.48).

G.6.3.3 Lateral Forces of CONCIC-2 AGV

The motorized wheels of CONCIC-2 AGV are located in the lateral center line of the AGV, and the vehicle is steered by varying the velocity of these two wheels. There are no steering action involved in these two driving wheels. The cornering force are therefore zero. Since the model assumed no side-slip at the motorized wheels, side-friction is assumed to balance the centripetal force at any time.

The casters are located in the longitudinal axis of the vehicle. When the velocity vector at the pivot point is not align with the wheel plane of the caster, the pivot point led the caster sideways as well as forward. As the results, a side-friction acts at the contact patch to prevent side-slip. The offset of the caster and the side friction results a torque to force the caster to rotate about the pivot point until its plane is in line with the velocity vector of the pivot point.

The side-friction of the casters can be calculated by using the formula (G.47).

$$F_{ln} = k_n \cdot N_i \qquad \text{(G.49)}$$

The coefficient of friction of the casters is not available from the manufacturer for CONCIC-2, it is chosen as 0.01 though the validation of the model. From the definition of side-friction, the direction of the force is always oppositely to the trend of side-slip and to align the caster to the direction of the velocity vector at the pivot point. The positive direction

of side-friction is defined along the angle β_1, or in other words, the positive direction of F_n is to have the caster rotate clockwise about the pivot point ($\dot{\delta} > 0$). When the angle between the +Y axis and the velocity vector at pivot point is defined as α_1, α_1 is calculated by (G.20) for CONCIC-2.

$$\left.\begin{aligned} \alpha_f &= \arctan\left(\frac{-k\cdot\Omega_z}{V_y}\right) \\ \alpha_r &= \arctan\left(\frac{k\cdot\Omega_z}{V_y}\right) \end{aligned}\right\} \qquad \text{(G.50)}$$

And the difference between the velocity vector of the pivot point and the caster heading is $(\alpha_1 - \delta_1)$. When $(\alpha_1 - \delta_1) > 0$, then F_{1n} acts in the positive direction. Otherwise, F_{1n} acts in the negative direction when $(\alpha_1 - \delta_1) < 0$. In the case of $(\alpha_1 - \delta_1) = 0$, there is no side-friction on the caster since the caster is in line with the velocity vector of the pivot point. Thus the sign of the lateral force is calculated by the following formula:

$$\arctan\left(\frac{-k\cdot\Omega_z}{V_y}\right) - \delta_f \qquad \text{(G.51)}$$

Where k is the wheel-base of the CONCIC-2 vehicle.

Hence the formula of the side-friction of casters of CONCIC-2 AGV is written as

$$\left.\begin{aligned} F_{fn} &= k_n \cdot N_f \cdot \text{sign}[\arctan(\frac{-k\cdot\Omega_z}{V_y})\ (-\delta_f)] \\ F_{rn} &= k_n \cdot N_r \cdot \text{sign}[\arctan(\frac{k\cdot\Omega_z}{V_y})\ (-\delta_r)] \end{aligned}\right\} \quad \text{(G.52)}$$

G.6.4 Equations of Motion of AGV with Formulated Forces

The external forces on the motorized wheels are summarized in the follows:

$$\left.\begin{aligned} F_{1t} &= \frac{n}{r_d}[k_t I_1 - \frac{Jn}{r_d}(\dot{V}_y - l\dot{\Omega}_z) - \frac{Dn}{r_d}(V_y - l\Omega_z) - T_f] \\ F_{2t} &= \frac{n}{r_d}[k_t I_2 - \frac{Jn}{r_d}(\dot{V}_y + l\dot{\Omega}_z) - \frac{Dn}{r_d}(V_y + l\Omega_z) - T_f] \\ F_{1f} &= k_1(1 + k_2 V_y - k_2 \cdot \cdot\Omega_z)\cdot N_1 \\ F_{2f} &= k_1(1 + k_2 V_y + k_2 \cdot \cdot\Omega_z)\cdot N_2 \end{aligned}\right\} \quad \text{(G.53)}$$

Where $k_1 = 0.007$, $k_2 = 0.01$.

Substituting the above equations into equations (G.27), the equations of motion of the AGV body are

$$\left.\begin{aligned}
(m+\frac{2n^2J}{r_d^2})\dot{V}_y &= \frac{nk_t}{r_d}(I_1+I_2) - (\frac{2n^2D}{r_d^2}+2k_1k_2N_d)V_y - 2k_1N_d \\
&\quad - F_{ff}\cos(\delta_f) + F_{fn}\cos(\beta_f) - F_{rf}\cos(\delta_r) + F_{rn}\cos(\beta_r) \\
(I_z+\frac{2n^2l^2}{r_d^2})\dot{\Omega}_z &= \frac{l\cdot n\cdot k_t}{r_d}(I_2-I_1) - (\frac{2n^2D}{r_d^2}+2k_1k_2N_d)l^2\Omega_z \\
&\quad + k\cdot[F_{rn}\sin(\beta_r) - F_{rf}\sin(\delta_r) - F_{fn}\sin(\beta_f) + F_{ff}\sin(\delta_f)]
\end{aligned}\right\} \quad (G.54)$$

The external forces acting on the casters are:

$$\left.\begin{aligned}
F_{fn} &= k_n\cdot N_f\cdot \text{sign}[\arctan(\frac{-k\cdot\Omega_z}{V_y}) - (-\delta_f)] \\
F_{rn} &= k_n\cdot N_r\cdot \text{sign}[\arctan(\frac{-k\cdot\Omega_z}{V_y}) - (-\delta_r)] \\
F_{rf} &= k_1(1+k_2V_{fp})\cdot N_f \\
F_{rf} &= k_1(1+k_2V_{rp})\cdot N_r
\end{aligned}\right\} \quad (G.55)$$

Substituting the above forces into the equations (G.28), the equations of motion of casters are:

$$\left.\begin{aligned}
I_{fz}\ddot{\delta}_f &= k_n\cdot N_f\, d\cdot \text{sign}[\arctan(\frac{-k\cdot\Omega_z}{V_y}) - (-\delta_f)] \\
I_{rz}\ddot{\delta}_r &= k_n\cdot N_r\cdot d\cdot \text{sign}[\arctan(\frac{-k\cdot\Omega_z}{V_y}) - (-\delta_r)]
\end{aligned}\right\} \quad (G.56)$$

Where $k_1 = 0.007$, $k_2 = 0.01$, and $k_n = 0.01$.

The angles β_f and β_r are calculated from

$$\left.\begin{aligned}\beta_f &= \delta_f + 90^\circ \\ \beta_r &= \delta_r + 90^\circ\end{aligned}\right\} \qquad \text{(G.57)}$$